POTENTIALS OF STEM CELL-DERIVED CARDIOMYOCYTES 'FROM DISEASE MODELING TO THERAPEUTIC STRATEGIES'

De Potentie van Pluripotente Stamcel Gedifferentieerde Hartspiercellen
'Van Ziekte Nabootsing tot Therapeutische Toepassingen'

Renée G. C. Maas

Potentials of Stem Cell derived cardiomyocytes. From disease modelling to therapeutic strategies. PhD Thesis with summary in Dutch. Utrecht University.

Cover design: Ridderprint | www.ridderprint.nl
Layout: Ridderprint | www.ridderprint.nl
Print: Ridderprint | www.ridderprint.nl
ISBN: 978-94-6483-793-3

POTENTIALS OF STEM CELL-DERIVED CARDIOMYOCYTES 'FROM DISEASE MODELING TO THERAPEUTIC STRATEGIES'

De Potentie van Pluripotente Stamcel Gedifferentieerde Hartspiercellen
'Van Ziekte Nabootsing tot Therapeutische Toepassingen'

(Met een samenvatting in de Nederlandse taal)

Proefschrift

ter verkrijging van de graad van doctor aan de Universiteit Utrecht op gezag van de rector magnificus, Prof. dr. H.R.B.M. Kummeling, ingevolge het besluit van het college voor promoties in het openbaar te verdedigen op

Woensdag 13 Maart 2024 des middags te 2.15 uur

door

Renée Goverdina Catharina Maas
geboren op 9 februari 1994
te Amersfoort

Promotoren:

Prof. dr. J.P.G. Sluijter
Prof. dr. P.A.F.M. Doevendans

Copromotoren:

Dr. J.W. Buikema
Dr. M. Harakalová

Het onderzoek beschreven in dit proefschrift is uitgevoerd binnen het Universitair medisch centrum Utrecht, het Regenerative Medicine Center te Utrecht, Nederland en aan de Universiteit van Stanford, Californië, Verenigde Staten van Amerika.

Het onderzoek beschreven in dit proefschrift werd (mede) mogelijk gemaakt met financiële steun van de stichting PLN (2018 'Cure PLN', 2019 'Crazy-idea' en 2020 'Crazy idea'), de Leducq grant (CURE-PLaN no.18CVD01), de Nederlandse Hartstichting (Dekker 03-003-2021-T025) en van de Nederlandse Organisatie voor Wetenschappelijk Onderzoek (NWO 2021 'HARVEY-18747-OTP'). De druk van dit proefschrift werd mede mogelijk gemaakt door financiële steun van de Hartstichting en de PLN stichting.

Beoordelingscommissie:

Prof. dr. J.M. Beekman
Prof. dr. A.N. Bovenschen
Prof. dr. P.C.J.J. Passier
Prof. dr. E. van Rooij
Prof. dr. J.P. van Tintelen (voorzitter)

Paranimfen:

Floor van den Dolder
Elana van Rooden-Meijer

Opgedragen aan mijn ouders en grootouders
die mij gezegend hebben met mijn kostbaarste talent;
de gave van nieuwsgierigheid en het verlangen naar een leven vol ontdekkingen.

TABLE OF CONTENTS

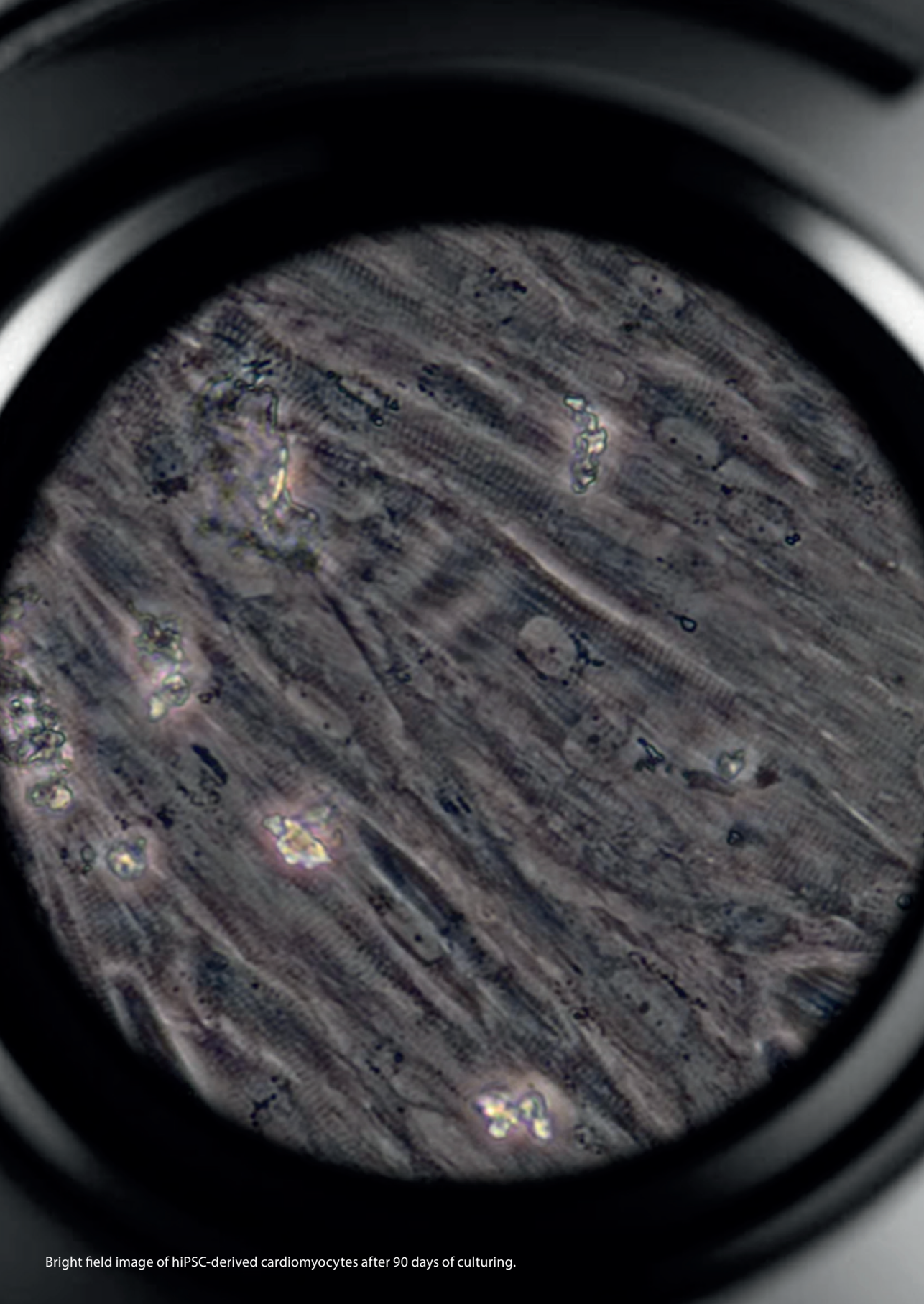

Bright field image of hiPSC-derived cardiomyocytes after 90 days of culturing.

Chapter 1

General Introduction and Thesis Outline

Renée G.C. Maas

GENERAL INTRODUCTION

This chapter describes the scientific content that incited the hypotheses and ideas investigated in this thesis. Firstly, it introduced the clinical significance of a genetic variation in cardiomyopathies, especially the dilated cardiomyopathy and arrhythmogenic cardiomyopathy, caused by a deleterious mutation of the arginine 14 codon in the phospholamban (PLN) gene (p.Arg14del). Secondly, it describes the knowledge derived from cardiogenesis and reproducible methods for the efficient generation of cardiomyocytes (CMs) derived from human induced pluripotent stem cells (hiPSCs). Lastly, it discusses the use of hiPSC-CMs for disease modeling and contemporary challenges encountered in drug research and postulates methodological alternatives.

1.1 Clinical relevance

In the past 30 years, the importance of cardiomyopathies as causes of morbidity and mortality, particularly in sudden cardiac death and heart failure, has been highlighted by the recognition of disease-causing genetic variants.[1] Genetic cardiomyopathies affect families following a Mendelian inheritance pattern with variable phenotype expression. They typically affect young patients and are important causes of sudden cardiac death in individuals who might otherwise be asymptomatic. The individual genetic makeup and environmental circumstances are responsible for a highly variable disease onset and progression. Despite major efforts to improve their condition with lifestyle alterations and medication, the natural course of cardiomyopathies cannot be halted, and gradual progress towards severely impaired cardiac function and death is generally inevitable. Progress has also been made in the management of several types of cardiomyopathies. However, advances in understanding these diseases show that cardiomyopathies represent complex genotypic and phenotypic entities.[2] Therefore, in the past decade, major progress has been made in detecting and, understanding the molecular and genetic basis of disease, pathophysiology, and clinical and radiological assessment of genetic cardiomyopathies.[3,4] These insights can potentially fuel enormous improvements for the early detection and novel therapeutic strategies of the future to prevent the detrimental effects of genetic cardiomyopathies.

1.2 PLN-R14del cardiomyopathy

The major inherited cardiomyopathies, dilated cardiomyopathy (DCM), arrhythmogenic cardiomyopathy (ACM), and hypertrophic cardiomyopathy (HCM), are characterized by arrhythmias and/or cardiac dysfunction often leading to progressive heart failure and sudden cardiac death.[5] In 40-60% of the patients with DCM and HCM, underlying pathogenic variants can be found, mainly located in genes encoding sarcomeric proteins[6,7]. In contrast, ACM is mainly caused in 60% of the patients by pathogenic variants in desmosomal genes.[8] Interestingly, one of the pathogenic mutations in both 10% of the DCM and 15% of

the ACM patients in the Netherlands was caused by a deleterious mutation of the arginine 14 codon in the phospholamban (PLN) gene (p.Arg14del).[9] Since the discovery of this mutation in a Greek family in 2006, thousands of patients have been identified in not only the Netherlands but also the USA, Canada, China, Germany, and Spain.[10–15]

PLN is a 52-amino acid protein located in the sarcoplasmic reticulum (SR) membrane that acts as a crucial reversible regulator of Ca^{2+} uptake in the CM.[16] In contrast to wildtype PLN, a deletion of arginine 14 codon (R14del) in the PLN gene (PLN-R14del) disrupts the conformational changes upon phosphorylation, resulting in inhibition of PLN pentamer formation and thus constitutive inhibition of sarcoplasmic/endoplasmic reticulum Ca^{2+} ATPase2a (SERCA2A/ATP2A2).[12,17] Therefore, PLN-R14del has been associated with irreversible super-inhibition of SERCA2A activity, preventing the influx of calcium into the sarcoplasmic reticulum. This process, in theory, delays the Ca^{2+} reuptake and induces prolonged muscle contraction. The pathophysiological mechanism causes several clinical features, including a dilated and/or arrhythmogenic heart muscle and the presence of cardiac fibrofatty replacement[18] and protein aggregates.[19] Compared to other mutation carriers, patients with a PLN mutation have a higher frequency of left ventricle structural and functional abnormalities, and they show the most pronounced diminished left ventricle function detected by echocardiography and cardiac magnetic resonance imaging (MRI).[20] Moreover, PLN-R14del hearts were compared with hearts with desmosomal, lamin A/C, sarcomeric, and desmin mutations and presented the highest amount of myocardial fibrosis, which is found in a distinct pattern in the posterolateral left ventricular wall.[21] Ultimately, it has been determined that PLN-R14del mutation carriers have a higher incidence of malignant ventricular arrhythmias with left ventricular ejection fraction <45%, premature sudden cardiac death, and end-stage heart failure when compared to DCM patients that do not carry this pathogenic variant.[22]

This mutation presents a highly variable phenotype, ranging from asymptomatic to cardiomyopathic. Its awareness is rather low, therefore, thousands of people can be carriers unknowingly.[20] This caveat is highly relevant because a substantial proportion of individuals who carry disease-causing genetic variants and are at risk of disease complications have incomplete and/or late-onset disease expression. To raise awareness of the mutation phenotype and more efficiently identify carriers and possibly develop new therapies, it is key to better understand the pathological mechanisms underlying this disease. It remains unclear how exactly the PLN-R14del mutation leads to such severe cardiomyopathy and malignant arrhythmias. Unfortunately, despite almost two decades worth of research about PLN-R14del cardiomyopathy, targeted treatment for these patients is lacking. Currently, efforts to identify a tailored therapy are ongoing, using state-of-the-art technology and through synergistic collaborations. With the development in finding therapeutics for this specific cardiovascular disease, bridges will be built toward the utility of these strategies for a plethora of other diseases.

1.3 Lessons learned from cardiogenesis

The important inventions of the microscope, sterile culturing, and defined mediums led to the creation of the first human immortal cell line in 1951.[23] These so-famously called HeLa cells were created by a tissue sample taken from a young woman with cervical cancer and quickly became invaluable to medical research. However, until today, due to the limited regenerative capacity of the heart, no successful passaging of adult human primary CMs nor cardiac stem cell isolation has been possible. This made the culturing of adult human CM models a challenge. For many years, signaling pathways that specify cardiac mesoderm and regulate cardiac proliferation have been extensively studied. Hereafter, wingless-related integration site (Wnt) signaling has proven to be essential in heart development [24] and the balance of Wnt regulation appears to play a critical role in cardiogenesis and, later on, shaping the cardiac fields.[25,26] In adult organisms, Wnt proteins regulate diverse cellular processes such as gene transcription and cell proliferation, migration, polarity, or division.[24] Since the discovery of embryonic stem cells by James Thomson and later, in 2006, the hiPSCs by Shinya Yamanaka have been heralded as major breakthroughs in stem cell research.[27,28] The knowledge derived from the developmental studies has been translated into reproducible methods for the efficient generation of cardiomyocytes (CMs) derived from human induced pluripotent stem cells (hiPSCs). The first attempts to differentiate hiPSCs into CMs about a decade ago resulted in very low numbers of hiPSC-CMs (5-10%), and the re-plating of these cells was a challenge.[29] Hereafter, the combination of monolayer cell culture with defined serum-free media, supplemented with growth factors involved in normal human embryological heart development, like Wnt agonists and antagonists, resulted in much higher efficiency (80–99%).[30,31] Altogether, the improvements over the last 70 years have tremendously improved the generation of stem cell-derived cardiomyocytes as a human cell source for in vitro disease modeling.

1.4 Cardiomyocyte generation and expansion

The discovery of hiPSCs offers unprecedented opportunities to study early human physiology and pathology at a cellular level.[32] Multiple embryonic pathways have been implicated in cardiac differentiation of pluripotent stem cells.[33] Understanding the particular role of the Wnt signaling pathway in heart formation has helped to develop pluripotent stem cell differentiation protocols that produce relatively pure cardiomyocyte populations[34] Currently, various hiPSC- CM differentiation protocols incorporate Wnt signaling activation via glycogen synthase kinase 3 beta (GSK-3β) inhibition (usually with a small molecule) from days 0 to 3. This is followed by Wnt inhibition via porcupine inhibition at days 3-5 to induce highly pure and dense hiPSC-CM cultures (**Figure 1**).[35]

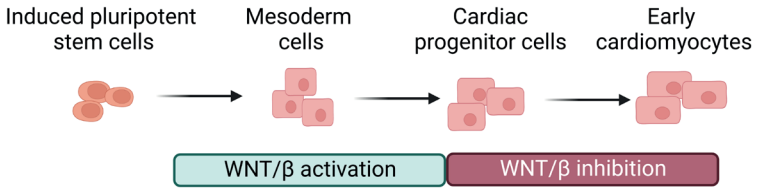

Figure 1. Generation of hIPSC-CMs by modulating the Wnt signaling pathway. Created with BioRender.com

A major limitation, however, remains the batch-to-batch variability of hiPSC-CM efficiency and the inability to robustly expand generally dense-cultured functional hiPSC-CMs for more than 5 fold.[36–39] Recently, we described that concomitant Wnt pathway regulation and removal of cell-cell contact inhibition via low cell density serial passaging resulted in a massive proliferative response of hiPSC-CMs (**Figure 2**).[40,41] The developmental clues and the role of the Wnt signaling pathway resulted not only in the efficient generation of hiPSC-CMs but also in a highly efficient detailed method for the expansion and passaging of functional hiPSC-CMs. However, the lack of maturity of the hiPSC-CMs generated by the described differentiation protocols is an important limitation to overcome for optimal human *in vitro* modeling.

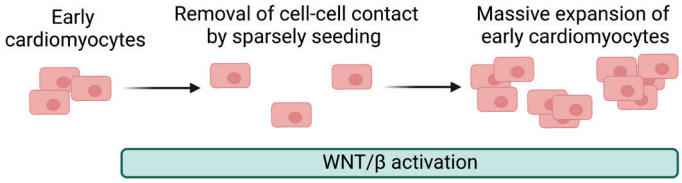

Figure 2. Expansion of hiPSC-CMs by modulating the Wnt signaling pathway. Created with BioRender.com

1.5 Cardiomyocyte maturation

HiPSC-CMs have emerged as a promising experimental tool for translational heart research. In theory, with the cardiac expansion method, hiPSC-CMs can provide an unlimited source of human cardiomyocytes that entail the use of human cardiac tissue or cells with minimal ethical and practical concerns. However, their usability as a human adult CM model is limited by their immature phenotype, represented in general by structural underdevelopment, metabolism based on glucose or lactate instead of fatty acids, slow Ca^{2+} signals, and negative force-frequency relationship that impact the features of electrophysiological parameters.[42–45] Applying hiPSC-CMs for adult cardiomyopathy disease modeling or drug research purposes, the immature status may influence to some extent the observed effects by impacting the excitation-contraction coupling. Therefore, to overcome this limitation,

many strategies have been invented to induce a mature phenotype of hiPSC-CMs. These strategies include 1) biochemical strategies such as; prolonged culture time; alterations in energy sources (**Figure 3**); hormones; cell-cell interactions/co-culturing; genetic manipulation and 2) biophysical strategies including extracellular matrices/substrate stiffness; biophysical stimulation; in vivo maturation; mechanical stretch and 3D cell culture have been described.[46,47] These different maturation methods can improve the modeling of complex adult cardiac physiology and disease.

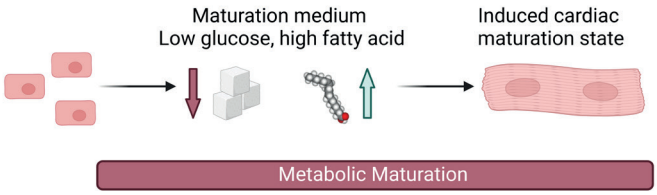

Figure 3. Maturation of hiPSC-CMs by modulating the physiologically appropriate levels of glucose and albumin-bound fatty acids. Created with BioRender.com

1.6 hiPSC-CM models

Next to cardiomyocyte generation, expansion, and maturation developments, the human-induced pluripotent stem cell (hiPSC) technology has yielded patient-derived cardiomyocytes that exhibit some of the hallmarks of cardiovascular disease and are therefore being used to model disease states. Some of the technical challenges were solved, such as the scaled production of pure cardiomyocytes in a quality-controlled way and the long-term cryopreserved hiPSC-CM biobanks. The generated 'more mature' cardiomyocytes have been used to study physiological and disease states, screen for novel therapeutic targets, and generate heart tissue for pharmaceutical testing. However, with the unlimited production of hiPSC-CMs, challenges arise for the scalability, sensitivity, and costs of hiPSC-CM disease modeling and robotic functional screening platforms. Each technique has its strengths, such as scalability or sensitivity, and needs to be considered carefully or combined to develop a full phenotypic screening (**Table 1**). By combining the different hiPSC-CM models, a full phenotypic screening would make it possible to study physiological disease states or to screen pharmaceutical or novel therapeutic compounds.

Table 1: Advantages and disadvantages in human iPSC-derived cardiomyocytes in vitro disease modeling platforms

Model	Advantage	Disadvantages	Format	Costs	Sensitivity	Scalability
EHTs	Sensitivity to cardiotoxins, physiological force, and slow action potential	Hypoxic conditions in center, risk of breaking.	24 wells	High	High	Low
Heart-on-a-chip	Allows ECM manipulation, mimics 3D cardiac environment	Limited imaging possibilities, Nonlinear cell alignment	48 wells	Middle	Middle	Low
Cardiac Spheroids	Recapitulating cell-cell interactions, reproducible, small 3D model	Lack of ECM, Nonlinear cell alignment.	384 wells	Low	Middle	High
Individual CMs	Heterogeneity analyses, Strong proliferation capacity	Far from physiological conditions, loss of cell-cell interactions	384 wells	Low	Low	Middle
2D Monolayers	Action potential and calcium wave propagation measurements, IF	Low on maturity, unable to recapitulate some disease phenotypes	384 wells	Low	Low	High

1.7 High-throughput integrative disease modeling and drug screenings

New therapies for genetic heart diseases have a high attrition rate, with only 1% reaching the stadium of a clinical trial.[48] This low number can partly be explained in part by a reliance on animal models, transformed cell lines, and heterologous recombinant systems for drug discovery. Because of their ease of culture, cell-based assays used in drug screening have historically depended on animal cells. However, these cells are generally short-term cultured and are limited in how well they reflect human biology. Moreover, the use of more physiologically relevant primary cells is restricted by availability and inherent variability. As previously described, the advent of hiPSC technology has opened up the possibility of technology platforms to perform compound screens of hiPSC-derived cardiomyocytes with relatively high throughput. It is essential to realize their potential for drug discovery. To date, hiPSCs have been used to model a growing list of heart diseases, providing proof of concept that their differentiated derivatives can recapitulate disease-associated pathologies. Moreover, in some cases, it has been shown that pathologies expressed by these cell-based disease models can be ameliorated by drugs known to be therapeutic for patients.[30] Based on an evaluation of multiple parameters including gene/mRNA/protein omics, mRNA/protein expression and electro-pathophysiology such as contractility and calcium handling, researchers will now be able to identify compounds that target molecules or pathways known to modulate cardiomyocytes, as well as those not previously associated with cardiomyocyte function

(**Figure 4**). This data will define a subset of chemical probes for interrogating cardiomyocyte phenotyping and provide validation of a platform for high-throughput screening of hiPSC-derived cardiomyocytes.

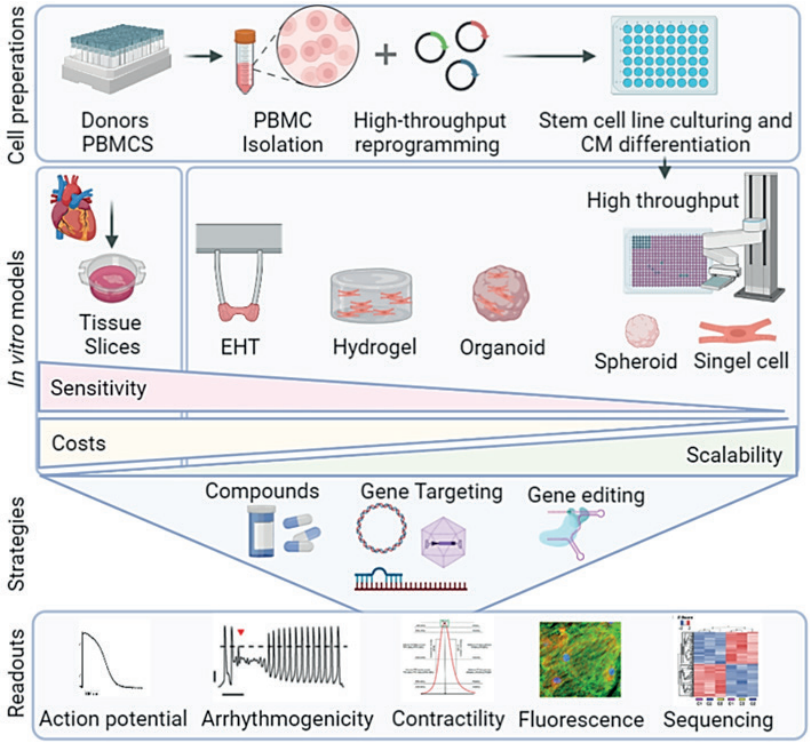

Figure 4. Graphical abstract of patient-derived human cardiomyocyte models for therapeutic screenings and disease modeling *in vitro*.

THESIS OUTLINE

The aim of this thesis is to shed light on the utilization of functional patient-derived human-induced pluripotent stem cell-derived cardiomyocytes (hiPSC-CMs) for disease modeling and high throughput screening of novel therapeutic strategies for genetic cardiomyopathies. This goal is achieved in two ways: firstly, by investigating the developmental clues of cardiogenesis for the generation of hiPSC-CMs, and secondly, by showing that the patient hiPSC-CMs can be conducted with scientifically sound methods using pragmatic in vitro disease models and innovative disease pathway analysis.

PART I: CLUES FROM HEART DEVELOPMENT TOWARDS OPTIMIZED HIPSC-CMS MODELS

In the first part of this thesis, we describe the steps of cardiogenesis and the pathways involved (**Chapter 2**). This leads to the identification of particular mechanisms involved in cardiomyocyte proliferation and the strategies for cardiomyocyte production, which are also presented here. By this rationale, differentiation strategies that have proven to generate hiPSC-CMs effectively may be repurposed for the massive expansion of hiPSC-CMs. We describe that concomitant GSK-3β inhibition and removal of cell-cell contact inhibition via low cell density serial passaging resulted in a massive proliferative response of hiPSC-CMs (**Chapter 3**). With this knowledge, we invented a highly efficient method for the expansion and passaging of functional hiPSC-CMs that can routinely be cryopreserved and subsequently used as a stable cell source for downstream applications (**Chapter 4**). This method is put in a new perspective in **Chapter 5**, in which live imaging in a hiPSC-CM culture system is used to follow the sequence of sarcomere breakdown during the mitotic phases of CM cell division. Again, going one step deeper in understanding and utilizing the mechanism of action, we will describe the magnitude of Wnt activation in hiPSC-CMs, which results in increased efficiency of non-viral vector incorporation. These findings give an insight into the regulation of sarcomere homeostasis during mitotic cell phases and provide a tool for further molecular and engineering studies (**Chapter 5**). However, the expanded hiPSC-CMs physiological immaturity severely limits their utility as a model system and their adoption for drug discovery. Therefore, we avail ourselves of a maturation media designed to provide oxidative substrates adapted to the metabolic needs of hiPSC-CMs. Part I concludes with a model of cardiac ischemic damage in metabolically matured hiPSC-CMs and exemplarily evaluates the cardioprotective effect of the RIP1 kinase inhibitor necrostatin-1 (**Chapter 6**).

PART II: MODELING THE PHOSHOLAMBAN R14DEL MUTATION USING PATIENT-SPECIFIC HIPSC-CMS

In the second part of this thesis, we aim to provide the most complete approach to investigating the molecular mechanism behind the genetic cardiomyopathy caused by the deletion of arginine 14 in the phospholamban gene (PLN-R14del). First, we will use a systematic review describing studies conducted to investigate the PLN-R14del disease (**Chapter 7**). We describe the currently available observational evidence that suggests a possible molecular mechanism and the therapeutic strategies used to improve the disease phenotype. Hereafter, we combined the approach of transcriptional regulation analysis in human primary tissue and validation in a unique long-term (160 days) matured hiPSC-CM model. We demonstrate a dysregulated PPARA-mediated mitochondrial fatty acid oxidation (FAO) signaling in PLN-R14del hearts and hiPSC-CMs. By activating PPARA in PLN-R14del hiPSC-CMs using bezafibrate, we observed an improved mitochondrial structure and calcium handling function, further indicating the importance of FAO in the molecular mechanism behind the PLN-R14del disease (**Chapter 8**). In

Chapter 9, we started by using transcriptomics of hiPSC-CMs and compared the differentially expressed pathways in PLN-R14del vs isogenic control. Here, we found the unfolded protein response as a compensatory mechanism of the PLN-R14del disease. We will show how this mechanism, directly and indirectly, suggests a mechanistic link between protein toxicity and PLN aggregate formation in the PLN-R14del-induced pathophysiology. Furthermore, we explored the therapeutic potential of activating the UPR with a small molecule activator, BiP (**Chapter 9**). In Chapters 8 and 9, we made use of only one severely affected PLN-R14del patient. To study the molecular mechanism of the PLN-R14del of various patients, we generated hiPSC lines derived from six patients carrying the pathogenic PLN-R14del variant and two non-carrier family members. (**Chapter 10**) In order to investigate these hiPSC-CMs of many PLN-R14del patients, we present a scalable, high-throughput screening-compatible workflow for the generation, maintenance, and optical analysis of cardiac spheroids in a 96-well-format (**Chapter 11**). Additionally, these small cardiac spheroids can be cryopreserved, allowing researchers to create next-generation living biobanks. Lastly, we use the spheroid model to study the PLN-R14del disease, screening hiPSC-CMs generated from 6 hiPSC lines. Here, we found the calcium handling parameters such as decay time, rise time, calcium transient duration, and peak value (amplitude) to be reduced in PLN-R14del spheroids derived from three individual patients (**Chapter 12**). Lastly, translating these findings back to clinical care, we will investigate the potential improvement of an AAV-mediated I-1c gene augmentation therapy on the PLN-R14del disease. Findings from the trial should be able to serve as pivotal evidence for therapy potentials and guidelines.

GENERAL DISCUSSION AND SUMMARY

As concluding considerations, we will put all the aforementioned findings into contemporary and future perspective, provide recommendations for future research, and provide an outlook for the future of hiPSC-CMs in disease modeling and therapeutic screening (**Chapter 13**). The thesis ends with a summary of the previous chapters (**Chapter 14**).

Table 2. Overview of the general introduction and related thesis chapters on the specific introduction sections.

Introduction section	Related thesis chapter number
1.1 Clinical relevance	Chapter 7
1.2 PLN-R14del cardiomyopathy	Chapters 7-10 & 12
1.3 Lessons learned from cardiogenesis	Chapter 2
1.4 Cardiomyocyte generation and expansion	Chapters 3-5
1.5 Cardiomyocyte maturation	Chapters 6, 8, 9, 12
1.6 hiPSC-CM models	Chapters 3-6 & 8-12
1.7 High-throughput integrative disease modeling and drug screenings	Chapters 11,12

REFERENCES

1. Towbin, J. A. INHERITED CARDIOMYOPATHIES. Circ. J. 78, 2347 (2014).
2. Robson, A. New insights into the genetics of cardiomyopathies. Nat. Rev. Cardiol. 18, 229–229 (2021).
3. Kaviarasan, V., Mohammed, V. & Veerabathiran, R. Genetic predisposition study of heart failure and its association with cardiomyopathy. The Egyptian Heart Journal 74, 1–17 (2022).
4. Lahoti, N., Jabbour, R. J., Ariff, B. & Wang, B. X. Cardiac MRI in cardiomyopathies. Future Cardiology vol. 18 51–65 Preprint at https://doi.org/10.2217/fca-2020-0233 (2022).
5. Bhuiyan, Z. Review of: 'Penetrance and disease expression of (likely) pathogenic variants associated with inherited cardiomyopathies in the general population'. Preprint at https://doi.org/10.32388/c17hcm (2022).
6. Pugh, T. J. et al. The landscape of genetic variation in dilated cardiomyopathy as surveyed by clinical DNA sequencing. Genetics in Medicine vol. 16 601–608 Preprint at https://doi.org/10.1038/gim.2013.204 (2014).
7. Akhtar, M. & Elliott, P. The genetics of hypertrophic cardiomyopathy. Glob Cardiol Sci Pract 2018, 36 (2018).
8. Groeneweg, J. A. et al. Clinical Presentation, Long-Term Follow-Up, and Outcomes of 1001 Arrhythmogenic Right Ventricular Dysplasia/Cardiomyopathy Patients and Family Members. Circ. Cardiovasc. Genet. 8, 437–446 (2015).
9. van der Zwaag, P. A. et al. Recurrent and founder mutations in the Netherlands-Phospholamban p.Arg14del mutation causes arrhythmogenic cardiomyopathy. Neth. Heart J. 21, (2013).
10. Cheung, C. C. et al. Phospholamban cardiomyopathy: a Canadian perspective on a unique population. Neth. Heart J. 27, 208–213 (2019).
11. DeWitt, M. M., MacLeod, H. M., Soliven, B. & McNally, E. M. Phospholamban R14 deletion results in late-onset, mild, hereditary dilated cardiomyopathy. J. Am. Coll. Cardiol. 48, 1396–1398 (2006).
12. Haghighi, K. et al. A mutation in the human phospholamban gene, deleting arginine 14, results in lethal, hereditary cardiomyopathy. Proc. Natl. Acad. Sci. U. S. A. 103, 1388–1393 (2006).
13. Jiang, X. et al. The phenotypic characteristic observed by cardiac magnetic resonance in a PLN-R14del family. Scientific Reports vol. 10 Preprint at https://doi.org/10.1038/s41598-020-73359-8 (2020).
14. López-Ayala, J. M. et al. Phospholamban p.arg14del Mutation in a Spanish Family With Arrhythmogenic Cardiomyopathy: Evidence for a European Founder Mutation. Revista Española de Cardiología (English Edition) vol. 68 346–349 Preprint at https://doi.org/10.1016/j.rec.2014.11.012 (2015).
15. Posch, M. G. et al. Genetic deletion of arginine 14 in phospholamban causes dilated cardiomyopathy with attenuated electrocardiographic R amplitudes. Heart Rhythm 6, 480–486 (2009).
16. Haghighi, K., Bidwell, P. & Kranias, E. G. Phospholamban Interactome in Cardiac Contractility and Survival: A New Vision of an OLD Friend. J. Mol. Cell. Cardiol. 0, 160 (2014).
17. Vafiadaki, E., Haghighi, K., Arvanitis, D. A., Kranias, E. G. & Sanoudou, D. Aberrant PLN-R14del Protein Interactions Intensify SERCA2a Inhibition, Driving Impaired Ca2+ Handling and Arrhythmogenesis. Int. J. Mol. Sci. 23, (2022).
18. Te Rijdt, W. P. et al. Myocardial fibrosis as an early feature in phospholamban p.Arg14del mutation carriers: phenotypic insights from cardiovascular magnetic resonance imaging. Eur. Heart J. Cardiovasc. Imaging 20, 92–100 (2019).
19. Te Rijdt, W. P. et al. Phospholamban p.Arg14del cardiomyopathy is characterized by phospholamban aggregates, aggresomes, and autophagic degradation. Histopathology 69, 542–550 (2016).
20. Hof, I. E. et al. Prevalence and cardiac phenotype of patients with a phospholamban mutation. Neth. Heart J. 27, 64–69 (2019).
21. Sepehrkhouy, S. et al. Distinct fibrosis pattern in desmosomal and phospholamban mutation carriers in hereditary cardiomyopathies. Heart Rhythm 14, 1024–1032 (2017).
22. Zwaag, P. A. van der et al. Phospholamban R14del mutation in patients diagnosed with dilated cardiomyopathy or arrhythmogenic right ventricular cardiomyopathy: evidence supporting the concept of arrhythmogenic cardiomyopathy. European Journal of Heart Failure vol. 14 1199–1207 Preprint at https://doi.org/10.1093/eurjhf/hfs119 (2012).
23. Vp, P. Cultivation of large cultures of HeLa cells in horse serum. Science 121, (1955).

24. Olson, E. N. & Srivastava, D. Molecular Pathways Controlling Heart Development. Science vol. 272 671–676 Preprint at https://doi.org/10.1126/science.272.5262.671 (1996).

25. Solloway, M. J. & Harvey, R. P. Molecular pathways in myocardial development: a stem cell perspective. Cardiovasc. Res. 58, 264–277 (2003).

26. Ueno, S. et al. Biphasic role for Wnt/beta-catenin signaling in cardiac specification in zebrafish and embryonic stem cells. Proc. Natl. Acad. Sci. U. S. A. 104, 9685–9690 (2007).

27. Thomson, J. A. et al. Isolation of a primate embryonic stem cell line. Proc. Natl. Acad. Sci. U. S. A. 92, (1995).

28. Takahashi, K. & Yamanaka, S. Induction of pluripotent stem cells from mouse embryonic and adult fibroblast cultures by defined factors. Cell 126, (2006).

29. Carvajal-Vergara, X. et al. Patient-specific induced pluripotent stem cell derived models of LEOPARD syndrome. Nature 465, 808 (2010).

30. Lian, X. et al. Directed cardiomyocyte differentiation from human pluripotent stem cells by modulating Wnt/β-catenin signaling under fully defined conditions. Nat. Protoc. 8, (2013).

31. Burridge, P. W., Holmström, A. & Wu, J. C. Chemically Defined Culture and Cardiomyocyte Differentiation of Human Pluripotent Stem Cells. Curr. Protoc. Hum. Genet. 87, 21.3.1 (2015).

32. Musunuru, K. et al. Induced Pluripotent Stem Cells for Cardiovascular Disease Modeling and Precision Medicine: A Scientific Statement From the American Heart Association. Circ Genom Precis Med 11, e000043 (2018).

33. Lee, J. H., Protze, S. I., Laksman, Z., Backx, P. H. & Keller, G. M. Human Pluripotent Stem Cell-Derived Atrial and Ventricular Cardiomyocytes Develop from Distinct Mesoderm Populations. Cell Stem Cell 21, 179–194.e4 (2017).

34. Batalov, I. & Feinberg, A. W. Differentiation of Cardiomyocytes from Human Pluripotent Stem Cells Using Monolayer Culture. Biomarker Insights vol. 10s1 BMI.S20050 Preprint at https://doi.org/10.4137/bmi.s20050 (2015).

35. Pahnke, A. et al. The role of Wnt regulation in heart development, cardiac repair and disease: a tissue engineering perspective. Biochem. Biophys. Res. Commun. 473, 698 (2016).

36. Mills, R. J. et al. Drug Screening in Human PSC-Cardiac Organoids Identifies Pro-proliferative Compounds Acting via the Mevalonate Pathway. Cell Stem Cell 24, 895–907.e6 (2019).

37. Sharma, A. et al. Stage-specific Effects of Bioactive Lipids on Human iPSC Cardiac Differentiation and Cardiomyocyte Proliferation. Sci. Rep. 8, 6618 (2018).

38. Titmarsh, D. M. et al. Induction of Human iPSC-Derived Cardiomyocyte Proliferation Revealed by Combinatorial Screening in High Density Microbioreactor Arrays. Sci. Rep. 6, (2016).

39. Uosaki, H. et al. Identification of chemicals inducing cardiomyocyte proliferation in developmental stage-specific manner with pluripotent stem cells. Circ. Cardiovasc. Genet. 6, (2013).

40. Buikema, J. W. et al. Wnt Activation and Reduced Cell-Cell Contact Synergistically Induce Massive Expansion of Functional Human iPSC-Derived Cardiomyocytes. Cell Stem Cell 27, 50–63.e5 (2020).

41. Maas, R. G. C. et al. Massive expansion and cryopreservation of functional human induced pluripotent stem cell-derived cardiomyocytes. STAR Protoc 2, 100334 (2021).

42. Mummery, C. L. et al. Differentiation of human embryonic stem cells and induced pluripotent stem cells to cardiomyocytes: a methods overview. Circ. Res. 111, (2012).

43. Denning, C. et al. Cardiomyocytes from human pluripotent stem cells: From laboratory curiosity to industrial biomedical platform. Biochim. Biophys. Acta 1863, 1728–1748 (2016).

44. Knight, W. E. et al. Maturation of Pluripotent Stem Cell-Derived Cardiomyocytes Enables Modeling of Human Hypertrophic Cardiomyopathy. Stem Cell Reports 16, 519–533 (2021).

45. Karakikes, I., Ameen, M., Termglinchan, V. & Wu, J. C. Human Induced Pluripotent Stem Cell-Derived Cardiomyocytes: Insights into Molecular, Cellular, and Functional Phenotypes. Circ. Res. 117, 80 (2015).

46. Ahmed, R. E., Anzai, T., Chanthra, N. & Uosaki, H. A Brief Review of Current Maturation Methods for Human Induced Pluripotent Stem Cells-Derived Cardiomyocytes. Front Cell Dev Biol 8, 178 (2020).

47. Tu, C., Chao, B. S. & Wu, J. C. Strategies for Improving the Maturity of Human Induced Pluripotent Stem Cell-Derived Cardiomyocytes. Circ. Res. 123, 512–514 (2018).

48. Wong, C. H., Siah, K. W. & Lo, A. W. Estimation of clinical trial success rates and related parameters. Biostatistics 20, 273 (2019).

PART I

From Heart Development Towards Optimal Cardiac *in Vitro* Models

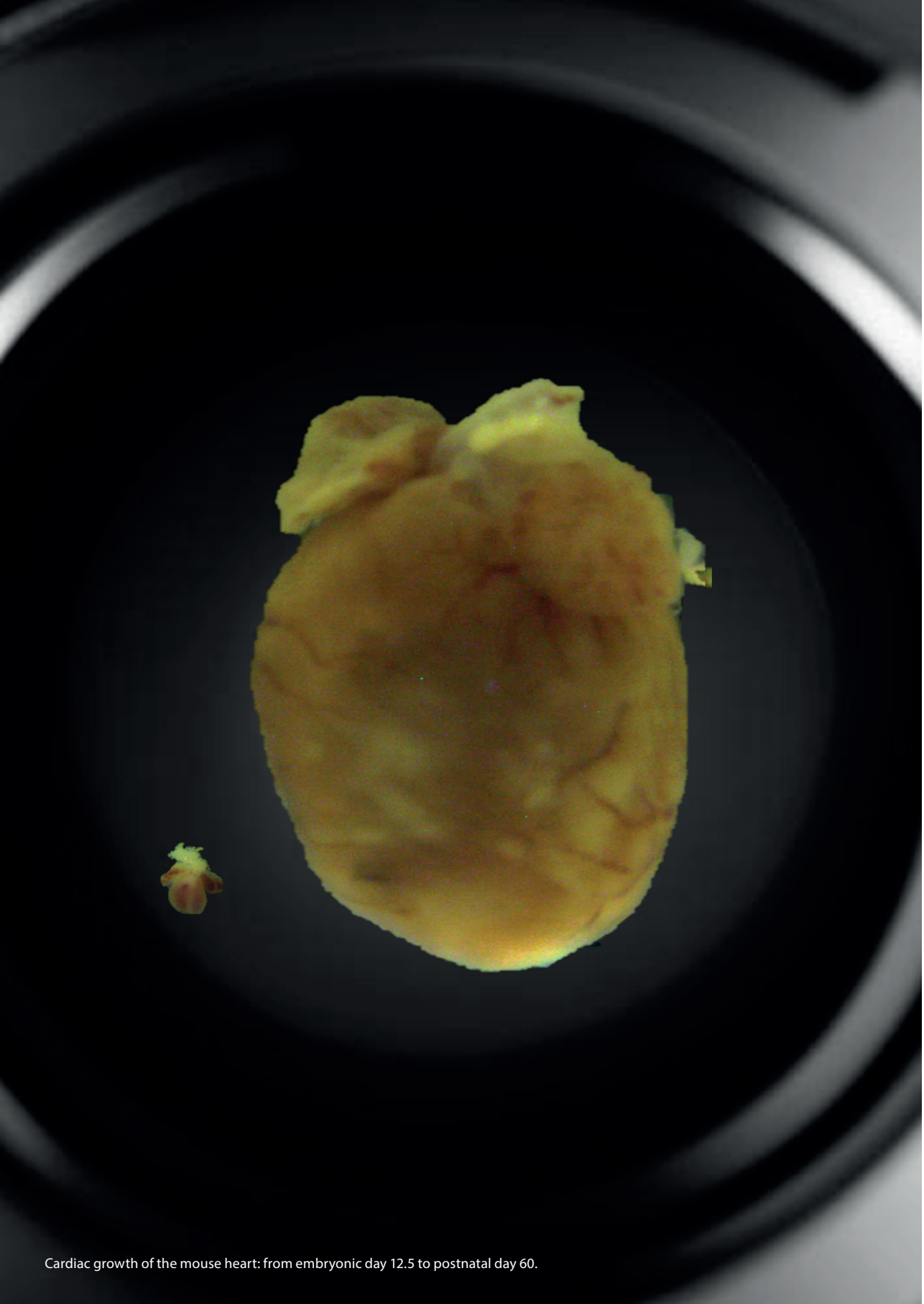

Cardiac growth of the mouse heart: from embryonic day 12.5 to postnatal day 60.

Chapter 2

Harnessing Developmental Cues for Cardiomyocyte Production

Published in: Development, 2023

Renée G.C. Maas, Floor van den Dolder*, Qianliang Yuan*, Jolanda van der Velden, Sean M. Wu, Joost P.G. Sluijter, Jan W. Buikema

*These authors contributed equally.

ABSTRACT

Developmental research has attempted to untangle the exact signals that control heart growth and size, with knockout studies in mice identifying pivotal roles for Wnt and Hippo signaling during embryonic and fetal heart growth. Despite this improved understanding, no clinically relevant therapies are yet available to compensate for the loss of functional adult myocardium and the absence of mature cardiomyocyte renewal that underlies cardiomyopathies of multiple origins. It remains of great interest to understand which mechanisms are responsible for the decline in proliferation in adult hearts and to elucidate new strategies for the stimulation of cardiac regeneration. Multiple signaling pathways have been identified that regulate the proliferation of cardiomyocytes in the embryonic heart and appear to be upregulated in postnatal injured hearts. In this Review, we highlight the interaction of signaling pathways in heart development and discuss how this knowledge has been translated into current technologies for cardiomyocyte production.

INTRODUCTION

Heart failure often results from the irreversible loss of functional myocardium or malfunctioning of the individual cardiomyocytes that comprise this tissue (De Boer et al., 2003; Fox et al., 2001; Gerber et al., 2000). This loss of functional cardiomyocytes can be acute or gradual and results in adverse remodeling of the remaining healthy myocardium (Olivetti et al., 1997; Saraste et al., 1997). In turn, myocardial dysfunction results in mechanical stress and upregulation of factors including angiotensin and norepinephrine, which all act to further promote detrimental myocardial remodeling (Colucci, 1997; Adhyapak, 2022). These alterations to extracellular matrix composition, cytoskeletal architecture and cell-cell connections occur in parallel with changes to the cardiac gene profile, such as reinduction of a fetal gene program (Parker et al., 1990; Bray et al., 2008).

Although clinical therapies for heart failure have significantly improved with multiple lines of heart failure drugs and mechanical circulatory support devices (Cook et al., 2015; Mancini and Burkhoff, 2005; Shen et al., 2022; Ponikowski et al., 2016), these treatments do not repair or replace malfunctioning myocardium. A central hurdle is that the adult heart is a largely postmitotic organ, where annual turnover is between 1-2% in young adults, and less than 0.5% in older adults (Bergmann et al., 2009; 2015). Thus, it is unsurprising that the adult heart lacks regenerative capacity post injury. In contrast, before birth, expansion of fetal cardiomyocytes is crucial for proper cardiogenesis and is tightly regulated by Wnt and Hippo signaling, with varying cardiomyocyte proliferation rates depending on location and developmental stage (Drenckhahn et al., 2008; Sturzu et al., 2015; Buikema et al., 2013; Rochais et al., 2009; von Gise et al., 2012; Qyang et al., 2007).

Remarkably, the early postnatal mammalian heart possesses regenerative potential (Haubner et al., 2016), but this regenerative response is lost 1 week after birth and scar tissue is formed in response to injury instead (Porrello et al., 2011; Ye et al., 2018; Zhu et al., 2018b). Translational cardiology aims to repair or replace a broken heart with autologous material (Laflamme and Murry, 2011; Ptaszek et al., 2012). The advent of patient-specific pluripotent stem cell sources represented a major advance for the field (Burridge et al., 2012), but the generation of large numbers of functional cardiomyocytes remains challenging due to their low proliferative rates (Tani et al., 2022). Here, we review how lessons from in vivo cardiomyocyte proliferation during mammalian cardiac development have been translated into technology to generate cardiomyocytes from human pluripotent stem cell sources.

LESSONS FROM CARDIAC DEVELOPMENT

Mesoderm formation

During development, most heart structures arise from the mesodermal germ layer. Mesoderm formation takes place at Carnegie stages (CS) 6-7 in humans and embryonic day (E) 6.5 in

mice, at the onset of gastrulation (Zhai et al., 2022). During gastrulation, cells from the blastocyst migrate to give rise to the endoderm and mesoderm. At the end of gastrulation, the three germ layers (endoderm, mesoderm and ectoderm) are specified. At the onset of mesoderm formation, the intraembryonic mesoderm subdivides into four distinct groups: the chordamesoderm, paraxial mesoderm, intermediate mesoderm and lateral plate mesoderm (Ivanovitch et al., 2021; Chan et al., 2013). Cardiopotent cells, also called cardiac progenitor cells, are derived from the lateral plate mesoderm during early gastrulation (Yamada and Takakuwa, 2012; Moretti et al., 2006; Garry and Olson, 2006). Cardiac progenitors are prepatterned within the primitive streak, with the atrial and ventricular cells arising at different anterior-posterior positions (Chan et al., 2013). Foxa2+ cardiac progenitors give rise primarily to the cardiovascular cells of the ventricles and are the first cardiogenic cells that migrate to the anterior side of the embryo (Bardot et al., 2017). These cells comprise approximately half of the cardiomyocyte population (Bardot et al., 2017). The right ventricle and outflow tract progenitors are found in anterior/distal primitive streak, where cells are exposed to a higher ratio of activin A to bone morphogenetic protein 4 (BMP4) signaling, whereas atrial progenitors are specified in the proximal primitive streak, where the activin A to BMP4 ratio is low (Ivanovitch et al., 2021).

Brachyury (T) gene expression is also required for the formation of posterior mesoderm in mice and zebrafish (Schulte-Merker and Smith, 1995; Herrmann et al., 1990). Basic fibroblast growth factor (FGF) and Activin A can promote the expression of the T homolog, Xbra, in the Xenopus presumptive ectoderm (Smith et al., 1991). T-box transcription factors and T are intrinsic factors that are crucial for the initiation of mesoderm differentiation and patterning of the primitive streak and are regulated by the Wnt signaling pathway from the adjacent embryonic midline and posterior regions of the embryo, indicating the importance of Wnt signaling at this stage of development (Yamaguchi et al., 1999).

Cardiac specification

Several transcription factors for cardiac development have been identified (Olson, 2006). These include MESP1, which specifies the cardiac mesodermal population and is expressed in the primitive streak around CS6-7 or E6.5. In MESP1-null embryos, severe cardiac abnormalities are observed, leading to cardiac lethality by E10.5 (Saga et al., 1999). Furthermore, in a double knockout of MESP1 and its homolog MESP2, mesoderm progenitors do not contribute to heart development, indicating that MESP1/2 expression is essential for cardiac mesoderm formation (Kitajima et al., 2000).

By CS8 or E7.5, specific regions of the mesoderm differentiate to form cardiovascular progenitor cells, which can be divided into cells that form the first heart field (FHF) and cells that form the second heart field (SHF) (Paige et al., 2015). When Wnt inhibitors such as dickkopf 1 (DKK1) or crescent are administered to posterior lateral plate mesoderm, heart

muscle development is induced and erythropoiesis is suppressed (Marvin et al., 2001, Naito et al., 2006). Meanwhile, ectopic expression of WNT8 or WNT3a in precardiac mesoderm inhibits heart muscle formation and promotes erythropoiesis (Marvin et al., 2001). In mouse embryonic stem cells, Wnt/β-catenin signaling acts biphasically; early treatment with Wnt3a stimulates mesoderm induction and cardiac differentiation, whereas late activation of β-catenin signaling impairs cardiac differentiation (Ueno et al., 2007). In combination with BMP and FGF, Wnt inhibition results in the activation of key upstream cardiac transcriptional regulatory genes NKX2-5, GATA4 and TBX5, which are required for the initiation of cardiac-like gene expression (Kelly et al., 2014).

The formation of the linear heart tube is mostly initiated by the contribution of the FHF, which eventually gives rise to the inflow tract and the majority of the left ventricle (Brade et al., 2013). FHF progenitors at this stage specifically express TBX5 and HCN4 (Später et al., 2013; Bruneau et al., 1999). The SHF develops slightly later and is less differentiated, providing cardiac progenitors that proliferate to promote the expansion of the heart tube (Kelly, 2012). The right ventricle and outflow tract are exclusively generated by the SHF (Buckingham et al., 2005). These SHF cardiomyocytes are marked with TBX1, ISL1 and HAND2 (Moretti et al., 2006; Stanley et al., 2002).

Together, these studies demonstrate that Wnt signals in different parts of the mesoderm are repressed as required for cardiac specification of these regions. Most in vitro protocols for directed cardiac differentiation of pluripotent stem cells incorporate this inhibition of Wnt signaling through the application of porcupine small-molecule inhibitors including IWP-2, IWR1 and Wnt-C59 (Lian et al., 2012; Burridge et al., 2014).

Developmental heart growth

Organ size regulation is an important aspect of cardiac development. The heart must grow large enough to generate sufficient cardiac output, and regional under- or overgrowth may result in septal wall defects, hypoplastic ventricle(s) or obstruction of the outflow tract(s) (Heallen et al., 2011). Heart growth during development is regulated by a combination of cardiomyocyte differentiation, proliferation and hypertrophy.

The human heart undergoes a dramatic proliferation period from CS9-CS16, resulting in a 600-fold increase in heart volume in just 3 weeks (de Bakker et al., 2016). First, the cardiac crescent fuses at the midline and gives rise to the FHF-derived linear heart tube, which subsequently commences beating and undergoes looping. Hereafter, the linear heart tube expands by drastic proliferation and recruitment of SHF cardiac progenitor cells that migrate from the pericardial cavity to the dorsal and caudal heart tube regions while undergoing differentiation (Kelly et al., 2014). Their rapid proliferation is regulated by canonical Wnt signaling (Günthel et al., 2018; Kwon et al., 2007). Upon the presence of the receptor-bound ligands WNT5A and WNT11, active β-catenin enters the nucleus, where it acts as a transcriptional co-activator of

the T-cell factor (TCF) and leukemia enhancer factor (LEF) transcription factors to activate Wnt target genes involved in cell proliferation such as axin 2 (AXIN2), cyclin D1 (CCND1) and lymphoid enhancer binding factor 1 (LEF1) (Cadigan and Waterman, 2012; Stamos and Weis, 2013) (**Figure 1**). Conversely, in the absence of Wnt ligands, a complex containing adenomatous polyposis coli (APC), casein kinase 1 (Ck1) and glycogen synthase kinase-3β (GSK-3β) mediates phosphorylation, ubiquitylation and, ultimately, degradation of β-catenin (Cadigan and Waterman, 2012; Stamos and Weis, 2013) (**Figure 1**). Conditional knockout studies for β-catenin in the SHF produce outflow tract abnormalities and impaired right ventricular development (Qyang et al., 2007; Lin et al., 2007).

After specification and terminal differentiation of cardiac progenitors into cardiomyocytes, the developing heart predominantly increases its size and mass via the proliferation of differentiated cardiomyocytes (Günthel et al., 2018) (**Table 1**). In mice, between E8.0 and E11.0, cardiomyocyte numbers increase 100-fold from 700 to 70,000 (De Boer et al., 2012) (**Figure 2A,C**). During this massive growth phase, the size of the individual cardiomyocytes remains relatively constant. After E11.0, proliferation continues but at a slower rate, with cardiomyocyte numbers approaching 1,000,000 by E18.5 (de Boer et al., 2012). The ballooning ventricles exhibit the highest proliferation rates during this period (Moorman and Christoffels, 2003; Moorman et al., 2010). By contrast, the atrioventricular canal, outflow tract and inner curvature regions have lower proliferation rates and thereby preserve the slow contraction characteristics of the heart tube (De Jong et al., 1992).

Proliferation rates may also vary within the same region depending on the developmental stage. Within the ventricles, proliferation rates are low during the formation of the trabecular network (Sedmera and Thompson, 2011). The trabeculae contribute to cardiac contractility, channel expression and energy metabolism, and start to develop at the luminal side of the myocardium by E9.5 or CS12 (Meyer et al., 2020; Günthel et al., 2018). Later in development, from CS12 until CS16, proliferation rates increase and the compacted ventricular chamber myocardium shows high expression of proliferative markers such as Ki67 and pHH3 (Buikema et al., 2013; Ye et al., 2015; Lin et al., 2015). These changes to ventricular proliferation rates are due to Wnt signaling. Canonical Wnt signaling is downregulated in the trabecular myocardium, which is consistent with the lower proliferation rates observed here (Buikema et al., 2013; Ye et al., 2015). By contrast, conditional knockout studies in mice have shown that epidermal growth factor receptor (EGFR) and Notch signaling are essential for trabecular development (Gassmann et al., 1995; Grego-Bessa et al., 2007). When proliferation rates in the ventricle increase, Wnt/β-catenin is essential for the exponential growth of the compacted ventricular myocardium; the increase in cardiomyocyte proliferation rates as you move from the inner trabeculae to outer compact myocardium corresponds with the graded activity of canonical Wnt signaling (Buikema et al., 2013; Ye et al., 2015). Consistent with this, β-catenin is mainly active in the compact myocardium, where it is expressed by the majority of proliferating cardiomyocytes (Buikema et al., 2013).

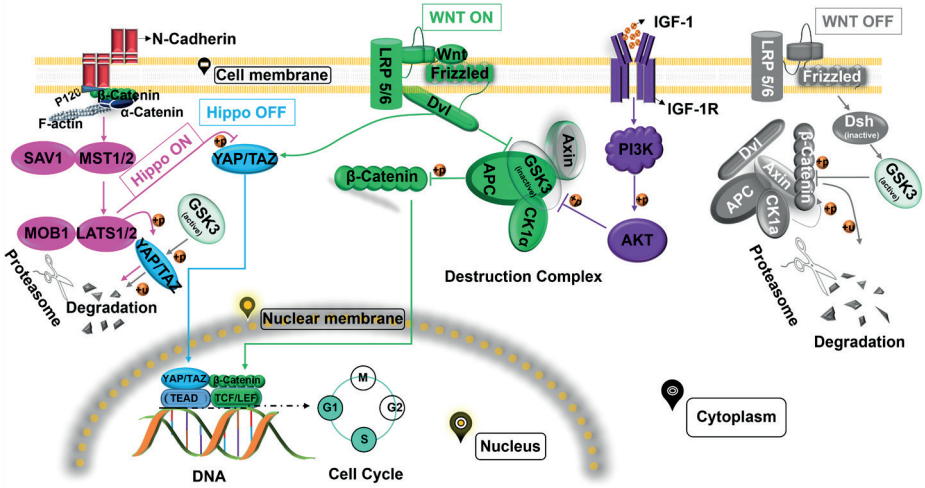

Figure 1. There is interplay between Wnt, Hippo and insulin signaling during cardiomyocyte proliferation. Activation of the Hippo, canonical Wnt or IGF1/PI3K/AKT signaling pathways causes YAP/TAZ and β-catenin to enter the nucleus and cluster with their DNA-binding partners TEAD and TCF/LEF, which activates transcription of target genes and induces cell cycle activation. Conversely, when Dsh is inactivated due to lack of Wnt proteins, activated GSK-3β can phosphorylate β-catenin or YAP/TAZ, ultimately resulting in their degradation by the proteasome. Hippo signaling induced by, for example, N-cadherin junction-mediated cell-cell contact leads to the degradation of the YAP/TAZ complex through the MST1/2-SAV1-LATS1/2-MOB1-YAP/TAZ cascade. IGF1/PI3K/AKT signaling can facilitate the entry of β-catenin into the nucleus via AKT kinase, which phosphorylates GSK-3β to inhibit its activation. AKT, RACα serine/threonine-protein kinase; APC, adenomatous polyposis coli protein; CK1α, casein kinase 1α; Dsh, disheveled; GSK-3β, glycogen synthase kinase-3; IGF1, insulin-like growth factor 1; IGF1R, IGF1 receptor; LATS1/2, large tumor suppressor homologue 1/2; LRP5/6, low-densitylipoprotein-related protein 5/6; MOB1, MOB kinase activator 1; MST1/2, mammalian STE20-like protein kinase 1/2; PI3 K, phosphoinositide 3-kinase; SAV1, protein Salvador homologue 1; TAZ, transcriptional coactivator with PDZ-binding motif; TCF/LEF, T-cell factor/lymphoid enhancer-binding factor; TEAD, TEA domain transcription factor family members; YAP, yes-associated protein; +p, phosphorylation; +u, ubiquitination.

After CS16 and E12.5, cardiomyocyte proliferation rates decline further to maintain normal heart and embryo size ratios until birth. Postnatal heart growth is regulated via cellular hypertrophy (Günthel, Barnett, and Christoffels, 2018) (**Figure 2 B,C**). The insulin-like growth factor (IGF)/Akt pathway appears to promote physiological (and pathogenic) hypertrophy by activation of the ERK/MAPK and the phosphoinositide 3-kinase (PI3K)/Akt pathways in postnatal cardiomyocytes (DeBosch et al., 2006; Liu et al., 1996; Li et al., 2011).

Table 1: Signaling pathways and regulators in heart development.

	Early embryonic development	Intermediate embryonic development	Late embryonic development	Early postnatal stages	Adolescence	Adulthood
Event(s)	Cardiac looping, EMT, proliferation	Cardiac expansion, chamber formation	Septation, valvulation, conduction system formation	Maturation, mitochondrial fatty acid oxidation	Bi-nucleation of cardiomyocytes	Hypotrophy
Pathways involved during heart development	Hippo, Notch, BMP, SMAD, TGF, FGF, Wnt, EGFR1	Hippo, Wnt, Notch, BMP, FGF, IGF, RA	TNFα, NF-κB, IL6, Notch/ HEY2	T3, cTnI, VHL/ HIF1, FAO, PGC1α	PPARA, Esrra, Mef2, Myod, SIRT1, E2f/Rb	T3, insulin, HOPX, VEGFB, IGF1, AMPK
Mouse development						
Developmental Stage	E9.5	E12.5	E18.5	P2	P13	P60
Heart size (mm)	0.2	0.8	1.1	1.8	5	8
Number of CMs	<10.000 (Alkass, 2015)	~70,000 (Alkass, 2015)	~1,000,000 (Alkass, 2015)	~1,700,000 (Alkass, 2015)	~2,500,000 (Alkass, 2015)	~2,500,000 (Alkass, 2015)
Proliferation (% ki67+)	N/A	45 (Lin, 2007)	N/A	28-37 (Alkass, 2015, Huang, 2018)	5 (Alkass, 2015)	0.01-1 (Castellan, 2020, Huang, 2018)
Proliferation (% PH3+)	N/A	2 (Lin, 2007)	N/A	10 (Gan, 2015)	2 (Gan, 2015)	N/A
Human development						
Developmental stage	CS3-4	CS4	CS6-7	1 month	20 years	>40 years
Heart size (mm)	0.003 (Günthel, 2018)	2 (Günthel, 2018)	10 (Dhanantwari, 2009)	~40 (Faber, 2021)	~110 (Mohammadi, 2016)	~120 (Mohammadi 2016)
Number of CMs	N/A	N/A	N/A	90,000,000 (Mollova, 2013)	3,200,000,000-3,700,000,000 (Bergmann, 2015, Mollova, 2013)	3,200,000,000 (Bergmann, 2015)
Proliferation (% ki67+)	N/A	N/A	N/A	0.5 (Ye, 2016)	0.04 (Mollova, 2013)	0.001 (Mollova, 2013)
Proliferation (% PH3+)	N/A	N/A	N/A	0.01 (Mollova, 2013)	0.005 (Mollova, 2013)	0 (Mollova, 2013)

MPK, AMP-activated protein kinase; BMP, bone morphogenetic protein; CS, Carnegie stage; cTnI, cardiac troponin I; E, embryonic day; EMT, epithelial-to-mesenchymal transition; EGFR1, epidermal growth factor receptor 1; Esrra, estrogen-related receptor alpha; FAO, fatty acid oxidation; FGF, fibroblast growth factor; HEY2, Hes related family BHLH transcription factor with YRPW motif 2; HOPX, homeodomain-only protein homeobox; IGF, insulin-like growth factor; IL6, interleukin 6; Mef2, MADS box transcription enhancer factor 2; Myod, myoblast determination protein 1; NF-κB, nuclear factor kappa-light-chain-enhancer of activated B cells; P, postnatal day; PGC1α, PPARγ coactivator 1 α; pHH3, phosphohistone H3; PPARA, peroxisome proliferator-activated receptor; RA, retinoic acid; Rb, retinoblastoma; SIRT1, sirtuin 1; SMAD, mothers against decapentaplegic; T3, thyroid hormone; TGF, transforming growth factor; TNFα, tumor necrosis factor α; VEGFB, vascular endothelial growth factor; VHL/HIF1, von Hippel-Lindau tumor suppressor protein/hypoxia-inducible factor-1.

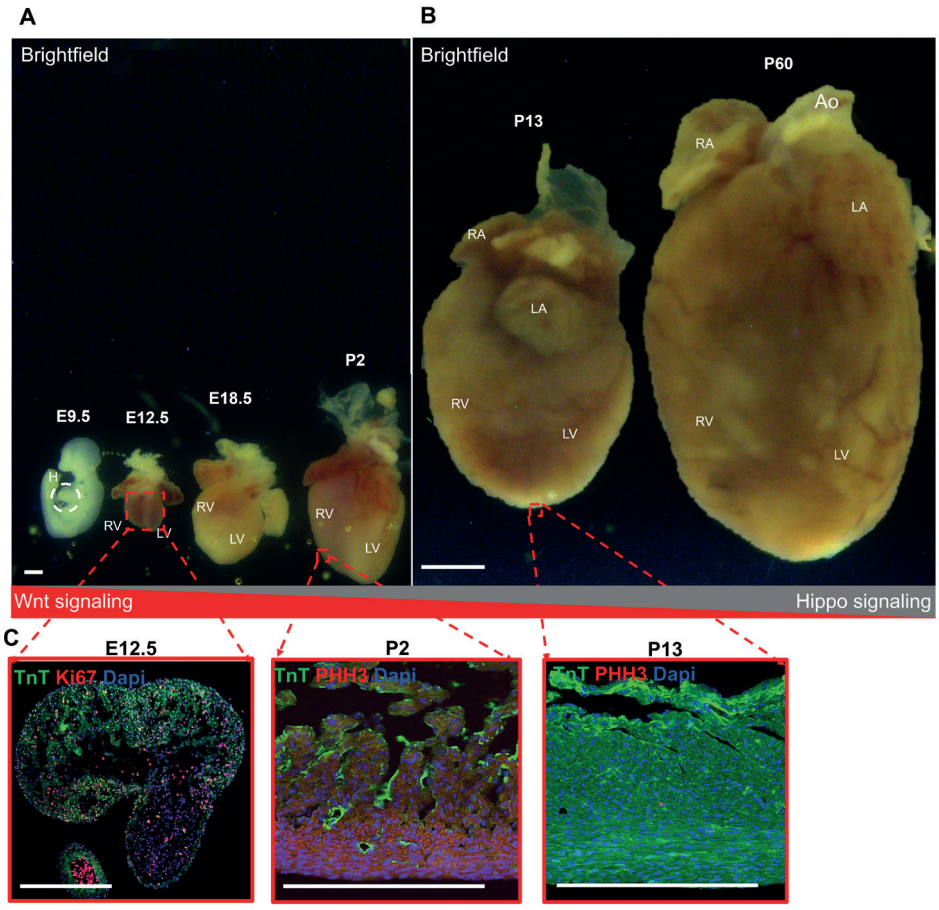

Figure 2. Heart size at selected stages of normal cardiac development. (A) Brightfield images capturing murine hyperplasia over embryonic day (E)9.5 (whole embryo; dashed white lines indicate the location of the heart), E12.5, E18.5 and postnatal day (P)2. (B) Brightfield images capturing murine hypertrophy from P13 to P60. (C) Immunofluorescent images showing pHH3+ cells in E12.5 and Ki67+ in LV cells of P2 and P13 hearts. pHH3 and Ki67 are proliferation markers and TnT is a cardiomyocyte marker. Ao, aorta; H, heart; LA, left atrium; LV, left ventricle; RA, right atrium; RV, right ventricle; TnT, troponin T; pHH3, phosphohistone H3. Figure is adapted from Buikema et al. (2013, 2020) and is available to view on Figshare alongside detailed Materials and Methods: 10.6084/m9.figshare.23607306. Scale bars: ~1 mm (A,C); 5 mm (B).

Interplay between Wnt, Hippo and IGF signaling during cardiomyocyte expansion

The major regulator of cardiac size is the Hippo pathway. This pathway regulates growth and progenitor genes such as SOX2, SNAI2, CCND1, CDC20 and MYCL in cardiomyocytes via the MST1/2-SAV1-LATS1/2-MOB1-YAP/TAZ cascade (Heallen et al., 2011) (**Figure 1**). YAP, a central protein within the Hippo signaling pathway, is activated at CS10 (Singh et al., 2016). Genetic inhibition of Hippo signaling in the embryonic heart leads to a lack of organ

size control and lethal cardiomegaly shortly after birth (von Gise et al., 2012). For example, mouse models harboring various embryonic deletions of the Hippo pathway members SAV1, MST1/2 and LATS2 display overgrown hearts and thickened ventricles owing to an excess of cardiomyocytes (Del Re, 2014). Downstream analysis in Hippo mutant hearts revealed that a lack of downregulation of canonical Wnt target genes and cell cycle regulators could explain the observed hyperplasia and cardiomegaly (Heallen et al., 2011). By contrast, upregulation of Hippo signaling leads to a downregulation of YAP and Wnt/β-catenin signaling to restrain heart size (Kim et al., 2017). Cardiac-specific deletion of YAP also impedes neonatal heart regeneration, resulting in a fibrotic response that generates scar tissue (Xin et al., 2013).

Cytoplasmic YAP/TAZ can also increase cytosolic retention of β-catenin, and thereby negatively regulate the Wnt/β-catenin signaling pathway (Imajo et al., 2012). Chromatin immunoprecipitation sequencing (ChIP-seq) indicated that YAP/TAZ and β-catenin form a common regulatory complex at the SOX2 and SNAI2 gene loci (Heallen et al., 2011). Activating YAP also leads to upregulation of the IGF/Akt pathway, resulting in the inhibition of GSK-3β, stabilization of β-catenin and transcription of Wnt target genes to enhance cardiomyocyte proliferation (Xin et al., 2011) (**Figure 1**). During development, IGF signaling directs cardiomyocyte proliferation between E9.5 and E12.5, and IGF knockout mice exhibit decreased ventricular proliferation (Li et al., 2011). Interestingly, knockout of IGF is non-lethal and by E14.5 the ventricular wall size is comparable with that of wild-type mice (Li et al., 2011; Díaz Del Moral et al., 2021).

The Wnt/β-catenin, IGF/Akt and Hippo/YAP pathways form a complex signaling network that regulates the balance between proliferation, differentiation and maturation of cardiomyocytes (**Figure 1**). It has generally been concluded that high Wnt, high IGF and low Hippo signaling results in proliferative growth of embryonic cardiomyocytes, whereas high Hippo signaling overrules Wnt and IGF to restrain cardiomyocyte proliferation and prevent cardiomegaly.

Cardiomyocyte cell biology in vitro

Developmental shortcuts for human pluripotent stem cell-derived cardiomyocyte differentiation

Cardiomyocytes derived from pluripotent stem cells represent a promising source of cells for disease modeling, drug screens and/or cardiac regenerative medicine (Madonna et al., 2019). The untangling of cues that drive cardiac development has identified growth factors, transcriptional regulators and signaling cascades that can promote the differentiation of cardiac cells from human embryonic stem cells (hESCs). Initial protocols for embryonic stem cell differentiation required formation of embryoid bodies to generate various cell types (Rungarunlert et al., 2009), and downstream applications for cardiac cell biology were limited due to extremely low percentages of cardiomyocyte yield (Osafune et al., 2008). Previously, co-culture of hESCs with visceral endoderm-like cells induced cardiomyocyte differentiation, producing beating

areas in ~35% of the culture surface (Mummery et al., 2003). Due to the addition of insulin and serum, however, only 2-3% of the cells were cardiomyocytes. The number of beating colonies increased 10-fold with the administration of serum- and insulin-free media, whereafter each beating colony contained ~25% cardiomyocytes. Moreover, in situ hybridization demonstrated that the streak ectoderm displays the highest level of mRNA for both Wnt3a and Wnt8c (Marvin et al., 2001). In retrospect, the expression of Wnt inhibitors in the ectoderm may be the underlying mechanism for the increased cardiomyocyte differentiation efficiency (Piccolo et al., 1999). Overall, it appears that the timing and relative expression of different growth factor combinations induce then pattern the cardiogenic mesoderm.

Subsequent studies identified important roles for the activin A, insulin, Wnt and BMP pathways in the establishment of cardiovascular cells (Klaus et al., 2007; Schneider and Mercola, 2001; Liu et al., 1999). Activin A and transforming growth factor β1 (TGFβ1) stimulation promotes cardiac mesoderm formation in mouse embryonic stem cells (Moretti et al., 2006; Kattman et al., 2 006) and addition of activin A and BMP4 induces endogenous Wnt signaling and mesoderm-like cells from human embryonic stem cell sources (Paige et al., 2010). Remarkably small changes in BMP4 and activin A concentrations can drive the specification of the FHF, the anterior SHF and the posterior SHF (Yang et al., 2022) from distinct stem cell-derived mesoderm populations (Kattman et al., 2011), ultimately affecting the relative numbers of atrial versus ventricular cardiomyocytes (Lee et al., 2017). Although cardiomyocytes produced in this way may be high quality, scaling up these protocols is challenging due to the stability and cost of growth factors involved, which must be precisely applied to achieve this delicate balance.

The ability to reprogram patient somatic cells into induced pluripotent stem cells (hiPSCs) represented a key turning point for the field (Takahashi et al., 2007). The potential to differentiate these patient-specific cells into many cell types, including functional cardiomyocytes (hiPSC-CMs) fueled a search for signaling molecules to replace the growth factors. In vitro, molecular inhibition of GSK-3β using small molecules such as CHIR99021 leads to nuclear accumulation of β-catenin and thus the transcription of Wnt target genes (Lian et al., 2012). Activation of Wnt signaling in monolayer-based hESC and hiPSC cultures results in efficient mesoderm-like cell formation, and subsequent inhibition of the Wnt signaling pathway promotes the terminal differentiation of these mesoderm-like cells into cardiomyocytes (Paige et al., 2010; Lian et al., 2012). The current standard in monolayer-based directed differentiation protocols uses this two-step Wnt pathway modulation to generate >80% hiPSC-CMs within 7 days of culture (Paige et al., 2010; Lian et al., 2012) (**Figure 3**). Altogether, the development of small molecule-based directed differentiation protocols has facilitated reliable and cost-effective production of both atrial and ventricular hiPSC-CMs. However, cell type heterogeneity presents a challenge, as homogeneous populations of subtype-specific cardiomyocytes are essential for drug discovery, cardiovascular disease modeling and cardiotoxicity screens (Zhang et al., 2009).

Developmental shortcuts for human pluripotent stem cell-derived cardiomyocyte expansion

Robust generation of large quantities of hiPSC-CMs from patient donors remains a significant hurdle. Conventional approaches to tackle this problem use large numbers of hiPSCs, which is very costly, and the differentiation efficiency is highly variable due to lack of control of important culture parameters (Laco et al., 2018). Moreover, the subsequent expansion of hiPSC-CM cultures is generally modest (<10-fold) (**Table 2**).

In vitro studies have identified multiple pathways controlling the proliferation of hiPSC-CMs. Computational approaches and chemical screens for cardiomyocyte proliferation regulators found 67 miRNAs targeting different components of the Hippo pathway (Diez-Cuñado et al., 2018) (**Table 2**). Hippo signaling appears to be upregulated in hiPSC-CMs cultured on plastic, but altering substrate stiffness has no effect on the fraction of proliferative cardiomyocytes, and none of the small molecule Hippo pathway inhibitors has been reported to enhance cardiomyocyte proliferation in vitro (Buikema et al., 2020).

The TGFβ pathway regulates the cell cycle in hiPSC-CMs, where it directly boosts the production of p27 in a Smad-dependent manner, allowing p27 to inhibit the activity of G1 cyclins (Toyoshima and Hunter, 1994; Kodo et al., 2016). The combined upregulation of CDK1, CCNB, CDK4 and CCND successfully upregulates cardiomyocyte proliferation markers in hiPSC-CMs (Mohamed et al., 2018), and inhibiting Wee1 and TGFβ promotes CDK1 phosphorylation, thus promoting G2/M phase entry (Mohamed et al., 2018) (**Table 2**).

Multiple hormones are implicated in the regulation of fetal growth, and many of these take on considerably different roles during early postnatal life. In utero, the human heart relies predominantly on high concentrations of carbohydrates, whereas the postnatal myocardium also uses fatty acid-rich substrates (Kolwicz et al., 2013). Insulin, prolactin, IGF1, IGF2 and thyroid-associated hormones are involved in anabolism during heart development (Díaz Del Moral et al., 2021). The growth factor IGF1 was shown to enhance the proliferation of hESC-derived cardiomyocytes via activation of the PI3K/Akt signaling pathway (McDevitt et al., 2005). Thyroid hormone or 3,5,3'-triiodothyronine (T3) inhibits proliferation and drives the maturation of cardiomyocytes before birth (Chattergoon et al., 2019). In parallel to IGF1, insulin increases proliferation of hiPSC-CMs and cardiac organoids (Mills et al., 2017) (**Table 2**).

Aurora B, aurora kinase B; bFGF, basic fibroblast growth factor; BrdU, 5-bromo-2'-deoxyuridine; CCNB, cyclin B1; CCND, cyclin D2; CDK1, cyclin-dependent kinase 1; CDK4, cyclin-dependent kinase 4; DOX, doxycycline; EdU, 5-ethynyl-2'-deoxyuridine; ERK, extracellular signal-regulated kinase; FGF1, fibroblast growth factor 1; FOXO, forkhead box transcription factors; G2/M, inter/mitosis and cytokinesis phase; GLI1, GLI family zinc finger 1; hESC-CM, human embryonic stem cell-derived cardiomyocyte; hiPSC-CM, human induced pluripotent stem cell-derived cardiomyocyte; hiPSC-CPC, human induced pluripotent stem cellderived cardiac progenitor

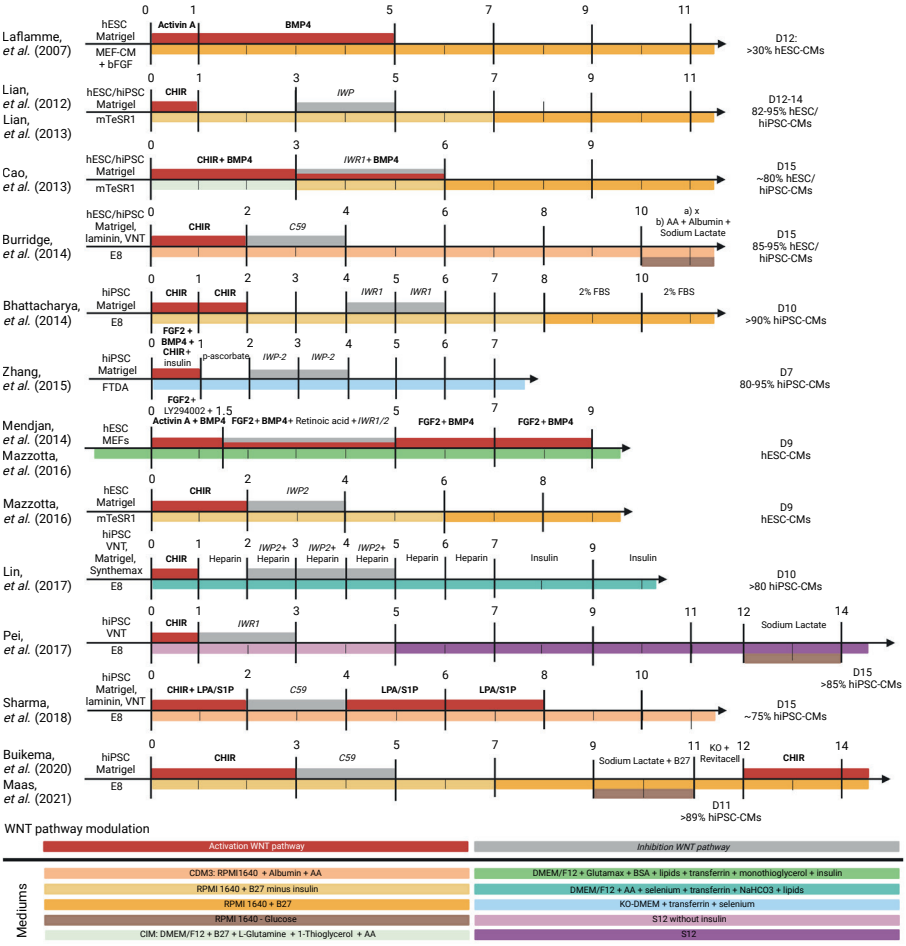

Figure 3. Summary of recent directed cardiac differentiation and expansion protocols for human pluripotent stem cell-derived cardiomyocytes. Schematics of pluripotent stem cell monolayer-based cardiomyocyte differentiation protocols. The days of each protocol are indicated by the vertical lines. Corresponding articles are shown on the left. Initial stem cell conditions, before the start of the differentiation, are shown to the left of day 0 on each timeline. Differentiation efficiency is indicated on the right side, where D indicates the day on which the differentiation efficiency was measured. The media used for differentiation are indicated by different colors below the time axis, with any additional components listed above the time axis. The red and grey boxes depicted above the time axis indicate activation or inhibition of the Wnt pathway, respectively. Key components responsible for modulating Wnt activity are indicated in bold for Wnt activation or italics for Wnt inhibition. Abbreviations: AA, L-ascorbic acid 2-phosphate; bFGF/FGF2, basic fibroblast growth factor; BMP4, bone morphogenetic protein 4; BSA, bovine serum albumin; CHIR, CHIR99021; DMEM, Dulbecco's Modified Eagle Medium; FBS, fetal bovine serum; hESCs, human embryonic stem cells; hiPSC, human induced pluripotent stem cells; IWP, inhibitor of Wnt production; KO-DMEM, knockout DMEM; LPA, lysophosphatidic acid; MEFs, mouse embryonic fibroblasts; RPMI, Roswell Park Memorial Institute medium; S1P, sphingosine-1-phosphate; VNT, vitronectin. E8, FDTA and mTeSR1 are stem cell media. C59 and IWR1 are inhibitors of the Wnt pathway. B27 is a commercially available cell culture supplement. Created with BioRender.com.

Table 2: Molecular targets for expansion of human pluripotent stem cell-derived cardiomyocytes

Pathways	Compound	Cell type +	Age (day)	culture format	Proliferation markers	Expansion (-fold)	ref
Hippo	67 miRNAs	hiPSC-CMs	38	2D, plastic	1.1% $pHH3^+$	N/A	Diez-Cuñado, 2018
Cyclins	CDK1, CCNB, CDK4, CCND	hiPSC-CMs	60	2D, plastic	25% EdU^+, 20% $pHH3^+$	N/A	Mohamed, 2018
TGFβ/ SMAD	Tgf-β, Wee1, CDK4, CCND	hiPSC-CMs	60	2D, plastic	12% EdU^+, 15% $pHH3^+$	N/A	Mohamed, 2018
PI3K	IGF-1	hESC-CMs	13-50	2D, plastic	0.4% $BrdU^+$	N/A	McDevitt, 2005
Wnt/FGF	CHIR99021 FGF1	hiPSC-CMs	30	2D, plastic	30% $Ki67^+$, 20% $BrdU^+$, 4% $pHH3^+$, 4% Auora B^+	N/A	Fan, 2020
Cell cycle inhibitors	(si)RNA: Rb1, Meis2	hiPSC-CMs	35	2D, plastic	30.8 EdU^+, 25,8% $Ki67^+$, 5,3% Auora B^+	N/A	Alam, 2019
Hippo, Wnt, ERK	CHIR99021 S1P/LPA	hiPSC-CMs	0-2	2D, plastic	40% $Ki67^+$, 4% $pHH3^+$	1.5	Sharma, 2018
Mevalonate	Compound 3	hiPSC-derived cardiac organoids	18	3D, ultra-low attachment plates	7.5% $Ki67^+$, 1% pHH3+	1.5	Mills, 2019
Wnt	CHIR99021	hiPSC-CMs	18	2D, high density microbioreactor	25% $Ki67^+$	1.5± 0.4	Titmarsh, 2016
Wnt/MAPK	BIO+SU+p38i	hiPSC-CMs	18	2D, plastic	3% EdU^+, 1.5% $BrdU^+$	1.5± 0.5	Uosaki, 2013
Mevalonate	Compound 65	hiPSC-derived cardiac organoids	14-16	3D	5% $Ki67^+$, 0.6% $pHH3^+$	2	Mills, 2017
Wnt	Wnt3a conditioned medium	hESC-derived Isl1 cardiovascular progenitors	6	2D, plastic	6,8% $pHH3^+$	6	Qyang, 2007
Activin/nodal, FGF/Wnt	A83-01, bFGF, CHIR	hiPSC-CMCs	12-15	2D, plastic	72.7 ± 1.5% $Ki67^+$	11	Vahdat, 2022
Wnt	CHIR99021	hiPSC-CM	12	3D, stirred spinner cultures	50% G2/M -$phase^+$	14-16	Laco, 2020
IL6/bFGF	IL6RIL6 chimera, bFGF	hiPSC-CM	14	2D, suspension culture system	N/A, Multiple passaging	25	Amit, 2011
FOXO inhibition	AS1842856	hiPSC-CM	10	2D, plastic	N/A, Multiple passaging	~40	Schade, 2022
Hedgehog	DOX, SB, IGF-1, SAG	hiPSC-CPCs	5	2D, plastic	8% GLI1 mRNA, 6% PTCH1 mRNA	75	Birket, 2015
Wnt/Insulin /Akt	CHIR99021, Cell-cell contact inhibition	hiPSC-CMs	11	2D, plastic	6% $pHH3^+$, 20% $Ki67^+$, 35% $CCND^+$, Multiple passaging	250	Buikema, 2020; Maas, 2021

cell; IGF1, insulin-like growth factor; Isl1, ISL LIM homeobox 1; MAPK, mitogen-activated protein kinase; Meis2, meis homeobox 2; p38i, p38 inhibitor; pHH3, phosphohistone H3; PI3K, phosphoinositide 3 kinases; Rb1, retinoblastoma; S1P/LPA, sphingosine-1-phosphate/ lysophosphatidic acid; SAG, smoothened agonist; SB, SB431542; (si)RNA, small interfering RNA; SMAD, mothers against decapentaplegic; TGFβ, transforming growth factor β.

However, insulin does not rescue cell cycle arrest, likely due to altered substrate use and fatty acid metabolism in the treated cardiomyocytes, so this effect is short-lived (Mills et al., 2017).

During development and hiPSC differentiation, the GSK-3β/ Wnt/β-catenin signaling cascade exerts multiphasic effects on cardiac differentiation and proliferation. The Wnt/β-catenin pathway is essential for cardiac repair and has been implicated in cardiac diseases (Titmarsh et al., 2016). Multiple studies in 2D and 3D in vitro cell models have described a significant proliferative effect of small molecules that inhibit GSK-3β and activate Wnt/β-catenin signaling, such as CHIR99021 (Buikema et al., 2013; Titmarsh et al., 2016; Sharma et al., 2018b; Uosaki et al., 2013) (**Table 2**).

Attempts have also been made to increase cardiomyocyte yield by first expanding the production of hiPSCs and then inducing cardiac differentiation (Le and Hasegawa, 2019). Conventional methods for this approach include the culture of hiPSCs in a 2D monolayer at larger surface areas (using T175 flasks, CompacT SelecT, roller bottles or CellCube) (Tohyama et al., 2017; Soares et al., 2014). Although these 2D culture monolayers can increase hiPSC cell number efficiently, hiPSC medium is very costly, and the differentiation efficiency is highly variable due to lack of control of important culture parameters such as the confluency of the hiPSCs and the timing of compound addition (Tohyama et al., 2017). More recently, advanced 3D culture strategies such as microcarriers, 3D aggregation and bioreactors have attracted interest and have proven suitable for large-scale culturing of hiPSCs (Borys et al., 2020; Abecasis et al., 2017). This 3D culture approach improves the efficiency of hiPSC-CM production and reduces variability in differentiation outcomes (Hofer and Lutolf, 2021). However, the cost of the medium and the need for dissociation during harvesting represent hurdles for subsequent differentiation applications (Le and Hasegawa, 2019).

Recently, we discovered that cell-cell contact promotes terminal differentiation and maturation, rather than proliferation, in densely cultured hiPSC-CMs (Buikema et al., 2020). Concomitant activation of Wnt signaling by CHIR99021 and cell-cell contact inhibition by low cell density serial passaging resulted in a massive proliferative response in the hiPSC-CMs (Buikema et al., 2020; Maas et al., 2021) (**Figure 4**).

These hiPSC-CMs exhibited immature functional properties, such as reduced contractility and underdeveloped sarcomeres; however, upon withdrawal of CHIR99021, cells quickly exited the cell cycle and terminally differentiated (Buikema et al., 2020). It appears that insulin is required for long-term hiPSC-CM culture recapitulating cardiac development (Lian et al., 2013;

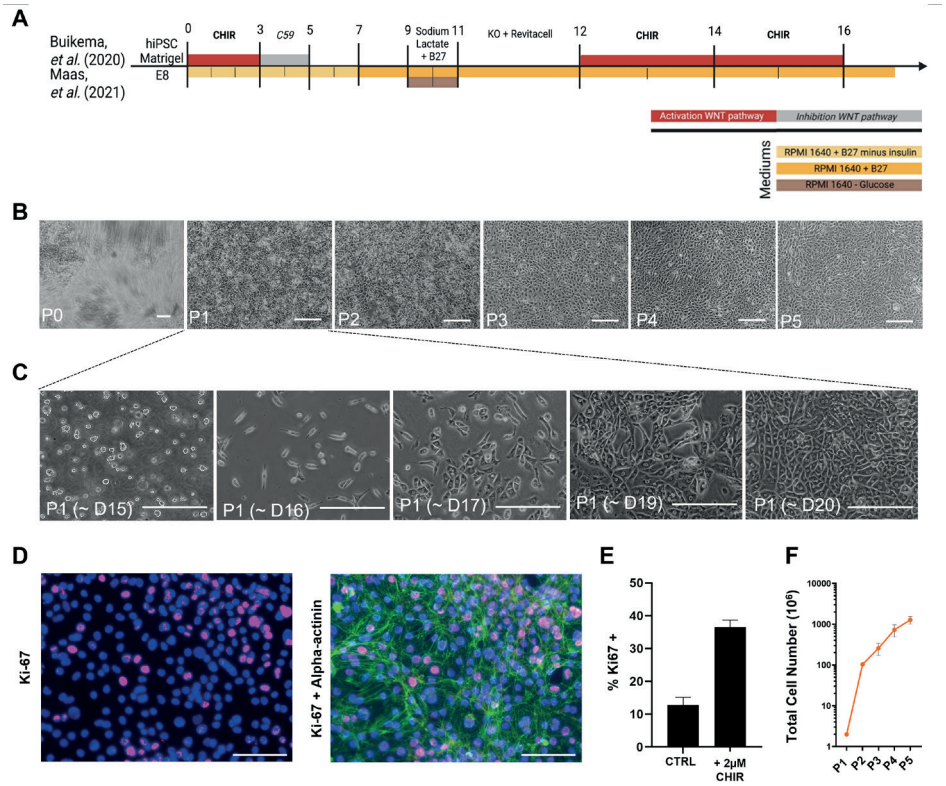

Figure 4. Overview of Wnt modulation during hiPSC-CM differentiation and expansion. (A) Schematic overview of human induced pluripotent stem cellderived cardiomyocyte (hiPSC-CM) differentiation. Created with BioRender.com. (B) Brightfield images of hiPSC-CMs over multiple passages including expansion illustrating the process of cell-cell contact removal via sparse passaging (~2.5×104 cells/cm2) with concomitant CHIR99021 administration in B27+insulin/RPMI media to facilitate massive expansion. (C) Brightfield images of hiPSC-CMs in expansion from days 15-20. (D) Immunofluorescence images of hiPSC-CMs stained for α-actinin (green), proliferation marker Ki67 (red) and nuclei (blue) as indicated. (E) Quantification of Ki67+ cells indicates that a 37% increase in hiPSC-CM proliferation can be promoted by administering 2 μM CHIR99021. (F) Quantification of hiPSC-CM number from P1 to P5 by sequentially expanding the hiPSC-CMs using CHIR99021 (CHIR). D, differentiation day; P, passage; RPMI, Roswell Park Memorial Institute medium. Figure is adapted from Maas et al. (2021) and is available to view on Figshare alongside detailed Materials and Methods: 10.6084/m9.figshare.23607282. Scale bars: 200 μM (B,C); 100 μM (D).

Govindsamy et al., 2018), so we also chose to optimize our protocol for proliferation induction with B-27 medium containing insulin. In summary, Wnt activation together with removal of cell-cell contacts transiently increases the window for massive expansion of immature hiPSC-CMs.

Massively expanded hiPSC-CMs are fully functional and could form a powerful source for tissue engineering applications and/or myocardial biopatches (Miyagawa et al., 2022; Gao et al., 2018). These protocols are still limited to producing a 100- to 250-fold increase

in cell number (Buikema et al., 2020; Maas et al., 2021) (**Table 2**), but they are pushing the production process towards clinically relevant cardiomyocyte numbers. For example, one batch of massively expanded hiPSC-CMs can be used to generate large numbers of 3D engineered heart tissues (EHTs) or to conduct large 2D screens (Hansen et al., 2010; Calpe and Kovacs, 2020). Moreover, hiPSC-CM-derived tissues or cell injections can form large grafts after transplantation into injured animal hearts (Shiba et al., 2016). Upon injection, previous studies have shown electrical coupling of hiPSCCMs to host myocardium, but also arrhythmic events (Hirt et al., 2012; Shiba et al., 2012). Recent work has shown that these arrhythmic events can be overcome via maturation-guided editing of hiPSC-CM ion channels, thereby improving electrophysiological function (Marchiano et al. 2023; Ottaviani et al., 2023). These approaches require 10-750 million cells for restoration of contractile function after ischemic injury in macaque monkeys (Anderson et al., 2014; Zhu et al., 2018a). Unfortunately, despite the recent methods to improve cardiomyocyte maturity, the overall maturation status of hiPSC-CMs with or without expansion remains low. Therefore, hiPSC-CM grafts retain different electrical properties compared with the host tissue, which could lead to increased arrhythmia risk (Fassina et al., 2022).

DISCUSSION

The further untangling of the cues that drive cardiomyocyte differentiation, proliferation and maturation will lead to increased understanding and improved drug screening options and treatments for cardiac diseases. This Review compares the pathways regulating heart growth in vivo with the molecular targets that promote in vitro cardiomyocyte production. The massive expansion of hiPSC-CMs that can be achieved via Wnt/β-catenin signaling modulation (**Table 2**, **Figure 3** and **Figure 4**) provides a framework for advanced basic and translational cell biology applications in cardiovascular medicine, and several preclinical trials are making use of these hiPSC-CMs (Sharma et al., 2018a; Hnatiuk et al., 2021).

The current knowledge from cardiac development has resulted in relatively easy methods for hiPSC-CM generation. Further understanding of exact cues for long-term proliferation and terminal differentiation, however, are required to produce unlimited numbers of mature cardiomyocytes. The recent discovery of partly-immortalized atrial cardiomyocytes represents a powerful approach for atrial disease modeling in vitro (Harlaar et al., 2022). However, their in vivo use may provoke safety concerns. Nevertheless, these approaches for expansion of cardiomyocytes illustrate that functional and beating cardiomyocytes can self-replicate before terminally differentiating upon growth stimuli withdrawal.

Interestingly, direct activation of Wnt/ β-catenin with CHIR99021 produces cardioprotective effects upon myocardial infarction in both small and large mammals (Fan et al., 2020). However, there is little evidence for induction of terminally differentiated cardiomyocyte proliferation after administration of CHIR99021 upon ischemic injury (Fan et al., 2020). This

lack of proliferative capacity in terminally differentiated cardiomyocytes is somewhat in line with developmental studies illustrating that Hippo signaling controls cell-cycle arrest in adult cardiomyocytes (Xin et al., 2011; Wang et al., 2014). Genetic modification of the Hippo/YAP signaling pathway results in dedifferentiation of adult myocardium with a subsequent regenerative response to ischemic injury (Leach et al., 2017; Monroe et al., 2019). Combined with novel DNA, RNA or nanoparticle local delivery technologies, signaling pathways hold promise as druggable targets in cardiovascular medicine (Braga et al., 2021). Future hiPSC-CM studies should focus on further simplification of the exact cues required for cardiomyocyte production, and should incorporate other myocyte subtypes required for regional repair of the heart, as well as more specific cardiac tissue generation.

Disclosures

J.W.B. and S.M.W. hold a patent on the expansion of hiPSC-derived cardiomyocytes.

Acknowledgments

R.G.C.M. is supported by a fellowship from the Stichting PLN. F.W.v.d.D. acknowledges support from the Dutch Cardiovascular Alliance. Q.Y. is supported by PhD fellowship from China Scholarship Council (201706170068). J.v.d.V. is supported by grants from Nederlandse Organisatie voor Wetenschappelijk Onderzoek–ZonMw (91818602 VICI), ZonMw and Hartstichting for the translational research program, project 95105003; the Dutch Cardiovascular Alliance grant Double Dose 2021; the Fondation Leducq grant number 20CVD01; and Proper Therapy project funded by the Nederlandse Organisatie voor Wetenschappelijk Onderzoek, domain Applied and Engineering Sciences (NWO-AES), the Association of Collaborating Health Foundations (Health~Holland), and ZonMw within the human models 2.0 call. S.M.W. is supported by the National Institutes of Health/National Institute of General Medical Sciences (1RM1GM131981-03); American Heart Association Established Investigator Award; Additional Ventures Foundation; National Science Foundation RECODE Project; and the Joan and Sanford I. Weill Department of Medicine Endowed Scholarship Fund. J.P.G.S. is supported by H2020-EVICARE (725229) of the European Research Council and ZonMw PSIDER grant (10250022110004). J.W.B. is supported by a Dekker Senior Clinical Scientist personal grant from the Hartstichting (03-003-2021-T025); Netherlands Heart Institute Fellowship; and CVON-Dosis young talent grant from the Hartstichting (CVON-Dosis 2014–40). Deposited in PMC for release after 12 months.

REFERENCES

1. Abecasis, B., Aguiar, T., Arnault, É., Costa, R., Gomes-Alves, P., Aspegren, A., Serra, M. and Alves, P. M. (2017). Expansion of 3D human induced pluripotent stem cell aggregates in bioreactors: bioprocess intensification and scaling-up approaches. J. Biotechnol. 246, 81-93.
2. Adhyapak, S. M. (2022). The impact of left ventricular geometry and remodeling on prognosis of heart failure in ischemic cardiomyopathy. J. Card. Surg. 37, 2168-2171.
3. Alam, P., Haile, B., Arif, M., Pandey, R., Rokvic, M., Nieman, M., Maliken, B. D., Paul, A., Wang, Y. G., Sadayappan, S. et al. (2019). Inhibition of senescence-associated genes Rb1 and Meis2 in adult cardiomyocytes results in cell cycle reentry and cardiac repair post-myocardial infarction. J. Am. Heart Assoc. 8, e012089.
4. Alkass, K., Panula, J., Westman, M., Wu, T. D., Guerquin-Kern, J. L. and Bergmann, O. (2015). No evidence for cardiomyocyte number expansion in preadolescent mice. Cell 163, 1026-1036.
5. Amit, M., Laevsky, I., Miropolsky, Y., Shariki, K., Peri, M. and Itskovitz-Eldor, J. (2011). Dynamic suspension culture for scalable expansion of undifferentiated human pluripotent stem cells. Nat. Protoc. 6, 572-579.
6. Anderson, M. E., Goldhaber, J., Houser, S. R., Puceat, M. and Sussman, M. A. (2014). Embryonic stem cell-derived cardiac myocytes are not ready for human trials. Circ. Res. 115, 335-338.
7. Bardot, E., Calderon, D., Santoriello, F., Han, S., Cheung, K., Jadhav, B., Burtscher, I., Artap, S., Jain, R., Epstein, J. et al. (2017). foxa2 identifies a cardiac progenitor population with ventricular differentiation potential. Nat. Commun. 8.
8. Bergmann, O., Bhardwaj, R. D., Bernard, S., Zdunek, S., Barnabeì-Heider, F., Walsh, S., Zupicich, J., Alkass, K., Buchholz, B. A., Druid, H. et al. (2009). Evidence for cardiomyocyte renewal in humans. Science 324, 98-102.
9. Bergmann, O., Zdunek, S., Felker, A., Salehpour, M., Alkass, K., Bernard, S., Sjostrom, S. L., Szewczykowska, M., Jackowska, T., Dos Remedios, C. et al. (2015). Dynamics of cell generation and turnover in the human heart. Cell 161.
10. Birket, M., Ribeiro, M., Verkerk, A., Ward, D., Leitoguinho, A. R., den Hartogh, S. C., Orlova, V. V., Devalla, H. D., Schwach, V., Bellin, M., et al. (2015). Expansion and patterning of cardiovascular progenitors derived from human pluripotent stem cells. Nat. Biotechnol. 33, 970-979.
11. Borys, B. S., So, T., Colter, J., Dang, T., Roberts, E. L., Revay, T., Larijani, L., Krawetz, R., Lewis, I., Argiropoulos, B. et al. (2020). Optimized serial expansion of human induced pluripotent stem cells using low–density inoculation to generate clinically relevant quantities in vertical–wheel bioreactors. Stem Cells Transl. Med. 9, 1036.
12. Brade, T., Pane, L. S., Moretti, A., Chien, K. R. and Laugwitz, K.-L. (2013). Embryonic heart progenitors and cardiogenesis. Cold Spring Harb. Perspect. Med. 3, a013847.
13. Braga, L., Ali, H., Secco, I. and Giacca, M. (2021). Non-coding RNA therapeutics for cardiac regeneration. Cardiovasc. Res. 117, 674-693.
14. Bray, M.-A., Sheehy, S. P. and Parker, K. K. (2008). Sarcomere alignment is regulated by myocyte shape. Cell Motil. Cytoskelet. 65, 641-651
15. Bruneau, B. G., Logan, M., Davis, N., Levi, T., Tabin, C. J., Seidman, J. G. and Seidman, C. E. (1999). Chamber-specific cardiac expression of Tbx5 and heart defects in holt-oram syndrome. Dev. Biol. 211, 100-108.
16. Buckingham, M., Meilhac, S. and Zaffran, S., (2005). Building the mammalian heart from two sources of myocardial cells. Nat. Rev. Genet. 6, 826-835.
17. Buikema, J. W., Mady, A. S., Mittal, N. V., Atmanli, A., Caron, L., Doevendans, P. A., Sluijter, J. P. G. and Domian, I. J. (2013). Wnt/β-catenin signaling directs the regional expansion of first and second heart field-derived ventricular cardiomyocytes. Development 140, 4165-4176
18. Buikema, J. W., Lee, S., Goodyer, W. R., Maas, R. G., Chirikian, O., Li, G., Miao, Y., Paige, S. L., Lee, D., Wu, H. et al. (2020). Wnt activation and reduced cell-cell contact synergistically induce massive expansion of functional human iPSC-derived cardiomyocytes. Cell Stem Cell 27, 50-63.e5
19. Burridge, P. W., Keller, G., Gold, J. and Wu, J. C. (2012). Production of de Novo cardiomyocytes: human pluripotent stem cell differentiation and direct reprogramming. Cell Stem Cell 10, 16-28.
20. Burridge, P. W., Matsa, E., Shukla, P., Lin, Z. C., Churko, J. M., Ebert, A. D., Lan, F., Diecke, S., Huber, B., Mordwinkin, N. M. et al. (2014). Chemically defined generation of human cardiomyocytes. Nat. Methods 11, 855-860.

21. Cadigan, K. M. and Waterman, M. L. (2012). TCF/LEFs and Wnt signaling in the nucleus. Cold Spring Harbor Perspect. Biol. 4, a007906.

22. Calpe, B. and Kovacs, W. J. (2020). High-throughput screening in multicellular spheroids for target discovery in the tumor microenvironment. Exp. Opin. Drug Discov. 15, 955-967.

23. Castellan, R. F. P., Thomson, A., Moran, C. M. and Gray, G. A. (2020). Electrocardiogram-gated Kilohertz Visualisation (EKV) Ultrasound allows assessment of neonatal cardiac structural and functional maturation and longitudinal evaluation of regeneration after injury. Ultrasound Med. Biol. 46, 167-179.

24. Chan, S. S., Shi, X., Toyama, A., Arpke, R. ÂW., Dandapat, A., Iacovino, M., Kang, J., Le, G., Hagen, H. ÂR., Garry, D. ÂJ. et al. (2013). Mesp1 patterns mesoderm into cardiac, hematopoietic, or skeletal myogenic progenitors in a context-dependent manner. Cell Stem Cell 12, 587-601.

25. Chattergoon, N. N., Louey, S., Scanlan, T., Lindgren, I., Giraud, G. D. and Thornburg, K. L. (2019). Thyroid hormone receptor function in maturing ovine cardiomyocytes. J. Physiol. 597, 2163-2176.

26. Colucci, W. S. (1997). Molecular and cellular mechanisms of myocardial failure. Am. J. Cardiol. 80, 15L-25L.

27. Cook, J. A., Shah, K. B., Quader, M. A., Cooke, R. H., Kasirajan, V., Rao, K. K., Smallfield, M. C., Tchoukina, I. and Tang, D. G. (2015). The total artificial heart. J. Thorac. Dis. 7, 2172-2180.

28. De Bakker, B. S., De Jong, K. H., Hagoort, J., De Bree, K., Besselink, C. T., De Kanter, F. E. C., Veldhuis, T., Bais, B., Schildmeijer, R., Ruijter, J. M. et al. (2016). An interactive three-dimensional digital atlas and quantitative database of human development. Science 354, aag0053.

29. De Boer, R. A., Pinto, Y. and Van Veldhuisen, D. (2003). The imbalance between oxygen demand and supply as a potential mechanism in the pathophysiology of heart failure: the role of microvascular growth and abnormalities. Microcirculation 10, 113-126.

30. De Boer, B. A., Van Den Berg, G., De Boer, P. A. J., Moorman, A. F. M. and Ruijter, J. M. (2012). Growth of the developing mouse heart: an interactive qualitative and quantitative 3D atlas. Dev. Biol. 368, 203-213.

31. De Jong, F., Opthof, T., Wilde, A. A., Janse, M. J., Charles, R., Lamers, W. H. and Moorman, A. F. (1992). Persisting zones of slow impulse conduction in developing chicken hearts. Circ. Res. 71, 240-250.

32. Debosch, B., Treskov, I., Lupu, T. S., Weinheimer, C., Kovacs, A., Courtois, M. and Muslin, A. J. (2006). Akt1 is required for physiological cardiac growth. Circulation 113, 2097-2104.

33. Del Re, D. P. (2014). The hippo signaling pathway: implications for heart regeneration and disease. Clin. Transl. Med.

34. Dhanantwari, P., Lee, E., Krishnan, A., Samtani, R., Yamada, S., Anderson, S., Lockett, E., Donofrio, M., Shiota, K., Leatherbury, L. et al. (2009). Human cardiac development in the first trimester: a high-resolution magnetic resonance imaging and episcopic fluorescence image capture atlas. Circulation 120, 343-351.

35. Dıaz Del Moral, S., Benaouicha, M., Mun oz-Chápuli, R. and Carmona, R. (2021). The insulin-like growth factor signalling pathway in cardiac development and regeneration. Int. J. Mol. Sci. 23, 234

36. Diez-Cuñ ado, M., Wei, K., Bushway, P. J., Maurya, M. R., Perera, R., Subramaniam, S., Ruiz-Lozano, P. and Mercola, M. (2018). miRNAs that induce human cardiomyocyte proliferation converge on the hippo pathway. Cell Rep. 23, 2168

37. Drenckhahn, J., Schwarz, Q. P., Gray, S., Laskowski, A., Kiriazis, H., Ming, Z., Harvey, R. P., Du, X.-J., Thorburn, D. R. and Cox, T. C. (2008). Compensatory growth of healthy cardiac cells in the presence of diseased cells restores tissue homeostasis during heart development. Dev. Cell 15, 521-533.

38. Faber, J. W., Hagoort, J., Moorman, A. F. M., Christoffels, V. M. and Jensen, B. (2021). Quantified growth of the human embryonic heart. Biol. Open 10, bio057059.

39. Fan, C., Oduk, Y., Zhao, M., Lou, X., Tang, Y., Pretorius, D., Valarmathi, M. T., Walcott, G. P., Yang, J., Menasche, P. et al. (2020). Myocardial protection by nanomaterials formulated with CHIR99021 and FGF1. JCI Insight 5, e132796.

40. Fassina, D., Costa, C. M., Longobardi, S., Karabelas, E., Plank, G., Harding, S. E. and Niederer, S. A. (2022). Modelling the interaction between stem cells derived cardiomyocytes patches and host myocardium to aid non-arrhythmic engineered heart tissue design. PLoS Comput. Biol. 18, e1010030.

41. Fox, K. F., Cowie, M. R., Wood, D. A., Coats, A. J., Gibbs, J. S., Underwood, S. R., Turner, R. M., Poole-Wilson, P. A., Davies, S. W. and Sutton, G. C. (2001). Coronary artery disease as the cause of incident heart failure in the population. Eur. Heart J. 22, 228-236.

42. Gao, L., Gregorich, Z. R., Zhu, W., Mattapally, S., Oduk, Y., Lou, X., Kannappan, R., Borovjagin, A. V., Walcott, G. P., Pollard, A. E. et al. (2018). Large cardiac muscle patches engineered from human induced-pluripotent stem cell-derived cardiac cells improve recovery from myocardial infarction in swine. Circulation 137, 1712-1730.

43. Gan, J., Sonntag, H.-J., Tang, M. K., Cai, D. and Lee, K. K. H. (2015). Integrative analysis of the developing postnatal mouse heart transcriptome. PLoS One 10, e0133288.

44. Garry, D. J. and Olson, E. N. (2006). A common progenitor at the heart of development. Cell 127, 1101-1104.

45. Gassmann, M., Casagranda, F., Orioli, D., Simon, H., Lai, C., Klein, R. and Lemke, G. (1995). Aberrant neural and cardiac development in mice lacking the ErbB4 neuregulin receptor. Nature 378, 390-394

46. Gerber, B. L., Rochitte, C. E., Melin, J. A., Mcveigh, E. R., Bluemke, D. A., Wu, K. C., Becker, L. C. and Lima, J. A. (2000). Microvascular obstruction and left ventricular remodeling early after acute myocardial infarction. Circulation 101.

47. Govindsamy, A., Naidoo, S. and Cerf, M. E. (2018). Cardiac development and transcription factors: insulin signalling, insulin resistance, and intrauterine nutritional programming of cardiovascular disease. J. Nutr. Metab. 2018, 8547976.

48. Grego-Bessa, J., Luna-Zurita, L., Del Monte, G., Bolós, V., Melgar, P., Arandilla, A., Garratt, A. N., Zang, H., Mukouyama, Y.-, Chen, H. et al. (2007). Notch signaling is essential for ventricular chamber development. Dev. Cell 12, 415-429.

49. Günthel, M., Barnett, P. and Christoffels, V. M. (2018). Development, proliferation, and growth of the mammalian heart. Mol. Ther. 26, 1599-1609.

50. Hansen, A., Eder, A., Boì^nstrup, M., Flato, M., Mewe, M., Schaaf, S., Aksehirlioglu, B. Ì^, Schwoì^rer, A., Uebeler, J. and Eschenhagen, T. (2010). Development of a drug screening platform based on engineered heart tissue. Circ. Res.

51. Harlaar, N., Dekker, S. O., Zhang, J., Snabel, R. R., Veldkamp, M. W., Verkerk, A. O., Fabres, C. C., Schwach, V., Lerink, L. J. S., Rivaud, M. R. et al. (2022). Conditional immortalization of human atrial myocytes for the generation of in vitro models of atrial fibrillation. Nat. Biomed. Eng. 6, 389-402.

52. Haubner, B. J., Schneider, J., Schweigmann, U., Schuetz, T., Dichtl, W., Velik-Salchner, C., Stein, J.-I. and Penninger, J. M. (2016). Functional recovery of a human neonatal heart after severe myocardial infarction. Circ. Res. 118, 216-221.

53. Heallen, T., Zhang, M., Wang, J., Bonilla-Claudio, M., Klysik, E., Johnson, R. L. and Martin, J. F. (2011). Hippo pathway inhibits Wnt signaling to restrain cardiomyocyte proliferation and heart size. Science 332, 458-461.

54. Herrmann, B. G., Labeit, S., Poustka, A., King, T. R. and Lehrach, H. (1990). Cloning of the T gene required in mesoderm formation in the mouse. Nature 343 , 617-622.

55. Hirt, M. N., Sörensen, N. A., Bartholdt, L. M., Boeddinghaus, J., Schaaf, S., Eder, A., Vollert, I., Sta¶Hr, A., Schulze, T., Witten, A. et al. (2012). Increased afterload induces pathological cardiac hypertrophy: a new in vitro model. Basic Res. Cardiol. 107, 307.

56. Hnatiuk, A. P., Briganti, F., Staudt, D. W. and Mercola, M. (2021). Human iPSC modeling of heart disease for drug development. Cell Chem. Biol. 28, 271-282.

57. Hofer, M. and Lutolf, M. P. (2021). Engineering organoids. Nat. Rev. Mater. 6, 402-420.

58. Huang, W., Feng, Y., Liang, J., Yu, H., Wang, C., Wang, B., Wang, M., Jiang, L., Meng, W., Cai, W., et al. (2018). Loss of microRNA-128 promotes cardiomyocyte proliferation and heart regeneration. Nat. Commun. 9, 700.

59. Imajo, M., Miyatake, K., Iimura, A., Miyamoto, A. and Nishida, E. (2012). A molecular mechanism that links Hippo signalling to the inhibition of Wnt/β-catenin signalling. EMBO J. 31, 1109-1122.

60. Ivanovitch, K., Soro-Barrio, P., Chakravarty, P., Jones, R. A., Bell, D. M., Mousavy Gharavy, S. N., Stamataki, D., Delile, J., Smith, J. C. and Briscoe, J. (2021). Ventricular, atrial, and outflow tract heart progenitors arise from spatially and molecularly distinct regions of the primitive streak. PLoS Biol. 19, e3001200

61. Kattman, S. J., Huber, T. L. and Keller, G. M. (2006). Multipotent Flk-1+ cardiovascular progenitor cells give rise to the cardiomyocyte, endothelial, and vascular smooth muscle lineages. Dev. Cell 11, 723-732.

62. Kattman, S. J., Witty, A. D., Gagliardi, M., Dubois, N. C., Niapour, M., Hotta, A., Ellis, J. and Keller, G. (2011). Stage-specific optimization of activin/nodal and BMP signaling promotes cardiac differentiation of mouse and human pluripotent stem cell lines. Cell Stem Cell 8, 228-240

63. Kelly, R. G. (2012). The second heart field. Curr. Top. Dev. Biol. 100, 33-65.

64. Kelly, R. G., Buckingham, M. E. and Moorman, A. F. (2014). Heart fields and cardiac morphogenesis. Cold Spring Harb. Perspect. Med. 4, a015750.

65. Kim, W., Khan, S. K., Gvozdenovic-Jeremic, J., Kim, Y., Dahlman, J., Kim, H., Park, O., Ishitani, T., Jho, E.-, Gao, B. et al. (2017). Hippo signaling interactions with Wnt/β-catenin and notch signaling repress liver tumorigenesis. J. Clin. Invest.

66. Kitajima, S., Takagi, A., Inoue, T. and Saga, Y. (2000). MesP1 and MesP2 are essential for the development of cardiac mesoderm. Development 127, 3215-3226.

67. Klaus, A., Saga, Y., Taketo, M. M., Tzahor, E. and Birchmeier, W. (2007). Distinct roles of Wnt/β-Catenin and Bmp signaling during early cardiogenesis. Proc. Natl. Acad. Sci. USA 104, 18531-18536

68. Kodo, K., Ong, S.-G., Jahanbani, F., Termglinchan, V., Hirono, K., Inanloorahatloo, K., Ebert, A. D., Shukla, P., Abilez, O. J., Churko, J. M. et al. (2016). iPSC-derived cardiomyocytes reveal abnormal TGF-β signalling in left ventricular non-compaction cardiomyopathy. Nat. Cell Biol. 18, 1031-1042.

69. Kolwicz, S. C., Jr., Purohit, S. and Tian, R. (2013). Cardiac metabolism and its interactions with contraction, growth, and survival of the cardiomyocte. Circ. Res. 113, 603-616.

70. Kwon, C., Arnold, J., Hsiao, E. C., Taketo, M. M., Conklin, B. R. and Srivastava, D. (2007). Canonical Wnt signaling is a positive regulator of mammalian cardiac progenitors. Proc. Natl. Acad. Sci. USA 104, 10894-10899.

71. Laco, F., Woo, T. L., Zhong, Q., Szmyd, R., Ting, S., Khan, F. J., Chai, C. L. L., Reuveny, S., Chen, A. and Oh, S. (2018). Unraveling the inconsistencies of cardiac differentiation efficiency induced by the GSK3β inhibitor CHIR99021 in human pluripotent stem cells. Stem Cell Rep. 10, 1851-1866.

72. Laco, F., Lam, A. T., Woo, T. L., Tong, G., Ho, V., Soong, P. L., Grishina, E., Lin, K. H., Reuveny, S. and Oh, S. K. (2020). Selection of human induced pluripotent stem cells lines optimization of cardiomyocytes differentiation in an integrated suspension microcarrier bioreactor. Stem Cell Res Ther. 11, 118.

73. Laflamme, M. A. and Murry, C. E. (2011). Heart regeneration. Nature 473, 326-335.

74. Leach, J. P., Heallen, T., Zhang, M., Rahmani, M., Morikawa, Y., Hill, M. C., Segura, A., Willerson, J. T. and Martin, J. F. (2017). Hippo pathway deficiency reverses systolic heart failure after infarction. Nature 550, 260-264.

75. Le, M. N. T. and Hasegawa, K. (2019). Expansion culture of human pluripotent stem cells and production of cardiomyocytes. Bioengineering 6, 48.

76. Lee, J. H., Protze, S. I., Laksman, Z., Backx, P. H. and Keller, G. M. (2017). Human pluripotent stem cell-derived atrial and ventricular cardiomyocytes develop from distinct mesoderm populations. Cell Stem Cell 21, 179-94.e4.

77. Li, P., Cavallero, S., Gu, Y., Chen, T. H. P., Hughes, J., Hassan, A. B., Brüning, J. C., Pashmforoush, M. and Sucov, H. M. (2011). IGF signaling directs ventricular cardiomyocyte proliferation during embryonic heart development. Development 138, 1795-1805.

78. Lian, X., Hsiao, C., Wilson, G., Zhu, K., Hazeltine, L. B., Azarin, S. M., Raval, K. K., Zhang, J., Kamp, T. J. and Palecek, S. P. (2012). Robust cardiomyocyte differentiation from human pluripotent stem cells via temporal modulation of canonical Wnt signaling. Proc. Natl. Acad. Sci. USA 109, E1848-E1857.

79. Lian, X., Zhang, J., Zhu, K., Kamp, T. J. and Palecek, S. P. (2013). Insulin inhibits cardiac mesoderm, not mesendoderm, formation during cardiac differentiation of human pluripotent stem cells and modulation of canonical Wnt signaling can rescue this inhibition. Stem Cells 31, 447-457.

80. Lin, L., Cui, L., Zhou, W., Dufort, D., Zhang, X., Cai, C.-L., Bu, L., Yang, L., Martin, J., Kemler, R. et al. (2007). β-catenin directly regulates Islet1 expression in cardiovascular progenitors and is required for multiple aspects of cardiogenesis. Proc. Natl. Acad. Sci. USA 104, 9313-9318.

81. Lin, Z., Zhou, P., Von Gise, A., Gu, F., Ma, Q., Chen, J., Guo, H., Van Gorp, P. R. R., Wang, D.-Z. and Pu, W. T. (2015). Pi3kcb links Hippo-YAP and PI3K-AKT signaling pathways to promote cardiomyocyte proliferation and survival. Circ. Res. 116, 35-45.

82. Liu, Q., Yan, H., Dawes, N. J., Mottino, G. A., Frank, J. S. and Zhu, H. (1996). Insulin-like growth factor II induces DNA synthesis in fetal ventricular myocytes in vitro. Circ. Res. 79, 716-726.

83. Liu, P., Wakamiya, M., Shea, M. J., Albrecht, U., Behringer, R. R. and Bradley, A. (1999). Requirement for Wnt3 in vertebrate axis formation. Nat. Genet. 22, 361-365.

84. Maas, R. G. C., Lee, S., Harakalova, M., Snijders Blok, C. J. B., Goodyer, W. R., Hjortnaes, J., Doevendans, P. A. F. M., Van Laake, L. W., Van Der Velden, J., Asselbergs, F. W. et al. (2021). Massive expansion and cryopreservation of functional human induced pluripotent stem cell-derived cardiomyocytes. STAR Protoc. 2, 100334.

85. Madonna, R., Van Laake, L. W., Botker, H. E., Davidson, S. M., De Caterina, R., Engel, F. B., Eschenhagen, T., Fernandez-Aviles, F., Hausenloy, D. J., Hulot, J.-S. et al. (2019). ESC working group on cellular biology of the heart: position paper for cardiovascular research: tissue engineering strategies combined with cell therapies for cardiac repair in ischaemic heart disease and heart failure. Cardiovasc. Res. 115, 488-500.

86. Mancini, D. and Burkhoff, D. (2005). Mechanical device-based methods of managing and treating heart failure. Circulation 112, 438-448.

87. Marchiano, S., Nakamura, K., Reinecke, H., Neidig, L., Lai, M., Kadota, S., Perbellini, F., Yang, X., Klaiman, J. M., Blakely, L. P. et al. (2023). Gene editing to prevent ventricular arrhythmias associated with cardiomyocyte cell therapy. Cell Stem Cell 30, 396-414.e9.

88. Marvin, M. J., Di Rocco, G., Gardiner, A., Bush, S. M. and Lassar, A. B. (2001). Inhibition of Wnt activity induces heart formation from posterior mesoderm. Genes Dev. 15, 316-327.

89. Mcdevitt, T. C., Laflamme, M. A. and Murry, C. E. (2005). Proliferation of cardiomyocytes derived from human embryonic stem cells is mediated via the IGF/PI 3-kinase/Akt signaling pathway. J. Mol. Cell. Cardiol. 39, 865-873.

90. Meyer, H. V., Dawes, T. J. W., Serrani, M., Bai, W., Tokarczuk, P., Cai, J., De Marvao, A., Henry, A., Lumbers, R. T., Gierten, J. et al. (2020). Genetic and functional insights into the fractal structure of the heart. Nature 584, 589-594.

91. Mills, R. J., Lee, I., Hou, C., Weng, C.-C., Li, S., Lieberman, B. P., Zeng, C., Mankoff, D. A. and Mach, R. H. (2017). Functional screening in human cardiac organoids reveals a metabolic mechanism for cardiomyocyte cell cycle arrest. Proc. Natl. Acad. Sci. U.S.A. 114, E8372-E8381.

92. Mills, R. J., Parker, B. L., Quaife-Ryan, G. A., Voges, H. K., Needham, E. J., Bornot, A., Ding, M., Andersson, H., Polla, M., Elliott D. A. et al. (2019). Drug screening in human PSC-cardiac organoids identifies pro-proliferative compounds acting via the mevalonate pathway. Cell Stem Cell 24, 895-907.e6.

93. Miyagawa, S., kainuma, S., Kawamura, T., Suzuki, K., Ito, Y., Iseoka, H., Ito, E., Takeda, M., Sasai, M., Mochizuki-Oda, N. et al. (2022). Case report: transplantation of human induced pluripotent stem cell-derived cardiomyocyte patches for ischemic cardiomyopathy. Front. Cardiovasc. Med. 9, 950829.

94. Mohamed, T. M. A., Ang, Y.-S., Radzinsky, E., Zhou, P., Huang, Y., Elfenbein, A., Foley, A., Magnitsky, S. and Srivastava, D. (2018). Regulation of cell cycle to stimulate adult cardiomyocyte proliferation and cardiac regeneration. Cell 173, 104-16.e12.

95. Mohammadi, S., Hedjazi, A., Sajjadian, M., Ghoroubi, N., Mohammadi, M. and Erfani, S. (2016). Study of the normal heart size in northwest part of Iranian population: a cadaveric study. J. Cardiovasc. Thorac. Res. 8, 119-125.

96. Mollova, M., Bersell, K., Walsh, S., Savla, J., Das, L. T., Park, S. Y., Silberstein, L. E., Dos Remedios, C. G., Graham, D., Colan, S. et al. (2013). Cardiomyocyte proliferation contributes to heart growth in young humans. Proc. Natl. Acad. Sci. USA 110, 1446-1451.

97. Monroe, T. O., Hill, M. C., Morikawa, Y., Leach, J. P., Heallen, T., Cao, S., Krijger, P. H. L., De Laat, W., Wehrens, X. H. T., Rodney, G. G. et al. (2019). YAP partially reprograms chromatin accessibility to directly induce adult cardiogenesis In Vivo. Dev. Cell 48, 765-79.e7

98. Moorman, A. F. M. and Christoffels, V. M. (2003). Cardiac chamber formation: development, genes, and evolution. Physiol. Rev. 83, 1223-1267.

99. Moorman, A. F., Van Den Berg, G., Anderson, R. H. and Christoffels, V. M. (2010). Early cardiac growth and the ballooning model of cardiac chamber formation. In Heart Development and Regeneration (ed. N. Rosenthal and R. P. Harvey), pp. 219-236. London: Elsevier.

100. Moretti, A., Caron, L., Nakano, A., Lam, J. T., Bernshausen, A., Chen, Y., Qyang, Y., Bu, L., Sasaki, M., Martin-Puig, S. et al. (2006). Multipotent embryonic isl1+ progenitor cells lead to cardiac, smooth muscle, and endothelial cell diversification. Cell 127, 1151-1165.

101. Mummery, C., Ward-Van Oostwaard, D., Doevendans, P., Spijker, R., Van Den Brink, S., Hassink, R., Van Der Heyden, M., Opthof, T., Pera, M., De La Riviere, A. B. et al. (2003). Differentiation of human embryonic stem cells to cardiomyocytes: role of coculture with visceral endoderm-like cells. Circulation 107, 2733-2740.

102. Naito, H., Melnychenko, I., Didié, M., Schneiderbanger, K., Schubert, P., Rosenkranz, S., Eschenhagen, T. and Zimmermann, W. H. (2006). Optimizing engineered heart tissue for therapeutic applications as surrogate heart muscle. Circulation 114, I72-I78.

103. Olivetti, G., Abbi, R., Quaini, F., Kajstura, J., Cheng, W., Nitahara, J. A., Quaini, E., Di Loreto, C., Beltrami, C. A., Krajewski, S. et al. (1997). Apoptosis in the failing human heart. N Engl. J. Med. 336, 1131-1141.

104. Olson, E. N. (2006). Gene regulatory networks in the evolution and development of the heart. Science 313, 1922-1927.

105. Osafune, K., Caron, L., Borowiak, M., Martinez, R. J., Fitz-Gerald, C. S., Sato, Y., Cowan, C. A., Chien, K. R. and Melton, D. A. (2008). Marked differences in differentiation propensity among human embryonic stem cell lines. Nat. Biotechnol.

106. Ottaviani, D., Ter Huurne, M., Elliott, D. A., Bellin, M. and Mummery, C. L. (2023). Maturing differentiated human pluripotent stem cells in vitro: methods and challenges. Development 150, dev201103.

107. Paige, S. L., Osugi, T., Afanasiev, O. K., Pabon, L., Reinecke, H. and Murry, C. E. (2010). Endogenous Wnt/β-catenin signaling is required for cardiac differentiation in human embryonic stem cells. PLoS One 5, e11134.

108. Paige, S. L., Plonowska, K., Xu, A. and Wu, S. M. (2015). Molecular regulation of cardiomyocyte differentiation. Circ. Res. 116, 341-353.

109. Parker, T. G., Packer, S. E. and Schneider, M. D. (1990). Peptide growth factors can provoke 'fetal' contractile protein gene expression in rat cardiac myocytes. J. Clin. Invest. 85, 507-514.

110. Piccolo, S., Agius, E., Leyns, L., Bhattacharyya, S., Grunz, H., Bouwmeester, T. and De Robertis, E. M. (1999). The head inducer cerberus is a multifunctional antagonist of nodal, BMP and Wnt signals. Nature 397, 707-710.

111. Ponikowski, P., Voors, A. A., Anker, S. D., Bueno, H., Cleland, J. G. F., Coats, A. J. S., Falk, V., González-Juanatey, J. R., Harjola, V.-P., Jankowska, E. A. et al. (2016). 2016 ESC guidelines for the diagnosis and treatment of acute and chronic heart failure: the task force for the diagnosis and treatment of acute and chronic heart failure of the ESC. Developed with the Special Contribution of the Heart Failure Association (HFA) of the ESC. Eur. J. Heart Fail 18, 891.

112. Porrello, E. R., Mahmoud, A. I., Simpson, E., Hill, J. A., Richardson, J. A., Olson, E. N. and Sadek, H. A. (2011). Transient regenerative potential of the neonatal mouse heart. Science 331, 1078-1080.

113. Ptaszek, L. M., Mansour, M., Ruskin, J. N. and Chien, K. R. (2012). Towards regenerative therapy for cardiac disease. Lancet 379, 933-942.

114. Qyang, Y., Martin-Puig, S., Chiravuri, M., Chen, S., Xu, H., Bu, L., Jiang, X., Lin, L., Granger, A., Moretti, A. et al. (2007). The renewal and differentiation of Isl1+ cardiovascular progenitors are controlled by a Wnt/β-Catenin pathway. Cell Stem Cell 1, 165-179.

115. Rochais, F., Mesbah, K. and Kelly, R. G. (2009). Signaling pathways controlling second heart field development. Circ. Res. 104, 933-942.

116. Rungarunlert, S., Techakumphu, M., Pirity, M. K. and Dinnyes, A. (2009). Embryoid body formation from embryonic and induced pluripotent stem cells: benefits of bioreactors. World J. Stem Cells 1, 11-21.

117. Saga, Y., Pulkki, K., Kallajoki, M., Henriksen, K., Parvinen, M. and Voipio-Pulkki, L.-M. (1999). MesP1 is expressed in the heart precursor cells and required for the formation of a single heart tube. Development 126, 3437-3447.

118. Saraste, A., Pulkki, K., Kallajoki, M., Henriksen, K., Parvinen, M. and Voipio-Pulkki, L.-M. (1997). Apoptosis in human acute myocardial infarction. Circulation 95, 320-323.

119. Schade, D., Drowley, L., Wang, Q. D., Plowright, A. T. and Greber, B. (2022). Phenotypic screen identifies FOXO inhibitor to counteract maturation and promote expansion of human iPS cell-derived cardiomyocytes. Bioorg. Med. Chem. 65.

120. Schneider, V. A. and Mercola, M. (2001). Wnt antagonism initiates cardiogenesis in Xenopus laevis. Genes Dev. 15.

121. Schulte-Merker, S. and Smith, J. C. (1995). Mesoderm formation in response to brachyury requires FGF signalling. Curr. Biol. 5, 62-67.

122. Sedmera, D. and Thompson, R. P. (2011). Myocyte proliferation in the developing heart. Dev. Dyn. 240, 1322-1334.

123. Sharma, A., Mckeithan, W. L., Serrano, R., Kitani, T., Burridge, P. W., Del Álamo, J. C., Mercola, M. and Wu, J. C. (2018a). Use of human induced pluripotent stem cell-derived cardiomyocytes to assess drug cardiotoxicity. Nat. Protoc.

124. Sharma, A., Zhang, Y., Buikema, J. W., Serpooshan, V., Chirikian, O., Kosaric, N., Churko, J. M., Dzilic, E., Shieh, A., Burridge, P. W. et al. (2018b). Stage-specific effects of bioactive lipids on human iPSC cardiac differentiation and cardiomyocyte proliferation. Sci. Rep. 8, 6618.

125. Shen, L., Jhund, P. S., Docherty, K. F., Vaduganathan, M., Petrie, M. C., Desai, A. S., KÃ¸Ber, L., Schou, M., Packer, M., Solomon, S. D. et al. (2022). Accelerated and personalized therapy for heart failure with reduced ejection fraction. Eur. Heart J. 43, 2573-2587.

126. Shiba, Y., Fernandes, S., Zhu, W.-Z., Filice, D., Muskheli, V., Kim, J., Palpant, N. J., Gantz, J., Moyes, K. W., Reinecke, H. et al. (2012). Human ES-cell-derived cardiomyocytes electrically couple and suppress arrhythmias in injured hearts. Nature 489, 322-325.

127. Shiba, Y., Gomibuchi, T., Seto, T., Wada, Y., Ichimura, H., Tanaka, Y., Ogasawara, T., Okada, K., Shiba, N., Sakamoto, K. et al. (2016). Allogeneic transplantation of iPS cell-derived cardiomyocytes regenerates primate hearts. Nature 538.

128. Singh, A., Ramesh, S., Cibi, D. M., Yun, L. S., Li, J., Li, L., Manderfield, L. J., Olson, E. N., Epstein, J. A. and Singh, M. K. (2016). Hippo signaling mediators Yap and Taz are required in the epicardium for coronary vasculature development. Cell Rep. 15, 1384-1393.

129. Smith, J. C., Price, B. M., Green, J. B., Weigel, D. and Herrmann, B. G. (1991). Expression of a Xenopus Homolog of Brachyury (T) is an immediate-early response to mesoderm induction. Cell 67, 79-87.

130. Soares, F. A. C., Chandra, A., Thomas, R. J., Pedersen, R. A., Vallier, L. and Williams, D. J. (2014). Investigating the feasibility of scale up and automation of human induced pluripotent stem cells cultured in aggregates in feeder free conditions. J. Biotechnol. 173, 53-58.

131. Später, D., Abramczuk, M. K., Buac, K., Zangi, L., Stachel, M. W., Clarke, J., Sahara, M., Ludwig, A. and Chien, K. R. (2013). A HCN4+ cardiomyogenic progenitor derived from the first heart field and human pluripotent stem cells. Nat. Cell Biol. 15, 1098-1106.

132. Stamos, J. L. and Weis, W. I. (2013). The β-catenin destruction complex. Cold Spring Harbor Perspect. Biol. 5, a007898.

133. Stanley, E. G., Biben, C., Elefanty, A., Barnett, L., Koentgen, F., Robb, L. and Harvey, R. P. (2002). Efficient Cre-mediated deletion in cardiac progenitor cells conferred by a 3'UTR-Ires-Cre Allele of the Homeobox Gene Nkx2-5. Int. J. Dev. Biol. 46, 431-439.

134. Sturzu, A. C., Rajarajan, K., Passer, D., Plonowska, K., Riley, A., Tan, T. C., Sharma, A., Xu, A. F., Engels, M. C., Feistritzer, R. et al. (2015). Fetal mammalian heart generates a robust compensatory response to cell loss. Circulation

135. Takahashi, K., Tanabe, K., Ohnuki, M., Narita, M., Ichisaka, T., Tomoda, K. and Yamanaka, S. (2007). Induction of pluripotent stem cells from adult human fibroblasts by defined factors. Cell 131, 861-872.

136. Tani, H., Tohyama, S., Kishino, Y., Kanazawa, H. and Fukuda, K. (2022). Production of functional cardiomyocytes and cardiac tissue from human induced pluripotent stem cells for regenerative therapy. J. Mol. Cell. Cardiol. 164, 83-91.

137. Titmarsh, D. M., Glass, N. R., Mills, R. J., Hidalgo, A., Wolvetang, E. J., Porrello, E. R., Hudson, J. E. and Cooper-White, J. J. (2016). Induction of human iPSC-derived cardiomyocyte proliferation revealed by combinatorial screening in high density microbioreactor arrays. Sci. Rep. 6, 24637.

138. Tohyama, S., Fujita, J., Fujita, C., Yamaguchi, M., Kanaami, S., Ohno, R., Sakamoto, K., Kodama, M., Kurokawa, J., Kanazawa, H. et al. (2017). Efficient large-scale 2D culture system for human induced pluripotent stem cells and differentiated cardiomyocytes. Stem Cell Rep. 9, 1406-1414.

139. Toyoshima, H. and Hunter, T. (1994). p27, a novel inhibitor of G1 Cyclin-Cdk protein kinase activity, is related to p21. Cell 78, 67-74.

140. Ueno, S., Weidinger, G., Osugi, T., Kohn, A. D., Golob, J. L., Pabon, L., Reinecke, H., Moon, R. T. and Murry, C. E. (2007). Biphasic role for Wnt/β-catenin signaling in cardiac specification in zebrafish and embryonic stem cells. Proc. Natl. Acad. Sci. U.S.A. 104, 9685-9690.

141. Uosaki, H., Magadum, A., Seo, K., Fukushima, H., Takeuchi, A., Nakagawa, Y., Moyes, K. W., Narazaki, G., Kuwahara, K., Laflamme, M. et al. (2013). Identification of chemicals inducing cardiomyocyte proliferation in developmental stage-specific manner with pluripotent stem cells. Circ. Cardiovasc. Genetics 6, 624-633.

142. Vahdat, S., Pahlavan, S., Mahmoudi, E., Barekat, M., Ansari, H., Bakhshandeh, B., Aghdami, N. and Baharvand, H. (2022). Expansion of human pluripotent stem cell-derived early cardiovascular progenitor cells by a cocktail of signaling factors. Sci. Rep. 9, 16006.

143. V on Gise, A., Lin, Z., Schlegelmilch, K., Honor, L. B., Pan, G. M., Buck, J. N., Ma, Q., Ishiwata, T., Zhou, B., Camargo, F. D. et al. (2012). YAP1, the nuclear target of hippo signaling, stimulates heart growth through cardiomyocyte proliferation but not hypertrophy. Proc. Natl. Acad. Sci. USA 109, 2394-2399.

144. Wang, Y., Hu, G., Liu, F., Wang, X., Wu, M., Schwarz, J. J. and Zhou, J. (2014). Deletion of yes-associated protein (YAP) specifically in cardiac and vascular smooth muscle cells reveals a crucial role for YAP in mouse cardiovascular development. Circ. Res. 114, 957-965.

145. Xin, M., Kim, Y., Sutherland, L. B., Qi, X., Mcanally, J., Schwartz, R. J., Richardson, J. A., Bassel-Duby, R. and Olson, E. N. (2011). Regulation of insulin-like growth factor signaling by Yap governs cardiomyocyte proliferation and embryonic heart size. Sci. Signal. 4, ra70.

146. Xin, M., Kim, Y., Sutherland, L. B., Murakami, M., Qi, X., Mcanally, J., Porrello, E. R., Mahmoud, A. I., Tan, W., Shelton, J. M. et al. (2013). Hippo pathway effector Yap promotes cardiac regeneration. Proc. Natl. Acad. Sci. U.S.A. 110, 13839.

147. Yamada, S. and Takakuwa, A. T. (ed.) (2012). Introduction – developmental overview of the human embryo. In The Human Embryo. IntechOpen.

148. Yamaguchi, T. P., Takada, S., Yoshikawa, Y., Wu, N. and Mcmahon, A. P. (1999). T (Brachyury) is a direct target of Wnt3a during paraxial mesoderm specification. Genes Dev. 13, 3185-3190.

149. Yang, D., Gomez-Garcia, J., Funakoshi, S., Tran, T., Fernandes, I., Bader, G. D., Laflamme, M. A. and Keller, G. M. (2022). Modeling human multi-lineage heart field development with pluripotent stem cells. Cell Stem Cell 29, 1382.

150. Ye, B., Hou, N., Xiao, L., Xu, Y., Boyer, J., Xu, H. and Li, F. (2015). APC controls asymmetric Wnt/β-catenin signaling and cardiomyocyte proliferation gradient in the heart. J. Mol. Cell. Cardiol. 89, 287-296

151. Ye, L., Qiu, L., Zhang, H., Chen, H., Jiang, C., Hong, H. and Liu, J. (2016). Cardiomyocytes in young infants with congenital heart disease: a three-month window of proliferation. Sci. Rep. 6, 23188.

152. Ye, L., D'Agostino, G., Loo, S. J., Wang, C. X., Su, L. P., Tan, S. H., Tee, G. Z., Pua, C. J., Pena, E. M., Cheng, R. B. et al. (2018). Early regenerative capacity in the porcine heart. Circulation 138, 2798-2808.

153. Zhai, J., Xiao, Z., Wang, Y. and Wang, H. (2022). Human embryonic development: from peri-implantation to gastrulation. Trends Cell Biol. 32, 18-29.

154. Zhang, J., Wilson, G. F., Soerens, A. G., Koonce, C. H., Yu, J., Palecek, S. P., Thomson, J. A. and Kamp, T. J. (2009). Functional cardiomyocytes derived from human induced pluripotent stem cells. Circ. Res. 104, e30-e41.

155. Zhu, K., Wu, Q., Ni, C., Zhang, P., Zhong, Z., Wu, Y., Wang, Y., Xu, Y., Kong, M., Cheng, H. et al. (2018a). Lack of remuscularization following transplantation of human embryonic stem cell-derived cardiovascular progenitor cells in infarcted nonhuman primates. Circ. Res. 122, 958-969.

156. Zhu, W., Zhang, E., Zhao, M., Chong, Z., Fan, C., Tang, Y., Hunter, J. D., Borovjagin, A. V., Walcott, G. P., Chen, J. Y. et al. (2018b). Regenerative potential of neonatal porcine hearts. Circulation 138, 2809-2816.

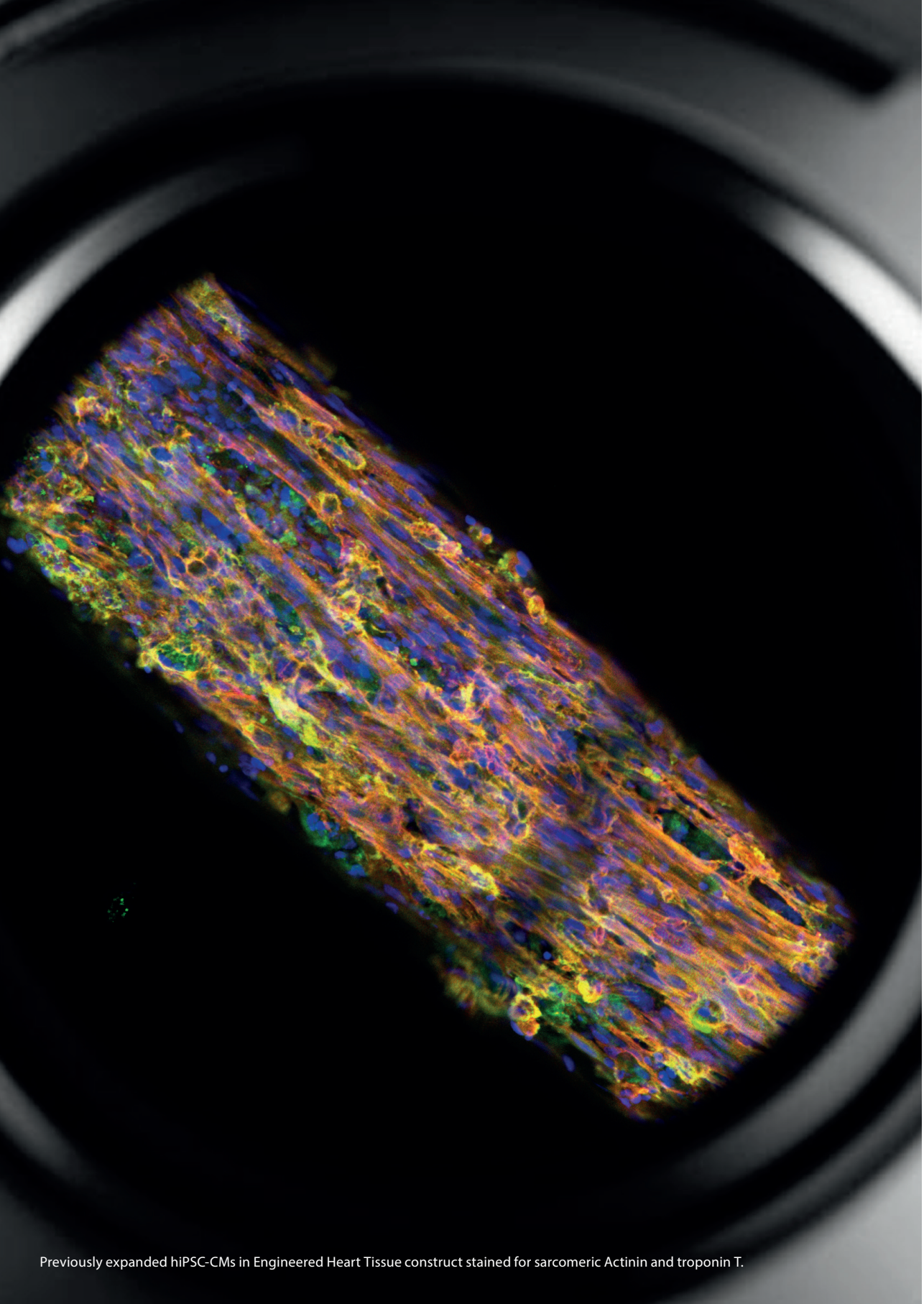

Previously expanded hiPSC-CMs in Engineered Heart Tissue construct stained for sarcomeric Actinin and troponin T.

Chapter 3

Wnt Activation and Reduced Cell-Cell Contact Synergistically Induce Massive Expansion of Functional Human iPSC-Derived Cardiomyocytes

Published in: Cell stem Cell, 2020

Jan W. Buikema*, Soah Lee*, **Renée G.C. Maas**§, William R. Goodyer§, Orlando Chirikian§, Guang Li, Yi Miao, Sharon L. Paige, Daniel Lee, Haodi Wu, David T. Paik, Siyeon Rhee, Lei Tian, Francisco X. Galdos, Nazan Puluca, Benjamin Beyersdorf, James Hu, Aimee Beck, Sneha Venkamatran, Srilatha Swami, Paul Wijnker, Maike Schuldt, Larissa M. Dorsch, Alain van Mil, Kristy Red-Horse, Joy Y. Wu, Caroline Geisen, Michael Hesse, Vahid Serpooshan, Stefan Jovinge, Bernd K. Fleischmann, Pieter A. Doevendans, Jolanda van der Velden, K. Christopher Garcia, Joseph C. Wu, Joost P.G. Sluijter, and Sean M. Wu

*These authors contributed equally.

§These authors contributed equally.

ABSTRACT

Modulating signaling pathways including Wnt and Hippo can induce cardiomyocyte proliferation in vivo. Applying these signaling modulators to human induced pluripotent stem cell-derived cardiomyocytes (hiPSC-CMs) in vitro can expand CMs modestly (<5-fold). Here, we demonstrate massive expansion of hiPSC-CMs in vitro (i.e., 100- to 250-fold) by glycogen synthase kinase-3β (GSK-3β) inhibition using CHIR99021 and concurrent removal of cell-cell contact. We show that GSK-3β inhibition suppresses CM maturation, while contact removal prevents CMs from cell cycle exit. Remarkably, contact removal enabled 10 to 25 times greater expansion beyond GSK-3β inhibition alone. Mechanistically, persistent CM proliferation required both LEF/TCF activity and AKT phosphorylation but was independent from yes-associated protein (YAP) signaling. Engineered heart tissues from expanded hiPSC-CMs showed comparable contractility to those from unexpanded hiPSC-CMs, demonstrating uncompromised cellular functionality after expansion. In summary, we uncovered a molecular interplay that enables massive hiPSC-CM expansion for large-scale drug screening and tissue engineering applications.

GRAPHICAL ABSTRACT

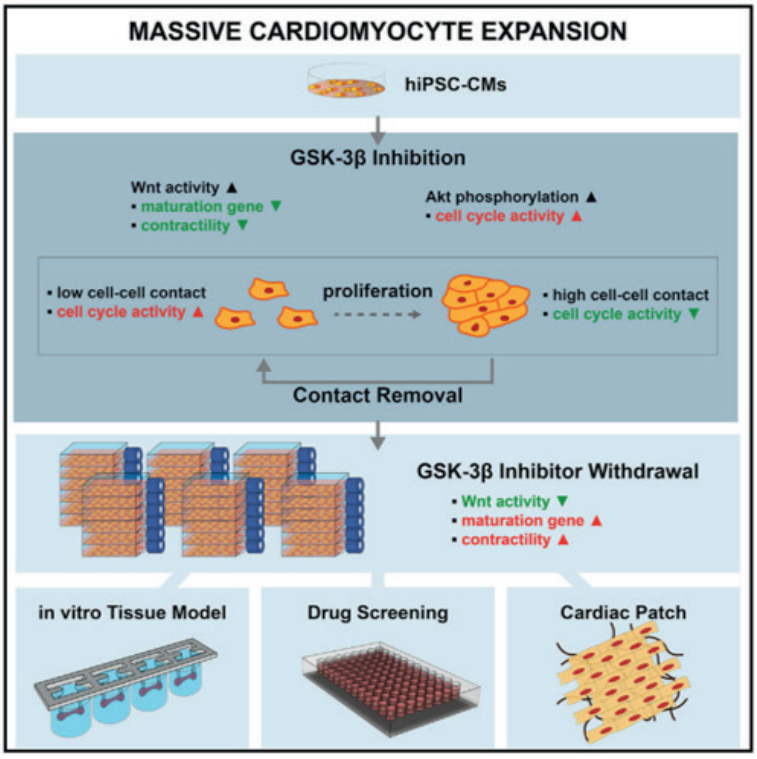

INTRODUCTION

Adult mammalian heart has limited capacity for regeneration. Cardiac injuries such as myocardial infarction lead to significant cardiomyocyte (CM) loss and subsequent heart failure with significant morbidity and mortality. Cell-based therapeutic approaches such as injection of stem cell-derived cells or transplantation of engineered cardiac tissue patches have shown promise to re-muscularize the damaged myocardium and enhance cardiac functions (Chong et al., 2014; Grego-Bessa et al., 2007; Liu et al., 2018; Ogle et al., 2016; Senyo et al., 2014; Shiba et al., 2016) . Since the myocardium is densely packed with CMs, cell-based therapy requires introductions of billions of human CMs (Chong et al., 2014; Liu et al., 2018) . In principle, pluripotent stem cells provide an unlimited supply of human CMs, however, in practice the generation of therapeutically relevant number of human CMs still remains an extremely labor-and time-intensive process, despite robust and highly efficient directed differentiation protocols.

To overcome this hurdle, several studies have focused on identifying molecules for promoting proliferation of differentiated CMs from pluripotent stem cells (PSCs) (Mills et al., 2019; Sharma et al., 2018; Titmarsh et al., 2016; Uosaki et al., 2013). However, when these molecules were applied to induce expansion of human PSC-derived CMs in vitro, the extent of proliferation has generally been modest (3-4-fold), which limits the use of these cells for cell-based therapeutic applications.

This modest extent of proliferation in vitro may result from contact inhibition of proliferation, which is a natural regulatory process of normal tissue morphogenesis, homeostasis, and regeneration. Contact inhibition of proliferation has been well-described in many cell types other than cardiomyocytes including epithelial cells and endothelial cells (Grazia Lampugnani et al., 2003; Kim and Asthagiri, 2011; Puliafito et al., 2012) , where cell proliferation is cell-density dependent. When human induced PSCs (hiPSCs) undergo directed cardiac specification and differentiation in vitro, the differentiated CMs become fully confluent in a dish. It is in this densely-packed cardiomyocytes condition that screening of mitogen candidates have been performed (Mills et al., 2017, 2019; Sharma et al., 2015; Titmarsh et al., 2016). Hence, we asked whether the removal of contact inhibition would further promote hiPSC-CM proliferation beyond that achieved in the presence of mitogen. In fact, a few previous studies including our earlier work on compensation of CM loss in the fetal heart by residual unablated CMs and another study on targeted disruption of cell-cell contacts in the mouse heart show evidence of cell cycle re-entry and enhanced CM proliferation in vivo (Li et al., 2015; Sturzu et al., 2015) . Therefore, we hypothesize that combined inhibition of cell-cell contacts and treatment with CM mitogen would enable continuous CM proliferation and expansion.

Here, we demonstrate for the first time the ability to massively expand functional hiPSC-CMs by continuous treatment of GSK-3β inhibitor CHIR-99021and concomitant removal of cell-cell contact. We chose CHIR-99021 (CHIR) as the hiPSC-CM mitogen because several studies

have previously demonstrated that it was the most potent CM mitogen in vitro (Mills et al., 2017,2019; Sharma et al., 2018; Titmarsh et al., 2016) . We show that hiPSC-CMs exhibit contact-mediated inhibition of proliferation, indicating that the removal of cell-cell contacts is essential to enable the maintenance of their proliferative capacity through continuous passaging. We show that the withdrawal of CHIR or treatment with C59, a small molecule Wnt antagonist, result in rapid cell-cycle exit and restoration of mature contractile, electrophysiological, and cellular characteristics. Further mechanistic studies identified the role of canonical Wnt signal via LEF/TCF to delay hiPSC-CM maturation, and the stimulatory role of AKT T308 and HSP27 phosphorylation in enhancing hiPSC-CM proliferation by increasing cell cycle activity. Lastly, we demonstrate that the expanded hiPSC-CMs exhibit fully differentiated and contractile phenotype as the unexpanded hiPSC-CM and are therefore an excellent cell source for the mass production of engineered heart tissues. Together, these studies reveal a novel and robust method, the mechanistic explanation, and a proof-of-principle demonstration of a translational approach to achieve massive hiPSC-CM expansion (>1 billion) needed for future cardiac regenerative strategies in patients with cardiomyopathy or congenital heart defects.

METHODS

Cell culture. Four previously established hiPSC lines (SCVI-111, Sendai virus reprogrammed, peripheral blood mononuclear cells (PBMCs), male; SCVI-113, Sendai virus reprogrammed, PBMCs, male; SCVI-202 Sendai virus reprogrammed, PBMCs, female; SCVI-273, Sendai virus reprogrammed, PBMCs, female (Matsa et al., 2016)) were maintained in DMEM/F12 (ThermoFisher) supplemented with the essential eight (E8) (Thermo Fisher) growth factors in a Matrigel (Corning) coated (1:400 for 24h) polystyrene 2D culture system. Upon 80–90% confluency, cells were dissociated in PBS with 0.5mM EDTA for 5–10 minutes at 37 °C. Dissociation was performed with gentle trituration to obtain small aggregates of undifferentiated hiPSCs. Passaging was performed in 1:15–20 splitting ratios or 10,000 cells per cm2 to achieve low density and reach full confluency within 4–5 days. For the first 24h after replating, 10βM of ROCK inhibitor Y-27632 was included in the hiPSC maintenance media. hiPSC-CM differentiation was performed using the previously described canonical Wnt stimulation and inhibition protocol (Lian et al., 2013) in RPMI 1640-based differentiation media supplemented with B27 minus insulin (Invitrogen). Between day 0–2, a gradient of CHIR99021 (Seleckchem) concentrations (3.0, 4.0, 5.0, 6.0, 7.0, 8.0 μM) was used. Between day 3–5, Wnt-C59 (2.0 μM) (Selleckchem) was added to the differentiation media. At day 7, B27 with insulin was added to the differentiation media. At day 11, wells that contain more than 80% beating cells were treated with TrypLE Select Enzyme 10X (Invitrogen) at 37 °C for 10–40 minutes. Gentle rocking was performed every 10 minutes. Preparations of single dissociated cells were generated with very gentle trituration and transferred to a 15 mL conical tube containing a wash buffer (PBS with 20% FBS). Cells were gently centrifuged at 1000 RPM for 3

minutes and immediately replated in 1:10 to 1:15 split ratios in RPMI 1640 + B27 1× with 10% Knock Out Serum Replacement (Gibco) and Thiazovivin 1.0 µM (Selleckchem). At day 12, hiPSC-CMs were further expanded for downstream assays in RPMI 1640 + B27 1× differentiation media supplemented with 2.0 to 4.0 µM CHIR99021 (Selleckchem). For the first 24h after passaging, 10% Knock Out Replacement Serum and Thiozovivin 1.0 µM were added to the differentiation media.

Generation of eGFP-anillin^{+} expressing hiPSCs. The previously described eGFP-anillin expression cassette (Hesse et al., 2012) was inserted into the AAV-CAGGS vector (Addgene #22212). hiPSCs (iLB-C1–30m-r12), kindly provided by Dr. O. Brüstle (Univ. of Bonn), were co-transfected (NEONTransfection, Invitrogen) with the AAV-CAGGS-eGFP-anillin vector, the hAAVS1 1L TALEN vector (Addgene #35431) and the hAAVS1 1R TALEN vector (Addgene, #35432) for targeted integration into the AAVS1 locus and several independent eGFP-anillin expressing hiPSC lines were generated. Targeted integration into the AAVS1 locus was proven by a PCR strategy, copy numbers were determined by qPCR. The eGFP-anillin+ expressing hiPSC line used was shown to have one specific AAVS1 integration and one random integration site without known functional consequence.

Contact inhibition study. For high cell-cell contact condition (i.e. dense), hiPSC-CMs were either left unpassaged or passaged without splitting, while for low cell-cell contact condition (i.e. sparse), the cells were passaged at 1:10 – 1:15 splitting ratio, depending on cell confluency of the original well. To examine paracrine effect, the conditioned media was collected from densely plated hiPSC-CMs, concentrated using Pierce™ protein concentrator (3K MWCO; Thermoscientific 88512). The concentrated factors were diluted with fresh expansion media (B27 + CHIR) at different ratios (1×, 0.1×, 0.01×), then given to sparsely plated hiPSC-CMs. To examine direct cell-cell contact effect, 100,000 hiPSC-CMs were plated in small surface area (i.e. 48-well-plate) to induce dense culture, while the same number of cells were plated in large surface (i.e. 6-well-plate) for sparse condition. For immunostaining, cells were fixed at 4% paraformaldehyde for 15 min at room temperature, washed three times with washing buffer (0.1% Tween-20/PBS), permeabilized and blocked with blocking buffer (3% bovine serum albumin/2% goat serum/0.01% saponin/PBS for 30 min at room temperature. Corresponding primary antibodies were diluted at desired ratio in blocking buffer (TnT: 1:250, Ki67: 1:200, phH3: 1:400) and were incubated with cells overnight at 4 °C on shaker. Next day, the cells were washed three times with washing buffer, each time for 5 min at room temperature on shaker. Then, the appropriate secondary antibodies were diluted in blocking buffer at 1:300 dilution ratio and were incubated with cells for 1 hr at room temperature on shaker. After the incubation, the samples were washed three times to remove any unbound secondary antibodies. Nuclei were counterstained using Dapi.

Cardiac tissue generation. Engineered Heart Tissues were with small modifications generated as described previously (Hansen et al., 2010). Briefly, induced pluripotent stem cell-derived cardiomyocytes were detached and resuspended in culture medium containing bovine fibrinogen (5 mg/ml), aprotinin (2.5 µg/ml) and 10% Matrigel. EHTs of 1×106 cardiomyocytes each were casted by mixing the reconstitution mix (97 µl/EHT) with thrombin (3 µl/EHT, 100 U/ml) and pipetting it into the casting molds. Fibrin polymerization (37 °C, 7% CO2, 98% RH, 2 h) led to the formation of a muscle strip. The EHTs were transferred to culture medium (Dulbecco's modified Eagle's medium) containing 10% horse serum, 1% penicillin/streptomycin, 10 µg/ml insulin and 33 µg/ml aprotinin and maintained at 21% oxygen, 7% CO2 and 37 °C in a humidified cell culture incubator for 25 days. Contractility measurements were performed in culture medium as described previously (Hansen et al., 2010).

Small molecules / growth factors. PNU74654, MK2206, CHIR99021, C59 and Palbociclib were obtained commercially. CHIR99021 and C59 were used depending on the assay at 2.0 or 4.0 µM final concentration and PNU74654, MK2206 and Palbociclib were used at 32, 1.0 and 1.0 µM, respectively. For in vitro studies, recombinant scFv-DKK1c and RSPO were expressed and purified as previously described (Janda et al., 2017) and used in final concentrations of 200 and 25 nM, respectively. Recombinant Wnt3A protein was purchased commercially and added in 100 ng/mL final concentration.

Protein expression analysis. Immunocytochemistry was performed with overnight incubation of primary antibodies (listed below) followed by 2-hour incubation with Alexa-conjugated fluorescent secondary antibodies. Immunostaining images were captured using confocal (Zeiss LSM 710) or epifluorescence (Leica DM IL) microscopy. Kinase phosphorylation screening assays were performed using the Proteome Profiler Human Phospho-Kinase Array Kit containing 43 human kinases. Western blotting was performed to validate the kinase screen results. Total protein expression was measured with a gel imager and quantified based on pixel intensity (BioRad). Only lanes from the same gel were used for displaying and quantification. Luciferase assays Day 12 hiPSC-CMs were transfected for 48 hours with a TCF reporter plasmid or the mutant reporter plasmid using Lipofectamine. 72 h after transfection cells were treated with various small molecules for an additional 24 h and then lysed and mixed with luciferase substrate. The expression of firefly luciferase was finally measured using a 96-well micro plate reader. Real-time PCR expression analysis For quantitative analysis of gene expression, RNA was extracted with a lysis buffer from hiPSC-CMs and stored at −80 °C. Total RNA from each sample was purified from cell lysate using a RNA purification kit. cDNA was made using a cDNA synthesis kit. Quantitative PCR was performed using a 96-well thermocycler system (Biorad) with SYBR Green substrate for 40 cycles. All primers sequences were obtained from the PrimerBank (Massachusetts General Hospital / Harvard Medical School) online database. Oligos were synthesized at Stanford University.

Single cell gene expression analysis. For single cell gene expression analysis, day 12 hiPSC-CMs were treated with DMSO, CHIR99021 or C59 for 24 hours. At the end of treatment hiPSC-CM aggregates were dispersed with TrypLE Select Enzyme as described above and dissociated with gentle trituration. Single cells were washed and re-suspended in ice cold RPMI 1640 with B27 supplement and then captured using the 10x Genomics platform. RNA amplification and generation of cDNA expression libraries were performed prior to sequencing using HiSeq-4000 (Illumina). The three data files (CTR, CHIR and C59) (GEO accession number: GSE148586) were merged and subsequent analysis was performed using Seurat software. Cells with poor quality and doublets/multiplets were filtered out based on aberrant gene numbers, total transcript counts, percentage of reads to mitochondrial genes, and housekeeping gene counts (GAPDH, SOD1, BLVRB, PSMB3). To remove batch effect, Seurat integration tool was employed (Stuart et al., 2019).

Flow cytometry. Freshly isolated hiPSC-CMs were fixed in PFA 4% for 5 min and incubated with primary antibody against TnT for 1 hr. After multiple washings, an Alexa488-conjugated mouse secondary antibody was added for 30 min of incubation followed by washings to remove unbound antibodies. Samples were then analyzed using the FACSCalibur® flow cytometer (BD Biosciences) and data processed using the FlowJo® software (TreeStar).

Electrophysiological studies. hiPSC-CM treated with DMSO, CHIR, or CHIR>C59 were passaged 3 times in RPMI 1640 + B27 Supplement for an equivalent number of days and seeded sparsely on Matrigel© coated 8 mm coverslips. Cells on coverslips were immersed in extracellular solution containing 140 mM NaCl, 2.8 mM KCl, 2 mM CaCl2, 2 mM MgCl2, 10 mM HEPES, and 10 mM glucose, at pH 7.4. Patch electrodes were filled with an intracellular solution containing 140 mM potassium gluconate, 10 mM NaCl, 2 mM MgCl2, 10 mM HEPES, 1 mM EGTA, 4 mM Mg-ATP, and 0.3 mM Na-GTP, at pH 7.3, hence, giving resistances of ~2–5 M'Ω. Spontaneous CM action potentials were recorded at room temperature using a sharp current clamp mode. For calcium transient recording, iPSC-CMs were loaded with 5 μM Fluo-4 AM for 5–10 mins at 37 °C and were washed 3 times afterward. Spontaneous calcium transients were observed at 37 °C with a Carl Zeiss LSM 510 confocal microscopy (Göttingen, Germany) and a 63× objective (Plan-Apochromat 63×/1.40 Oil DIC M27). Calcium signalings were recorded using line-scanning mode, and the Imaging data were analyzed with a custom-made Mat lab algorithm. Transient amplitude was expressed as ΔF/F0.

Single cell patterning and contractility. For single cell contractile assays, hiPSC-CMs were plated on polyacrylamide hydrogels of 10 kPa stiffness with micro-patterned Matrigel© to achieve a final hiPSC-CM aspect ratio of 7:1 (Lee et al., 2020). After 3–6 days of culture in the presence of DMSO, CHIR, or CHIR>C59, contractility of hiPSC-CMs were measured by recording contractile motion of at least 10 individual cells per group using high speed microscope

camera (frame rate: 75 fps, shutter speed: 1/150 sec) and motion velocity analysis was performed using Sony Cell Motion Imaging System (SI8000) (Hayakawa et al., 2014). Briefly, motion velocity analysis calculates contraction/relaxation velocity and deformation distance by computationally measuring movement of pixels in the consecutive video images. Since cells are patterned into known surface area (1800 μm2) and attached to hydrogel substrate of known stiffness (10 kPa), maximum contractile force was calculated using Young's modulus equation.

$$max.\,contractile\,force = \frac{max.\ contractile\,deformation\,distance}{initial\,cell\,length\,determined\,by\,patterning\,(112\,\mu m)} \times \frac{Surface\,Area}{Young's\,modulus}$$

After recordings, cells were fixed immuno-stained with antibodies to cTnT and α-actinin, counterstained with DAPI, and imaged using Zeiss LSM710 confocal microscope. Quantification of sarcomere alignment was performed using FIJI software with an additional analysis package (Orientation J) to determine the angle of z-disc-registered sarcomeric α-actinin. For example, 90 ° angle of z-disc-registered sarcomeric α-actinin represents myofibril alignment along cellular long axis.

Biophysical effect examination using hydrogel substrate. To modulate substrate stiffness, polyacrylamide hydrogels were prepared as previously described (Lee et al., 2019, 2020). Briefly, 40% of acrylamide and 2% bisacrylamide stock solution was diluted with deionized water to make polyacrylamide hydrogel precursor solution with the final concentration of acrylamide at 8% and the final concentration of bisacrylamide at 0.06%, 0.15%, and 0.6%, to achieve hydrogel stiffness of 1, 10, and 60 kPa, respectively. The hydrogel precursor solution was sandwiched between two coverslips and photo-crosslinked under light (365 nm, 4 mW/cm2) for 5 min. After photocrosslinking the hydrogel, one coverslip was peeled off to reveal a hydrogel substrate. Day 24 hiPSC-CMs were plated on the hydrogel substrate and cultured for 5 days in expansion media (B27+CHIR 2μM) for 5 days before fixation. Immunostaining was done as described above. Rabbit-derived Yap antibody was diluted at 1:50.

YAP inhibition study. To pharmacologically inhibit YAP activity, a well-known inhibitor, verteporfin (SML0534, Sigma) was administered to day 22 hiPSC-CMs at different concentrations (0.1, 1, 10, 50, 100 μM) for 24 hours. 50, 100 μM verteporfin treatment led to cell death. Next day, the cells were fixed and stained for YAP, TnT, and Ki67 as described above.

***In vivo studies* in mice.** Pregnant mice at gestational day 16.5 and 4-day-old CD1 mice (Jackson Laboratory, Bar Harbor, ME) were given 4–6 consecutive daily intraperitoneally injections of CHIR at a dose of 50mg/kg. After 4 days (embryonic studies) or 6 days (neonatal studies) post-injection, euthanasia was performed by first sedating the mice via isoflurane (inhalant, 2% in 100% oxygen, neonate placed on a warm pad), followed by a secondary cervical dislocation. Death was verified after euthanasia and prior to disposal. All animal experiments were approved by the animal care and use committee (APLAC) at Stanford University. All experiments were performed in accordance with relevant guidelines and regulations of Stanford University. Body and heart weights were measured by a blinded observer. Freshly isolated adult hearts were dissected from mouse chest cavity and washed in PBS to remove excess blood. The postnatal hearts were incubated in 30% sucrose in phosphate buffered solution (PBS) overnight followed by stepwise incubation with a graded concentration of OCT in PBS for cryo-sectioning. Following cryopreservation, hearts were cut into 10 µm sections and lightly fixed in 4% paraformaldehyde in PBS prior to immunostaining. All quantitative analyses of the histological sections were performed on numerically coded animals in an observer-blinded fashion to prevent subjective bias in data analysis.

Statistical analysis. Cell counts were performed with Luna-FL fluorescence cell counter, BD flow cytometry system, Image J software or manually. Numerical data are presented individually or as mean ± standard deviation (SD), standard error (SE) or standard error of the mean (SEM). Statistical significance was performed using Excel or Prism software. Values of $p<0.05$ were considered statistically significant.

Key resources table

REAGENT or RESOURCE	SOURCE	IDENTIFIER
Antibodies		
Cardiac Troponin T	Fisher	MS-295
KI67	Abcam	Ab15580
Phospho-Histone 3	Cell Signaling	9701
alpha sarcomeric actinin	Sigma-Aldrich	A7811
MLC2V	Abcam	ab48003
phospo AKT T308	Cell Signaling	#9275
Cyclin D2	Santa Cruz	SC-452
YAP	Santa Cruz	SC15407
Proteome Profiler Human Phospho-Kinase Array Kit	R&D systems	ARY003B
Biological Samples		
TCF reporter plasmid	Addgene	M50
Mutant TCF reporter plasmid	Addgene	M51
Chemicals, Peptides, and Recombinant Proteins		
CHIR99021	Selleckchem	S2924 / S1263
C59	Selleckchem	S737
Verteporfin	Sigma	SML0534
PNU74654	Selleckchem	S8429
MK2206	Selleckchem	S1078
Palbociclib	Selleckchem	S1116
Wnt3A	R&D systems	5036-WN-010
Lipofectamine	Invitrogen	L3000001
luciferase substrate	Promega	E1910
Critical Commercial Assays		
Bovine fibrinogen	Sigma	F8630
Aprotin	Sigma	A1153
Matrigel	Corning	35234
Thrombin	Sigma	T7513
Insulin	Sigma	I9278
ROCK inhibitor Y-27632	Selleckchem	S1049
RNeasy Plus Mini Kit	Qiagen	74134
HotStart-IT Sybr	Invitrogen	75762
Superscript cDNA kit	Invitrogen	11904018
RPMI 1640	Invitrogen	12633012
B27 supplement	Invitrogen	17504044
Deposited Data		
Single cell RNA sequencing	10x	GSE148586
Experimental Models: Cell Lines		
hiPSC line	Stanford Biobank	SCVI111
hiPSC line	Stanford Biobank	SCVI113
hiPSC line	Stanford Biobank	SCVI202
hiPSC line	Stanford Biobank	SCVI273
Experimental Models: Organisms/Strains		
C57BL/6J Mice	Jackson Laboratory	000664
Software and Algorithms		
Prism 8	Graphpad	
Excel 2016	Microsoft	
Seurat	Satijalab.org	
FlowJo®	TreeStar	

RESULTS

Glycogen synthase kinase-3β (GSK-3β) inhibition promotes hiPSC-CM proliferation in a cell-density dependent manner through direct cell-cell contact

Previous studies have shown CHIR-mediated GSK-3β inhibition leads to cardiomyocyte proliferation in mouse fetal heart, embryonic stem cell-derived cardiomyocytes (Buikema et al., 2013a, 2013b) and hiPSC-CM (Mills et al., 2017; Sharma et al., 2018). Despite the known role of GSK-3β inhibitor as a mitogen, the extent of cardiomyocyte proliferation has been reported to be modest (< 3- to 5-fold increase in total cell number) (Mills et al., 2017; Sharma et al., 2018) and were all performed in densely-plated cell cultures. We investigated whether disruption of cell-cell contact by low-density passaging would further promote hiPSC-CM proliferation. iPSC lines from healthy individuals were differentiated into cardiomyocytes using small molecule-based Wnt-modulated protocol (**Figure 1A**) (Lian et al., 2012, 2013). The differentiating cells displayed stage-specific gene expression for pluripotent stem cells (NANOG), mesoderm (MESP1) and cardiac progenitor cells (Isl1) before committing to the cardiomyogenic lineage (**Figure S1A–B**). When hiPSC-CMs were passaged at low-density, the total cell number increased by 8-, 8-, and 4-folds at each passage, resulting overall in a 241-fold increase in hiPSC-CM number (**Figure 1B**). In contrast, the fold-change in cell number in densely passaged group and w/o passaging group remained comparable, and at the end of three passages or 3 weeks, the number increase was ~10-fold (Figure 1B). The CM number increase with low-density passage was supported by their increase in cell cycle activity (**Figure 1C–F**) compared with densely passaged or un-passaged CMs assessed by cell cycle marker Ki67 (**Figure 1C–D**). Moreover, fraction of mitotic CMs was at 1% without passaging and remained at 1% upon passaging at high cell density, but it was only when CMs were passaged at low-density that led to significant increase in mitotic CM fraction up to 10% (**Figure 1E–F**). This indicates that the maintenance of low cell density is necessary to sustain active cell cycle activity in CMs. Taken together, we demonstrate that massive expansion of hiPSC-CMs can be achieved through sparse passaging in the presence of CHIR. We then asked whether hiPSC-CMs at high cell density inhibit CM proliferation and induce cell cycle exit by their secretion of anti-proliferative paracrine factors (**Figure 1G**). We did not find any significant changes in the proportion of Ki67-expressing hiPSC-CMs between different conditioned media treatment groups (**Figure 1H–I**). Next, we examined whether the presence of cell-cell contact induces cell cycle exit in hiPSC-CMs (**Figure 1J**). Interestingly, densely plated hiPSC-CMs significantly down-regulated Ki67 and pHH3, suggesting that cell-cell contact inhibits cell cycle activity in hiPSC-CMs (**Figure 1K–N**). Taken together, we demonstrate here that cell-cell contact is a major barrier to hiPSC-CM proliferation and that prevention of cell-cell contact is critical to maintain CHIR-induced CM proliferation.

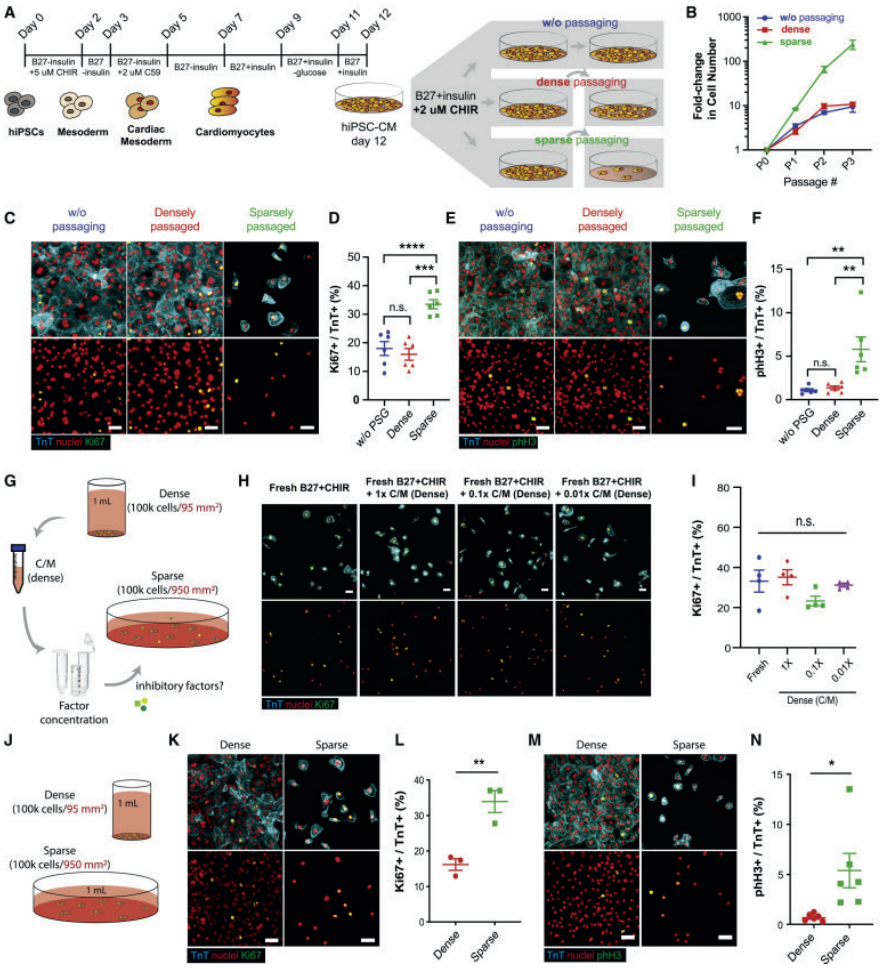

Figure 1: GSK-3β inhibition promotes hiPSC-CM proliferation in a cell-density dependent manner. (A) Schematic of Wnt-modulated directed cardiac differentiation and subsequent expansion. Day 12, hiPSC-CMs were plated densely (~100,000 cells/cm2), sparsely (~10,000 cells/cm2) for serial passaging or cultured without passaging (~500,000-1M cells/cm2) in the presence of CHIR99021 (CHIR) (2.0 M) (B) Graph displaying growth of hiPSC-CMs represented as fold increase over day 12 for each passage (P) number. Data are means ± SEM. (C) Immunohistochemistry for proliferation marker Ki67 (green), cardiac troponin T (TnT) (cyan) and nuclei (red) in hiPSC-CMs for the indicated culture conditions. (D) Quantification of the Ki67+ hiPSC-CMs mentioned in C. Immunofluorescence (E) and quantification (F) of the mitotic phospho-histone H3 (pHH3) (green), TnT (cyan) and nuclei (red) in hiPSC-CMs cultured in varying cell densities. Data (B-F) are in means ± SEM. *p<0.05, ****p<0.001, n.s. p>0.05 by One-way ANOVA with Tukey's post hoc multiple comparisons test. (G) Illustration of conditioned-media of densely cultured cells, subsequent factor concentration and application to sparsely cultured hiPSC-CMs. (H) Immunofluorescence images for the indicated antibodies in sparsely passaged hiPSC-CMs cultured with varying concentrations of conditioned medium from densely cultured hiPSC-CMs. (I) Quantification of the percentages of Ki67+/TnT+ cells in H. Data are means ± SEM. n.s. p>0.05 by One-way ANOVA Dunnett's post hoc multiple comparisons to control "no C/M" group (blue open circle). (J) Schematic of culturing fixed hiPSC-CMs cell numbers with (dense) or without (sparse) cell-cell contact. Immunofluorescence (K) and quantification (L) of the percent proliferative (Ki67+/TnT+) cells with (dense) and without sparsely cell-cell contact. Same for mitotic (pHH3+/TnT+) cells (M) and (N). Data are means ± SEM. *p<0.05, **p<0.01 by unpaired t-test. Supplementary Table 1 specifies the replicates per experiment.

Glycogen synthase kinase-3β inhibition and low-density passaging result in massive expansion of beating hiPSC-CMs

To determine the maximum extent of hiPSC-CMs expansion through combined GSK-3β inhibition and low-density passaging, we treated hiPSC-CMs continuously with or without 2.0 μM CHIR (CHIR vs. CTR), and serially passaged at low-density (**Figure 2A**). Remarkably, in the presence of CHIR, the beating hiPSC-CMs continue to divide without notable cell death (**Figure S1C**) and can be passaged up to 4–5 times over 60+ days (**Figure 2B–D**). Control dimethyl-sulfoxide (DMSO)-treated hiPSC-CMs cease to proliferate after the first or second passage (**Figure 2B–D**). Interestingly, despite the capacity for continuous cell division in the presence of CHIR, these hiPSC-CMs remain capable of spontaneous beating (Supplementary Movie 1). Typically, ~2 million hiPSC-CMs (e.g. 1 well in a 6-well plate) at day 12 of differentiation generate 300–900 million hiPSC-CMs (**Figure 2E**). In addition, the expansion capacity was reproducible in CMs from 4 different iPSC lines (CVI-111, CVI 113, CVI 202 and CVI 273) (**Figure 2F**). Moreover, no significant difference in expansion capacity was observed among the same batch of day 12 CVI-111 hiPSC-CMs that were either cryopreserved or used directly (**Figure S1D**). In total, continuous treatment of day 12 hiPSC-CMs with CHIR for >30 days resulted in 100 to 250-fold increase in total CM number when compared to CTR hiPSC-CMs at similar time points (**Figure 2G–H**). Furthermore, CHIR-treatment appeared to maintain, if not slightly enrich, CM purity as opposed to control DMSO-treated hiPSC-CMs which decreased CM purity with each passage (**Figure 2I–J**), most likely due to over-growth of non-myocytes. To examine the progression of cell cycle activity of CHIR-treated hiPSC-CMs over multiple passaging, the percentage of troponin T (TnT) positive hiPSC-CMs that express the cell cycle marker Ki67 was assessed at each passage after treatment with CHIR or DMSO (CTR) (**Figure S1E**). Interestingly, while CTR hiPSC-CMs showed a rapid decline in their expression of Ki67 with each passage where only a small number of proliferative cells can be observed after passage 2 (P2), CHIR-treatment with low-density passaging resulted in significant ($P = 4.42E-05$) extension (up to 5 passages) of the presence of proliferating cells. Moreover, we found that CHIR-treated hiPSC-CMs indeed proceed through each stage of the cell cycle, undergo cytokinesis and remain more mono-nucleated (**Figure 2K–M** and **S1F–I**). Furthermore, our immunostaining data suggests that hiPSC-CMs disassemble their aligned sarcomeres during active mitosis, suggesting the diminution or absence of active hiPSC-CM beating during the mitotic phase of cell division (**Figure 2K–M**). Collectively, these data support the ability of GSK-3 inhibition and contact removal via serial passaging to maintain hiPSC-CM proliferation.

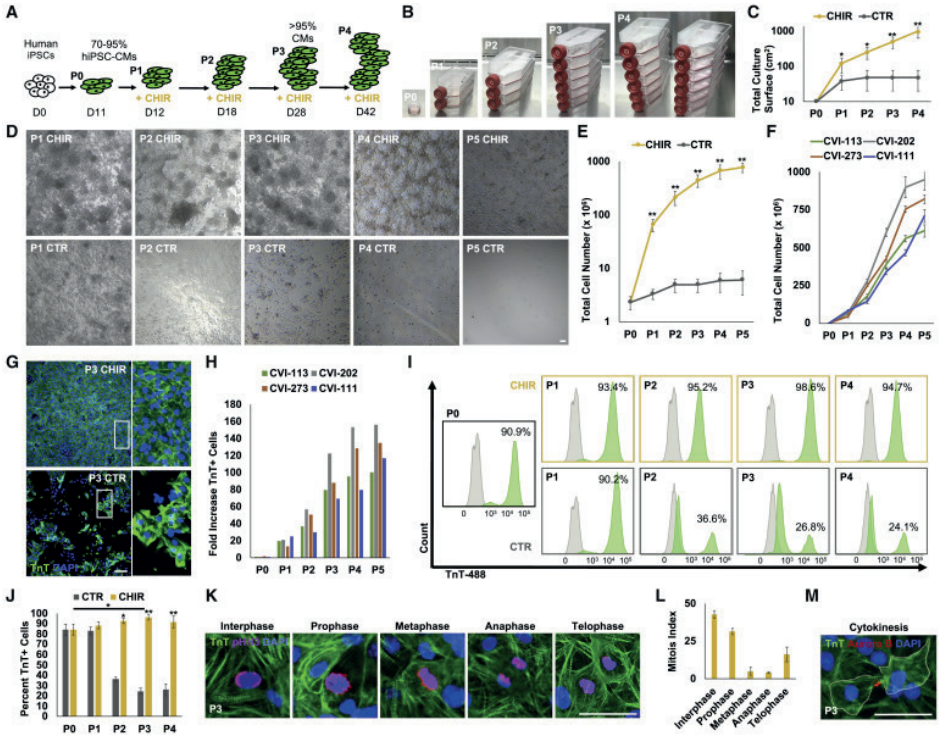

Figure 2: GSK-3β inhibition and long-term low-density passaging results in massive expansion of beating hiPSC-CMs. (A) Schematic timeline of hiPSC-CM expansion and passaging. (B) Representative images of hiPSC-CM flasks from initial 10 cm2 confluent dish at passage 0 (P0) to multiple T-175 cm2 cell culture flasks at end of passage 4. (C) Total surface area (cm2) coverage by hiPSC-CMs at each passage. (D) Representative bright-field images of hiPSC-CMs treated with CHIR (2.0 M) or DMSO (CTR) prior to being passaged. Note that CHIR-treated cells reach confluence again prior to next passaging while DMSO-treated cells become progressive more sparse. Same dilution factor was applied to both treatment conditions. (E) Quantification of total cell numbers from P0 to P5. (F) Graph displaying the expansion for multiple passages (P) of low-density cultured and CHIR treated CMs derived from the 4 indicated hiPSC lines. (G) Immunofluorescence analysis for TnT expression at P3 for hiPSC-CMs treated with DMSO (CTR) or CHIR. (H) Fold increase in TnT+ cells at each passage in CHIR-treated over DMSO treated cells for 4 indicated hiPSC lines. (I) Representative flow cytometry plots of TnT expression (green) and unstained controls (grey) in DMSO (CTR) and CHIR-treated cells for the indicated passage number. (J) Average percentages of TnT+ cells from flow cytometric analysis in (I). (K) Representative confocal microscopy images of P3 (> day 28) CHIR-treated hiPSC-CMs at different phases of mitoses. (L) Quantification of proliferating hiPSC-CMs at distinct mitotic phases from (K). (M) Immunofluorescence image of Aurora B kinase expression in TnT+ cells undergoing cytokinesis. Scale bars represent 100µm, Bar charts represent mean±SD. *p<0.05 and **p<0.005 by unpaired t-test. Supplementary Table 1 specifies the replicates per experiment.

Single-cell phenotypic assessment of hiPSC-CMs following CHIR treatment.

CM maturation is accompanied by formation of highly structured sarcomere, bi- or multi-nucleation, and cell cycle exit (Bassat et al., 2017; Bersell et al., 2009; Senyo et al., 2014; Uygur and Lee, 2016). The observed massive expansion of beating hiPSC-CMs following GSK-3β inhibition and low-density plating (**Figure 2**) raises the possibility that besides cell-cell contact

inhibition (**Figure 1**), prevention of maturation may also in part explain their retained capacity to proliferate. Patterned CHIR-treated single CM that is undergoing mitotic cell division marked by pHH3, exhibited complete sarcomere disassembly (**Figure 3A**). Moreover, control (CTR) hiPSC-CMs demonstrated highly organized and aligned sarcomeres, while CHIR-treated hiPSC-CMs on micropatterns exhibited markedly reduced alignment and organization of sarcomeres (**Figure 3A–B**). Quantification of z-disc-registered sarcomeric α-actinin confirmed the observed sarcomere disorganization in CHIR-treated hiPSC-CMs (**Figure 3C–D**). Interestingly, when the Wnt inhibitor C59 was added to cells that had previously expanded with CHIR treatment (CHIR>C59), these cells improved their sarcomeric organization (**Figure 3B–D**). This supports the reversibility of GSK-3β inhibition signaling effects on hiPSC-CMs. Imaging-based assessment of contractile properties of CTR and CHIR-treated hiPSC-CMs demonstrated a decrease in force generation with CHIR treatment (**Figure 3E**) that recovered upon replacing CHIR with C59 or after the withdrawal of CHIR (data not shown). Additional single-cell calcium studies of age-matched CTR- and CHIR-treated and CHIR withdrawn hiPSC-CMs showed no difference in their spontaneous action potentials, calcium transients, beating frequency nor amplitude (**Figure 3F–H**). Real-time quantitative PCR analysis revealed CHIR-treated hiPSC-CMs downregulate markers associated with cardiomyocyte maturation (MYL2, TNNI3, MYOM2), excitation (GJA1), contractility (RYR2) and metabolism (COX6A2, CKMT) compared to those treated with DMSO or C59, supporting maturation arrest phenotype at transcriptional level (**Figure 3I–K**).

To further characterize global transcriptional changes in individual hiPSC-CMs in response to GSK-3β inhibition, we performed single-cell RNA sequencing in day 12 hiPSC-CMs treated for 24 hours with either DMSO (CTR), CHIR (4.0 μM), or C59 (4.0 μM) (**Figure 3L**). We captured a total of 8,381 cells and performed 93,552 mean reads per cell resulting in a median of 1,297 genes analyzed per cell. Unsupervised analysis revealed 5 cell populations characterized as non-proliferative and proliferative ventricular CMs, non-proliferative and proliferative atrial CMs and fibroblast, present in all 3 treatment samples (**Figure S2A–D**). We found that Wnt target genes such as AXIN2 and LEF1 were upregulated in almost all cells treated with CHIR (**Figure 3M**). Furthermore, mature cardiac genes were dramatically downregulated in CHIR-treated hiPSC-CMs and conversely correlated with the up-regulation of Wnt signaling target genes (**Figure 3N**). Interestingly, CHIR treatment resulted in a larger subset of proliferative and immature atrial and ventricular-like hiPSC-CMs (**Figure 3O–P** and **Figure S2E**). Importantly, GSK-3β inhibition did not result in increased expression of the cardiac progenitor markers such as CKIT, ISL1 or MESP1/2 (**Figure S2F**), suggesting that expansion of functional hiPSC-CM with CHIR does not lead to expansion of a rare population of residual cardiac mesoderm or second-heart-field progenitor cells (Wu et al., 2008). Furthermore, expression of key cardiac transcription factors such as GATA4, TBX5, MEF2C and NKX2.5 (Ieda et al., 2010), did not alter significantly in hiPSC-CMs treated with CHIR versus CTR and C59 (**Figure S2G**). Overall, these data strongly support the inhibition of hiPSC-CM maturation by CHIR/GSK-3β inhibition, a phenomenon that has also been observed in second heart field-derived cardiac progenitor cells and other cell types (Sato et al., 2004; Yin et al., 2014).

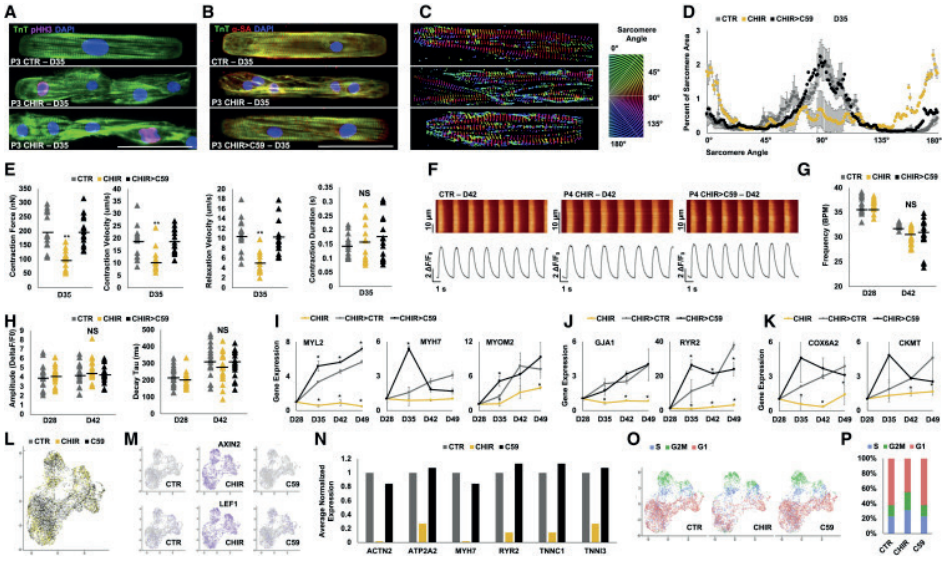

Figure 3: Phenotypic assessment of hiPSC-CMs following GSK-3β inhibition and removal of cell-cell contact inhibition (A-B) Confocal microscopy images of P3 (D35) hiPSC-CMs treated previous with either DMSO (1:5000) (CTR) or CHIR (2.0 μM) since P0 and (for CHIR-treated cells) subsequently treated for 6 days with either continuation of CHIR (2.0 μM) or replacement of CHIR with C59 (2.0 μM) (CHIR>C59) and immunostained on micropatterned surfaces for the expression of troponin T (TnT) and alpha-s actinin (α-SA) or phospho Histone H3 (pHH3). Treated hiPSC-CMs were micropatterned as single cells to adopt rectangular morphology with 7:1 aspect ratio. (C-D) Representative images of distribution of sarcomere fiber alignment. Color codes represent angle of α-SA with respect to cellular long axis (e.g. Z-disc-registered α-SA angle = 90o) (n=10) (E) Contractility measurements in cells treated in (B). (F) Ca^{2+} transients (Fluo-4AM) fluorescence expressed relative to baseline [F/F0] in hiPSC-CMs at day (D) 42 in hiPSC-CMs treated with DMSO (CTR), CHIR (CHIR) or CHIR followed by C59 (CHIR>C59). Plots displaying the Ca^{2+} transient (G) Frequency, (H) Amplitude and Decau Tau for each group. Fold increases in the expression of sarcomere (I), electrophysiological (J), and metabolic genes (K) at the indicated days in hiPSC-CMs treated with CHIR from D12 to D28 followed by either continued treatment with CHIR, CHIR withdraw (CHIR>CTR) or replacement of CHIR with C59 (CHIR>C59). (L) UMAP plots of day 12 hiPSC-CMs treated with DMSO (1:2500) (grey), CHIR (4.0 μM) (yellow), or C59 (4.0 μM) (black) for 24 hrs. (M) UMAP plots for indicated treatments and genes of single-cell sequencing data. (N) Average normalized (over CTR) expression of the selected mature cardiac genes for indicated treatments. (O) UMAP plots for cell cycle analysis, S-phase (S)(blue), G2/M-phase (G2M)(green) and G1-phase (red) for the indicated treatments. (P) Bar graph displaying the percentage of cells from (L) in S, G2M, or G1 phase for indicated treatments. Scale bars represent 100μm. Dot plots represent biological replicates and average. Bar charts represent mean. Graphs represent average±SD. *p<0.05 and **p<0.005 by unpaired t-test. NS=not significant. Supplementary Table 1 specifies the replicates per experiment.

YAP activity is uncoupled from cell density-dependent CHIR-induced hiPSC-CM proliferation.

The Hippo signaling pathway has been shown to regulate heart growth and Wnt signaling-mediated cardiomyocyte proliferation (Heallen et al., 2011). Hippo pathway consists of a core kinase cascade that modulates activity of transcriptional co-activator, yes-associated protein (YAP), which is one of the major nuclear effectors of Hippo pathway. Previous studies have

shown that overexpression of active YAP is sufficient to induce cardiomyocyte proliferation (Bassat et al., 2017; von Gise et al., 2012; Lin et al., 2015). We examined whether YAP is responsible for density-dependent proliferation of CHIR-treated hiPSC-CMs. Immunostaining of YAP revealed that ratio of nuclear to cytoplasmic YAP increases when hiPSC-CMs are sparsely plated (**Figure 4A–B**). Given the positive correlation between nuclear YAP translocation and cardiomyocyte proliferation **(Figure 1K–N, ,4A4A–B**), we next asked whether this increase in YAP nuclear translocation results from mechanosensing of stiffness. Since densely-packed hiPSC-CMs would sense their microenvironment to be softer than sparsely-plated hiPSC-CMs that are cultured directly over tissue culture plastic, we addressed whether substrate stiffness could alter the proliferation of hiPSC-CMs via YAP activity (**Figure 4C**). Interestingly, we found no difference in the fraction of Ki67+ CMs with changing substrate stiffness (**Figure 4D–E**), despite a significant increase in nuclear translocation of YAP when hiPSC-CMs were cultured on stiff hydrogel (60 kPa) or rigid plastic (**Figure 4F–G**). In line with this finding, reduced YAP nuclear translocation via treatment of verteporfin (**Figure 4H–I**), an inhibitor of YAP nuclear translocation, did not lead to a reduction in hiPSC-CM proliferation (**Figure 4J–K**). In summary, these data demonstrate an uncoupling of CHIR and cell-cell contact regulated hiPSC-CM proliferation from nuclear YAP activity.

Mechanistic analysis of GSK-3β inhibition and low-density culture on hiPSC-CM proliferation reveals an interplay between canonical Wnt and AKT signaling

To further elucidate the underlying molecular mechanisms, we first examined whether CHIR acts downstream of Wnt ligand binding to its receptor Frizzled and co-receptor low-density lipoprotein receptor 5/6 (LRP 5/6) (Nusse and Clevers, 2017). We found that a panel of Wnt ligands (i.e. canonical Wnt agonist Wnt3A and a previously described Wnt surrogate ligand scFv-DKK1c (Janda et al., 2017; Yan et al., 2017) in combination with R-Spondin (RSPO)) robustly mediated immature hiPSC-CM expansion comparable to CHIR-treatment, suggesting CHIR acts downstream of Wnt ligand activity (**Figure S3A–G**).

Since GSK-3β is known to be involved in multiple cellular processes beyond canonical Wnt signaling modulation (Beurel et al., 2015) and we show here that cell contact is a potent inhibitor of hiPSC-CM proliferation, we sought to examine whether a β-catenin-independent mechanism is involved in hiPSC-CM proliferation. Interestingly, we found that while CHIR-induced activation of the TCF/LEF luciferase reporter was completely abolished in the presence of PNU74654, a specific TCF/LEF β-catenin signaling blocker (Trosset et al., 2006) (**Figure 5A**), the CHIR-mediated hiPSC-CM proliferation decreased only by ~50% (**Figure 5B**). This suggests that a β-catenin-independent mechanism contributes to roughly half of the proliferative activity observed with CHIR treatment. We confirmed, by real time quantitative PCR, the induction of Wnt signaling target gene expression (e.g. Axin2, LEF, and CCND2) following CHIR treatment in hiPSC-CMs and the ability of PNU74654 treatment to abolish this increase

(**Figure 5C**). We also show that the expression of markers of hiPSC-CM maturation (MYL2, MYH7, MYOM1) were down-regulated by CHIR treatment and recovered fully upon the co-treatment with PNU746554 (**Figure 5C**). These results demonstrate that β-catenin-mediated canonical Wnt signaling prevents hiPSC-CM maturation and is responsible for roughly 50% of the observed CHIR-induced expansion of hiPSC-CMs.

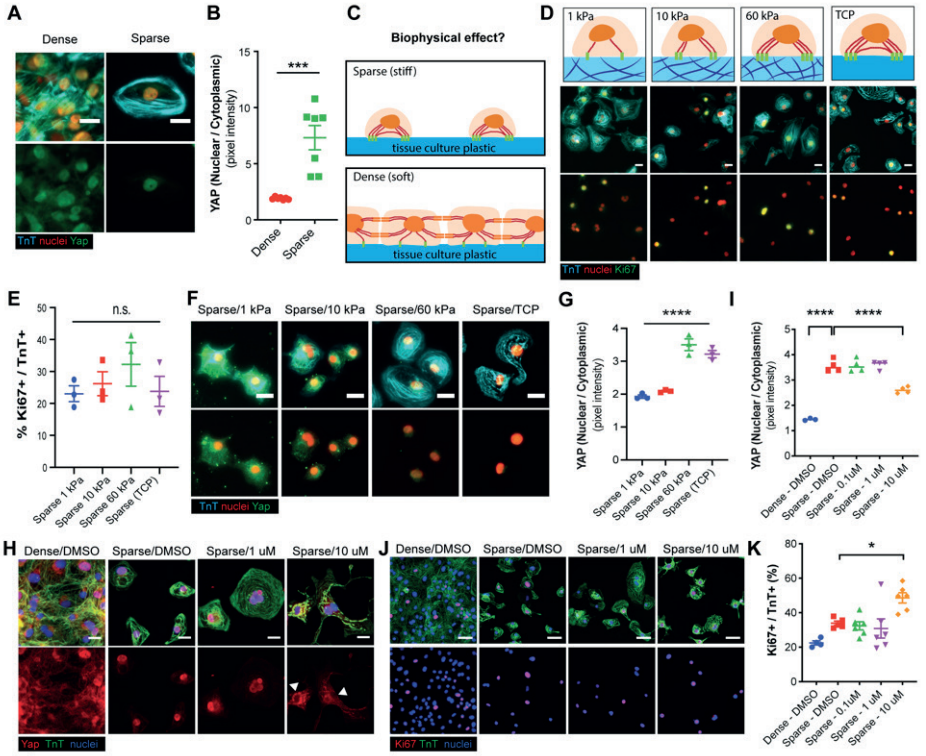

Figure 4: Density-dependent CHIR-induced hiPSC-CM proliferation is uncoupled from YAP activity. (A) Representative immunofluorescence images for yes-associated protein (YAP)(green), cardiac troponin T (TnT) (cyan) and nuclei (red) in dense or sparse culture conditions. (B) Graph displaying nuclear/cytoplasmic YAP ratios for the indicated culture condition. Data are means ± SEM. ****p<0.0001 by unpaired t test. (C) Schematic displaying potential biophysical effects of sparse and dense cell culture on cell-sensing of the substrate stiffness. (D) Immunofluorescence for Ki67 (green), TnT (cyan) and nuclei (red) in hiPSC-CMs cultured on substrates with varying stiffness (kPa) or on tissue culture plastic (TCP)(infinite stiffness). (E) Quantification of the percent Ki67+/TnT+ cells for the indicated substrate stiffness in D. (F) Representative immunofluorescence images as in A of hiPSC-CMs cultured sparsely on the substrates as in D. (G) Nuclear/cytoplasmic ratios of YAP in hiPSC-CMs in F. YAP expression (I) and (H) in hiPSC-CMs cultured in sparse or dense culture conditions with or without YAP inhibitor Verteporfin (1.0 or 10 μM). Immunofluorescence (J) and quantification (K) for ki67+ (red), TnT+ (green) cells (blue) for the same conditions as in H. Data are means ± SEM. *p<0.05. ****p<0.0001 by One-way ANOVA Dunnett's post hoc multiple comparisons to control "Sparse-DMSO" group. Supplementary Table 1 specifies the replicates per experiment.

To identify the β-catenin-independent process that accounts for the low density plus CHIR-mediated hiPSC-CM proliferation, we screened a library of 43 kinases with known functions (**Figure 5D** and **S4A**) and found a significant upregulation of AKT1/2/3 phosphorylation at residue T308 (**Figure 5D**), a residue that is required for AKT activation and cell division (Liu et al., 2014). In addition, we found an increased phosphorylation of HSP27, an AKT binding protein, as well as p70S6K, a downstream AKT target (**Figure 5D**) (Conejo et al., 2002; Song et al., 2005). Using an antibody directed against the T308 residues of phosphorylated AKT (pAKT), we confirmed by western blotting that the active (i.e. phosphorylated) form of AKT is rapidly increased following CHIR treatment at low cell density (**Figure 5E–F**). Immunostaining of day 12 hiPSC-CMs revealed that T308 pAKT was abundantly expressed in the cytoplasm of mitotic hiPSC-CMs in the CHIR-treated group (**Figure 5G and S4B**).

Next, we assessed the contribution of T308 pAKT in hiPSC-CM proliferation by using a previously described highly selective AKT phosphorylation inhibitor MK2206 (Lindsley et al., 2007). When co-treated with MK2206, CHIR and low density-induced hiPSC-CM proliferation decreased by ~50% compared with CHIR treatment alone and pAKT expression reduced (**Figure 5G–I**). Furthermore, we found while MK2206 treatment inhibits AKT T308 phosphorylation (**Figure 5I**), it does not affect downstream β-catenin signaling, as assessed by the LEF/TCF luciferase reporter (**Figure 5J**), nor does it alter the expression of genes associated with CM maturation or Wnt signaling (**Figure 5K**). These data reveal the presence of β-catenin-independent signaling that target downstream effects of GSK-3β inhibition and low cell density via activation of AKT signaling to induce hiPSC-CM proliferation (**Figure 5L**). (PI3K)-AKT pathway is a well-known regulator of Cyclin D2 protein stabilization and cell-cycle progression (Mirzaa et al., 2014). Interestingly, the addition of MK2206 (AKT inhibitor) or PNU74654 (LEF/TCF inhibitor) reduced amounts of Cyclin D2 positive hiPSC-CMs (**Figure 5MN**), indicating that Cyclin D2 activity integrates the contribution by β-catenin signaling and AKT phosphorylation to overall hiPSC-CM proliferation. Previously, Type D cyclins were reported to assemble with Cyclin-dependent-kinases 4/6 (CDK4/6) and form enzymatically active holoenzyme complexes to propel cell cycle progression (Sherr et al., 2016). To address whether CDK4/6 also play an integrative role in CHIR and low cell density-mediate proliferation, CHIR-treated, sparse hiPSC-CMs were treated with palbociclib, a potent small molecular inhibitor of CDK4/6, and shown mitosis was nearly completely abrogated (**Figure 5O–P**). Taken together, these data demonstrate that GSK-3β inhibition and concomitant cell contact removal induce a molecular interplay to enhance LEF/TCF activity via canonical β-catenin signaling and activate AKT phosphorylation at T308 to enhance Cyclin D2 activity and promote hiPSC-CM proliferation.

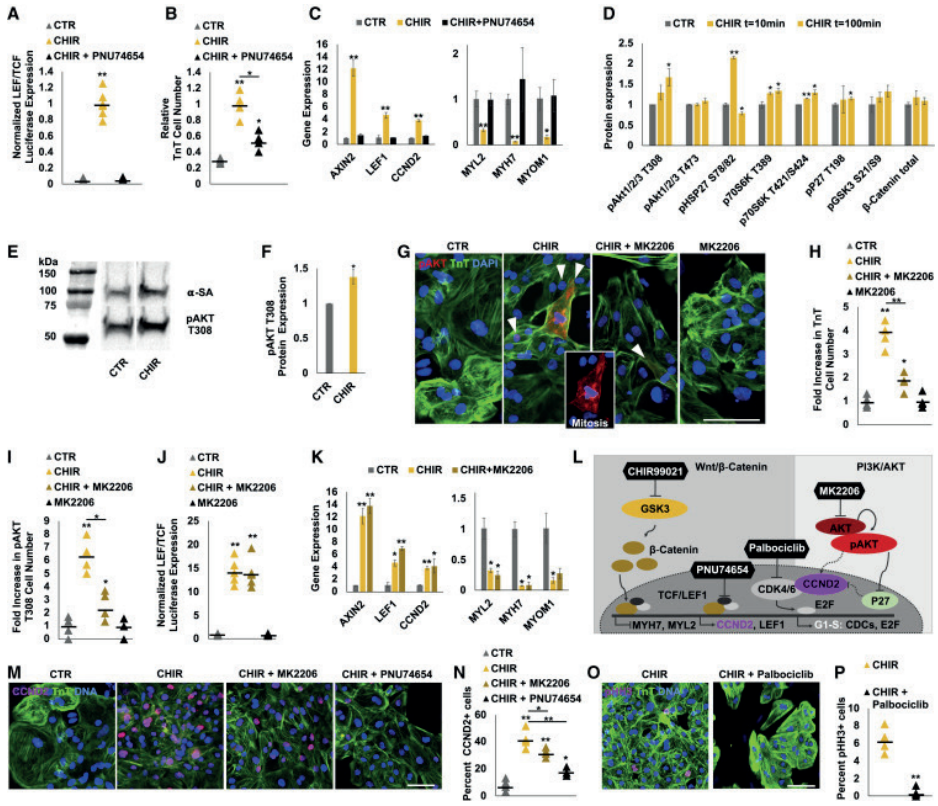

Figure 5: CHIR and low-density plating activate β-catenin and AKT signaling to enhance hiPSC-CM proliferation via Cyclin D2-dependent kinases and prevent maturation via repression of sarcomere gene expression. (A) TOPFlash (TCF/LEF) luciferase analysis of hiPSC-CMs treated with CTR or CHIR in the presence/absence of PNU74654 for 24 hrs. (B) Fold increase in TnT+ cell number after DMSO (CTR) or CHIR (2.0 μM) treatment in the presence/absence of PNU74654 (32 μM). (C) Normalized gene expression of Wnt target genes and maturation markers after treatment with CTR or the indicated compounds. Note the complete recovery of maturation gene expression when canonical Wnt signaling is abolished by PNU74654 treatment. (D) A mini-screen of 43 kinase targets after CHIR treatment demonstrated an increase in phosphorylation (p) levels at AKT, HSP27, and others. (E) Confirmation of AKT T308 phosphorylation by Western Blotting analysis. (F) Quantification of pAKT protein expression level after CHIR treatment. (G) Immunofluorescence analysis for pAKT T308 expression in TnT+ (green) day 20 hiPSC-CMs cultured for 6 days with the indicated treatment. Quantification of the number of TnT+ (H) and pAKT T308+ (I) cells for each treatment with the indicated compounds. (J) TOPFlash luciferase analysis of hiPSC-CMs after treatment of CHIR for 24 hrs in the presence/absence of MK2206 (1.0 μM). (K) Expression of Wnt target genes and maturation markers after treatment with CTR or the indicated compounds. Note that AKT signaling is not changing the Wnt dependent maturation related gene expression. (L) A schematic diagram of the inhibitory relationship between GSK3 and downstream canonical Wnt signaling and their de-repression with CHIR. The role of PNU74654 to inhibit β-catenin-TCF/LEF activity is highlighted. Dashed lines indicate a correlation between AKT-CCND2. (M) Immunofluorescence analysis for Cyclin D2 (CCND2) (pink) expression in TnT+ (green) day 20 hiPSC-CMs cultured for 6 days with the indicated compounds. Quantification of the number of CCND2+/TnT+ cells per treatment group (N). (O) Immunofluorescence analysis for phospho Histone H3 (pHH3) (pink) and TnT (green) expression at day 20 hiPSC-CMs cultured for 6 days with the indicated compounds. Quantification of the number of pHH3+/TnT+ cells per treatment group (P). Scale bars represent 100μm, dot plots represent biological replicates and average. Bar charts represent mean±SD. *p<0.05 and **p<0.005 by unpaired t-test. Supplementary Table 1 specifies the replicates per experiment.

Long-term GSK-3β inhibition does not preclude terminal differentiation and maturation of expanded hiPSC-CMs and their capacity to form functional cardiac tissue

Given the diverse role for GSK-3β signaling to regulate cell lineage commitment and differentiation, a prolonged exposure to CHIR raises concerns regarding possibilities of hiPSCCM phenotype conversion or oncogenic transformation that prevent them from appropriate maturation following expansion, a finding that would significantly hamper their use for tissue engineering applications or regenerative approaches. To address this, we expanded hiPSC-CMs for 4 serial passages in continuous presence of CHIR followed by its withdrawal from the culture media for several weeks. When compared to age-matched controls, previously long-term expanded cells had phenotypically recovered to normal as assessed by immunohistochemistry for α-sarcomeric actinin and real-time PCR for several mature sarcomeric and ion channel genes (**Figure 6A–B**). Next, as a functional proof-of-principle, we created engineered heart tissues from P4 CHIR expanded hiPSC-CMs and age-matched non-expanded CMs (**Figure 6C**). Mass-produced (**Figure 6D**) engineered heart tissues from expanded hiPSC-CMs exhibited normal sarcomere alignment and fully functional integration when applied in engineered heart tissues (**Figure 6E**). Moreover, mass produced engineered heart tissues from multiple hiPSC lines (CVI-111 and CVI-273) have comparable or slightly enhanced functional properties when compared to those generated from age-matched unexpanded control cells (**Figure 6F and Supplementary Movie 5 and 6**). The proliferative response of hiPSC-CMs to GSK-3β inhibition raises the possibility that CHIR may act to stimulation cell division in proliferation-competent CMs when applied the late embryonic or postnatal heart in vivo. To investigate this, pregnant mice at E16.5 was treated with a once daily injection of CHIR or DMSO carrier (CTR) for 4 consecutive days, followed by harvesting. Interestingly, at E20.5 CHIR-treated embryos contained 1.8-fold increase in mitotic CMs when compared to the embryos treated with DMSO control (**Figure S5A–C**). Analysis of individual cell size revealed no difference in the size of single CMs in hearts from CHIR-administered mice compared to those treated with DMSO (**Figure S5D–E**). These data suggest the potential for residual hyperplasia of CMs during late gestation with GSK-3β inhibition, despite substantially attenuated proliferative effect compared to in vitro CHIR-treated hiPSC-CMs. Furthermore, GSK-3β inhibition with daily CHIR injections for 6 consecutive days in postnatal mice (P10) did not result in increased myocardial growth when compared to controls (**Figure S5F–G**). These data support the progressive decline in proliferative capacity of embryonic CMs in vivo and the likely inhibitory effects of cell-cell contact that prevents significant CM expansion upon in vivo GSK-3β inhibition.

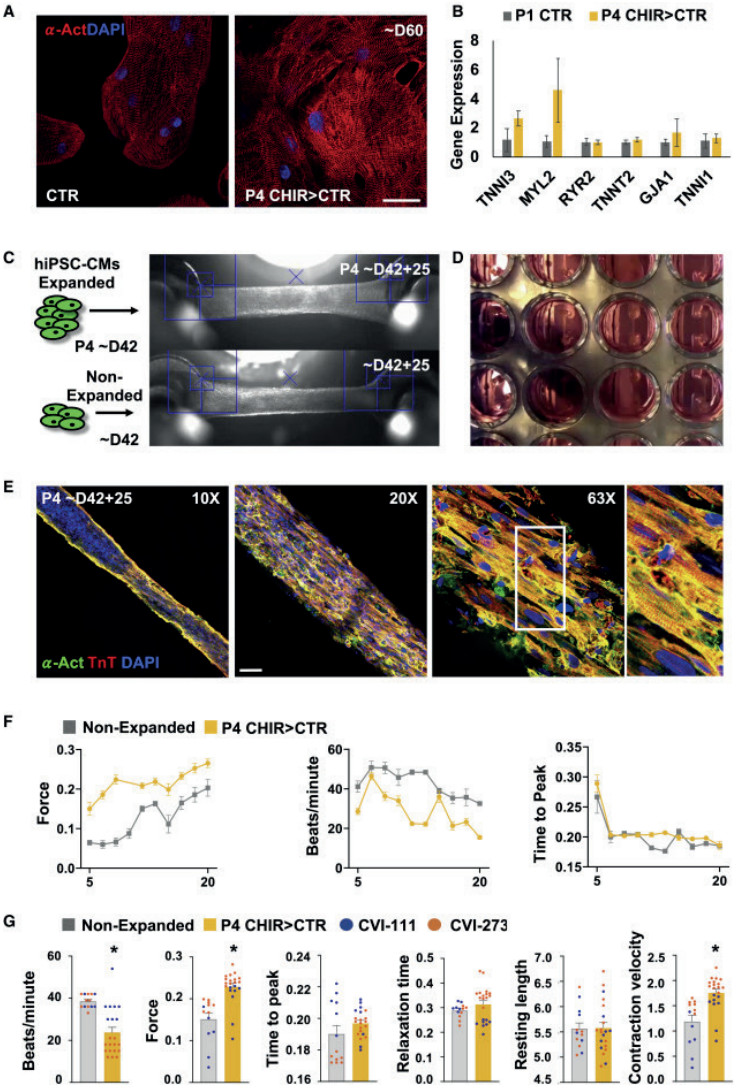

Figure 6: Long-term GSK3 inhibition with low-density plating does not preclude hiPSC-CMs terminal differentiation and maturation in functional cardiac tissue. (A) Immunofluorescence image of alpha-actinin (α-Act) and (B) qPCR analysis of sarcomeric gene expression in passage 4 (P4) expanded vs non-expanded hiPSC-CMs at day 42 (~D42) of differentiation. (C) Brightfield images of engineered heart tissues produced from non-expanded or P4 expanded hiPSC-CMs at ~D42 and further cultured for 25-days. (D) Brightfield image of engineered heart tissues in a 24-well plate format. (E) Immunofluorescence microscopy images of alpha-actinin (α-Act) and Troponin T (TnT) in cardiac tissue generated from previously expanded hiPSC-CMs. (F) Graphs displaying development of contraction force (mN), beating rate and time to peak (T1) in heart tissues generated from previously expanded (P4 CHIR>CTR) (yellow) or non-expanded (grey) hiPSC-CMs measured at different time points after cardiac tissue formation. (G) Plots for contraction analysis in engineered heart tissue 14 days after formation for the indicated treatment and hiPSC lines. Scale bars represent 100µm. Bar charts represent mean±SD. Dot plots represents biological replicates and mean±SEM. *p<0.05 by unpaired t-test. Supplementary Table 1 specifies the replicates per experiment.

DISCUSSION

A major goal of cardiac regenerative medicine is the restoration of functional cardiac tissue in damaged or defected hearts. Identification of a strategy to stimulate proliferation of preexisting CMs would allow for repairing failing hearts induced by CM loss and generating patient-specific, engineered heart tissue for regenerative therapy or drug screening applications. Here, we achieved massive expansion of functional hiPSC-CMs in vitro through concomitant GSK-3β inhibition and removal of cell-cell contact. While we and others have previously demonstrated the ability of canonical Wnt signaling activation or direct GSK-3β inhibition to transiently expand mouse and human PSC-CMs in vitro, the extent remained modest (<10-fold) (Buikema et al., 2013b; Mills et al., 2019; Sharma et al., 2018; Titmarsh et al., 2016; Uosaki et al., 2013). In this study, we show that direct cell-cell contact is a major inhibitor for continuous CM proliferation, and the modest expansion of hiPSC-CMs by GSK-3β inhibition alone can be overcome by removal of cell-cell contact following multiple passages, which can cumulatively result in a 250-fold expansion (**Figure 1 and 2**). Mechanistically, we demonstrate that GSK-3β inhibition suppresses CM maturation via LEF/TCF activity, while concomitant removal of cell-cell contact stimulates the cell cycle activation by AKT T308 phosphorylation (**Figure 3 and 5**). The combined CHIR treatment with low density hiPSC-CM culture allowed for continuous cell cycle activation and CM proliferation, independent from upregulation of YAP activity (**Figure 1 and 4**) These findings support the role of Wnt/ β-catenin signaling in suppressing hiPSC-CM maturation and uncover a role of cell-cell contact in inhibiting CM proliferation. As a proof-of-concept, we show the feasibility of using hiPSC-CMs expanded by the presented method for mass production of engineered heart tissues (**Figure 6**). We believe the ability to generate hiPSC-CMs at this scale will greatly facilitate in vitro disease modeling, high throughput drug screening and in vivo tissue engineering applications. In summary, we demonstrate massive expansion of human cardiomyocytes in vitro by simultaneously "removing brakes and pushing accelerators" (He and Zhou, 2017).

Our finding here complements the recent studies demonstrating the generation of a large number of cardiac cells for regenerative applications with noted differences. First, this study reveals an important finding that mitotic cardiomyocytes quickly lose proliferation capacity via juxtacrine signaling (**Figure 1**), highlighting the importance of removal of cell-cell contact. Contact inhibition of cell proliferation is an essential regulatory process to control tissue growth during embryonic development and tissue homeostasis, and is known to be dysregulated in uncontrolled tumor growth (Kim et al., 2011). Historically for continuous cell growth upon reaching high cell confluence, reducing cell density and removing contact inhibition have been standard in vitro cell culture procedure, also known as passaging. However, passaging of hiPSC-CMs has not been possible because passaging alone leads to expanding only nonmyocytes (**Figure 2F** and **2H**). We show a remarkable role of CHIR in delaying hiPSC-CM maturation and widening their mitotic window to enable continuous CM passaging and expansion (**Figure 2** and **3**). In addition, this study represents a unique

strategy to generate a massive amount of CMs from differentiated CMs. Earlier studies have shown to produce cardiovascular progenitor cells using growth factor combinations during hiPSC differentiation or small molecules plus overexpression of reprogramming factor for direct lineage conversion into cardiovascular progenitors (Birket et al., 2015; Zhang et al., 2016). Given the mix population of the differentiated progeny of multipotent cardiovascular progenitors, this strategy to generate a massive amount of pure hiPSC-CMs provides a unique opportunity. For example, ~10 billion hiPSC-CMs (the total estimated number of CMs in an adult heart) with >95% purity can be prepared from two 6-wells plate of day 12 hiPSC-CMs. Mechanistically, none of previous studies that demonstrated the ability of GSK-3β inhibition and Wnt signaling to induce CM division (Buikema et al., 2013b; Heallen et al., 2011; Kerkela et al., 2008; Titmarsh et al., 2016; Tseng et al., 2006; Uosaki et al., 2013), has reported that canonical Wnt signaling activation via GSK-3β inhibition prevents CM maturation and extends the proliferative window of immature CMs (**Figure 2 and 5**). Furthermore, we report CHIR/low density-induced hiPSC-CM proliferation is independent from YAP activity (**Figure 4**), which was previously shown to be sufficient for promoting cardiomyocyte proliferation mediated by β-catenin (Heallen et al., 2011; Mills et al., 2017). Since β-catenin was a required mediator of Hippo signaling to induce cardiomyocyte proliferation and cardiomegaly (Heallen et al., 2011), CHIR treatment may have overwritten the effect of YAP modulation, thereby revealing a YAP-independent effect of contact inhibition. Further study is being actively conducted to further elucidate the underlying molecular mechanisms.

One concern associated with massively expanding CMs is the possibility of their oncogenic transformation. We demonstrate that after the withdrawal of CHIR, hiPSC-CMs can mature normally and display a similar degree of sarcomere organization, electrophysiological response, and force generation as control hiPSC-CMs that were withheld from GSK-3β inhibition (**Figure 3 and Figure 6**). Gene expression analysis showed an increase in most sarcomere and ion-channel gene expression upon withdrawal of GSK-3β inhibition (**Figure 3**). Furthermore, we observed that proliferating hiPSC-CMs are mostly mononucleated (**Figure 2** and **3**) and that after withdrawal of CHIR, the number of binucleated CMs increased while the fraction of cell-cycle-entered hiPSC-CMs decreased (**Figure S1H–I).** Our single-cell RNA sequencing data also supports the maintenance of the immature state of hiPSC-CMs by Wnt signaling pathway activation as a mean to extend their proliferative window, leading to a moderate level of increase in the expression of cell cycle proteins compared with untreated hiPSC-CMs (**Figure 3** and **5** and **S2**). Taken together, this confirms that GSK-3β inhibition in immature hiPSC-CMs serves to increase proliferation by arresting these cells from their normal maturation process and not by driving these beating CMs into an alternative fate that is more proliferative, as with overexpression of cell cycle genes, which should minimize the potential for oncogenic transformation.

Finally, one of the most promising therapeutic strategies to treat ischemic heart failure is to generate new CMs in an injured myocardium. Our in vivo studies indicate CHIR treatment during late gestation results in significantly more mitotic CMs, while this effect was not found

10 days after birth (**Figure S5**). This indicates that GSK-3β inhibition alone is not sufficient for cardiac regeneration in the postnatal and adult phases. Nevertheless, these findings point to the potential for residual hyperplasia of CMs during late gestation with Wnt stimulation as a therapy for certain forms of congenital heart disease such as hypoplastic left heart syndrome since a recent in-depth study indicates dysregulation of Wnt signaling as one of the contributors to impaired growth (Liu et al., 2017).

SUMMARY

We demonstrated a strategy for the massive expansion of beating hiPSC-CMs with simultaneous GSK-3β inhibition and low cell density culture that ultimately generated a 250-fold increase in the number of hiPSC-CMs, which is suitable for multiple translational/regenerative applications. Furthermore, the in vivo control of late gestational CM proliferation may lead to promising regenerative strategies for treating patients with congenital heart defects.

Study Limitations

Some limitations should be considered when interpreting the results of this study. First, while we observed a strong expansion capacity of day 12 hiPSC-CMs, this capacity is not unlimited. This suggests that additional factors contribute to the proliferative decline of hiPSCCM with maturation. In line with this finding we found that late gestational but not postnatal administration of CHIR is able to increase in vivo cardiomyocyte proliferation. Second, our mechanics studies focused on the inhibition of GSK-3β signaling to stimulate hiPSC-CM proliferation. While we identified the powerful negative effect of cell-cell contact on hiPSC-CM proliferation, the precise molecular mechanism of this effect remains unknown. Whether the engagement of cell surface molecules between two adjacent cells leads to a change in downstream signaling event that suppresses hiPSC-CM proliferation will require further investigation.

Acknowledgements

This work was supported by a UMC Utrecht Clinical Fellowship and Netherlands Heart Institute Fellowship (to J.B.); Stanford Child Health Research Institute Postdoctoral Fellowship and NIH NRSA Postdoctoral Fellowship 5F32HL142205 (to S.L.); NIH Pathway to Independence Award 1K99HL127295–01A1 (to V.S.); The Richard and Helen DeVos Foundation (to S.J.); Netherlands Heart Foundation (CVON-Dosis 2014–40), and Netherlands Organization for Sciences (NWO)-ZonMW (VICI 91818602) (to J.V.); R01 HL145676, R01 HL146690 and P01 HL141084 (to J.C.W); NIH (OD004411, HL099776, LM012179), and the Endowed Faculty Scholar Award of Lucile Packard Foundation for Children and Child Health Research Institute at Stanford (to S.M.W.). The sequencing data was generated on an HiSeq purchased with funds from NIH under award

number S10OD018220. We thank members of the Sean Wu lab for manuscript critique and Andrew Olson at the Stanford Neuroscience Imaging Core Facility for assistance with confocal imaging.

Footnotes

Publisher's Disclaimer: This is a PDF file of an unedited manuscript that has been accepted for publication. As a service to our customers we are providing this early version of the manuscript. The manuscript will undergo copyediting, typesetting, and review of the resulting proof before it is published in its final form. Please note that during the production process errors may be discovered which could affect the content, and all legal disclaimers that apply to the journal pertain.

Declaration of Conflict of Interest

A provisional patent has been filed with the US Patent and Trademark Office regarding the effect of bioactive lipids plus Wnt signaling activation on hiPSC-CM proliferation/expansion.

REFERENCES

1. Lee, S., Yang, H., Chen, C., Venkatraman, S., Darsha, A., Wu, S.M., Wu, J.C., and Seeger, T. (2020). Simple Lithography-Free Single Cell Micropatterning using Laser-Cut Stencils. JoVE e60888.
2. Bassat, E., Mutlak, Y.E., Genzelinakh, A., Shadrin, I.Y., Umansky, K.B., Yifa, O., Kain, D., Rajchman, D., Leach, J., Bassat, D.R., et al. (2017). The extracellular matrix protein agrin promotes heart regeneration in mice. Nature 547, 179–184.
3. Bersell, K., Arab, S., Haring, B., and Kühn, B. (2009). Neuregulin1/ErbB4 signaling induces cardiomyocyte proliferation and repair of heart injury. Cell 138, 257–270.
4. Beurel, E., Grieco, S.F., and Jope, R.S. (2015). Glycogen synthase kinase-3 (GSK3): regulation, actions, and diseases. Pharmacol. Ther. 148, 114–131.
5. Birket, M.J., Ribeiro, M.C., Verkerk, A.O., Ward, D., Leitoguinho, A.R., den Hartogh, S.C., Orlova, V.V., Devalla, H.D., Schwach, V., Bellin, M., et al. (2015). Expansion and patterning of cardiovascular progenitors derived from human pluripotent stem cells. Nat. Biotechnol. 33, 970–979.
6. Buikema, J.W., Zwetsloot, P.-P.M., Doevendans, P.A., Sluijter, J.P.G., and Domian, I.J. (2013a). Expanding Mouse Ventricular Cardiomyocytes through GSK-3 Inhibition. Curr Protoc Cell Biol 61, 23.9.1-23.9.10.
7. Buikema, J.W., Mady, A.S., Mittal, N.V., Atmanli, A., Caron, L., Doevendans, P.A., Sluijter,J.P.G., and Domian, I.J. (2013b). Wnt/β-catenin signaling directs the regional expansion of first and second heart field-derived ventricular cardiomyocytes. Development 140, 4165–4176.
8. Chong, J.J.H., Yang, X., Don, C.W., Minami, E., Liu, Y.-W., Weyers, J.J., Mahoney, W.M., Van Biber, B., Cook, S.M., Palpant, N.J., et al. (2014). Human embryonic-stem-cell-derived cardiomyocytes regenerate non-human primate hearts. Nature 510, 273–277.
9. Conejo, R., de Alvaro, C., Benito, M., Cuadrado, A., and Lorenzo, M. (2002). Insulin restores differentiation of Ras-transformed C2C12 myoblasts by inducing NF-kappaB through an AKT/P70S6K/p38-MAPK pathway. Oncogene 21, 3739–3753.
10. von Gise, A., Lin, Z., Schlegelmilch, K., Honor, L.B., Pan, G.M., Buck, J.N., Ma, Q., Ishiwata, T., Zhou, B., Camargo, F.D., et al. (2012). YAP1, the nuclear target of Hippo signaling, stimulates heart growth through cardiomyocyte proliferation but not hypertrophy. Proc. Natl. Acad. Sci. U.S.A. 109, 2394–2399.
11. Grazia Lampugnani, M., Zanetti, A., Corada, M., Takahashi, T., Balconi, G., Breviario, F., Orsenigo, F., Cattelino, A., Kemler, R., Daniel, T.O., et al. (2003). Contact inhibition of VEGF- induced proliferation requires vascular endothelial cadherin, beta-catenin, and the phosphatase DEP-1/CD148. J. Cell Biol. 161, 793–804.
12. Grego-Bessa, J., Luna-Zurita, L., Monte, G. del, Bolós, V., Melgar, P., Arandilla, A., Garratt, A.N., Zang, H., Mukouyama, Y., Chen, H., et al. (2007). Notch Signaling is Essential for Ventricular Chamber Development. Dev Cell 12, 415–429.
13. Hansen, A., Eder, A., Bönstrup, M., Flato, M., Mewe, M., Schaaf, S., Aksehirlioglu, B., Schwoerer, A.P., Schwörer, A., Uebeler, J., et al. (2010). Development of a drug screening platform based on engineered heart tissue. Circ. Res. 107, 35–44.
14. Hayakawa, T., Kunihiro, T., Ando, T., Kobayashi, S., Matsui, E., Yada, H., Kanda, Y., Kurokawa, J., and Furukawa, T. (2014). Image-based evaluation of contraction-relaxation kinetics of human-induced pluripotent stem cell-derived cardiomyocytes: Correlation and complementarity with extracellular electrophysiology. J. Mol. Cell. Cardiol. 77, 178–191.
15. He, L., and Zhou, B. (2017). Cardiomyocyte proliferation: remove brakes and push accelerators. Cell Research 27, 959–960.
16. Heallen, T., Zhang, M., Wang, J., Bonilla-Claudio, M., Klysik, E., Johnson, R.L., and Martin, J.F. (2011). Hippo Pathway Inhibits Wnt Signaling to Restrain Cardiomyocyte Proliferation and Heart Size. Science 332, 458–461.
17. Hesse, M., Raulf, A., Pilz, G.-A., Haberlandt, C., Klein, A.M., Jabs, R., Zaehres, H., Fügemann,C.J., Zimmermann, K., Trebicka, J., et al. (2012). Direct visualization of cell division using high-resolution imaging of M-phase of the cell cycle. Nature Communications 3, 1–12.
18. Ieda, M., Fu, J.-D., Delgado-Olguin, P., Vedantham, V., Hayashi, Y., Bruneau, B.G., and Srivastava, D. (2010). Direct reprogramming of fibroblasts into functional cardiomyocytes by defined factors. Cell 142, 375–386.

19. Janda, C.Y., Dang, L.T., You, C., Chang, J., de Lau, W., Zhong, Z.A., Yan, K.S., Marecic, O.,Siepe, D., Li, X., et al. (2017). Surrogate Wnt agonists that phenocopy canonical Wnt and β-catenin signalling. Nature 545, 234–237.

20. Kerkela, R., Kockeritz, L., MacAulay, K., Zhou, J., Doble, B.W., Beahm, C., Greytak, S., Woulfe, K., Trivedi, C.M., Woodgett, J.R., et al. (2008). Deletion of GSK-3β in mice leads to hypertrophic cardiomyopathy secondary to cardiomyoblast hyperproliferation. J Clin Invest 118, 3609–3618.

21. Kim, J.-H., and Asthagiri, A.R. (2011). Matrix stiffening sensitizes epithelial cells to EGF and enables the loss of contact inhibition of proliferation. J Cell Sci 124, 1280–1287.

22. Kim, N.-G., Koh, E., Chen, X., and Gumbiner, B.M. (2011). E-cadherin mediates contact inhibition of proliferation through Hippo signaling-pathway components. Proc. Natl. Acad. Sci. U.S.A. 108, 11930–11935.

23. Li, J., Gao, E., Vite, A., Yi, R., Gomez, L., Goossens, S., van Roy, F., and Radice, G.L. (2015). Alpha-catenins control cardiomyocyte proliferation by regulating Yap activity. Circ. Res. 116, 70–79.

24. Lian, X., Hsiao, C., Wilson, G., Zhu, K., Hazeltine, L.B., Azarin, S.M., Raval, K.K., Zhang, J., Kamp, T.J., and Palecek, S.P. (2012). Robust cardiomyocyte differentiation from human pluripotent stem cells via temporal modulation of canonical Wnt signaling. Proc. Natl. Acad. Sci. U.S.A. 109, E1848-1857.

25. Lian, X., Zhang, J., Azarin, S.M., Zhu, K., Hazeltine, L.B., Bao, X., Hsiao, C., Kamp, T.J., and Palecek, S.P. (2013). Directed cardiomyocyte differentiation from human pluripotent stem cells by modulating Wnt/β-catenin signaling under fully defined conditions. Nat Protoc 8, 162–175.

26. Lin, Z., Zhou, P., von Gise, A., Gu, F., Ma, Q., Chen, J., Guo, H., van Gorp, P.R.R., Wang, D.-Z., and Pu, W.T. (2015). Pi3kcb links Hippo-YAP and PI3K-AKT signaling pathways to promote cardiomyocyte proliferation and survival. Circ. Res. 116, 35–45.

27. Lindsley, C.W., Barnett, S.F., Yaroschak, M., Bilodeau, M.T., and Layton, M.E. (2007). Recent progress in the development of ATP-competitive and allosteric Akt kinase inhibitors. Curr Top Med Chem 7, 1349–1363.

28. Liu, P., Begley, M., Michowski, W., Inuzuka, H., Ginzberg, M., Gao, D., Tsou, P., Gan, W.,Papa, A., Kim, B.M., et al. (2014). Cell-cycle-regulated activation of Akt kinase by phosphorylation at its carboxyl terminus. Nature 508, 541–545.

29. Liu, X., Yagi, H., Saeed, S., Bais, A.S., Gabriel, G.C., Chen, Z., Peterson, K.A., Li, Y., Schwartz, M.C., Reynolds, W.T., et al. (2017). The complex genetics of hypoplastic left heart syndrome. Nat. Genet. 49, 1152–1159.

30. Liu, Y.-W., Chen, B., Yang, X., Fugate, J.A., Kalucki, F.A., Futakuchi-Tsuchida, A., Couture, L.,Vogel, K.W., Astley, C.A., Baldessari, A., et al. (2018). Human embryonic stem cell-derived cardiomyocytes restore function in infarcted hearts of non-human primates. Nat. Biotechnol. 36, 597–605.

31. Matsa, E., Burridge, P.W., Yu, K.-H., Ahrens, J.H., Termglinchan, V., Wu, H., Liu, C., Shukla, P., Sayed, N., Churko, J.M., et al. (2016). Transcriptome Profiling of Patient-Specific Human iPSC-Cardiomyocytes Predicts Individual Drug Safety and Efficacy Responses In Vitro. Cell Stem Cell 19, 311–325.

32. Mills, R.J., Titmarsh, D.M., Koenig, X., Parker, B.L., Ryall, J.G., Quaife-Ryan, G.A., Voges, H.K.,Hodson, M.P., Ferguson, C., Drowley, L., et al. (2017). Functional screening in human cardiac organoids reveals a metabolic mechanism for cardiomyocyte cell cycle arrest. Proc Natl Acad Sci USA 114, E8372–E8381.

33. Mills, R.J., Parker, B.L., Quaife-Ryan, G.A., Voges, H.K., Needham, E.J., Bornot, A., Ding, M., Andersson, H., Polla, M., Elliott, D.A., et al. (2019). Drug Screening in Human PSC-Cardiac Organoids Identifies Pro-proliferative Compounds Acting via the Mevalonate Pathway. Cell Stem Cell 24, 895-907.e6.

34. Mirzaa, G., Parry, D.A., Fry, A.E., Giamanco, K.A., Schwartzentruber, J., Vanstone, M., Logan, C.V., Roberts, N., Johnson, C.A., Singh, S., et al. (2014). De novo CCND2 mutations leading to stabilization of cyclin D2 cause megalencephaly-polymicrogyria-polydactyly-hydrocephalus syndrome. Nat. Genet. 46, 510–515.

35. Nusse, R., and Clevers, H. (2017). Wnt/β-Catenin Signaling, Disease, and Emerging Therapeutic Modalities. Cell 169, 985–999.

36. Ogle, B.M., Bursac, N., Domian, I., Huang, N.F., Menasché, P., Murry, C.E., Pruitt, B., Radisic, M., Wu, J.C., Wu, S.M., et al. (2016). Distilling complexity to advance cardiac tissue engineering. Sci Transl Med 8, 342ps13.

37. Puliafito, A., Hufnagel, L., Neveu, P., Streichan, S., Sigal, A., Fygenson, D.K., and Shraiman, B.I. (2012). Collective and single cell behavior in epithelial contact inhibition. PNAS 109, 739–744.

38. Sato, N., Meijer, L., Skaltsounis, L., Greengard, P., and Brivanlou, A.H. (2004). Maintenance of pluripotency in human and mouse embryonic stem cells through activation of Wnt signaling by a pharmacological GSK-3-specific inhibitor. Nat. Med. 10, 55–63.

39. Senyo, S.E., Lee, R.T., and Kühn, B. (2014). Cardiac regeneration based on mechanisms of cardiomyocyte proliferation and differentiation. Stem Cell Res 13, 532–541.

40. Sharma, A., Zhang, Y., Buikema, J.W., Serpooshan, V., Chirikian, O., Kosaric, N., Churko, J.M., Dzilic, E., Shieh, A., Burridge, P.W., et al. (2018). Stage-specific Effects of Bioactive Lipids on Human iPSC Cardiac Differentiation and Cardiomyocyte Proliferation. Scientific Reports 8, 6618.

41. Sharma, P., Abbasi, C., Lazic, S., Teng, A.C.T., Wang, D., Dubois, N., Ignatchenko, V., Wong, V., Liu, J., Araki, T., et al. (2015). Evolutionarily conserved intercalated disc protein Tmem65 regulates cardiac conduction and connexin 43 function. Nature Communications 6, 8391.

42. Sherr, C.J., Beach, D., and Shapiro, G.I. (2016). Targeting CDK4 and CDK6: From Discovery to Therapy. Cancer Discov 6, 353–367.

43. Shiba, Y., Gomibuchi, T., Seto, T., Wada, Y., Ichimura, H., Tanaka, Y., Ogasawara, T., Okada, K., Shiba, N., Sakamoto, K., et al. (2016). Allogeneic transplantation of iPS cell-derived cardiomyocytes regenerates primate hearts. Nature 538, 388–391.

44. Song, G., Ouyang, G., and Bao, S. (2005). The activation of Akt/PKB signaling pathway and cell survival. J. Cell. Mol. Med. 9, 59–71.

45. Stuart, T., Butler, A., Hoffman, P., Hafemeister, C., Papalexi, E., Mauck, W.M., Hao, Y., Stoeckius, M., Smibert, P., and Satija, R. (2019). Comprehensive Integration of Single-Cell Data. Cell 177, 1888-1902.e21.

46. Sturzu, A.C., Rajarajan, K., Passer, D., Plonowska, K., Riley, A., Tan, T.C., Sharma, A., Xu, A.F., Engels, M.C., Feistritzer, R., et al. (2015). The Fetal Mammalian Heart Generates a Robust Compensatory Response to Cell Loss. Circulation 132, 109–121.

47. Titmarsh, D.M., Glass, N.R., Mills, R.J., Hidalgo, A., Wolvetang, E.J., Porrello, E.R., Hudson, J.E., and Cooper-White, J.J. (2016). Induction of Human iPSC-Derived Cardiomyocyte Proliferation Revealed by Combinatorial Screening in High Density Microbioreactor Arrays. Scientific Reports 6, 1–15.

48. Trosset, J.-Y., Dalvit, C., Knapp, S., Fasolini, M., Veronesi, M., Mantegani, S., Gianellini, L.M., Catana, C., Sundström, M., Stouten, P.F.W., et al. (2006). Inhibition of protein-protein interactions: the discovery of druglike beta-catenin inhibitors by combining virtual and biophysical screening. Proteins 64, 60–67.

49. Tseng, A.-S., Engel, F.B., and Keating, M.T. (2006). The GSK-3 Inhibitor BIO Promotes Proliferation in Mammalian Cardiomyocytes. Chemistry & Biology 13, 957–963.

50. Uosaki, H., Magadum, A., Seo, K., Fukushima, H., Takeuchi, A., Nakagawa, Y., Moyes, K.W., Narazaki, G., Kuwahara, K., Laflamme, M., et al. (2013). Identification of chemicals inducing cardiomyocyte proliferation in developmental stage-specific manner with pluripotent stem cells. Circ Cardiovasc Genet 6, 624–633.

51. Uygur, A., and Lee, R.T. (2016). Mechanisms of Cardiac Regeneration. Dev Cell 36, 362–374.

52. Wu, S.M., Chien, K.R., and Mummery, C. (2008). Origins and fates of cardiovascular progenitor cells. Cell 132, 537–543.

53. Yan, K.S., Janda, C.Y., Chang, J., Zheng, G.X.Y., Larkin, K.A., Luca, V.C., Chia, L.A., Mah, A.T., Han, A., Terry, J.M., et al. (2017). Non-equivalence of Wnt and R-spondin ligands during Lgr5 + intestinal stem-cell self-renewal. Nature 545, 238–242.

54. Yin, X., Farin, H.F., van Es, J.H., Clevers, H., Langer, R., and Karp, J.M. (2014). Niche-independent high-purity cultures of Lgr5+ intestinal stem cells and their progeny. Nat. Methods 11, 106–112.

55. Zhang, Y., Cao, N., Huang, Y., Spencer, C.I., Fu, J.-D., Yu, C., Liu, K., Nie, B., Xu, T., Li, K., et al. (2016). Expandable Cardiovascular Progenitor Cells Reprogrammed from Fibroblasts. Cell Stem Cell 18, 368–381.

SUPPLEMENTARY

The **supplementary figures 1-5** and **supplementary table 1** can be downloaded from: https://www.cell.com/cms/10.1016/j.stem.2020.06.001/attachment/ce0d8e61-0e51-41c9-8d8e-f9ba8fb7160a/mmc1

Or:

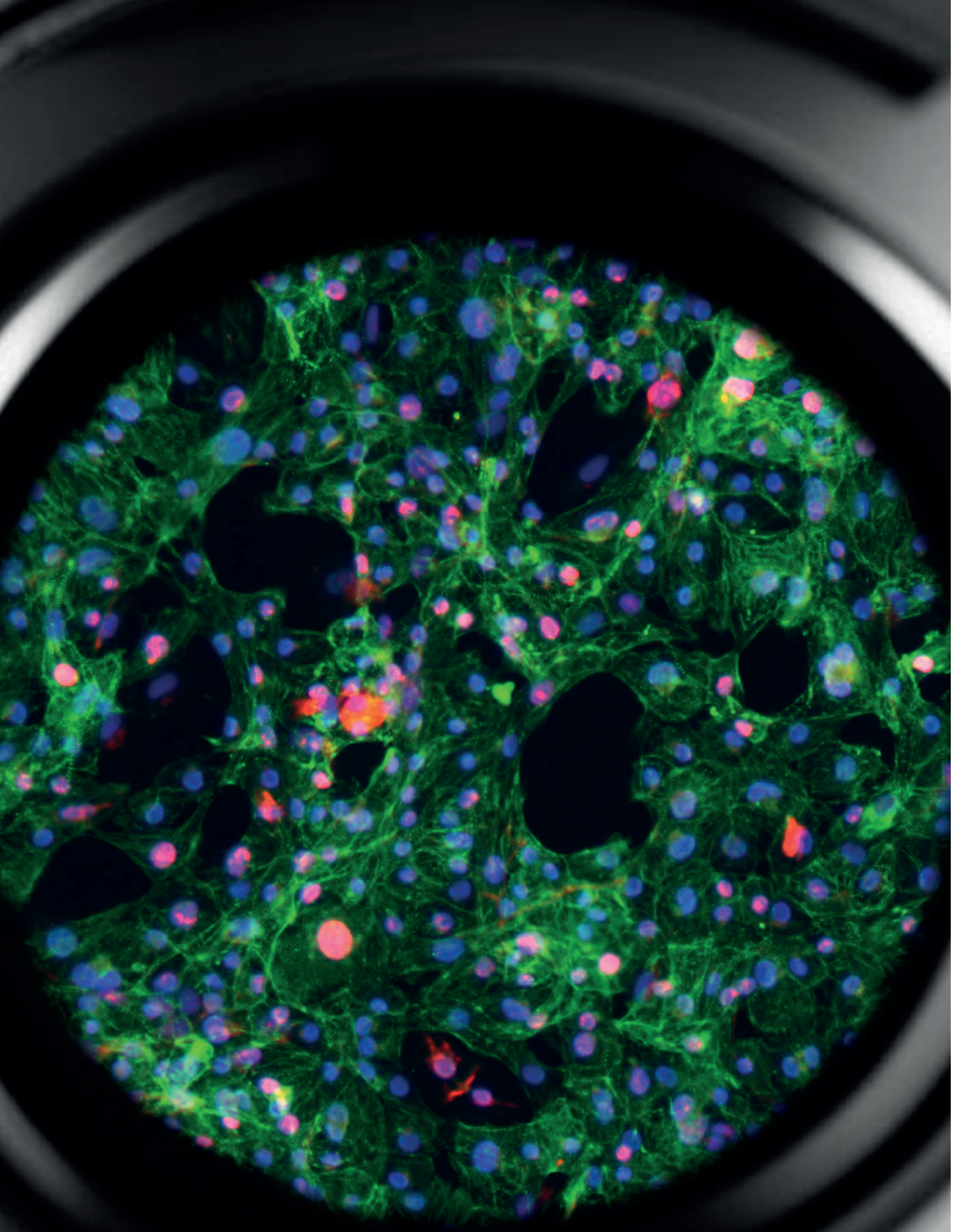

Proliferation stain of expanding stem cell-derived cardiomyocytes.

Chapter 4

Massive Expansion and Cryopreservation of Functional Human Induced Pluripotent Stem Cell-Derived Cardiomyocytes

Published in: Cell STAR Protocols, 2021

Renée G.C. Maas*, Soah Lee*, Magdalena Harakalova, Christian J.B. Snijders Blok, William R. Goodyer, Jesper Hjortnaes, Pieter A.F.M. Doevendans, Linda W. Van Laake, Jolanda van der Velden, Folkert W. Asselbergs, Joseph C. Wu, Joost P.G. Sluijter, Sean M. Wu[§] and Jan W. Buikema[§]

[*]These authors contributed equally.
[§]These authors contributed equally

ABSTRACT

Since the discovery of human induced pluripotent stem cells (hiPSCs), numerous strategies have been established to efficiently derive cardiomyocytes from hiPSCs (hiPSC-CMs). Here, we describe a cost-effective strategy for the subsequent massive expansion (>250-fold) of high-purity hiPSC-CMs relying on two aspects: removal of cell-cell contacts and small-molecule inhibition with CHIR99021. The protocol maintains CM functionality, allows cryopreservation, and the cells can be used in downstream assays such as disease modeling, drug and toxicity screening, and cell therapy. For complete details on the use and execution of this protocol, please refer to Buikema (2020).

GRAPHICAL ABSTRACT

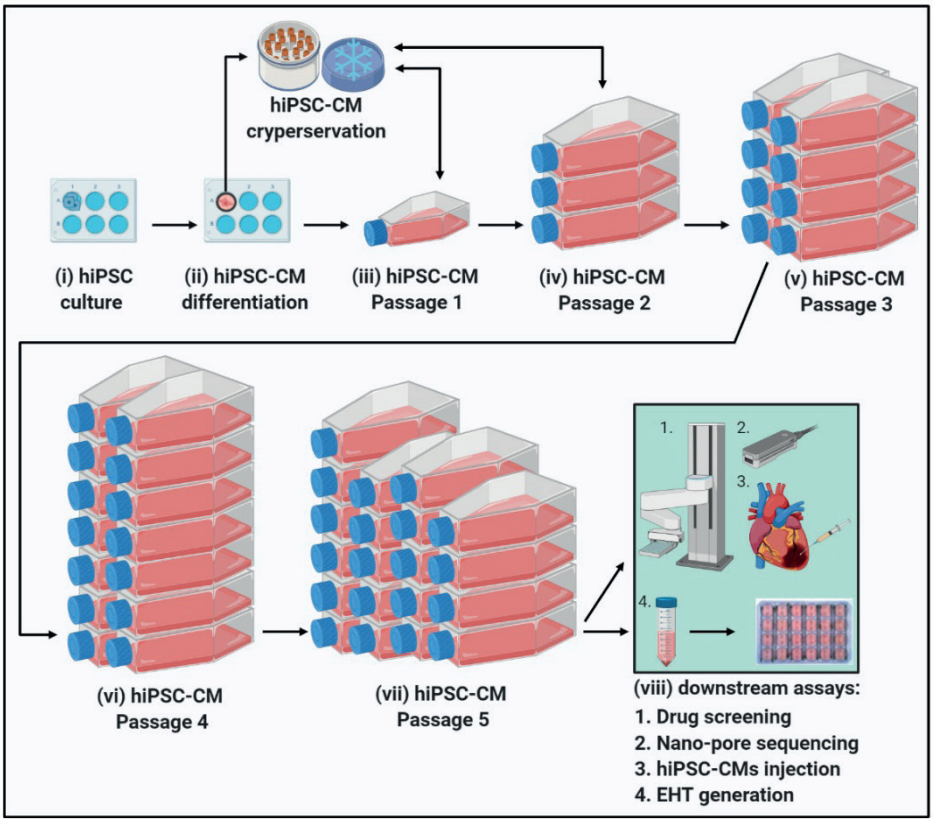

Created with BioRender.com

METHODS

Before You Begin

Timing: 30 min

In a sterile hood, dilute Matrigel to a concentration of 1.2 mg/ml in 4°C RPMI-1640 in a 50 ml tube on ice. Prepare aliquots of 1 ml in 15 ml tubes on ice and store at -20°C. Remove one Matrigel aliquot (1 ml) from the freezer, and add 11 ml of cold RPMI-1640 to a final concentration of 0.1mg/mL (empirically up to 5x lower concentrations of Matrigel are working). Gently mix the Matrigel solution to thaw and dissolve the Matrigel. Immediately add 1 ml/well Matrigel in RPMI-1640 for 6-well plates, 1,5 ml/flask for T25s, 2,5 ml/flask for T75, or 5 ml/flask for T175 flasks. Allow the Matrigel to set for 30 minutes at 37°C before use. The Matrigel-coated plates and flasks can be stored at 4 °C for up to 3 weeks.

Note: Keep Matrigel on ice to avoid solidification during the coating procedure. Boxes with pipet tips can be pre-chilled at -20°C.

MATERIALS AND EQUIPMENT

- hiPSC E8 complete medium: In a sterile environment, mix E8 basal medium, E8 supplement (2% (vol/vol) and penicillin/streptomycin (1% (vol/vol)).

  Note: We recommend to aliquot the E8 supplement (-20°C) and medium (4°C) and prepare weekly aliquots of the complete medium by pre-warming the required amount. The basal medium can be stored at –20°C for up to 1 year. After preparation, hiPSC E8 complete medium can be stored at 4°C for up to 1 month.

- 10 mM stock Y27632 (Y): In a sterile environment, add 31.2246 mL DMSO to 100 mg Y27632.

  Note: Prepare aliquots of 2-10 µL and store at −80°C for up to 6 months. After thawing the aliquot can be stored at 4°C for 2 weeks.

- E8 + 5 µM Y-27632: In a sterile environment, add 0.05% Y-27632 (1:2000 dilution of the 10mM stock) to the hiPSC E8 complete medium.

  Note: After preparation, this medium can be stored at 4°C for up to 1 week.

- 40 mM stock CHIR99021 (CHIR): In a sterile environment, add 1.2455 mL DMSO to 25 mg CHIR.

  Note: Prepare aliquots of 2-10 µL and store at −80°C for up to 1 year. Avoid re-freezing of the aliquots.

- CM differentiation medium (B27): In a sterile environment, mix RPMI 1640, 2% B-27 minus insulin (1:50) and 1% penicillin/streptomycin (1:100).

- CM differentiation medium + 7 µM CHIR: In a sterile environment, add 0.0267% CHIR (1:3750 dilution of the 40mM stock) into CM differentiation medium.

  Note: After preparation, do not store this medium to avoid repeated freeze-thaw cycles of CHIR.

- CM differentiation medium + 8 µM CHIR: In a sterile environment, add 0.02% CHIR (1:5000 dilution of the 40 mM CHIR stock) into CM differentiation medium.

  Note: After preparation, do not store this medium to avoid repeated freeze-thaw cycles of CHIR.

- Wnt-C59 (20 mM): In a sterile environment, add 1302.2 µL DMSO to 10 mg Wnt-C59.

  Note: Prepare aliquots of 50 µL format and store at –80°C for up to 2 years. Avoid re-freezing of the aliquots.

- CM differentiation medium + 2 µM Wnt-C59: In a sterile environment, add 0,01% Wnt-C59 (1:10.000 dilution of the 20 mM Wnt-C59 stock) into CM differentiation medium.

  Note: After preparation, do not store this medium to avoid repeated freeze-thaw cycles of Wnt-C59.

  •CM culture medium (CM): In a sterile environment mix RPMI 1640, 2% B-27 supplement (1:50) and 1% penicillin/streptomycin (1:100).

- CM purification medium (PM): In a sterile environment mix RPMI 1640 no glucose, 2% B-27 supplement (1:50) and 1% penicillin/streptomycin (1:100).

- CM replating medium (RM): In a sterile environment, add 0.1% Y-27632 (1:1000 dilution of the 10mM stock) and 10% KO serum replacement (1:10) into CM culture medium.

  Note: After preparation, all cardiac culture mediums can be stored at 4°C for up to 1 month.

  CM expansion medium (EM) (with 2 µM CHIR): In a sterile environment, add 0.005% CHIR (1:20.000 dilution of the 40 mM CHIR stock) into CM culture medium.

  Note: After preparation, we do not recommend storing this medium.

- CM splitting medium (SM) (with 2 µM CHIR): In a sterile environment, add 0.005% CHIR (1:20.000 dilution of the 40 mM CHIR stock), 0.1% Y-27632 (1:1000 dilution of the 10mM stock), and 10% KO serum replacement (1:10) replacement into CM culture medium.

  Note: After preparation, we do not recommend storing this medium.

- CM thawing medium (TM): In a sterile environment, add 1% Revitacell (1:100) and 10% KO serum replacement (1:10) into CM culture medium. Protect medium from light.

  CRITICAL: Revitacell is light-sensitive. Protect Revitacell from light.

  Note: After preparation, this medium can be stored at 4°C for up to 1 week.

  Note: We recommend to prepare aliquots of 100-500 µL Revitcell and store at –20°C for up to 1 year.

- Permeabilization and blocking buffer: This buffer contains PBS, 5% BSA and 0,3% Triton-X-100.

- Flow cytometry buffer: This buffer contains 50 ml of PBS and 1% BSA and 0.3% Triton-X-100.

- Wash buffer: This buffer contains 50 ml of PBS and 1% BSA.
  Note: After preparation, all buffers can be stored at 4°C for up to 1 month.

Alternatives:

- 6-Well cell culture plates: Greiner, cat. no. 657160.
- T25 cell culture flasks: Greiner, cat. no. 690170.
- T75 cell culture flasks: Greiner, cat. no. 658170.
- T175 cell culture flasks: Greiner, cat. no. 660160.
- Centrifuge tubes: 15 ml, Greiner, cat. no. 188280.
- Room temperature CoolCell cell freezing container (-1 °C /minute cell freezing).
- Cryovials: VWR, cat. no. 479-6846.
- Counting slides: Countess, Cat. no C10228.
- BSL2 biosafety cabinet: e.g., Telstar EF.
- Cell Counter: e.g, Countess II FL Automated Cell Counter from Life Technologies.
- Cell culture incubator (37°C, 5% CO2, 21% O2): e.g. Panasonic MCO 170.
- 37°C water bath: e.g., Julabo Pura.

Key Resources Tables

Table 1. key culture format cultivation table

STEPS	Culture format	#Culture formats	Start amount of cells (10^4 / cm^2)	Total amount of cells after each step (10^4)	Volume of medium/format	Timing
hiPSC culturing	6 wells plate	1 well	~2	~300	2 mL per wells	4 d
Cardiac differentiation	6 wells plate	1 well	~30	~700	3 mL per wells	11 d
Passage 1	T75 flask	1x	~2.5	~2100	7 mL per T75 flask	~4 d
Passage 2	T175 flask	3x	~4	~7000	21 ml per T175 flask	~5 d
Passage 3	T175 flask	8x	~5	~20000	21 ml per T175 flask	~6 d
Passage 4	T175 flask	14x	~8	~35000	21 ml per T175 flask	~7 d
Passage 5	T175 flask	20x	~10	~50000	21 ml per T175 flask	~8 d

Table 2. key resources table

REAGENT or RESOURCE	SOURCE	IDENTIFIER
Antibodies		
Anti-α-actinin, primary mouse monoclonal antibody	Merck,	A7811
Anti-Ki67, primary rabbit polyclonal antibody	Abcam	AB833
Propidium Iodide (PI)	Cell Signaling	4087S
Goat Anti-mouse Alexa Fluor 488	Invitrogen	A11029
Goat Anti-rabbit Alexa Fluor 568	Invitrogen	A11011
Chemicals, peptides, and recombinant proteins		
B-27 supplement minus insulin (B27-insulin)	Thermo fisher	A1895601
B-27 supplement plus insulin (B27+insulin)	Thermo fisher	17504-044
Bovine Serum Albumin Fraction V	Roche	10735086001
CHIR-99021	Selleckchem	S2924
EDTA	Thermo fisher	15575020
Essential 8 (E8) medium	Thermo fisher	A1517001
Paraformaldehyde solution 4% in 1x PBS, pH 7.0 – 7.6	Santa Cruz	SC281692
PBS, pH 7.4	Thermo fisher	10010072
KnockOut™ (KO) Serum Replacement	Thermo fisher	10828
Matrigel, growth Factor Reduced, Basement Membrane Matrix	Corning	356230
Penicillin/streptomycin	Thermo fisher	15140
Triton X-100	Merck	X100-1L
TrypLE™ Select Enzyme (10X)	Thermo fisher	A12177
Trypan Blue Solution, 0.4%	Thermo fisher	15250061
RevitaCell	Thermo fisher	A2644501
ROCK inhibitor Y-27632	Biorbyt	orb60104
RPMI 1640 medium	Thermo fisher	11875
RPMI 1640 medium no glucose	Thermo fisher	11879020
STEMdiff™ Cardiomyocyte Freezing Medium	Stemcell	05030
Wnt-C59	Tocris	5148
Experimental Models: Cell Lines		
Human induced pluripotent stem cell lines	(Stanford Cardiovascular Institute (S-CVI) Biobank)	CVI-111 (control 1) CVI-114 (control 2) CVI-273 (control 3)

STEP-BY-STEP METHOD DETAILS

hiPSC culturing

Timing: 30 min

1. When the hiPSCs are 80–90% confluent (usually about 3 to 4 days after passaging) aspirate the old medium, then add 1 ml room temperature 0.5 mM EDTA to each well. At this point, 2.5 to 3 million cells should be present in each well of the 6-well culture plate.
2. Incubate the plate at room temperature and wait for 3-5 minutes.
3. Aspirate the EDTA and flush the hiPSC with a 1 ml tip filled with 1 ml E8 + 5 μM Y27632, dispense the medium over the surface of the plate well until all the cells are detached and gently mix 2-5 times using the 1 ml tip.

4. Add the required cell amount from the 1 ml cell suspension into each well of a Matrigel-coated plate with room temperature warm 2ml E8 + 5 µM Y27632 (split ratio of 1:13 is performed here).
5. Place the plate in the incubator and make side-to-side movements to equally disperse the cells in every well.
6. Each day aspirate the medium and add 2 ml of fresh room temperature hiPSC E8 complete medium per well.
7. When the hiPSCs are 80–90% confluent they are ready to start the differentiation. At this point, equal dispersed hiPSC colonies should be present in each well.
   CRITICAL: The starting seeding cell density is very critical for efficient cardiac differentiation. The initial plating density and/or the time of expansion prior to initiation of differentiation may require optimization for different cell lines or expansion conditions. We recommend plating at a 1:10-1:20 splitting ratio with a cell density of 80-90% within 3-4 days.
   Note: Karyotyping of the hiPSC lines is advised. Thereafter, hiPSC can be safely passaged for 20 times before another karyotyping is advised. Passaging over 40 times could lead in spontaneous differentiation of the hiPSC lines, resulting in inefficient differentiations.
   Pause point: The hiPSC can be maintained in hiPSC E8 complete medium and passaged every 3-4 days before starting differentiation and hiPSC-CM expansion.

hiPSC-CM differentiation

Timing: 10 min per day

8. Day 0: Prepare 3 mL/well of the appropriate concentration of CHIR per hiPSC line in CM differentiation medium. For every differentiation apply 2 concentrations of CHIR for an optimal window concentration per differentiation per plate.
   CRITICAL: Do not refreeze and thaw the CHIR aliquots since this molecule is unstable after thawing and freezing.
   Note: Other differentiation protocols can be used to generate hiPSC-CMs before the expansion. Here, we have used the B27[3], Heparin[4] and CDM3[2] medium, which were all sufficient for the massive expansion of hiPSC-CMs.
   Note: Though we identified 7 and 8 µM CHIR in the B27 protocol as the optimal concentration for the three lines that we tested, other lines may respond to CHIR treatment differently. We recommend testing concentrations of 2-8 µM of CHIR in heparin[4] or CDM3[2] medium and 5-10 µM of CHIR in B27[3] medium differentiations.
9. Day 1: On top of the original medium, add carefully 2 ml/well of 37°C-preheated CM differentiation medium. Put the plate back into the 37°C, 5% CO2, 21% O2 incubator.
10. Day 2: On top of the original medium, add carefully 1 ml/well of 37°C-preheated CM differentiation medium. Put the plate back into the 37°C, 5% CO2, 21% O2 incubator.
    Note: Here we use the addition of medium on day 1 and day 2 to the original medium of step 8. This protocol is effective to gradual decrease the CHIR concentration, mimicking

the first steps of embryonic heart development. However, other differentiation protocols such as 2 days of CHIR medium is also possible to generate hiPSC-CMs for the CM expansion.

11. Day 3: Aspirate the old medium and add carefully 3 mL/well of 37°C-preheated CM differentiation medium with 2 µM Wnt-C59 to each well of the 6-well plate. Put the plate back into the 37°C, 5% CO2, 21% O2 incubator.
    Note: During differentiation, the cell death rate is high. Remove dead cell debris as much as possible by shaking and aspirating the medium completely.
12. Day 5: Aspirate the medium and add 3 mL/well of 37°C-preheated CM differentiation medium. Put the plate back into the 37°C, 5% CO2, 21% O2 incubator.
13. Day 7: Aspirate the medium and add 3 mL/well of 37°C-preheated CM culture medium. Put the plate back into the 37°C, 5% CO2, 21% O2 incubator. Robust spontaneous contraction should occur by day 8-9.
14. Day 9: Aspirate the medium and add 2 mL ml/well of 37°C-preheated CM purification medium. Put the plate back into the 37°C, 5% CO2, 21% O2 incubator.
15. Day 11: The cardiomyocytes are now ready for cardiac expansion.

Replating of differentiated hiPSC-CMs

Timing: 30 min

Between day 10 and day 14 the hiPSC-derived cardiomyocytes can be used for most successful cardiac expansion. Here, we use monolayers with spontaneous contracting cells on day 11 (Movie 1). From a 6 well plate format, select the most optimal well(s) by microscopic observe the amount of beating cardiomyocytes.

CRITICAL: For efficient hiPSC-CM expansion, use wells where a beating percentage between 50-90% can be observed under the bright field microscope (confluent contracting wells roughly contain ~90% CMs).

16. Aspirate the medium and incubate hiPSC-CMs with pure TrypLE™ Select (10X) for 15-45 min at 37°C (0,75 mL of TrypLE per 9.6-cm2 growth surface).
    Note: Use the pure TrypLE™ Select (10X) for efficient dissociation of the hiPSC-CMs. Other reagents such as TrypLE™ Express or Trypsin will result in an inefficient dissociation and low viability.
17. After incubation for ~15 minutes, gently shake to detach the hiPSC-CMs. If cells do not detach yet, then repeat incubation for 1 or 2 times (up to 45 minutes). When cells come off the culture plate, add 2 ml per 25-cm2 warm RPMI-1640 per flask and dispense over the surface of the plate until all the cells are detached and gently mix 2-5 times using the 5 ml pipette.
    Note: Premature dissociation by pipetting results in shear stress-induced cell death, therefore shaking and longer incubations with TrypLE™ Select (10X) is advised.
18. Transfer the cell suspension to a 15-ml tube.
19. Centrifuge the cell suspension at 200xg for 3 min at room temperature.

20. Aspirate the supernatant and resuspend the cell suspension in 1 ml/flask of 37°C-preheated of the CM replating medium.
21. Count the cell suspension.
22. Re-plate passage 1 (P1) of hiPSC-CMs in the culture system of choice in a culture surface split ratio of 1:10-20 and add 37°C-preheated CM replating medium in the volume according to table 1.
    Note: If Animal-free and chemical defined is not desired, the Knock-out serum can be replaced with 10% FBS in the replating medium.
23. Remove the Matrigel coating from the flasks and immediately add the cell solution to the prepared culture flasks/plates.
24. Put the flask into the incubator and distribute the cells by moving the flask in short side-to-side and back-and-forth motions. Incubator conditions should be set to 37°C, 5% CO2, 21% O2, and 90% humidity. Proceed to step 25.

hiPSC-CM expansion

Timing: 30 min

25. Day 1: After attachment and recovery of passage 1 (P1) hiPSC-CM for 24 hours start the expansion process by replacing the replating medium with 37°C-preheated cardiac expansion medium according to Table 1 every other day or once every three days. For most cell lines 2 µM CHIR induces efficient expansion of hiPSC-CMs.
    CRITICAL: Even though we found that 2 µM of CHIR is the optimal concentration for the expansion of hiPSC-CMs from three different donors that we tested, it should be noted that cell line-to-line and molecular batch-to-batch variabilities are possible. Therefore, it is recommended to optimize CHIR concentrations between 1-3 µM.
    Note: The protocol for the generation of hiPSC-CMs can be variable. Here, the differentiation methods; B27[3], Heparin[4], and CDM3[2] are used to produce CMs, which can be efficiently expanded (Please see **Figure 1**).
26. After 3-5 days, the hiPSC-CMs will reach 70-80% confluency and should be passaged to inhibit cell-cell contact. Aspirate the medium, wash with PBS. Add 1 ml of room temperature warm TrypLE per 25-cm2 growth surface and incubate the hiPSC-CMs for 10–15 min at 37°C.
27. After incubation for ~15 minutes, detach the hiPSC-CMs with a 5 or 10 ml tip filled with 2 ml per 25-cm2 37°C-preheated RPMI-1640 and dispense over the surface of the plate well until all the cells are detached and gently mix 2-5 times using the 5 ml pipette.
    Note: The dissociation of expanding hiPSC-CMs will be more quickly and easier than the dissociation of d11 differentiated hiPSC-CMs, which sometimes requires prolonged incubation with TrypLE™ Select (10X).

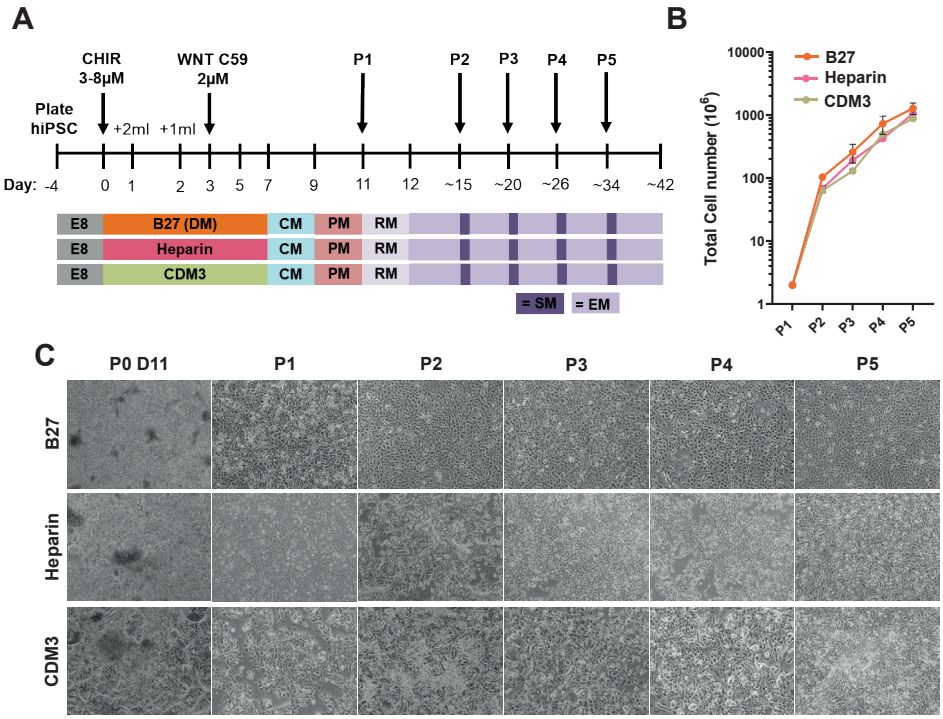

Figure 1: Massive expansion of hiPSC-CMs from various differentiation methods. (A) Schematic representation of Wnt-based directed cardiac differentiation and subsequent expansion of hiPSC-CMs generated by three different medium compositions ((B27; Lian et al., 2012; Heparin; Lin et al., 2017, and CDM3; Burridge et al., 2014). Timeline indicating B27-medium with insulin and additional CHIR99021 (CHIR) usage required for expansion. Abbreviations: CM; CM culture medium, PM; CM purification medium, RM; CM replating medium, EM; CM expansion medium, SM; CM splitting medium, P; passage. (B) Graph displaying the hiPSC-CM expansion capacity from hiPSC-CMs generated by the indicated differentiation method. One hiPSC line was used for these experiments. n=7, n=2, n=2 respectively from P0 day 11 to P5. Data are represented as mean ± SD. (C) Bright-field images at different time points of hiPSC-CM expansion with the input of the indicated differentiation methods. Scale bar, 200 µm.

28. Transfer the cell suspension to a new 15 ml tube.
29. Centrifuge the cell suspension at 200xg for 3 min at room temperature.
30. Aspirate the supernatant and resuspend the cell suspension in 1 ml/tube 37°C-preheated of the CM splitting medium supplemented with optimal CHIR concentration.
31. Count the cell suspension.
    Note: If cell numbers are high per tube, resuspend hiPSC-CMs in a larger amount of medium before counting the cell suspension (1 ml per 10 million).
32. Add 37°C-preheated CM splitting medium to the hiPSC-CMs, in the density and volume according to table 1.

33. Remove the Matrigel solution from new flasks and immediately add the cell solution to the prepared culture flasks/plates.
34. Put the flask into the incubator and distribute the cells in the well by moving the flask in short side-to-side and back-and-forth motions. Incubator conditions should be set to 37°C, 5% CO2, 21% O2, and 90% humidity.
35. Refresh the expansion medium every other day in the volume according to table 1. After 5-8 days, the hiPSC-CMs will reach 70-80% confluency and should be passaged to inhibit cell-cell contact. Repeat step 26-34 for passag e 2-5. By every passage, split the hiPSC-CMs in a lower splitting ratio and flasks according to table 1.
    Note: By higher passage numbers hiPSC-CMs proliferation gradually slows down and further passaging then P4-5 usually does not result in increased cell numbers.
    (Please see Figure 2 for representative morphologies during hiPSC-CM passaging)
    CRITICAL: Replacement of medium is recommended for every other day in order to provide fresh nutrients and stable concentrations of CHIR for expanding hiPSC-CMs. For weekend free culturing it is possible to stretch the medium changing interval accordingly while increasing the medium volume in table 1 with 1.5X.
36. After substantial expansion of the CM population, CHIR withdrawal from the medium results in the decrease of hiPSC-CMs proliferation, and subsequent regular CM culture medium change intervals can be extended for long term culturing or downstream assays.

    PAUSE POINT: After passage 1 or passage 2, the expanded hiPSC-CMs can be efficiently frozen for biobanking and thawing upon analysis (See freezing of hiPSC-CMs; Steps 35-40, **Figure 2**).

Freezing of hiPSC-derived CMs

Timing: 30 min

Note: Volumes are given for one cryovial.

35. Count the CMs after the dissociation as described in the 'Replating of differentiated hiPSC-CMs' section.
    CRITICAL: Use hiPSC-CMs in passage 1-2 for the cryopreservation and biobanking to generate viable and expandable cultures.
36. Transfer the desired cell suspension for freezing to a 15-ml tube.
37. Centrifuge the cell suspension at 200xg for 3 min at room temperature.
38. Remove the supernatant and resuspend the CM in STEMdiff™ Cardiomyocyte Freezing Medium. Use 0.5 ml medium for 0.5-2 x 106 CMs and 1 ml of freezing medium for 2-8 x 106 CMs per vial.
    Note: Keep the cell suspension on ice.
39. Freeze the vials at –80 °C overnight in a CoolCell or 2-propanol-filled freezing container.
40. Transfer the vials to liquid nitrogen or –150 °C for long-term storage.

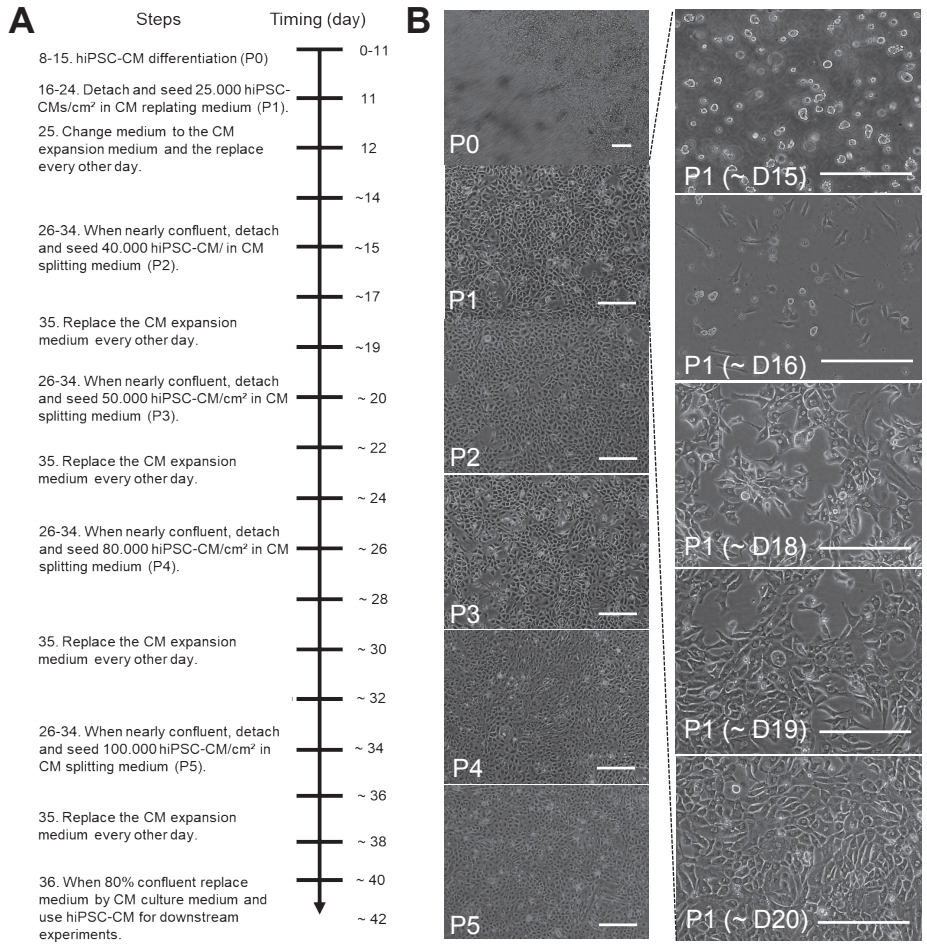

Figure 2: Visualized timeline of hiPSC-CM expansion. (A) Timeline diagram displaying the steps required for expansion and passaging of hiPSC-CMs. (B) Time-lapse images of cell morphology at the indicated passage numbers and/or culture days (D). Left: Images of cell confluency on day of passaging for P0-5. Right: Daily consecutive images of P1 hiPSC-CMs demonstrating cell seeding density and growth speed between P1 and P2. Replating at day 151-15, start of CHIR9021 (CHIR) treatment at day 12-16 the next day, cell cluster formation at day 14-19 is observed the days after and a nearly confluent monolayer before passaging at D18-206-21 the next passage. Scale bar: 200µm. Abbreviations: D; day, P; passage.

Thawing of hiPSC-derived CMs

Timing: 30 min

41. Prepare 9 ml of RPMI medium in a 15-ml tube on RT.
42. Prepare a Matrigel coated T75 per 3-6 x 106 and a T175 for 7-14 x 106 hiPSC-CMs.
43. Collect the vial with hiPSC-CMs from the liquid nitrogen and thaw the cells at 37 °C till only a little clump is visible. Do not thaw more than three vials of CMs at one time.

44. Transfer the cell suspension to the 15-ml tube, drop by drop and swirl the tube while adding the cell suspension. The dropwise addition of medium to the cell suspension is critical to minimize osmotic shock.
45. Centrifuge the cell suspension at 200xg for 3 min at room temperature.
46. Remove the supernatant and resuspend the hiPSC-CMs in the desired volume of CM thawing medium.
47. Count the cells within the cell suspension.
48. Aspirate the liquid from the Matrigel-coated flasks, and seed the CMs into the Matrigel-coated flasks, according to the format amount in **Table 1**.
49. Put the flask into the incubator and distribute the cells in the well by moving the flask in short side-to-side and back-and-forth motions. Incubator conditions should be set to 37°C, 5% CO2, 21% O2, and 90% humidity.
50. Replace the thawing medium with CM expansion medium the next day. The hiPSC-CMs should be attached, beating, and can be used for expansion (step 19) or downstream assays.
    (Please see **Figure 3** for representative viability, morphology, and proliferation rate after thawing of hiPSC-CM)

Flow cytometry analyses of dissociated hiPSC–CMs

Timing: 1.5 h, plus 30 min for dissociation of CMs

51. Dissociate the CMs as described in the 'Replating of differentiated hiPSC-CMs' section.
52. After counting the hiPSC-CMs, collect 100.000 CMs from the cell suspension in 1,5 ml tubes.
53. Centrifuge the cell suspension at 200xg for 3 min at room temperature.
54. Discard the supernatant and add 50 µl 4% PFA.
55. Incubate 10 minutes at room temperature.
56. Centrifuge the cell suspension at 200xg for 3 min at room temperature.
57. Discard the supernatant and add 1 ml PBS.
    Pause Point: The fixed hiPSC-CMs can be stored at 4°C for up to 4 weeks.

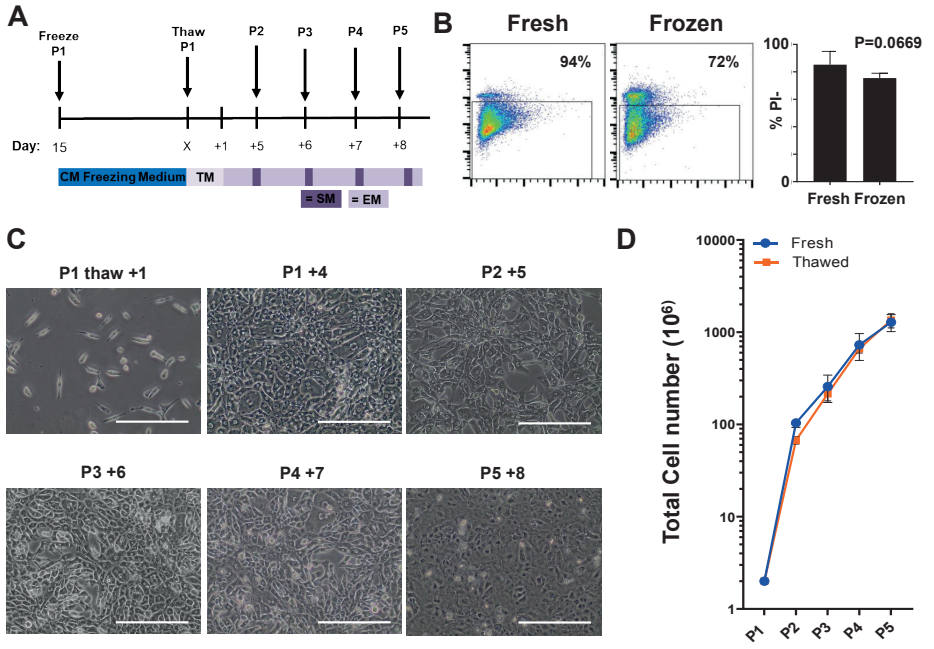

Figure 3: Cryopreservation and subsequent expansion of beating hiPSC-CMs. (A) Schematic representation of small molecule-based Wnt-modulated directed cardiac differentiation and subsequent cryopreservation and expansion. hiPSC-CMs can be stored in liquid nitrogen after passage 1 and after thawing expanded for 5 passages (P) before downstream assays. Abbreviations: TM; CM thawing medium, EM; CM expansion medium, SM; CM splitting medium, P; passage. (B) Left panels are flow cytometer detection of dead cells with propidium iodide (PI) after detaching or after thawing of cardiomyocytes, cryopreserved on day 15 of differentiation. Right is the quantification of fresh vs thawed PI % (n=5 per condition, P<0.05, paired T-test.). (C) Representative images of the thawed hiPSC-CMs before starting the expansion protocol and during passaging (scale bar: 100 µm). (D) Quantification of cardiomyocyte expansion curve of fresh vs thawed hiPSC-CMs, n=7, n=5 respectively from thawed P10 to P5.

58. Transfer the cell suspension to a FACS tube.
59. Centrifuge the cell suspension at 4 °C for 3 min at 200xg and discard the supernatant.
60. Resuspend 1 × 105 cells in 50 µl of permeabilization buffer containing 5% BSA and 0.3% Triton-X-100.
61. Incubate the cells for 30 min at 4 °C.
62. Resuspend in 50 µl of flow cytometry buffer containing the α-actinin antibody (1:300 dilution) and in another FACS tube resuspend 1 × 105 cells in 50 µl of flow cytometry buffer with the respective isotype control (e.g., FITC mouse IgM, κ isotype (1:200 dilution)) and 1 × 105 cells in 50 µl of flow cytometry buffer for negative control.
63. Incubate the cells for 30 min at 4°C.

64. Wash the cells with 2.5 ml of flow cytometry buffer and centrifuge at 200xg for 5 min at 4°C; discard the supernatant and repeat the wash two more times.
65. Resuspend in 50 µl of flow cytometry buffer containing the secondary-antibody Goat-anti-mouse (1:300 dilution).
66. Analyse the cells with a flow cytometer, adjusting the gates according to the standard gating strategy as shown in **Figure 4**.

A

CELL LINE	CTR. 1 *N* = 9	CTR. 2 *N* = 4	CTR. 3 *N* = 4	AVERAGE *N* = 25
AACTININ-POSITIVE CELLS P1 (%)	84 ± 12	88 ± 14	93 ± 8	89 ± 12
AACTININ-POSITIVE CELLS P5 (%)	88 ± 10	92 ± 1	91 ± 5	91 ± 5
FOLD INCREASE	2229 ± 1070	1129 ± 203	1303 ± 49	1343 ± 374

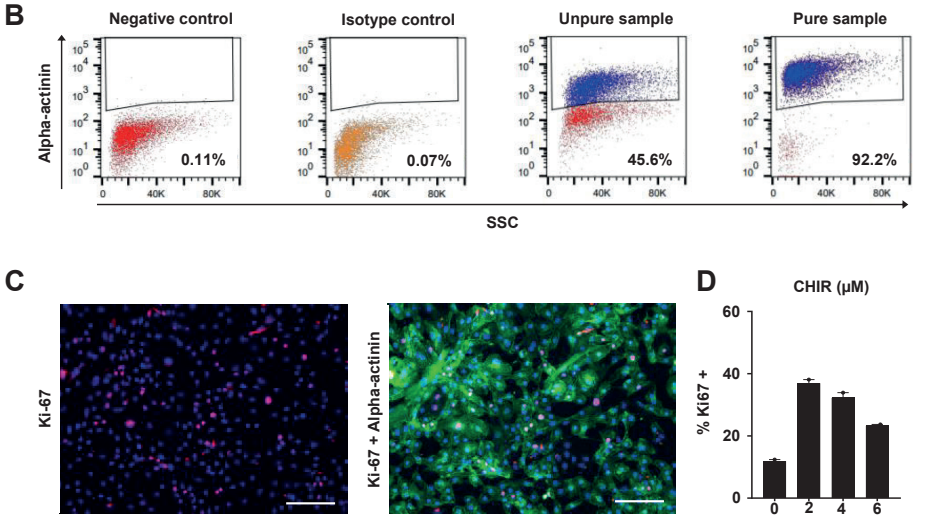

Figure 4. Differentiation efficiency and expansion capacity in different control hiPSC lines. (A) Quantitative analysis of small molecule-based Wnt-modulated directed cardiac differentiation at the passage (P) number P1 and P5. Replicate numbers refer to the number of performed expansion experiments from individual differentiation batches. The percentages of increase in hiPSC-CMs are relative to the input of day 11 hiPSC-CMs. Mean values ± s.d. are given. (B) Representative gating strategy for α-actinin positive hiPSC-CMs in a pure population of hiPSC-CMs versus negative control, isotype control, and an impure or un-purified hiPSC-CM culture. The number of α-actinin positive analyzed cells is 25 × 10^5. SSC – side scatter. (C) Representative immunofluorescence for proliferation assessed by Ki67 expression after 48 hours of CHIR treatment. Immunofluorescence: Hoechst (blue), Ki67 (red), and α-actinin (green). Scale bar: 200 µm. (D) Quantitative graph indicates high proliferation (37%) of cardiomyocytes stimulated with the optimal dose of 2 µM CHIR.

Expected Outcomes

The efficient expansion of functional CMs (up to a 250-fold increase of CM number within 3-5 weeks) can be obtained from multiple hiPSC lines. For the method described here, hiPSC-CMs from 3 different differentiation protocols were all suitable for expansion in cardiac expansion medium, though the expansion capacity of the hiPSC-CMs differentiated using the B27 differentiation protocol appears to be the most robust (**Figure 1**). Before starting the expansion steps, hiPSC-CMs microscopically should have high amounts of beating areas by d8-9 and should be used between day 11 and day 14 of differentiation. After low cell-density replating of hiPSC-CMs in culture flasks, addition CHIR to the cardiac culture medium efficiently induces hiPSC-CM proliferation and subsequent passaging (**Figure 2**). After 3-5 days of expansion, the hiPSC-CMs will reach a near confluent monolayer. The cryopreservation steps allow for biobanking of large batches of hiPSC-CMs that can be stored before expansion or after passage 1 or 2. Thawing of cryopreserved hiPSC-CMs is efficient (74% viable hiPSC-CMs, and during subsequent expansion hiPSC-CMs exhibit a similar growth curve when compared to fresh unfrozen hiPSC-CMs (**Figure 3**). After passage 2, we do not recommend to biobank the expanding hiPSC-CMs due to lower viability upon recovery. In a successful differentiation batch the expression of cardiac sarcomere protein α-actinin is usually more than 80%, and expanding cells should remain α-actinin positive during subsequent passaging. Upon CHIR optimization, up to 37% of the hiPSC-CMs will be positive for proliferative cell marker Ki-67 (**Figure 4**).

Limitations

Despite high hiPSC-CM differentiation efficiency (85%–99%) in 2D monolayer cultures (85%–99%), yet, batch-to-batch and cell line-to-line variability remains an issue for stable CM production. In our protocol, we provide the possibility to robustly expand and/or further purify hiPSC-CM cultures via serial passaging and cell contact inhibition. This ultimately allows for a 250 fold expansion of day 11 hiPSC-CMs. However, we have noticed that also cell line-to-line and batch-to-batch variabilities exist. Moreover, the expansion capacity decreases when cells are passaged multiple times.

Another limitation of our method is that hiPSC-CMs differentiation should be at least 50% (Flow cytometry positive for α-actinin) to induce an efficient proliferative response at day 11. One explanation for the absence of massive proliferation of unpure hiPSC-CM cultures would be cell-cycle inhibiting paracrine signaling factors secreted by the other cell types. Alternatively, in low efficiency cultures (<50%) the CM are phenotypically different from efficiently differentiated hiPSC-CMs (>70%). Lastly, when it comes to cryopreservation of hiPSC-CMs the cell viability after thawing reduces from P1 to P5 (70% to 28%), which was similar to the non-expanded age-matched CMs. Therefore, cryopreservation hiPSC-CMs is recommended up to passage 2. HiPSC-CMs exceeding passage 2 are suitable for the use in direct downstream assays.

Troubleshooting

Problem 1: There are many dead hiPSC after passaging, is this normal?

Potential Solution: The hiPSCs need to be monitored under a microscope and the dissociation needs to be stopped at the right time. When light sheds through the colonies and the hiPSCs can be easily flushed off the plate, the dissociation is successful. Use 0.5 mM EDTA solution and 10 µM Y27632 in the E8 complete medium is necessary.

Problem 2: The hiPSC colonies are too dense in the middle, is this a problem?

Potential Solution: The hiPSCs need to be equally divided over the wells to enable full monolayer differentiation with high efficiencies. Mechanically dissociate the detached hiPSC 5-10 times till the clumps are only 3-5 cells big. Move plate more times side-to-side in the incubator and leave cells for 24 hours.

Problem 3: The hiPSCs look abnormal or the proliferation speed is slow.

Potential Solution: Wait for some passages before starting cardiac differentiation. Perform mycoplasma test and karyotyping to rule out any hiPSC cell line abnormalities.

Problem 4: No spontaneous contraction on day 11.

Potential Solution: See solutions concerning problems during the cultivation of hiPSCs. Optimize the CHIR concentrations from 5-10 µM per hiPSC line. Do not re-freeze CHIR aliquots.

Problem 5: Many dead hiPSC-CMs are present upon thawing, is this normal?

Potential Solution: We observe a cell viability between 60-90% upon thawing by using CMs on passage 1-2. Pipette cells carefully with a 5 ml pipette. Place the thawed cells directly into the replating medium. Add 1:100 Revitacell to promote cell survival and 10% KO serum can be added to promote cell survival after thawing.

Problem 6: No hiPSC-CMs are attached to the culture flask after replating.

Potential Solution: Allow Matrigel to incubate at 37C for 1 hour. Check culture flask on complete coating coverage. Pipette cells carefully with a 5 ml pipette. Add 1:100 Revitacell to promote cell survival. Add 10% KO serum to promote cell survival. Seed cell number as described in **Table 1**.

Problem 7: Many dead hiPSC-CMs after replating, is this normal?

Potential Solution: Pipette carefully with 5 ml pipette, add 10 µM Y27632 to promote cell survival, add 10% KO serum to promote cell survival, decrease CHIR concentration, seed cell number as described in **Table 1**.

Problem 8: The hiPSC-CMs are low in their proliferation rate during passaging.

Potential Solution: Optimize the CHIR concentration and add the CHIR every other day. Do not re-freeze CHIR aliquots. Use a lower splitting ratio in the first 3 passages (1:20-1:5) and increase the splitting ratio upon passage 3 and passage 4 to 1:2. Do not split after passage 4. Only use differentiated cell populations with ≥70% α-actinin-positive cells.

ACKNOWLEGEMENTS

This work was supported by a UMC Utrecht Clinical Fellowship, Netherlands Heart Institute Fellowship, and CVON-Dosis young talent grant (to J.W.B.); Stanford Child Health Research Institute Postdoctoral Fellowship and NIH NRSA Postdoctoral Fellowship 5F32HL142205 (to S.L.); R01 HL145676, R01 HL146690, and P01 HL141084 (to J.C.W); NIH (OD004411, HL099776, LM012179) and the Joan and Sanford I. Weill Scholar Fund (to S.M.W.); Netherlands Heart Foundation (CVON-Dosis 2014–40), and Netherlands Organization for Sciences (NWO)-ZonMW (VICI 91818602) (to J.V.); Dutch Research Council (NWO) VENI grant no. 016.176.136 (M.H.); Foundation Leducq (Cure-PLaN) (to R.G.C.M., M.H., and F.A.). R.G.C.M. is supported by a grant of the PLN Foundation. F.W.A. is supported by UCL Hospitals NIHR Biomedical Research Centre; Horizon2020 ERC-2016-COG EVICARE (725229), Horizon 2020 BRAV3 (SC1-BHC-07-2019) and ZonMw-TAS program (no. 116002016) (to J.S.). We thank Prof. Joseph Wu (University of Stanford, USA) for the provision of the SCVI-111, SCVI-114, and SCVI-273 hiPSC lines. The graphical abstract was created with BioRender.com.

REFERENCES

1. Buikema, J.W. Wnt activation and reduced cell-cell contact synergistically induce massive expansion of functional human iPSC-derived cardiomyocytes. Cell Stem Cell 2020;1, 50-63.
2. Burridge PW, Matsa E, Shukla P, Lin ZC, Churko JM, Ebert AD, Lan F, Diecke S, Huber B, Mordwinkin NM, Plews JR, Abilez OJ, Cui B, Gold JD, Wu JC. Chemically defined generation of human cardiomyocytes. Nat Methods. 2014 Aug;11(8):855-60.
3. Lian X, Hsiao C, Wilson G, Zhu K, Hazeltine LB, Azarin SM, Raval KK, Zhang J, Kamp TJ, Palecek SP. Robust cardiomyocyte differentiation from human pluripotent stem cells via temporal modulation of canonical wnt signaling. Proc Natl Acad Sci U S A. 2012;109:E1848-1857
4. Lin Y, Linask KL, Mallon B, Johnson K, Klein M, Beers J, Xie W, Du Y, Liu C, Lai Y, Zou J, Haigney M, Yang H, Rao M, Chen G. Heparin Promotes Cardiac Differentiation of Human Pluripotent Stem Cells in Chemically Defined Albumin-Free Medium, Enabling Consistent Manufacture of Cardiomyocytes. Stem Cells Transl Med. 2017 Feb;6(2):527-538.

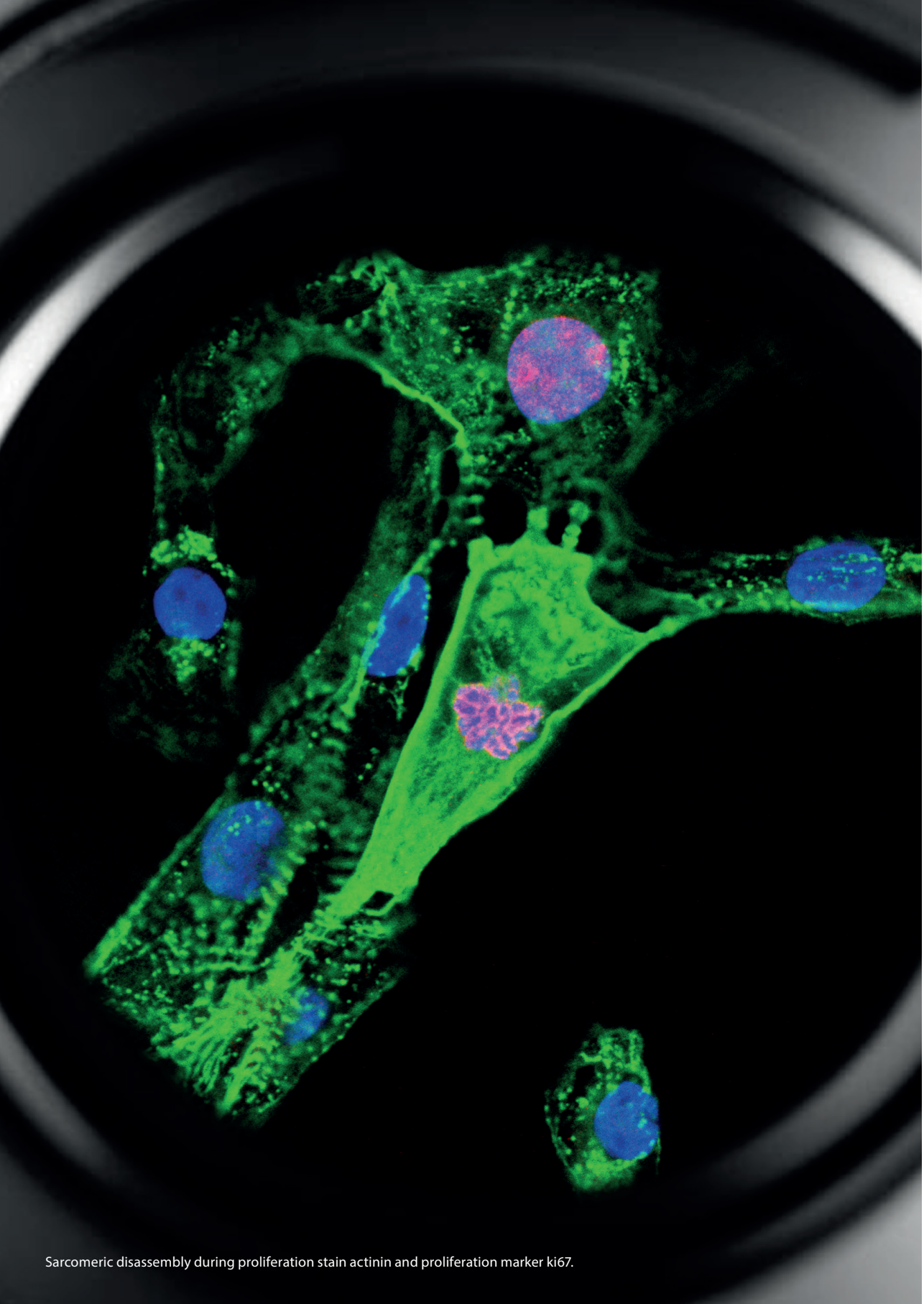

Sarcomeric disassembly during proliferation stain actinin and proliferation marker ki67.

Chapter 5

Sarcomere Disassembly and Transfection Efficiency in Proliferating Human iPSC-Derived Cardiomyocytes

Published in: Journal of Cardiovascular Development and Disease, 2022

Renée G.C. Maas*, Qianliang Yuan*, Ellen C. J. Brouwer, Jiayi Pei, Christian Snijders Blok, Marko A. Popovic, Nanne J. Paauw, Niels Bovenschen, Jesper Hjortnaes, Magdalena Harakalova, Pieter A. Doevendans, Joost P. G. Sluijter, Jolanda van der Velden, and Jan W. Buikema

*These authors contributed equally to this work.

ABSTRACT

Contractility of the adult heart relates to the architectural degree of sarcomeres in individual cardiomyocytes (CMs) and appears to be inversely correlated with the ability to regenerate. In this study we utilized multiple imaging techniques to follow the sequence of sarcomere disassembly during mitosis resulting in cellular or nuclear division in a source of proliferating human pluripotent stem cell-derived cardiomyocytes (hiPSC-CMs). We observed that both mono- and binuclear hiPSC-CMs give rise to mononuclear daughter cells or binuclear progeny. Within this source of highly proliferative hiPSC-CMs, treated with the CHIR99021 small molecule, we found that Wnt and Hippo signaling was more present when compared to metabolic matured non-proliferative hiPSC-CMs and adult human heart tissue. Furthermore, we found that CHIR99021 increased the efficiency of non-viral vector incorporation in high-proliferative hiPSC-CMs, in which fluorescent transgene expression became present after the chromosomal segregation (M phase). This study provides a tool for gene manipulation studies in hiPSC-CMs and engineered cardiac tissue. Moreover, our data illustrate that there is a complex biology behind the cellular and nuclear division of mono- and binuclear CMs, with a shared-phenomenon of sarcomere disassembly during mitosis.

INTRODUCTION

The contractile tissue of the heart is composed of a mixture of different cells, including approximately 35% cardiomyocytes (CMs).[1] Proper contraction of CMs is dictated by the architecture of the sarcomeres and appears together with polyploidy inversely correlated with self-renewal. Higher sarcomere architectural organization is related to maturity of the heart[2], while immature organization of sarcomeres correlates to the capacity of CMs to proliferate.[3] Previous studies in rodent hearts have shown that during embryonic and early postnatal hyperplastic growth phases the CMs gradually disassemble their sarcomeres during mitosis to ensure cytokinesis.[4-6]

Unlike in fish[7], mammals display hyperplastic growth shortly after birth, which is subsequentially silenced leading to heart growth predominantly originating from cellular hypertrophy.[8] The hypertrophic growth dynamic is accompanied by increased ploidy and multinucleation of the adult heart.[9-10] The exact dynamics of human CM multinucleation and self-duplication in relation to sarcomere architecture remain largely unknown. Moreover, reliable determination of CM cytokinesis, multinucleation, self-duplication and nuclear ploidy is challenging.[11-13]

The advances in human-induced pluripotent stem cells (hiPSCs) biology allow for efficient directed differentiation into CMs (hiPSC-CMs), thereby relying on biphasic Wnt signal modulation and resulting in up to 95% pure populations of hiPSC-CMs.[14-16] Currently, hiPSC-CMs are widely used in mechanistic studies, drug testing and tissue engineering.[17-18]. We and others demonstrated that a third phase of Wnt signal modulation in immature CMs results in a maturation block while prolongating the window for CM proliferation.[3,9,20-22] Using this strategy, it now becomes feasible to maintain 30–50% of Ki67 positive cells and up to 10% of mitotic CMs after day 12 of hiPSC-CM differentiation.[3,21] Here we utilized live imaging in a hiPSC-CM culture system to follow the sequence of sarcomere breakdown during the mitotic phases of CM cell division. We observed that cytokinesis in hiPSC-CMs originates from mononuclear and binuclear CMs and for both routes of duplication the sarcomere breakdown was present during the mitotic phases. Moreover, we observed that a mitotic cell figure, suggestive for the sequence of sarcomere breakdown, was also present during the process of binucleation.

Molecular genetic modification in hiPSC-CMs represents an essential tool for the mechanistic validations and functions of genes and proteins, but is limited by technical challenges to transfect low-proliferative hiPSC-CMs.[23] Here, we show that Wnt activation in hiPSC-CMs results in sarcomere breakdown during mitosis and that increased cell cycle activity facilitates increased efficiency of non-viral vector incorporation. These findings give an insight in the regulation of sarcomere homeostasis during mitotic cell phases and provide a tool for further molecular and engineering studies.

METHODS

Maintenance of hiPSC. hiPSC obtained from the Stanford Cardiovascular Institute Biobank (SCVI-111 and SCVI-273) were non-enzymatically passaged using 0.5 mM EDTA (Thermo Fisher, Waltham, MA, USA) every 4 days as previously described.[3] In brief, cells were incubated with 0.5 mM EDTA-PBS at room temperature for 5–8 min until cells began to separate uniformly throughout the colonies. PBS-EDTA was removed and hiPSC colonies were washed off swiftly using 1 mL E8 complete medium (Thermo Fisher, Waltham, MA, USA). hiPSC clumps were passaged in a ratio of 1:10 routinely at 80% confluence. To improve cell survival, split ratio reliability and to reduce selective pressure, 10 μM of ROCK inhibitor (Y-27632, Stemcell Technologies, Vancouver, BC, Canada) was added to the E8 complete medium for the first 24 h after cell passaging. Matrigel (Corning, Somerville, MA, USA, 1:400) coated plates (Corning, Somerville, MA, USA) were used for hiPSC culture and PSC Cryopreservtion Kit (Gibco, Waltham, MA, USA) was used for the cryopreservation of hiPSC.

Differentiation of hiPSC into Cardiomyocytes. To obtain hiPSC-derived CMs, hiPSCs were grown to ~90% confluence in a 6-well format. hiPSC cells were maintained in E8 complete medium for at least three passages before starting cardiac lineage differentiations. The cells were efficiently differentiated as previously described, using the RPMI/B27 minus insulin medium (Gibco, Waltham, MA, USA) supplemented with 7–8 μM CHIR99021 (cell line specific) (SelleckChem, Houston, TX, USA) for the first 2 days and 2 μM Wnt-C59 (SelleckChem, Houston, TX, USA) for another 48 h. The proliferation of hiPSC-CMs can be conducted by the removal of cell–cell contacts and small-molecule inhibition with CHIR99021.[3] Subsequential multiple low-density passaging and reintroduction of 2–3 μM CHIR99021 (cell line specific) to the RPMI/B27 media results in an expansion of hiPSC-CMs.[3]

Metabolic Maturation of iPSC-CMs. In order to mature the CMs, we used a previously described metabolic maturation medium.[24] After re-plating and purification, the RPMI/B27 medium was replaced by the maturation medium for a minimum of 3 weeks. Metabolic maturation medium was composed in RPMI 1640 (Thermo Fisher Scientific, Waltham, MA, USA, 11875119) with B27 supplement (Thermo Fisher Scientific, Waltham, MA, USA, 17504-044). Maturation media was composed in DMEM without glucose (Thermo Fisher Scientific, Waltham, MA, USA, 11966025) supplemented with 3 mM glucose (Sigma Aldrich, Saint Louis, MO, USA, G7021), 10 mM L-lactate (Sigma Aldrich, Saint Louis, MO, USA, 71718), 5 μg/mL Vitamin B12 (Sigma Aldrich, Saint Luis, MO, USA, V6629), 0.82 μM Biotin (Sigma Aldrich, Saint Louis, MO, USA, B4639), 5 mM Creatine monohydrate (Sigma Aldrich, Saint Louis, MO, USA, C3630), 2 mM Taurine (Sigma Aldrich, Saint Louis, MO, USA, T0625), 2 mM L-carnitine (Sigma Aldrich, Saint Louis, MO, USA, C0283), 0.5 mM Ascorbic acid (Sigma Aldrich, Saint Louis, MO, USA, A8960), 1 × NEAA (Thermo Fisher Scientific, Waltham, MA, USA, 11140), 0.5% (*w/v*) Albumax (Thermo

Fisher Scientific, Waltham, MA, USA, 11020021), 1 × B27 and 1% KOSR (Thermo Fisher Scientific, Waltham, MA, USA, 10828028). The medium was refreshed every 3–4 days.

Immunofluorescence. hiPSC-CMs after two days of expansion were seeded into a µ-Plate 96 well (Ibidi) with a density of ~5 × 10^4 cells/well for continuously culturing with RPMI/B27 and RPMI/B27 supplemented with CHIR99021 (3 µM) for six days. Media was refreshed every other day. At day 6, the cells were washed and fixed with 4% formaldehyde for 10 min at room temperature, permeabilized with 0.25% PBS-Triton for 5 min and then blocked with 10% donkey serum for 30 min. The cells were then incubated overnight at 4 °C with primary antibodies for cTnT (TNNT2 [1C11], Ab8295, dilution 1:250, Abcam, Cambridge, UK) and Ki67 (D3B5, dilution 1:400, Cell Signaling Technology, Danvers, MA, USA). Next, the cells were incubated with the corresponding secondary Alexa fluor-555 and –647 antibodies (1:400 dilution, Life Technologies, Carlsbad, CA, USA) for 1 h at room temperature. Nuclear DNA was labeled with DAPI. Images were acquired by an Eclipse Ti2 inverted microscope system (Nikon, Tokio, Japan). Z-stacks function was performed with 0.2 um thickness containing 11 frames under the 40×/0.95 NA objective in wide-field mode. All the images were processed afterwards for 3D deconvolution by NIS elements analysis software. Analysis and quantifications were performed with a maximum intensity projection by Image J.

Time-Lapse Imaging. Time-lapse sequence was implemented in order to keep track of hiPSC-CMs single cell cycle phases. hiPSC-CMs were replated on a Matrigel-coated 8-well chamber (Ibidi, Grafelfing, Germany) with a density of 1 × 10^5 cells/well. The cells were treated with 3 µM CHIR99021 for 2 days, then subjected to time-lapse imaging on an Eclipse Ti2 inverted microscope system (Nikon, Tokio, Japan) for imaging under the objective of 10×/0.45 NA. Cells were kept at an Okolab enclosure with temperature 37 °C, 5% CO_2 and 95% humidity. Each frame was acquired every 5 min until 12–24 h. Nuclear morphology varied in mitotic phases were captured from mononucleated or binucleated cells. To keep track of mCherry expression in hiPSC-CMs, The time-lapse sequence was developed 12 h post-transfection of hiPSC-CMs with the mCherry plasmid on an Eclipse Ti2 inverted microscope system (Nikon, Tokio, Japan) using bright-field mode/or confocal mode with a 10×/0.45 NA objective. Images were taken every 5 min for 12 h.

RNA Sequencing for CM Proliferation Genes. hiPSC-CMs collected at passage 1–3 and during maturation (day 77, 84 and 97) were obtained from a healthy donor hiPSC-CMs. RNA was isolated using ISOLATE II RNA Mini Kit (Meridian Biosciences, Cincinnati, OH, USA) according to the manufacturers' instructions with minor adjustments. After the isolation of mRNA, libraries were prepared using the NEXTflexTM Rapid RNA-seq Kit (Perkin Elmer, Waltham, MA, USA). Libraries were sequenced on the Nextseq500 platform (Illumina, San Diego, CA, USA), producing single-end reads of 75 bp. Reads were aligned to the human

reference genome GRCh37 using STAR v2.4.2a. Picard's AddOrReplaceReadGroups v1. (http://broadinstitute.github.io/picard/ (accessed on 4 June 2020)) was used to add read groups to the BAM files, which were sorted with Sambamba v0.4.5 and transcript abundances were quantified with HTSeq-count v0.6.1p1 using the union mode. Subsequently, reads per kilobase per million mapped reads (RPKMs) were calculated with edgeR's RPKM function.

Transfection of hiPSC-CMs with mCherry. hiPSC-CMs were transfected (ViaFect (6:1), Promega, Madison, WI, USA) with 100 ng/cm^2 PF256-H2B-mCherry and 20% FBS (Gibco). After 3 days, cells were harvested for FACS analysis, and fluorescent images were acquired with the EVOS (Life Technologies, Carlsbad, CA, USA). For quantification, nuclear expression (mCherry) was calculated as a percentage of positive nucleus to total nucleus (Hoechst 33342, Invitrogen, Waltham, MA, USA). The time-lapse imaging was developed with a 12 h post-transfection of hiPSC-CMs with mCherry plasmid on an LIPSI Ti2 inverted microscope system (Nikon, Tokio, Japan) using wide-field mode or confocal mode with a 10×/0.45 NA air objective. Images were taken every 5 min for 12 h.

FACS Analysis of Transfection Efficiency. After transfection, cells were dissociated via digestion with TrypLE™ Select (10×, Gibco, Waltham, MA, USA) and fixed in 4% paraformaldehyde (PFA). Next, immunostaining was performed on cells fixed with 4% paraformaldehyde (PFA) in PBS. Cells were incubated with anti-α-Actinin (clone A7811, Sigma Aldrich, Saint Louis, MO, USA) or anti-Ki67 (clone A833, Abcam, Cambridge, UK) labeled with Alexa-488 using 1:300 Alexa Fluor 488 (Thermo Fischer Scientific, Waltham, MA, USA) and 0.1 µg/mL Hoechst (33342, Invitrogen, Waltham, MA, USA). The staining was performed in PBS with 5% BSA (Roche) and 0.3% Triton-x-100 (Sigma Aldrich, Saint Louis, MO, USA). Stained cells were analyzed and sorted on an Astrios FACS (BD Pharmingen, San Diego, CA, USA). Data were collected from at least 10,000 events.

Statistical analysis. Statistical analysis was conducted by Graphpad Prism software version 9. Data significance was statistically determined using an unpaired Student's *t*-test for the comparison of two normally distributed datasets. One-way ANOVA or two-way ANOVA was performed with a Tukey's multiple comparisons test to evaluate statistical differences among multiple datasets. Data plots are displayed as mean ± standard error of mean (sem), unless specified otherwise, and a p-value < 0.05 was set to determine statistical significance.

RESULTS

Sarcomere Organization of hiPSC-CMs during Cell Cycle Phases

To visualize sarcomere organization during the cell cycle phases (G0, G1/S/G2 and M-phase), we differentiated hiPSC lines (Stanford Cardiovascular Institute 273 (SCVI-273 or SCVI-111) into CMs and performed imaging for sarcomere proteins and cell cycle marker expression (Ki67). Day 11 hiPSC-CMs were dissociated, replated and treated with glycogen synthase-3 beta (GSK3β) inhibitor to activate canonical Wnt signaling to maintain the proliferative capacity of early hiPSC-CMs.[3,24] (Figure 1A). To confirm purity after passage 1 (P1), hiPSC-CMs were stained for cardiac troponin T (cTnT) and cell counting indicated the presence of >95% pure CMs (**Figure 1B, 1C**). High resolution confocal imaging of hiPSC-CMs, stained for Ki67 and cTnT, demonstrated that CMs in G0 phase and G1/S/G2 phase had the highest degree of organized sarcomeres and were spontaneously beating, while cells in M phase, especially during metaphase, anaphase and telophase, disassembled their sarcomeres, had a rolled-up morphology and were not lively contracting (**Figure 1D, 1E** and **Supplementary Figure 1**). Interestingly, we observed that both mononuclear and binuclear hiPSC-CMs were found in G0 phase. Automated quantification of the amount of troponin T lines confirmed that quiescent CMs (G0) expressed more lines when compared to Ki67 positive CMs ($p < 0.05$). These results indicate that sarcomere breakdown, by reduced Troponin T lines, is present in hiPSC-CMs that undergo cytokinesis.

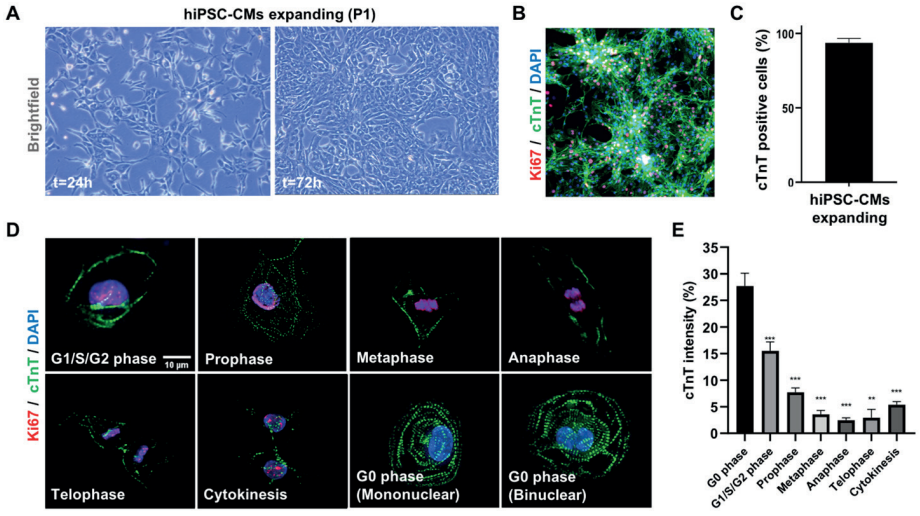

Figure 1. hiPSC-CMs sarcomere disassembly during mitosis. (A) Bright-field images of expanding hiPSC-CMs at passage 1 (P1). (B) Immunofluorescence for cardiac troponin T (cTnT), Ki67 and DAPI in hiPSC-CMs expanded with 3 µM CHIR99021 for 2 days. (C) Quantification of cTnT positive cells represented as a percentage of total cells (n = 3). (D) Representative immunofluorescence wide-field images of cTnT, Ki67 and DAPI during the different cell cycle phases of hiPSC-CMs. Note: during metaphase, anaphase and telophase the hiPSC-CM have a rolled-up morphology while contraction is absent. Scale bar indicates 10 µm. (E) Quantification of cTnT density analyzed by image J (n = 50). Bar plot represents mean cTnT intensity ± SEM. Significance assessed by unpaired t-test and defined by ** $p < 0.01$, and *** $p < 0.001$.

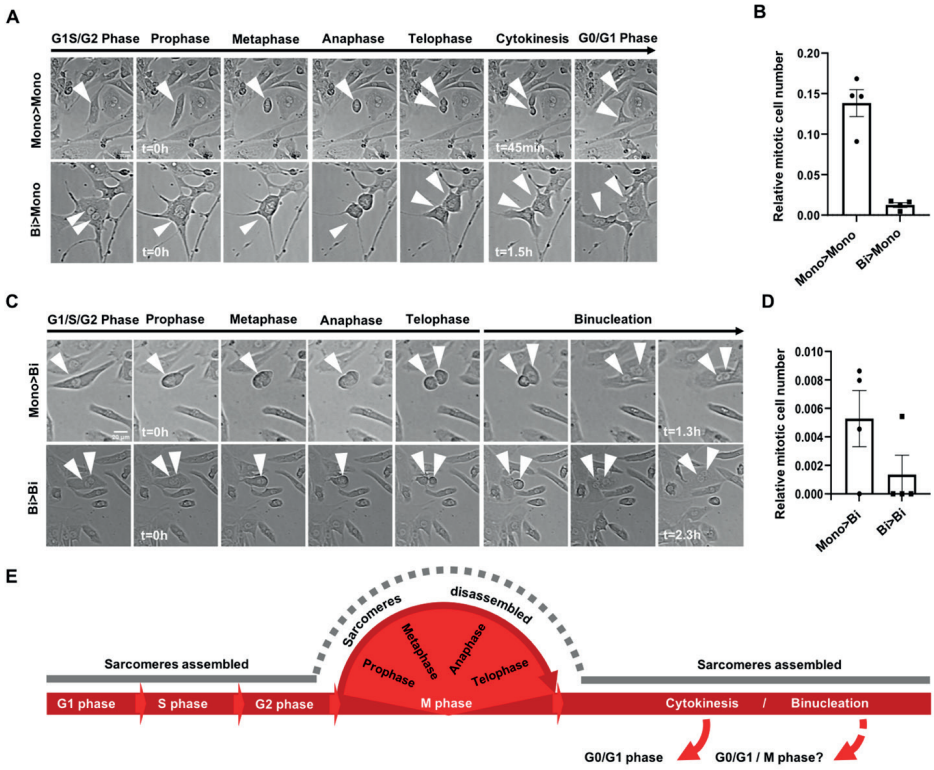

Figure 2. Time-lapse analysis of cytokinesis and binucleation in hiPSC-CMs. (A) Mononuclear (Mono > Mono) or binuclear (Bi > Mono) hiPSC-CMs undergoing cytokinesis after chromosomal segregation (rolled-up morphology). Time is indicated in hours (h). Scale bar indicates 20 µm. (B) Relative number of mitotic mononuclear (Mono > Mono) or binuclear (Bi > Mono) hiPSC-CMs undergoing cytokinesis. Average consists of 4 replicates including, in total, 105 mitotic cells of 771 counted cells for the SCVI-273 hiPSC line. Error bars indicate standard error (C) Bright-field time-lapse images showing binucleation and chromosomal segregation of pre-existent mononuclear (Mono > Bi) or binuclear (Bi > Bi) hiPSC-CMs. Time is indicated in hours (h). Scale bar indicates 20 µm. (D) Relative number of mitotic mononuclear (Mono > Bi) or binuclear (Bi > Bi) hiPSC-CMs undergoing binucleation. Average consists of 4 replicates including, in total, 105 mitotic cells of 771 counted cells for the SCVI-273 hiPSC line. Error bars indicate standard error. (E) Schematic diagram visualizing cell cycle in relation to status of the sarcomeres.

Live Tracing of Mitotic Figures in hiPSC-CMs

To assess longitudinal characterization of CMs in M-phase (segregation of chromosomes) and their progeny, we recorded time-lapse videos of proliferating SCVI-273 hiPSC-CMs and analyzed the fraction of cells that went through the M-phase, indicated by a rolled-up morphology during the anaphase.[13] We identified that both mononuclear (~13% of total) and binuclear cells (~1.5% of total) can enter the M-phase to segregate their chromosomes to give rise to two daughter cells (**Figure 2A, 2B**). Interestingly, binuclear CMs also (re)entered the M phase instead of directly providing one nucleus to each daughter cell (Figure 2A, arrows in lower panel).

Moreover, we observed that both mononuclear (~0.5% of total) and binuclear (~0.1% of total) hiPSC-CMs entered the M-phase to become or remain binuclear (**Figure 2C, 2D**). We repeated these experiments in SCVI-111 hiPSC-CMs treated with CHIR99021 and found that all four sequences were present with similar distributions, the binuclear-to-binuclear transition being the rarest event (**Supplementary Figure 2**). Given our study (**Figure 1**) on sarcomere density during M-phase it appears that for each form of nuclear or cytoplasmic division of hiPSC-CMs, cells underwent chromosomal segregation accompanied by sarcomere breakdown (**Figure 2E**).

Gene Expression Analysis of Long-Term Proliferating, Matured Non-Proliferative hiPSC-CMs and Adult Human Heart Tissue

To provide more background on the cell cycle status of immature hiPSC-CMs, which were long-term cultured with GSK3β inhibitor CHIR99021 and sequential serially passaged (up to P4), we performed gene expression profiling for each serial passage (P1 (day ~18), P2 (day ~24) and P3 (day ~35)) and compared this to long-term metabolic matured hiPSC-CMs of day 77, 84 and 97. Confirmative immunohistochemistry for α-actinin and Ki67 demonstrated that proliferation rates (Ki67 positivity) were decreased when reaching a higher passaging number in expanding CMs.[25] (**Figure 3A**). In contrast, in long-term metabolic matured hiPSC-CMs, we observed almost complete absence of proliferative cells.[25] (**Figure 3A**). Moreover, higher organization of sarcomeres was visible in mature versus immature hiPSC-CMs (**Figure 3A, lower left panel**).

Whole genome RNA sequencing revealed that the expression of sarcomere genes in mature CMs and human heart tissue, such as TNNI3 and TNNT2, were inversely correlated to genes associated with proliferation, such as TOP2A, MKI67 and CCND2 (**Figure 3B**). The opposite phenomenon was observed in the gene expression of proliferative CMs from P1, P2 and P3. Furthermore, genes associated with embryonic signaling pathways, including Wnt and Hippo, were upregulated in proliferating hiPSC-CMs when compared to quiescent CMs (**Figure 3B**). Analysis of M-phase, G2 phase, S phase and G1 phase-related genes showed an increase in the long-term Wnt-treated hiPSC-CMs from P1 to P3 versus the metabolic maturated CMs from day 77, 84 and 97 and adult human hearts (**Figure 3C**). Altogether, these data showed that in hiPSC-CMs, the cell cycle gene expression is inversely correlated to sarcomere gene expression and maturity of CMs.

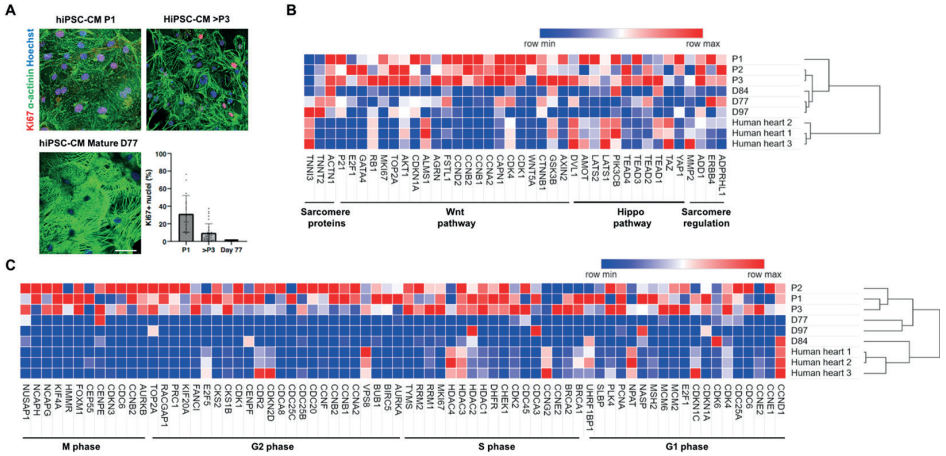

Figure 3. Selected gene expression profiles for developmental growth and cell cycle regulators in serially passaged immature hiPSC-CMs and metabolic matured hiPSC-CMs. (A) Representative immunofluorescence for Hoechst (blue), Ki67 (red), and a-actinin (green) in hiPSC-CMs treated with CHIR99021 at passage 1 (P1) and 4 (p > 3), versus metabolic matured hiPSC-CMs at day 77. Graph displays the percentage of Ki67 positive nuclei per condition (P1, >P3 or day 77) (n = 3 differentiations with 17, 32 and 24 quantified images). (B) Heatmap showing the expression patterns of 40 selected genes involved in the proliferation and/or development of hiPSC-CMs between expanding hiPSC-CMs (passage 1–3), metabolic matured hiPSC-CMs (day 77, 84 and 97) and adult human heart tissue. (C) Heatmap showing the expression patterns of cell cycle phase-related genes between expanding hiPSC-CMs (passages 1–3), metabolic matured hiPSC-CMs (day 77, 84 and 97) and adult human heart tissue. Red indicates high expression and blue indicates low expression of represented genes. Heatmaps are clustered and show the RPKMs for the selected genes.

GSK3β Inhibition Increases Non-Viral Vector Incorporation Efficiency in hiPSC-CMs

The efficiency of non-viral vector incorporation in low-proliferative hiPSC-CMs is usually below 20%, which highly challenges its usefulness in, e.g., molecular knockdown experiments.[26] We reasoned that GSK3β inhibition in hiPSC-CMs, promoting a high-proliferative status, would also potentially enhance the incorporation and expression of introduced plasmid DNA. To this end, we used day 30 high-proliferative hiPSC-CMs treated with CHIR99021 and low-proliferative non-GSK3β inhibition treated age-matched controls and transfected these for 72 h with a PF256-H2B-mCherry plasmid (mCherry expression controlled by the histone cluster 1 promotor in the presence of Lipofectamine or ViaFect transfection reagent.[27] Non-viral vector incorporation efficiency was measured by flowcytometry for mCherry and Hoechst and fluorescence-based immunohistochemistry for α-actinin and expression of mCherry 72 h after the start of transfection (**Supplementary Figure 3A–C**). We observed that in the presence of CHIR99021 30.5 ± 4.9% of day 30, high-proliferative hiPSC-CMs expressed mCherry versus 10.8 ± 5.4% (p = 0.03) of low-proliferative hiPSC-CMs cultured without a GSK3β inhibitor (Figure 4A). To investigate the cell cycle-independent effects of the GSK3β inhibition of non-viral vector incorporation efficacy, we also transfected day ~80 metabolic matured

and non-proliferative hiPSC-CMs in the presence or absence of CHIR99021. We found that in the presence of CHIR99021, non-proliferative CMs expressed mCherry in 12 ± 0.6%, while in the absence of CHIR99021, matured CMs were mCherry positive in 8.3 ± 0.8% (p = 0.89) (**Figure 4B**). Additionally, we compared ViaFect with Lipofectamine 3000 transfection reagent and found that CHIR99021 treatment increased the transfection efficiency in both reagents by more than 50% (**Figure S3D**). To confirm general transfection efficiency and potential non-cell cycle-dependent effects of CHIR99021, we utilized a common source of indefinitely proliferating HEK293 cells and transfected these with and without GSK3β inhibition. In HEK293 cells we observed no significant increase in transfection efficiency when CHIR99021 was added to the media versus the DMSO carrier control (33.8% vs. 35.8%, p = 0.93) (**Figure 4C**). Next, we confirmed the expression of mCherry in the fraction of CMs, which were treated with CHIR99021 via immunohistochemistry for α-actinin and endogenous mCherry fluorescence (**Figure 4D**). These data illustrate that CHIR99021 promotes non-viral vector uptake in hiPSC-CMs predominantly via a cell cycle-dependent way.

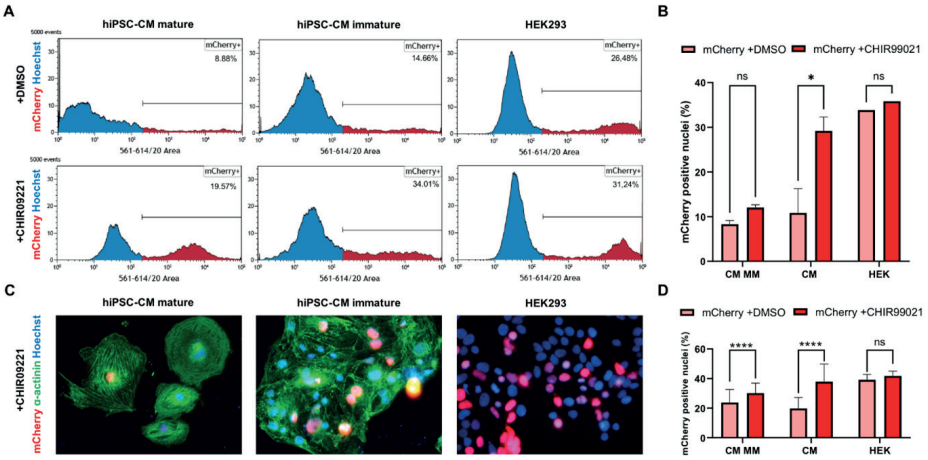

Figure 4. Transfection efficiency in immature hiPSC-CMs vs. mature hiPSC-CMs and HEK293 cells. (A) Quantitative flow-cytometry graph indicating high transfection efficiency of up to 34% in immature and up to 20% in mature hiPSC-CM treated with 2 μM of CHIR99021, 100 ng/mL mCherry plasmid and with ViaFect transfection reagent. (B) Bar graph displaying mean mCherry transfection efficiency in immature (CM) and mature (MM) hiPSC-CMs and HEK293 cells (HEK) treated with CHIR99021 or DMSO carrier control in the presence of ViaFect or Lipofectamin transfection reagent. Mean flow-cytometry values of 3 biological replicates are represented and error bars indicate standard deviation. (C) Representative immunofluorescence for Hoechst (blue), mCherry (red) and α-actinin (green) after 72 h of transfection treatment (ViaFect) in hiPSC-CMs and HEK293 cells treated with CHIR99021. (D) Quantitative bar graph representing mean transfection efficiency in a fraction of hiPSC-CMs or HEK293 cells by mCherry expression of high transfection efficiency. Experiments performed 3 biological replicates. Error bars indicated standard deviation. * indicates $p < 0.05$, ** indicates $p < 0.01$).

Live Tracing of Non-Viral Vector-Based Fluorescence Expression in hiPSC-CMs

Based on our data, it appears that the cell cycle-related effects of CHIR99021 are the most crucial for the transfection efficiency in hiPSC-CMs (**Figure 4).** To demonstrate that indeed the active cycling hiPSC-CMs were to express the mCherry plasmid first, we recorded time-lapse videos in bright-field and immunofluorescence mode for 12 h starting at 1-day post-transfection of the cells. After 24 h and 36 h of transfection we observed a pattern of mainly neighboring cells that started to express the mCherry fluorescent protein (**Figure 5A**). Quantification of neighboring cells confirmed that 75.25% were paired mCherry positive cells, while 14.35% of mCherry positive cells were unpaired and 10.4% were binucleated cells (Figure 5B). Next, we analyzed our time-lapse videos for cells that showed a rolled-up morphology during mitosis and found that the fraction of cells undergoing cytokinesis started to express mCherry protein mainly right after cytokinesis had occurred (**Figure 5C**). In cells that became binucleate after mitosis we noticed an expression of mCherry in both nuclei upon completion of the binucleation process (**Figure 5D**). These data indicate that incorporation of vectors occurs before or during M-phase, while expression of the PF256-H2B-mCherry vector starts immediately after the M-phase.

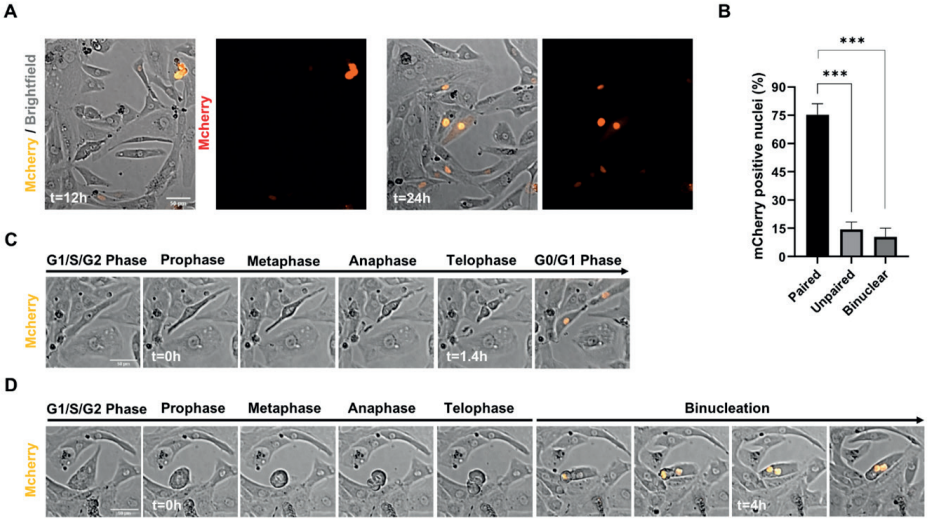

Figure 5. Time-lapse analysis of non-viral vector mCherry incorporation in proliferating hiPSC-CMs. (A) Representative time-lapse images of the mCherry positive hiPSC-CMs 12 h and 24 h post-transfection with mCherry-H2B plasmid and ViaFect transfection reagent. (B) Quantification of the mCherry positive paired, unpaired and binucleated cells represented in percentages (n = 100). Data are shown as mean ± SEM. *** $p < 0.001$ as calculated by Student's t-test. (C) Selected time-lapse images visualizing mCherry expression in a mononuclear hiPSC-CM undergoing cytokinesis. (D) Selected time-lapse images demonstrating mCherry expression after binucleation of a mononuclear hiPSC-CM. Time is indicated in hours (h). Scale bar indicates 50 µm.

DISCUSSION

The cardiomyocyte compartment of the human heart is largely non-mitotic and with an annual cell turnover lower than 1%, this explains the lack of true regenerative capacity.[28] In the neonatal period, CMs still proliferate and the heart possesses a capacity to regenerate upon injury, while in the adult myocardium the rate of CM self-renewal becomes too low to compensate for potential cell loss by, e.g., myocardial infarction. In mammals, cardiac growth by hyperplasia changes to hypertrophy early after birth, coinciding with increasing DNA content of the CMs via multinucleation and nuclear polyploidization.[11] Previous studies have shown a correlation between the amount of diploid CMs and substantial regenerative capacity, raising the hypothesis that multinucleation and/or polyploidy forms a block for CM proliferation and heart regeneration.[9,10,25,29,30] On the contrary, there is evidence for self-duplication of multinucleated CMs, suggesting a more complex situation of ploidy in relation to cardiac repair.[31,32] For this study, we utilized time-lapse recordings to study the sequence of sarcomere distribution during mitosis, followed by cytokinesis, multinucleation or self-duplication in massively expanding hiPSC-CMs.

In **Figure 1** we demonstrate that during mitosis of hiPSC-CMs, sarcomere breakdown is predominantly activated during the metaphase, anaphase and telophase and cells transiently stop contracting during cytokinesis. After cytokinesis and the following G0 or G1/S/G2 phases, the sarcomeres are restored and spontaneous beating is reinitiated. Moreover, we observe that in hiPSC-CMs the sequence of mitosis is followed by cytokinesis and self-duplication versus multinucleation (**Figure 2**). Remarkably, for all of these sequences, we noticed that chromosomal segregation (M-phase), accompanied by sarcomere disassembly were both present during mitosis (**Figure 1** and **Figure 2**). Mechanistically, we show that Wnt and Hippo genes are highly expressed in the high-proliferative juvenile hiPSC-CMs versus non-proliferative metabolic matured CMs (**Figure 3**). In addition, we demonstrate in **Figure 4** that high-proliferative hiPSC-CMs in G1/S/G2 or M phase can incorporate non-viral vectors at a much higher degree than low-proliferative or non-proliferative hiPSC-CMs. Our data also indicates that the earliest expression of such vectors is present in CMs that just have gone through M phase/chromosomal segregation (**Figure 5**). Collectively, our study provides information on sarcomere density during mitosis and sequential cytokinesis, self-duplication or multinucleation. Our live-tracing studies (**Figure 2** and **Supplementary Figure 2**) indicated that cell cycle activity of hiPSC-CMs was varying among different cell lines. We observed that cytokinesis occurred in 13–40%, self-duplication in 1.5–2.5% and multinucleation in 0.6–1.7% of events. Multinucleation as a result of a binuclear cells going through the M phase formed a rare event (0.1–0.2%). The observation that binucleated cells can self-duplicate is in line with previous studies in mice that have found that regenerative capacity also originates from pre-existing and multinucleated CMs.[31,32] The occurrence of binucleation, however, is 5–10 times lower than self-renewal in our hiPSC-CM system, in which we concurrently activate Wnt signaling and remove cell–cell contacts (**Figure 2B, 2D** and **Figure 5B**). Therefore, this

higher incidence of cytokinesis from mononucleated cells in our system also appears to be in line with the concept that diploid cells are the most powerful for endogenous heart regeneration.[10] The observation that hiPSC-CMs disassemble their sarcomeres followed by temporary quiescence is potentially explanatory for the low number of cell division in the adult human heart, which cannot allow itself "to skip a beat". Besides the heart, the process of multinucleation as a result of a cytokinetic cell division also occurs in skeletal muscle and forms of cancer. Previous studies have demonstrated that this multinucleation process is reflected in hiPSC-derived muscle progenitor and cancer cell line models.[33-35]

Additionally, our non-viral vector gene transfection studies show that efficiency is highly related to the proliferative status of hiPSC-CMs. Although multiple methods of genetic modifications exist (i.e., lipofectamine-mediated transfection, and viral-based transduction), their efficiency, cytotoxicity, safety, and cost remain unsatisfactory and often below 10–20%.[26] We used our live hiPSC-CM imaging setup to study the transfection in proliferating (canonical Wnt activation) versus non-proliferating hiPSC-CMs. We found that hiPSC-CMs after chromosomal segregation (mitotic figure) were the first cells expressing a non-viral vector-based fluorescent protein. A smaller fraction of cells incorporates non-viral vector DNA in a cell cycle-independent manner. This improved approach for gene transfection is directly usable for research involving molecular studies and cardiac tissue engineering applications.

Several limitations should be considered when interpreting the results of our study. Although we used expanding hiPSC-CMs reaching purity of up to 98%, for our time-lapse videos we were not able to live trace sarcomere, and therefore, there is potentially a risk of other cell types being recorded and analyzed. Secondly, CHIR99021, a potent GSK3β inhibitor present in our expansion culture system, could potentially also have non-cell cycle-related effects leading to increased transfection rates. Our data in Figure 5, however, indicates that activation of the cell cycle and M phase is needed for early incorporation of non-viral vectors. Lastly, the lack of environmental cues in our in vitro system put limitations on the interpretation of the described event of self-duplication as a potential route for heart regeneration.

This study demonstrates that there is a complex landscape in hiPSC-CM proliferation, multinucleation and self-duplication. Moreover, enhanced incorporation of non-viral vectors is related to Wnt activation and cell cycle activity of hiPSC-CMs, which forms a strong tool for molecular gene studies in hiPSC-CMs and cardiac tissue engineering.

ACKNOWLEDGEMENTS

We thank Joseph C. Wu from Stanford University for providing lines SCVI-111 and SCVI-273. We thank Amsterdam UMC (location VUmc; O2 building) Microscopy and Cytometry Core Facility (MCCF) for the technological support.

REFERENCES

1. Banerjee, I.; Fuseler, J.W.; Price, R.L.; Borg, T.K.; Baudino, T.A. Determination of cell types and numbers during cardiac development in the neonatal and adult rat and mouse. Am. J. Physiol. Circ. Physiol. 2007, 293, H1883–H1891. [Google Scholar] [CrossRef] [PubMed]
2. Guo, Y.; Jardin, B.D.; Zhou, P.; Sethi, I.; Akerberg, B.N.; Toepfer, C.N.; Ai, Y.; Li, Y.; Ma, Q.; Guatimosim, S.; et al. Hierarchical and stage-specific regulation of murine cardiomyocyte maturation by serum response factor. Nat. Commun. 2018, 9, 3837. [Google Scholar] [CrossRef] [PubMed]
3. Maas, R.G.; Lee, S.; Harakalova, M.; Blok, C.J.S.; Goodyer, W.R.; Hjortnaes, J.; Doevendans, P.A.; Van Laake, L.W.; van der Velden, J.; Asselbergs, F.W.; et al. Massive expansion and cryopreservation of functional human induced pluripotent stem cell-derived cardiomyocytes. STAR Protoc. 2021, 2, 100334. [Google Scholar] [CrossRef] [PubMed]
4. Fan, X.; Hughes, B.G.; Ali, M.; Cho, W.J.; Lopez, W.; Schulz, R. Dynamic Alterations to α-Actinin Accompanying Sarcomere Disassembly and Reassembly during Cardiomyocyte Mitosis. PLoS ONE 2015, 10, e0129176. [Google Scholar] [CrossRef]
5. Ahuja, P.; Perriard, E.; Perriard, J.-C.; Ehler, E. Sequential myofibrillar breakdown accompanies mitotic division of mammalian cardiomyocytes. J. Cell Sci. 2004, 117, 3295–3306. [Google Scholar] [CrossRef]
6. Porrello, E.R.; Mahmoud, A.I.; Simpson, E.; Hill, J.A.; Richardson, J.A.; Olson, E.N.; Sadek, H.A. Transient Regenerative Potential of the Neonatal Mouse Heart. Science 2011, 331, 1078–1080. [Google Scholar] [CrossRef]
7. Jopling, C.; Sleep, E.; Raya, M.; Martí, M.; Raya, A.; Belmonte, J.C.I. Zebrafish heart regeneration occurs by cardiomyocyte dedifferentiation and proliferation. Nature 2010, 464, 606–609. [Google Scholar] [CrossRef]
8. Bergmann, O.; Zdunek, S.; Felker, A.; Salehpour, M.; Alkass, K.; Bernard, S.; Sjostrom, S.L.; Szewczykowska, M.; Jackowska, T.; Dos Remedios, C.; et al. Dynamics of Cell Generation and Turnover in the Human Heart. Cell 2015, 161, 1566–1575. [Google Scholar] [CrossRef]
9. Senyo, S.E.; Steinhauser, M.L.; Pizzimenti, C.L.; Yang, V.K.; Cai, L.; Wang, M.; Wu, T.-D.; Guerquin-Kern, J.-L.; Lechene, C.P.; Lee, R.T. Mammalian heart renewal by pre-existing cardiomyocytes. Nature 2013, 493, 433–436. [Google Scholar] [CrossRef]
10. Patterson, M.; Barske, L.; Van Handel, B.; Rau, C.D.; Gan, P.; Sharma, A.; Parikh, S.; Denholtz, M.; Huang, Y.; Yamaguchi, Y.; et al. Frequency of mononuclear diploid cardiomyocytes underlies natural variation in heart regeneration. Nat. Genet. 2017, 49, 1346–1353. [Google Scholar] [CrossRef]
11. Derks, W.; Bergmann, O. Polyploidy in Cardiomyocytes. Circ. Res. 2020, 126, 552–565. [Google Scholar] [CrossRef] [PubMed]
12. Ponnusamy, M.; Li, P.-F.; Wang, K. Understanding cardiomyocyte proliferation: An insight into cell cycle activity. Cell. Mol. Life Sci. 2017, 74, 1019–1034. [Google Scholar] [CrossRef]
13. Neininger, A.; Long, J.H.; Baillargeon, S.M.; Burnette, D.T. A simple and flexible high-throughput method for the study of cardiomyocyte proliferation. Sci. Rep. 2019, 9, 15917. [Google Scholar] [CrossRef]
14. Paige, S.L.; Osugi, T.; Afanasiev, O.K.; Pabon, L.; Reinecke, H.; Murry, C.E. Endogenous Wnt/β-Catenin Signaling Is Required for Cardiac Differentiation in Human Embryonic Stem Cells. PLoS ONE 2010, 5, e11134. [Google Scholar] [CrossRef] [PubMed]
15. Lian, X.; Hsiao, C.; Wilson, G.; Zhu, K.; Hazeltine, L.B.; Azarin, S.M.; Raval, K.K.; Zhang, J.; Kamp, T.J.; Palecek, S.P. Cozzarelli Prize Winner: Robust cardiomyocyte differentiation from human pluripotent stem cells via temporal modulation of canonical Wnt signaling. Proc. Natl. Acad. Sci. USA 2012, 109, E1848–E1857. [Google Scholar] [CrossRef] [PubMed]
16. Lian, X.; Zhang, J.; Azarin, S.M.; Zhu, K.; Hazeltine, L.B.; Bao, X.; Hsiao, C.; Kamp, T.; Palecek, S.P. Directed cardiomyocyte differentiation from human pluripotent stem cells by modulating Wnt/β-catenin signaling under fully defined conditions. Nat. Protoc. 2013, 8, 162–175. [Google Scholar] [CrossRef] [PubMed]
17. Buikema, J.W.; Zwetsloot, P.-P.M.; Doevendans, P.A.; Domian, I.J.; Sluijter, J.P.G. Wnt/β-Catenin Signaling during Cardiac Development and Repair. J. Cardiovasc. Dev. Dis. 2014, 1, 98–110. [Google Scholar] [CrossRef]
18. Buikema, J.W.; Wu, S.M. Untangling the Biology of Genetic Cardiomyopathies with Pluripotent Stem Cell Disease Models. Curr. Cardiol. Rep. 2017, 19, 30. [Google Scholar] [CrossRef]

19. Titmarsh, D.M.; Glass, N.R.; Mills, R.J.; Hidalgo, A.; Wolvetang, E.J.; Porrello, E.R.; Hudson, J.E.; Cooper-White, J.J. Induction of Human iPSC-Derived Cardiomyocyte Proliferation Revealed by Combinatorial Screening in High Density Microbioreactor Arrays. Sci. Rep. 2016, 6, 24637. [Google Scholar] [CrossRef]

20. Sharma, A.; Zhang, Y.; Buikema, J.W.; Serpooshan, V.; Chirikian, O.; Kosaric, N.; Churko, J.M.; Dzilic, E.; Shieh, A.; Burridge, P.W.; et al. Stage-specific Effects of Bioactive Lipids on Human iPSC Cardiac Differentiation and Cardiomyocyte Proliferation. Sci. Rep. 2018, 8, 6618. [Google Scholar] [CrossRef]

21. Buikema, J.W.; Mady, A.S.; Mittal, N.; Atmanli, A.; Caron, L.; Doevendans, P.A.; Sluijter, J.; Domian, I.J. Wnt/β-catenin signaling directs the regional expansion of first and second heart field-derived ventricular cardiomyocytes. Development 2013, 140, 4165–4176. [Google Scholar] [CrossRef]

22. Mills, R.J.; Titmarsh, D.M.; Koenig, X.; Parker, B.L.; Ryall, J.G.; Quaife-Ryan, G.A.; Voges, H.K.; Hodson, M.P.; Ferguson, C.; Drowley, L.; et al. Functional screening in human cardiac organoids reveals a metabolic mechanism for cardiomyocyte cell cycle arrest. Proc. Natl. Acad. Sci. USA 2017, 114, E8372–E8381. [Google Scholar] [CrossRef] [PubMed]

23. Brunner, S.; Fürtbauer, E.; Sauer, T.; Kursa, M.; Wagner, E. Overcoming the Nuclear Barrier: Cell Cycle Independent Nonviral Gene Transfer with Linear Polyethylenimine or Electroporation. Mol. Ther. 2002, 5, 80–86. [Google Scholar] [CrossRef] [PubMed]

24. Feyen, D.A.M.; McKeithan, W.L.; Bruyneel, A.A.N.; Spiering, S.; Hörmann, L.; Ulmer, B.; Zhang, H.; Briganti, F.; Schweizer, M.; Hegyi, B.; et al. Metabolic Maturation Media Improve Physiological Function of Human iPSC-Derived Cardiomyocytes. Cell Rep. 2020, 32, 107925. [Google Scholar] [CrossRef] [PubMed]

25. Buikema, J.W.; Lee, S.; Goodyer, W.R.; Maas, R.G.; Chirikian, O.; Li, G.; Miao, Y.; Paige, S.L.; Lee, D.; Wu, H.; et al. Wnt Activation and Reduced Cell-Cell Contact Synergistically Induce Massive Expansion of Functional Human iPSC-Derived Cardiomyocytes. Cell Stem Cell 2020, 27, 50–63.e5. [Google Scholar] [CrossRef] [PubMed]

26. Tan, S.H.; Tao, Z.; Loo, S.; Su, L.; Chen, X.; Ye, L. Non-viral vector based gene transfection with human induced pluripotent stem cells derived cardiomyocytes. Sci. Rep. 2019, 9, 14404. [Google Scholar] [CrossRef]

27. Nam, H.-S.; Benezra, R. High Levels of Id1 Expression Define B1 Type Adult Neural Stem Cells. Cell Stem Cell 2009, 5, 515–526. [Google Scholar] [CrossRef]

28. Bergmann, O.; Bhardwaj, R.D.; Bernard, S.; Zdunek, S.; Barnabé-Heider, F.; Walsh, S.; Zupicich, J.; Alkass, K.; Buchholz, B.A.; Druid, H.; et al. Evidence for Cardiomyocyte Renewal in Humans. Science 2009, 324, 98–102. [Google Scholar] [CrossRef]

29. Bersell, K.; Arab, S.; Haring, B.; Kühn, B. Neuregulin1/ErbB4 Signaling Induces Cardiomyocyte Proliferation and Repair of Heart Injury. Cell 2009, 138, 257–270. [Google Scholar] [CrossRef]

30. Kühn, B.; Del Monte, F.; Hajjar, R.J.; Chang, Y.-S.; Lebeche, D.; Arab, S.; Keating, M.T. Periostin induces proliferation of differentiated cardiomyocytes and promotes cardiac repair. Nat. Med. 2007, 13, 962–969. [Google Scholar] [CrossRef]

31. Wang, W.E.; Li, L.; Xia, X.; Fu, W.; Liao, Q.; Lan, C.; Yang, D.; Chen, H.; Yue, R.; Zeng, C.S.; et al. Dedifferentiation, Proliferation, and Redifferentiation of Adult Mammalian Cardiomyocytes After Ischemic Injury. Circulation 2017, 136, 834–848. [Google Scholar] [CrossRef] [PubMed]

32. D'Uva, G.; Aharonov, A.; Lauriola, M.; Kain, D.; Yahalom-Ronen, Y.; Carvalho, S.; Weisinger, K.; Bassat, E.; Rajchman, D.; Yifa, O.; et al. ERBB2 triggers mammalian heart regeneration by promoting cardiomyocyte dedifferentiation and proliferation. Nat. Cell Biol. 2015, 17, 627–638. [Google Scholar] [CrossRef] [PubMed]

33. Van der Wal, E.; Herrero-Hernandez, P.; Wan, R.; Broeders, M.; In't Groen, S.L.; van Gestel, T.J.; van IJcken, W.F.J.; Cheung, T.H.; van der Ploeg, A.T.; Schaaf, G.J.; et al. Large-Scale Expansion of Human iPSC-Derived Skeletal Muscle Cells for Disease Modeling and Cell-Based Therapeutic Strategies. Stem Cell Rep. 2018, 10, 1975–1990. [Google Scholar] [CrossRef] [PubMed]

34. Chal, J.; Oginuma, M.; Al Tanoury, Z.; Gobert, B.; Sumara, O.; Hick, A.; Bousson, F.; Zidouni, Y.; Mursch, C.; Moncuquet, P.; et al. Differentiation of pluripotent stem cells to muscle fiber to model Duchenne muscular dystrophy. Nat. Biotechnol. 2015, 33, 962–969. [Google Scholar] [CrossRef] [PubMed]

35. Ariizumi, T.; Ogose, A.; Kawashima, H.; Hotta, T.; Umezu, H.; Endo, N. Multinucleation followed by an acytokinetic cell division in myxofibrosarcoma with giant cell proliferation. J. Exp. Clin. Cancer Res. 2009, 28, 44. [Google Scholar] [CrossRef]

SUPPLEMENTARY

The **supplementary figures 1-3** and **supplementary videos 1-4** can be downloaded from: https://www.mdpi.com/article/10.3390/jcdd9020043/s11

Or:

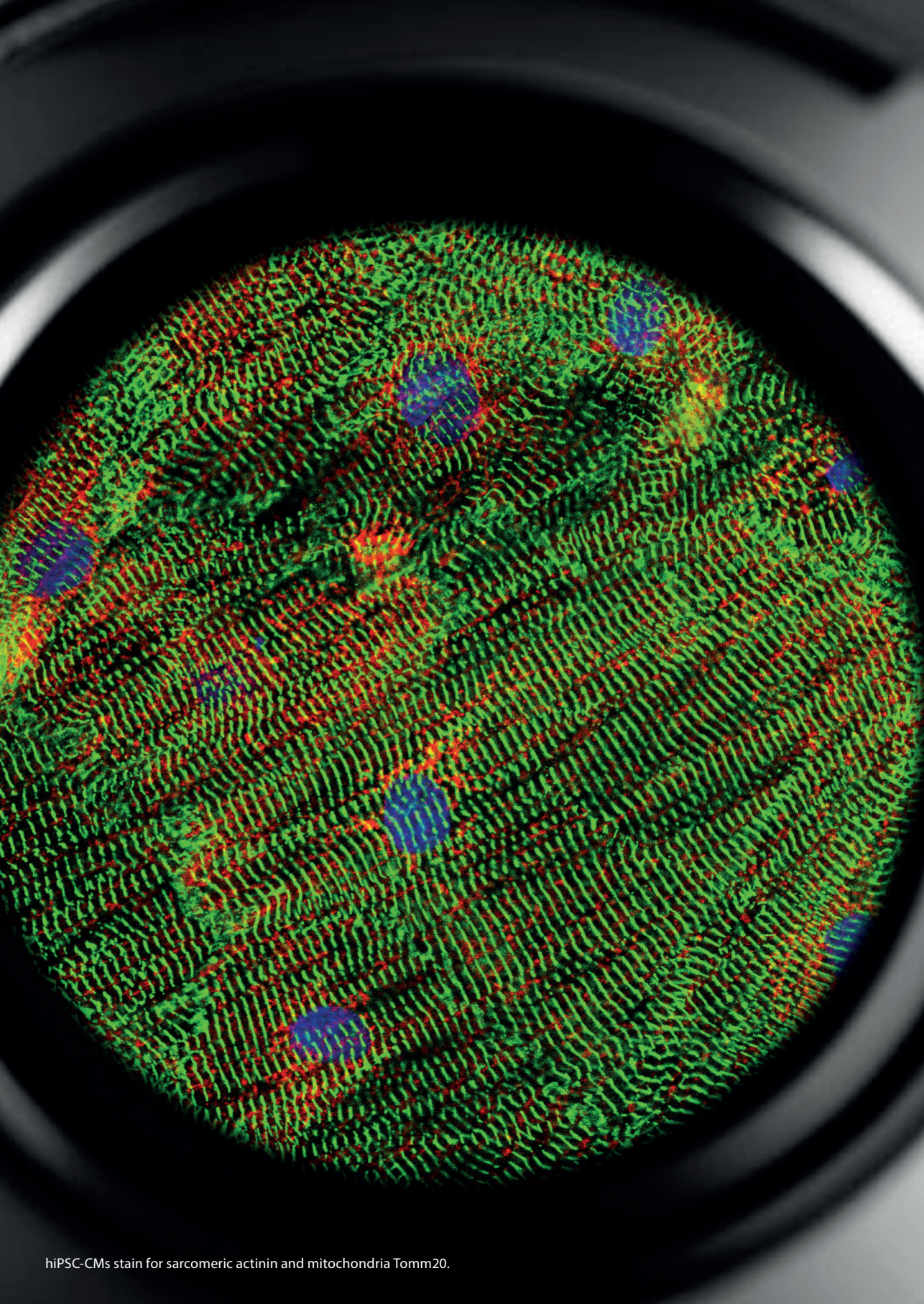

hiPSC-CMs stain for sarcomeric actinin and mitochondria Tomm20.

Chapter 6

Metabolic Maturation Increases Susceptibility to Hypoxia-induced Damage in Human iPSC-Derived Cardiomyocytes

Published in: Stem Cells Translational Medicine, 2022

Marijn C. Peters, **Renée G.C. Maas**, Iris van Adrichem, Pieter A. Doevendans, Mark Mercola, Tomo Šarić, Jan W. Buikema, Alain van Mil, Steven A.J. Chamuleau, Joost P.G. Sluijter, Anna P. Hnatiuk*, and Klaus Neef*

*These authors contributed equally.

ABSTRACT

Development of new cardioprotective approaches using in vivo models of ischemic heart disease remains challenging as differences in cardiac physiology, phenotype and disease progression between humans and animals influence model validity and prognostic value. Furthermore, economical and ethical considerations have to be taken into account, especially when using large animal models with relevance for conducting pre-clinical studies. The development of human induced pluripotent stem cell-derived cardiomyocytes (iPSC-CMs) has opened new opportunities for in vitro studies on cardioprotective compounds. However, the immature cellular phenotype of iPSC-CMs remains a roadblock for disease modelling. Here, we show that metabolic maturation renders the susceptibility of iPSC-CMs to hypoxia further towards a clinically representative phenotype. iPSC-CMs cultured in conventional medium did not show significant cell death after exposure to hypoxia. In contrast, metabolically matured (MM) iPSC-CMs showed inhibited mitochondrial respiration after exposure to hypoxia and increased cell death upon increased durations of hypoxia. Furthermore, we confirmed the applicability of MM iPSC-CMs for in vitro studies of hypoxic damage by validating the known cardioprotective effect of necroptosis inhibitor necrostatin-1. Our results provide important steps to improving and developing valid and predictive human in vitro models of ischemic heart disease.

GRAPHICAL ABSTRACT

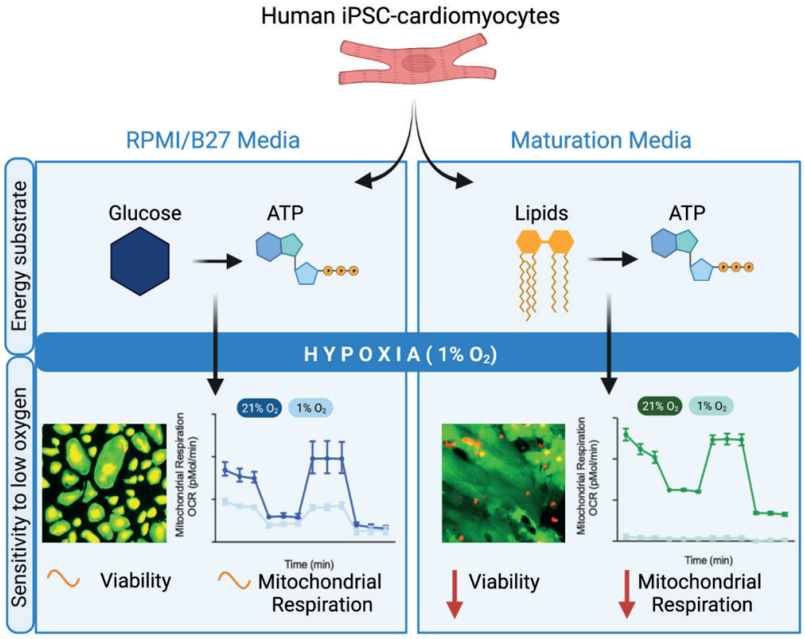

Significance Statement

The immaturity of human iPSC-derived cardiomyocytes (iPSC-CMs) remains a roadblock for disease modelling. This study shows that only after metabolic maturation in low glucose, high oxidative substrate media, iPSC-CMs become susceptible to hypoxia-induced cellular damage. Inhibition of necroptosis prevented hypoxia-induced decrease in mitochondrial respiration and cell death in metabolically matured iPSC-CMs. Together, these findings suggest that metabolically matured iPSC-CMs are susceptible to hypoxia damage, representing a key step for establishing valid in vitro models of cardiac ischemia.

INTRODUCTION

Ischemic heart disease is a major cause of death worldwide.[1] The decrease in oxygen and nutrient availability in the myocardium leads to cardiomyocyte (CM) death and therefore loss of cardiac contractile force.[2] Current clinical therapies focus on early reperfusion of the ischemic tissue, thereby decreasing the tissue damage which occurs after myocardial infarctions. To develop improved therapeutic approaches to protect the heart from ischemic damage, both animal models and *in vitro* disease modelling platforms have been used frequently. However, although cardioprotective factors have shown promising therapeutic effects in *in vitro* cell models and in animal experiments, they often failed in showing clear beneficial effects in clinical trials.[3] The roles of comorbidities, ageing, and the use of medication, often neglected in preclinical models, have been considered as reasons for translational failure.[4] Moreover, existing models do not robustly reflect the human CM-specific pathophysiology due to marked differences between CMs from humans compared to other species[5], e.g., with respect to calcium handling[6], electrophysiology[6], myofilament composition[7,8], maturation expression profile[9], and metabolism.[10] The development of human induced pluripotent stem cell (iPSC) technology[11] and their differentiation to cardiomyocytes (CMs)[12] opened doors for more suitable human-based cardiac disease modelling by the generation of patient-specific CMs[13] and pre-clinical screening of therapeutics.[14,15] Despite the mentioned advantages linked to their human origin, iPSC-CMs, typically derived from a 20-day differentiation protocol, display a foetal rather than adult CM phenotype.[16,17] Adult human CMs generate 90% of their energy from mitochondrial oxidative phosphorylation while neonatal rat CMs and iPSC-CMs use glycolysis as their main energy source[18], as reflected in a lower expression of TCA cycle and fatty acid β-oxidation markers.[19,20] Thus, human iPSC-CMs can have limited clinical validity and predictive value as models of pathophysiological processes, especially when linked to oxidative metabolic processes.[19,21] Several studies focussed on increasing the maturation of iPSC-CMs by stimulating the post-natal shift from anaerobic glycolysis-dependent metabolism to aerobic β-oxidation.[18,22–24] Recently, a study showed increased cell death of iPSC-CMs metabolically matured for 8 days in glucose deprived, fatty acid rich media, upon submission to *in vitro* ischemia-reperfusion injury by applying two hours of complete oxygen deprivation (0% O_2) followed by four hours of reperfusion (20% O_2).[25] In a similar attempt, we

have shown that three weeks of culture in a medium with physiological levels of glucose and Ca^{2+}, supplemented with a fine-tuned composition of additives, induced metabolic, structural, electrophysiological and mechanical iPSC-CM maturation characterized by lower resting membrane potential, rapid depolarization, increased sarcoplasmic reticulum calcium cycling, increased contractile force and enhanced fatty acid oxidation, in line with cardiomyocyte maturation during cardiac development.[18] In this study, we sought to investigate the utilization of metabolically matured iPSC-CMs to model cardiac ischemic damage and exemplarily evaluate the cardioprotective effect of the RIP1 kinase inhibitor necrostatin-1.

METHODS

Cell culture. The female iPSC line SCVI-273 (Sendai virus reprogrammed) was kindly provided by Joseph Wu, Stanford University.[26] The female iPSC line NP0141-31B was generated in the Šarić group from peripheral blood mononuclear cells, also using the Sendai virus reprogramming method.[27,28] This line is deposited as cell line UKKi032-C at the European Bank for induced Pluripotent Stem Cells (EBiSC, www.ebisc.org) and is listed at the international online registry hPSCreg (www.hpscreg.eu). iPSCs were cultured in Essential 8 medium (Gibco, A1517001) in 0,1 mg/mL matrigel (Corning, CLS356252) coated-6 well plates. When reaching 80-90% confluency, directed differentiation to CMs was initiated by changing medium to RPMI 1640 (ThermoFisher Scientific, 11875085) supplemented with 2% B27 minus insulin (ThermoFisher Scientific, A1895601) (B27- medium) and 7 µM CHIR99021 (Selleck Chemicals, S2924). After 3 days, B27-medium was changed and supplemented with 2 µM Wnt-C59 (R&D systems, 5148) to inhibit canonical Wnt signaling. On day 7, the medium was changed to RPMI 1640 and 2% B27 plus insulin supplement (ThermoFisher Scientific, 17504001) (B27+ medium) and on day 9 to RPMI 1640 without glucose (ThermoFisher Scientific, 118979020) and 2% B27 plus insulin for purification (depletion of non-CM cells). On day 11 cells were re-plated in RPMI/B27 plus insulin supplemented with 10% KnockOut serum replacement (KOSR, ThermoFisher Scientific, 108280028) and 10 µM selective Rock-1 inhibitor Y-27632 (Selleck Chemicals, S1049). After the second purification on day 14 for two days in RPMI 1640 without glucose, the medium was changed to RPMI/B27 plus insulin. On day 20, the purification medium was changed to maturation medium[18] or cells were kept in RPMI/B27 plus insulin. Cells were matured in maturation medium for three weeks before re-plating with medium changes every four days.

Damage induction. 4 days before applying hypoxic conditions at day 20, the medium was changed to medium containing variable nutrient compositions (**Supplementary table 1**). Ischemia was induced by incubation at 5% O_2 in a hypoxia incubator (In-VitroCell NU-5800, NuAire) providing continuous oxygen monitoring or ~1% O_2 using the GasPak EZ Pouch system (BD, 260683) with indicator strips to confirm O_2 concentrations below 1%.

Preconditioning protective treatment. Before hypoxia, the medium was changed to media of variant nutrient composition (**Supplementary table 1**). iPSC-CMs were preconditioned with 60 µM necroptosis inhibitor Necrostatin-1 (Nec-1, Abcam ab141053) for 24 hours.

Lactate dehydrogenase, glucose and lactate measurements. Media glucose and lactate levels were determined using the Accutrend plus device (Roche, 05050472023) and verified using the glucose (Sigma, MAK083-1KT) and lactate colorimetric kits (Sigma, MAK064-1KT). Lactate dehydrogenase levels were determined using the LDH assay colorimetric kit (Abcam, ab102526) according to manufacturer's instructions.

Immunofluorescent staining. Live dead assay was performed using EthD1/calcein AM staining with the LIVE/DEAD Kit, for mammalian cells (ThermoFisher Scientific, L3224) according to manufacturer's instructions and imaging was performed using the EVOS Floid microscope (ThermoFisher Scientific, AMF5000). The ratio of EthD1 to Calcein AM was determined by dividing the number of EthD1-positive cells by the number of Calcein AM-positive cells per image. The averages of 5 images were used per condition. For immunofluorescence stainings, after fixation in 4% paraformaldehyde for 30 minutes, cells were permeabilized in 0,1% Triton-X100 (Sigma, 11332481001) before blocking in 10% normal goat serum/1% BSA (Sigma, A9418). Primary antibodies used were: ACTN1 (Sigma-Aldrich, A7811, 1:200), cardiac troponin T (Abcam, ab45932, 1:100), Ki-67 (Abcam, ab8330, 1:200), pH3 (Cell Signaling Technology, #9701, 1:200), TOMM20 (Abcam, ab56783, 1:200) and Aurora B kinase (Abcam, ab2254, 1:100). Detection was mediated by incubation with AlexaFluor antibody conjugates (ThermoFisher Scientific) and nuclei were visualised using DAPI (ThermoFisher Scientific, 62248). Mounting was performed using Fluoromount-G mounting medium (ThermoFisher Scientific, 00-4958-02). For apoptotic cell death analysis, TUNEL assays (Roche, 11684795910) were performed according to the manufacturer's instructions. Imaging was performed on a confocal microscope (Leica Sp8x, LAS X imaging software) and image analysis using ImageJ (1.51a, Java 1.8.0.231).

Flow cytometry. Cells were gently dissociated (multi tissue dissociation kit, Miltenyi Biotec, 130-110-204) and incubated with LIVE/DEAD fixable green dead cell stain kit (ThermoFisher Scientific, L23101). This kit contains a fixable fluorescent dye that binds to amines. In viable cells, this amine-reactive dye binds amines on the outer cell surface, as opposed to dead cells in which the dye can additionally bind internal amines due to membrane disruption. After staining, cells were fixed (inside fix solution, Miltenyi Biotec, 130-090-477) and stained with primary antibodies (diluted in inside perm solution, Miltenyi Biotec, 130-090-477). ACTN1-VioBlue (Miltenyi Biotec, 130-127-354, 1:10) and cardiac Troponin-T VioBlue (Miltenyi Biotec, 130-120-402, 1:10) were used as conjugated antibodies. As a control, universal isotype control

antibodies (REA, Miltenyi Biotec, 130-096-932) were used. Media and washes were collected to obtain a complete representation, including detached cells. The samples were analysed using a FACS Canto system (BD Bioscience, FACSDiva software 6.0) and FlowJo software (BD Bioscience, v10).

Beating rate analysis. iPSC-CM beating rate was microscopically determined (Olympus CKX53) and recorded (Hero 8 GoPro camera). Beats per minute were quantified by counting the number of contractions of individual cells from 10 second videos.

Seahorse analysis. Mitochondrial respiration was measured using a XF24 Extracellular Flux Analyzer (Seahorse Bioscience, Agilent) to assess the effect of hypoxia on the electron transport chain complexes. XF24 plates (Agilent, 103518-100) were used and coated with 0.1 mg/mL Matrigel (Corning, CLS356252) before cells were seeded at a density of $1{,}0x10^5$ cells per well. 24 hours or 4 hours before Seahorse analysis, plates were placed in a GasPak EZ Pouch system to induce hypoxia following manufacturer's instructions. One hour before measurement cells were washed three times with Seahorse XF DMEM Basal Medium (Agilent, 103680-100), supplemented with 2% B27, 4 mM glutamine (Gibco, 25030081), 10 mM glucose (ThermoFisher Scientific, 15023021), and 1% chemically defined lipid concentrate (ThermoFisher Scientific, 11905031). Oxygen consumption rate (OCR) was determined using XF Cell Mito Stress Assay (Agilent, 103015-100) with subsequent additions of: (1) ATP synthase inhibitor: 2.5 mM oligomycin, (2) uncoupler: 2.5 mM carbonyl cyanide 4-(trifluoromethoxy) phenylhydrazone (FCCP) and (3) Complex I/II inhibitors: 2.5 mM Rotenone/Antimycin A. At the end of measurement, the oxygen consumption rate (OCR) values were normalized to cell numbers per well as assessed by Hoechst 33342 (Thermofisher Scientific) staining at 20x magnification imaging using the Evos microscope and ImageJ[29]. Baseline respiration was calculated by subtracting the OCR, after addition of rotenone and antimycin A, from the respiration as measured at the first time point. ATP production was calculated as the OCR at the first time point minus the OCR after oligomycin infusion. The proton leak was determined by subtracting the OCR after FCCP infusion from the value after oligomycin infusion. Maximal OCR was calculated as the difference between the OCR after FCCP infusion and after rotenone and antimycin A infusion. Respiratory capacity was calculated by subtracting the difference between the OCR before the addition of inhibitors and after rotenone and antimycin A infusion from the OCR after FCCP infusion. Lastly, non-mitochondrial respiration was defined as the OCR after rotenone and antimycin A infusion. The experiment was done in 1-2 biological replicates, with each replicate consisting of 5 technical repeats per condition.

Statistical analysis. iPSC lines from two donors were used and the number (N) depicted in individual figures represents the number of independent experiments performed. Each

experiment was performed with both cell lines. Statistical analysis was performed using Prism 8 (GraphPad) software. Normality was assessed using a Shapiro-Wilk test. To compare two normally distributed groups, a Student's t-test was performed. For three or more groups and the assessment of one parameter, one-way ANOVA statistical test was used. With multiple parameters and three or more groups, a two-way ANOVA was used. For one-way ANOVA and two-way ANOVA, Dunnett multiple comparisons was used as post-hoc analysis to determine significance at a P<0,05. Results are shown as mean ± SEM.

RESULTS

Immature iPSC-CMs are not sensitive to hypoxia

Human iPSCs were subjected to directed differentiation to cardiomyocytes (iPSC-CMs) using the Wnt pathway inhibition differentiation protocol[27,28], resulting in a homogeneous, autonomously contractile cell population robustly expressing CM-defining markers troponin T and ACTN1 (**Figure 1a-c**) and only low ratios of cells expressing proliferation marker Ki67 (5,9% ± 0,8%; **Figure 1d**), similar to values reported for neonatal mice and young infant hearts.[30,31] To test the sensitivity of these, presumably immature, iPSC-CMs to oxygen and nutrient deprivation, we cultured the cells in four different media of variable nutrient compositions (**Supplementary table 1**) before exposure to hypoxia: 1) DMEM-Glu/L (25 mM glucose, 10% KOSR), 2) RPMI-Glu/B27 (11,1 mM glucose, 2% B27), 3) RPMI/B27 (0mM glucose, 2% B27), and 4) RPMI-Lac/L (0 mM glucose, lactate, 10% KOSR). DMEM-Glu/L is highest in glucose and lipids, followed by RPMI-Glu/B27 with high glucose and low lipids, where both types are commonly used to maintain iPSC-CMs after differentiation. RPMI/B27 and RPMI-Lac/L are both used during the purification steps of iPSC differentiation into CMs and contain no glucose where RPMI/B27 is low in lipids. RPMI-Lac/L contains additional lactate and higher lipid concentration to inhibit glycolysis and stimulate the use of the respiratory chain[32]. Incubation in 1% O_2 for 24 hours did not lead to increased cell death of iPSC-CMs in high-glucose media (DMEM-Glu/L, RPMI-Glu/B27) and no-glucose and low-lipid media (RPMI/B27) compared to incubation in 21% O_2 (**Figure 1e, f**). Only exposure to 1% O_2 for 24 hours in no-glucose, high-lipid and high-lactate medium (RPMI-Lac/L) induced minimal, yet significantly increased cell death (ethidium homodimer-1 [EthD1] / calcein AM ratio: 0,02 ± 0,005 [21% O_2] vs. 0,11 ± 0,004 [1% O_2]; P=0,04). To validate the assessment of cell death, we included a Triton X-100 treatment as a positive control, that resulted in 100% cell death for all media conditions (**Figure 1e**). To more accurately quantify results, we repeated the respective experiments using RPMI-Lac/L medium and analysed via flow cytometry using an amine-reactive dye to detect membrane disruption. Although in 12 of 30 experiments a small reduction in cell viability was observed, differences were statistically non-significant in flow cytometric analyses (viable cells: 85% ± 1,9% [21% O_2] vs. 78,3 ± 3,0 [1% O_2]; P=0,1; **Figure 1g, h**). These findings show immature iPSC-CMs are insensitive to hypoxic damage irrespective of media glucose content. The presence of lipids and lactate in combination with low glucose media led to minimal, yet detectable hypoxic damage in immature iPSC-CMs.

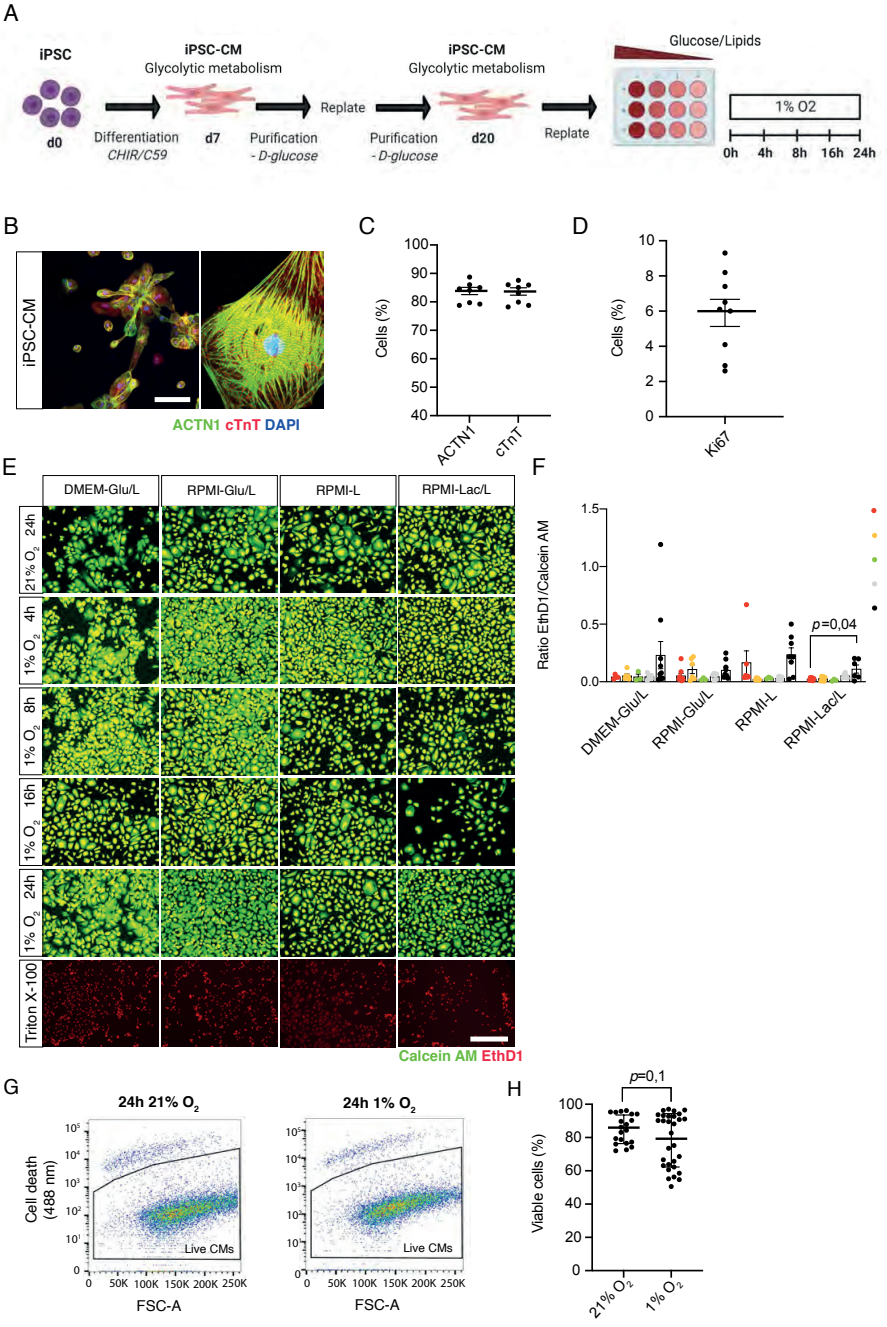
A
iPSC
d0
Differentiation
CHIR/C59
iPSC-CM
Glycolytic metabolism
d7
Purification
- D-glucose
Replate
iPSC-CM
Glycolytic metabolism
Purification
- D-glucose
d20
Replate
Glucose/Lipids
1% O2
0h 4h 8h 16h 24h
B
iPSC-CM
ACTN1 cTnT DAPI
C
Cells (%)
ACTN1
cTnT
D
Cells (%)
Ki67
E
DMEM-Glu/L
RPMI-Glu/L
RPMI-L
RPMI-Lac/L
21% O2 24h
1% O2 4h
1% O2 8h
1% O2 16h
1% O2 24h
Triton X-100
Calcein AM EthD1
F
Ratio EthD1/Calcein AM
p=0,04
0h
4h
8h
16h
24h
DMEM-Glu/L
RPMI-Glu/L
RPMI-L
RPMI-Lac/L
G
24h 21% O2
24h 1% O2
Cell death (488 nm)
Live CMs
FSC-A
H
p=0,1
Viable cells (%)
21% O2
1% O2

◄ Figure 1. Hypoxia does not induce damage in iPSC-CMs
A. Schematic representation of experimental setup. B, C. ACTN1 and cTnT expression of iPSC-CMs assessed by immunofluorescence microscopy (B) and flow cytometry (C) (n=8) D. Ki67 expression of iPSC-CMs assessed by flow cytometry (n=9). E. Ethidium homodimer-1 (EthD1)/Calcein AM staining of iPSC-CMs cultured in four different media (DMEM-Glu/L, RPMI-Glu/B27, RPMI-B27, RPMI-Lac/L) with indicated nutrient compositions, exposed to indicated O_2 concentrations and durations. Arrowheads indicate a representative selection of EthD1-positive cells. F. Quantification (n=8) and media compositions of E. G. Flow cytometry analysis of viability of iPSC-CMs cultured for 24 hours in 21% O_2 or 1% O_2 and quantification (H) (n=30). Data is collected from 2-3 technical replicates (exact amounts specified in separate panels), 3 biological replicates (cardiac differentiations) of 2 cell lines. H: 3 technical replicates from 10 biological replicates (cardiac differentiations). Data were analysed using one-way ANOVA and Dunnett multiple comparison. *P<0,05. Scale bar: 200µm. Data are shown as mean ± SEM.

Metabolically matured iPSC-CMs are sensitive to hypoxia

To investigate whether maturation of iPSC-CMs would increase susceptibility to hypoxia, we applied the recently published protocol for metabolic maturation (MM)[18] (**Figure 2a**), resulting in increased ratio of ACTN expressing cells (83,3% ± 1,3% [RPMI/Lac/L (non-MM)] vs. 94,4% ± 2,6% [MM]; P<0,01; **Figure 2b, c**) and decreased ratio of proliferating KI67 expressing cells (5,9% ± 0,77% [non-MM] vs. 1,4% ± 0,32% [MM]; P<0,01; **Figure 2d**). MM iPSC-CMs displayed a significant increase in cell death after 16 and 24 hours of hypoxia (fold increase EthD1/calcein AM ratio compared to normoxic: 1,78 ± 0,14 [1% O_2, 16 hours]; 1,83 ± 0,15 [1% O_2, 24 hours]; **Figure 2e, f**). Hypoxia induced damage of MM iPSC-CMs was confirmed by an increase in media lactate dehydrogenase concentration (**Figure 2g**) (25,0 ± 0,01 [U/l; 21% O_2] vs 39,4 ± 5,8 [U/l; 1% O_2, 24 hours], P<0,05) and a reduction in cell viability assessed via flow cytometry (56,5% ± 2,8% [21% O_2] vs 14,0% ± 1,2% [1% O_2, 24 hours]; P<0,001; **Figure 2h, i**). Additionally, analyses of iPSC-CM beating rates after 24 hours exposure to 1% O_2 showed significant decrease only for MM (**Supplementary figure 1**).

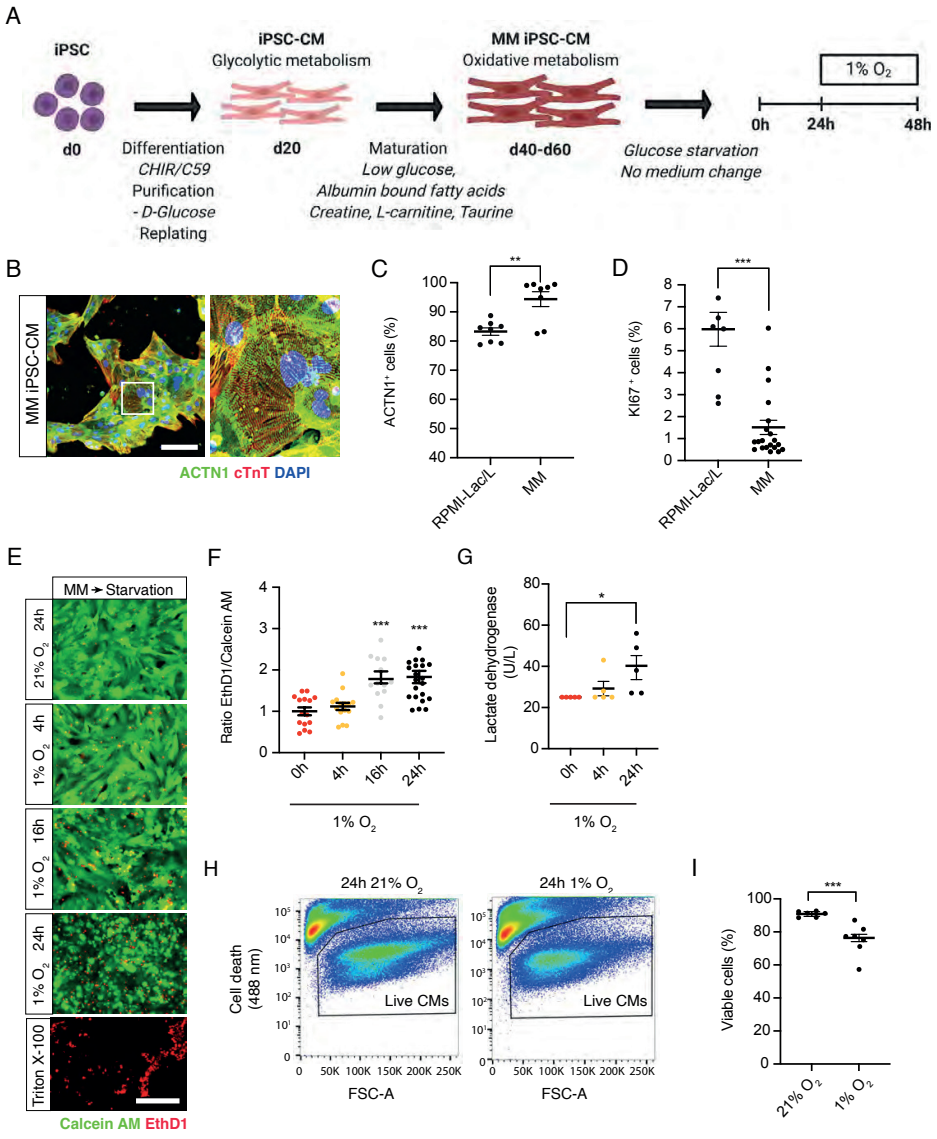

Figure 2. Hypoxia induces cell death of MM iPSC-CMs

A. Schematic representation of experimental setup. B, C. ACTN1 and cTnT expression of MM iPSC-CMs by immunofluorescence microscopy (B) and flow cytometric analysis of ACTN1 expression (C) (n=8, 2 cell lines, 2 biological replicates, 2 technical replicates). D. KI67 expression of MM iPSC-CMs compared to non-MM iPSC-CMs (n=20, 2 cell lines, 5 biological replicates, 2 technical replicates). E, F. EthD1/Calcein AM staining (LIVE/DEAD assay) of MM iPSC-CMs exposed to 21% O_2 for 24 hours or 1% O_2 for 4, 8, 16, or 24 hours and quantification (F) (n=15, 2 cell lines, 4 biological replicates, 1-2 technical replicates). G. Lactate dehydrogenase media levels of day 40 matured iPSC-CMs exposed to 1% O_2 (n=5, 2 cell lines, 2 biological replicates, 1-2 technical replicates). H, I. Flow cytometry analysis of MM iPSC-CMs viability after 24 hours exposure to 21% O_2 or 1% O_2 and quantification (I) (n=7, 2 cell lines, 3 biological replicates, 1-2 technical replicates). Data was analysed using one-way ANOVA and Dunnett multiple comparison. *P<0,05; ** P<0,01; ***P<0,001. Scale bar: 200 µm. Data are shown as mean ± SEM.

Although iPSC-CMs are continuously exposed to an atmospheric concentration of 21% O_2 during cell culture conditions, in myocardial tissue, normoxic oxygen concentrations can be substantially lower.[33] We therefore assessed whether a decrease from 21% O_2 to a more physiological cardiac normoxia of 5% O_2 would already induce damage in MM iPSC-CMs (**Figure 3a**). Although hypoxia did not change the fraction of ACTN1-positive MM iPSC-CMs in the surviving population ($ACTN1^+$: 92,7 ± 3,35% [24 hours, 21% O2] vs. 93,8 ± 1,7%, P = 0,74 [24 hours, 1% O_2]; **Supplemental figure 2**), both, incubation in 5% O_2 and 1% O_2, decreased myofibrillar organization, as shown by immunostaining for ACTN1 and cardiac troponin T (cTnT) (**Figure 3b, c**).

An increased ratio of apoptotic ($TUNEL^+$) iPSC-CMs was observed in MM after short periods (4 hours) of exposure to 5% O_2 (25,5% ± 1,2%), similar to 1% O_2 (23,7% ± 1,6%), compared to atmospheric 21% O_2 (15,4% ± 0,83%; p<0,05; **Figure 3d, e**). Longer hypoxia periods (24 hours) increased percentage of apoptotic iPSC-CMs to 41,5% ± 4,5% (5% O_2) and 37,6% ± 3,5% (1% O_2) compared to 12,0% ± 1,5% (21% O_2; p<0,001; **Figure 3d, e**). We did not observe a significant difference in the ratio of apoptotic iPSC-CMs between 5% and 1% O_2, both after short- (4 hours) or long-term (24 hours) incubation. We collected media after hypoxia for 4 and 24 hours to assess glucose, lactate and lactate dehydrogenase concentrations and found significantly increased glucose consumption after 24 hours at both 5% and 1% O_2, reducing glucose levels below the detection limit of 0,6 mM (**Figure 3f**).

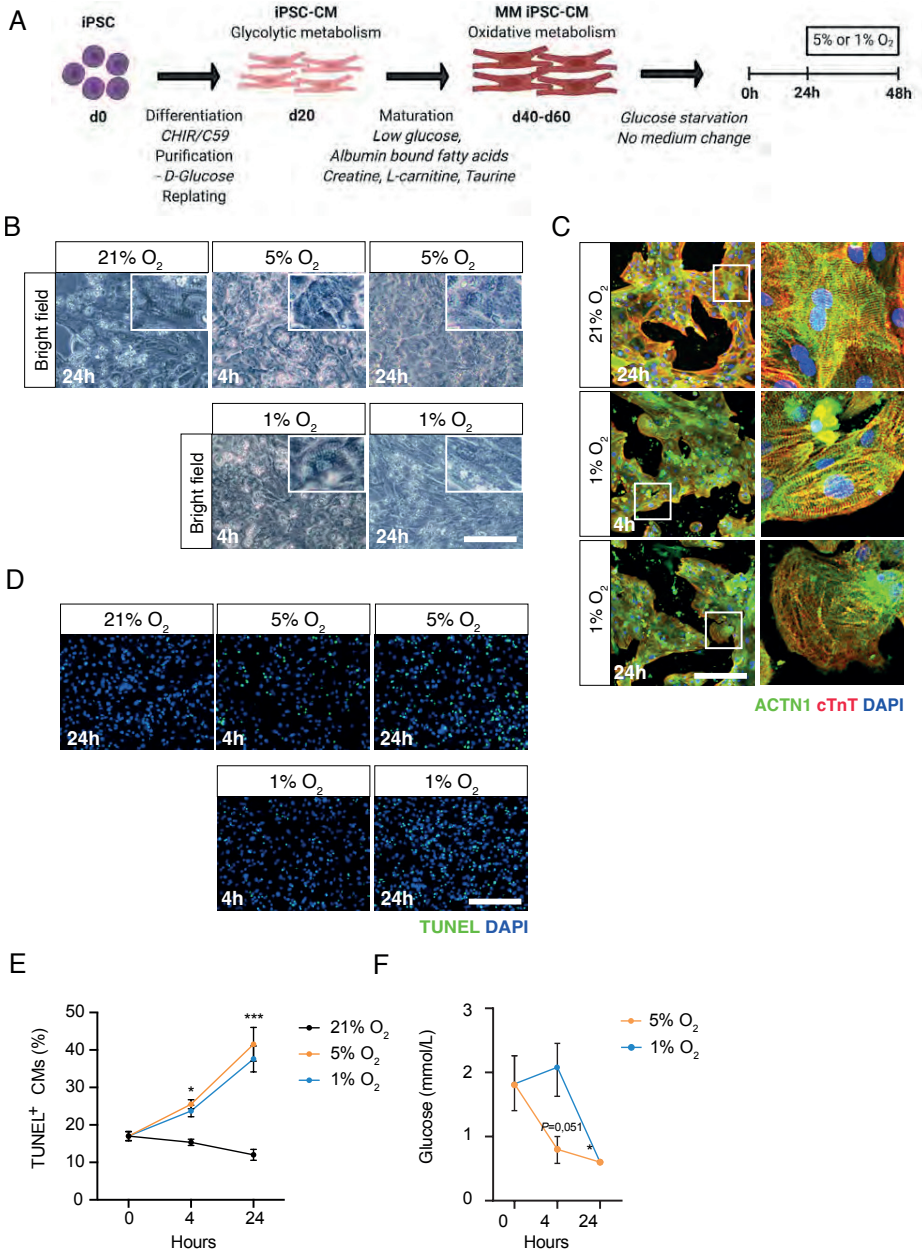

Figure 3. Mild hypoxia is sufficient to induce cell death in MM iPSC-CMs
Schematic representation of experimental set-up. **B**. Bright-field images of MM iPSC-CMs exposed to indicated hypoxia conditions. **C**. Microscopic images of ACTN1 and cTnT immunostainings. Square indicates area of close-up. **D**. Microscopic images of TUNEL staining of MM iPSC-CMs. **E**. Quantification of TUNEL staining. **F-H**. Glucose (**F**) and lactate (**G**) concentrations in media after 4 to 24 hours incubation of MM iPSC-CMs at indicated hypoxia conditions. E: 3 technical replicates from 6 biological replicates (cardiac differentiations) (n=28); F, G: 2 technical replicates from 3 biological replicates (cardiac differentiations) (n=5). Data were analysed using one-way ANOVA and Dunnett multiple comparison. *P<0,05; **P<0,01; ***P<0,001. Scale bar: 200 µm. Data are shown as mean ± SEM.

Metabolic profiling of non-MM and MM iPSC-CMs after hypoxia exposure

To investigate whether hypoxia affects mitochondrial function of iPSC-CMs, we compared the oxygen consumption rates (OCR) of MM iPSC-CMs and non-MM iPSC-CMs 40 days after differentiation in normoxia and hypoxia (1% O_2) using Seahorse metabolic analysis. To study the role of glucose in hypoxia-mediated mitochondrial damage in the non-MM iPSCs, we used RPMI-Glu/B27 as high glucose medium and RPMI-Lac/L as low glucose medium (**Figure 1**). In normoxia, MM iPSC-CMs showed the highest OCR, indicating increased used of oxidative phosphorylation (**Figure 4a-c**). Under hypoxic conditions, non-MM iPSC-CMs cultured in RPMI-Glu/L maintained responsiveness, while non-MM iPSC-CMs cultured in RPMI-Lac/L lost responsiveness to the mitochondrial respiratory chain inhibitors (**Figure 4a, b**). Glucose deprived (RPMI-Lac/L) non-MM iPSC-CMs showed decreased OCR in normoxia compared to non-MM iPSC-CMs in glucose-rich medium (RPMI-Glu/B27) illustrating metabolic starvation caused by the absence of glucose (**Figure 4a, b**). While MM iPSC-CMs showed the highest OCR in normoxic conditions and similar responses to the mitochondrial inhibitors as the non-MM iPSC-CMs in glucose medium, 24 hours of hypoxia caused a massive drop in OCR and complete loss of mitochondrial flexibility in MM iPSC-CMs as non-MM iPSC-CMs maintained responsiveness to oligomycin, FCCP and antimycin A and rotenone. 24 hours hypoxia significantly decreased basal respiration, ATP production and maximal respiration in both non-MM and MM iPSC-CMs where the strongest decrease in OCR was observed in MM iPSC-CMs. Spare respiratory capacity and non-mitochondrial respiration was only significantly decreased in MM iPSC-CMs and not in non-MM iPSC-CMs. Additionally, comparative analysis of non-MM and MM-iPSC-CMs cultured in the same plate showed an increased ratio of apoptotic cells ($TUNEL^+$) in MM iPSC-CMs (4 hours, 1% O_2: 23,8% ± 1,5%; 24 hours, 1% O_2: 93,0% ± 2,4% vs. 21% O_2: 7,92% ± 1,09%; P<0,001), while no increase in apoptosis was observed for non-MM iPSC-CMs (4 hours, 1% O_2: 1,18% ± 0,2%; 24 hours, 1% O_2: 10,6% ± 6,6% vs. 21% O_2: 1,1% ± 0,23%; P>0,05; **Figure 4d, e**). This showed metabolic maturation in MM is responsible for increased sensitivity to hypoxia. All together, these results provide further support for our findings that MM iPSC-CMs depend on oxidative phosphorylation and consequently are more sensitive to hypoxia than non-MM iPSC-CMs cultured in glucose-rich or low glucose/lactate media. These results strongly suggest that iPSC-CMs, cultured conventionally and in the presence of glucose, resemble the immature embryonic CM phenotype with respect to their energy substrate utilization, active metabolic pathways, and survival upon low oxygen exposure. In contrast, MM iPSC-CMs cultured with lipids as the primary energy source, more closely resemble adult CMs, consistent with previous reports[18]. We found that MM iPSC-CMs are more sensitive to hypoxia, leading to minimized mitochondrial function, DNA fragmentation, and ultimately apoptosis.

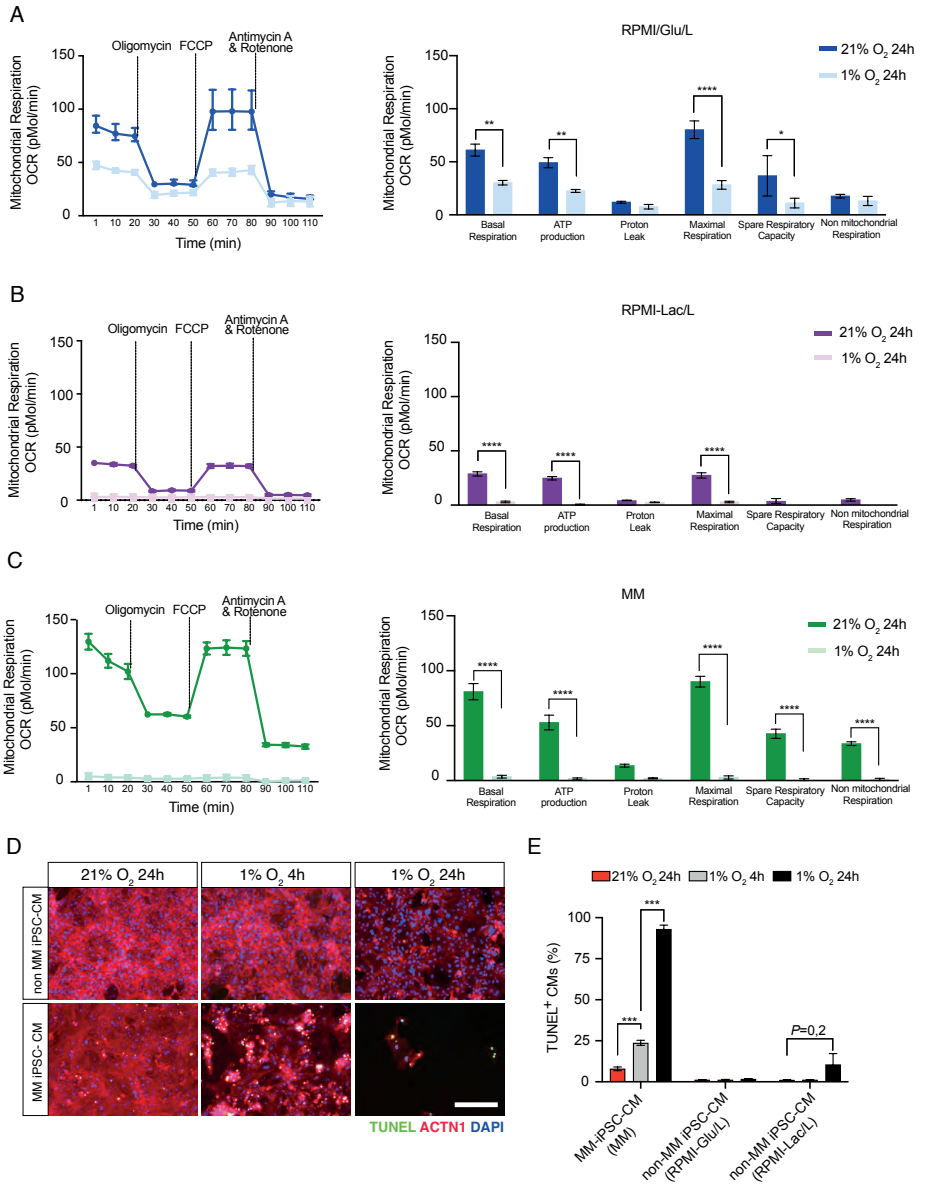

Figure 4. Metabolic profiling of non-MM iPSC-CMs and MM iPSC-CMs exposed to hypoxia
A-C. Normalized real-time oxygen consumption rate (OCR) of non-MM iPSC-CMs in RPMI-Glu/B27 (**A**), RPMI-B27 (**B**) and MM iPSC-CMs (**C**) in normoxia (21% O_2, 24 hours), short-term hypoxia (1% O_2, 4 hours) or long-term hypoxia (1% O_2, 24 hours) by Seahorse extracellular flux analyser. Cells were treated with oligomycin, FCCP, and antimycin A and rotenone to measure mitochondrial respiration. **D**. Comparative images of TUNEL staining of cardiomyocytes used in metabolic profiling. **E**. Quantification of TUNEL staining. A-C: 2 cell lines, 2 biological replicates, 1-2 technical replicates (n=5). Scale bar: 200 µm. Data was analysed using one-way ANOVA and Dunnett multiple comparison. *P<0,05; **P<0,01; ***P<0,001; ****P<0,0001. Data are shown as mean ± SEM.

Preconditioning with Nec-1 protects metabolically matured iPSC-CMs from hypoxic injury

To determine the utility of our damage model as a platform to screen for protective agents, we preconditioned the cells with the necroptosis inhibitor necrostatin-1 (Nec-1) and assessed whether the previously found protective effects[34,35] could be reproduced (**Figure 5a**). Supplementation of MM-iPSCs with Nec-1 24 hours prior to hypoxia, indeed resulted in a significant decrease in cell death compared to control (fold change EthD1/calcein AM ratio: 0,47 ± 0,06 with Nec-1, P<0,01; **Figure 5b, c**). MM iPSC-CMs preconditioned with Nec-1 showed a significant increase in OCR (**Figure 5d, e**), as opposed to non-MM iPSC-CMs (**Supplemental figure 3**). Furthermore, Nec-1 preconditioning increased the expression of the mitochondrial outer membrane protein TOMM20 compared to control, indicating increased cellular mitochondrial content (**Figure 5f, g**).

DISCUSSION

In the present study, we confirmed that the conventional method for differentiation of iPSC-CMs using RPMI/B27-based medium (RPMI-Glu/B27) generates cells with low sensitivity to hypoxia and consequential cell death. We furthermore demonstrated that applying metabolic maturation of iPSC-CMs increased sensitivity to hypoxia, rendering these matured cells better models for *in vitro* models of cardiac ischemia. The observed ability of conventionally cultured, non-MM iPSC-CMs to increase the glycolytic flux in anaerobic conditions is in line with the characteristics of foetal immature CMs having a higher threshold for oxygen insufficiency.[36–38] During development, arterial blood oxygen saturation fluctuates around 3% O_2, which would be considered a hypoxic condition in the adult human heart, with respect to activation of hypoxia-induced gene expression.[37] However, foetal immature CMs are conditioned to low oxygen pressures during development and thus rely on anaerobic energy pathways for metabolism and cardiac growth. Mechanistically, it has been shown that transcription factor hypoxia-inducible factor 1 (HIF1) is stabilized in foetal CMs under low oxygen pressures and plays a key role in maintaining and enhancing glycolytic metabolism via LDH-A regulation in the compact myocardium and counteracting CM maturation.[23,38,39]

Also in iPSC-CMs the inhibition of HIF1 has been shown to lead to CM maturation and a metabolic shift from aerobic glycolysis towards oxidative phosphorylation.[24] Frequently used "high glucose" cell culture media containing glucose at concentrations of ~15 mmol/L do not relate to human physiology, with local glucose concentrations of ~3 mmol/L, and have been considered obstructive for iPSC-CM maturation.[40] Furthermore, a four-fold postnatal increase in concentration of circulating fatty acids enables and drives increased activation of fatty acid β-oxidation pathways in adult cardiomyocytes.[40,41] Despite relying mainly on metabolization of glucose, we did observe a decrease in mitochondrial respiration rate in non-MM iPSC-CMs following hypoxia. This could be related to the short intermittent reoxygenation step required

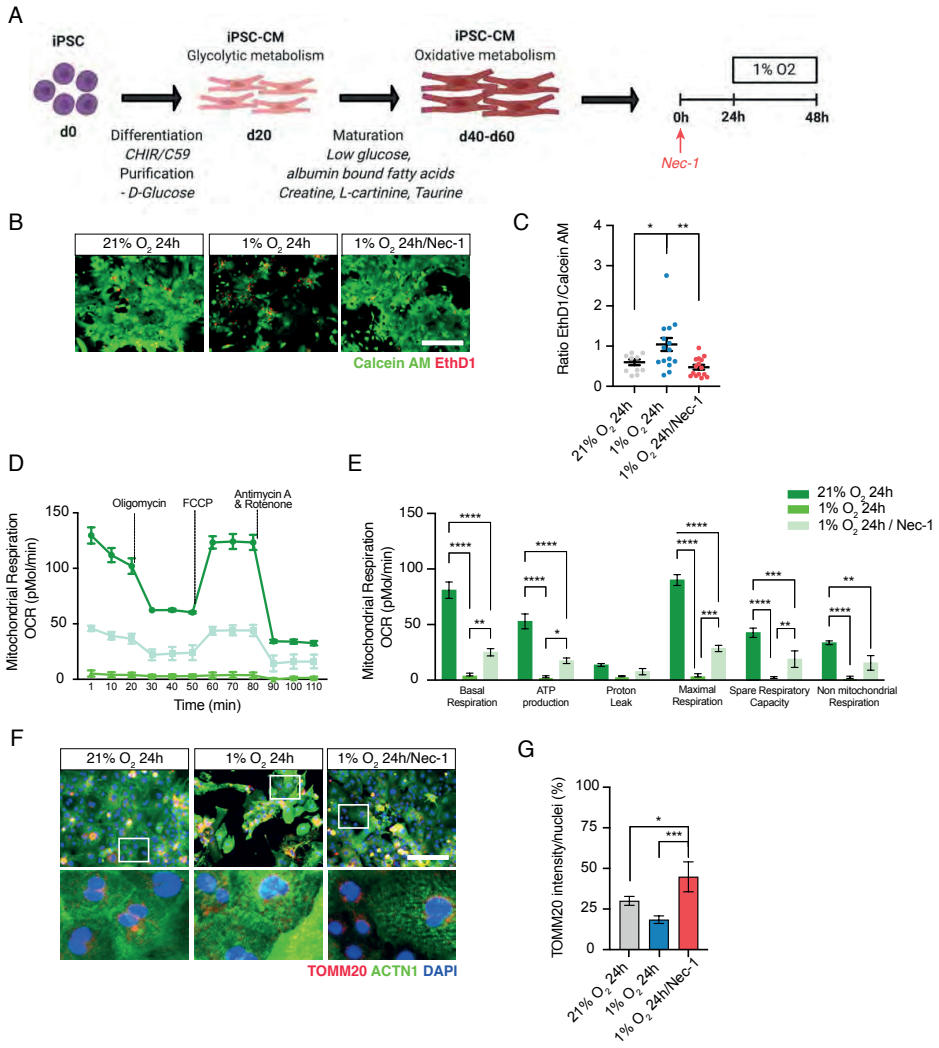

Figure 5. Preconditioning with Nec-1 protects MM iPSC-CMs from hypoxia

A. Schematic representation of experimental set-up. **B**. EthD1/Calcein AM staining of MM iPSC-CMs exposed to 21% O_2 or 1% O_2 for 24 hours in the absence or presence of necroptosis inhibitor Nec-1. **C**. Quantification of **B**. **D-E**. Normalized real-time oxygen consumption rate (OCR) of iPSC-CMs MM iPSC-CMs in normoxia (21% O_2, 24 hours), long-term ischemia (1% O_2, 24 hours), or long-term hypoxia preconditioned with Nec-1 for 24 hours by Seahorse extracellular flux analyser. Cells were treated with oligomycin, FCCP, and antimycin A and rotenone to measure mitochondrial respiration. **F**. Immunofluorescent staining of sarcomeres (ACTN1, green) and mitochondria (TOMM20, red) of cells used for metabolic profiling. **G**. Quantification of TOMM20 staining. D-F: 2 cell lines, 2 biological replicates, 1-2 technical replicates (n=5). Scale bars: 200 µm. Data were analysed using two-way ANOVA. *P<0,05; **P<0,01; ***P<0,001; ****P<0,0001. Data are shown as mean ± SEM.

for Seahorse metabolic profiling analysis. Cell damage from reperfusion is caused by the release of reactive oxygen species upon the sudden increase in oxygen availability[42]. Hypoxia and reoxygenation have previously been shown to induce only limited damage and prolonged hypoxia without reoxygenation did not affect beating frequency in immature iPSC-CMs[36]. This is in line with our results of maintained beating frequency in immature, non-MM iPSC-CMs after prolonged hypoxia. A previously observed limited effect of hypoxia compared to reperfusion injury on calcium overload related cellular damage in immature iPSC-CMs[43], potentially explains why our seahorse results do show a response of iPSC-CMs in RPMI-media to hypoxia. During late human embryonal development, the glycolytic metabolism is insufficient to generate adequate ATP levels for cardiac contractions leading to the metabolic shift towards oxidative phosphorylation.[39] The increased oxygen availability around birth destabilizes the HIF1 transcription factor complex, resulting in the mitochondrial shift towards more energy-efficient oxidative phosphorylation-based metabolism.[38,44] With this increased availability of ATP, CMs mature with a concomitant increase in ploidy, myofibrillar organization, and number of mitochondria providing for increased energy demands of cardiac contractility.[39] However, these necessary changes in functional and structural phenotype seem to limit metabolic flexibility. We observed that MM iPSC-CMs, as opposed to non-MM iPS-CMs were sensitive to hypoxia-induced cell death and showed decreased mitochondrial respiration after 4 hours of hypoxia. Additionally, lactate production plays a vital role in glycolysis and was not observed in normoxic conditions or in short-term hypoxia, but did increase in long-term hypoxia, indicating that MM iPSC-CMs eventually shift towards oxidative phosphorylation of fatty acids. This observation was in line with the drop in glucose levels in these conditions without an increase in lactate production. Interestingly, we showed that 5% O_2, considered physiological normoxia in most tissue[33], induced a similar degree of cell death as 1% O_2 for MM iPSC-CMs. This suggests, that in our model hypoxia-induced cell death pathways are already induced at a decrease from atmospheric 21% O_2 to 5% O_2, in contrast to previous studies suggesting 0,5-2% O_2 as effective cellular hypoxia[43]. This difference in physiological tissue normoxia and cell culture normoxia is an important factor to take into account when further developing *in vitro* hypoxia models. Within this study, differentiation of iPSC to iPSC-CMs is conducted at atmospheric O_2, whereas during cardiac development *in vivo* CMs differentiate and mature at lower physiological concentrations (5-8% O_2).[33,37] We have shown, while glycolytic non-MM iPSC-CMs were insensitive to hypoxia, MM iPSC-CMs showed increased sensitivity to hypoxia and even physiological O_2 concentrations. Using a monolayer of a single cell-type in an *in vitro* setting alongside hyperoxia during cardiac differentiation are likely to contribute further to sensitivity to O_2 concentration considered physiological. Further investigation could determine thresholds of specific O_2 concentrations resulting in activation of hypoxia signalling (e.g., HIF1α stabilization) in iPSC-CMs. This could be followed up by hypoxia studies using viable cardiac tissue slices[45] or engineered heart tissues[46] to circumvent limitations of monolayer single cell-type models, although obviously

more cost- and technology-intensive, thus probably less promising for high-throughput applications and screens.

Finally, we confirmed the applicability of MM iPSC-CM to model hypoxic damage by validating the protective effects of the necroptosis inhibitor Nec-1, in contrast to conventional, non-MM iPSC-CM culture conditions. In summary, we have shown that MM iPSC-CMs display increased sensitivity to hypoxic injury, which is more reminiscent of adult CMs and therefore represent an improved model for human ischemic heart disease *in vitro*.

ACKNOWLEDGEMENTS

The authors would like to acknowledge Joseph Wu (Stanford Medicine, USA) for providing the CVI-273 hiPS cell line. We thank Maike Kreutzenbeck and Rebecca Dieterich (Šarić group, University of Cologne) for their technical support with the generation and characterisation of the NP0141-31B / UKKi032-C iPSC line. M.C.P. and K.N. were supported by a Netherlands Cardiovascular Research Initiative (CVON) grant (REMAIN 2014B27) and a Health~Holland LSH-TKI grant (DELICATE LSHM19086). M.M. is supported by the National Institutes Health (5P01HL141084 and 1R01HL152055) and Foundation Leducq (CUREPLaN). T.Š. was supported by the Innovative Medicine Initiative Joint Undertaking (IMI-JU) funded by the European Commission and the European Federation of Pharmaceutical Industries and Associations (EFPIA, grant agreement No. 115582, "European Bank for induced Pluripotent Stem Cells, EBiSC). J.P.G.S and R.G.C.M were supported by the PLN foundation, J.P.G.S and A.v.M. were supported by Horizon2020 ERC-2016-COG-EVICARE (grant number 725229) and BRAVE (grant number 874827).

Disclosure of Potential Conflicts of Interest

The authors disclose no conflicts of interest.

REFERENCES

1. Virani SS, Alonso A, Benjamin EJ, et al. Heart Disease and Stroke Statistics—2020 Update: A Report from the American Heart Association.; 2020. doi:10.1161/CIR.0000000000000757
2. Oerlemans MIFJ, Koudstaal S, Chamuleau SA, De Kleijn DP, Doevendans PA, Sluijter JPG. Targeting cell death in the reperfused heart: Pharmacological approaches for cardioprotection. Int J Cardiol. 2013;165(3):410-422. doi:10.1016/j.ijcard.2012.03.055
3. Hausenloy DJ, Garcia-Dorado D, Bøtker HE, et al. Novel targets and future strategies for acute cardioprotection: Position Paper of the European Society of Cardiology Working Group on Cellular Biology of the Heart. Cardiovasc Res. 2017;113(6):564-585. doi:10.1093/cvr/cvx049
4. Ferdinandy P, Hausenloy DJ, Heusch G, Baxter GF, Schulz R. Interaction of Risk Factors, Comorbidities, and Comedications with Ischemia/Reperfusion Injury and Cardioprotection by Preconditioning, Postconditioning, and Remote Conditioning. Pharmacol Rev. 2014;66(4):1142-1174.
5. Milani-Nejad N, Janssen PML. Small and Large Animal Models in Cardiac Contraction Research: Advantages and Disadvantages. Pharmacol Ther. 2014;141(3):1-5. doi:10.1016/j.pharmthera.2013.10.007.Small
6. Pond AL, Scheve BK, Benedict AT, et al. Expression of distinct ERG proteins in rat, mouse, and human heart. Relation to functional I(Kr) channels. J Biol Chem. 2000;275(8):5997-6006. doi:10.1074/jbc.275.8.5997
7. Swynghedauw B. Developmental and functional adaptation of contractile proteins in cardiac and skeletal muscles. Physiol Rev. 1986;66(3):710-771. doi:10.1152/physrev.1986.66.3.710
8. Marian AJ. On mice, rabbits and human heart failure. Circulation. 2005;111(18):2276-2279. doi:10.1161/01.CIR.0000167559.13502.9A.On
9. Uosaki H, Taguchi Y h. Comparative Gene Expression Analysis of Mouse and Human Cardiac Maturation. Genomics, Proteomics Bioinforma. 2016;14(4):207-215. doi:10.1016/j.gpb.2016.04.004
10. Karakikes I, Ameen M, Termglinchan V, Wu JC. Human Induced Pluripotent Stem Cell-Derived Cardiomyocytes: Insights into Molecular, Cellular, and Functional Phenotypes. Circ Res. 2015;117(1):80-88. doi:10.1161/CIRCRESAHA.117.305365
11. Takahashi K, Tanabe K, Ohnuki M, et al. Induction of Pluripotent Stem Cells from Adult Human Fibroblasts by Defined Factors. Cell. 2007;131(5):861-872. doi:10.1016/j.cell.2007.11.019
12. Burridge PW, Keller G, Gold JD, Wu JC. Production of de novo cardiomyocytes: Human pluripotent stem cell differentiation and direct reprogramming. Cell Stem Cell. 2012;10(1):16-28. doi:10.1016/j.stem.2011.12.013
13. van Mil A, Balk GM, Neef K, et al. Modelling inherited cardiac disease using human induced pluripotent stem cell-derived cardiomyocytes: Progress, pitfalls, and potential. Cardiovasc Res. 2018;114(14):1828-1842. doi:10.1093/cvr/cvy208
14. Li Q, Wang J, Wu Q, Cao N, Yang HT. Perspective on human pluripotent stem cell-derived cardiomyocytes in heart disease modeling and repair. Stem Cells Transl Med. 2020;9(10):1121-1128. doi:10.1002/sctm.19-0340
15. Hnatiuk AP, Briganti F, Staudt DW, Mercola M. Human iPSC modeling of heart disease for drug development. Cell Chem Biol. 2021;28(3):271-282. doi:10.1016/j.chembiol.2021.02.016
16. Robertson C, Tran DD, George SC. Concise review: Maturation phases of human pluripotent stem cell-derived cardiomyocytes. Stem Cells. 2013;31(5):829-837. doi:10.1002/stem.1331
17. Herron TJ. Calcium and voltage mapping in hiPSC-CM monolayers. Cell Calcium. 2016;59(2-3):84-90. doi:10.1016/j.ceca.2016.02.004
18. Feyen DAM, McKeithan WL, Bruyneel AAN, et al. Metabolic Maturation Media Improve Physiological Function of Human iPSC-Derived Cardiomyocytes. Cell Rep. 2020;32(3). doi:10.1016/j.celrep.2020.107925
19. Ulmer BM, Eschenhagen T. Human pluripotent stem cell-derived cardiomyocytes for studying energy metabolism. Biochim Biophys Acta - Mol Cell Res. 2020;1867(3):118471. doi:10.1016/j.bbamcr.2019.04.001
20. Tohyama S, Hattori F, Sano M, et al. Distinct metabolic flow enables large-scale purification of mouse and human pluripotent stem cell-derived cardiomyocytes. Cell Stem Cell. 2013;12(1):127-137. doi:10.1016/j.stem.2012.09.013
21. Fillmore N, Levasseur JL, Fukushima A, et al. Uncoupling of glycolysis from glucose oxidation accompanies the development of heart failure with preserved ejection fraction. 2018:1-12.

22. Ulmer BM, Stoehr A, Schulze ML, et al. Contractile Work Contributes to Maturation of Energy Metabolism in hiPSC-Derived Cardiomyocytes. Stem Cell Reports. 2018;10(3):834-847. doi:10.1016/j.stemcr.2018.01.039

23. Horikoshi Y, Yan Y, Terashvili M, et al. Fatty acid-treated induced pluripotent stem cell-derived human cardiomyocytes exhibit adult cardiomyocyte-like energy metabolism phenotypes. Cells. 2019;8(1095):1-21.

24. Hu D, Linders A, Yamak A, et al. Metabolic maturation of human pluripotent stem cellderived cardiomyocytes by inhibition of HIF1α and LDHA. Circ Res. 2018;123(9):1066-1079. doi:10.1161/CIRCRESAHA.118.313249

25. Hidalgo A, Glass N, Ovchinnikov D, et al. Modelling ischemia-reperfusion injury (IRI) in vitro using metabolically matured induced pluripotent stem cell-derived cardiomyocytes. APL Bioeng. 2018;2(2). doi:10.1063/1.5000746

26. Kitani T, Ong SG, Lam CK, et al. Human-Induced Pluripotent Stem Cell Model of Trastuzumab-Induced Cardiac Dysfunction in Patients with Breast Cancer. Circulation. 2019;139(21):2451-2465. doi:10.1161/CIRCULATIONAHA.118.037357

27. Matsa E, Burridge PW, Yu KH, et al. Transcriptome Profiling of Patient-Specific Human iPSC-Cardiomyocytes Predicts Individual Drug Safety and Efficacy Responses In Vitro. Cell Stem Cell. 2016;19(3):311-325. doi:10.1016/j.stem.2016.07.006

28. Hamad S, Derichsweiler D, Papadopoulos S, et al. Generation of human induced pluripotent stem cell-derived cardiomyocytes in 2D monolayer and scalable 3D suspension bioreactor cultures with reduced batch-to-batch variations. Theranostics. 2019;9(24):7222-7238. doi:10.7150/thno.32058

29. Schneider CA, Rasband WS, Eliceiri KW. ImageJ. U. S. National Institutes of Health, Bethesda, Maryland, USA. doi:10.3389/fimmu.2021.731361

30. Ye L, Qiu L, Zhang H, et al. Cardiomyocytes in Young Infants with Congenital Heart Disease: A Three-Month Window of Proliferation. Sci Rep. 2016;6:1-9. doi:10.1038/srep23188

31. Kretzschmar K, Post Y, Bannier-Hélaouët M, et al. Profiling proliferative cells and their progeny in damaged murine hearts. Proc Natl Acad Sci U S A. 2018;115(52):E12245-E12254. doi:10.1073/pnas.1805829115

32. Balafkan N, Mostafavi S, Schubert M, et al. A method for differentiating human induced pluripotent stem cells toward functional cardiomyocytes in 96-well microplates. Sci Rep. 2020;10(1):1-14. doi:10.1038/s41598-020-73656-2

33. Carreau A, Hafny-Rahbi B El, Matejuk A, Grillon C, Kieda C. Why is the partial oxygen pressure of human tissues a crucial parameter? Small molecules and hypoxia. J Cell Mol Med. 2011;15(6):1239-1253. doi:10.1111/j.1582-4934.2011.01258.x

34. Oerlemans MIFJ, Liu J, Arslan F. Inhibition of RIP1-dependent necrosis prevents adverse cardiac remodeling after myocardial ischemia – reperfusion in vivo. 2012. doi:10.1007/s00395-012-0270-8

35. Feyen D, Gaetani R, Liu J, et al. Increasing short-term cardiomyocyte progenitor cell (CMPC) survival by necrostatin-1 did not further preserve cardiac function. 2018:83-91. doi:10.1093/cvr/cvt078

36. Häkli M, Kreutzer J, Mäki AJ, et al. Human induced pluripotent stem cell-based platform for modeling cardiac ischemia. Sci Rep. 2021;11(1):1-13. doi:10.1038/s41598-021-83740-w

37. J. Patterson A, Zhang L. Hypoxia and Fetal Heart Development. Curr Mol Med. 2010;10(7):653-666. doi:10.2174/156652410792630643

38. Ascuitto RJ, Ross-Ascuitto NT. Substrate metabolism in the developing heart. Semin Perinatol. 1996;20(6):542-563. doi:10.1016/S0146-0005(96)80068-1

39. Menendez-Montes I, Escobar B, Palacios B, et al. Myocardial VHL-HIF Signaling Controls an Embryonic Metabolic Switch Essential for Cardiac Maturation. Dev Cell. 2016;39(6):724-739. doi:10.1016/j.devcel.2016.11.012

40. Slaats RH, Schwach V, Passier R. Metabolic environment in vivo as a blueprint for differentiation and maturation of human stem cell-derived cardiomyocytes. Biochim Biophys Acta - Mol Basis Dis. 2020;1866(10):165881. doi:10.1016/j.bbadis.2020.165881

41. Lopaschuk GD, Jaswal JS. Energy metabolic phenotype of the cardiomyocyte during development, differentiation, and postnatal maturation. J Cardiovasc Pharmacol. 2010;56(2):130-140. doi:10.1097/FJC.0b013e3181e74a14

42. Ferrari R, Ceconi C, Curello S, et al. Role of oxygen free radicals in ischemic and reperfused myocardium. Am J Clin Nutr. 1991;53. doi:10.1093/ajcn/53.1.215S

43. Wei W, Liu Y, Zhang Q, Wang Y, Zhang X, Zhang H. Danshen-Enhanced Cardioprotective Effect of Cardioplegia on Ischemia Reperfusion Injury in a Human-Induced Pluripotent Stem Cell-Derived Cardiomyocytes Model. Artif Organs. 2017;41(5):452-460. doi:10.1111/aor.12801

44. Neary MT, Ng KE, Ludtmann MHR, et al. Hypoxia signaling controls postnatal changes in cardiac mitochondrial morphology and function. J Mol Cell Cardiol. 2014;74:340-352. doi:10.1016/j.yjmcc.2014.06.013

45. Pitoulis FG, Watson SA, Perbellini F, Terracciano CM. Myocardial slices come to age: An intermediate complexity in vitro cardiac model for translational research. Cardiovasc Res. 2020;116(7):1275-1287. doi:10.1093/CVR/CVZ341

46. Giacomelli E, Meraviglia V, Campostrini G, et al. Human-iPSC-Derived Cardiac Stromal Cells Enhance Maturation in 3D Cardiac Microtissues and Reveal Non-cardiomyocyte Contributions to Heart Disease. Cell Stem Cell. 2020;26(6):862-879.e11. doi:10.1016/j.stem.2020.05.004

SUPPLEMENTARY

The **supplementary figures 1-3 and** the **supplementary table 1** can be downloaded from: https://oup.silverchair-cdn.com/oup/backfile/Content_public/Journal/stcltm/11/10/10.1093_stcltm_szac061/1/szac061_suppl_supplementary_material.pdf?Expires=1709309449&Signature=Sj12XddBRKJ6KHwIevyyjrvJqHxkrPRkHLKaSAZhIibFCa9bDVzwFqWB7SG-TSMMH3Kn1kPiGW0Umx44dLnmB-iGvut4EYhBp4w-08gr6s2NBpsm-yK059qLBlXfZyJSQ9FKrXN8-rKj1G4MT2vkd5lqCGXWvNsw2HhCRg~xVhTVZb-R6cmsbESsf2hYVxKZAphs5VqTliNrexckv0KKcvOCPEg0VhZ2AwD7elKrOu3CvlenvGDBt9bp-7UkXsfjmWbXzfK-NFQlxC6-cru8uHZQEsTaHfSUmu80liJW71JWoODlUVjLLrN~YZ4WhNn-BcJeyV-fxmcHs~~k-FjN~AKA__&Key-Pair-Id=APKAIE5G5CRDK6RD3PGA

Or:

PART II

Modelling the phospholamban R14del mutation using patient-specific hiPSC-CMs

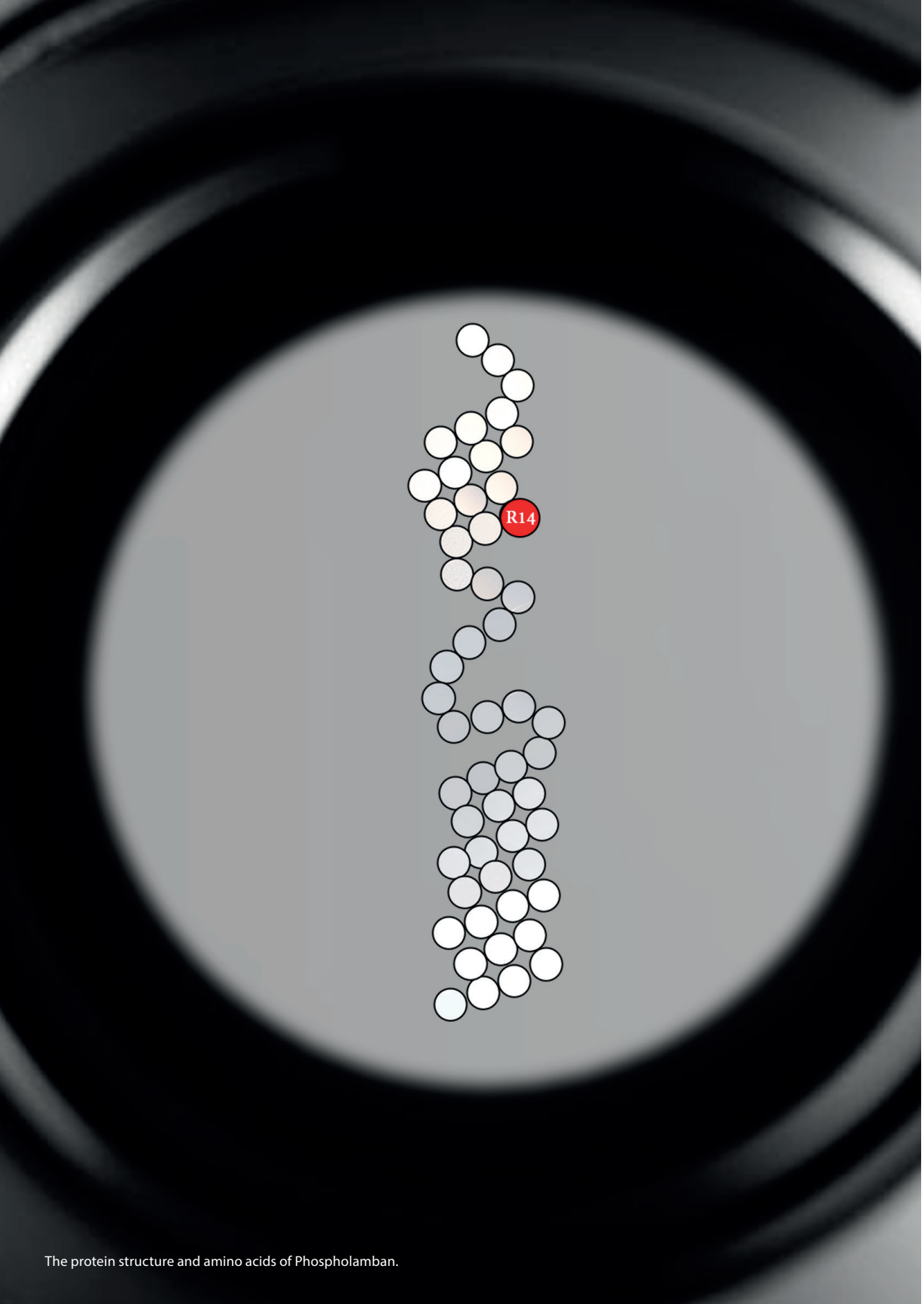

The protein structure and amino acids of Phospholamban.

Chapter 7

Phospholamban R14del Cardiomyopathy: a Systematic Summary of the Pathophysiological Mechanisms

Manuscript submitted to Circulation Research

Renée G.C. Maas, Luuk Kerckhaert , Judy Broersma,
Pieter. A. Doevendans, Joost. P.G. Sluijter, Francesca Stillitano

ABSTRACT

Phospholamban (PLN) encodes for a transmembrane sarcoplasmic reticulum (SR) phosphoprotein and is crucial in the regulation of calcium cycling in cardiomyocytes by interacting with the calcium pump sarco(endo)plasmic reticulum calcium ATPase 2a (SERCA2a). The deletion of amino acid arginine 14 in the cardiac-enriched protein phospholamban (PLN-R14del) potentially leads to a super-inhibitory effect towards SERCA2a, causing disturbed calcium handling and decreased contractility in cardiomyocytes. However, the functional consequences of this mutation and the mechanisms underlying PLN-R14del cardiomyopathy remain poorly understood. The purpose of this systematic review is to summarize the research studies conducted on understanding the molecular mechanisms causing PLN-R14del cardiomyopathy. This review will emphasize the impact that the discovery of PLN-R14del had on fueling insights into the basic biology of calcium handling, protein toxicity, metabolism, and fibrosis, and reinforce the idea that PLN is a crucial dynamic regulator of SERCA2a that contributes to the speed and force of calcium-driven muscle contraction. Finally, the elucidation of the mechanisms involved in cardiomyopathy onset and progression from this causative gene will lead to the development of novel therapeutic agents, which were summarized here.

INTRODUCTION

In 2006, the deletion of arginine 14 (p.Arg14del) within the phospholamban protein (PLN-R14del) was discovered to cause severe cardiomyopathy in members of a Greek family.[1] Since then, this mutation has been identified in thousands of cardiomyopathy patients across various countries, including the USA, Canada, China, Japan, Vietnam, Italy, Germany, Spain, and the Netherlands (**Figure 1**).[1–8] Notably, in the Dutch population, the PLN-R14del founder mutation has emerged as one of the most prevalent genetic mutations associated with cardiomyopathy. More than 1600 carriers have been identified so far, and this number continues to grow.[9,10] In the Netherlands, PLN-R14del is responsible for approximately 10% to 15% of patients with dilated cardiomyopathy (DCM) and 15% with arrhythmogenic cardiomyopathy (ACM)[11]. Remarkably, this mutation accounts for about 25% of the annual heart transplants performed in the Netherlands, underlining its significant impact on cardiac health.[10]

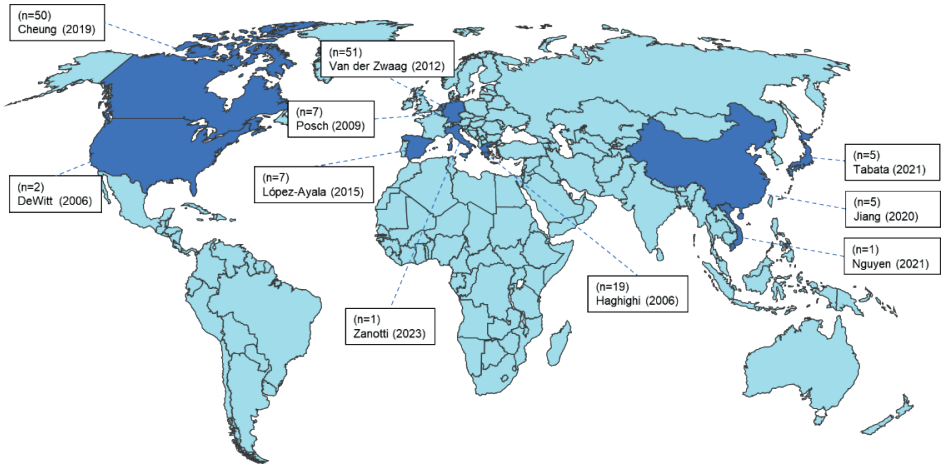

Figure 1. World map illustrating the global distribution of PLN-R14del carriers, which have been identified in 10 different countries around the world (dark blue color). N= number of patients described per study.

Phospholamban is a small protein consisting of 52 amino acids and is encoded by the *PLN* gene. Its primary role is the regulation of the calcium pump known as Sarco(endo)plasmic reticulum calcium ATPase 2a (SERCA2a) within cardiomyocytes. The normal function of PLN has been extensively reviewed.[12,13] Nevertheless, the precise mechanisms and implications of the PLN-R14del mutation in causing heart disease remain unclear and subject to controversy, warranting ongoing research efforts. In this review, we systematically summarize all studies describing the PLN-R14del mutation and discuss the pathological phenotypes in addressing the PLN-R14del cardiomyopathy.

Clinical alterations in PLN-R14del patients

The onset of PLN-R14del disease differs among patients and seems to be age-dependent. Typically, most patients begin experiencing symptoms at an average age ranging from 40 to 48 years.[14–16] However, there is evidence of patients under 30 years old exhibiting ventricular tachycardia. Conversely, many PLN-R14del carriers remain asymptomatic[17], highlighting the significant variability in disease penetrance associated with this mutation. In a Spanish family, a disease penetration of 75% was reported.[5] Several factors may contribute to an individual's disease onset and progression, including additional mutations, alterations in the PLN interactome[18], external stressors like intense physical activity[19–22], or combinations thereof. Interestingly, no association has been found between participation in high dynamic sports and malignant ventricular arrhythmias in PLN-R14del carriers.[17] Therefore, further understanding of the interplay between genetic and environmental factors is crucial for both the diagnosis and management of this condition. To date, no studies have described an explanation for this disease penetrance variability.

The clinical spectrum of the disease phenotype associated with PLN-R14del mutation varies from early stage ECG and ultrasound strain abnormalities to a moderate stage consisting of reduced left ventricular function, and ultimately progression into congestive biventricular failure, potentially accompanied by arrhythmias.[23–28] At the structural level, the PLN-R14del mutation results in a biventricular phenotype, characterized by the presence of fibrosis, dilation of the heart, fibrofatty tissue replacement, and the formation of protein aggregates. These structural changes within the heart may provide the substrates necessary for the occurrence of ventricular arrhythmias.[29] Notably, certain ECG abnormalities, such as low-voltage ECG with attenuated R amplitudes and inverted T-waves, are early indicators of the disease in individuals with the PLN-R14del mutation and can be attributed to the presence of cardiac fibrosis.[30,31] Importantly, attenuated R amplitudes can serve as an early ECG marker, irrespective of any echocardiographic abnormalities, indicating a mutation-related remodeling process that precedes the onset of ventricular dysfunction.[6]

Since the discovery of PLN-R14del, several studies have investigated the underlying mechanisms of PLN-R14del cardiomyopathy. However, despite all efforts, PLN-R14del patients still wait desperately for customized therapy or even a curative treatment. In an attempt to understand the pathological characteristics of the disease, we performed a systematic search of studies providing the current knowledge on PLN-R14del cardiomyopathy, focusing on the structural and cellular characteristics of the disease (**Table 1**). The literature search was based on the following terminology in the title and/or abstract: ''PLN R14del''; ''Phospholamban R14del''; ''p.Arg14del''; ''PLN Arg14del''; ''Phospholamban Arg14del''; ''R14del''. The selected studies and data extraction were independently evaluated. The search found 82 studies, of which 81 fulfilled the selection criteria (**Supplementary Table 1**). Forty studies described the mutation effects in human patients, sixteen studies were performed in mice, seven in patient-

derived induced pluripotent stem cell-derived models, one paper described the PLNR14del pig model and one PLNR14del zebrafish model was reported.

Table 1: Systematic summary of clinical and research studies in PLN-R14del cardiomyopathy. Studies are sorted based on the year of publication.

First author and year of publication	Species	Type of study	Main findings
Haghighi (2006)[32]	Human, Mouse	Clinical and pathological examination, Genetic analysis, *in vivo*, *in vitro*	The PLN-R14del mutation was identified in a Greek family. PLN-R14Del mice recapitulate human cardiomyopathy. Possibly super-inhibition of SERCA2a by mutant monomeric PLN.
DeWitt (2006)[33]	Human	Clinical examination, Genetic analysis	Screening of a cohort of 260 unrelated DCM patients for mutations in the *PLN* gene, identified 1 family with PLN-R14del.
Posch (2009)[34]	Human	Clinical examination, Genetic analysis	PLN-R14del causes abnormal ECG phenotype with low R amplitudes irrespective of echocardiographic abnormalities. Indication for fibrosis as a primary process.
Haghighi (2012)[35]	Mouse	Pathological examination, *in vivo*, *ex vivo*, *in silico*	PLN-R14del is misrouted to the sarcolemma, in absence of endogenous PLN, alters NKA activity which subsequently leads to cardiac remodeling.
Ceholski (2012)[36]	n/a	*in silico*	PLN-R14del has a dominant-negative effect on SERCA2a function. Hydrophobic imbalance in the cytoplasmic domain of PLN might be a predictor of DCM.
Van der Zwaag (2012)[37]	Human	Clinical examination, Pathological examination, Genetic analysis	PLN mutation carriers diagnosed with DCM show arrhythmogenic phenotype and cardiomyopathy as well, including sudden cardiac death at a young age.
Van der Zwaag (2013)[38]	Human	Epidemiological analysis, Genetic analysis	Geographic origin of PLN-R14del is likely East-Friesland (The Netherlands), where the R14del variant originated 575-825 years ago.
Van der Heijden (2013)[39]	n/a	Review	Reviewed PLN studies till 2013. In the near future, the goal should be to identify all carriers of the PLN-R14del mutation to be able to prevent SCD.
Groeneweg (2013)[40]	Human	Clinical examination, Pathological examination, Genetic analysis	Due to the discovery of the ACM phenotype, the number of PLN-R14del patients contributes substantially to the revised TFC of ACM cardiomyopathy.
Gho (2014)[41]	Human	Pathological Examination	Using a novel histological quantification method, myocardial fibrosis is mainly present in the LPW and adipose tissue in the RV wall.
Van Rijsingen (2014)[42]	Human	Clinical examination, Genetic analysis	PLN-R14del carriers are at high risk for VA and end-stage heart failure. No association between participation in high dynamic sports and malignant Vas.
Bhonsale (2015)[43]	Human	Genetic Analysis	Pathogenic mutations were identified in 577 patients (241 families) from USA and Dutch ARVD/C cohorts. 5.7% carried the PLN-R14del mutation.
Vostrikov (2015)[44]	n/a	*in silico*	Deletion of R14 weakens membrane interaction in the cytoplasmic domain, causing a loss of function. Phosphorylation does not reverse the inhibitory effect.

First author and year of publication	Species	Type of study	Main findings
Young (2015)[45]	n/a	Review	Reviewed PLN mutants Arg9 and Arg14 and how the synergistic changes in SR calcium homeostasis led to impaired cardiac contractility and DCM.
Karakikes (2015)[46]	hiPSC-CMs	*in vitro*, Pathological examination, Genetic restoration	Gene correction using TALENs in hiPSC-CMs ameliorate PLN-R14del associated phenotype in vitro. Knock-down of mutant R14del or overexpression of WT PLN also reversed disease phenotype.
López-Ayala (2015)[47]	Human	Clinical examination, Genetic analysis	A Spanish family was reported exhibiting a disease penetration of 75%. ECG abnormalities are often found in carriers, with low-voltage/attenuated R amplitudes.
Fish (2016)[48]	Human	Genetic analysis	No PLN-R14del mutation was found in 315 African patients with ACM (n = 111), DCM (n = 95), HCM (n = 40) or PC (n = 69). One PLN c.25C > T (p.R9C) mutation was detected (mutation prevalence = 0.2%).
Milano (2016)[49]	Human	Clinical examination, Genetic analysis	Rare genetic variants, including PLN-R14del, contribute to the risk of sudden cardiac death.
Te Rijdt (2016)[50]	Human	Clinical examination, Pathological examination	PLN-R14del cardiomyopathy is characterized by large perinuclear PLN aggregates, which form aggresomes and are degraded via autophagy.
Stillitano (2016)[51]	hiPSC-CMs	*in vitro*, Pathological examination, functional readout, Genetic restoration	Three-dimensional EHT shows impaired cardiac contractility due to PLN-R14del. Genomic editing using TALENs restores contractile function.
Opbergen (2017)[52]	n/a	Review	Review outlines the intracellular cardiac calcium dynamics and relates pathophysiological signaling.
Sepehrkhouy (2017)[53]	Human	Pathological examination	PLN-associated cardiomyopathies exhibit a distinct fibrosis pattern from other hereditary cardiomyopathies. Fibrosis is most prominently present in the LPW.
Te Rijdt (2017)[54]	Human	Pathological examination, Genetic analysis	Using immunohistochemical staining of PLN protein aggregates, PLN-R14del cardiomyopathy can be diagnosed sensitively and specifically.
Nannenberg (2018)[55]	Human	Clinical Examination	Study evaluated ascertainment bias on survival. In PLN-R14del-positive patients, the median age of survival increased from 63.5% (2010) to 65.2 years (2012).
Wu (2018)[56]	Pig	*ex vivo*, model characterization	Generation of PLNR14del pigs via CRISPR/Cpf1-mediated gene editing and somatic cell nuclear transfer. Heart H&E staining results of 3 months old PLNR14del piglets showed no signifcant differences in tissue morphology or cell shape and size.
Hof (2019)[57]	n/a	Review	Reviewed studies till 2017. The most striking characteristic is the low-voltage ECGs. Therefore, cardiac and genetic screening is strongly recommended.
Te Rijdt (2019)[58]	Human	Clinical examination, Pathological examination, Genetic analysis	PLN-R14del phenotype is biventricular, is characterized by fibrofatty replacement and fibrosis, and exhibits a distinct molecular signature compared to ACM.
Cheung (2019)[59]	Human	Clinical examination Genetic analysis	A Canadian cohort of PLN-R14del patients exhibited similar disease phenotypes as Dutch patients, including VA and ECG abnormalities.

First author and year of publication	Species	Type of study	Main findings
Doevendans (2019)[60]	n/a	Cure Phospholamban-Induced Cardiomyopathy (CURE-PlaN)	CURE-PlaN network funded by the Foundation Leducq was started in 2019 with the ultimate goal of developing innovative disease-specific therapeutic modalities.
Stroik (2020)[61]	hiPSC-CMs	In vitro, functional readout	Viral expression of a SERCA2a-activating PLN mutant improves calcium cycling and synchronicity in PLN-R14del hiPSC-CMs.
Eijgenraam (2020)[62]	Mouse	Clinical examination, Pathological examination, Genetic analysis, In vivo, *ex vivo*, drug screening	Homozygous transgenic PLN-R14del mice exhibit the same cardiac phenotype as human PLN-R14del cardiomyopathy patients, yet in an accelerated manner. Eplerenone or metoprolol did not improve cardiac function or survival in the mice.
Bleijendaal (2020)[63]	Human	*in silico*	Diagnosis of PLN-R14del cardiomyopathy can be improved using machine learning and deep learning model methods by screening for abnormal T-waves.
Jiang (2020)[64]	Human	Clinical examination	PLN-R14del family found in Southwestern China, exhibiting similar symptoms as previously described. CMR on the LPW is important for early disease discovery.
Menzel (2020)[65]	Human, Mouse	Molecular dynamics simulations, Protein analysis, functional readout	Phosphorylation at either Ser16 or Thr17 converted PLN into a target for the phospho-adaptor protein 14-3-3 with different affinities. Phosphorylation of Thr17 therefore may become crucial for 14-3-3 recruitment to PLN-R14del.
Pei & Maas (Preprint, 2020)[66]	Human	Genetic analysis, Pathological examination, Genetic analysis, *ex vivo*	Authors report differentially acetylated TF and expressed genes in FAO metabolisms and their downstream target in PLN-R14del hearts.
Taha (2021)[67]	Human	Clinical examination	Echocardiographic characteristics of 281 PLN-R14del carriers. Pre-symptomatic mutation carriers with apical PSS in the apex are at higher risk of Vas.
Van de Leur (2021)[68]	Human	Clinical Examination	DNN was developed on ECGs of 69 patients and evaluated on 17 patients. DNN visualizes disease-specific ECG features and reveals yet unidentified features.
Lopes (2021)[69]	Human	Clinical examination	ECG-based identification was strongly improved by using a transfer learning approach with sex classification. The QRS complex was found to be the most important region in the ECG for PLN-R14del identification.
Nguyen (2021)[70]	Human	Clinical examination, Genetic analysis	Screening of a Vietnamese cohort of 230 familial and sporadic DCM patients for 58 genes. The diagnostic yield of PLNR41del was 2%.
Feyen (2021)[71]	hiPSC-CMs	*in vitro*, Pathological examination, Genetic analysis, functional readout, rescue with drug	Single-cell RNA sequencing of PLN-R14del-CMs revealed the induction of the UPR pathway. PLN-R14del hiPSC-CMs treated with a UPR activator (BiP) showed a dose-dependent amelioration of the contractility deficit.
Cuello (2021)[72]	hiPSC-CMs	*in vitro*, pathological examination, functional readout, rescue with drug	RNA-seq and proteomic analyses on PLNR14del-CMs revealed dysfunction between the ER and mitochondria. Transduction of PLN-R14del EHTs with the Ca^{2+}-binding proteins GcaMP6f/parvalbumin improved the disease phenotype.

First author and year of publication	Species	Type of study	Main findings
Raad (2021)[73]	Humanized Mouse	Clinical and pathological examination, functional readout, *in vivo*, *ex vivo*	Humanized PLN-R14del mice exhibited adverse electrophysiological remodeling, absence of significant structural or hemodynamic changes, and increased arrhythmia susceptibility.
Verstraelen (2021)[74]	Human	Clinical examination	This study developed a new mutation-specific prediction model that improved risk stratification for primary prevention of ICD implantation by developing a new mutation-specific prediction model for malignant VA in PLN-R14del carriers.
Te Rijdt (2021)[75]	Human	Clinical trial: The PHOspholamban Related Cardiomyopathy Intervention Study (iPHORECAST)	This study investigates if pre-emptive treatment of 42 presymptomatic PLN-R14del carriers using 50 mg eplerenone, can reduce disease progression and postpone the onset of overt disease.
Haghighi (2021)[76]	Humanized Mouse	Clinical examination, Pathological examination, functional readout, *in vivo*, *ex vivo*, rescue with drug	Humanized PLN-R14del mice exhibited impairment of atrioventricular conduction, in association with VA, which appeared to originate from the right ventricle in vivo. KN93 reversed this proarrhythmic parameter.
Koch (2021)[77]	n/a	*in silico*, *in vitro*	Mathematical modeling and preliminary analyses suggest that the PLN-R14del could impair noise filtering, offering a new perspective on how this mutation causes cardiac arrhythmias.
Grote Beverborg (2021)[78]	Mouse	Clinical examination, Pathological examination, functional readout, *in vivo*, *ex vivo*, gene silencing rescue	Mice harboring the PLN-R14del pathogenic variant recapitulate the DCM phenotype; subcutaneous administration of PLN-ASO prevents PLN protein aggregation, cardiac dysfunction, and leads to a 3-fold increase in survival rate.
Taha (2021)[79]	Human	Clinical examination	LVMD has incremental prognostic value on top of LVEF in PLN-R14del carriers, particularly in those with preserved LVEF.
Eijgenraam (2021)[80]	Mouse	Clinical examination, Pathological examination, functional readout, *in vivo*, *ex vivo*	Progression of PLN-R14Δ/Δ mice was investigated by echocardiography, ECG, tissue analysis, and transcriptomics and proteomics in week 3, 4, and 5 of age.
Van der Klooster (2021)[81]	Human	Clinical Examination	In 7.2% of cardiomyocytes from PLNR14del patients, homogeneously distributed p62 accumulation was present.
De Brouwer (2021)[82]	Human	Clinical Examination	Analysis of 933 PLN-R14del patients showed that low-voltage ECGs predict sustained VA and are more common in females, yet the prognostic value is greater in males.
Kamel (2021)[83]	Zebrafish	Clinical examination, Pathological examination, functional readout, *in vivo*, *ex vivo*, rescue with drug	Zebrafish harboring the PLN-R14del pathogenic variant recapitulate alterations of cardiac intracellular Ca^{2+} dynamics already at the embryonic stages. In the adult heart, PLN-R14del-CMs show alterations in APD, clear variations in cardiac output, and cardiac remodeling. Istaroxime enhances cardiac output.

First author and year of publication	Species	Type of study	Main findings
Tabata (2021)[84]	Human	Clinical examination	Authors discovered 5 PLN-R14del patients in Japan. All patients were diagnosed with DCM, developed end-stage heart failure, and experienced VT.
Badone (2021)[85]	hiPSC-CMs	*in vitro*, functional readout, pathological examination	PLN-R14del-CMs showed altered calcium handling. PST3093 was not effective in the mutant-CMs but affected Ca^{2+} dynamics parameters in the isogenic controls.
De Boer (2021)[86]	n/a	Review	Described the PLN-R14del as an example of a monogenic driver of DCM with specific pathomechanisms.
Driessen (2021)[87]	Human	Clinical examination	Buccal mucosa cells labeled with anti-plakoglobin antibodies revealed that the scores of PLN p.Arg14del patients were comparable to controls ($p > 0.209$), suggesting differences in underlying etiology.
Van der Voorn (2022)[88]	Human	Clinical examination, immuno-assay	Collagen turnover ratio was significantly higher in patients with T wave inversion or premature ventricular contractions during an exercise tolerance test.
Mittal (2022)[89]	hiPSC	*in vitro*, model characterisation	Study generated hiPSC lines from five PLN-R14del carriers and three non-carrier family members. All eight lines show the correct characterisation of pluripotency.
Dave (2022)[90]	Humanized Mouse	Pathological examination, *in vivo* gene editing using CRISPR/Cas9	Humanized PLN-R14del mice are more susceptible to developing VT; disruption of an hPLN-R14del allele by AAV9-CRISPR/Cas9 improves cardiac function and reduces VT susceptibility.
Monda (2022)[91]	n/a	Review	Reviewed studies till 2021. Focuses mainly on PLNR14del's ACM pathophysiology, clinical manifestation, risk stratification for sudden cardiac death, and management.
Eijgenraam (2022)[92]	Mouse	Clinical examination, Pathological examination, functional readout, *in vivo*, *ex vivo*	Progression of PLN-R14Δ/Δ mice were investigated. Administration of a PLN-targeting antisense oligonucleotide halted further cardiac dysfunction, resulting in an increased life span and almost eliminated PLN aggregates.
Deiman (2022)[93]	n/a	Review	In this review, an overview of how precision medicine can be approached as a treatment strategy for PLNR14del is discussed.
Vera (2022)[94]	hiPSC	*in vitro,* model characterisation	Study generated hiPSC lines from two PLN-R14del carriers. All lines show the correct characterisation of pluripotency.
Pei & Maas (Preprint, 2022)[95]	Human	Genetic analysis, Pathological examination, Genetic analysis, *ex vivo*	Authors report differentially acetylated TF and expressed genes in FAO metabolisms and their downstream target in PLN-R14del hearts and hiPSC-CMs of PLN-R14del patients.
Vafiadaki (2022)[96]	Humanized Mouse, HEK293, H9c2 cells	Protein interactions, *ex vivo*, *in vitro*, *in silico*	Pulldown assays reveal that PLN-R14del exhibits increased binding to SERCA2a and HAX-1, SERCA2a activity is inhibited, causing a cascade of molecular events contributing to impaired Ca^{2+}-homeostasis and arrhythmogenesis.
Rogalska (2023)[97]	Mouse, hiPSC-CMs	RNA-Sequencing splicing analysis	>200 significant alternative splicing events and profiles were observed in the LV and RV. The most affected biological process was "cardiac cell action potential" and 2 genes (TRPM4/CAMK2D) which encode proteins regulating calcium homeostasis.

First author and year of publication	Species	Type of study	Main findings
Aboumsallem (2023)[98]	Mouse	multi-omics characterization	Cell-death and tissue-repair pathways were enriched and energy derivation processes were downregulated in hearts of 7 weeks old homozygous PLN-R14del mouse model.
Kumar (2023)[99]	Humanized Mouse	Pathological examination, functional readout, *in vivo*, *ex vivo*, rescue with drug	Changes in Ca^{2+} handling and myofilament proteins resulted in decreased contractility. The depressive contractile effects were prevented by omecamtiv mecarbil, while MYK-461 had no effects.
Van der Meer (2023)[10]	n/a	newspaper article	Authors estimate that approximately 25% of all transplanted patients carry the PLN-R14del mutation. Authors summarize the history, clinical onset, pathophysiology potential therapies, and patient participation.
Vafiadaki (2023)[100]	n/a	Review	Reviewed studies till 2022 provide an overview on PLN-R14del disease pathophysiology and therapeutic approaches.
Zanotti 2023[8]	Human	Clinical examination, Pathological examination, protein analysis, *ex vivo*	Authors detected alteration in histology and the formation of perinuclear aggresomes in skeletal muscle tissue from an Italian patient carrying PLN-R14del.
Cleary (Preprint, 2023)[101]	HEK293	Protein interactions, *in vitro*, *in silico*	PLN-R14del proteins showed significantly increased pentamer to monomer ratios and an increased affinity for homo-oligomerization and decreased binding affinity for SERCA compared to WT. Authors suggest that the R14del mutation stabilizes PLN in its pentameric form, decreasing its ability to regulate SERCA.
De Brouwer (2023)[102]	Human	Clinical trial: The PHOspholamban Related Cardiomyopathy Intervention Study (iPHORECAST)	multicentre randomized trial 'intervention in PHOspholamban RElated CArdiomyopathy STudy' (i-PHORECAST) showed no significant improvement after eplerenone treatment in asymptomatic PLN p.Arg14del carriers.
Maniezzi (Preprint, 2023)[103]	Mouse	*ex vivo*, Functional readouts, Genetic/ Protein analysis	PLN-R14del mouse cardiomyocytes shows a reduced ability to inhibit SERCA2a, arguing super-inhibition. Metabolism was found decreased and ER stress increased. The drug PST3093 showed no effect in PLN-R14del cardiomyocytes.'
Van Lint[22]	Human	Clinical Examination	The authors found no association between the amount of exercise and the susceptibility to develop ACM, DCM, VA, or HF in PLN p.(Arg14del) carriers.
Doevendans PA (2023) [104]	n/a	Pro-Con Statement	The author speculates whether all carriers should be offered preventive treatment. Con: These therapeutic steps are experimental and not ready to be offered to patients.
de Boer (2023)[105]	n/a	Pro-Con Statement	The author speculates whether all carriers should be offered preventive treatment. Pro: PLN-R14del carriers have a 50% lifetime risk of developing severe disease, therefore we should not hesitate to offer pre-emptive medication.
Taha (2023)[106]	Human	Clinical Examination	Deep neural network was able to discriminate PLN variant carriers (n = 278) from control subjects (n = 621) in echocardiographic deformation curves.

First author and year of publication	Species	Type of study	Main findings
Balducci (2023)[107]	hiPSC	*in vitro*, model characterisation	Study generated hiPSC lines from five PLN-R14del carriers who were asymptomatic at the time of blood collection and one non-carrier family member. All six lines show the correct characterisation of pluripotency.
Stege (2023)[108]	Mouse	Clinical examination, Pathological examination, functional readout, *ex vivo*	Dwarf open reading frame (DWORF) overexpression delayed cardiac fibrosis, heart failure and increased life span >2-fold by reducing abnormal ER clusters in homozygous R14del mice.
Van der Voorn (2023)[109]	Human	Genotyping array cohort study for HRC polymorphism frequencies	The p.(Ser96Ala) polymorphism was not associated with life-threatening arrhythmias or heart failure-related events of 848 PLN-R14del carriers.

Abbreviations: ACM = Arrhythmogenic Cardiomyopathy; ASO= antisense oligonucleotides; APD = Action Potential Duration; ASO=AntiSense Oligonucleotides; Ca^{2+} = Calcium; CaMKII = Calmodulin dependent kinase II; CM = Cardiomyocyte; CMR = Cardiac Magnetic Resonance; DCM = Dilated Cardiomyopathy; DNN= Deep Neural Network; ECG = Electrocardiogram; EHT = Engineered heart tissue; ER = Endoplasmic Reticulum; FAO = fatty acid oxidation; HCM = Hypertropic Cardiomyopathy; HF = Heart Failure; HRC = histidine-rich Ca^{2+} binding; ICD = Implantable Cardioverter-Defibrillator; iPSC = induced Pluripotent Stem Cell; LV = left ventricle; LVEF = Left Ventricular Ejection Fraction; LPW = left posterolateral wall; LVMD = Left Ventricular Mechanical Dispersion; NKA = Na/K-ATPase; PC = peripartum cardiomyopathy; PLN = Phospholamban; PLN-R14del/p.Arg14del = Deletion of arginine 14 in PLN gene; Preprint = manuscripts published on BioRxiv or ResearchSquare. PSS = Post-Systolic Shortening; RV =Right Ventricle; SCD = Sudden Cardiac Death; SERCA2a = Sarco/endoplasmic reticulum Ca^{2+}-ATPase 2a; TALENs= Transcription Activator Like Effector Nucleases; TF= Transcription Factor; TFC = Task Force Criteria; UPR = Unfolded Protein Response; VA = Ventricular Arrhythmia; VT = Ventricular tachycardia.

Cellular and molecular alterations in PLN-R14del Cardiomyopathy

The major features of PLN-R14del disease that could be linked to the pathogenic mutation include cellular and molecular dysfunctions such as protein aggregation/toxicity, arrhythmogenesis, metabolic dysfunction, reduced cardiac function, fibrosis, resulting in a structural cardiomyopathy phenotype. However, the contributing mechanisms underlying these PLN-R14del pathophysiological features remain unclear. Here, we review the current knowledge on how PLN-R14del mutation causes the panoply of DCM and ACM manifestations and the potential molecular mechanisms contributing to the disease pathophysiology.

Calcium cycling and contractile force.

The PLN protein is a crucial regulator of cardiac contractility by modulating calcium (Ca^{2+}) transport via SERCA2a and its functioning has been extensively reviewed.[110] In brief, when dephosphorylated, PLN binds to SERCA2a through intramembrane protein-protein interactions to lower its affinity for Ca^{2+}, thereby decreasing the Ca^{2+} uptake into the sarcoplasmic reticulum (SR), which results in the contraction of the cardiomyocyte.[111,112] Phosphorylation of PLN reverses this inhibition, stimulating calcium transport into the SR and increasing the rate of relaxation. PLN phosphorylation is regulated by protein kinase A (PKA)

at serine 16 and/or Ca^{2+}/calmodulin-dependent protein kinase II (CaMKII) at the threonine 17 residue. As more Ca^{2+} is accumulated in the SR, a greater Ca^{2+} store is available for release in a subsequent beat, leading to enhanced contractile force.[113]

Production of pluripotent stem cells (hiPSC) from human adult somatic tissues provides the opportunity to generate large numbers of PLN-R14del patient-specific stem cells.[89,94,107] The first direct evidence of PLN-R14del mutation affecting calcium cycling has been shown in these (hiPSC)-derived cardiomyocytes (iPSC-CMs) from a DCM patient carrying the mutation.[46] This study revealed progressive dysregulation of Ca^{2+} cycling in PLN-R14del hiPSC-CMs, characterized by oscillations and extra peaks, a hallmark of an arrhythmic profile[114,115], which is consistent with the increased arrhythmogenic vulnerability seen in patients with this mutation. Similarly, irregular Ca^{2+} transients were observed in a PLN-R14del knock-in hiPSC line generated by inserting the mutation in a control iPSC line via CRISPR/Cas9.[61] Subsequently, a study from Cuello et al. showed prolonged late Ca^{2+} decay time and a Ca^{2+} concentration-dependent increase in irregular beating patterns in 2D PLN-R14del-CMs, but no observations of abnormal Ca^{2+} waveforms were reported. A deeper calcium transient analysis was performed by Badone et al., in the same PLN-R14del hiPSC line used by Cuello et al. where heterogeneous calcium transient profiles in the cell population of both wild-type and mutant lines were observed.[85] However, the majority of mutant cells showed a typical profile characterized by fast rise and decay time as compared to wild-type, indicating increased SERACA2a activity, possibly due to a loss of PLN inhibitory function as a consequence of the mutation. These data are in contrast with the current described theory of a "super-inhibitory" effect of PLN-R14del and indicate that PLN-R14del mutation might have other, yet unknown, consequences. Interestingly, all studies using engineered heart tissues (EHTs) reported a reduced contractile force in EHTs generated from multiple PLN-R14del patient lines or healthy donor introduced R14del.[51,71,72] EHTs contain more relevant physiological structures compared to 2D culturing techniques and can promote cell phenotype, metabolic activity, maturation, and functionality, leading to more reliable and more predictive models. The variation of PLN-R14del calcium handling outcomes in 2D hiPSC-CMs might be explained by the inefficient model format which it would be interesting to study the calcium handling in 3D hiPSC-CMs models harboring the PLN-R14del disease.

The first mouse models, overexpressing PLN-R14Del, revealed histopathologic abnormalities, super-inhibition of the Ca^{2+} affinity for SERCA2a, and premature death.[1,35] Calcium kinetic and contractile parameters have been further investigated in isolated cardiomyocytes from a novel knock-in humanized PLN-R14del mouse model.[76] The study reported depressed calcium cycling and contractile parameters, specifically in right ventricular (RV) myocytes from young mutant mice (12-13 weeks). This suggests that the arrhythmogenic phenotype associated with the PLN-R14del mutation may originate in the RV compartment during early stages. In the same mouse model, at 12 months of age, contractile parameters and calcium transients

were considerably reduced in the RV of PLN-R14del cardiomyocytes.[99] Moreover, myofilament calcium sensitivity increased in both ventricles of these mutant mice. These findings indicate that myofilament calcium function in disturbed in both ventricles, but abnormal myocyte calcium cycling and contractility are primarily limited to the RV over the long term.

In another recent study, RNA-Sequencing splicing analysis revealed more than 200 different alternative splicing events and profiles in the LV and RV of PLN-R14del versus healthy mouse hearts.[97] Interestingly, in the RV, the most affected biological process was associated with "cardiac cell action potential". Furthermore, the splicing of two key genes, *TRPM4* and *CAMK2D*, which encode proteins that regulate calcium homeostasis in the heart, was altered in PLN-R14del mouse hearts and hiPSC-CMs. This suggests that abnormal splicing may influence calcium homeostasis in the heart, potentially contributing to the increased risk of arrhythmogenesis in PLN-R14del arrhythmogenic cardiomyopathy.

These findings collectively present, for the first time, distinct differences in calcium cycling and contractility within specific heart compartments affected by PLN-R14del disease. The reason why the PLN-R14del mutation affects the right ventricle, specifically in this mouse model, is not fully understood. However, it is known that there are intrinsic differences in the physiology and metabolism between the left and right ventricles. Additionally, compensatory mechanisms in the LV may mask any effects of the PLN-R14del mutation in this compartment. Further studies are needed to fully elucidate the mechanisms underlying the compartment-specific effects of PLN-R14del mutation in the heart.

Ventricular tachycardia

One of the most concerning clinical features of PLN-R14del mutation is the risk of malignant ventricular tachycardia (VT), which can be life-threatening. This risk appears to be age-dependent, with the incidence of VT increasing over time.[11,74] Even if an individual does not exhibit any symptoms, they may still be at risk for developing complications associated with the mutation. Therefore, early identification of high-risk individuals who carry the PLN-R14del mutation is crucial. This allows for close monitoring and timely intervention, which can help prevent life-threatening ventricular arrhythmias and/or slow down the progression of heart failure.

In a recent study using artificial intelligence, echocardiographic deformation imaging was employed to predict the risk of VT in pre-symptomatic mutation carriers.[106] This technique allows for the assessment of both regional and global myocardial deformation patterns, offering valuable insights into the heart's mechanical function. The study identified significant alterations in mechanical function, particularly in the apical region, among pre-symptomatic PLN-R14del mutation carriers, indicating an increased risk of VT.[116] These findings suggest that deformation imaging could be a valuable tool for identifying individuals at a heightened risk

of developing VT. They may also pave the way for future research to explore the potential therapeutic strategies for managing apical mechanical alterations in PLN-R14del carriers to prevent the development of VT. However, it is essential to determine the optimal frequency and timing of follow-up echocardiograms to monitor changes in mechanical behavior and adjust preventive strategies will be crucial for effective clinical management.

Recent studies in mouse models of PLN-R14del disease revealed the ability to detect abnormal cardiac function and increased arrhythmogenic vulnerability in pre-symptomatic hPLN-R14del mice, which reflect similarities to pre-symptomatic PLN-R14del patients.[62,73,76,90] The study by Dave et al. is particularly exciting, as it demonstrates the potential therapeutic benefits of allele-specific disruption of the PLN-R14del mutation using in vivo AAV9/CRISPR-Cas9. The ability to improve cardiac function and reduce VT susceptibility to wild-type levels is a significant achievement and offers new hope for patients in the early stages of PLN-R14del disease. These studies suggest that the combination of animal models of PLN-R14del disease and emerging therapeutic strategies, such as allele-specific disruption of the PLN-R14del mutation using genome editing approaches, has the potential to revolutionize the treatment of this disease and possibly other inherited cardiomyopathies.

Super-inhibition of SERCA2a

Mechanistically, the arginine residues (Arg9, Arg13, and Arg14) of PLN interact transiently with SERCA-Glu606, while for the phosphorylated PLN, the phosphate group at Ser16 forms strong interactions with SERCA-Arg604 and SERCA-Lys605.[117] This dynamic interplay is essential for the regulation of SERCA2a activity. However, the R14del mutation disrupts the R-R-X-S motif crucial for the phosphorylation of Ser16 by PKA, thereby limiting the extent to which SERCA2a inhibition can be reversed.[118] In addition, R14del appears to disrupt the mutant protein's coil domain, an essential structure that provides structural flexibility to PLN, enabling conformational changes associated with PLN phosphorylation and its association with SERCA2a.[36,96,119] Consequently, in the context of PLN-R14del-related disease, this mutation is believed to exert a constitutive inhibitory effect on SERCA2a, even when phosphorylated by PKA and activated CaMKII. This persistent inhibition leads to increased cytosolic Ca^{2+}, which can have several consequences, including the phosphorylation of the S2814 site of the ryanodine receptor 2 (RyR2), resulting in the release of more calcium from the sarcoplasmic reticulum into the cytosol, which can contribute to disturbances in cardiac function and potentially lead to arrhythmias or contractile dysfunction.[120] The concept of "super-inhibition" of SERCA2a by PLN-R14del has been substantiated by previous research findings. Haghighi et al. demonstrated the super-inhibition of SERCA activity in both co-transfected HEK-293 cells and transgenic mice overexpressing the mutation. Importantly, they observed that the dominant effect of the mutation could not be completely removed by phosphorylation mediated by PKA.[121] Furthermore, Vafiadaki et al. confirmed this increased inhibitory effect

by reporting increased binding of PLN-R14del to SERCA2a and HAX-1, a protein, which binds directly to PLN, modulating its activity either by enhancing its inhibitory action on SERCA2a. This strengthened interaction intensifies the inhibitory effect of PLN-R14del on SERCA2a.[122] As a result, calcium reuptake is further impaired, leading to increased release of Ca^{2+} from the SR into the cytosol. These disruptions in calcium handling can trigger various cardiac events, including after-contractions, transient inward currents, and arrhythmogenic delayed afterdepolarizations (DADs).[123–125] However, it's important to note that some studies have reported contradictory findings regarding the influence of PLN-R14del on SERCA2a. For instance, Badone et al. observed increased SERCA2a function in PLN-R14del-hiPSC-CMs due to a loss of PLN's inhibitory function.[126] Furthermore, a recent preprint study from the same research group demonstrated hyperdynamic Ca^{2+} handling and reduced SERCA2a inhibition by PLN-R14del in ventricular cardiomyocytes from 8-12 weeks-old transgenic mice.[103] In isolated CMs from homozygous R14del mice, an enhanced calcium reuptake was observed[108], which is in line with the publications above on altered calcium reuptake by mutant PLN-R14del. These findings challenge the notion of super-inhibition of SERCA2a, which could have explained the previously observed ACM phenotype. Nevertheless, the constitutively unrestrained function of SERCA2a may, in the long term, negatively impact myocyte function as well. In summary, the PLN-R14del mutation's effects on SERCA2a function remain a subject of debate and ongoing research. These findings imply that factors beyond the super-inhibition of SERCA2a may contribute to the development of PLN-R14del-induced DCM/ACM. Further investigation is needed to fully elucidate the complex mechanisms underlying these conditions in individuals with this genetic mutation.

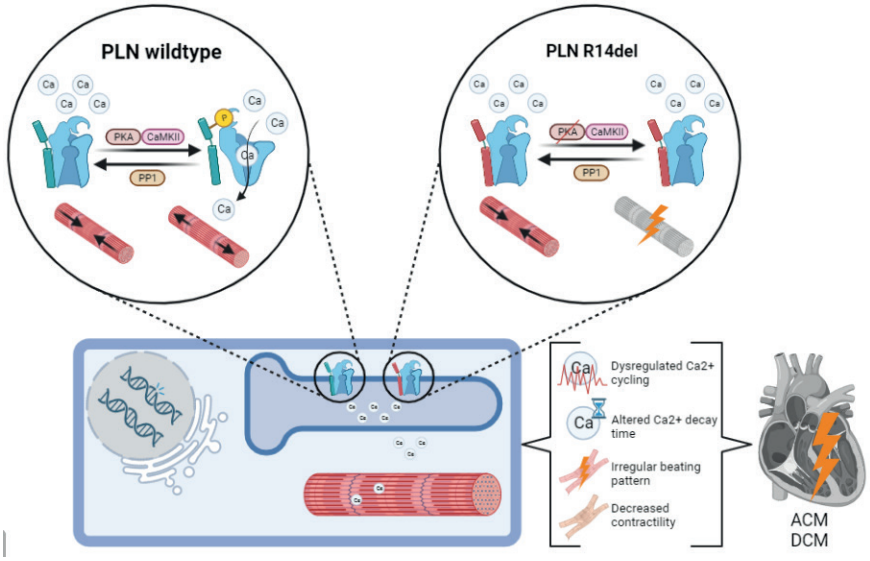

Figure 2: Regulation of calcium uptake and contractility in PLN wildtype versus PLN-R14del. In PLN wildtype, PLN phosphorylation is regulated by protein kinase A (PKA) at serine 16 and/or Ca^{2+}/calmodulin-dependent protein kinase II (CaMKII) at the threonine 17 residue. The type 1 protein phosphatase (PP1) dephosphorylation of PLN, thereby inhibiting SERCA2a's affinity for Ca^{2+}. The cytosolic Ca^{2+} binds to troponin, causing conformational changes in the sarcomere, which leads to the interaction of thick and thin filaments of the sarcomere and muscle contraction. In PLN-R14del, the R-R-X-S motif crucial for the phosphorylation of Ser16 by PKA is disrupted, thereby limiting the extent to which SERCA2a inhibition can be reversed. Hypothetically, the enhanced cytosolic Ca^{2+} levels result in defective muscle contraction and/or relaxation, which is the cause of various muscle diseases.

PLN Monomer vs Pentamers

PLN exists in a dynamic equilibrium between its monomeric and pentameric form, which is influenced by its phosphorylation state. While PLN monomers seem to be important for the reversible inhibition of SERCA, the function of PLN pentamer has not been fully elucidated and has been proposed to function as 1) storage for active monomers[127], 2) an ion channel[128], and/or 3) a SERCA binding partner required for the regulation of cardiac contractility[129]. Indeed, in both synthetic and cell membranes, PLN was found to form pentamers to regulate the concentration of active monomers available to bind SERCA and keep its function within a physiological window.[130] Other studies suggested that the pentamer structure displays a channel-forming architecture that could allow the passage of small ions such as Ca^{2+}[131] or Cl^{-} [132]. However, both electrochemical measurements and free energy calculations provide strong evidence that PLN, whether in bellflower or pinwheel configurations, does not conduct Ca^{2+} or Cl^{-} ions.[133] A recent study showed that PLN pentamers are not entirely passive but interact with SERCA in a 1:1 complex, influencing cardiomyocyte contractility and PLN phosphorylation dynamics.[134] This interaction with SERCA2a appears to act as buffers, fine-tuning SERCA turnover and regulation via monomeric PLN.[135,136] As a consequence,

depolymerization of the PLN pentamer would be necessary to activate the inhibitory function of the PLN monomers.[137,138] Interestingly, PLN pentamers are found next to SERCA2a, and PKA preferentially phosphorylates PLN pentamers. This suggests a model in which PLN pentamers not only delay the phosphorylation of PLN monomeric but also indirectly regulate SERCA by prolonging SERCA-PLN interaction, thus revealing an additional role for PLN pentamers in the regulatory process.[139] Moreover, the deletion of amino acid 14 in PLN has been shown to partially destabilize the PLN pentamer, potentially increasing the concentration of PLN monomer.[140] However, a recent preprint study described the hyper-stabilization of PLN-R14del pentamers which leads to a decrease in the population of PLN monomers available to inhibit SERCA.[101] This enhanced pentamer stability and impaired PLN binding dynamics could potentially lead to a decreased binding of R14del-PLN to SERCA, which contradicts the previous observation.

Moreover, a mathematical model of the PLN-R14del regulatory network suggests that this mutation could impair molecular noise filtering in the β-adrenergic signaling network. In this study, simulations show that phosphorylation delay and bistability, due to cooperative dephosphorylation of pentamers, act as complementary filters that reduce the effect of random fluctuations in PKA activity, thereby ensuring consistent monomer phosphorylation and SERCA activity despite noisy upstream signals. This suggests that molecular noise filtering in the β-adrenergic signaling network may be important in preventing cardiac arrhythmias.[141] Further studies will be needed to confirm these findings and determine the precise mechanisms by which molecular noise filtering in the β-adrenergic signaling network is disrupted by the PLN-R14del mutation. Nevertheless, the study highlights the potential importance of understanding the regulatory networks underlying cardiac function and the potential impact of genetic mutations on these networks.

PLN binding partners

In addition to its canonical interaction with SERCA2a, PLN forms a multimeric complex interacting, directly and indirectly, with several partners including Protein Phosphatase I (PP1), inhibitor-1 (I-1), the anti-apoptotic HS-1 associated protein X-1 (HAX-1), and the small Heat shock protein 20 (Hsp20)[142,143], which regulate SR calcium-cycling and contractility. Thus, the PLN-R14del mutation could affect PLN binding partners and lead to aberrant calcium handling, arrhythmia, and cellular damage.[144] Indeed, a recent study revealed alterations in PLN-R14del interactions to multiple known binding partners (SERCA2a, HAX-1, PP1 Regulatory Subunit 3A and histidine-rich calcium-binding protein, HRC) causing inhibition of SERCA2a activity, and leading to impaired SR Ca^{2+} cycling and depressed cardiac function.[145] Interestingly, a new PLN-binding protein has been identified in mouse ventricular tissue.[146] This study demonstrated that phosphorylation at either Ser^{16} or Thr^{17} converted PLN into a target for the phospho-adaptor protein 14-3-3 with different affinities. 14-3-3 protein protected PLN phosphorylation sites from dephosphorylation and the exogenous addition

of 14-3-3 to β-adrenergic-stimulated cardiomyocytes led to prolonged SERCA activation.[147] Since the phosphorylation of Ser16 is disrupted in the PLN-R14del, phosphorylation of Thr17 by CaMKII might become highly important for 14-3-3 recruitment to the PLN-R14del protein. Understanding the inhibitory mechanism of PLN-R14del and its reversal upon phosphorylation or Ca^{2+} increase is essential for developing novel interventional strategies.

Protein Toxicity and Unfolded Protein Response

Due to the limited regenerative capacity of cardiomyocytes, the survival of the existing cardiomyocytes by protein quality control is critical for optimal cardiomyocyte function.[148,149] Pathological circumstances such as oxidative stress[150], disturbance of calcium homeostasis[151], and protein misfolding[152] cause ER stress.[153,154] Consequent disturbed protein homeostasis results in increased misfolded proteins, followed by the formation of protein aggregates and aggresomes.[155] PLN-R14del cardiomyopathy has been associated with large cytoplasmic perinuclear PLN-containing aggregates in both human[156–158] and mouse heart tissues.[159,160] Te Rijdt et al. have demonstrated that PLN aggregates have a typical appearance of aggresomes, where PLN aggregates colocalize with p62 and microtubule-associated protein light chain 3 (LC3)[161], indicating evidence for protein aggregates degradation.[162] A recent study identified a homogeneous distribution of p62-positive aggregates in the myocardium of PLN-R14del patients, independent of fibrosis distribution.[158] These data suggest that the autophagy system is not able to remove all the mutant PLN protein, resulting in the accumulation of p62-positive proteotoxic perinuclear aggregates in the cardiomyocytes[163], which can interfere with cellular function, and ultimately induce cell death.[164] Interestingly, immunohistochemical analysis in specimens harvested during left ventricular assist device (LVAD) implantation is a highly sensitive and specific method for demonstrating PLN protein aggregates and for diagnosing PLN-R14del cardiomyopathy.[165] Moreover, a recent study by Eijgenraam et al,[166] showed that alterations in proteostasis and PLN protein aggregation were already present before functional impairments were observed in homozygous PLN-R14 mice. Misfolded/aggregated proteins can accumulate within the endoplasmic reticulum (ER), causing activation of the unfolded protein response (UPR). Cuello et al,[167] have recently shown impairment of the ER compartment and activation of UPR in a patient-specific PLN-R14del iPSC line compared to the isogenic control. Similarly, Feyen et al,[168] observed an increased ER stress and UPR in PLN-R14del hiPSC-CMs. More importantly, they found that activation of the UPR preserves cell function and, therefore, plays a protective role in alleviating ER stress and potentially blunts disease pathogenesis. Pharmacological and molecular modulation of the UPR suggests a compensatory role in PLN R14del cardiomyopathy. These findings have high value as they could be harnessed therapeutically to delay the onset or slow down the progression of the disease.

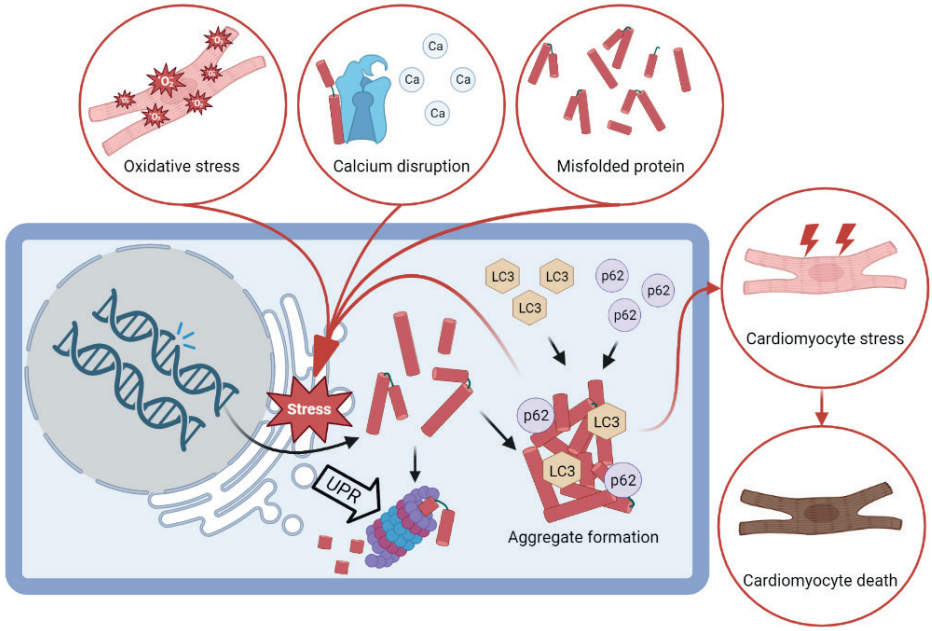

Figure 3: Protein Toxicity and Unfolded Protein Response in PLN-R14del. In PLN-R14del, the misfolded PLN-R14del protein, calcium disruption, and oxidative stress can lead to increased ER stress. Increased ER stress can lead to higher protein folding toxicity and the activation of the UPR and autophagy proteins LC3 and P62. If the autophagy system is not able to remove all the mutant PLN protein, this results in the accumulation of p62-positive proteotoxic perinuclear aggregates in the cardiomyocytes, which cause cardiomyocyte stress and ultimately induce cell death.

Mitochondrial disruption and reduced fatty acid oxidation.

Given the unrelenting contraction, cardiomyocytes rely on mitochondria for continuous ATP production. Fuel utilization and energy production are crucial and contribute to the balance between glucose and fatty acid oxidation (FAO). Impaired mitochondrial function in the failing heart can occur due to several reasons, including increased reactive oxygen species (ROS), dysregulation of Ca^{2+} homeostasis, impairment of mitochondrial dynamics, and alterations in transcriptional regulation of mitochondrial proteins, which lead to a reduced mitochondrial oxidative metabolism and ATP production.[169] A recent non-peer-reviewed study analyzed the transcriptional regulation profiling in end-stage hearts from PLN-R14del patients and healthy donors, using multi-omics approaches. They identified differentially acetylated promoters and enhancers (H3K27ac ChIPseq), annotated enriched transcription factor (TF) binding motifs located in those regions, and differentially expressed genes (RNA-seq).[170] By integrating the information at the DNA and RNA levels, they detected the downregulation of key TF regulators in FAO metabolism and their downstream target in PLN-R14del hearts as compared to controls. In addition, histological analysis, immunofluorescence staining, and transmission

electron microscopy showed accumulation of lipid droplets and a disrupted morphology of mitochondria in mutant samples compared to controls, indicating insufficient FAO, which might contribute to lipotoxicity, and eventually cardiomyocyte death.[171] Successively, a study performed in both PLN-R14del hiPSC-CMs and derived engineered heart tissues (EHTs) showed a lower abundance of mitochondria, perinuclear lipid accumulation, altered post-translational modifications of key metabolic enzymes such as PDH (Pyruvate dehydrogenase) and AMPK (AMP-activated protein kinase), and oxidative stress, as a consequence of ER/mitochondria contact site disruption in mutant samples compared to isogenic controls.[172,173] Taken together, these data indicate PLN-R14del-mediated dysfunction of the ER/mitochondria compartment as a novel molecular disease mechanism and a target for future treatments.

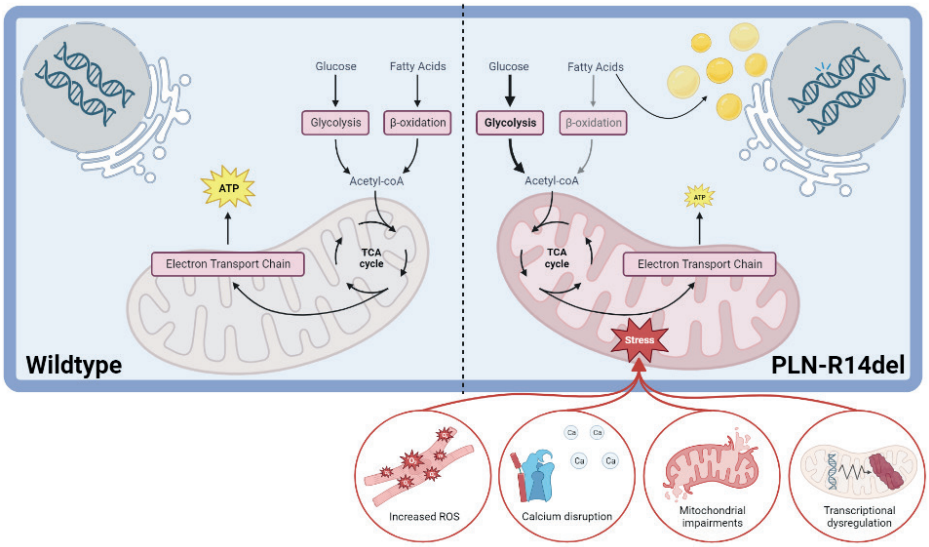

Figure 4: Metabolic function in PLN wildtype versus PLN-R14del. In healthy cells, cardiomyocytes balance between glucose and fatty acid β-oxidation for energy production. In PLN-R14del, impaired mitochondrial function and stress can occur due to increased reactive oxygen species (ROS), Calcium disruption, mitochondrial impairments, and alterations in the transcriptional regulation of mitochondrial proteins. During mitochondrial stress, energy substrate utilization switches to glycolysis, thereby impairing the FAO and resulting in the accumulation of perinuclear lipids.

Fibrosis; localization and the effect of fatty infiltration

Cardiac fibrosis is a frequent finding during the histological examination of heart tissues from PLN-R14del patients with end-stage disease.[174,175] Significant replacement fibrosis and myofibrillar disarrangement have been first identified in the PLN-R14del patients belonging to the large Greek family with clinical manifestation of DCM and ACM.[176] Similar findings have been shown in a transgenic and homozygous PLN-R14del mouse model.[160,176] Generally, the

deposition of excess fibrous connective tissue is the result of a disturbed balance between the synthesis and degradation of extracellular matrix proteins due to myofibroblast activation.[177] Interestingly, PLN-R14del hearts were compared with hearts with desmosomal, lamin A/C, sarcomeric, and desmin mutations and presented the highest amount of myocardial fibrosis which is found in a distinct pattern in the posterolateral left ventricular wall.[178] Further studies in Dutch patient populations have demonstrated a more detailed analysis using digital quantification and identified a distinct pattern of interstitial fibrosis, most prominently located in the subepicardial layer of the posterolateral wall of the left ventricle in PLN-R14del patients compared to controls and other hereditary cardiomyopathies.[179–182] Fibrosis is associated with low R amplitudes and inverted T waves found on ECGs of PLN-R14del patients.[183,184] Using a novel method of high-resolution systematic digital histological quantification of fibrosis and fatty infiltration in transversal cardiac slides, Gho et al. determined the exact patterns of fatty changes in PLN-R14del hearts.[185] They found that fatty changes in the myocardial tissue were observed in the entire right ventricular (RV) wall and partially in the epicardial layer of the left ventricle (LV) posterolateral wall. Overall, the amount of adipose tissue infiltration was more pronounced in the RV than in the LV. The observations share this conclusion in several other studies, where fibrofatty replacement was mainly observed in the epicardial layer of the RV wall and limited fibrofatty alterations were seen in the LV wall.[186–189] Fibrofatty replacement could be induced by increased sensitivity to wall stress and metabolic demand in the RV.[190] Additionally, a recent preprint has revealed increased lipid droplet accumulation in both the hearts and stem cell-derived cardiomyocytes of PLN-R14del patients. Here, the authors identified key transcription factors involved in the affected (lipid) metabolism, even before the onset of RV wall stress.[95] Another recent study has linked lipid droplet accumulation in PLN-R14del to the impairment of the ER/mitochondria compartment.[72] Nonetheless, the exact pathophysiological mechanism and metabolic changes behind the source of adipose structures in PLN-R14del cardiomyopathy remain to be investigated. Still, the exact pathophysiological mechanism responsible for the segregated and distinct pattern of fibrosis in PLN-R14del hearts remains to be elucidated.

Onset of pathological myofibroblast activation and fibrosis

Despite fibrosis being a crucial process in the repair of damaged tissue, progressive fibrosis can lead to myocardial stiffness, dysfunction, and arrhythmias.[191,192] Sepehrkhouy et al.[178] speculated that the pattern of predominantly posterolateral epicardial fibrosis is induced by increased sensitivity to wall stress on the heart. This wall stress could be induced when cardiomyocytes are more vulnerable to mechanical forces. For example, the aggregation of remnant PLN protein found in cardiomyocytes[81] or disturbed calcium handling can result in the maladaptive remodeling of the macromolecular protein complexes, leading to enhanced mechanical force within the cardiomyocyte.[52] Interestingly, te Rijdt et al. have observed a specific predominance of fibrosis in the inferolateral wall of the left ventricle in PLN-R14del

carriers with preserved LV systolic function, suggesting that fibrosis is an early feature of PLN-R14del cardiomyopathy.[193] They hypothesized that the inferolateral wall could be more vulnerable due to regional molecular changes caused by the mutation or that the regional susceptibility could result from exposure to higher mechanical stress.[194] This finding could suggest that cardiac fibrosis is an early feature of PLN-R14del cardiomyopathy before LV function decreases. In fact, recent data show that total collagen turnover correlates weakly to moderately with clinical parameters in PLN-R14del patients.[88] The occurrence of fibrosis is then speculated to be a primary process triggered by the PLN-R14del mutation, which eventually leads to ventricular arrhythmias and heart failure. Additionally, an independent association between the presence of fibrosis and the occurrence of ventricular arrhythmias has been demonstrated.[195] Hence, the heterogeneity of fibrosis depends on both the spatial size and the degree of heterogeneity: a larger size and larger degree of heterogeneity make the formation of arrhythmias more probable.[196] Recent data show that total collagen turnover correlates weakly to moderately with clinical parameters in PLN-R14del patients.[197] These findings may help to understand the disease onset and to improve the identification and diagnosis of PLN-R14del patients.

Inflammation

Inflammation is a hallmark of heart failure and plays a crucial role in the progression of cardiac dysfunction in both DCM and ACM.[198,199] However, very little is known about the role of inflammation in DCM/ACM associated with PLN-R14del mutation. Recently, an unbiased approach of combined transcriptomics and proteomics revealed a progressive increase of myocardial inflammation in the hearts of homozygous PLN-R14del mice.[200] Interestingly, a strong infiltration of immune cells was observed in the sub-epicardial region of the heart in a knock-in PLN-R14del zebrafish model.[201] Together the results of these studies suggest that inflammation might impact PLN-R14del disease progression and emphasize the clinical relevance of inflammation in the severity of PLN-R14del-induced cardiomyopathy. Further investigation is needed to understand the specific mechanisms by which inflammation contributes to disease progression in PLN-R14del-associated cardiomyopathy. This could involve studying the interactions between immune cells, cytokines, and other signalling molecules in the heart. In addition, it would be important to investigate whether the extent of inflammation correlates with disease severity in PLN-R14del-associated cardiomyopathy patients. This could involve analyzing patient samples and medical records to identify potential biomarkers of inflammation and disease progression. A recent study used a label-free whole myocardium multi-omics analysis in homozygous PLN-R14del (PLN-R14Δ/Δ) mice and identified four biomarkers associated with all-cause mortality; proline and arginine-rich end leucine-rich repeat protein (PRELP), cytoskeleton-associated protein 4 (CKAP4), S100 calcium-binding protein A11 (S100A11) and annexin A1 (ANXA1).[98] These biomarkers play roles in disease progression (cell death and tissue repair pathways) and the regulation of the inflammatory

response. These common pathways and biomarkers could have a clinical potential and prognostic associations merit further investigation to develop optimal management and therapeutic strategies for PLN0R14del patients. Moreover, given the potential role of inflammation in disease progression, it would be important to explore therapeutic interventions that target the immune system in PLN-R14del-associated cardiomyopathy. This could involve testing anti-inflammatory drugs or other immune-modulating therapies in animal models or clinical trials.

Current treatments for PLNR14del patients

The current optimal medical treatment in patients carrying the PLNR14del mutation follows the guidelines for heart failure and arrhythmias for the prevention of sudden cardiac death (SCD).[202,203] The pharmaceutical therapeutic agents that are used include β-blockers and angiotensin-converting enzyme (ACE) inhibitors.[204] Due to a lack of specificity, these medical treatments only slow down the progression of the disease at best and possibly alleviate the symptoms to some degree. In most cases of disease progression, additional interventions have to be implemented,[205,206] such as implantable cardioverter-defibrillators (ICD), a left ventricular assist device (LVAD)[207] or a heart transplant for patients with end-stage PLN-R14del disease. In the Netherlands, about 25% of the heart transplants performed yearly are PLN-R14del related.[208] However, heart transplants are limited by donor shortage, surgical complications, and long-term effects of immunosuppressive therapy.[209] Therefore, a better understanding of the molecular mechanisms could result in a tailored PLN-R14del-specific therapy. Since the discovery of PLN-R14del cardiomyopathy, many studies focusing on this disease have been performed. Here, we summarize the potential pharmacological agents available which could be more promising in treating PLNR14del compared to the current strategies (**Table 2**).

Table 2: Systematic table including all treatment strategies performed and outcomes. Studies are sorted based on the mechanism of action.

Therapy Strategy	Target	Executed study	Positive outcome	Disadvantages	ref
Current treatments					
ICD	Arrhythmias	Executed in 46% of DCM-PLN-R14del patients.	Reduces the risk of deadly arrhythmias.	up to 120 months.[210]	211,212
LVAD	LV	Executed in 30% of PLN patients.	Bridge to transplantation or as an alternative for destination therapy.	Therapy is still associated with substantial morbidity.	213
HTx	Whole heart	Executed in 18% of the DCM-PLN-R14del patients.	Most optimal treatment strategy up till now.	Not many hearts are available.	214
Calcium regulation strategies					
Istraoxime	SERCA2a activator	Tested in PLN-R14del zebrafish embryos and isolated adult CMs.	Ameliorates the in vivo Ca^{2+} dysregulation and improves cardiac relaxation.	Plasma half-life of less than 1 hour, intravenous injections required. Acceleration of Ca^{2+} uptake has been shown to promote arrhythmias.[215]	216
PST3093	"Selective" SERCA2a activator	PLN-R14del mouse and hiPSC-CMs	PST3093 affects Ca^{2+} dynamics parameters in PLN-R14del corrected CMs.	WT only responded and tended to convert the corrected pattern into the R14del phenotype.	103,217
KN93	CaMKII inhibitor	PLN-R14del Mouse quiescent LV and RV myocytes.	KN93 reversed the proarrhythmic phenotype. Compensatory expression of key genes associated with Ca^{2+}-cycling.	Interacts but to inhibit CaMKII specifically, the more affinized compound is necessary.[218]	219
Parvalbumin-encoding virus	Ca^{2+}-binding protein	PLN-R14del hiPSC-CMs and EHTs.	UPR expression was reduced and led to dynamic alterations within the ER-mitochondrial compartment.	No force restoration. A large fraction of the expressed parvalbumin resided in the nucleus.	220
GCaMP6f -encoding virus	Ca^{2+}-buffering protein	PLN-R14del hiPSC-CMs and EHTs.	Improved contractile force and mitochondria number. Reduction of UPR expression, dynamic alterations within the ER-mitochondrial compartment.	No difference in Ca^{2+} transient amplitude was detected.	221
Metoprolol	β-blocker	PLN-R14del Mouse	Metoprolol significantly ($p < 0.05$) decreased heart rate.	No increase in the survival rate.	222
DWORF	SERCA activator	PLN-R14del Mouse	Overexpression delayed cardiac fibrosis, heart failure and increased life span >2-fold.	DWORF did not improve calcium handling, possibly due to enhanced calcium reuptake in R14del mice.	108
Contractility modulation					
Omecamtiv mecarbil	selective cardiac myosin activator	Humanized PLN-R14del mice	Study found that the depressive contractile effects were prevented without affecting Ca^{2+} homeostasis.	Induces continuous activation of resting myosin ATPase and increases myocardial oxygen consumption.	99

Therapy Strategy	Target	Executed study	Positive outcome	Disadvantages	ref
Mavacamten (MYK-461)	selective cardiac myosin inhibitor	Humanized PLN-R14del mice	Can decrease the contractility without affecting Ca^{2+} transients	No improvement in the decreased contractile function was found in this study.	99
Anti-fibrotic strategies					
Eplerenone	Antifibrotic agent	PLN-R14del Mouse	Reduced ventricular dilatation.	No improvement in contractile dysfunction or survival rate.	223
Eplerenone	Antifibrotic agent	Clinical trial iPHORECAST with 42 presymptomatic PLN-R14del carriers.	Study pre-emptive established antifibrotic effects, and reduce disease progression.	No significant improvement in asymptomatic PLN p.Arg14del carriers.	102,224
ER stress modulation					
BiX	Induces BiP expression	PLN-R14del hiPSC-CMs and EHTs.	Enhanced contractility to and nearly complete force restoration.	Biphasic, as a high concentration of BiX, leads to decreased contractility.	225
Metabolism modulation					
Bezafibrate	PPARA agonist	PLN-R14del hiPSC-CMs and cardiac spheroids.	re-activates mitochondrial FAO and improves Ca^{2+} transients.	Hyperhomocysteinemia risk, No major long-term outcome trials with clear results are available.	95
PLN gene/protein regulation					
TALENs	PLN-R14del	PLN-R14del hiPSC-CMs	TALEN-correction ameliorates the PLN-R14del phenotype in hiPSC-CMs and EHTs.	Early stage of development and with ethical concerns, this technique is still far from clinical application.	226,227
rAAV2	PLN-R14del	CRISPR-engineered PLN-R14del hiPSC-CMs	rAAV2-driven expression of PLN rescues arrhythmic Ca^{2+} transients and alleviates decreased Ca^{2+} transport.	The CUPID 2 trial (AAV1/SERCA2a) did not reduce terminal events in the overall study population.	228
AAV6	PLN	Patient-specific PLN-R14del hiPSC-CMs	AAV-PLN overexpression reduced irregular calcium transients and hypertrophic factors.	Safety concerns due to the use of delivery vectors.	229
ASOs (KD)	PLN	Homozygous PLN-R14del mice	KD of the *PLN* gene expression leads to decreased protein aggregation, fibrosis, and improved survival in PLN-R14del mice.	Targeting both mutated and non-mutated PLN mRNA might induce lethal dilated cardiomyopathy.[230]	231
CRISPR/Cas9	PLN-R14del	Humanized PLN-R14del mice	Specific disruption of mutant PLN allele leads to reduced susceptibility to developing ventricular tachycardia.	Safety concerns due to possible off-target effects and the use of delivery vectors.	232

Abbreviations: AMPK = adenosine monophosphate-activated protein kinase; ASOs = antisense oligonucleotides; EF = Ejection fraction; EHT = Engineered heart tissue; FAO = Fatty acid oxidation; hESC-CMs = human embryonic stem cell-derived cardiomyocytes; HF= Heart failure; hiPSC-CMs = Human Induced Pluripotent Stem Cell-Derived Cardiomyocytes; HTx=heart transplantation; ICD= Implantable Cardioverter Defibrillator; KD = Knock-down, LV = Left Ventricle; LVAD= Left Ventricular Assist Device; modRNA = modified RNA; siRNA = small interfering RNA; shRNA = short hairpin RNA; TALENs = transcription activator-like effector nucleases; TF = Transcription Factor.

DISCUSSION

PLN-R14del-associated cardiomyopathy is a complex disease that encompasses a spectrum of phenotypes, including both autosomal-dominant DCM and the association with ventricular arrhythmias. The disease is causing global concern with now 10 countries describing many patients carrying the p.Arg14del variant (**Figure 1**). Notably, understanding the role of the PLN mutation in this disease provides critical insights into the broader context of heart failure pathophysiology, contributing to a comprehensive understanding of heart diseases.[233] Here, we have systematically gathered the studies describing PLN cardiomyopathy and the potential molecular mechanisms underlying the disease pathophysiology (**Table 1**, **Supplementary Table 1**).

Importantly, clinicians have observed variability in disease penetrance, which includes the diversity in disease onset, differing from young symptomatic patients and elderly asymptomatic mutation carriers.[234] With this variability, a mosaic pattern of cardiomyocytes with and without PLN aggregates was observed.[235–237] Multiple mechanisms such as allelic imbalance or environmental factors could play a role[238], where (epi)genomic analysis may unravel key modifiers and risk factors affecting the disease development.[239] A recent study by van der Voorn revealed that the p.(Ser96Ala) Polymorphism in Histidine-Rich Calcium Binding Protei, previously described as a secondary hit in cardiomyopathies, was not associated with life-threatening arrhythmias or heart failure-related events of 848 PLN-R14del carriers.[109] Allelic imbalance is a process where two alleles of a gene are transcribed differentially and thereby expressed at different levels in a cell. Allelic imbalance has been identified in 88% of genes in human tissues[240], which can be either tissue-specific or genome-wide.[240,241]

Additionally, more research is required focusing on the development and progression of PLN-R14del disease before heart failure occurs. For this, a human heart biobank was recently established, in which heart tissues and medical data from deceased donors are stored and can be used for scientific research.[242] The collection of heart tissue from pre-symptomatic individual carriers will allow to study of early-stage disease mechanisms. Moreover, animal models represent potential approaches to studying disease onset and progression. Indeed, the recent development of PLN-R14del mouse models, together with the PLN-R14del zebrafish model, has helped identify early-stage molecular mechanisms of PLN-R14del disease. In addition, a pig model of PLN-R14del disease has been generated[60], which could offer advantages over mouse and zebrafish models, especially in terms of cardiovascular physiology and disease manifestation, as they have a cardiac system that is anatomically and functionally more similar to humans. Pig models will better facilitate the efforts to delineate the molecular and cellular mechanisms underlying the pathogenesis of the PLN-R14del clinical phenotype and evaluate potential therapeutic interventions.

However, animal models could give different outcomes compared to humans, as seen with the Istaroxime study in zebrafish[243] versus the Istaroxime (PST3093) analogue compound in

hiPSC-CMs.[244] Even within animal models, such as the PLN-R14del mouse and humanized mouse model, variations in the phenotypes occur (**Table 1**). Patient-specific iPSC-derived cardiomyocytes generated from both symptomatic and asymptomatic individual carriers could represent valuable human-based models to study PLN-R14del pathophysiology. However, the maturation status of the cells and the expression level of phospholamban should be carefully considered and controlled, as these factors could influence the cellular response to PLN-R14del mutation. Additionally, other factors such as genetic background and environmental factors could influence disease development and progression, so it is important to carefully consider these variables when using these human-based models to study disease mechanisms.

The primary objective in understanding the pathogenesis of PLN-R14del cardiomyopathy is to pave the way for innovative, disease-specific treatments. These goals have been pursued through the significant efforts of organizations such as the PLN Foundation and collaborative research initiatives like the Leducq Transatlantic Network of Excellence consortium, known as CURE-PLaN.[60] In both of these contexts, the final aim is to develop effective therapeutic approaches, which encompass two primary approaches: corrective gene therapy and the identification of pharmacological agents that can deplete or neutralize the pathological PLN protein.

Furthermore, there are ongoing grants and research initiatives aimed at advancing our understanding and developing innovative therapies for PLN-R14del disease. These encompass heart vector-mediated gene therapy[245], prime editing gene therapy[246], as well as the exploration of oligonucleotide chemistries, gene editing, and gene modulation[247]. Currently, whether all PLN-R14del carriers should be offered preventive treatment due to the 50% lifetime risk of developing severe disease and if these therapeutic steps are ready is under debate within the scientific community.[104,105]

Here, we have systematically summarized the therapies that have been explored for their effectiveness in addressing PLN-R14del cardiomyopathy (**Table 2**). The discovery of an existing pharmacological agent would represent the most rapid and straightforward approach to treating patients.

For example, a lower UPR activity or induced stress in life might explain the accelerated manifestation of symptoms observed in some patients and could potentially lead to the more severely affected PLN-R14del patients due to an elevated vulnerability to proteotoxicity. Modulating the UPR activity might subsequently normalize the disease phenotype.[248] Moreover, as described above, the PLN-R14del mutation might not only directly regulate SERCA2a and Ca^{2+} re-entry, but also regulate other binding partners[249], and could cause impairment of inter-organelle communication between ER and mitochondria. Ca^{2+}-binding proteins GCaMP6f and parvalbumin mainly reduced the UPR expression and led to dynamic

alterations within the ER-mitochondrial compartment and only GCaPM6f was associated with significantly improved force development in PLN-R14del EHTs.[72] Recently, a SR localized micropeptide called dwarf open reading frame (DWORF) was discovered to have the opposite function of PLN. DWORF overexpression in homozygous R14del mice did prevent abnormal S/ER cluster formation but did not result in an additional increase in calcium reuptake due to an already enhanced calcium reuptake.[108] Both findings argue that aberrant S/ER formation is the key mechanism, rather than targeting the super-inhibition of SERCA2a, in the development of PLN-R14del cardiomyopathy. Together, altered PLN protein conformation could affect the localization and interaction of proteins crucial for ER/mitochondria integrity. By the reduction of protein toxicity, cardiomyocyte cell loss, fibrosis, and cardiac dysfunction could be prevented.

As the main function of PLN is the regulation of calcium by the modulation of SERCA, multiple therapeutic strategies have been tested to modulate calcium handling. The CaMKII inhibitor KN93 reversed the proarrhythmic phenotype in myocytes of PLN-R14del mice, consequently suggesting its anti-arrhythmic application and especially potentially preventing SCD.[100,108100] On the contrary, Metoprolol (β-blocker) significantly decreased the heart rate and showed no increase in the survival rate of PLN-R14del mice.[62] Given the molecular effects of β-blocker are not based on a modulation of CaMKII, it seems the community is open and motivated for new pharmacologic drugs for CaMKII inhibition Still, Ca^{2+} scavenging[250] could be beneficial to improve impaired Ca^{2+}-homeostasis and prevent arrhythmogenesis. If the PLN-R14del results in enhanced calcium reuptake, rather than the previously described super-inhibition, increasing calcium S/ER reuptake could be ineffective in PLN-R14del cardiomyopathy and need to be further evaluated before more therapeutic testing.

Conversely, the option of gene correction therapy, with the potential to directly correct the mutation in the PLN gene, offers a potentially superior strategy. Nonetheless, significant obstacles, including ethical considerations and the development of effective methods for delivering gene therapy into the target cells, must be overcome. In both scenarios, implementing additional model systems, such as the porcine model, could prove highly beneficial. This is due to the high similarity between porcine and human cardiac anatomy, electrophysiology and coronary circulation.[251] Consequently, potential agents could be tested using these model systems, providing greater knowledge of their mechanism of action and possible side effects. Nevertheless, the pursuit of both gene therapy and pharmacological treatment options is ongoing, to advance our understanding and improving therapeutic options for PLN-R14del cardiomyopathy.

CONCLUSION

PLN-R14del mutation has been shown to affect various aspects of cardiomyocyte function, including calcium handling, contractility, metabolism, and protein homeostasis. The exact mechanisms underlying the development and progression of PLN-R14del cardiomyopathy are still not fully understood, and there is a need for further research to identify the key pathways involved and potential therapeutic targets. It is also important to investigate the relationship between the different abnormalities observed in PLN cardiomyopathy, as they may have complex interrelationships and contribute to the overall disease phenotype. Ultimately, a better understanding of the molecular mechanisms underlying PLN-R14del cardiomyopathy could lead to the development of more effective treatments for this devastating disease.

ACKNOWLEDGEMENTS

We thank the PLN Foundation for the support and knowledge as a structural basis for this review. We thank Prof. Marc Baldus and Anamika Gaur for their input and expertise on the PLN monomer-pentamer interaction information.

FUNDING

R.G.C.M. and L.K. are supported by the PLN Foundation. R.G.C.M. is also supported by the Dutch Research Council (NWO)-HARVEY (grant number 18747). F.S. and P.A.D. are supported by the Fondation Leducq CUREPlaN (grant number 18CVD01). J.P.G.S. is supported by Horizon2020 ERC-2016-COG-EVICARE (grant number 725229). P.A.D. and J.P.G.S. are supported by ZonMw Psider-Heart and NWO- HARVEY.

CONFLICTS OF INTEREST

The authors declare that there is no conflict of interest regarding the publication of this paper.

DATA AVAILABILITY

No new data were generated or analysed in support of this research.

REFERENCES

1. Haghighi, K. et al. A mutation in the human phospholamban gene, deleting arginine 14, results in lethal, hereditary cardiomyopathy. Proc. Natl. Acad. Sci. U. S. A. 103, (2006).
2. Cheung, C. C. et al. Phospholamban cardiomyopathy: a Canadian perspective on a unique population. Neth. Heart J. 27, 208–213 (2019).
3. DeWitt, M. M., MacLeod, H. M., Soliven, B. & McNally, E. M. Phospholamban R14 deletion results in late-onset, mild, hereditary dilated cardiomyopathy. J. Am. Coll. Cardiol. 48, (2006).
4. Jiang, X. et al. The phenotypic characteristic observed by cardiac magnetic resonance in a PLN-R14del family. Sci. Rep. 10, 1–6 (2020).
5. López-Ayala, J. M. et al. Phospholamban p.arg14del mutation in a Spanish family with arrhythmogenic cardiomyopathy: evidence for a European founder mutation. Rev. Esp. Cardiol. 68, (2015).
6. Posch, M. G. et al. Genetic deletion of arginine 14 in phospholamban causes dilated cardiomyopathy with attenuated electrocardiographic R amplitudes. Heart Rhythm 6, (2009).
7. van der Zwaag, P. A. et al. Phospholamban R14del mutation in patients diagnosed with dilated cardiomyopathy or arrhythmogenic right ventricular cardiomyopathy: evidence supporting the concept of arrhythmogenic cardiomyopathy. Eur. J. Heart Fail. 14, 1199–1207 (2012).
8. Zanotti, S. et al. Characterization of Skeletal Muscle Biopsy and Derived Myoblasts in a Patient Carrying Arg14del Mutation in Gene. Cells 12, (2023).
9. Hof, I. E. et al. Prevalence and cardiac phenotype of patients with a phospholamban mutation. Neth. Heart J. 27, 64–69 (2019).
10. van der Meer, P., van Rooij, E. & Doevendans, P. A. [Cardiomyopathy due to a mutation in the phospholamban gene: a high-impact genetic abnormality]. Ned. Tijdschr. Geneeskd. 167, (2023).
11. van der Zwaag, P. A. et al. Phospholamban R14del mutation in patients diagnosed with dilated cardiomyopathy or arrhythmogenic right ventricular cardiomyopathy: evidence supporting the concept of arrhythmogenic cardiomyopathy. Eur. J. Heart Fail. 14, 1199–1207 (2012).
12. Young, H. S., Ceholski, D. K. & Trieber, C. A. Deception in simplicity: hereditary phospholamban mutations in dilated cardiomyopathy. Biochem. Cell Biol. 93, (2015).
13. Haghighi, K. et al. A mutation in the human phospholamban gene, deleting arginine 14, results in lethal, hereditary cardiomyopathy. Proc. Natl. Acad. Sci. U. S. A. 103, (2006).
14. van der Zwaag, P. A. et al. Phospholamban R14del mutation in patients diagnosed with dilated cardiomyopathy or arrhythmogenic right ventricular cardiomyopathy: evidence supporting the concept of arrhythmogenic cardiomyopathy. Eur. J. Heart Fail. 14, 1199–1207 (2012).
15. van Rijsingen, I. A. W. et al. Outcome in phospholamban R14del carriers: results of a large multicentre cohort study. Circ. Cardiovasc. Genet. 7, 455–465 (2014).
16. Bhonsale, A. et al. Impact of genotype on clinical course in arrhythmogenic right ventricular dysplasia/cardiomyopathy-associated mutation carriers. Eur. Heart J. 36, 847–855 (2015).
17. van Rijsingen, I. A. W. et al. Outcome in phospholamban R14del carriers: results of a large multicentre cohort study. Circ. Cardiovasc. Genet. 7, 455–465 (2014).
18. Haghighi, K., Bidwell, P. & Kranias, E. G. Phospholamban interactome in cardiac contractility and survival: A new vision of an old friend. J. Mol. Cell. Cardiol. 77, 160–167 (2014).
19. van Rijsingen, I. A. W. et al. Outcome in phospholamban R14del carriers: results of a large multicentre cohort study. Circ. Cardiovasc. Genet. 7, 455–465 (2014).
20. Peterson, D. F. et al. Aetiology and incidence of sudden cardiac arrest and death in young competitive athletes in the USA: a 4-year prospective study. Br. J. Sports Med. 55, 1196–1203 (2021).
21. Harmon, K. G. Incidence and Causes of Sudden Cardiac Death in Athletes. Clin. Sports Med. 41, 369–388 (2022).
22. van Lint, F. H. M. et al. Exercise does not influence development of phenotype in PLN p.(Arg14del) cardiomyopathy. Neth. Heart J. 31, 291–299 (2023).

23. van der Zwaag, P. A. et al. Phospholamban R14del mutation in patients diagnosed with dilated cardiomyopathy or arrhythmogenic right ventricular cardiomyopathy: evidence supporting the concept of arrhythmogenic cardiomyopathy. Eur. J. Heart Fail. 14, 1199–1207 (2012).

24. van Opbergen, C. J. M., Delmar, M. & van Veen, T. A. B. Potential new mechanisms of pro-arrhythmia in arrhythmogenic cardiomyopathy: focus on calcium sensitive pathways. Netherlands Heart Journal vol. 25 157–169 Preprint at https://doi.org/10.1007/s12471-017-0946-7 (2017).

25. Taha, K. et al. Early Mechanical Alterations in Phospholamban Mutation Carriers: Identifying Subclinical Disease Before Onset of Symptoms. JACC Cardiovasc. Imaging 14, 885–896 (2021).

26. Haghighi, K. et al. A mutation in the human phospholamban gene, deleting arginine 14, results in lethal, hereditary cardiomyopathy. Proc. Natl. Acad. Sci. U. S. A. 103, (2006).

27. van Rijsingen, I. A. W. et al. Outcome in phospholamban R14del carriers: results of a large multicentre cohort study. Circ. Cardiovasc. Genet. 7, 455–465 (2014).

28. Te Riele, A. S. J. M. et al. Mutation-positive arrhythmogenic right ventricular dysplasia/cardiomyopathy: the triangle of dysplasia displaced. J. Cardiovasc. Electrophysiol. 24, 1311–1320 (2013).

29. van Rijsingen, I. A. W. et al. Outcome in phospholamban R14del carriers: results of a large multicentre cohort study. Circ. Cardiovasc. Genet. 7, 455–465 (2014).

30. Kamath, S. A. et al. Low voltage on the electrocardiogram is a marker of disease severity and a risk factor for adverse outcomes in patients with heart failure due to systolic dysfunction. Am. Heart J. 152, 355–361 (2006).

31. Te Rijdt, W. P. et al. Myocardial fibrosis as an early feature in phospholamban p.Arg14del mutation carriers: phenotypic insights from cardiovascular magnetic resonance imaging. Eur. Heart J. Cardiovasc. Imaging 20, 92–100 (2019).

32. Haghighi, K. et al. A mutation in the human phospholamban gene, deleting arginine 14, results in lethal, hereditary cardiomyopathy. Proc. Natl. Acad. Sci. U. S. A. 103, (2006).

33. DeWitt, M. M., MacLeod, H. M., Soliven, B. & McNally, E. M. Phospholamban R14 deletion results in late-onset, mild, hereditary dilated cardiomyopathy. J. Am. Coll. Cardiol. 48, (2006).

34. Posch, M. G. et al. Genetic deletion of arginine 14 in phospholamban causes dilated cardiomyopathy with attenuated electrocardiographic R amplitudes. Heart Rhythm 6, (2009).

35. Haghighi, K. et al. The human phospholamban Arg14-deletion mutant localizes to plasma membrane and interacts with the Na/K-ATPase. J. Mol. Cell. Cardiol. 52, (2012).

36. Ceholski, D. K., Trieber, C. A. & Young, H. S. Hydrophobic imbalance in the cytoplasmic domain of phospholamban is a determinant for lethal dilated cardiomyopathy. J. Biol. Chem. 287, 16521–16529 (2012).

37. van der Zwaag, P. A. et al. Phospholamban R14del mutation in patients diagnosed with dilated cardiomyopathy or arrhythmogenic right ventricular cardiomyopathy: evidence supporting the concept of arrhythmogenic cardiomyopathy. Eur. J. Heart Fail. 14, 1199–1207 (2012).

38. van der Zwaag, P. A. et al. Recurrent and founder mutations in the Netherlands-Phospholamban p.Arg14del mutation causes arrhythmogenic cardiomyopathy. Neth. Heart J. 21, 286–293 (2013).

39. van der Heijden, J. F. & Hassink, R. J. The phospholamban p.Arg14del founder mutation in Dutch patients with arrhythmogenic cardiomyopathy. Neth. Heart J. 21, 284–285 (2013).

40. Groeneweg, J. A. et al. Arrhythmogenic right ventricular dysplasia/cardiomyopathy according to revised 2010 task force criteria with inclusion of non-desmosomal phospholamban mutation carriers. Am. J. Cardiol. 112, 1197–1206 (2013).

41. Gho, J. M. I. H. et al. High resolution systematic digital histological quantification of cardiac fibrosis and adipose tissue in phospholamban p.Arg14del mutation associated cardiomyopathy. PLoS One 9, e94820 (2014).

42. van Rijsingen, I. A. W. et al. Outcome in phospholamban R14del carriers: results of a large multicentre cohort study. Circ. Cardiovasc. Genet. 7, 455–465 (2014).

43. Bhonsale, A. et al. Impact of genotype on clinical course in arrhythmogenic right ventricular dysplasia/cardiomyopathy-associated mutation carriers. Eur. Heart J. 36, 847–855 (2015).

44. Vostrikov, V. V., Soller, K. J., Ha, K. N., Gopinath, T. & Veglia, G. Effects of naturally occurring arginine 14 deletion on phospholamban conformational dynamics and membrane interactions. Biochim. Biophys. Acta 1848, 315–322 (2015).

45. Young, H. S., Ceholski, D. K. & Trieber, C. A. Deception in simplicity: hereditary phospholamban mutations in dilated cardiomyopathy. Biochem. Cell Biol. 93, (2015).

46. Karakikes, I. et al. Correction of human phospholamban R14del mutation associated with cardiomyopathy using targeted nucleases and combination therapy. Nat. Commun. 6, 6955 (2015).

47. López-Ayala, J. M. et al. Phospholamban p.arg14del mutation in a Spanish family with arrhythmogenic cardiomyopathy: evidence for a European founder mutation. Rev. Esp. Cardiol. 68, (2015).

48. Fish, M. et al. Mutation analysis of the phospholamban gene in 315 South Africans with dilated, hypertrophic, peripartum and arrhythmogenic right ventricular cardiomyopathies. Sci. Rep. 6, 22235 (2016).

49. Milano, A. et al. Sudden Cardiac Arrest and Rare Genetic Variants in the Community. Circ. Cardiovasc. Genet. 9, 147–153 (2016).

50. Te Rijdt, W. P. et al. Phospholamban p.Arg14del cardiomyopathy is characterized by phospholamban aggregates, aggresomes, and autophagic degradation. Histopathology 69, 542–550 (2016).

51. Stillitano, F. et al. Genomic correction of familial cardiomyopathy in human engineered cardiac tissues. Eur. Heart J. 37, 3282–3284 (2016).

52. van Opbergen, C. J. M., Delmar, M. & van Veen, T. A. B. Potential new mechanisms of pro-arrhythmia in arrhythmogenic cardiomyopathy: focus on calcium sensitive pathways. Netherlands Heart Journal vol. 25 157–169 Preprint at https://doi.org/10.1007/s12471-017-0946-7 (2017).

53. Sepehrkhouy, S. et al. Distinct fibrosis pattern in desmosomal and phospholamban mutation carriers in hereditary cardiomyopathies. Heart Rhythm 14, 1024–1032 (2017).

54. Te Rijdt, W. P. et al. Phospholamban immunostaining is a highly sensitive and specific method for diagnosing phospholamban p.Arg14del cardiomyopathy. Cardiovasc. Pathol. 30, 23–26 (2017).

55. Nannenberg, E. A. et al. Effect of Ascertainment Bias on Estimates of Patient Mortality in Inherited Cardiac Diseases. Circ Genom Precis Med 11, e001797 (2018).

56. Wu, H. et al. Engineering CRISPR/Cpf1 with tRNA promotes genome editing capability in mammalian systems. Cell. Mol. Life Sci. 75, 3593–3607 (2018).

57. Hof, I. E. et al. Prevalence and cardiac phenotype of patients with a phospholamban mutation. Neth. Heart J. 27, 64–69 (2019).

58. Te Rijdt, W. P. et al. Myocardial fibrosis as an early feature in phospholamban p.Arg14del mutation carriers: phenotypic insights from cardiovascular magnetic resonance imaging. Eur. Heart J. Cardiovasc. Imaging 20, 92–100 (2019).

59. Cheung, C. C. et al. Phospholamban cardiomyopathy: a Canadian perspective on a unique population. Neth. Heart J. 27, 208–213 (2019).

60. Doevendans, P. A., Glijnis, P. C. & Kranias, E. G. Leducq Transatlantic Network of Excellence to Cure Phospholamban-Induced Cardiomyopathy (CURE-PLaN). Circ. Res. 125, 720–724 (2019).

61. Stroik, D. R. et al. Viral expression of a SERCA2a-activating PLB mutant improves calcium cycling and synchronicity in dilated cardiomyopathic hiPSC-CMs. J. Mol. Cell. Cardiol. 138, 59–65 (2020).

62. Eijgenraam, T. R. et al. The phospholamban p.(Arg14del) pathogenic variant leads to cardiomyopathy with heart failure and is unreponsive to standard heart failure therapy. Sci. Rep. 10, 9819 (2020).

63. Bleijendaal, H. et al. Computer versus cardiologist: Is a machine learning algorithm able to outperform an expert in diagnosing a phospholamban p.Arg14del mutation on the electrocardiogram? Heart Rhythm 18, 79–87 (2021).

64. Jiang, X. et al. The phenotypic characteristic observed by cardiac magnetic resonance in a PLN-R14del family. Sci. Rep. 10, 1–6 (2020).

65. Menzel, J. et al. 14-3-3 binding creates a memory of kinase action by stabilizing the modified state of phospholamban. Sci. Signal. 13, (2020).

66. Pei, J. et al. Transcriptional regulation profiling reveals disrupted lipid metabolism in failing hearts with a pathogenic phospholamban mutation. bioRxiv 2020.11.30.402792 (2020) doi:10.1101/2020.11.30.402792.

67. Taha, K. et al. Early Mechanical Alterations in Phospholamban Mutation Carriers: Identifying Subclinical Disease Before Onset of Symptoms. JACC Cardiovasc. Imaging 14, 885–896 (2021).

68. van de Leur, R. R. et al. Discovering and Visualizing Disease-Specific Electrocardiogram Features Using Deep Learning: Proof-of-Concept in Phospholamban Gene Mutation Carriers. Circ. Arrhythm. Electrophysiol. 14, e009056 (2021).

69. Lopes, R. R. et al. Improving electrocardiogram-based detection of rare genetic heart disease using transfer learning: An application to phospholamban p.Arg14del mutation carriers. Comput. Biol. Med. 131, 104262 (2021).

70. Nguyen, T. V. et al. Genetic Determinants and Genotype-Phenotype Correlations in Vietnamese Patients With Dilated Cardiomyopathy. Circ. J. 85, 1469–1478 (2021).

71. Feyen, D. A. M. et al. Unfolded Protein Response as a Compensatory Mechanism and Potential Therapeutic Target in PLN R14del Cardiomyopathy. Circulation (2021) doi:10.1161/CIRCULATIONAHA.120.049844.

72. Cuello, F. et al. Impairment of the ER/mitochondria compartment in human cardiomyocytes with PLN p.Arg14del mutation. EMBO Mol. Med. 13, e13074 (2021).

73. Raad, N. et al. Arrhythmia Mechanism and Dynamics in a Humanized Mouse Model of Inherited Cardiomyopathy Caused by Phospholamban R14del Mutation. Circulation 144, 441–454 (2021).

74. Verstraelen, T. E. et al. Prediction of ventricular arrhythmia in phospholamban p.Arg14del mutation carriers-reaching the frontiers of individual risk prediction. Eur. Heart J. 42, 2842–2850 (2021).

75. Te Rijdt, W. P. et al. Rationale and design of the PHOspholamban RElated CArdiomyopathy intervention STudy (i-PHORECAST). Neth. Heart J. (2021) doi:10.1007/s12471-021-01584-5.

76. Haghighi, K. et al. Impaired Right Ventricular Calcium Cycling Is an Early Risk Factor in R14del-Phospholamban Arrhythmias. J Pers Med 11, (2021).

77. Koch, D. et al. Molecular noise filtering in the β-adrenergic signaling network by phospholamban pentamers. Cell Rep. 36, 109448 (2021).

78. Grote Beverborg, N. et al. Phospholamban antisense oligonucleotides improve cardiac function in murine cardiomyopathy. Nat. Commun. 12, 5180 (2021).

79. Taha, K. et al. Optimal echocardiographic assessment of myocardial dysfunction for arrhythmic risk stratification in phospholamban mutation carriers. Eur. Heart J. Cardiovasc. Imaging (2021) doi:10.1093/ehjci/jeab178.

80. Eijgenraam, T. R. et al. Protein Aggregation Is an Early Manifestation of Phospholamban p.(Arg14del)-Related Cardiomyopathy: Development of PLN-R14del-Related Cardiomyopathy. Circ. Heart Fail. 14, e008532 (2021).

81. van der Klooster, Z. J. et al. P62-positive aggregates are homogenously distributed in the myocardium and associated with the type of mutation in genetic cardiomyopathy. J. Cell. Mol. Med. 25, (2021).

82. de Brouwer, R. et al. Sex-specific aspects of phospholamban cardiomyopathy: The importance and prognostic value of low-voltage electrocardiograms. Heart Rhythm (2021) doi:10.1016/j.hrthm.2021.11.009.

83. Kamel, S. M. et al. Istaroxime treatment ameliorates calcium dysregulation in a zebrafish model of phospholamban R14del cardiomyopathy. Nat. Commun. 12, 7151 (2021).

84. Tabata, T. et al. Phospholamban p.Arg14del Cardiomyopathy: A Japanese Case Series. Intern. Med. (2021) doi:10.2169/internalmedicine.8594-21.

85. Badone, B. et al. Characterization of the PLN p.Arg14del Mutation in Human Induced Pluripotent Stem Cell-Derived Cardiomyocytes. Int. J. Mol. Sci. 22, (2021).

86. de Boer, R. A. et al. Targeted therapies in genetic dilated and hypertrophic cardiomyopathies: from molecular mechanisms to therapeutic targets. A position paper from the Heart Failure Association (HFA) and the Working Group on Myocardial Function of the European Society of Cardiology (ESC). Eur. J. Heart Fail. (2021) doi:10.1002/ejhf.2414.

87. Driessen, H. E. et al. Buccal Mucosa Cells as a Potential Diagnostic Tool to Study Onset and Progression of Arrhythmogenic Cardiomyopathy. Int. J. Mol. Sci. 23, (2021).

88. van der Voorn, S. M. et al. Exploring the Correlation Between Fibrosis Biomarkers and Clinical Disease Severity in PLN p.Arg14del Patients. Front Cardiovasc Med 8, 802998 (2021).

89. Mittal, N. et al. Generation of human induced pluripotent stem cell (iPSC) lines derived from five patients carrying the pathogenic phospholamban-R14del (PLN-R14del) variant and three non-carrier family members. Stem Cell Res. 60, 102737 (2022).

90. Dave, J. et al. Gene editing reverses arrhythmia susceptibility in humanized PLN-R14del mice: modeling a European cardiomyopathy with global impact. Cardiovasc. Res. (2022) doi:10.1093/cvr/cvac021.

91. Monda, E. et al. Clinical and Molecular Characteristics of Patients with PLN R14del Cardiomyopathy: State-of-the-Art Review. Cardiogenetics vol. 12 112–121 Preprint at https://doi.org/10.3390/cardiogenetics12010012 (2022).

92. Eijgenraam, T. R. et al. Antisense Therapy Attenuates Phospholamban p.(Arg14del) Cardiomyopathy in Mice and Reverses Protein Aggregation. Int. J. Mol. Sci. 23, (2022).

93. Deiman, F. E., Bomer, N., van der Meer, P. & Grote Beverborg, N. Review: Precision Medicine Approaches for Genetic Cardiomyopathy: Targeting Phospholamban R14del. Curr. Heart Fail. Rep. (2022) doi:10.1007/s11897-022-00558-x.

94. Vera, C. D. et al. Generation of two induced pluripotent stem cell lines carrying the phospholamban R14del mutation for modeling ARVD/C. Stem Cell Res. 63, 102834 (2022).

95. Harakalova, M. et al. Transcriptional regulation profiling reveals PPARA-mediated fatty acid oxidation as a novel therapeutic target in phospholamban R14del cardiomyopathy. (2022) doi:10.21203/rs.3.rs-1902254/v1.

96. Vafiadaki, E., Haghighi, K., Arvanitis, D. A., Kranias, E. G. & Sanoudou, D. Aberrant PLN-R14del Protein Interactions Intensify SERCA2a Inhibition, Driving Impaired Ca Handling and Arrhythmogenesis. Int. J. Mol. Sci. 23, (2022).

97. Rogalska, M. E. et al. Isoform changes of action potential regulators in the ventricles of arrhythmogenic phospholamban-R14del humanized mouse hearts. Metabolism 138, 155344 (2023).

98. Aboumsallem, J. P. et al. Multi-omics analyses identify molecular signatures with prognostic values in different heart failure aetiologies. J. Mol. Cell. Cardiol. 175, 13–28 (2023).

99. Kumar, M. et al. Myofilament Alterations Associated with Human R14del-Phospholamban Cardiomyopathy. Int. J. Mol. Sci. 24, (2023).

100. Vafiadaki, E., Glijnis, P. C., Doevendans, P. A., Kranias, E. G. & Sanoudou, D. Phospholamban R14del disease: The past, the present and the future. Front Cardiovasc Med 10, 1162205 (2023).

101. Cleary, S. R. et al. Dilated cardiomyopathy variant R14del increases phospholamban pentamer stability, blunting dynamic regulation of cardiac calcium handling. bioRxiv : the preprint server for biology (2023) doi:10.1101/2023.05.26.542463.

102. de Brouwer, R. et al. A randomized controlled trial of eplerenone in asymptomatic phospholamban p.Arg14del carriers. Eur. Heart J. 44, 4284–4287 (2023).

103. Maniezzi, C. et al. Early consequences of the phospholamban mutation PLN-R14del+/- in a transgenic mouse model. bioRxiv 2023.04.05.535536 (2023) doi:10.1101/2023.04.05.535536.

104. Doevendans, P. A. Should we offer preventive treatment to all carriers of PLN p.(Arg14del) variant? Neth. Heart J. 31, 289–290 (2023).

105. Boer, D. & Rudolf, A. Should we offer preventive treatment to all carriers of PLN p.(Arg14del) variant? Neth. Heart J. 31, 287–288 (2023).

106. Taha, K. et al. Deep neural network-based clustering of deformation curves reveals novel disease features in PLN pathogenic variant carriers. Int. J. Cardiovasc. Imaging 39, 2149–2161 (2023).

107. Balducci, V. et al. Generation and characterization of novel human induced pluripotent stem cell (iPSC) lines originating from five asymptomatic individuals carrying the PLN-R14del pathogenic variant and a non-carrier relative. Stem Cell Res. 72, 103208 (2023).

108. Stege, N. M. et al. DWORF Extends Life Span in a PLN-R14del Cardiomyopathy Mouse Model by Reducing Abnormal Sarcoplasmic Reticulum Clusters. Circ. Res. 133, 1006–1021 (2023).

109. van der Voorn, S. M. et al. Lack of Evidence for the Role of the p.(Ser96Ala) Polymorphism in Histidine-Rich Calcium Binding Protein as a Secondary Hit in Cardiomyopathies. Int. J. Mol. Sci. 24, (2023).

110. MacLennan, D. H. & Kranias, E. G. Phospholamban: a crucial regulator of cardiac contractility. Nat. Rev. Mol. Cell Biol. 4, 566–577 (2003).

111. van der Zwaag, P. A. et al. Phospholamban R14del mutation in patients diagnosed with dilated cardiomyopathy or arrhythmogenic right ventricular cardiomyopathy: evidence supporting the concept of arrhythmogenic cardiomyopathy. Eur. J. Heart Fail. 14, 1199–1207 (2012).

112. Bers, D. M., Despa, S. & Bossuyt, J. Regulation of Ca2+ and Na+ in normal and failing cardiac myocytes. Ann. N. Y. Acad. Sci. 1080, (2006).

113. Tada, M. & Toyofuku, T. Molecular regulation of phospholamban function and expression. Trends Cardiovasc. Med. 8, (1998).

114. Shah, D. et al. Modeling of -Related Dilated Cardiomyopathy Using Human Induced Pluripotent Stem Cells. Cells 8, (2019).

115. Lan, F. et al. Abnormal calcium handling properties underlie familial hypertrophic cardiomyopathy pathology in patient-specific induced pluripotent stem cells. Cell Stem Cell 12, (2013).

116. Taha, K. et al. Early Mechanical Alterations in Phospholamban Mutation Carriers: Identifying Subclinical Disease Before Onset of Symptoms. JACC Cardiovasc. Imaging 14, 885–896 (2021).

117. Weber, D. K. et al. Structural basis for allosteric control of the SERCA-Phospholamban membrane complex by Ca and phosphorylation. Elife 10, (2021).

118. Vostrikov, V. V., Soller, K. J., Ha, K. N., Gopinath, T. & Veglia, G. Effects of naturally occurring arginine 14 deletion on phospholamban conformational dynamics and membrane interactions. Biochim. Biophys. Acta 1848, 315–322 (2015).

119. Kim, J. et al. Dysfunctional conformational dynamics of protein kinase A induced by a lethal mutant of phospholamban hinder phosphorylation. Proc. Natl. Acad. Sci. U. S. A. 112, 3716–3721 (2015).

120. Laver, D. R. Ca2+ stores regulate ryanodine receptor Ca2+ release channels via luminal and cytosolic Ca2+ sites. Clin. Exp. Pharmacol. Physiol. 34, (2007).

121. Haghighi, K. et al. A mutation in the human phospholamban gene, deleting arginine 14, results in lethal, hereditary cardiomyopathy. Proc. Natl. Acad. Sci. U. S. A. 103, (2006).

122. Vafiadaki, E., Haghighi, K., Arvanitis, D. A., Kranias, E. G. & Sanoudou, D. Aberrant PLN-R14del Protein Interactions Intensify SERCA2a Inhibition, Driving Impaired Ca Handling and Arrhythmogenesis. Int. J. Mol. Sci. 23, (2022).

123. ter Keurs, H. E., Zhang, Y. M. & Miura, M. Damage-induced arrhythmias: reversal of excitation-contraction coupling. Cardiovasc. Res. 40, (1998).

124. ter Keurs, H. E. The interaction of Ca2+ with sarcomeric proteins: role in function and dysfunction of the heart. Am. J. Physiol. Heart Circ. Physiol. 302, (2012).

125. Mark D. McCauley, X. H. T. W. Ryanodine Receptor Phosphorylation, Calcium/Calmodulin-dependent Protein Kinase II, and Life-threatening Ventricular Arrhythmias. Trends Cardiovasc. Med. 21, 48 (2011).

126. Badone, B. et al. Characterization of the PLN p.Arg14del Mutation in Human Induced Pluripotent Stem Cell-Derived Cardiomyocytes. Int. J. Mol. Sci. 22, (2021).

127. Becucci, L. et al. On the Function of Pentameric Phospholamban: Ion Channel or Storage Form? Biophys. J. 96, L60–L62 (2009).

128. Smeazzetto, S., Henkel, M., Ferri, T., Thiel, G. & Moncelli, M. R. Ion Channel Activity of Pentameric Phospholamban. Biophys. J. 98, 328a (2010).

129. Glaves, J. P., Primeau, J. O., Espinoza-Fonseca, L. M., Lemieux, M. J. & Young, H. S. The Phospholamban Pentamer Alters Function of the Sarcoplasmic Reticulum Calcium Pump SERCA. Biophys. J. 116, (2019).

130. Kimura, Y., Kurzydlowski, K., Tada, M. & MacLennan, D. H. Phospholamban inhibitory function is activated by depolymerization. J. Biol. Chem. 272, 15061–15064 (1997).

131. Kovacs, R. J., Nelson, M. T., Simmerman, H. K. & Jones, L. R. Phospholamban forms Ca2+-selective channels in lipid bilayers. J. Biol. Chem. 263, 18364–18368 (1988).

132. Oxenoid, K. & Chou, J. J. The structure of phospholamban pentamer reveals a channel-like architecture in membranes. Proc. Natl. Acad. Sci. U. S. A. 102, (2005).

133. Becucci, L. et al. On the Function of Pentameric Phospholamban: Ion Channel or Storage Form? Biophys. J. 96, L60–L62 (2009).

134. Glaves, J. P., Primeau, J. O., Espinoza-Fonseca, L. M., Lemieux, M. J. & Young, H. S. The Phospholamban Pentamer Alters Function of the Sarcoplasmic Reticulum Calcium Pump SERCA. Biophys. J. 116, (2019).

135. Akin, B. L., Hurley, T. D., Chen, Z. & Jones, L. R. The structural basis for phospholamban inhibition of the calcium pump in sarcoplasmic reticulum. J. Biol. Chem. 288, 30181–30191 (2013).

136. Glaves, J. P., Primeau, J. O., Espinoza-Fonseca, L. M., Lemieux, M. J. & Young, H. S. The Phospholamban Pentamer Alters Function of the Sarcoplasmic Reticulum Calcium Pump SERCA. Biophys. J. 116, (2019).

137. Mark D. McCauley, X. H. T. W. Ryanodine Receptor Phosphorylation, Calcium/Calmodulin-dependent Protein Kinase II, and Life-threatening Ventricular Arrhythmias. Trends Cardiovasc. Med. 21, 48 (2011).

138. Kimura, Y., Kurzydlowski, K., Tada, M. & MacLennan, D. H. Phospholamban inhibitory function is activated by depolymerization. J. Biol. Chem. 272, 15061–15064 (1997).

139. Wittmann, T., Lohse, M. J. & Schmitt, J. P. Phospholamban pentamers attenuate PKA-dependent phosphorylation of monomers. J. Mol. Cell. Cardiol. 80, (2015).

140. DeWitt, M. M., MacLeod, H. M., Soliven, B. & McNally, E. M. Phospholamban R14 deletion results in late-onset, mild, hereditary dilated cardiomyopathy. J. Am. Coll. Cardiol. 48, (2006).

141. Koch, D. et al. Molecular noise filtering in the β-adrenergic signaling network by phospholamban pentamers. Cell Rep. 36, 109448 (2021).

142. Kranias, E. G. & Hajjar, R. J. Modulation of cardiac contractility by the phospholamban/SERCA2a regulatome. Circ. Res. 110, 1646–1660 (2012).

143. Haghighi, K., Bidwell, P. & Kranias, E. G. Phospholamban interactome in cardiac contractility and survival: A new vision of an old friend. J. Mol. Cell. Cardiol. 77, 160–167 (2014).

144. Kranias, E. G. & Hajjar, R. J. Modulation of cardiac contractility by the phospholamban/SERCA2a regulatome. Circ. Res. 110, 1646–1660 (2012).

145. Vafiadaki, E., Haghighi, K., Arvanitis, D. A., Kranias, E. G. & Sanoudou, D. Aberrant PLN-R14del Protein Interactions Intensify SERCA2a Inhibition, Driving Impaired Ca Handling and Arrhythmogenesis. Int. J. Mol. Sci. 23, (2022).

146. Menzel, J. et al. 14-3-3 binding creates a memory of kinase action by stabilizing the modified state of phospholamban. Sci. Signal. 13, (2020).

147. Menzel, J. et al. 14-3-3 binding creates a memory of kinase action by stabilizing the modified state of phospholamban. Sci. Signal. 13, (2020).

148. Te Rijdt, W. P. et al. Phospholamban p.Arg14del cardiomyopathy is characterized by phospholamban aggregates, aggresomes, and autophagic degradation. Histopathology 69, 542–550 (2016).

149. Tarone, G. & Brancaccio, M. Keep your heart in shape: molecular chaperone networks for treating heart disease. Cardiovasc. Res. 102, 346–361 (2014).

150. Vasconcellos, L. R. C. et al. Protein aggregation as a cellular response to oxidative stress induced by heme and iron. Proc. Natl. Acad. Sci. U. S. A. 113, E7474–E7482 (2016).

151. Torres, M., Encina, G., Soto, C. & Hetz, C. Abnormal calcium homeostasis and protein folding stress at the ER: A common factor in familial and infectious prion disorders. Commun. Integr. Biol. 4, 258–261 (2011).

152. Soto, C. & Pritzkow, S. Protein misfolding, aggregation, and conformational strains in neurodegenerative diseases. Nat. Neurosci. 21, 1332–1340 (2018).

153. Te Rijdt, W. P. et al. Phospholamban p.Arg14del cardiomyopathy is characterized by phospholamban aggregates, aggresomes, and autophagic degradation. Histopathology 69, 542–550 (2016).

154. Lin, J. H., Walter, P. & Benedict Yen, T. S. Endoplasmic Reticulum Stress in Disease Pathogenesis. Annual Review of Pathology: Mechanisms of Disease vol. 3 399–425 Preprint at https://doi.org/10.1146/annurev.pathmechdis.3.121806.151434 (2008).

155. Glick, D., Barth, S. & Macleod, K. F. Autophagy: cellular and molecular mechanisms. J. Pathol. 221, 3–12 (2010).

156. Te Rijdt, W. P. et al. Phospholamban p.Arg14del cardiomyopathy is characterized by phospholamban aggregates, aggresomes, and autophagic degradation. Histopathology 69, 542–550 (2016).

157. Te Rijdt, W. P. et al. Phospholamban immunostaining is a highly sensitive and specific method for diagnosing phospholamban p.Arg14del cardiomyopathy. Cardiovasc. Pathol. 30, 23–26 (2017).

158. van der Klooster, Z. J. et al. P62-positive aggregates are homogenously distributed in the myocardium and associated with the type of mutation in genetic cardiomyopathy. J. Cell. Mol. Med. 25, (2021).

159. Eijgenraam, T. R. et al. The phospholamban p.(Arg14del) pathogenic variant leads to cardiomyopathy with heart failure and is unreponsive to standard heart failure therapy. Sci. Rep. 10, 9819 (2020).

160. Eijgenraam, T. R. et al. Protein Aggregation Is an Early Manifestation of Phospholamban p.(Arg14del)-Related Cardiomyopathy: Development of PLN-R14del-Related Cardiomyopathy. Circ. Heart Fail. 14, e008532 (2021).

161. Te Rijdt, W. P. et al. Phospholamban p.Arg14del cardiomyopathy is characterized by phospholamban aggregates, aggresomes, and autophagic degradation. Histopathology 69, 542–550 (2016).

162. Cohen-Kaplan, V. et al. p62- and ubiquitin-dependent stress-induced autophagy of the mammalian 26S proteasome. Proc. Natl. Acad. Sci. U. S. A. 113, E7490–E7499 (2016).

163. van der Klooster, Z. J. et al. P62-positive aggregates are homogenously distributed in the myocardium and associated with the type of mutation in genetic cardiomyopathy. J. Cell. Mol. Med. 25, (2021).

164. Rothermel, B. A. & Hill, J. A. Myocyte autophagy in heart disease: friend or foe? Autophagy 3, (2007).

165. Te Rijdt, W. P. et al. Phospholamban immunostaining is a highly sensitive and specific method for diagnosing phospholamban p.Arg14del cardiomyopathy. Cardiovasc. Pathol. 30, 23–26 (2017).

166. Eijgenraam, T. R. et al. Protein Aggregation Is an Early Manifestation of Phospholamban p.(Arg14del)-Related Cardiomyopathy: Development of PLN-R14del-Related Cardiomyopathy. Circ. Heart Fail. 14, e008532 (2021).

167. Cuello, F. et al. Impairment of the ER/mitochondria compartment in human cardiomyocytes with PLN p.Arg14del mutation. EMBO Mol. Med. 13, e13074 (2021).

168. Feyen, D. A. M. et al. Unfolded Protein Response as a Compensatory Mechanism and Potential Therapeutic Target in PLN R14del Cardiomyopathy. Circulation (2021) doi:10.1161/CIRCULATIONAHA.120.049844.

169. Lopaschuk, G. D., Karwi, Q. G., Tian, R., Wende, A. R. & Dale Abel, E. Cardiac Energy Metabolism in Heart Failure. Circulation Research vol. 128 1487–1513 Preprint at https://doi.org/10.1161/circresaha.121.318241 (2021).

170. Pei, J. et al. Transcriptional regulation profiling reveals disrupted lipid metabolism in failing hearts with a pathogenic phospholamban mutation. bioRxiv 2020.11.30.402792 (2020) doi:10.1101/2020.11.30.402792.

171. Sletten, A. C., Peterson, L. R. & Schaffer, J. E. Manifestations and mechanisms of myocardial lipotoxicity in obesity. J. Intern. Med. 284, 478–491 (2018).

172. Lopaschuk, G. D., Karwi, Q. G., Tian, R., Wende, A. R. & Dale Abel, E. Cardiac Energy Metabolism in Heart Failure. Circulation Research vol. 128 1487–1513 Preprint at https://doi.org/10.1161/circresaha.121.318241 (2021).

173. Cuello, F. et al. Impairment of the ER/mitochondria compartment in human cardiomyocytes with PLN p.Arg14del mutation. EMBO Mol. Med. 13, e13074 (2021).

174. Ritterhoff, J. & Tian, R. Metabolism in cardiomyopathy: every substrate matters. Cardiovasc. Res. 113, (2017).

175. Sepehrkhouy, S. et al. Distinct fibrosis pattern in desmosomal and phospholamban mutation carriers in hereditary cardiomyopathies. Heart Rhythm 14, 1024–1032 (2017).

176. Haghighi, K. et al. A mutation in the human phospholamban gene, deleting arginine 14, results in lethal, hereditary cardiomyopathy. Proc. Natl. Acad. Sci. U. S. A. 103, (2006).

177. Piek, A., de Boer, R. A. & Silljé, H. H. W. The fibrosis-cell death axis in heart failure. Heart Fail. Rev. 21, 199 (2016).

178. Sepehrkhouy, S. et al. Distinct fibrosis pattern in desmosomal and phospholamban mutation carriers in hereditary cardiomyopathies. Heart Rhythm 14, 1024–1032 (2017).

179. Gho, J. M. I. H. et al. High resolution systematic digital histological quantification of cardiac fibrosis and adipose tissue in phospholamban p.Arg14del mutation associated cardiomyopathy. PLoS One 9, e94820 (2014).

180. Te Rijdt, W. P. et al. Phospholamban p.Arg14del cardiomyopathy is characterized by phospholamban aggregates, aggresomes, and autophagic degradation. Histopathology 69, 542–550 (2016).

181. Sepehrkhouy, S. et al. Distinct fibrosis pattern in desmosomal and phospholamban mutation carriers in hereditary cardiomyopathies. Heart Rhythm 14, 1024–1032 (2017).

182. Posch, M. G. et al. Genetic deletion of arginine 14 in phospholamban causes dilated cardiomyopathy with attenuated electrocardiographic R amplitudes. Heart Rhythm 6, (2009).

183. Te Rijdt, W. P. et al. Myocardial fibrosis as an early feature in phospholamban p.Arg14del mutation carriers: phenotypic insights from cardiovascular magnetic resonance imaging. Eur. Heart J. Cardiovasc. Imaging 20, 92–100 (2019).

184. Posch, M. G. et al. Genetic deletion of arginine 14 in phospholamban causes dilated cardiomyopathy with attenuated electrocardiographic R amplitudes. Heart Rhythm 6, (2009).

185. Gho, J. M. I. H. et al. High resolution systematic digital histological quantification of cardiac fibrosis and adipose tissue in phospholamban p.Arg14del mutation associated cardiomyopathy. PLoS One 9, e94820 (2014).

186. Te Rijdt, W. P. et al. Phospholamban p.Arg14del cardiomyopathy is characterized by phospholamban aggregates, aggresomes, and autophagic degradation. Histopathology 69, 542–550 (2016).
187. Sepehrkhouy, S. et al. Distinct fibrosis pattern in desmosomal and phospholamban mutation carriers in hereditary cardiomyopathies. Heart Rhythm 14, 1024–1032 (2017).
188. Te Rijdt, W. P. et al. Myocardial fibrosis as an early feature in phospholamban p.Arg14del mutation carriers: phenotypic insights from cardiovascular magnetic resonance imaging. Eur. Heart J. Cardiovasc. Imaging 20, 92–100 (2019).
189. Te Rijdt, W. P. et al. Distinct molecular signature of phospholamban p.Arg14del arrhythmogenic cardiomyopathy. Cardiovasc. Pathol. 40, 2–6 (2019).
190. Sepehrkhouy, S. et al. Distinct fibrosis pattern in desmosomal and phospholamban mutation carriers in hereditary cardiomyopathies. Heart Rhythm 14, 1024–1032 (2017).
191. Maione, A. S. et al. Fibrosis in Arrhythmogenic Cardiomyopathy: The Phantom Thread in the Fibro-Adipose Tissue. Front. Physiol. 11, (2020).
192. Mandawat, A. et al. Progression of Myocardial Fibrosis in Nonischemic DCM and Association With Mortality and Heart Failure Outcomes. JACC Cardiovasc. Imaging 14, 1338–1350 (2021).
193. Te Rijdt, W. P. et al. Myocardial fibrosis as an early feature in phospholamban p.Arg14del mutation carriers: phenotypic insights from cardiovascular magnetic resonance imaging. Eur. Heart J. Cardiovasc. Imaging 20, 92–100 (2019).
194. Te Rijdt, W. P. et al. Phospholamban p.Arg14del cardiomyopathy is characterized by phospholamban aggregates, aggresomes, and autophagic degradation. Histopathology 69, 542–550 (2016).
195. Liang, C., Wang, K., Li, Q., Bai, J. & Zhang, H. Influence of the distribution of fibrosis within an area of myocardial infarction on wave propagation in ventricular tissue. Sci. Rep. 9, 1–14 (2019).
196. Kazbanov, I. V., ten Tusscher, K. H. W. J. & Panfilov, A. V. Effects of Heterogeneous Diffuse Fibrosis on Arrhythmia Dynamics and Mechanism. Sci. Rep. 6, 20835 (2016).
197. van der Voorn, S. M. et al. Exploring the Correlation Between Fibrosis Biomarkers and Clinical Disease Severity in PLN p.Arg14del Patients. Front Cardiovasc Med 8, 802998 (2021).
198. Torre-Amione, G. Immune activation in chronic heart failure. Am. J. Cardiol. 95, (2005).
199. Asatryan, B. et al. Inflammation and Immune Response in Arrhythmogenic Cardiomyopathy: State-of-the-Art Review. Circulation 144, 1646–1655 (2021).
200. Eijgenraam, T. R. et al. Protein Aggregation Is an Early Manifestation of Phospholamban p.(Arg14del)-Related Cardiomyopathy: Development of PLN-R14del-Related Cardiomyopathy. Circ. Heart Fail. 14, e008532 (2021).
201. Kamel, S. M. et al. Istaroxime treatment ameliorates calcium dysregulation in a zebrafish model of phospholamban R14del cardiomyopathy. Nat. Commun. 12, 7151 (2021).
202. Ponikowski, P. et al. [2016 ESC Guidelines for the diagnosis and treatment of acute and chronic heart failure]. Kardiol. Pol. 74, 1037–1147 (2016).
203. Priori, S. G. et al. [2015 ESC Guidelines for the management of patients with ventricular arrhythmias and the prevention of sudden cardiac Death. The Task Force for the Management of Patients with Ventricular Arrhythmias and the Prevention of Sudden Cardiac Death of the European Society of Cardiology]. G. Ital. Cardiol. 17, 108–170 (2016).
204. Eijgenraam, T. R. et al. The phospholamban p.(Arg14del) pathogenic variant leads to cardiomyopathy with heart failure and is unreponsive to standard heart failure therapy. Sci. Rep. 10, 9819 (2020).
205. Eijgenraam, T. R. et al. The phospholamban p.(Arg14del) pathogenic variant leads to cardiomyopathy with heart failure and is unreponsive to standard heart failure therapy. Sci. Rep. 10, 9819 (2020).
206. van der Zwaag, P. A. et al. Phospholamban R14del mutation in patients diagnosed with dilated cardiomyopathy or arrhythmogenic right ventricular cardiomyopathy: evidence supporting the concept of arrhythmogenic cardiomyopathy. Eur. J. Heart Fail. 14, 1199–1207 (2012).
207. Vaidya, Y., Riaz, S. & Dhamoon, A. S. Left Ventricular Assist Devices. in StatPearls (StatPearls Publishing, 2021).
208. Dubbel Dutch. https://dubbeldutchdenver.com/pln-letter-to-inform-community-in-north-america.

209. Ponikowski, P. et al. 2016 ESC Guidelines for the diagnosis and treatment of acute and chronic heart failure: The Task Force for the diagnosis and treatment of acute and chronic heart failure of the European Society of Cardiology (ESC)Developed with the special contribution of the Heart Failure Association (HFA) of the ESC. Eur. Heart J. 37, (2016).

210. Abbasi, M., Negarandeh, R., Norouzadeh, R. & Mogadam, A. R. S. The Challenges of Living With an Implantable Cardioverter Defibrillator: A Qualitative Study. Iran. Red Crescent Med. J. 18, (2016).

211. van der Zwaag, P. A. et al. Phospholamban R14del mutation in patients diagnosed with dilated cardiomyopathy or arrhythmogenic right ventricular cardiomyopathy: evidence supporting the concept of arrhythmogenic cardiomyopathy. Eur. J. Heart Fail. 14, 1199–1207 (2012).

212. Bleijendaal, H. et al. Computer versus cardiologist: Is a machine learning algorithm able to outperform an expert in diagnosing a phospholamban p.Arg14del mutation on the electrocardiogram? Heart Rhythm 18, 79–87 (2021).

213. Felix, S. E. A. et al. The role of long-term mechanical circulatory support in patients with advanced heart failure. Neth. Heart J. 28, 115–121 (2020).

214. van der Zwaag, P. A. et al. Phospholamban R14del mutation in patients diagnosed with dilated cardiomyopathy or arrhythmogenic right ventricular cardiomyopathy: evidence supporting the concept of arrhythmogenic cardiomyopathy. Eur. J. Heart Fail. 14, 1199–1207 (2012).

215. Liu, B. et al. Conditional Up-Regulation of SERCA2a Exacerbates RyR2-Dependent Ventricular and Atrial Arrhythmias. Int. J. Mol. Sci. 21, (2020).

216. Kamel, S. M. et al. Istaroxime treatment ameliorates calcium dysregulation in a zebrafish model of phospholamban R14del cardiomyopathy. Nat. Commun. 12, 7151 (2021).

217. Badone, B. et al. Characterization of the PLN p.Arg14del Mutation in Human Induced Pluripotent Stem Cell-Derived Cardiomyocytes. Int. J. Mol. Sci. 22, (2021).

218. Junho, C. V. C., Caio-Silva, W., Trentin-Sonoda, M. & Carneiro-Ramos, M. S. An Overview of the Role of Calcium/Calmodulin-Dependent Protein Kinase in Cardiorenal Syndrome. Front. Physiol. 0, (2020).

219. Haghighi, K. et al. Impaired Right Ventricular Calcium Cycling Is an Early Risk Factor in R14del-Phospholamban Arrhythmias. J Pers Med 11, (2021).

220. Cuello, F. et al. Impairment of the ER/mitochondria compartment in human cardiomyocytes with PLN p.Arg14del mutation. EMBO Mol. Med. 13, e13074 (2021).

221. Cuello, F. et al. Impairment of the ER/mitochondria compartment in human cardiomyocytes with PLN p.Arg14del mutation. EMBO Mol. Med. 13, e13074 (2021).

222. Eijgenraam, T. R. et al. The phospholamban p.(Arg14del) pathogenic variant leads to cardiomyopathy with heart failure and is unreponsive to standard heart failure therapy. Sci. Rep. 10, 9819 (2020).

223. Eijgenraam, T. R. et al. The phospholamban p.(Arg14del) pathogenic variant leads to cardiomyopathy with heart failure and is unreponsive to standard heart failure therapy. Sci. Rep. 10, 9819 (2020).

224. Te Rijdt, W. P. et al. Rationale and design of the PHOspholamban RElated CArdiomyopathy intervention STudy (i-PHORECAST). Neth. Heart J. (2021) doi:10.1007/s12471-021-01584-5.

225. Feyen, D. A. M. et al. Unfolded Protein Response as a Compensatory Mechanism and Potential Therapeutic Target in PLN R14del Cardiomyopathy. Circulation (2021) doi:10.1161/CIRCULATIONAHA.120.049844.

226. Stillitano, F. et al. Genomic correction of familial cardiomyopathy in human engineered cardiac tissues. Eur. Heart J. 37, 3282–3284 (2016).

227. Karakikes, I. et al. Correction of human phospholamban R14del mutation associated with cardiomyopathy using targeted nucleases and combination therapy. Nat. Commun. 6, 6955 (2015).

228. Stroik, D. R. et al. Viral expression of a SERCA2a-activating PLB mutant improves calcium cycling and synchronicity in dilated cardiomyopathic hiPSC-CMs. J. Mol. Cell. Cardiol. 138, 59–65 (2020).

229. Karakikes, I. et al. Correction of human phospholamban R14del mutation associated with cardiomyopathy using targeted nucleases and combination therapy. Nat. Commun. 6, 6955 (2015).

230. Haghighi, K. et al. Human phospholamban null results in lethal dilated cardiomyopathy revealing a critical difference between mouse and human. J. Clin. Invest. 111, 869–876 (2003).

231. Grote Beverborg, N. et al. Phospholamban antisense oligonucleotides improve cardiac function in murine cardiomyopathy. Nat. Commun. 12, 5180 (2021).

232. Dave, J. et al. Gene editing reverses arrhythmia susceptibility in humanized PLN-R14del mice: modeling a European cardiomyopathy with global impact. Cardiovasc. Res. (2022) doi:10.1093/cvr/cvac021.

233. Luo, M. & Anderson, M. E. Mechanisms of altered Ca2+ handling in heart failure. Circ. Res. 113, 690–708 (2013).

234. van der Zwaag, P. A. et al. Phospholamban R14del mutation in patients diagnosed with dilated cardiomyopathy or arrhythmogenic right ventricular cardiomyopathy: evidence supporting the concept of arrhythmogenic cardiomyopathy. Eur. J. Heart Fail. 14, 1199–1207 (2012).

235. Te Rijdt, W. P. et al. Phospholamban immunostaining is a highly sensitive and specific method for diagnosing phospholamban p.Arg14del cardiomyopathy. Cardiovasc. Pathol. 30, 23–26 (2017).

236. van der Klooster, Z. J. et al. P62-positive aggregates are homogenously distributed in the myocardium and associated with the type of mutation in genetic cardiomyopathy. J. Cell. Mol. Med. 25, (2021).

237. Feyen, D. A. M. et al. Unfolded Protein Response as a Compensatory Mechanism and Potential Therapeutic Target in PLN R14del Cardiomyopathy. Circulation (2021) doi:10.1161/CIRCULATIONAHA.120.049844.

238. van Rijsingen, I. A. W. et al. Outcome in phospholamban R14del carriers: results of a large multicentre cohort study. Circ. Cardiovasc. Genet. 7, 455–465 (2014).

239. Montag, J. et al. Intrinsic MYH7 expression regulation contributes to tissue level allelic imbalance in hypertrophic cardiomyopathy. J. Muscle Res. Cell Motil. 38, (2017).

240. Battle, A., Brown, C. D., Engelhardt, B. E. & Montgomery, S. B. Genetic effects on gene expression across human tissues. Nature 550, (2017).

241. Pinter, S. F. et al. Allelic Imbalance Is a Prevalent and Tissue-Specific Feature of the Mouse Transcriptome. Genetics 200, (2015).

242. Website. Eerste Nederlandse donorbank voor harten opent volgende week zijn deuren. Stichting PLN http://plnheart.org/eerste-nederlandse-donorbank-voor-harten-opent-volgende-week-zijn-deuren/ (2020).

243. Kamel, S. M. et al. Istaroxime treatment ameliorates calcium dysregulation in a zebrafish model of phospholamban R14del cardiomyopathy. Nat. Commun. 12, 7151 (2021).

244. Badone, B. et al. Characterization of the PLN p.Arg14del Mutation in Human Induced Pluripotent Stem Cell-Derived Cardiomyocytes. Int. J. Mol. Sci. 22, (2021).

245. Projecten. NWO https://www.nwo.nl/onderzoeksprogrammas/open-technologieprogramma/projecten.

246. From pluripotent stem cells to prime editing gene therapy for inherited cardiomyopathies. ZonMw Projects https://projecten.zonmw.nl/nl/project/pluripotent-stem-cells-prime-editing-gene-therapy-inherited-cardiomyopathies.

247. ^ES. EU Horizon grant for NLHI coordinated consortium Geremy. Netherlands Heart Institute https://heart-institute.nl/eu-horizon-grant-for-nlhi-coordinated-consortium-geremy/ (2023).

248. Feyen, D. A. M. et al. Unfolded Protein Response as a Compensatory Mechanism and Potential Therapeutic Target in PLN R14del Cardiomyopathy. Circulation (2021) doi:10.1161/CIRCULATIONAHA.120.049844.

249. Menzel, J. et al. 14-3-3 binding creates a memory of kinase action by stabilizing the modified state of phospholamban. Sci. Signal. 13, (2020).

250. Cuello, F. et al. Impairment of the ER/mitochondria compartment in human cardiomyocytes with PLN p.Arg14del mutation. EMBO Mol. Med. 13, e13074 (2021).

251. Clauss, S. et al. Characterization of a porcine model of atrial arrhythmogenicity in the context of ischaemic heart failure. PLoS One 15, (2020).

SUPPLEMENTARY FILE

Systematic review output per search term

Search terms, in title and/or abstract: PLN R14del; Phospholamban R14del; p.Arg14del; PLN Arg14del; Phospholamban Arg14del; R14del. Databases used: pubmed.gov, bioRxiv, ResearchSquare.

Total results: 82

Final literature search day: 28-12-2023

Excluded: one author corrections (nr. 50).

Papers used for manuscript: 81

1:	van der Voorn SM, van Drie E, Proost V, Dimitrova K, Netherlands Acm/Pln Registry, Ernst RF, James CA, Tichnell C, Murray B, Calkins H, Saguner AM, Duru F, Ellinor PT, Bezzina CR, Jurgens SJ, van Tintelen JP, van Veen TAB. Lack of Evidence for the Role of the p.(Ser96Ala) Polymorphism in Histidine-Rich Calcium Binding Protein as a Secondary Hit in Cardiomyopathies. Int J Mol Sci. 2023 Nov 3;24(21):15931. doi: 10.3390/ijms242115931. PMID: 37958923; PMCID: PMC10648441.
2:	Stege NM, Eijgenraam TR, Oliveira Nunes Teixeira V, Feringa AM, Schouten EM, Kuster DWD, van der Velden J, Wolters AHG, Giepmans BNG, Makarewich CA, Bassel- Duby R, Olson EN, de Boer RA, Silljé HHW. DWORF Extends Life Span in a
	PLN-R14del Cardiomyopathy Mouse Model by Reducing Abnormal Sarcoplasmic Reticulum Clusters. Circ Res. 2023 Dec 8;133(12):1006-1021. doi: 10.1161/CIRCRESAHA.123.323304. Epub 2023 Nov 13. PMID: 37955153; PMCID:PMC10699510.
3:	Balducci V, Scardigli F, Harakalova M, Peter van Tintelen J, Doevendans PA, Costa KD, Turnbull IC, P G Sluijter J, Stillitano F. Generation and characterization of novel human induced pluripotent stem cell (iPSC) lines originating from five asymptomatic individuals carrying the PLN-R14del pathogenic variant and a non-carrier relative. Stem Cell Res. 2023 Sep 21;72:103208. doi: 10.1016/j.scr.2023.103208. Epub ahead of print. PMID:37748331.
4:	Taha K, van de Leur RR, Vessies M, Mast TP, Cramer MJ, Cauwenberghs N, Verstraelen TE, de Brouwer R, Doevendans PA, Wilde A, Asselbergs FW, van den Berg MP, D'hooge J, Kuznetsova T, Teske AJ, van Es R. Deep neural network-based clustering of deformation curves reveals novel disease features in PLN pathogenic variant carriers. Int J Cardiovasc Imaging. 2023 Aug 11. doi: 10.1007/s10554-023-02924-9. Epub ahead of print. PMID:37566298.
5:	de Boer RA. Should we offer preventive treatment to all carriers of PLN p.(Arg14del) variant? : Pro: Provide pre-emptive treatment to asymptomatic carriers. Neth Heart J. 2023 Aug;31(7-8):287-288. doi:10.1007/s12471-023-01793-0. Epub 2023 Jul 26. PMID: 37493902; PMCID:PMC10400733.
6:	Doevendans PA. Should we offer preventive treatment to all carriers of PLN p.(Arg14del) variant? : Con: Do no harm to asymptomatic carriers. Neth Heart J. 2023 Aug;31(7-8):289-290. doi: 10.1007/s12471-023-01794-z. Epub 2023 Jul 25. PMID: 37491506; PMCID: PMC10400497.
7:	van Lint FHM, Hassanzada F, Verstraelen TE, Wang W, Bosman LP, van der Zwaag PA, Oomen T, Calkins H, Murray B, Tichnell C, Beuren TMA, Asselbergs FW, Houweling A, van den Berg MP, Wilde AAM, James CA, van Tintelen JP. Exercise does not influence development of phenotype in PLN p.(Arg14del) cardiomyopathy. Neth Heart J. 2023 Aug;31(7-8):291-299. doi: 10.1007/s12471-023-01800-4. Epub 2023 Jul 20. PMID: 37474840; PMCID: PMC10400740.
8:	Zanotti S, Ripolone M, Napoli L, Velardo D, Salani S, Ciscato P, Priori S, Kukavica D, Mazzanti A, Diamanti L, Vegezzi E, Moggio M, Corti S, Comi G, Sciacco M. Characterization of Skeletal Muscle Biopsy and Derived Myoblasts in a Patient Carrying Arg14del Mutation in Phospholamban Gene. Cells. 2023 May 17;12(10):1405. doi: 10.3390/cells12101405. PMID: 37408239; PMCID: PMC10216566.

9:	Cleary SR, Teng ACT, Kongmeneck AD, Fang X, Phillips TA, Cho EE, Kekenes-Huskey P, Gramolini AO, Robia SL. Dilated cardiomyopathy variant R14del increases phospholamban pentamer stability, blunting dynamic regulation of cardiac calcium handling. bioRxiv [Preprint]. 2023 May 28:2023.05.26.542463. doi: 10.1101/2023.05.26.542463. PMID: 37292897; PMCID: PMC10245957.
10:	de Brouwer R, Te Rijdt WP, Hoorntje ET, Amin A, Asselbergs FW, Cox MGPJ, van der Heijden JF, Hillege H, Karper JC, Mahmoud B, van der Meer P, Oomen A, Te Riele ASJM, Silljé HHW, Tan HL, van Tintelen JP, van Veldhuisen DJ, Westenbrink BD, Wiesfeld ACP, Willems TP, van der Zwaag PA, Wilde AAM, de Boer RA, van den Berg MP. A randomized controlled trial of eplerenone in asymptomatic phospholamban p.Arg14del carriers. Eur Heart J. 2023 May 20:ehad292. doi:10.1093/eurheartj/ehad292. Epub ahead of print. PMID: 37210081.
11:	Maniezzi, C., Eskandr, M., Florindi, C., Ferrandi, M., Barassi, P., Sacco, E., Pasquale, V., Maione, A. S., Pompilio, G., Oliveira Nunes Teixeira, V., de Boer, R. A., Silljé, H. H., Lodola, F., & Zaza, A. Early consequences of the phospholamban mutation PLN-R14del+/- in a transgenic mouse model. bioRxiv, 2023.04.05.535536. https://doi.org/10.1101/2023.04.05.535536.
12:	Vafiadaki E, Glijnis PC, Doevendans PA, Kranias EG, Sanoudou D. Phospholamban R14del disease: The past, the present and the future. Front Cardiovasc Med. 2023 Apr 18;10:1162205. doi: 10.3389/fcvm.2023.1162205. PMID: 37144056; PMCID:PMC10151546.
13:	van der Meer P, van Rooij E, Doevendans PA. Cardiomyopathie door mutatie in het phospholamban-gen [Cardiomyopathy due to a mutation in the phospholamban gene: a high-impact genetic abnormality]. Ned Tijdschr Geneeskd. 2023 Apr 19;167:D7274. Dutch. PMID: 37078560.
14:	Kumar M, Haghighi K, Koch S, Rubinstein J, Stillitano F, Hajjar RJ, Kranias EG, Sadayappan S. Myofilament Alterations Associated with Human R14del-Phospholamban Cardiomyopathy. Int J Mol Sci. 2023 Jan 31;24(3):2675. doi:10.3390/ijms24032675. PMID: 36768995; PMCID: PMC9917359.
15:	Aboumsallem JP, Shi C, De Wit S, Markousis-Mavrogenis G, Bracun V, Eijgenraam TR, Hoes MF, Meijers WC, Screever EM, Schouten ME, Voors AA, Silljé HHW, De Boer RA. Multi-omics analyses identify molecular signatures with prognostic values in different heart failure aetiologies. J Mol Cell Cardiol. 2023 Feb;175:13-28. doi: 10.1016/j.yjmcc.2022.12.001. Epub 2022 Dec 6. PMID:36493852.
16:	Rogalska ME, Vafiadaki E, Erpapazoglou Z, Haghighi K, Green L, Mantzoros CS, Hajjar RJ, Tranter M, Karakikes I, Kranias EG, Stillitano F, Kafasla P, Sanoudou D. Isoform changes of action potential regulators in the ventricles of arrhythmogenic phospholamban-R14del humanized mouse hearts. Metabolism. 2023 Jan;138:155344. doi: 10.1016/j.metabol.2022.155344. Epub 2022 Nov 12. PMID:36375644.
17.	Jiayi Pei, Renee G.C. Maas, Karen R. Gaar-Humphreys, Johannes M.I.H. Gho, Emilia Nagyova, Christian J.B. Snijders Blok, Iris van Adrichem, René van Es, Shahrzad Sepehrkhouy, Dries Feyen, Noortje A. M. van den Dungen, Nico Lansu, Jorg Calis, Niels van de Kaaij, Nicolaas de Jonge, Linda W. van Laake, Anneline S.J.M. te Riele, Manon M. Huibers, Roel A. de Weger, Marianne C. Verhaar, J. Peter van Tintelen, Frédéric Maxime Vaz, Boudewijn Burgering, Alain van Mil, Jan W. Buikema, Aryan Vink, Ioannis Karakikes, Mark Mercola, Pieter A. Doevendans, Joost P. G. Sluijter, Frank G. van Steenbeek, Caroline Cheng, Michal Mokry, Folkert W. Asselbergs, Magdalena Harakalova. Transcriptional regulation profiling reveals PPARA-mediated fatty acid oxidation as a novel therapeutic target in phospholamban R14del cardiomyopathy, 28 October 2022, PREPRINT (Version 1) available at Research Square [https://doi.org/10.21203/rs.3.rs-1902254/v1]
18:	Vafiadaki E, Haghighi K, Arvanitis DA, Kranias EG, Sanoudou D. Aberrant PLN-R14del Protein Interactions Intensify SERCA2a Inhibition, Driving Impaired Ca²⁺ Handling and Arrhythmogenesis. Int J Mol Sci. 2022 Jun 22;23(13):6947. doi: 10.3390/ijms23136947. PMID: 35805951; PMCID: PMC9266971.
19:	Vera CD, Manhas A, Shenoy SP, Wheeler MT, Sallam K, Wu JC. Generation of two induced pluripotent stem cell lines carrying the phospholamban R14del mutation for modeling ARVD/C. Stem Cell Res. 2022 Aug;63:102834. doi:10.1016/j.scr.2022.102834. Epub 2022 Jun 6. PMID: 35700631; PMCID: PMC9476586.
20:	Deiman FE, Bomer N, van der Meer P, Grote Beverborg N. Review: Precision Medicine Approaches for Genetic Cardiomyopathy: Targeting Phospholamban R14del. Curr Heart Fail Rep. 2022 Aug;19(4):170-179. doi: 10.1007/s11897-022-00558-x.Epub 2022 Jun 14. PMID: 35699837; PMCID: PMC9329159.

21: Eijgenraam TR, Stege NM, Oliveira Nunes Teixeira V, de Brouwer R, Schouten EM, Grote Beverborg N, Sun L, Später D, Knöll R, Hansson KM, Amilon C, Janzén D, Yeh ST, Mullick AE, van der Meer P, de Boer RA, Silljé HHW. Antisense Therapy Attenuates Phospholamban p.(Arg14del) Cardiomyopathy in Mice and Reverses Protein Aggregation. Int J Mol Sci. 2022 Feb 22;23(5):2427. doi: 10.3390/ijms23052427. PMID: 35269571; PMCID: PMC8909937.

22. Monda, E.; Blasi, E.; De Pasquale, A.; Di Vilio, A.; Amodio, F.; Caiazza, M.; Diana, G.; Lioncino, M.; Perna, A.; Verrillo, F.; et al. Clinical and Molecular Characteristics of Patients with PLN R14del Cardiomyopathy: State-of-the-Art Review. Cardiogenetics 2022, 12, 112-121. https://doi.org/10.3390/cardiogenetics12010012

23: Mittal N, Dave J, Harakalova M, van Tintelen JP, Asselbergs FW, Doevendans PA, Costa KD, Turnbull IC, Stillitano F. Generation of human induced pluripotent stem cell (iPSC) lines derived from five patients carrying the pathogenic phospholamban-R14del (PLN-R14del) variant and three non-carrier family members. Stem Cell Res. 2022 Apr;60:102737. doi: 10.1016/j.scr.2022.102737. Epub 2022 Mar 1. PMID: 35247838.

24: Dave J, Raad N, Mittal N, Zhang L, Fargnoli A, Oh JG, Savoia ME, Hansen J, Fava M, Yin X, Theofilatos K, Ceholski D, Kohlbrenner E, Jeong D, Wills L, Nonnenmacher M, Haghighi K, Costa KD, Turnbull IC, Mayr M, Cai CL, Kranias EG, Akar FG, Hajjar RJ, Stillitano F. Gene editing reverses arrhythmia susceptibility in humanized PLN-R14del mice: modeling a European cardiomyopathy with global impact. Cardiovasc Res. 2022 Feb 22:cvac021. doi:10.1093/cvr/cvac021. Epub ahead of print. PMID: 35191471.

25: van der Voorn SM, Bourfiss M, Te Riele ASJM, Taha K, Vos MA, de Brouwer R, Verstraelen TE, de Boer RA, Remme CA, van Veen TAB. Exploring the Correlation Between Fibrosis Biomarkers and Clinical Disease Severity in PLN p.Arg14del Patients. Front Cardiovasc Med. 2022 Jan 13;8:802998. doi: 10.3389/fcvm.2021.802998. PMID: 35097021; PMCID: PMC8793805.

26: Driessen HE, van der Voorn SM, Bourfiss M, van Lint FHM, Mirzad F, Onsri LE, Vos MA, van Veen TAB. Buccal Mucosa Cells as a Potential Diagnostic Tool to Study Onset and Progression of Arrhythmogenic Cardiomyopathy. Int J Mol Sci.2021 Dec 21;23(1):57. doi: 10.3390/ijms23010057. PMID: 35008484; PMCID: PMC8744793.

27: Badone B, Ronchi C, Lodola F, Knaust AE, Hansen A, Eschenhagen T, Zaza A. Characterization of the PLN p.Arg14del Mutation in Human Induced Pluripotent Stem Cell-Derived Cardiomyocytes. Int J Mol Sci. 2021 Dec 16;22(24):13500. doi:10.3390/ijms222413500. PMID: 34948294; PMCID: PMC8709382.

28: de Boer RA, Heymans S, Backs J, Carrier L, Coats AJS, Dimmeler S, Eschenhagen T, Filippatos G, Gepstein L, Hulot JS, Knöll R, Kupatt C, Linke WA, Seidman CE, Tocchetti CG, van der Velden J, Walsh R, Seferovic PM, Thum T. Targeted therapies in genetic dilated and hypertrophic cardiomyopathies: from molecular mechanisms to therapeutic targets. A position paper from the Heart Failure Association (HFA) and the Working Group on Myocardial Function of the European Society of Cardiology (ESC). Eur J Heart Fail. 2022 Mar;24(3):406-420. doi: 10.1002/ejhf.2414. Epub 2022 Jan 14. PMID: 34969177; PMCID: PMC9305112.

29: Tabata T, Kuramoto Y, Ohtani T, Miyawaki H, Miyashita Y, Sera F, Kioka H, Higo S, Asano Y, Hikoso S, Sakata Y. Phospholamban p.Arg14del Cardiomyopathy: A Japanese Case Series. Intern Med. 2022 Jul 1;61(13):1987-1993. doi:10.2169/internalmedicine.8594-21. Epub 2021 Dec 18. PMID: 34924461; PMCID:PMC9334245.

30: Kamel SM, van Opbergen CJM, Koopman CD, Verkerk AO, Boukens BJD, de Jonge B, Onderwater YL, van Alebeek E, Chocron S, Polidoro Pontalti C, Weuring WJ, Vos MA, de Boer TP, van Veen TAB, Bakkers J. Istaroxime treatment ameliorates calcium dysregulation in a zebrafish model of phospholamban R14del cardiomyopathy. Nat Commun. 2021 Dec 9;12(1):7151. doi: 10.1038/s41467-021-27461-8. PMID: 34887420; PMCID: PMC8660846.

31: de Brouwer R, Meems LMG, Verstraelen TE, Mahmoud B, Proost V, Wilde AAM, Bosman LP, van Drie E, van der Zwaag PA, van Tintelen JP, Houweling AC, van den Berg MP, de Boer RA. Sex-specific aspects of phospholamban cardiomyopathy: The importance and prognostic value of low-voltage electrocardiograms. Heart Rhythm. 2022 Mar;19(3):427-434. doi: 10.1016/j.hrthm.2021.11.009. Epub 2021 Nov 9. PMID:34767988.

32: van der Klooster ZJ, Sepehrkhouy S, Dooijes D, Te Rijdt WP, Schuiringa FSAM, Lingeman J, van Tintelen JP, Harakalova M, Goldschmeding R, Suurmeijer AJH, Asselbergs FW, Vink A. P62-positive aggregates are homogenously distributed in the myocardium and associated with the type of mutation in genetic cardiomyopathy. J Cell Mol Med. 2021 Mar;25(6):3160-3166. doi: 10.1111/jcmm.16388. Epub 2021 Feb 18. PMID: 33605084; PMCID: PMC7957157.

33: Eijgenraam TR, Boogerd CJ, Stege NM, Oliveira Nunes Teixeira V, Dokter MM, Schmidt LE, Yin X, Theofilatos K, Mayr M, van der Meer P, van Rooij E, van der Velden J, Silljé HHW, de Boer RA. Protein Aggregation Is an Early Manifestation of Phospholamban p.(Arg14del)-Related Cardiomyopathy: Development of PLN-R14del-Related Cardiomyopathy. Circ Heart Fail. 2021 Nov;14(11):e008532. doi:10.1161/CIRCHEARTFAILURE.121.008532. Epub 2021 Sep 30. PMID: 34587756; PMCID:PMC8589082.

34: Taha K, Verstraelen TE, de Brouwer R, de Bruin-Bon RHACM, Cramer MJ, Te Rijdt WP, Bouma BJ, de Boer RA, Doevendans PA, Asselbergs FW, Wilde AAM, van den Berg MP, Teske AJ. Optimal echocardiographic assessment of myocardial dysfunction for arrhythmic risk stratification in phospholamban mutation carriers. Eur Heart J Cardiovasc Imaging. 2021 Sep 13:jeab178. doi: 1093/ehjci/jeab178. Epub ahead of print. PMID: 34516619.

35: Grote Beverborg N, Später D, Knöll R, Hidalgo A, Yeh ST, Elbeck Z, Silljé HHW, Eijgenraam TR, Siga H, Zurek M, Palmér M, Pehrsson S, Albery T, Bomer N, Hoes MF, Boogerd CJ, Frisk M, van Rooij E, Damle S, Louch WE, Wang QD, Fritsche-Danielson R, Chien KR, Hansson KM, Mullick AE, de Boer RA, van der Meer P. Phospholamban antisense oligonucleotides improve cardiac function in murine cardiomyopathy. Nat Commun. 2021 Aug 30;12(1):5180. doi:10.1038/s41467-021-25439-0. PMID: 34462437; PMCID: PMC8405807.

36: Koch D, Alexandrovich A, Funk F, Kho AL, Schmitt JP, Gautel M. Molecular noise filtering in the β-adrenergic signaling network by phospholamban pentamers. Cell Rep. 2021 Jul 27;36(4):109448. doi:10.1016/j.celrep.2021.109448. PMID: 34320358; PMCID: PMC8333238.

37: Haghighi K, Gardner G, Vafiadaki E, Kumar M, Green LC, Ma J, Crocker JS, Koch S, Arvanitis DA, Bidwell P, Rubinstein J, van de Leur R, Doevendans PA, Akar FG, Tranter M, Wang HS, Sadayappan S, DeMazumder D, Sanoudou D, Hajjar RJ, Stillitano F, Kranias EG. Impaired Right Ventricular Calcium Cycling Is an Early Risk Factor in R14del-Phospholamban Arrhythmias. J Pers Med. 2021 Jun 3;11(6):502. doi: 10.3390/jpm11060502. PMID: 34204946; PMCID: PMC8226909.

38: Te Rijdt WP, Hoorntje ET, de Brouwer R, Oomen A, Amin A, van der Heijden JF, Karper JC, Westenbrink BD, Silljé HHW, Te Riele ASJM, Wiesfeld ACP, van Gelder IC, Willems TP, van der Zwaag PA, van Tintelen JP, Hillege JH, Tan HL, van Veldhuisen DJ, Asselbergs FW, de Boer RA, Wilde AAM, van den Berg MP. Rationale and design of the PHOspholamban RElated CArdiomyopathy intervention Study (i-PHORECAST). Neth Heart J. 2022 Feb;30(2):84-95. doi:10.1007/s12471-021-01584-5. Epub 2021 Jun 18. PMID: 34143416; PMCID: PMC8799798.

39: Verstraelen TE, van Lint FHM, Bosman LP, de Brouwer R, Proost VM, Abeln BGS, Taha K, Zwinderman AH, Dickhoff C, Oomen T, Schoonderwoerd BA, Kimman GP, Houweling AC, Gimeno-Blanes JR, Asselbergs FW, van der Zwaag PA, de Boer RA, van den Berg MP, van Tintelen JP, Wilde AAM. Prediction of ventricular arrhythmia in phospholamban p.Arg14del mutation carriers-reaching the frontiers of individual risk prediction. Eur Heart J. 2021 Jul 31;42(29):2842-2850. doi:10.1093/eurheartj/ehab294. PMID: 34113975; PMCID: PMC8325776.

40: Raad N, Bittihn P, Cacheux M, Jeong D, Ilkan Z, Ceholski D, Kohlbrenner E, Zhang L, Cai CL, Kranias EG, Hajjar RJ, Stillitano F, Akar FG. Arrhythmia Mechanism and Dynamics in a Humanized Mouse Model of Inherited Cardiomyopathy Caused by Phospholamban R14del Mutation. Circulation. 2021 Aug 10;144(6):441-454. doi: 10.1161/CIRCULATIONAHA.119.043502. Epub 2021 May 24. PMID: 34024116; PMCID: PMC8456417.

41: Cuello F, Knaust AE, Saleem U, Loos M, Raabe J, Mosqueira D, Laufer S, Schweizer M, van der Kraak P, Flenner F, Ulmer BM, Braren I, Yin X, Theofilatos K, Ruiz-Orera J, Patone G, Klampe B, Schulze T, Piasecki A, Pinto Y, Vink A, Hübner N, Harding S, Mayr M, Denning C, Eschenhagen T, Hansen A. Impairment of the ER/mitochondria compartment in human cardiomyocytes with PLN p.Arg14del mutation. EMBO Mol Med. 2021 Jun 7;13(6):e13074. doi: 10.15252/emmm.202013074. Epub 2021 May 16. PMID: 33998164; PMCID: PMC8185541.

42: Feyen DAM, Perea-Gil I, Maas RGC, Harakalova M, Gavidia AA, Arthur Ataam J, Wu TH, Vink A, Pei J, Vadgama N, Suurmeijer AJ, Te Rijdt WP, Vu M, Amatya PL, Prado M, Zhang Y, Dunkenberger L, Sluijter JPG, Sallam K, Asselbergs FW, Mercola M, Karakikes I. Unfolded Protein Response as a Compensatory Mechanism and Potential Therapeutic Target in PLN R14del Cardiomyopathy. Circulation. 2021 Aug 3;144(5):382-392. doi: 10.1161/CIRCULATIONAHA.120.049844. Epub 2021 Apr 30. PMID: 33928785; PMCID: PMC8667423.

43: Nguyen TV, Tran Vu MT, Do TNP, Tran THN, Do TH, Nguyen TMH, Tran Huynh BN, Le LA, Nguyen Pham NT, Nguyen TDA, Nguyen TMN, Le NHP, Pham Nguyen V, Ho Huynh TD. Genetic Determinants and Genotype-Phenotype Correlations in Vietnamese Patients With Dilated Cardiomyopathy. Circ J. 2021 Aug 25;85(9):1469-1478. doi: 10.1253/circj.CJ-21-0077. Epub 2021 May 20. PMID: 34011823.

44: Lopes RR, Bleijendaal H, Ramos LA, Verstraelen TE, Amin AS, Wilde AAM, Pinto YM, de Mol BAJM, Marquering HA. Improving electrocardiogram-based detection of rare genetic heart disease using transfer learning: An application to phospholamban p.Arg14del mutation carriers. Comput Biol Med. 2021 Apr;131:104262. doi: 10.1016/j.compbiomed.2021.104262. Epub 2021 Feb 11. PMID:33607378.

45: van de Leur RR, Taha K, Bos MN, van der Heijden JF, Gupta D, Cramer MJ, Hassink RJ, van der Harst P, Doevendans PA, Asselbergs FW, van Es R. Discovering and Visualizing Disease-Specific Electrocardiogram Features Using Deep Learning: Proof-of-Concept in Phospholamban Gene Mutation Carriers. Circ Arrhythm Electrophysiol. 2021 Feb;14(2):e009056. doi: 10.1161/CIRCEP.120.009056. Epub 2021 Jan 5. PMID: 33401921; PMCID: PMC7892204.

46: Taha K, Te Rijdt WP, Verstraelen TE, Cramer MJ, de Boer RA, de Bruin-Bon RHACM, Bouma BJ, Asselbergs FW, Wilde AAM, van den Berg MP, Teske AJ. Early Mechanical Alterations in Phospholamban Mutation Carriers: Identifying Subclinical Disease Before Onset of Symptoms. JACC Cardiovasc Imaging. 2021 May;14(5):885-896. doi: 10.1016/j.jcmg.2020.09.030. Epub 2020 Nov 18. Erratum in: JACC Cardiovasc Imaging. 2021 Jul;14(7):1493. PMID: 33221241.

47: Maas R, Pei J, Gaar-Humphreys K, Gho J, Nagyova E, Blok CS, Adrichem Iv, Es Rv, Sepehrkhouy S, Feyen D, Dungen Nvd, Lansu N, Calis J, Kaaij Nvd, de Jonge N, Laake Lv, Riele At, Huibers M, de Weger R, Verhaar MC, Tintelen JPv, Vaz F, Burgering B, Mil Av, Buikema J, Vink A, Karakikes I, Mercola M, Doevendans PA, Sluijter J, Steenbeek Fv, Cheng C, Mokry M, Asselbergs F, Harakalova M. Transcriptional regulation profiling reveals PPARA-mediated fatty acid oxidation as a novel therapeutic target in phospholamban R14del cardiomyopathy. Research Square; 2022. DOI: 10.21203/rs.3.rs-1902254/v1.

48: Jiang X, Xu Y, Sun J, Wang L, Guo X, Chen Y. The phenotypic characteristic observed by cardiac magnetic resonance in a PLN-R14del family. Sci Rep. 2020 Oct 5;10(1):16478. doi: 10.1038/s41598-020-73359-8. PMID: 33020536; PMCID:PMC7536202.

49: Menzel J, Kownatzki-Danger D, Tokar S, Ballone A, Unthan-Fechner K, Kilisch M, Lenz C, Urlaub H, Mori M, Ottmann C, Shattock MJ, Lehnart SE, Schwappach B. 14-3-3 binding creates a memory of kinase action by stabilizing the modified state of phospholamban. Sci Signal. 2020 Sep 1;13(647):eaaz1436. doi: 10.1126/scisignal.aaz1436. PMID: 32873725.

50: Eijgenraam TR, Boukens BJ, Boogerd CJ, Schouten EM, van de Kolk CWA, Stege NM, Te Rijdt WP, Hoorntje ET, van der Zwaag PA, van Rooij E, van Tintelen JP, van den Berg MP, van der Meer P, van der Velden J, Silljé HHW, de Boer RA. Author Correction: The phospholamban p.(Arg14del) pathogenic variant leads to cardiomyopathy with heart failure and is unresponsive to standard heart failure therapy. Sci Rep. 2020 Oct 2;10(1):16710. doi: 10.1038/s41598-020-70780-x. Erratum for: Sci Rep. 2020 Jun 17;10(1):9819. PMID: 33009422; PMCID: PMC7532180.

51: Bleijendaal H, Ramos LA, Lopes RR, Verstraelen TE, Baalman SWE, Oudkerk Pool MD, Tjong FVY, Melgarejo-Meseguer FM, Gimeno-Blanes FJ, Gimeno-Blanes JR, Amin AS, Winter MM, Marquering HA, Kok WEM, Zwinderman AH, Wilde AAM, Pinto YM. Computer versus cardiologist: Is a machine learning algorithm able to outperform an expert in diagnosing a phospholamban p.Arg14del mutation on the electrocardiogram? Heart Rhythm. 2021 Jan;18(1):79-87. doi:10.1016/j.hrthm.2020.08.021. Epub 2020 Sep 8. PMID: 32911053.

52: Eijgenraam TR, Boukens BJ, Boogerd CJ, Schouten EM, van de Kolk CWA, Stege NM, Te Rijdt WP, Hoorntje ET, van der Zwaag PA, van Rooij E, van Tintelen JP, van den Berg MP, van der Meer P, van der Velden J, Silljé HHW, de Boer RA. The phospholamban p.(Arg14del) pathogenic variant leads to cardiomyopathy with heart failure and is unreponsive to standard heart failure therapy. Sci Rep. 2020 Jun 17;10(1):9819. doi: 10.1038/s41598-020-66656-9. Erratum in: Sci Rep. 2020 Oct 2;10(1):16710. PMID: 32555305; PMCID: PMC7300032.

53: Stroik DR, Ceholski DK, Bidwell PA, Mleczko J, Thanel PF, Kamdar F, Autry JM, Cornea RL, Thomas DD. Viral expression of a SERCA2a-activating PLB mutant improves calcium cycling and synchronicity in dilated cardiomyopathic hiPSC-CMs. J Mol Cell Cardiol. 2020 Jan;138:59-65. doi: 10.1016/j.yjmcc.2019.11.147. Epub 2019 Nov 18. PMID: 31751570; PMCID: PMC7035975.

54: Doevendans PA, Glijnis PC, Kranias EG. Leducq Transatlantic Network of Excellence to Cure Phospholamban-Induced Cardiomyopathy (CURE-PLaN). Circ Res. 2019 Sep 13;125(7):720-724. doi: 10.1161/CIRCRESAHA.119.315077. Epub 2019 Sep 12. PMID: 31513489.

55: Cheung CC, Healey JS, Hamilton R, Spears D, Gollob MH, Mellor G, Steinberg C, Sanatani S, Laksman ZW, Krahn AD. Phospholamban cardiomyopathy: a Canadian perspective on a unique population. Neth Heart J. 2019 Apr;27(4):208-213. doi: 1007/s12471-019-1247-0. PMID: 30806910; PMCID: PMC6439019.

56: Te Rijdt WP, Asimaki A, Jongbloed JDH, Hoorntje ET, Lazzarini E, van der Zwaag PA, de Boer RA, van Tintelen JP, Saffitz JE, van den Berg MP, Suurmeijer AJH. Distinct molecular signature of phospholamban p.Arg14del arrhythmogenic cardiomyopathy. Cardiovasc Pathol. 2019 May-Jun;40:2-6. doi: 10.1016/j.carpath.2018.12.006. Epub 2018 Dec 21. PMID: 30763825.

57: Hof IE, van der Heijden JF, Kranias EG, Sanoudou D, de Boer RA, van Tintelen JP, van der Zwaag PA, Doevendans PA. Prevalence and cardiac phenotype of patients with a phospholamban mutation. Neth Heart J. 2019 Feb;27(2):64-69. doi:10.1007/s12471-018-1211-4. PMID: 30547415; PMCID: PMC6352623.

58: Nannenberg EA, van Rijsingen IAW, van der Zwaag PA, van den Berg MP, van Tintelen JP, Tanck MWT, Ackerman MJ, Wilde AAM, Christiaans I. Effect of Ascertainment Bias on Estimates of Patient Mortality in Inherited Cardiac Diseases. Circ Genom Precis Med. 2018 Oct;11(10):e001797. doi: 10.1161/CIRCGEN.117.001797. PMID: 30354299.

59: Te Rijdt WP, Ten Sande JN, Gorter TM, van der Zwaag PA, van Rijsingen IA, Boekholdt SM, van Tintelen JP, van Haelst PL, Planken RN, de Boer RA, Suurmeijer AJH, van Veldhuisen DJ, Wilde AAM, Willems TP, van Dessel PFHM, van den Berg MP.

Myocardial fibrosis as an early feature in phospholamban p.Arg14del mutation carriers: phenotypic insights from cardiovascular magnetic resonance imaging. Eur Heart J Cardiovasc Imaging. 2019 Jan 1;20(1):92-100. doi: 10.1093/ehjci/jey047. PMID: 29635323.

60: Te Rijdt WP, van der Klooster ZJ, Hoorntje ET, Jongbloed JDH, van der Zwaag PA, Asselbergs FW, Dooijes D, de Boer RA, van Tintelen JP, van den Berg MP, Vink A, Suurmeijer AJH. Phospholamban immunostaining is a highly sensitive and specific method for diagnosing phospholamban p.Arg14del cardiomyopathy. Cardiovasc Pathol. 2017 Sep-Oct;30:23-26. doi: 10.1016/j.carpath.2017.05.004. Epub 2017 May 30. PMID: 28759816.

61: Sepehrkhouy S, Gho JMIH, van Es R, Harakalova M, de Jonge N, Dooijes D, van der Smagt JJ, Buijsrogge MP, Hauer RNW, Goldschmeding R, de Weger RA, Asselbergs FW, Vink A. Distinct fibrosis pattern in desmosomal and phospholamban mutation carriers in hereditary cardiomyopathies. Heart Rhythm. 2017 Jul;14(7):1024-1032. doi: 10.1016/j.hrthm.2017.03.034. Epub 2017 Mar 30. PMID: 28365402.

62: van Opbergen CJ, Delmar M, van Veen TA. Potential new mechanisms of pro-arrhythmia in arrhythmogenic cardiomyopathy: focus on calcium sensitive pathways. Neth Heart J. 2017 Mar;25(3):157-169. doi: 10.1007/s12471-017-0946-7. PMID: 28102477; PMCID: PMC5313453.

63: Stillitano F, Turnbull IC, Karakikes I, Nonnenmacher M, Backeris P, Hulot JS, Kranias EG, Hajjar RJ, Costa KD. Genomic correction of familial cardiomyopathy in human engineered cardiac tissues. Eur Heart J. 2016 Nov 14;37(43):3282-3284. doi: 10.1093/eurheartj/ehw307. Epub 2016 Jul 22. PMID:27450564; PMCID: PMC6425468.

64: Te Rijdt WP, van Tintelen JP, Vink A, van der Wal AC, de Boer RA, van den Berg MP, Suurmeijer AJ. Phospholamban p.Arg14del cardiomyopathy is characterized by phospholamban aggregates, aggresomes, and autophagic degradation. Histopathology. 2016 Oct;69(4):542-50. doi: 10.1111/his.12963. Epub 2016 May 12. PMID: 26970417.

65: Milano A, Blom MT, Lodder EM, van Hoeijen DA, Barc J, Koopmann TT, Bardai A, Beekman L, Lichtner P, van den Berg MP, Wilde AA, Bezzina CR, Tan HL. Sudden Cardiac Arrest and Rare Genetic Variants in the Community. Circ Cardiovasc Genet. 2016 Apr;9(2):147-53. doi: 10.1161/CIRCGENETICS.115.001263. Epub 2016 Jan 22. PMID: 26800703.

66: Karakikes I, Stillitano F, Nonnenmacher M, Tzimas C, Sanoudou D, Termglinchan V, Kong CW, Rushing S, Hansen J, Ceholski D, Kolokathis F, Kremastinos D, Katoulis A, Ren L, Cohen N, Gho JMIH, Tsiapras D, Vink A, Wu JC, Asselbergs FW, Li RA, Hulot JS, Kranias EG, Hajjar RJ. Correction of human phospholamban R14del mutation associated with cardiomyopathy using targeted nucleases and combination therapy. Nat Commun. 2015 Apr 29;6:6955. doi:10.1038/ncomms7955. PMID: 25923014; PMCID: PMC4421839.

67: Fish M, Shaboodien G, Kraus S, Sliwa K, Seidman CE, Burke MA, Crotti L, Schwartz PJ, Mayosi BM. Mutation analysis of the phospholamban gene in 315 South Africans with dilated, hypertrophic, peripartum and arrhythmogenic right ventricular cardiomyopathies. Sci Rep. 2016 Feb 26;6:22235. doi: 10.1038/srep22235. Erratum in: Sci Rep. 2016 May 18;6:25863. PMID: 26917049; PMCID: PMC4808831.

68: López-Ayala JM, Boven L, van den Wijngaard A, Peñafiel-Verdú P, van Tintelen JP, Gimeno JR. Phospholamban p.arg14del mutation in a Spanish family with arrhythmogenic cardiomyopathy: evidence for a European founder mutation. Rev Esp Cardiol (Engl Ed). 2015 Apr;68(4):346-9. doi: 10.1016/j.rec.2014.11.012. Epub 2015 Feb 17. PMID: 25700660.

69: Vostrikov VV, Soller KJ, Ha KN, Gopinath T, Veglia G. Effects of naturally occurring arginine 14 deletion on phospholamban conformational dynamics and membrane interactions. Biochim Biophys Acta. 2015 Jan;1848(1 Pt B):315-22. doi:10.1016/j.bbamem.2014.09.007. Epub 2014 Sep 22. PMID: 25251363; PMCID:PMC4258429.

70: Young HS, Ceholski DK, Trieber CA. Deception in simplicity: hereditary phospholamban mutations in dilated cardiomyopathy. Biochem Cell Biol. 2015 Feb;93(1):1-7. doi: 10.1139/bcb-2014-0080. Epub 2014 Dec 1. PMID: 25563649.

71: Bhonsale A, Groeneweg JA, James CA, Dooijes D, Tichnell C, Jongbloed JDH, et al. Impact of genotype on clinical course in arrhythmogenic right ventricular dysplasia/cardiomyopathy-associated mutation carriers. Eur Heart J. 2015 Apr 7;36(14):847–55.

72: van Rijsingen IA, van der Zwaag PA, Groeneweg JA, Nannenberg EA, Jongbloed JD, Zwinderman AH, Pinto YM, Dit Deprez RH, Post JG, Tan HL, de Boer RA, Hauer RN, Christiaans I, van den Berg MP, van Tintelen JP, Wilde AA. Outcome in phospholamban R14del carriers: results of a large multicentre cohort study. Circ Cardiovasc Genet. 2014 Aug;7(4):455-65. doi: 10.1161/CIRCGENETICS.113.000374. Epub 2014 Jun 8. PMID: 24909667.

73: Gho JM, van Es R, Stathonikos N, Harakalova M, te Rijdt WP, Suurmeijer AJ, van der Heijden JF, de Jonge N, Chamuleau SA, de Weger RA, Asselbergs FW, Vink A. High resolution systematic digital histological quantification of cardiac fibrosis and adipose tissue in phospholamban p.Arg14del mutation associated cardiomyopathy. PLoS One. 2014 Apr 14;9(4):e94820. doi:10.1371/journal.pone.0094820. PMID: 24732829; PMCID: PMC3986391.

74: Groeneweg JA, van der Zwaag PA, Olde Nordkamp LR, Bikker H, Jongbloed JD, Jongbloed R, Wiesfeld AC, Cox MG, van der Heijden JF, Atsma DE, de Boer K, Doevendans PA, Vink A, van Veen TA, Dooijes D, van den Berg MP, Wilde AA, van Tintelen JP, Hauer RN. Arrhythmogenic right ventricular dysplasia/cardiomyopathy according to revised 2010 task force criteria with inclusion of non-desmosomal phospholamban mutation carriers. Am J Cardiol. 2013 Oct 15;112(8):1197-206. doi:10.1016/j.amjcard.2013.06.017. Epub 2013 Jul 19. PMID: 23871674.

75: van der Heijden JF, Hassink RJ. The phospholamban p.Arg14del founder mutation in Dutch patients with arrhythmogenic cardiomyopathy. Neth Heart J. 2013 Jun;21(6):284-5. doi: 10.1007/s12471-013-0413-z. PMID: 23595706; PMCID:PMC3661881.

76: van der Zwaag PA, van Rijsingen IA, de Ruiter R, Nannenberg EA, Groeneweg JA, Post JG, Hauer RN, van Gelder IC, van den Berg MP, van der Harst P, Wilde AA, van Tintelen JP. Recurrent and founder mutations in the Netherlands-Phospholamban p.Arg14del mutation causes arrhythmogenic cardiomyopathy. Neth Heart J. 2013 Jun;21(6):286-93. doi: 10.1007/s12471-013-0401-3. PMID: 23568436;PMCID: PMC3661879.

77: van der Zwaag PA, van Rijsingen IA, Asimaki A, Jongbloed JD, van Veldhuisen DJ, Wiesfeld AC, Cox MG, van Lochem LT, de Boer RA, Hofstra RM, Christiaans I, van Spaendonck-Zwarts KY, Lekanne dit Deprez RH, Judge DP, Calkins H, Suurmeijer AJ, Hauer RN, Saffitz JE, Wilde AA, van den Berg MP, van Tintelen JP. Phospholamban R14del mutation in patients diagnosed with dilated cardiomyopathy or arrhythmogenic right ventricular cardiomyopathy: evidence supporting the concept of arrhythmogenic cardiomyopathy. Eur J Heart Fail. 2012 Nov;14(11):1199-207. doi: 10.1093/eurjhf/hfs119. Epub 2012 Jul 20. PMID: 22820313; PMCID: PMC3475434.

78:	Ceholski DK, Trieber CA, Young HS. Hydrophobic imbalance in the cytoplasmic domain of phospholamban is a determinant for lethal dilated cardiomyopathy. J Biol Chem. 2012 May 11;287(20):16521-9. doi: 10.1074/jbc.M112.360859. Epub 2012 Mar 16. PMID: 22427649; PMCID: PMC3351288.
79:	DeWitt MM, MacLeod HM, Soliven B, McNally EM. Phospholamban R14 deletion results in late-onset, mild, hereditary dilated cardiomyopathy. J Am Coll Cardiol. 2006 Oct 3;48(7):1396-8. doi: 10.1016/j.jacc.2006.07.016. Epub 2006 Sep 12. PMID: 17010801.
80:	Haghighi K, Pritchard T, Bossuyt J, Waggoner JR, Yuan Q, Fan GC, Osinska H, Anjak A, Rubinstein J, Robbins J, Bers DM, Kranias EG. The human phospholamban Arg14-deletion mutant localizes to plasma membrane and interacts with the Na/K-ATPase. J Mol Cell Cardiol. 2012 Mar;52(3):773-82. doi: 10.1016/j.yjmcc.2011.11.012. Epub 2011 Dec 1. PMID: 22155237; PMCID: PMC3376549.
81:	Posch MG, Perrot A, Geier C, Boldt LH, Schmidt G, Lehmkuhl HB, Hetzer R, Dietz R, Gutberlet M, Haverkamp W, Ozcelik C. Genetic deletion of arginine 14 in phospholamban causes dilated cardiomyopathy with attenuated electrocardiographic R amplitudes. Heart Rhythm. 2009 Apr;6(4):480-6. doi: 10.1016/j.hrthm.2009.01.016. Epub 2009 Jan 18. PMID: 19324307.
82:	Haghighi K, Kolokathis F, Gramolini AO, Waggoner JR, Pater L, Lynch RA, Fan GC, Tsiapras D, Parekh RR, Dorn GW 2nd, MacLennan DH, Kremastinos DT, Kranias EG. A mutation in the human phospholamban gene, deleting arginine 14, results in lethal, hereditary cardiomyopathy. Proc Natl Acad Sci U S A. 2006 Jan 31;103(5):1388-93. doi: 10.1073/pnas.0510519103. Epub 2006 Jan 23. PMID: 16432188; PMCID: PMC1360586.

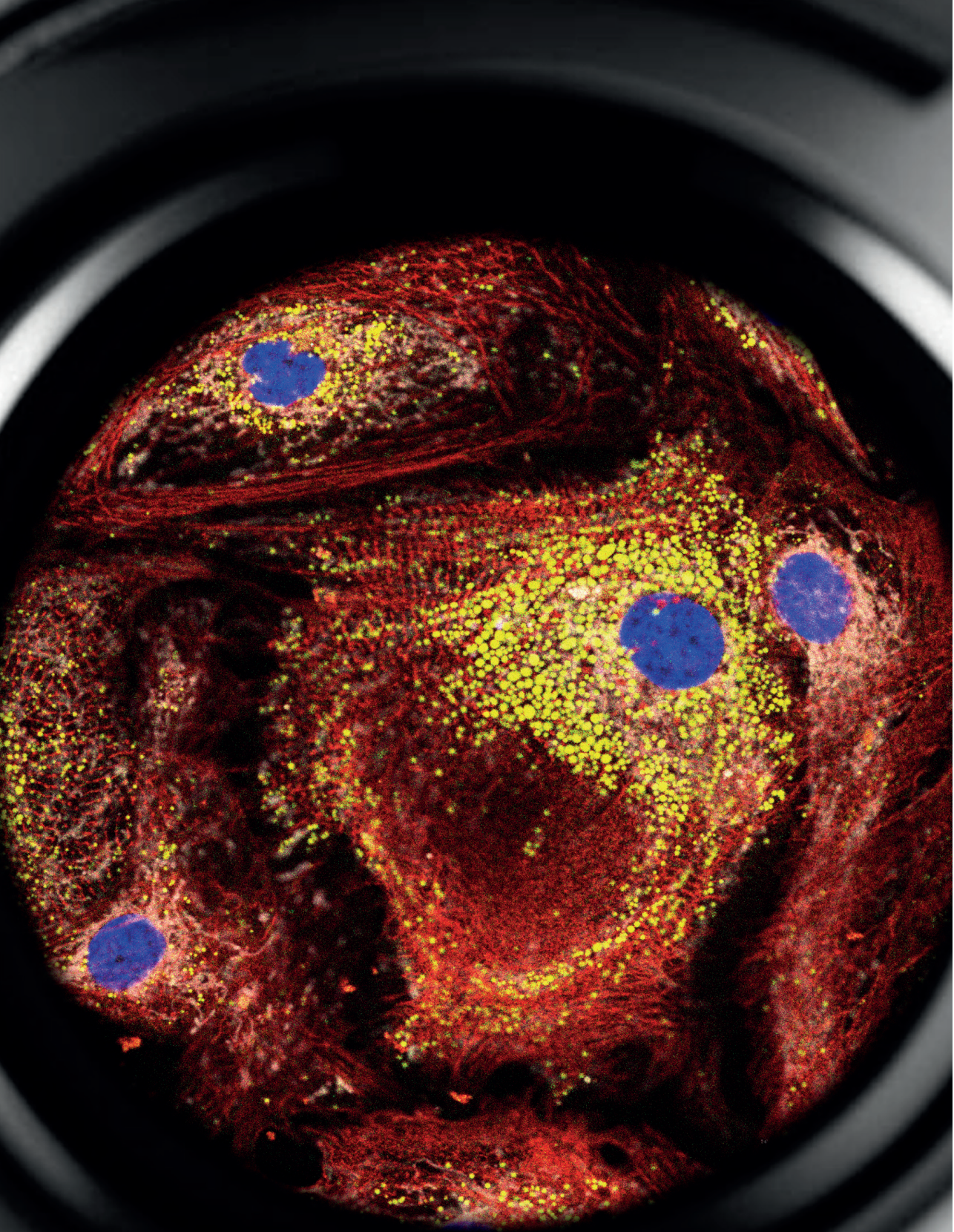

PLN patient-derived hiPSC-CMs stained for sarcomeric troponin and lipid droplets.

Chapter 8

Transcriptional Regulation Profiling Reveals PPARA-Mediated Fatty Acid Oxidation as a Novel Therapeutic Target in Phospholamban R14del Cardiomyopathy

Manuscript in preparation, available on Research Square

Renée G.C. Maas*, Jiayi Pei*, Karen R. Gaar-Humphreys, Johannes M.I.H. Gho, Emilia Nagyova, Christian J.B. Snijders Blok, Iris van Adrichem, René van Es, Shahrzad Sepehrkhouy, Dries Feyen, Noortje A. M. van den Dungen, Nico Lansu, Jorg Calis, Niels van de Kaaij, Nicolaas de Jonge, Linda W. van Laake, Anneline S.J.M. te Riele, Manon M. Huibers, Roel A. de Weger, Marianne C. Verhaar, J. Peter van Tintelen, Frédéric Maxime Vaz, Boudewijn Burgering, Alain van Mil, Jan W. Buikema, Aryan Vink, Ioannis Karakikes, Mark Mercola, Pieter A. Doevendans, Joost P. G. Sluijter, Frank G. van Steenbeek, Caroline Cheng, Michal Mokry§, Folkert W. Asselbergs§, Magdalena Harakalova§

*These authors contributed equally.

§These authors contributed equally.

ABSTRACT

Carriers of the R14del pathogenic variant in the phospholamban (PLN) gene develop severe cardiomyopathy with extracellular adipocyte infiltration and intracellular cardiomyocyte mitochondrial disturbances. However, the basis of this metabolic dysregulation tailoring potential treatment targets is unknown. Here, we present a combined approach of transcriptional regulation analysis in human primary tissue and validation in a unique long-term (160 days) matured human induced pluripotent stem cell-derived cardiomyocyte (hiPSC-CM) model. We demonstrate a dysregulated PPARA-mediated mitochondrial fatty acid oxidation (FAO) signalling in PLN-R14del hearts and hiPSC-CMs. PLN-R14del hiPSC-CMs also displayed a higher preference for glycolysis over FAO and presented limited flexibility in energy substrate switching leading to enhanced lipid droplet storage. By activating PPARA in PLN-R14del hiPSC-CMs using bezafibrate, we observed an improved mitochondrial structure and calcium handling function, further indicating the importance of FAO in the disease and the potential of PPARA agonists as a novel therapeutic strategy in cardiomyopathies.

INTRODUCTION

The R14del (c.40_42delAGA, p.Arg14del) pathogenic variant in the phospholamban (PLN) gene is associated with biventricular cardiomyopathy with a high risk of life-threatening ventricular arrhythmias, often presenting as dilated cardiomyopathy (DCM) or arrhythmogenic cardiomyopathy (ACM).[1,2] It explains a large proportion of Dutch DCM and ACM patients and has also been identified in many other countries.[3,4] PLN is a small phosphoprotein located in the cardiomyocyte sarcoplasmic reticulum and the nuclear membrane and is the major regulator of SERCA2a/ATP2A2 activity and calcium (Ca^{2+}) cycling.[1] We and others have shown that mechanisms within the nuclear, endoplasmic/sarcoplasmic reticulum and mitochondrial network are impaired in PLN-R14del cardiomyopathy.[5–7] Despite these efforts, no effective treatment is available for PLN-R14del variant carriers to prevent disease development. Macroscopically, PLN-R14del hearts show biventricular subepicardial fibrofatty tissue replacement of the myocardium, which is characterised by extensive interstitial fibrosis, adipocyte infiltration, and islands of isolated cardiomyocytes between adipocytes.[8–10] This adipocyte infiltration and fibrosis create an anatomical barrier resulting in the reentry of the electrical impulse and thereby an increased risk of fatal arrhythmias.[11,12] A novel adult zebrafish plna R14del model also displays this adipocyte accumulation and mitochondrial damage in the diseased myocardium,[13] while the available murine models show mitochondrial impairment in the absence of adipocyte accumulation.[14,15] Mitochondrial dysfunction decreases ATP production, thereby opening the sensitive K^+ channels on the sarcolemma channels, which reduces cardiomyocyte excitability and impairs electrical conduction in the heart.[16] Besides altered electrical conduction, metabolic changes also affect cardiac ion channel gating, intracellular calcium handling, and fibrosis formation; all well-known aspects of PLN-R14del pathophysiology.[16] However, the majority of studies have focused on calcium regulation by PLN,[14,17] little effort has been put into elucidating the basis for the metabolic aberrations in human PLN-R14del cardiomyopathy. The presence of myocardial fibrofatty infiltration is accompanied by intracellular cardiomyocyte lipid abnormalities in cardiomyopathies in adults, such as those due to variants in PKP2 and PNPLA2.[18,19] Several forms of childhood cardiomyopathies caused by mutations in the mitochondrial fatty acid oxidation (FAO) pathway genes, such as HADHA, HADHB, CPT2, and ACADVL, also show intracellular cardiomyocyte lipid droplet storage and adipocyte infiltration in the myocardium and other organs.[20] A recent study has linked lipid droplet accumulation in PLN-R14del to the endoplasmic reticulum stress.[6] However, little is known about the transcriptional regulation of this process and what (metabolic) factors influence lipid droplet accumulation. A limited number of lipid droplets, which store unutilized fatty acids (FAs) by mitochondria for energy production, are present in healthy cardiomyocytes. However, an increased lipid droplet deposition is associated with impaired FAO.[21] While FAs are the primary energy source in healthy adult cardiomyocytes, diseased cardiomyocytes switch from FAO to glycolysis for energy production, resembling the energy balance of the fetal heart.[22,23] Yet, this switch to

fetus-like energy management is insufficient to meet adult energy consumption needs and it will disturb the capacity of FAO-based ATP synthesis, leading to further starvation of the heart and disease progression.[24] The impaired lipid metabolism could hereby contribute to the disease progression in PLN-R14del cardiomyocytes and warrant further investigation. Here, we explored the role of transcriptional regulation on disturbed (lipid) metabolism in PLN-R14del cardiomyopathy. We showed that even after the removal of the dominant fibrofatty replacement in the subepicardial layer, the fingerprint of (lipid) metabolic dysregulation was still present in the remaining human myocardium. We further confirmed the disturbed (lipid) metabolism in human-induced pluripotent stem cell-derived cardiomyocytes (hiPSC-CMs) from PLN-R14del carriers. We also identified key transcription factors involved in the affected (lipid) metabolism, which can serve as promising targets for future therapeutic strategies. Furthermore, we examined the preference of energy sources and the metabolic flexibility in switching energy sources between PLN-R14del and wildtype hiPSC-CMs, including the effect of major energy substrate depletion. Finally, we employed two rescue methods, namely CRISPR/Cas9-based gene correction and an FAO-modulating compound bezafibrate), to investigate the association of the PLN-R14del pathogenic variant with intracellular lipid accumulation, mitochondrial lipid metabolism and the Ca^{2+} handling properties. Collectively, our data on the negative effects of energy substrate dysregulation in PLN-R14del cardiomyopathy provide novel insights into the new therapeutic strategies and clinical practice (i.e. drug repurposing).

METHODS

Study design and samples. This study was approved by the Biobank Research Ethics Committee, University Medical Centre Utrecht, Utrecht, The Netherlands, under protocol number 12-387 (cardiac tissues), and 14-513 (skin biopsies). Written informed consent was obtained or in certain cases waived by the ethics committee when obtaining informed consent was not possible due to the death of the individual.

Cardiac tissues: Heart samples collected at autopsy or transplantation were obtained from a homogeneous cohort of PLN-R14del variant positive patients (n=6). Four control hearts obtained from rejected organ donors (n=3) or autopsy (n=1) were used as a reference. To further elaborate on PLN-R14del-specific changes, hearts from patients with ischemic cardiomyopathy (n=4) and non-ischemic cardiomyopathy based on pathogenic variants in genes encoding sarcomeric proteins (n=6) were also included. An overview of cardiac tissues is presented in **Table S1A**. Cardiac tissues used for ChIP-seq and RNA-seq were obtained from regions halfway between the atrioventricular valves and the apex and were stored at -80°C. The epicardial region, where fibrofatty replacement profoundly occurred, was excluded in PLN-R14del hearts and the cardiomyocyte-rich myocardial region was included in this study. From each individual, an adjacent block of tissue from the same biopsy was used for ChIP-seq and was paraffin-embedded and stained with Masson's trichrome (**Fig.S8A**). High-resolution

systematic digital histological quantification of fibrosis and fatty tissue in trichrome stained slides was used to create schematic overviews showing mean fibrosis or adipose tissue in the PLN-R14del and control groups (**Fig.S8B**). If applicable, macroscopically visible regions of subepicardial fat or myocardial fibrofatty replacement were removed from frozen tissue blocks and 12-30 tissue slices of 10 µm thick were cut to achieve a comparable amount of myocardial tissue in the sequenced material. For all the other samples ten 10 µm thick frozen slices were collected.

Chromatin H3K27ac immunoprecipitation and sequencing of human cardiac tissues. Chromatin was isolated from frozen cardiac tissues using the MAGnify™ Chromatin Immunoprecipitation System kit (Life Technologies) according to the manufacturer's instructions. In brief, the obtained cardiac tissue was crosslinked with 1% formaldehyde and the crosslinking was stopped by adding 1.25 M glycine. Cells were lysed using the kit-provided lysis buffer and nuclei were sonicated using Covaris microTUBE (duty cycle 5%, intensity 2, 200 cycles per burst, 60s cycle time, 10 cycles). Sheared chromatin was diluted based on the expected number of isolated cells and was incubated with an anti-H3K27ac antibody (ab4729, Abcam) pre-coupled to magnetic beads for 2 hours at 4°C. Beads were extensively washed and crosslinking was reversed by the kit-provided reverse crosslinking buffer with 20 mg/mL Proteinase K. DNA was purified using ChIP DNA Clean & Concentrator kit (Zymo Research). Isolated DNA was additionally sheared, end repaired, sequencing adaptors were ligated and the library was amplified by PCR using primers with sample-specific barcodes according to our modification to the manufacturer's recommendations.[2] After PCR, the library was purified and checked for the proper size range and for the absence of adaptor dimers on a 2% agarose gel and sequenced on SOLiD Wildfire sequencer.

Histone acetylation data processing. *ChIP-seq peak identification:* Sequencing reads were mapped against the reference genome (hg19 assembly, GRCh37) using the BWA package (-c, –l 25, -k 2, -n 10).[3] Multiple reads mapping to the same location and strand have been collapsed to single reads and only uniquely placed reads were used for peak/region calling. Regions were called using Cisgenome 2.0 (–e 150 -maxgap 200 –minlen 200).[4] Next, to obtain a common reference, region coordinates from all PLN-R14del and control samples were stretched to at least 2000 base pairs and collapsed into a single common list. Overlapping regions were merged based on their outmost coordinates. Only the autosomal regions supported by at least 2 independent datasets were further analysed. Sequencing reads from each ChIP-seq library were overlapped with the common region list, to set the H3K27ac occupancy for every region-sample pair. Obtained regions were further analysed using 4 analyses.

Detection of differentially acetylated regions: Regions with differential H3K27ac occupancy between PLN-R14del and control hearts were identified using DESeq2 standard settings

($p<0.05$ as calculated by Wald test)[5] and are referred to as 'differentially acetylated regions' (**Table S2A**). Supervised hierarchical clustering was performed with quantile normalised (limma::normalizeQiantiles() function in R), log^2 transformed and median centred read counts per common region. To avoid the log^2 transformation of zero values, one read was added to each region.

Gene annotated to differentially acetylated regions and pathway analysis: Region to gene annotation was performed in silico using a conservative window of +/-5kb from the transcription start site, **Table S2B** and **2C**. ToppFun and STRING were used for gene list enrichment analysis and candidate gene prioritisation based on functional annotations and protein interaction networks.[6,7] For ToppFun, the list of hyper- and hypoacetylated genes was tested using probability density function p-value calculation method, FDR B&H correction, p-value cut-off of 0.05, and gene limit of 1-2,000 genes per term (**Table S2D**). Since the pre-build gene/protein networks integrated into ToppFun were not created using the same criteria and the 126 annotated number of genes varies significantly, we also reported genes belonging to known disease pathways even below the p-value threshold (where indicated). For protein network interaction visualisation STRING v10.0 was used with a minimum required interaction score at the highest confidence setting for all differentially acetylated peaks.

Enrichment of TFBMs in differentially acetylated regions: A total of 3,396 cardiac DNAse hypersensitivity sites (DHS) were obtained from the ENCODE database (Heart_OC, Primary frozen heart tissue from NICHD donor ID:1104, Male, Caucasian, 35 years old)[8] overlapping with all differentially acetylated regions in the PLN-R14del vs. control group (both hypo- and hyperacetylated) were used for this analysis. The genomic sequence of DHS was repeat masked and the enrichment of TFBM was calculated against the shuffled sequences using the Analysis Motif of Enrichment (AME tool) of the MEME Suite with the following settings: motif database: human (HOCOMOCO v9), background model sequence set to 0.29182,0.20818,0.20818,0.29 182, pseudo count added to a motif column: 0.25, Wilcoxon rank-sum test (quick), $p<0.05$, **Table S3A**), number of multiple tests for Bonferroni correction: #Motifs× #PartitionsTested = 426×1 = 426[9]. The functional annotation of the enriched TFs was performed as described above (**Table 141 S3B**). Protein network interaction was performed as explained above using the high confidence interaction score.

PLN-specificity analysis of differentially acetylated regions: Sequencing reads from each ChIP-seq sample (PLN-R14del (n=6), control (n=4), ischemic (n=4), and sarcomeric (n=6) groups) were compared to the common differentially acetylated region list to set the H3K27ac occupancy for every region-sample pair. Raw read counts were quantile normalised (limma::normalizeQiantiles() function in R), log2 transformed and median centred (to avoid log^2 transformation of zero values, one read was added to each region). The median value from each sample group was used to construct an n x k table where n = 4 (one value per 150 each sample type) and k represent the number of differentially acetylated regions. The

k-means (nstart = 200) function in R was used to partition the regions into 12 different clusters. To enable the reproducibility of identified clusters, the set.seed(10) R command was called before the clustering. Annotation of clusters with PLN-specific patterns was performed as described above (**Table S4**).

RNA sequencing of human cardiac tissues and transcriptome analysis. RNA was isolated using ISOLATE II RNA Mini Kit (Bioline) according to the manufacturer's instructions with minor adjustments. After the selection of mRNA, libraries were prepared using the NEXTflexTM Rapid RNA-seq Kit (Bioo Scientific). Libraries were sequenced on the Nextseq500 platform (Illumina), producing single-end reads of 75bp. Reads were aligned to the human reference genome GRCh37 using STAR v2.4.2a.[10] Picard's AddOrReplaceReadGroups v1.98 (http://broadinstitute.github.io/picard/) was used to add read groups to the BAM files, which were sorted with Sambamba v0.4.5 and transcript abundances were quantified with HTSeq-count v0.6.1p1 using the union mode.[11,12] Subsequently, reads per kilobase per million mapped reads (RPKMs) were calculated with edgeR's RPKM function.[13] DESeq2 was used to identify differentially expressed genes using the cutoff of $p<0.05$ in the Galaxy environment using the default settings (**Table S5A**).[14] Gene enrichment analysis was performed using ToppFun and STRING as explained above (**Table S5B and 5C**).[6,7]

Characterization of cardiac tissues by immunofluorescence and electron microscopy. Immunofluorescence staining of Oil Red O was also performed to detect lipid droplets in frozen cardiac tissues from 4 control and 6 PLN-R14del hearts, which were included in two sequencing experiments. Electron microscopy was also performed to further investigate lipid droplets present in these cardiac tissues. Images were acquired using a Leica SP8X confocal microscope and processed using ImageJ. Processed images were compared using the Student's t-test (#$p<0.1$, *$p < 0.05$; **$p < 0.01$; ***$p < 0.001$, 0.001 and ****$P \leq .0001$). Besides, DAPI, ATP2A2, TNNI3, and metabolic-related proteins (HADHA and PPARA), were examined in these cardiac tissues using immunofluorescence staining. Nuclear PPARA signal was quantified by a customised pipeline using CellProfiler 4.0.6. Briefly, the images were uploaded as hyperstack images including the channels stained for DAPI, PPARA, and TNNI3. The first module is the ColortoGray module which splits the images into 3 grayscale images from each channel. Next, the nuclei were identified using the entifyPrimaryObjects module. All objects between 10 and 240 pixels in the blue channel were identified based on specific shape and intensity parameters. The boundaries of the cardiomyocytes were determined using the IdentifyPrimaryObjects module which identified all pixels that were stained with TNNI3. Cardiomyocyte nuclei were determined using the MaskObject module, in which previously identified nuclei overlapped with the identified cardiomyocytes. And those that were not overlapping were recognized as non-myocyte nuclei. Quality control

was performed using the EditObjectsManually module to accurately bin cardiomyocyte and non-myocyte nuclei. To identify the nuclear PPARA signal of the cardiomyocyte nuclei, a mask was first made on the PPARA channel using the MaskImage module resulting in an image showing only the PPARA signal within the cardiomyocyte nuclei. The signal was then identified using the IdentifyPrimaryObjects module. The MaskObjects module was then used to assign each PPARA signal to a single parent nucleus. Intensity measurements were made for both the cardiomyocyte nuclei and the PPARA signal using the MeasureObjectIntensity module. Data for the PPARA signal per individual nuclei was then exported to a CSV file using the ExporttoSpreadsheet module. Full details of the pipeline can be seen in the attached CellProfiler file. All data was represented as Mean ± SD and two-way ANOVA was used for statistical analysis (*$p < 0.05$; **$p < 0.01$; ***$p < 0.001$, 0.001 and ****$P \leq .0001$). The list of antibodies is shown in **Table S8**.

Differentiation of hiPSC into cardiomyocytes. Reprogrammed Sendai (kit) accordingly as described before.[15] Briefly, hiPSCs (>p20 <p50) were grown to ~90% confluence in 6 wells format and maintained in E8 medium for at least three passages before starting cardiac lineage differentiation. Upon differentiation, the medium was changed to medium without insulin (INS- medium), as insulin inhibits cardiac mesoderm formation. On day zero (day 0), 3 ml/well INS- medium was supplemented with 6-8 µM CHIR99021 (Selleck Chemicals). After one night of incubation, an additional 2 ml of the INS- medium was carefully added (day 1), and an additional 1 ml of the INS- medium was added on day 2. On day 3, the medium was replaced by a 3 ml/well INS- medium supplemented with 2 µM Wnt-C59 (Tocris Bioscience). Afterwards, the culturing medium was changed every other day and contracting cells were generally seen between day 7 and day 9. After day 9, the INS- medium was changed to 3 ml/well INS+ medium. To metabolically select and purify hiPSC-CMs, INS+ was replaced with a purification medium (without D-glucose) for 2 days. Purified hiPSC-CMs were continuously cultured in INS+ for 2 days to recover. On day 15 hiPSC-CMs were detached by 10 mins incubation of 10X TrypLE select 10X (Thermo Fisher) at 37°C. Detached cells in TrypLE solution were flushed using INS+ medium and cell pellets were obtained by centrifuging at 300g for 3 minutes. After aspiration, hiPSC-CMs were resuspended in INS+ medium supplemented with 5 uM ROCK inhibitor and 10% KO-serum (Thermo Fisher) and filtered through a 100 µm pore filter (Corning). Approximately three million hiPSC-CMs were re-plated into Matrigel-coated wells in a 6-well plate and further cultured for 2 days in INS+ medium for recovery. To ensure the purity of hiPSC-CMs, they were cultured in a purification medium for 2 days before all cell-based experiments in this study (e.g. RNA-seq and Seahorse assays).

Media used for the cultivation of iPSC-CMs. To mature hiPSC-CMs, we used the maturation medium developed in the Mercola lab.[16] After the 2nd purification as indicated above,

INS+ medium was replaced by the maturation medium for a minimum of 3 weeks, which metabolically matured hiPSC-CMs. Next, to study the metabolic capacity of hiPSC-CMs, they were continuously cultured in a glucose-rich medium or lipid-rich medium for another 3 weeks before the Seahorse assays and the immunofluorescence analyses. An overview of culture media is shown in **Table S6**.

RNA isolation and transcriptome analysis of hiPSC-CMs using RNA-seq. Total RNA was isolated from cells using TriZol (Ambion) according to the manufacturer's instructions. DNase treatment was carried out using the RNase-Free DNase Set (Qiagen). The quality of total RNA was first examined using Bioanalyzer 6000 Pico Kit (Agilent), and mRNA was selected. Libraries were prepared and sequenced as indicated before. Raw counts per gene per sample were imported to the Galaxy server and differentially expressed genes (**Table S7**) between PLN-R14del and control hiPSC-CMs were identified using DESeq2 as indicated above.[14]

Metabolic measurements of iPSC-CMs using Seahorse assay. Metabolic activity of purified hiPSC-CMs was determined by mitochondrial fatty acid β-oxidation (FAO) and cytosolic glycolysis using the Seahorse XFe24 Extracellular Flux Analyzer (Seahorse Bioscience). Briefly, long-term cultured hiPSC-CMs (77-159 days old) were first seeded to Matrigel-coated Seahorse XFe24 assay plates at a density of 50,000 cells/well and cultured in the standard culture medium for 2 days. Afterwards, the standard culture medium was replaced by a glucose-rich or lipid-rich medium and refreshed every other day. To measure the oxygen consumption rate (OCR, pmol/min/µg protein) and extracellular acidification rate (ECAR, mpH/min/µg of protein), hiPSC-CMs were first washed three times with 0.5 ml fresh Seahorse medium (Agilent Technologies/Seahorse Bioscience) supplemented with 2% B27, 1% Chemically Defined Lipid Concentrate (Gibco), 4mM L-glutamine (Gibco), and 10mM glucose (Agilent, 103577-100) and then kept in the same medium for 1 hour in a non-CO_2 incubator at 37 °C. Afterwards, 100 µM etomoxir (ETO, a specific irreversible inhibitor of carnitine palmitoyltransferase 1, Agilent) was added to determine FAO dependency by measuring the oxygen consumption rate (OCR, pmol/min/µg protein), followed by the addition of 50 mM 2-Deoxy-D-glucose (2DG competitive glycolytic inhibitor, Sigma Aldrich) to determine cytosolic glycolysis by measuring extracellular acidification rate (ECAR, mpH/min/µg of protein).[17] Three measurements were taken before and after each injection and mixing cycle. Both OCR and ECAR were compared between PLN-R14del and wild-type hiPSC-CMs. Besides, immunofluorescent staining with alpha-actinin antibody, DAPI, and Nile-red was performed to demonstrate the purity and the accumulated lipids of both PLN-R14del and wild-type hiPSC-CMs included in the Seahorse assay (**Fig.S9**).

Seahorse mitochondrial FAO assay by measuring OCR: Each parameter for % OCR from baseline we assessed and calculated as described below: (1) Baseline: the last measurement of basal

respiration before ETO injection (time point 3) was normalised to 100%, and the base measurement was defined by combining three measurements normalised to time point 3. (2) FAO: the three measurements after ETO injection normalised to time point 3. (3) Glycolysis: the three measurements after 2-DG injection normalised to time point 3. (4) FAO dependency: the percentage of fatty acids dependence was calculated by quantifying the change in basal OCR after ETO-inhibited FAO compared to the total mitochondrial function from other substrate oxidation. (5) Metabolic flexibility: the maximal respiration due to the utilisation of other substrates was determined by the OCR after 2-DG-inhibited glycolysis.

Seahorse glycolysis assay by measuring ECAR: Each parameter for % ECAR from baseline was measured and processed as follows: (1) Baseline: the last measurement of baseline before ETO injection (time point 3) was normalised to 100%, and the base measurement was defined by combining three measurements normalised to time point 3. (2) Glycolysis: the three measurements after ETO injection normalised to time point 3. Glycolysis was quantified as the maximum percentage increase of ECAR over baseline. (3) Glycolysis inhibition: the three measurements after 2-DG injection normalised to time point 3. (4) Glycolysis dependency: the degree of glycolysis dependency was determined by the reduction of glycolysis after 2-DG injection. (5) Glycolytic reserve was determined by the average ECAR level after ETO injection subtracted from the average ECAR level after 2-DG injection.

Statistical analysis of OCR and ECAR measurements: The Seahorse experiments were performed using 3 biological replicates, with each replicate consisting of 5–12 technical repeats per condition. OCR and ECAR rates were normalised to the non-glycolytic acidification rate per well and all values were further normalised to the in situ nuclear staining cell counts (Mean ± SD, n=3 counts/well). To compare OCR and ECAR between PLN-R14del and wild-type hiPSC-CMs, an unpaired t-test or one-way ANOVA (biological replicates n=3, n=5-12 wells per replicate) was used. All data was represented as Mean ± SD and significance was displayed by *p < 0.05; **p < 0.01; ***p < 0.001, 0.001 and ****P ≤.0001. All ANOVA tests were subsequently analysed using Tukey's post hoc test. Statistical analysis was performed using the GraphPad Prism 8.3 software.

Bezafibrate application. Bezafibrate, a PPAR-agonist, was applied to control and PLN-R14del hiPSC-CMs. Briefly, all hiPSC-CMs were cultured in the maturation medium for 120 days. Bezafibrate was dissolved in dimethyl sulfoxide (DMSO) and added to hiPSC-CMs at 100 μM. After 24hr incubation, all hiPSC-CMs with and without treatment were fixed for immunofluorescence staining purposes as described below.

Optical Ca^{2+} transient analysis. Ca^{2+} transient analysis was performed to evaluate Ca^{2+} handling property between control and PLN-R14del hiPSC-CMs with and without bezafibrate

treatment. Briefly, cells were loaded 30 min in FluoroBrite DMEM Media (Thermo Fisher) supplemented with 1.25 µM Cal-520 (Abcam) and 0.02% Pluronic F-127 solution (Sigma Aldrich). Spontaneous calcium transients were recorded between two and three weeks after plating. Video streams of Cal-520 (the green channel) lasting 10 seconds at 33 fps were automatically scanned by a Leica Thunder microscope. Image analysis was conducted using Cyteseer (Vala Sciences, California, USA) as previously described.[18] The physiological parameters; peak value (normalized area under the peak trace), rise time and decay time were automatically calculated for each time series. Data tables were analyzed with Microsoft Excel and drug responses and bar plots were generated with GraphPad Prism 9 software.

Characterization of hiPSC-CMs by immunofluorescence staining. HiPSC-CMs were cultured on Matrigel-coated coverslips, fixed in paraformaldehyde (4%), and permeabilized in blocking/permeabilization buffer (5% BSA/0,3% Triton-X-100 in PBS) for 30 minutes. Primary antibodies were added and incubated in 1:5 diluted blocking/permeabilization buffer DPBS overnight at 4°C. Cells were washed four times with PBS (5 mins each time) and incubated with Alexa-conjugated secondary antibodies diluted in 1:5 blocking/permeabilization buffer in the dark at room temperature for 1 hr. Cells were washed as previously described and nuclei were stained using 1 µg/ml Hoechst (Life Technologies) for 15 mins. Coverslips were mounted using Fluoromount-G (Southern Biotech) and images were acquired using a Leica SP8X confocal microscope. Immunofluorescence stainings of Nile-red were quantified by the lipid mask macro of Image J, displaying the number of lipids/nuclei and were quantified using one-way ANOVA (n=3/3 coverslips/images per well, n=3 biological replicates, n=>10 wells per condition). Details of antibodies were shown in **Table S8**.

RESULTS

Identification of histone acetylation changes in PLN-R14del cardiac tissue

H3K27ac histone acetylation regulates gene transcription and contributes to phenotypic responses in heart diseases.[25] Therefore, we performed H3K27ac ChIP-seq to study histone acetylation changes in 6 PLN-R14del versus 4 control hearts (**Fig.1A and Table S1A**). We identified 28,149±9,538, and 182 25,721±8,460 H3K27ac enriched regions within PLN-R14del and control hearts, respectively. We subsequently combined regions that were identified in at least two independent samples into a set of 23,356 regions to assess differentially acetylated regions between control and PLN-R14del groups. In total, 2,107 autosomal regions showed differential H3K27ac levels between PLN-R14del and control hearts (**Fig.1B and Table S2A**). Compared to controls, regions with higher H3K27ac levels in PLN-R14del hearts are referred to as hyperacetylated regions (n=1,149) and regions with lower H3K27ac levels in PLN-R14del hearts are referred to as hypoacetylated regions (n=958, **Fig.1C** and **Fig.S1**).

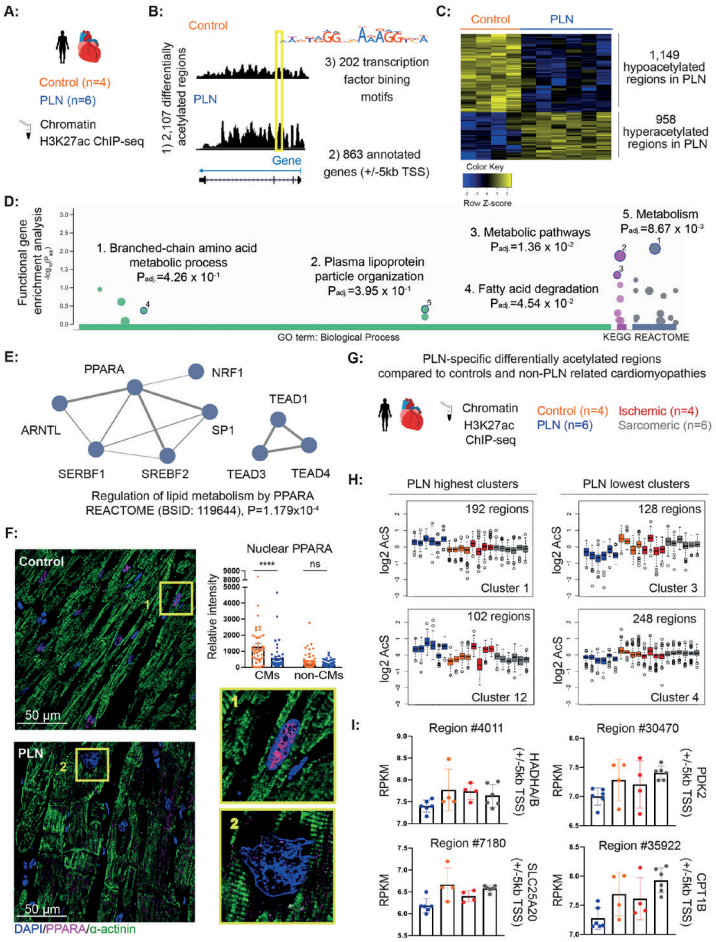

Figure 1: Identification of differentially acetylated DNA regulation regions in PLN-R14del cardiomyopathy compared to the controls and other cardiomyopathies. **A**) An overview illustrating 487 the study design of comparing histone acetylation between PLN-R14del cardiomyopathy and the healthy controls using H3K27ac ChIP-seq. **B**) A workflow indicating the production of three main datasets obtained from identified histone acetylated regions: dataset 1) 2,107 differentially acetylated regions between PLN-R14del and controls; dataset 2) 863 genes annotated to differentially acetylated regions in the +/-5kb window from the gene's transcription start site; dataset 3) 202 transcription factor binding motifs (TFBMs) enriched within the sequences of differentially acetylated regions. **C**) Heatmap showing top 100 differentially acetylated regions in cardiac tissue from PLN-R14del versus control hearts (dataset 1). **D**) Functional gene enrichment analysis using annotated genes in the vicinity of hypoacetylated regions pointed towards altered metabolism-related biological functions (dataset 2). **E**) PPARA and its interacting TFs involved in lipid metabolism obtained from TFBMs enriched in differentially acetylated regions (dataset 3). **F**) Immunofluorescence staining and quantification of nuclear PPARA signals (magenta) in PLN-R14del and control hearts. The nucleus was stained in blue and α-actinin in green. Confocal images were taken at 63x magnification. CMs: identified cardiomyocytes in the tissues; non-CMs: non-cardiomyocytes in the tissues. **G**) An overview showing additional biopsies from patients with ischemic cardiomyopathy and sarcomeric non-ischemic cardiomyopathy (non-PLN-related cardiomyopathies), besides PLN-R14del and control hearts as indicated in A). **H**) K-mean clustering analysis showing four PLN-R14del-specific clusters based on acetylation signals (AcS). **I**) Examples of genes involved in mitochondrial metabolism annotated to regions from PLN-R14del-lowest clusters (cluster 3 and 4) shown in H).

Genes annotated to differentially acetylated regions in PLN-R14del cardiac tissues are enriched in metabolic pathways

To identify genes potentially regulated by the differentially acetylated regions, we focused on regions in close vicinity to promoters and annotated genes 5,000 bases up- and downstream from the transcription start site of a gene as used previously (**Fig.1B**).[25,26] Out of 968 hyperacetylated regions, 295 genes were identified in close vicinity to 251 hyperacetylated regions, and out of 1,149 hypoacetylated regions, 568 genes were identified in the close vicinity to 462 hypoacetylated regions (**Fig.1C, Table S2B** and **2C**). To examine which biological processes and pathways are affected, we performed gene set enrichment analysis using genes annotated to differentially acetylated regions. We observed that hyperacetylation-related genes were mostly involved in fibrosis, (cardiovascular) development, and chromatin assembly (**Table S2D and Fig.S2**), while hypoacetylation-related genes were related to metabolism (**Fig.1D and Table S2E**).

The transcription factor binding motifs (TFBMs) overrepresented in hypoacetylated regions are enriched in metabolic pathways

To identify possible upstream acting transcription factors (TFs), which regulate genes involved in the pathogenesis of the disease, we studied the overrepresentation of TFBMs in differentially acetylated regions. By using the DNA sequences of all differentially acetylated regions in PLN-R14del versus control hearts (**Fig.1B**), we detected enrichment in 202 TFBMs and annotated them to 200 TF-encoding genes (**Table S3A**). Consistently, several of the most enriched biological processes annotated to TFs pointed towards altered metabolism, such as adipogenesis and mitochondrial structure (**Table S3B and Fig.S3**). Notably, PPARA, a major regulator of cardiomyocyte lipid metabolism, particularly FAO, was also annotated from enriched motifs together with other interacting TFs (**Fig.1E**). Therefore, we further investigated the localization of PPARA in cardiac tissues by immunofluorescence staining and observed a significant decrease in the nuclear PPARA signal of PLN-R14del cardiomyocytes versus the controls, whereas the PPARA signal in non-myocyte cells remained comparable between PLN-R14del and control hearts (**Fig.1F**).

Hypoacetylated regions associated with metabolic pathways specific for PLN-R14del cardiomyopathy as compared to other cardiomyopathies

Besides non-failing control hearts, we also compared PLN-R14del hearts with other cardiomyopathies, including ischemic cardiomyopathy (n=4) and non-ischemic dilated cardiomyopathy (sarcomeric group, n=6, **Fig.1G**). K-mean clustering analysis revealed four PLN-R14del-specific clusters when compared to other cardiomyopathy groups and the controls (**Fig.1H, Fig.S4**, and **Table S4A**). Genes located in the vicinity of these PLN-R14del-specific clusters were again highly enriched in metabolic signalling (**Table S4B and 4C**, and **Fig.S5**). Examples of metabolic genes, including HADHA/HADHB, SLC25A20, PDK2, and CPT1B,

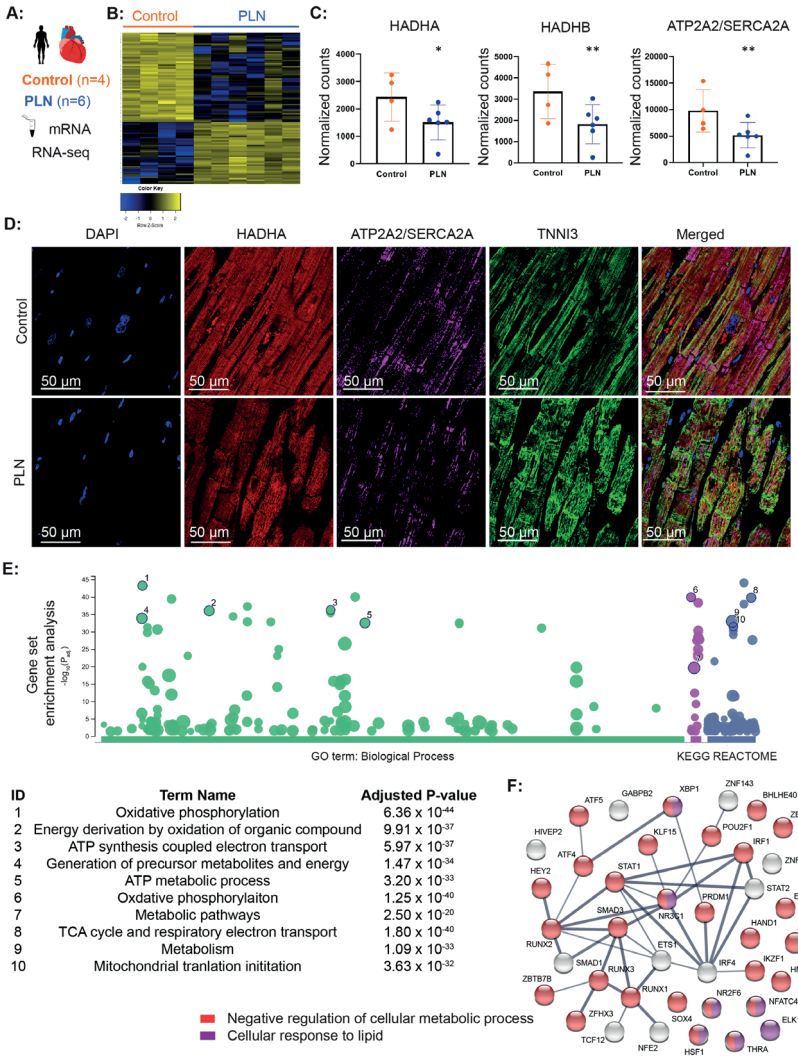

ID	Term Name	Adjusted P-value
1	Oxidative phosphorylation	6.36×10^{-44}
2	Energy derivation by oxidation of organic compound	9.91×10^{-37}
3	ATP synthesis coupled electron transport	5.97×10^{-37}
4	Generation of precursor metabolites and energy	1.47×10^{-34}
5	ATP metabolic process	3.20×10^{-33}
6	Oxdative phosphorylaiton	1.25×10^{-40}
7	Metabolic pathways	2.50×10^{-20}
8	TCA cycle and respiratory electron transport	1.80×10^{-40}
9	Metabolism	1.09×10^{-33}
10	Mitochondrial tranlation inititation	3.63×10^{-32}

Figure 2: Identification of differentially expressed genes between PLN-R14del and control hearts using RNA-seq. **A**) An overview illustrating the study design of comparing transcriptome between PLN-R14del and control hearts using RNA-seq after poly(A) selection. **B**) Heatmap showing top 100 differentially expressed genes in cardiac tissue from PLN-R14del versus control hearts. **C**) Examples of 3 differentially expressed genes between PLN-R14del and control hearts. **D**) PLN-R14del heart showed lower ATP2A2/SERCA2A signal (purple) and HADHA signal (red) compared to the control heart using immunofluorescence staining, confirming its levels in the RNA-seq data. Nuclei were stained by DAPI (blue) and sarcomeres were stained by TNNI3 (green). Confocal images were taken at 63x magnification. **E**) Enrichment analysis using downregulated genes indicated the top enriched biological processes and pathways were related to metabolism. **F**) Protein-protein-interaction network using 39 TFs from the integrative analysis pointed toward (negatively) affected metabolism. Protein-coding genes involved in "Negative regulation of cellular metabolic process" are shown in red, protein-coding genes involved in "Cellular response to lipid" are shown in purple, and protein-coding genes that are not involved in these two processes are shown in light grey.

which were annotated in PLN-R14del-specific hypoacetylated clusters were shown in **Fig.1I.** Combined, we detected differentially acetylated regions that distinguish PLN-R14del from other types of cardiomyopathies and they annotated metabolic-related genes were profoundly affected.

Enriched metabolic pathways by differentially expressed genes in PLN-R14del hearts
Besides differentially acetylated regions, we obtained 1,668 up- and 1,873 downregulated genes in PLN-R14del versus control hearts using RNA-seq (**Fig.2A and Fig.2B, Table S5A**). In line with the well-established suppression of SERCA2A/ATP2A2 at the protein level,[6] we showed its suppression at the mRNA level for the first time. Additionally, metabolic genes, such as HADHA and HAHDB, which were annotated from PLN-R14del-specific hypoacetylated clusters, also showed significantly lower mRNA levels in PLN-R14del versus control hearts (**Fig.2C**). We further demonstrated decreased HADHA and SERCA2A/ATP2A2 protein levels in PLN-R14del versus the control heart by immunofluorescence staining (**Fig.2D**). Consistent with enriched biological processes and pathways by annotated genes from differentially acetylated regions, fibrosis, (cardiovascular) development, and chromatin assembly were enriched by upregulated genes (Table S5B) and metabolism (oxidative phosphorylation, ATP metabolic process, metabolic pathways, etc.) were enriched by downregulated genes (**Fig.2E** and **Table S5C**). Notably, among 200 TFs annotated from differentially acetylated regions, 39 TFs showed significantly altered mRNA levels in PLN-R14del versus control hearts, including 26 up- and 13 down-regulated TF-coding genes. Enriched protein-protein-interaction network by 39 TF-coding genes again suggests (negatively) affected metabolism (**Fig.2F**). Thus, we identified a panel of upstream TFs and downstream targets in metabolic processes, which were disrupted in PLN-R14del cardiomyopathy.

Differentially expressed genes in PLN-R14del hiPSC-CMs suggest altered lipid metabolic pathways

Monolayers of hiPSC-CMs have been used to study the molecular mechanisms underlying several major cardiomyopathies, including ion-related, structural, and metabolic cardiomyopathies. However, the physiological immaturity of hiPSC-CMs severely limits their utility as a prediction model for adolescent genetic myopathies. To improve the cardiac immaturity limitation, we cultured hiPSC-CMs for 160 days in a maturation media designed to provide oxidative substrates adapted to the metabolic needs[27] (**Table S6**). These long-term cultured hiPSC-CMs showed well-developed structural and mitochondrial organization as stained by the sarcomeric and mitochondrial marker (**Fig.S7A**). Hereafter, we studied the transcriptome profiles in PLN-R14del and healthy control hiPSC-CMs (**Fig.3A and Table S1B**). First, we examined markers of cytoskeletal components (ACTN1, TNNT2, MYH7, and MYL2), ion channels (KCNA5 and KCNJ4), and mitochondrial components (ATP5F1A and HSP60), and lipid metabolism (PPARA, ACAT1, FABP3, and Nile red staining). In general, we observed an increase in mRNA levels of most markers from short- and long-term (25 and 160 days, respectively)

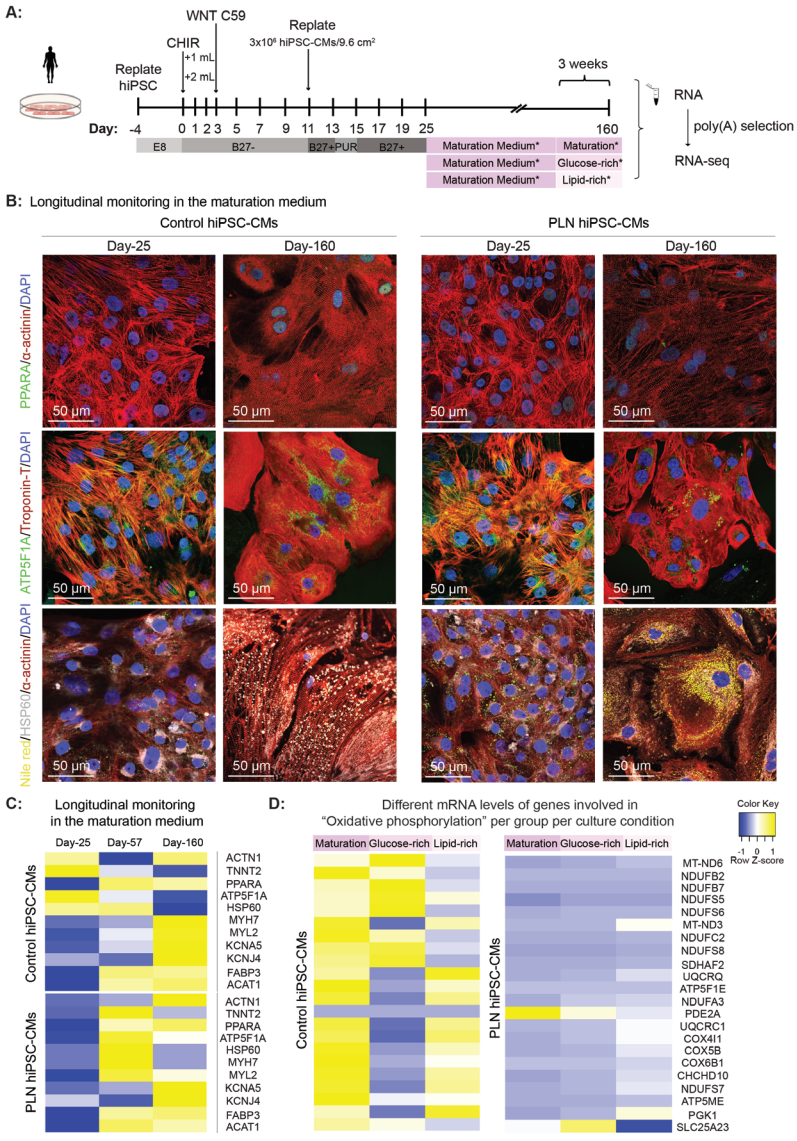

Figure 3: Characterization of long-term cultured human induced pluripotent stem cell-derived cardiomyocytes (hiPSC-CMs) and identification of differentially expressed genes between PLN-R14del and control hiPSC-CMs. **A**) An overview illustrating the study design of comparing transcriptome between long-term cultured PLN-R14del and control hiPSC-CMs in three different media. **B**) Metabolic marker (PPARA), sarcomeric markers (alpha-actinin and troponin-T), mitochondrial markers (ATP5A and HSP60), and lipid droplets (Nile red) were examined in short-term (20 days) and long-term (160 days) cultured PLN-R14del and control hiPSC-CMs using immunofluorescence staining. Nuclei were stained by DAPI (blue). Confocal images were taken at 63x magnification. **C**) Heatmap showing the mRNA expression levels of selected markers in sarcomeres, ion channels, and metabolism in both PLN-R14del and control hiPSC-CMs were shown from the proliferation stage to the maturation stage. **D**) Heatmap showing the mRNA expression levels of genes involved in oxidative phosphorylation (GO: 0006119) in control and PLN-R14del hiPSC-CMs cultured in three different media.

cultured PLN-R14del and healthy control hiPSC-CMs and confirmed these observations at the protein level by immunofluorescence staining (**Fig.3B** and **Fig.3C**). Therefore, we extended the culture time of hiPSC-CMs in the following experiments, which showed an overall improved maturation status but a more distinguishable metabolism-phenotype between PLN-R14del and control hiPSC-CMs. Since our data obtained from PLN-R14del hearts indicated a disrupted lipid metabolism, we cultured control and PLN-R14del hiPSC-CMs to further elucidate the metabolic activities in three culture media containing different amounts of glucose and lipids, which are the two main metabolic substrates for cardiomyocytes (**Fig.3A**). In total, we identified 952, 1,321, and 2,104 differentially expressed genes in PLN-R14del versus control hiPSC-CMs cultured in the maturation, the glucose-rich,

and the lipid-rich medium, respectively (**Table S7A-C**). Notably, regardless of culture media, pathway enrichment analyses using downregulated genes in PLN-R14del versus control hiPSC-CMs consistently pointed towards metabolic activities, such as oxidative phosphorylation/GO:0006119 (**Fig.3D, Fig.S8A-C**, and **Table S7D-F**). However, it is important to note that the metabolic genes involved in the enriched biological processes (i.e., oxidative phosphorylation), which were shared among three conditions, were not the same (Fig.S8D-F). Similarly, regardless of culture media, pathway enrichment analyses using upregulated genes in PLN-R14del versus control hiPSC-CMs consistently pointed towards fibrosis and (cardiovascular) development, which were in line with the results obtained from the *ex vivo* human cardiac tissues (**Table S7D-F**).

Disturbed fatty acid oxidation (FAO) and metabolic flexibility in PLN-R14del hiPSC-CMs Besides the downregulated transcriptional regulation of lipid metabolism in PLN-R14del cardiomyopathy, a significantly lower cellular metabolic activity/viability was also observed in PLN-R14del versus control hiPSC-CMs (**Fig.4A**). This suppression remained when excessive glucose or FAs were given to the cells (**Fig.S7B-C**). To further elucidate whether the obtained transcriptomic data could predict affected metabolism in PLN-R14del cardiomyopathy, we compared the FAO metabolism, a key metabolic program in cardiomyocytes (**Fig.4B**), by evaluating mitochondrial respiration via ETO-inhibited FAO and 2-DG-inhibited glycolysis using the Seahorse analysis (**Fig.4C**). In the maturation medium, which contains both glucose and FAs, we observed a comparable oxygen consumption rate (OCR) between PLN-R14del and control hiPSC-CMs at the baseline level and after ETO-inhibited FAO (**Fig.4E**), suggesting a similar FAO-dependence of both groups. However, after blocking glycolysis by 2-DG, we observed an increased OCR in control hiPSC-CMs, whereas the OCR of PLN-R14del hiPSC-CMs continued to decline significantly, suggesting control hiPSC-CMs are less dependent on glycolysis and have more metabolic adaptive characteristics than PLN-R14del hiPSC-CMs. Similarly, in the glucose-rich medium, OCR was comparable between PLN-R14del and control hiPSC-CMs at the baseline level (**Fig.4F**). After blocking glycolysis, a significantly higher OCR was observed in control versus PLN-R14del hiPSC-CMs, once again suggesting better metabolic flexibility and substrate utilisation in control hiPSC-CMs. Notably, in the lipid-rich medium, the

basal OCR was significantly lower in PLN-R14del versus control hiPSC-CMs (**Fig.4G**), implying an impaired FAO in the PLN-R14del hiPSC-CMs at the beginning. Although OCRs of both PLN-R14del and control hiPSC-CMs decreased after FAO- and glycolysis-blockages, OCRs remained significantly lower in PLN-R14del hiPSC-CMs than in the controls. These findings suggest that despite the presence of excess lipids in the medium, PLN-R14del hiPSC-CMs are less capable of utilizing their FAO metabolism to produce the required energy, therefore being more glycolysis-dependent.

Higher glucose dependency in PLN-R14del hiPSC-CMs

Glucose metabolism, another major metabolic program in cardiomyocytes (**Fig.4B**), was also studied. We measured the extracellular acidification rate (ECAR) to study the activity of the glycolytic pathway in PLN-R14del and wild-type hiPSC-CMs by manipulating the FAO and glucose metabolism using ETO and 2-DG, respectively (**Fig.4D**). In the maturation medium, basal ECAR levels were comparable between both groups, but it became significantly lower in PLN-R14del versus control hiPSC-CMs after FAO- and glycolysis-blockages (**Fig.4H**), indicating a higher glycolysis dependency of PLN-R14del hiPSC-CMs. A significantly higher glycolytic reserve was also observed in PLN-R14del hiPSC-CMs than in the controls. In the glucose-rich medium, ECAR levels remained comparable between both groups at the basal level, after blocking FAO, and after blocking glycolysis (**Fig.4I**). However, the decline of ECAR after glycolysis-blockage was more profound in PLN-R14del versus control hiPSC-CMs, suggesting a higher glycolysis-dependence and a higher glycolytic reserve of PLN-R14del hiPSC-CMs. In the lipid-rich medium, basal ECAR levels were comparable between both groups (**Fig.4J**). Interestingly, a higher ECAR was shown in PLN-R14del versus control hiPSC-CMs after FAO-blockage, which decreased profoundly after glycolysis-blockage, again, confirming the higher glycolysis-dependency in PLN-R14del hiPSC-CMs. These results imply our in vitro maturation-induced PLN-R14del hiPSC-CM mimics the heart failure-related metabolic alterations consisting of the energy production reduction by mitochondria through oxidative phosphorylation and an increase in (anaerobic) glycolysis.

Intracellular lipid droplet accumulation is a key feature of PLN-R14del cardiomyopathy

Data acquired from the cardiac tissues and/or hiPSC-CMs at DNA, RNA, protein, and functional levels consistently pointed towards altered metabolism in PLN-R14del versus control groups, particularly FAO. Since lipid accumulation is known as the hallmark of impaired FAO, we examined the lipid accumulation in cardiac tissues and hiPSC-CMs. First, we performed a digital quantification in heart slices assessing the percentage of adipose tissue, which showed an increased adipocyte deposition in PLN-R14del versus control hearts (**Fig.S8**). Next, we used Nile red to localise intracellular lipid droplets in snap-frozen and paraffin-embedded tissues and observed a more frequent perinuclear accumulation of lipid droplets in PLN-R14del

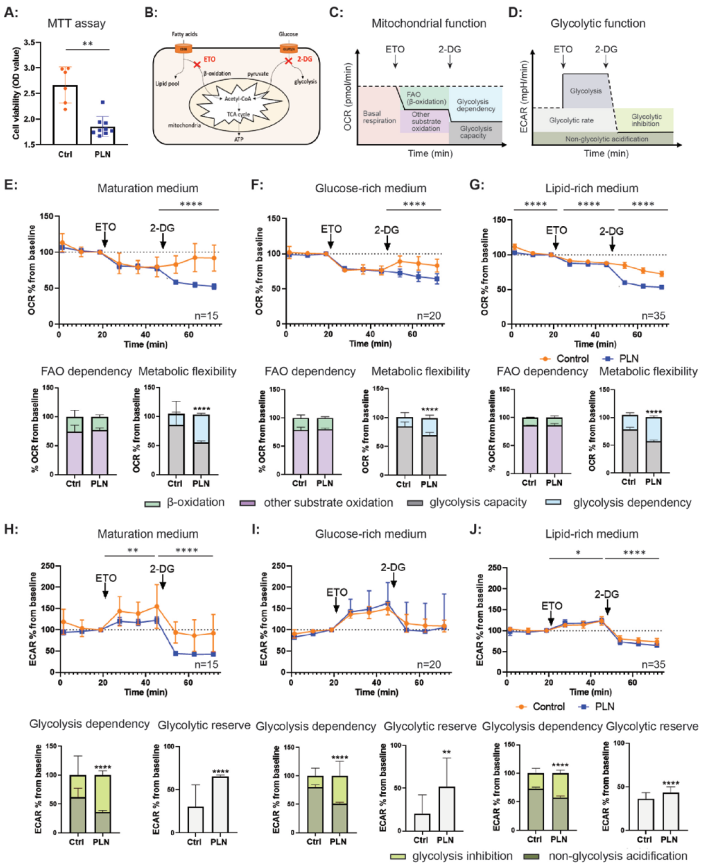

Figure 4: Examination of metabolic activity between PLN-R14del and control hiPSC-CMs. **A**) Tetrazolium assay showed a significantly lower general metabolic activity in PLN-R14del hiPSC-CMs when compared to the controls. **B**) A simple diagram illustrating utilization pathways of fatty acids and glucose in cardiomyocytes and two commonly used compounds, etomoxir (ETO) and 2-deoxyglucose (2-DG), to study the capacity of these pathways by blocking their utilization, respectively. **C**) An overview illustrating Seahorse XF24 Extracellular Flux assay, which measures the oxygen consumption rate (OCR) to study the activity of the fatty acid oxidation (FAO) in PLN and wild-type hiPSC-CMs by manipulating the FAO and glucose metabolism using etomoxir (ETO) and 2-deoxyglucose (2-DG). **D**) An overview illustrating Seahorse XF24 Extracellular Flux assay, which measures extracellular acidification rate (ECAR) to study the activity of the glycolytic pathway in PLN-R14del and wild-type hiPSC-CMs by manipulating the FAO and glucose metabolism using ETO and 2-DG. **E-G**) OCR of hiPSC-CMs cultured in the maturation medium, the glucose-rich medium, and the lipid-rich medium, respectively (grey arrow indicates a switch in energy substrates). Quantification of OCR values at the basal level, after ETO injection, and after 2-DG injection, were normalised to nuclei count. The degree of FAO dependency is determined by the reduction of mitochondrial function after ETO injection, and the degree of metabolic flexibility is determined by the OCR after 2-DG injection. **H-J**) ECAR of hiPSC-CMs cultured in the maturation medium, the glucose-rich medium, and the lipid-rich medium, respectively (grey arrow indicates a switch in energy substrates). Quantification of ECAR values at the baseline level, after ETO injection, and after 2-DG injection, were normalised to nuclei count. The degree of glycolysis dependency is determined by the total glycolysis minus the non-glycolytic acidification (after 2-DG injection). The glycolytic reserve ability is determined by ECAR after ETO injection minus ECAR after 2-DG injection. Data are expressed as mean ±SD, biological replicates are 3 individual differentiations with each N= 5-12 wells. One-way ANOVA with Tukey's post-hoc comparison or Student's t-tests were used, P<0.05, **P<0.01, ***P<0.001, ****P<0.0001.

cardiac tissue than in the control (**Fig.5A**). Transmission electron microscopy revealed a significantly lower mitochondrial length (aspect ratio) and a significantly higher accumulation of intracellular lipid droplets in PLN-R14del versus control hearts (**Fig.5B and Fig.5C**), suggesting impaired mitochondrial FAO. In line with the hearts, highly accumulated intracellular lipid droplets were observed in PLN-R14del versus control hiPSC-CMs, regardless of different culturing media (**Fig.5D**). Combined, these findings suggested intracellular lipid droplet accumulation is a key feature in PLN-R14del cardiomyopathy.

CRISPR/Cas9-based correction of PLN-R14del attenuated intracellular lipid accumulation

We used CRISPR/Cas9-based gene editing to correct PLN-R14del mutation[28] and observed a significant reduction of intracellular lipid droplets in R14del-corrected hiPSC-CMs (isogenic control, **Fig.6A**). Interestingly, hiPSC-CMs derived from an asymptomatic PLN-R14del carrier and the homozygous hiPSC-CMs showed a comparable amount of the lipid droplets as in PLN-R14del hiPSC-CMs. These findings suggested a tight relationship between PLN-R14del mutation and impaired lipid metabolism, thereby leading to intracellular lipid droplet accumulation. PPARA-targeted drug increased Ca^{2+} handling and mitochondrial trifunctional protein levels in PLN-R14del hiPSC-CMs. We also applied a PPARA agonist (bezafibrate) to further investigate PPARA-mediated FAO in PLN-R14del cardiomyocytes. First, we measured the Ca^{2+} transient in control and PLN-R14del hiPSC-CMs with and without bezafibrate treatment. We observed significantly increased rise and decay time in treated versus untreated PLN-R14del hiPSC-CMs (**Fig.6B**), whereas the treatment did not affect Ca^{2+} handling in control hiPSC-CMs. Next, we examined HADHA and HADHB levels, encoding the mitochondrial trifunctional protein involved in the FAO pathway, which showed suppressed histone acetylation and transcriptional levels in PLN-R14del versus control hearts (**Fig.1I** and **Fig.2C**). We confirmed the suppression of HADHA and HADHB in long-term cultured untreated PLN-R14del cardiomyocytes and further showed elevated HADHA and HADHB levels in bezafibrate-treated PLN-R14del cardiomyocytes (**Fig.6C**). Whereas, the treatment did not alter HADHA and HADHB levels in control hiPSC-CMs. Combined, these findings suggested disturbed HADHA/HADHB-involved FAO in PLN-R14del hiPSC-CMs, the potential association between PPARA-mediated FAO and Ca^{2+} handling, and the role of PPARA as a promising therapeutic target in PLN-R14del cardiomyopathy.

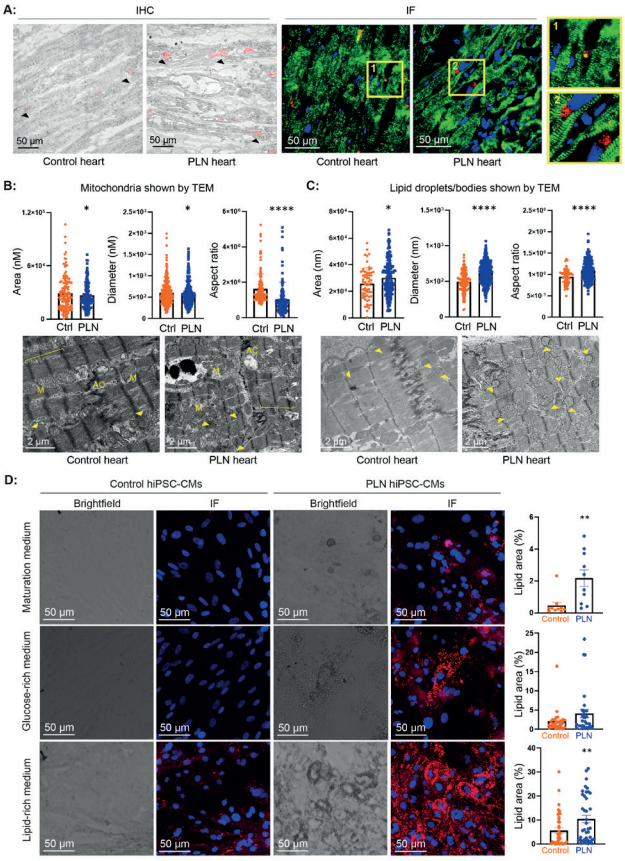

Figure 5: Lipid accumulation and impaired mitochondria in PLN-R14del cardiac tissues and hiPSC-CMs. **A**) Left: Examples of Nile red staining (red, indicated by black arrows) in control and PLN-R14del paraffin-embedded cardiac tissues using immunohistochemical staining (IHC). Images were taken at 40x magnification. Right: Examples of Nile red staining (red) in control and PLN-R14del snap-frozen cardiac tissues using immunofluorescence staining (IF). Confocal images were taken at 63x magnification. Nuclei were stained by DAPI (blue) and sarcomeres were stained by TNNI3 (green). **B**) Bar graphs showing impaired detected mitochondria in PLN-R14del versus control hearts using transmission electron microscopy (TEM). Each dot represents an individual mitochondrial from control and PLN hearts. Representative TEM image of the control heart (bottom left) showing regular myofilaments arranged in sarcomeres (brackets), variable-sized mitochondria (M) arranged in rows in between myofibrils, lipid droplets (yellow arrows) and profiles of the intercalated disc with a large mixed-type junction (area composita, AC) in between cardiomyocytes. Whereas, representative TEM image of the PLN-R14del heart (bottom right) shows irregular myofilaments arranged in sarcomeres (brackets), variable-sized mitochondria (M) located around the myofibrils, lipid droplets (yellow arrows) and profiles of the intercalated disc with a large mixed-type junction (AC) in between cardiomyocytes. Multiple shape descriptors were determined for manually traced lipid droplets and mitochondria. **C**) Bar graphs showing higher coverage by lipid droplets and bigger lipid droplets in PLN-R14del versus control hearts using TEM. Representative TEM images (below) showing manually traced lipid droplets (indicated by yellow arrows) in the control and PLN-R14del hearts. Each dot represents an individual lipid droplet from control and PLN hearts. TEM images were collected from 3 healthy controls (67 traced lipid droplets and 128 traced mitochondria) and 1-2 PLN-R14del hearts (177 traced lipid droplets and 129 traced mitochondria). Data are expressed as mean ±SD. Unpaired T-test was used, *P<0.05, ****P<0.0001. Scale bar: 2 µM. **D**) Examples of Nile red staining to demonstrate the lipid accumulation in long-term cultured (160 days) PLN-R14del and control hiPSC-CMs in three different media. Bar graph showing a higher lipid accumulation (red) in PLN-R14del versus control hiPSC-CMs in three different media.

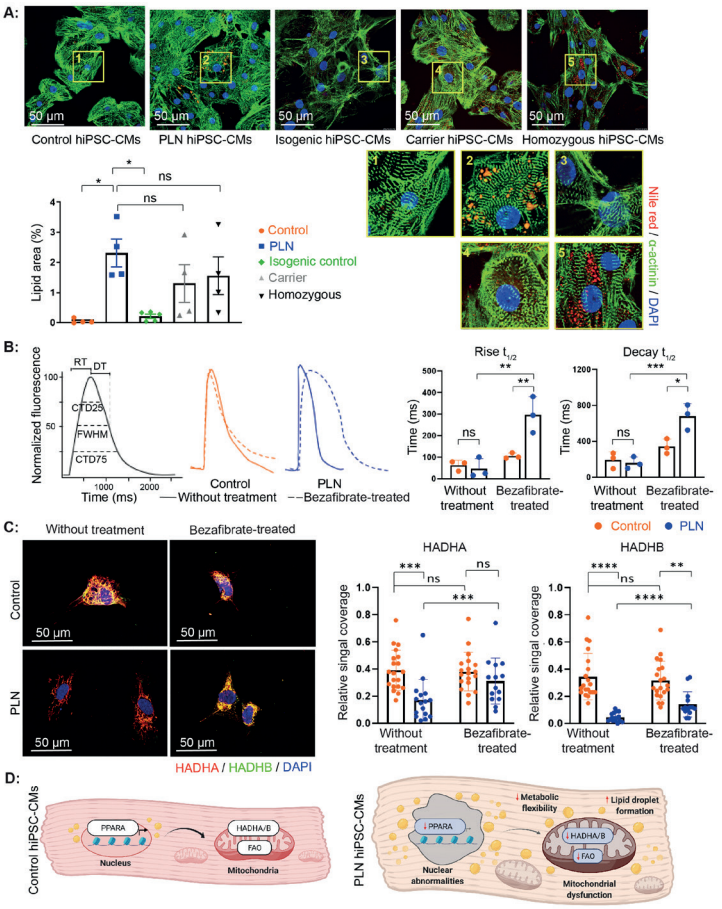

Figure 6: Genetic engineering and agonist therapy as novel treatment strategies targeting dysregulated lipid metabolism in PLN-R14del cardiomyopathy. **A**) Immunofluorescence images of Nile red staining showing the lipid accumulation in all hiPSC-CMs groups. Nuclei were stained by DAPI (blue). Bar graph showing a significantly higher intracellular lipid formation in PLN-R14del hiPSC-CMs when compared to the healthy controls as well as the isogenic controls in which PLN-R14del was corrected (n ≥ 4 per group), whereas the lipid accumulation in hiPSC-CMs from PLN-R14del patient, an asymptomatic PLN-R14del carrier, and a homozygous PLN-R14del group reamined comparable. Data were normalised to nuclei and shown as mean ±SEM. One-way ANOVA was used, **P<0.01, ***P<0.001. **B**) Ca^{2+} transient parameters for examining the Ca^{2+} 590 handling property in hiPSC-CMs, including rise time (RT), decay time (DT), calcium full-width half maximum (FWHM), duration at 25% decline from maximum amplitude (CTD25), and duration at 75% decline from maximum amplitude (CTD75). Representative calcium transient in control and PLN-R14del hiPSC-CMs with and without bezafibrate treatment (dashed and solid line, respectively). Each trace is an average DF/F 0 versus time plot (33 Hz) in each well and three wells per condition per group were included in this analysis. **C**) Immunofluorescence staining of HADHA (red) and HADHB (green) in control and PLN-R14del hiPSC-CMs with and without bezafibrate treatment. Nuclei were stained by DAPI (blue). All images were taken at 63x magnification. Bar graphs showing significantly elevated HADHA and HADHB levels after bezafibrate treatment in PLN-R14del, but not in the control hiPSC-CMs. Data was normalised to the number of nuclei. Each dot represents the normalized data per obtained images and shown as mean ±SD. Two-way ANOVA was used in the bezafibrate treatment experiment, ns= not significant, **P<0.01, ***P<0.001, ****P<0.0001. **D**) Schematic overview of PPARA-mediated FAO dysregulation and impaired lipid metabolism in PLN-R14del versus control cardiomyocytes

DISCUSSION

In this study, we provide new information on changes in chromatin activity and global transcriptional regulation in human myocardium obtained from patients with PLN-R14del cardiomyopathy compared to other types of cardiomyopathy and healthy controls. Multi-omics integration points to the inhibited mitochondrial function and (lipid) metabolism in PLN-R14del hearts based on the changed histone acetylation levels of annotated gene promoters, predicted TFBMs and altered gene expression. These datasets will serve as the basis for upcoming biomarker and novel therapeutic strategies. We particularly focused on the inhibited PPARA-mediated FAO in PLN-R14del hearts. PPARA is a key TF that regulates cardiac lipid metabolism to enhance FAO.[29] It is predominantly located within the nucleus,[30] however, external signals and pathways regulate the transport of PPARA from the nucleus to other subcellular compartments and mediate the biological functions of PPARA.[31] We obtained the enriched TFBM of PPARA in differentially acetylated promoters between PLN-R14del and controls. Although the histone acetylation of PPARA promoter and mRNA level of PPARA remained comparable between PLN-R14del and control hearts, we showed a significant decline of PPARA signal inside cardiomyocyte nuclei in PLN-R14del hearts. Taken together, the loss of nuclear PPARA in PLN-R14del cardiomyocytes suggested suppressed PPARA-mediated biological processes that take place inside nuclei, including substrate inflexibility promoting FFA uptake and lipid accumulation, and ensuing cardiovascular complications. The promoters of PPARA-regulated downstream targets in lipid metabolism, such as HADHA, HADHB, MLYCD, and PNPLA2,[32,33,34] showed suppressed acetylation levels in PLN-R14del hearts. Furthermore, by comparing PLN-R14del hearts with non-PLN-R14del-related cardiomyopathies, we identified PLN-R14del-specific regions and many annotated genes in these regions also involved in lipid metabolism (e.g. AGPAT2, HADHA, HADHB, MLYCD, PLPP1, and PTGDS). Additionally, several of these metabolic genes also showed decreased mRNA levels in PLN-R14del versus control hearts, including HADHA and HADHB. In line with these omics-based data, we also observed accumulated lipid droplets and abnormal mitochondrial morphology in PLN-R14del hearts. Combined, the impaired PPARA-regulated FAO could play a critical role in PLN-R14del cardiomyopathy. A recent study also showed that 18-33 days old PLN-R14del engineered heart tissues had impaired energy metabolism reflected at the protein level, including suppressed FAs metabolism and accumulation of lipid droplets.[6] Here, we further explored and identified affected genes in the metabolic regulation in long-term cultured PLN-R14del and control hiPSC-CMs (>110 days). We demonstrated for the first time that PLN-R14del hiPSC-CMs displayed a lower FAO profile than the controls at both mRNA and functional levels, and this suppression pattern remained consistent even though PLN-R14del hiPCS-CMs were given excessive amounts of FAs or glucose, indicating the profoundly impaired lipid metabolism. FAO changes serve as an indicator of an early adapted or maladapted metabolic response.[35] Normally, the majority of the energy demand of the heart comes from mitochondrial FAO, especially free circulating FAs.[36] In contrast, diseased cardiomyocytes suffer from a decreased FAO and an increased intracellular lipid accumulation resulting in lipotoxicity and cell death.[37,38] We also showed lipid accumulation and a decreased cell viability of PLN-

R14del hiPSC-CMs, further suggesting the importance of impaired FAO as a key pathological mechanism underling PLN-R14del cardiomyopathy. Notably, we observed enhanced Ca^{2+} handling properties and elevated mitochondrial trifunctional protein levels (HADHA and HADHB) in PLN-R14del hiPSC-CMs after bezafibrate treatment, a PPARA-targeting agonist. Several FDA/EMA-approved PPARA agonists, including bezafibrate, have shown protective effects on cardiomyopathies by restoring the FA metabolism.[39,40] However, to the best of our knowledge, we showed for the first time, the potential of bezafibrate in re-activating mitochondrial FAO and improving Ca^{2+} transients, which provides a novel strategic path for developing precision medicine for PLN-R14del patients, such as targeting FAO upstream regulators (i.e. PPARA). Besides FAO suppression, the activation of glycolysis-related genes was shown in murine cardiomyocytes carrying another PLN pathogenic variant (p.Arg9Cys).[41] We also showed PLN-R14del hiPSC-CMs exhibited a preference for glucose utilisation. Increased glucose utilisation, which further inhibits FAO by malonyl coenzyme A-mediated inhibition, has been shown in cardiomyocytes from hypertrophic cardiomyopathies and failing hearts.[33,42] The switch from FAs to glucose utilisation can be due to its faster uptake in the cells and the lower oxygen consumption.[43] Like lipotoxicity, increased glucose levels can have deleterious effects on cardiomyocytes by introducing oxidative stress-related cell death and decreasing contractile force.[44,45] Thus, the glucose-dependent energy metabolism is associated with the progression of cardiac dysfunction and could be an early pathological process in PLN-R14del hearts.[42] Last but not least, we also observed reduced metabolic flexibility in PLN-R14del hiPSC-CMs. Healthy cardiomyocytes have the flexibility of switching substrates for energy production under different conditions.[42] This metabolic flexibility is a critical factor for maintaining normal cardiac function and preventing the progression of diseased hearts.[46] Impaired metabolic flexibility has also been observed in mouse cardiomyocytes with the depletion of Ryr2, which show reduced mRNA levels of key regulators in the FA metabolism (e.g. Ppargc1a, Pparα, Pparγ, and Klf15) as well as the glucose metabolism (e.g. Glut4 and Pck1).[47] Therefore, restoring balanced metabolic activity is beneficial for 435 PLN-R14del cardiomyopathy. It is important to note that histone acetylation and transcriptome changes in PLN-R14del versus control hearts are derived from both cardiomyocytes and non-myocyte cell types, such as endothelial cells and fibroblasts that are abundant in the heart.[48] Non-myocyte cell types in the heart also contribute to the disease progression.[49] Therefore, the responsible cell type(s) or mechanisms for the adipocyte infiltration by either the activation of the already existing pool of adipocytes or transdifferentiation of (cardiac) cells into adipocytes remain unclear. However, we have previously shown that the majority of the bulk data came from cardiomyocytes when compared to 11 non-myocyte cell types in both inherited and acquired heart disease.[25,26] The impaired mitochondrial FAO indicated by the bulk data was 444 validated in PLN-R14del hiPSC-CMs at transcriptional and functional levels, highlighting the possibility of FAO abnormalities as early pathological signs in PLN-R14del cardiomyocytes. Nevertheless, future studies should also focus on investigating interactions between cardiomyocytes and non-myocyte cells during the cardiac energy rearrangement

as well as the impact of lipid disturbances in PLN-R14del cardiomyopathy. In conclusion, we revealed valuable information on the histone acetylation activities and the transcriptome regulation in PLN-R14del hearts and PLN-R14del hiPSC-CMs when compared with controls. Integrating this data, we demonstrated a disturbed energy metabolism in PLN-R14del and identified upstream TFs regulating impaired FAO. CRISPR-Cas9-based therapy to correct PLN-R14del and bezafibrate treatment to re-active mitochondrial FAO further illustrated the tight relationships between the mutation, impaired FAO, lipid accumulation, and Ca^{2+} handling and shed light to future therapeutic strategies for PLN-R14del patients.

ACKNOWLEDGMENTS

We are very thankful to the patients and their families for providing valuable cardiac tissue for research purposes. We further thank Marc P. Buijsrogge (in memoriam) for collecting cardiac tissues and Joyce van Kuik, Erica Sierra-de Koning and Petra van der Kraak for technical assistance with tissue processing. We thank Utrecht Sequencing Facility for providing sequencing service and data. Utrecht Sequencing Facility is subsidised by the University Medical Centre Utrecht, Hubrecht Institute, Utrecht University and The Netherlands X-omics Initiative (NWO project 184.034.019). We thank Prof. Joseph C. Wu from Stanford University for providing lines SCVI-111 and SCVI-273. Both first shared authors contributed equally and have the right to put their names forward for CV purposes.

SOURCES OF FUNDING

This work was supported by the Dutch PLN patient organisation Foundation PLN (JYP, RGCM, MH, JMIHG, FWA), Leducq grant (CURE-PLaN no. 18CVD01 to JYP, RGCM, JC, DF, IK, MM, PAD, JPvT,, MH, FWA), the NWO VENI grant (no. 016.176.136 to MH), ZonMW Open Competition grant (CONTRACT no. 09120012010018 to KGH, FWA, MH), National Institute of Health grants R01 LM010098 (MH, FWA) and R01HL152055, P01HL141084 (MM), Dutch Cardiovascular Alliance (DCVA) grant (DOUBLE-DOSE no. 2020B005 to MH, FvS, FWA, JPvT), ERA-CVD grant (SCALE no. 2019T109 to JYP, FvS, MH), Netherlands Foundation for Cardiovascular Excellence (CC), two NWO VIDI grants (no. 91714302 to CC and no. 016096359 to MCV), the ErasmusMC fellowship grant (CC), the RM fellowship grant of the UMC Utrecht (CC), and UCL Hospitals NIHR Biomedical Research Centre grant BRC86A (FWA), Horizon2020 ERC-2016-COG EVICARE (725229), Horizon 2020 BRAV3 (SC1-BHC-07-2019), NWO-TTP program (Harvey 2021/TTW/01038252), and ZonMW-PSIDER (ZonMw file No: 40-46800-98-018) to JS.

DISCLOSURES

None

REFERENCES

1. Feyen, D. A. M. et al. Unfolded Protein Response as a Compensatory Mechanism and Potential Therapeutic Target in PLN R14del Cardiomyopathy. Circulation 144, (2021).
2. Pei, J., van den Dungen, N. A. M., Asselbergs, F. W., Mokry, M. & Harakalova, M. Chromatin Immunoprecipitation Sequencing (ChIP-seq) Protocol for Small Amounts of Frozen Biobanked Cardiac Tissue. Methods Mol. Biol. 2458, 97–111 (2022).
3. Li, H. & Durbin, R. Fast and accurate long-read alignment with Burrows-Wheeler transform. Bioinformatics 26, 589–595 (2010).
4. Ji, H. et al. An integrated software system for analyzing ChIP-chip and ChIP-seq data. Nat. Biotechnol. 26, 1293–1300 (2008).
5. Huber, W. et al. Orchestrating high-throughput genomic analysis with Bioconductor. Nat. Methods 12, 115–121 (2015).
6. Chen, J., Bardes, E. E., Aronow, B. J. & Jegga, A. G. ToppGene Suite for gene list enrichment analysis and candidate gene prioritization. Nucleic Acids Res. 37, W305–11 (2009).
7. Franceschini, A. et al. STRING v9.1: protein-protein interaction networks, with increased coverage and integration. Nucleic Acids Res. 41, D808–15 (2013).
8. Rosenbloom, K. R. et al. ENCODE data in the UCSC Genome Browser: year 5 update. Nucleic Acids Res. 41, D56–63 (2013).
9. McLeay, R. C. & Bailey, T. L. Motif Enrichment Analysis: a unified framework and an evaluation on ChIP data. BMC Bioinformatics vol. 11 (2010).
10. Dobin, A. et al. STAR: ultrafast universal RNA-seq aligner. Bioinformatics 29, 15–21 (2013).
11. Tarasov, A., Vilella, A. J., Cuppen, E., Nijman, I. J. & Prins, P. Sambamba: fast processing of NGS alignment formats. Bioinformatics vol. 31 2032–2034 (2015).
12. Anders, S., Pyl, P. T. & Huber, W. HTSeq--a Python framework to work with high-throughput sequencing data. Bioinformatics 31, 166–169 (2015).
13. Robinson, M. D., McCarthy, D. J. & Smyth, G. K. edgeR: a Bioconductor package for differential expression analysis of digital gene expression data. Bioinformatics 26, 139–140 (2010).
14. Love, M. I., Huber, W. & Anders, S. Moderated estimation of fold change and dispersion for RNA-seq data with DESeq2. Genome Biol. 15, 550 (2014).
15. Sharma, A. et al. High-throughput screening of tyrosine kinase inhibitor cardiotoxicity with human induced pluripotent stem cells. Sci. Transl. Med. 9, (2017).
16. Feyen, D. A. M. et al. Metabolic Maturation Media Improve Physiological Function of Human iPSC-Derived Cardiomyocytes. Cell Rep. 32, 107925 (2020).
17. Kim, C. et al. Studying arrhythmogenic right ventricular dysplasia with patient-specific iPSCs. Nature 494, 105 (2013).
18. Cerignoli, F. et al. High Throughput Measurement of Ca2+ Dynamics for Drug Risk Assessment in Human Stem Cell-derived Cardiomyocytes by Kinetic Image Cytometry. J. Pharmacol. Toxicol. Methods 66, 246 (2012). Haghighi K, Kolokathis F, Gramolini AO, Waggoner JR, Pater L, Lynch RA, Fan G-C, Tsiapras D, Parekh RR, Dorn GW, II, MacLennan DH, Kremastinos DT, Kranias EG. A mutation in the human phospholamban gene, deleting arginine 14, results in lethal, hereditary cardiomyopathy. Proc Natl Acad Sci U S A 2006;103:1388.
2. Rijsingen IAW van, Zwaag PA van der, Groeneweg JA, Nannenberg EA, Jongbloed JDH, Zwinderman AH, Pinto YM, Dit Deprez RHL, Post JG, Tan HL, Boer RA de, Hauer RNW, Christiaans I, Berg MP van den, Tintelen JP van, Wilde AAM. Outcome in phospholamban R14del carriers: results of a large multicentre cohort study. Circ Cardiovasc Genet 2014;7:455–465.

3. Zwaag PA van der, Rijsingen IAW van, Asimaki A, Jongbloed JDH, Veldhuisen DJ van, Wiesfeld ACP, Cox MGPJ, Lochem LT van, Boer RA de, Hofstra RMW, Christiaans I, Spaendonck-Zwarts KY van, Lekanne dit Deprez RH, Judge DP, Calkins H, Suurmeijer AJH, Hauer RNW, Saffitz JE, Wilde AAM, Berg MP van den, Tintelen JP van. Phospholamban R14del mutation in patients diagnosed with dilated cardiomyopathy or arrhythmogenic right ventricular cardiomyopathy: evidence supporting the concept of arrhythmogenic cardiomyopathy. Eur J Heart Fail 2012;14:1199–1207.
4. Hof IE, Heijden JF van der, Kranias EG, Sanoudou D, Boer RA de, Tintelen JP van, Zwaag PA van der, Doevendans PA. Prevalence and cardiac phenotype of patients with a phospholamban mutation. Neth Heart J 2019;27:64–69.
5. Doevendans PA, Glijnis PC, Kranias EG. Leducq Transatlantic Network of Excellence to Cure Phospholamban-Induced Cardiomyopathy (CURE-PLaN). Circ Res 2019;125:720–724.
6. Karakikes I, Stillitano F, Nonnenmacher M, Tzimas C, Sanoudou D, Termglinchan V, Kong C-W, Rushing S, Hansen J, Ceholski D, Kolokathis F, Kremastinos D, Katoulis A, Ren L, Cohen N, Gho JMIH, Tsiapras D, Vink A, Wu JC, Asselbergs FW, Li RA, Hulot J-S, Kranias EG, Hajjar RJ. Correction of human phospholamban R14del mutation associated with cardiomyopathy using targeted nucleases and combination therapy. Nat Commun 2015;6:6955.
7. Cuello F, Knaust AE, Saleem U, Loos M, Raabe J, Mosqueira D, Laufer S, Schweizer M, Kraak P van der, Flenner F, Ulmer BM, Braren I, Yin X, Theofilatos K, Ruiz-Orera J, Patone G, Klampe B, Schulze T, Piasecki A, Pinto Y, Vink A, Hübner N, Harding S, Mayr M, Denning C, Eschenhagen T, Hansen A. Impairment of the ER/mitochondria compartment in human cardiomyocytes with PLN p.Arg14del mutation. EMBO Mol Med 2021;13:e13074.
8. Te Rijdt WP, Tintelen JP van, Vink A, Wal AC van der, Boer RA de, Berg MP van den, Suurmeijer AJH. Phospholamban p.Arg14del cardiomyopathy is characterized by phospholamban aggregates, aggresomes, and autophagic degradation. Histopathology 2016;69:542–550.
9. Gho JMIH, Es R van, Stathonikos N, Harakalova M, Rijdt WP te, Suurmeijer AJH, Heijden JF van der, Jonge N de, Chamuleau SAJ, Weger RA de, Asselbergs FW, Vink A. High resolution systematic digital histological quantification of cardiac fibrosis and adipose tissue in phospholamban p.Arg14del mutation associated cardiomyopathy. PLoS One 2014;9:e94820.
10. Te Rijdt WP, Asimaki A, Jongbloed JDH, Hoorntje ET, Lazzarini E, Zwaag PA van der, Boer RA de, Tintelen JP van, Saffitz JE, Berg MP van den, Suurmeijer AJH. Distinct molecular signature of phospholamban p.Arg14del arrhythmogenic cardiomyopathy. Cardiovasc Pathol 2019;40:2–6.
11. Sepehrkhouy S, Gho JMIH, Es R van, Harakalova M, Jonge N de, Dooijes D, Smagt JJ van der, Buijsrogge MP, Hauer RNW, Goldschmeding R, Weger RA de, Asselbergs FW, Vink A. Distinct fibrosis pattern in desmosomal and phospholamban mutation carriers in hereditary cardiomyopathies. Heart Rhythm 2017;14:1024–1032.
12. Justus M. B. Anumonwo TH. Fatty Infiltration of the Myocardium and Arrhythmogenesis: Potential Cellular and Molecular Mechanisms. Front Physiol 2018;9.
13. Te Rijdt WP, Ten Sande JN, Gorter TM, Zwaag PA van der, Rijsingen IA van, Boekholdt SM, Tintelen JP van, Haelst PL van, Planken RN, Boer RA de, Suurmeijer AJH, Veldhuisen DJ van, Wilde AAM, Willems TP, Dessel PFHM van, Berg MP van den. Myocardial fibrosis as an early feature in phospholamban p.Arg14del mutation carriers: phenotypic insights from cardiovascular magnetic resonance imaging. Eur Heart J Cardiovasc Imaging 2019;20:92–100.
14. Kamel SM, Opbergen CJM van, Koopman CD, Verkerk AO, Boukens BJD, Jonge B de, Onderwater YL, Alebeek E van, Chocron S, Polidoro Pontalti C, Weuring WJ, Vos MA, Boer TP de, Veen TAB van, Bakkers J. Istaroxime treatment ameliorates calcium dysregulation in a zebrafish model of phospholamban R14del cardiomyopathy. Nat Commun 2021;12.
15. Eijgenraam TR, Boukens BJ, Boogerd CJ, Marloes Schouten E, Kolk CWA van de, Stege NM, Rijdt WP te, Hoorntje ET, Zwaag PA van der, Rooij E van, Tintelen JP van, Berg MP van den, Meer P van der, Velden J van der, Silljé HHW, Boer RA de. The phospholamban p.(Arg14del) pathogenic variant leads to cardiomyopathy with heart failure and is unreponsive to standard heart failure therapy. Sci Rep 2020;10:1–13.
16. Raad N, Bittihn P, Cacheux M, Jeong D, Ilkan Z, Ceholski D, Kohlbrenner E, Zhang L, Cai CL, Kranias EG, Hajjar RJ, Stillitano F, Akar FG. Arrhythmia Mechanism and Dynamics in a Humanized Mouse Model of Inherited Cardiomyopathy Caused by Phospholamban R14del Mutation. Circulation 2021;144.

17. Opbergen CJM van, Braven L den, Delmar M, Veen TAB van. Mitochondrial Dysfunction as Substrate for Arrhythmogenic Cardiomyopathy: A Search for New Disease Mechanisms. Front Physiol 2019;0.

18. Haghighi K, Gardner G, Vafiadaki E, Kumar M, Green LC, Ma J, Crocker JS, Koch S, Arvanitis DA, Bidwell P, Rubinstein J, Leur R van de, Doevendans PA, Akar FG, Tranter M, Wang H-S, Sadayappan S, DeMazumder D, Sanoudou D, Hajjar RJ, Stillitano F, Kranias EG. Impaired Right Ventricular Calcium Cycling Is an Early Risk Factor in R14del-Phospholamban Arrhythmias. Journal of Personalized Medicine 2021;11.

19. Shah K, Wei C-Y, Kim C-S, Wong J, Wen J-Y, Tirasawasdichai T, Wang C, -S. Vincent Chen H. Modeling Arrhythmogenic Right Ventricular Dysplasia/Cardiomyopathy with Patient-Specific iPSCs. Human iPS Cells in Disease Modelling. Springer, Tokyo; 2016. p27–43.

20. Haemmerle G, Moustafa T, Woelkart G, Büttner S, Schmidt A, Weijer T van de, Hesselink M, Jaeger D, Kienesberger PC, Zierler K, Schreiber R, Eichmann T, Kolb D, Kotzbeck P, Schweiger M, Kumari M, Eder S, Schoiswohl G, Wongsiriroj N, Pollak NM, Radner FPW, Preiss-Landl K, Kolbe T, Rülicke T, Pieske B, Trauner M, Lass A, Zimmermann R, Hoefler G, Cinti S, Kershaw EE, Schrauwen P, Madeo F, Mayer B, Zechner R. ATGL-mediated fat catabolism regulates cardiac mitochondrial function via PPAR-α and PGC-1. Nat Med 17:1076.

21. Lawrence Merritt J, II, Norris M, Kanungo S. Fatty acid oxidation disorders. Annals of Translational Medicine 2018;6.

22. Goldberg IJ, Trent CM, Christian Schulze P. Lipid Metabolism and Toxicity in the Heart. Cell Metab 2012;15:805.

23. Christian Schulze P, Drosatos K, Goldberg IJ. Lipid Use and Misuse by the Heart. Circ Res 2016;118:1736.

24. Osorio JC, Stanley WC, Linke A, Castellari M, Diep QN, Panchal AR, Hintze TH, Lopaschuk GD, Recchia FA. Impaired Myocardial Fatty Acid Oxidation and Reduced Protein Expression of Retinoid X Receptor-α in Pacing-Induced Heart Failure. Circulation.

25. Carvajal K, Moreno-Sánchez R. Heart Metabolic Disturbances in Cardiovascular Diseases. Archives of Medical Research.

26. Kolwicz SC Jr, Purohit S, Tian R. Cardiac metabolism and its interactions with contraction, growth, and survival of cardiomyocytes. Circ Res 2013;113:603–616.

27. Dávila-Román VG, Vedala G, Herrero P, Fuentes L de las, Rogers JG, Kelly DP, Gropler RJ. Altered myocardial fatty acid and glucose metabolism in idiopathic dilated cardiomyopathy. J Am Coll Cardiol 2002;40:271–277.

28. Pei J, Harakalova M, Treibel TA, Lumbers RT, Boukens BJ, Efimov IR, Dinter JT van, González A, López B, El Azzouzi H, Dungen N van den, Dijk CGM van, Krebber MM, Ruijter HM den, Pasterkamp G, Duncker DJ, Nieuwenhuis EES, Weger R de, Huibers MM, Vink A, Moore JH, Moon JC, Verhaar MC, Kararigas G, Mokry M, Asselbergs FW, Cheng C. H3K27ac acetylome signatures reveal the epigenomic reorganization in remodeled non-failing human hearts. Clin Epigenetics 2020;12:1–18.

29. Pei J, Schuldt M, Nagyova E, Gu Z, Bouhaddani S el, Yiangou L, Jansen M, Calis JJA, Dorsch LM, Blok CS, Dungen NAM van den, Lansu N, Boukens BJ, Efimov IR, Michels M, Verhaar MC, Weger R de, Vink A, Steenbeek FG van, Baas AF, Davis RP, Uh HW, Kuster DWD, Cheng C, Mokry M, Velden J van der, Asselbergs FW, Harakalova M. Multi-omics integration identifies key upstream regulators of pathomechanisms in hypertrophic cardiomyopathy due to truncating MYBPC3 mutations. Clin Epigenetics 2021;13:1–20.

30. Feyen DAM, McKeithan WL, Bruyneel AAN, Spiering S, Hörmann L, Ulmer B, Zhang H, Briganti F, Schweizer M, Hegyi B, Liao Z, Pölönen RP, Ginsburg KS, Lam CK, Serrano R, Wahlquist C, Kreymerman A, Vu M, Amatya PL, Behrens CS, Ranjbarvaziri S, Maas RGC, Greenhaw M, Bernstein D, Wu JC, Bers DM, Eschenhagen T, Metallo CM, Mercola M. Metabolic Maturation Media Improve Physiological Function of Human iPSC-Derived Cardiomyocytes. Cell Rep 2020;32.

31. Feyen DAM, Perea-Gil I, Maas RGC, Harakalova M, Gavidia AA, Arthur AJ, Wu TH, Vink A, Pei J, Vadgama N, Suurmeijer AJ, Te Rijdt WP, Vu M, Amatya PL, Prado M, Zhang Y, Dunkenberger L, Sluijter JPG, Sallam K, Asselbergs FW, Mercola M, Karakikes I. Unfolded Protein Response as a Compensatory Mechanism and Potential Therapeutic Target in PLN R14del Cardiomyopathy. Circulation 2021;144.

32. Finck BN. The PPAR regulatory system in cardiac physiology and disease. Cardiovasc Res 2007;73:269–277.

33. Grygiel-Górniak B. Peroxisome proliferator-activated receptors and their ligands: nutritional and clinical implications - a review. Nutr J 2014;13:1–10.

34. Umemoto T, Fujiki Y. Ligand-dependent nucleo-cytoplasmic shuttling of peroxisome proliferator-activated receptors, PPARα and PPARγ. Genes Cells 2012;17.

35. Schuier AM, Wood PA. Mouse Models for Disorders of Mitochondrial Fatty Acid β-Oxidation. ILAR J 2002;43:57–65.

36. Weeghel M van, Abdurrachim D, Nederlof R, Argmann CA, Houtkooper RH, Hagen J, Nabben M, Denis S, Ciapaite J, Kolwicz SC, Lopaschuk GD, Auwerx J, Nicolay K, Des Rosiers C, Wanders RJ, Zuurbier CJ, Prompers JJ, Houten SM. Increased cardiac fatty acid oxidation in a mouse model with decreased malonyl-CoA sensitivity of CPT1B. Cardiovascular Research.

37. Shi J, Qu Q, Liu H, Zhang Y, Cui W, Chen P, Lv H. Case Report: PNPLA2 Gene Complex Heterozygous Mutation Leading to Neutral Lipid Storage Disease With Myopathy. Front Integr Neurosci 2021;14.

38. Rech M, J J F, Glatz JFC, Bilsen M van, Schroen B, Nabben M. Assessing fatty acid oxidation flux in rodent cardiomyocyte models. Scientific Reports.

39. Martínez MS, García A, Luzardo E, Chávez-Castillo M, Olivar LC, Salazar J, Velasco M, Quintero JJR, Bermúdez V. Correction: Energetic metabolism in cardiomyocytes: molecular basis of heart ischemia and arrhythmogenesis. Vessel Plus.

40. Haffar T, Bérubé-Simard F, Bousette N. Impaired fatty acid oxidation as a cause for lipotoxicity in cardiomyocytes. Biochem Biophys Res Commun 2015;468:73–78.

41. Hickson-Bick DLM, Buja ML, McMillin JB. Palmitate-mediated Alterations in the Fatty Acid Metabolism of Rat Neonatal Cardiac Myocytes. Journal of Molecular and Cellular Cardiology.

42. Burke MA, Chang S, Wakimoto H, Gorham JM, Conner DA, Christodoulou DC, Parfenov MG, DePalma SR, Eminaga S, Konno T, Seidman JG, Seidman CE. Molecular profiling of dilated cardiomyopathy that progresses to heart failure. JCI Insight 2016;1.

43. Pascual F, Coleman RA. Fuel availability and fate in cardiac metabolism: A tale of two substrates. Biochim Biophys Acta 2016;1861:1425–1433.

44. Fillmore N, Lopaschuk GD. Targeting mitochondrial oxidative metabolism as an approach to treat heart failure. Biochimica et Biophysica Acta (BBA) - Molecular Cell Research.

45. Davargaon RS, Sambe AD, V SMV. Toxic effect of high glucose on cardiomyocytes, H9c2 cells: Induction of oxidative stress and ameliorative effect of trolox. Journal of Biochemical and Molecular Toxicology.

46. Taegtmeyer H, Sen S, Vela D. Return to the fetal gene program. Annals of the New York Academy of Sciences.

47. Taegtmeyer H, Golfman L, Sharma S, Razeghi P, Arsdall M. Linking Gene Expression to Function: Metabolic Flexibility in the Normal and Diseased Heart. Annals of the New York Academy of Sciences.

48. Bround MJ, Wambolt R, Luciani DS, Kulpa JE, Rodrigues B, Brownsey RW, Allard MF, Johnson JD. Cardiomyocyte ATP production, metabolic flexibility, and survival require calcium flux through cardiac ryanodine receptors in vivo. J Biol Chem 2013;288:18975–18986.

49. Hong F, Xu P, Zhai Y. The Opportunities and Challenges of Peroxisome Proliferator-Activated Receptors Ligands in Clinical Drug Discovery and Development. International Journal of Molecular Sciences.

50. Home P. Safety of PPAR agonists. Diabetes Care 2011;34 Suppl 2:S215–S219.

51. Khuchua Z, Glukhov AI, Strauss AW, Javadov S. Elucidating the Beneficial Role of PPAR Agonists in Cardiac Diseases. International Journal of Molecular Sciences.

52. Pinto AR, Ilinykh A, Ivey MJ, Kuwabara JT, D'Antoni ML, Debuque R, Chandran A, Wang L, Arora K, Rosenthal N, Tallquist MD. Revisiting Cardiac Cellular Composition. Circ Res 2016;118:400.

53. Pingzhu Zhou WTP. Recounting cardiac cellular composition. Circ Res 2016;118:368.

54. Pei J, Dungen NAM van den, Asselbergs FW, Mokry M, Harakalova M. Chromatin Immunoprecipitation Sequencing (ChIP-seq) Protocol for Small Amounts of Frozen Biobanked Cardiac Tissue. Methods Mol Biol 2022;2458:97–111.

55. Li H, Durbin R. Fast and accurate long-read alignment with Burrows-Wheeler transform. Bioinformatics 2010;26:589–595.

56. Ji H, Jiang H, Ma W, Johnson DS, Myers RM, Wong WH. An integrated software system for analyzing ChIP-chip and ChIP-seq data. Nat Biotechnol 2008;26:1293–1300.

57. Huber W, Carey VJ, Gentleman R, Anders S, Carlson M, Carvalho BS, Bravo HC, Davis S, Gatto L, Girke T, Gottardo R, Hahne F, Hansen KD, Irizarry RA, Lawrence M, Love MI, MacDonald J, Obenchain V, Oleś AK, Pagès H, Reyes A, Shannon P, Smyth GK, Tenenbaum D, Waldron L, Morgan M. Orchestrating high-throughput genomic analysis with Bioconductor. Nat Methods 2015;12:115–121.

58. Chen J, Bardes EE, Aronow BJ, Jegga AG. ToppGene Suite for gene list enrichment analysis and candidate gene prioritization. Nucleic Acids Res 2009;37:W305–W311.

59. Franceschini A, Szklarczyk D, Frankild S, Kuhn M, Simonovic M, Roth A, Lin J, Minguez P, Bork P, Mering C von, Jensen LJ. STRING v9.1: protein-protein interaction networks, with increased coverage and integration. Nucleic Acids Res 2013;41:D808–D815.

60. Rosenbloom KR, Sloan CA, Malladi VS, Dreszer TR, Learned K, Kirkup VM, Wong MC, Maddren M, Fang R, Heitner SG, Lee BT, Barber GP, Harte RA, Diekhans M, Long JC, Wilder SP, Zweig AS, Karolchik D, Kuhn RM, Haussler D, Kent WJ. ENCODE data in the UCSC Genome Browser: year 5 update. Nucleic Acids Res 2013;41:D56–D63.

61. McLeay RC, Bailey TL. Motif Enrichment Analysis: a unified framework and an evaluation on ChIP data. BMC Bioinformatics.

62. Dobin A, Davis CA, Schlesinger F, Drenkow J, Zaleski C, Jha S, Batut P, Chaisson M, Gingeras TR. STAR: ultrafast universal RNA-seq aligner. Bioinformatics 2013;29:15–21.

63. Tarasov A, Vilella AJ, Cuppen E, Nijman IJ, Prins P. Sambamba: fast processing of NGS alignment formats. Bioinformatics.

64. Anders S, Pyl PT, Huber W. HTSeq--a Python framework to work with high-throughput sequencing data. Bioinformatics 2015;31:166–169.

65. Robinson MD, McCarthy DJ, Smyth GK. edgeR: a Bioconductor package for differential expression analysis of digital gene expression data. Bioinformatics 2010;26:139–140.

66. Love MI, Huber W, Anders S. Moderated estimation of fold change and dispersion for RNA-seq data with DESeq2. Genome Biol 2014;15:550.

67. Sharma A, Burridge PW, McKeithan WL, Serrano R, Shukla P, Sayed N, Churko JM, Kitani T, Wu H, Holmström A, Matsa E, Zhang Y, Kumar A, Fan AC, Del Álamo JC, Wu SM, Moslehi JJ, Mercola M, Wu JC. High-throughput screening of tyrosine kinase inhibitor cardiotoxicity with human induced pluripotent stem cells. Sci Transl Med 2017;9.

68. Kim C, Wong J, Wen J, Wang S, Wang C, Spiering S, Kan NG, Forcales S, Puri PL, Leone TC, Marine JE, Calkins H, Kelly DP, Judge DP, Chen H-SV. Studying arrhythmogenic right ventricular dysplasia with patient-specific iPSCs. Nature 2013;494:105.

69. Cerignoli F, Charlot D, Whittaker R, Ingermanson R, Gehalot P, Savtchenko A, Gallacher DJ, Towart R, Price JH, McDonough PM, Mercola M. High Throughput Measurement of Ca2+ Dynamics for Drug Risk Assessment in Human Stem Cell-derived Cardiomyocytes by Kinetic Image Cytometry. J Pharmacol Toxicol Methods 2012;66:246.

SUPPLEMENTARY TABLES

Supplementary table 1 can be downloaded from: https://assets.researchsquare.com/files/rs-1902254/v1/e49a3acc04361a0cb84717f0.png

Table S1: A) An overview of cardiac tissues, B) An overview of hiPSC-CM lines.

Supplementary table 2 can be downloaded from: https://assets.researchsquare.com/files/rs-1902254/v1/03767b120cd27b5a481a8c7c.xlsx

Table S2: (A) Differentially acetylated regions between PLN-R14del and control hearts (dataset 1), B) genes annotated to hyperacetylated regions in PLN-R14del hearts (dataset 2), C) Genes annotated to hypoacetylated regions in PLN-R14del hearts (dataset 2), D) Gene enrichment analysis of annotated genes from hyperacetylated regions in PLN-R14del versus control hearts, E) Gene enrichment analysis of annotated genes from hypoacetylated regions in PLN-R14del versus control hearts.

Supplementary table 3 can be downloaded from: https://assets.researchsquare.com/files/rs-1902254/v1/6904b54b7b218b6d55cc58d9.xlsx

Table S3: A) Enriched transcription factor binding motifs in differentially acetylated regions and TFs coding genes (dataset 3), B) Gene enrichment analysis of transcription factor coding genes.

Supplementary table 4 can be downloaded from: https://assets.researchsquare.com/files/rs-1902254/v1/4c19006c98d4c67f3c296c2c.xlsx

Table S4: A) Altered regulatory regions that were specific in PLN-R14del hearts when compared with the controls and hearts with ischemic or non-ischemic dilated cardiomyopathy, B) Annotated genes from the hyper- and the hypoacetylated regions that were PLN-R14del-specific when compared with the other groups, C) Gene enrichment analysis of annotated genes from PLN-R14del-specific regions.

Supplementary table 5 can be downloaded from: https://assets.researchsquare.com/files/rs-1902254/v1/06f99ca8be68ffa170179499.xlsx

Table S5: A) Differentially expressed genes between PLN-R14del and control hearts, B) Gene enrichment analysis of upregulated genes in PLN-R14del versus control hearts, C) Gene enrichment analysis of downregulated genes in PLN-R14del versus control hearts.

Supplementary table 6 can be downloaded from: https://assets.researchsquare.com/files/rs-1902254/v1/25976e0975e8525f6305abe4.xlsx

Table S6: Media used for culturing hiPSC-CMs and their detailed compositions.

Supplementary table 7 can be downloaded from: https://assets.researchsquare.com/files/rs-1902254/v1/4b3265a4b8c96e37f16cb31d.xlsx

Table S7: A) Differentially expression genes between PLN-R14del and wild-type hiPSC-CMs cultured in the maturation medium, B) Differentially expression genes between PLN-R14del and wild-type hiPSC-CMs cultured in the glucose-rich medium, C) Differentially expression genes between PLN-R14del and wild-type hiPSC-CMs cultured in the lipid-rich medium, D) Gene enrichment analysis of differentially expressed genes between PLNR14del and wild-type hiPSC-CMs cultured in the maturation medium, E) Gene enrichment analysis of differentially expressed genes between PLN-R14del a nd wild-type hiPSC-CMs cultured in the glucose-rich medium, F) Gene enrichment analysis of differentially expressed genes between PLN-R14del and wild-type hiPSC-CMs cultured in the lipid-rich medium.

Supplementary table 8 can be downloaded from: https://assets.researchsquare.com/files/rs-1902254/v1/3d4d4b75b30aaad7d6f76e3c.xlsx

Table S8: Sheet1 contains an overview of antibodies and stainings.

SUPPLEMENTARY FIGURES

Supplementary Figure 1 can be downloaded from: https://assets.researchsquare.com/files/rs-1902254/v1/e49a3acc04361a0cb84717f0.png

Supplementary Figure 1: A) Heatmap representing differentially acetylated regions between PLN-R14del and control group. B) Flowchart representing the detection and annotation of differentially acetylated regions in PLNR14del patients versus controls. C) Manhattan plot showing the differentially acetylated regions in PLN-R14del versus control hearts. Green: hyperacetylated regions; Red: hypoacetylated regions; Black: non-significant regions.

Supplementary Figure 2 can be downloaded from: https://assets.researchsquare.com/files/rs-1902254/v1/a3db1858b3158e47981958f1.png

Supplementary Figure 2: A) Four differentially acetylated regions depicted using the UCSC Genome Browser. In each example, the region overlaps with the putative promoter (upstream region, 5'UTR, first exons in region tracks) and shows a significant difference between PLN-R14del patients and controls (dot plots). Arrow beginning indicates gene transcription start site. AcS = acetylation 437 signal. ENCODE = publicly available ENCODE consortium data default display. H3K27ac = layered H3K27ac ChIPseq data in 6 cell types (GM12878 - red, H1-hESC – orange, HSMM – green, HUVEC – light blue, K562 – dark blue, NHEK – purple, NHLF – pink). DHS – DNaseI hypersensitivity clusters in 125 cells, TFs = ChIPseq for 161 TFs. B) Selected examples of enriched protein-protein interaction networks using protein-coding genes annotated to differentially annotated regions.

Supplementary Figure 3 can be downloaded from: https://assets.researchsquare.com/files/rs-1902254/v1/977dcee472f47c215db074e3.png

Supplementary Figure 3: A) Selected examples of protein-protein-interaction networks using annotated transcription factors (TFs) that were predicted to binding to motifs enriched in differentially acetylated regions. B) Selected examples of TFs with both differentially acetylated promoter as well as their corresponding motifs enriched in differentially acetylated regions. Dot plots represent the acetylation signal (AcS) measured for each sample.

Supplementary Figure 4 can be downloaded from: https://assets.researchsquare.com/files/rs-1902254/v1/7e4d95a33e96fef1d7530156.png

Supplementary Figure 4: PLN-specificity analysis of differentially acetylated regions (ChIP-seq): K-mean clustering of PLN R14del cardiomyopathy (red), healthy controls (green), ischemic cardiomyopathy (dark blue) and sarcomeric non-ischemic cardiomyopathy (light blue) based on H3K27ac signal was used to partition the regions into 12 different clusters. A) K-mean clusters showing PLN-specific hyper- and hypoacetylation regions when compared with controls and hearts with ischemic or non-ischemic dilated cardiomyopathy in general; B) Examples of 8 PLN-specific regions and genes in the vicinity of these regions (LINC01140, WIPF1, OSR1, IFFO2, LTBP1,GCGR, or CNNM4). No genes have been annotated in the vicinity of region 1689.

Supplementary Figure 5 can be downloaded from: https://assets.researchsquare.com/files/rs-1902254/v1/fcc80eaa09bc453ce53de50a.png

Supplementary Figure 5: Genes annotated to PLN-specific differentially acetylated regions (ChIP-seq): As an effort to identify differentially acetylated regions in the vicinity of genes involved in lipid metabolism possibly linked to fibrofatty tissue replacement in PLN group, this figure shows selected examples of STRING protein database used to detect interacting proteins annotated to differentially annotated regions as part of the GO term 'lipid metabolic process' (GO:0006629). Only the highest confidence interactions are displayed. Disconnected nodes were removed from the network image. Dot plots represent the acetylation signal (AcS) measured for each sample.

Supplementary Figure 6 can be downloaded from: https://assets.researchsquare.com/files/rs-1902254/v1/c396eec02044df4930781f58.png

Supplementary Figure 6: Differentially expressed genes between patients and controls (RNA-seq): A) Top 5 enriched Pathway and GO: Biological process terms by upregulated genes in PLN versus control hearts. Notably, the most upregulated genes are part of fibrosis pathways and extracellular matrix organization. B) Top 5 enriched Pathway and GO: Biological process terms by downregulated genes in PLN versus control hearts. Note the enrichment of metabolic pathways. C) Transcription factor (TF) coding genes, which were predicted to bind to enriched motifs in H3K27ac ChIPseq differentially acetylated regions, with altered mRNA expression levels between PLN and control hearts.

Supplementary Figure 7 can be downloaded from: https://assets.researchsquare.com/files/rs-1902254/v1/35bc8505201af85fabf9b6d4.png

Supplementary Figure 7: A) Representative immunofluorescence images showing the well developed mitochondrial organization (stained by Tomm20 in red) and sarcomere (stained by α-actinin in green) in long-termed cultured control and PLN-R14del hiPSC-Cms. Nuclei were stained by DAPI (blue). B) Seahorse XF Cell Mito Stress Test demonstrated a lower oxygen consumption rate (OCR) in PLN-R14del hiPSC-CMs than the controls, suggesting an impaired mitochondrial function in PLN-R14del hiPSC-CMs.

Supplementary Figure 8 can be downloaded from: https://assets.researchsquare.com/files/rs-1902254/v1/d16d47c689fca3a5d93dd40b.png

Supplementary Figure 8: A) Enrichment analysis using downregulated genes in PLN-R14del versus control hiPSC-CMs cultured in the maturation medium pointed towards altered metabolic-related biological functions. B) Enrichment analysis using downregulated genes in PLN-R14del versus control hiPSC-CMs cultured in the glucose-rich medium pointed towards altered metabolic-related biological functions. C) Enrichment analysis using downregulated genes in PLN-R14del versus control hiPSC-CMs cultured in the lipid-rich medium pointed towards altered metabolic-related biological functions. D) STRING protein-protein-interaction network highlighting oxidative phosphorylation-related protein-coding genes (red) that were downregulated in PLNR14del hiPSC-CMs cultured in the maturation medium. E) STRING protein-protein-interaction network highlighting oxidative phosphorylation-related protein-coding genes (red) that were downregulated in PLN-R14del hiPSC-CMs cultured in the glucose-rich medium. F) STRING protein-protein-interaction network highlighting oxidative phosphorylation-related protein-coding genes (red) that were downregulated in PLN-R14del hiPSC-CMs cultured in the lipid-rich medium.

Supplementary Figure 9 can be downloaded from: https://assets.researchsquare.com/files/rs-1902254/v1/b8527354b1fbacbf752abf31.png

Supplementary Figure 9: A) Histological slides derived from the same tissue region as used for H3K27ac ChIPseq and RNA-seq stained with Masson's trichrome (red – cardiomyocytes, blue – fibrosis, white – fatty tissue). LV = left ventricle; Sept = septum. Black line indicates the removal of fibro-fatty tissue replacement prior to ChIPseq. B) Schematic overview showing the mean fatty tissues in control and PLN-R14del hearts using a colour scale. Epicardial fat was excluded from the analysis. LV = left ventricle, RV = right ventricle, Post. = posterior, Ant.= anterior.

Supplementary Figure 10 can be downloaded from: https://assets.researchsquare.com/files/rs-1902254/v1/c2cfa5894c8fe1561f521945.jpg

Supplementary Figure 10: Representative immunofluorescence images showing the purity and the accumulated lipids in wild-type control and PLN-R14del hiPSC-CMs used in the Seahorse assay.

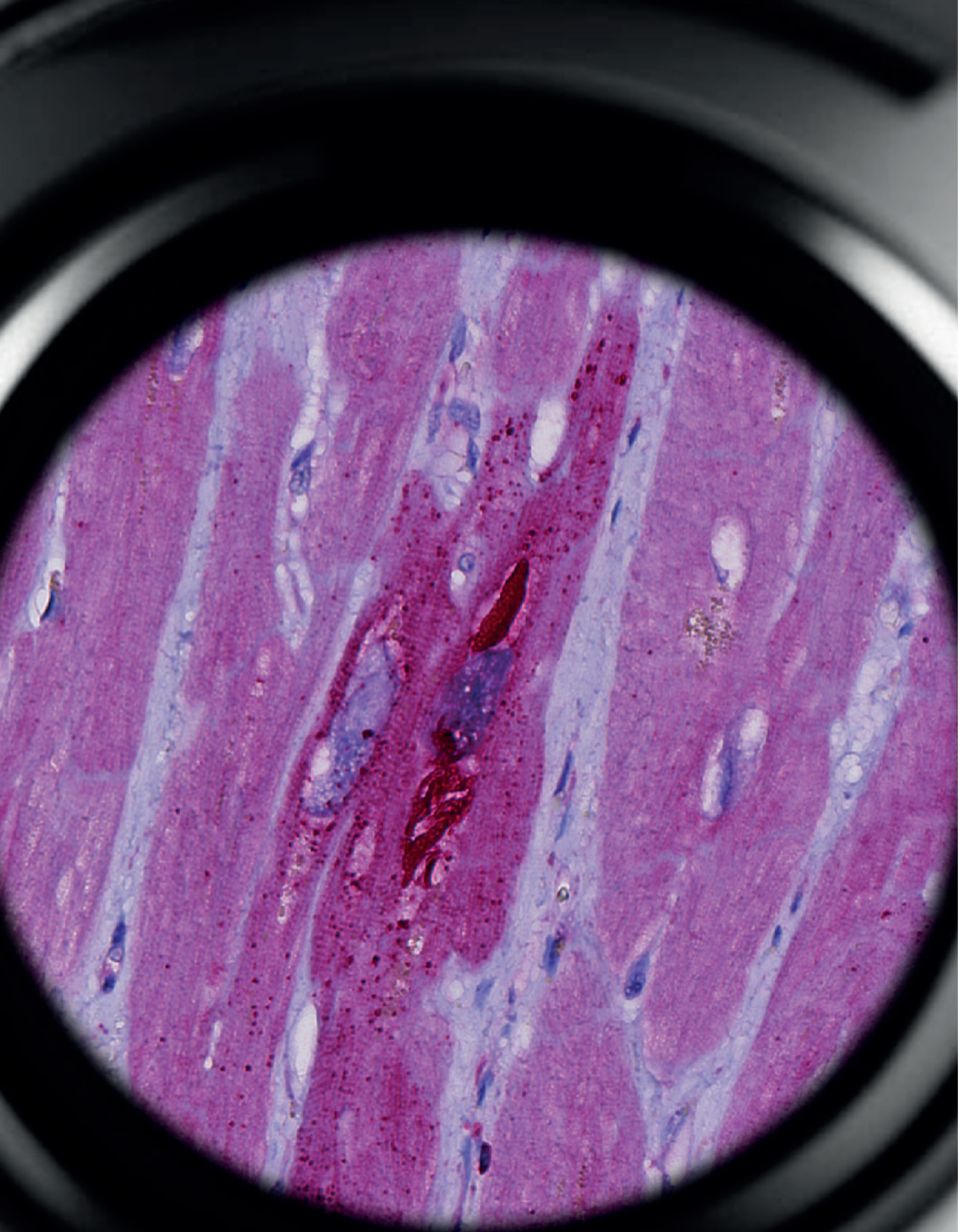

The heart of a PLN patient stained for binding immunoglobulin protein (BIP).

Chapter 9

Unfolded Protein Response as a Compensatory Mechanism and Potential Therapeutic Target in PLN R14del Cardiomyopathy

Published in: Circulation, 2021

Dries A.M. Feyen*, Isaac Perea-Gil*, **Renée G.C. Maas**, Magdalena Harakalova, Alexandra A. Gavidia, Jennifer Ataam Arthur, Ting-Hsuan Wu, Aryan Vink, Jiayi Pei, Nirmal Vadgama, Albert J. Suurmeijer, Wouter P. te Rijdt, Michelle Vu, Prashila L. Amatya, Maricela Prado, Yuan Zhang, Logan Dunkenberger, Joost P.G. Sluijter, Karim Sallam, Folkert W. Asselbergs, Mark Mercola, Ioannis Karakikes

*These authors contributed equally.

ABSTRACT

Phospholamban (PLN) is a critical regulator of calcium cycling and contractility in the heart. The loss of arginine at position 14 in PLN (R14del) is associated with dilated cardiomyopathy with a high prevalence of ventricular arrhythmias. How the R14 deletion causes dilated cardiomyopathy is poorly understood, and there are no disease-specific therapies. We used single-cell RNA sequencing to uncover PLN R14del disease mechanisms in human induced pluripotent stem cells (hiPSC-CMs). We used both 2-dimensional and 3-dimensional functional contractility assays to evaluate the impact of modulating disease-relevant pathways in PLN R14del hiPSC-CMs. Modeling of the PLN R14del cardiomyopathy with isogenic pairs of hiPSC-CMs recapitulated the contractile deficit associated with the disease in vitro. Single-cell RNA sequencing revealed the induction of the unfolded protein response (UPR) pathway in PLN R14del compared with isogenic control hiPSC-CMs. The activation of UPR was also evident in the hearts from PLN R14del patients. Silencing of each of the 3 main UPR signaling branches (IRE1, ATF6, or PERK) by siRNA exacerbated the contractile dysfunction of PLN R14del hiPSC-CMs. We explored the therapeutic potential of activating the UPR with a small molecule activator, BiP (binding immunoglobulin protein) inducer X. PLN R14del hiPSC-CMs treated with BiP protein inducer X showed a dose-dependent amelioration of the contractility deficit in both 2-dimensional cultures and 3-dimensional engineered heart tissues without affecting calcium homeostasis. Together, these findings suggest that the UPR exerts a protective effect in the setting of PLN R14del cardiomyopathy and that modulation of the UPR might be exploited therapeutically.

INTRODUCTION

Phospholamban (PLN) encodes a critical regulatory protein of Ca^{2+} cycling and is a primary mediator of the β-adrenergic effects, resulting in enhanced cardiac output.[1] The levels of PLN and its degree of phosphorylation profoundly influence the activation state of the sarcoplasmic reticulum calcium ATPase (SERCA2a). In the dephosphorylated state, PLN interacts with SERCA2a and shifts its Ca^{2+} activation toward lower apparent Ca^{2+} affinity. On protein kinase A–mediated phosphorylation, the inhibitory interaction between PLN and SERCA2a is abolished, and the apparent Ca^{2+} affinity is raised. Thus, PLN is the rate-determining factor for Ca^{2+} reuptake by SERCA2a and a key regulator of contractility in the heart. Dilated cardiomyopathy (DCM) is the leading cause of heart failure, and familial DCM is responsible for up to a third of the reported cases.[2] Various pathogenic genetic variants have been linked to DCM, including mutations in the coding region of the PLN gene. DCM caused by the deletion of the arginine 14 codon in the PLN gene (R14del) is associated with prevalent ventricular arrhythmias, heart failure, and sudden cardiac death.[3,4] The limited mechanistic understanding of how the R14del contributes to the overall clinical presentation translates to the lack of disease-specific therapeutic strategies. In this study, we investigated the molecular underpinnings of PLN R14del-induced cardiomyopathy by leveraging the power of human induced pluripotent stem cells (hiPSCs), CRISPR/Cas9 genome editing, and single-cell RNA sequencing (scRNA-seq) technologies. PLN R14del hiPSC-derived cardiomyocytes (hiPSC-CMs) faithfully recapitulated the contractile dysfunction observed in PLN R14del-induced cardiomyopathy. At the molecular level, we observed an elevated endoplasmic reticulum (ER) stress and unfolded protein response (UPR) in the PLN R14del hiPSC-CMs compared with isogenic controls. Molecular and pharmacological modulation of the UPR pathway revealed a protective role of the UPR activation in PLN R14del hiPSC-CMs. Our findings suggest a mechanistic link between proteostasis and PLN R14del-induced pathophysiology that could be exploited to develop therapeutic strategies for PLN R14del cardiomyopathy.

METHODS

Human iPSC reprogramming and culture. Peripheral blood mononuclear cells (PBMCs) were reprogrammed to hiPSCs using the CytoTune™-iPS 2.0 Sendai Reprogramming Kit (Thermo Fisher Scientific) according to the manufacturer's instructions with modifications. PBMCs were expanded in StemPro-34 SFM media (Life Technologies) supplemented with cytokines: SCF (100 ng/mL), FLT-3 (100 ng/mL), IL-3 (20 ng/mL), IL-6 (20 ng/mL) and EPO (2 U/mL). After six days, 2 x105 PBMCs were transduced with the three CytoTune® 2.0 reprogramming vectors in one well of a 24-well plate in 0.5 mL in complete StemPro-34 SFM. Twenty-four hours post-transduction the PBMCs were pelleted by centrifugation, resuspended in fresh complete StemPro-34 SFM and plated in one Matrigel-coated well of a 24-well plate. Three days later the media was replaced with StemPro-34 SFM without cytokines and cultured

for an additional 3 days. The cells were gradually transitioned into E8 stem cell medium in a step-wise manner over 5-6 days by replacing 20% of the media each day. Stem cell-like colonies were manually picked about two weeks post transduction and expanded in E8 stem cell media (Life Technologies) on plates coated with human ESC-qualified Matrigel (BD Biosciences) under hypoxic conditions (5% O_2, 5% CO_2) at 37°C. Cells were dissociated with Gentle Cell Dissociation Reagent (StemCell Technologies) with E8 medium supplemented with 2.5 μM Y-27632 (SelleckChem).

Immunofluorescence analysis of pluripotency markers. The hiPSCs were seeded in Matrigel-coated well in a 96-plate (Greiner Bio-One) and cultured for 4-5 days. The cells were washed with PBS, fixed with 4% paraformaldehyde. After permeabilizing with 0.3% Triton-X diluted in PBS supplemented with 2% BSA, 2% FBS, the cells were incubated with primary antibodies (Human Pluripotent Stem Cell Immunocytochemistry Kit, R&D System; Tra-1, Millipore) overnight at 4 °C. After washing, cells were incubated with secondary antibodies Alex Fluor 488/555 / Hoechst 33342 (Invitrogen). Images were taken on an IC200 Kinetic Imaging Cytometer (Vala Sciences; 20x 0.75 N.A.) and further processed using ImageJ software (National Institutes of Health).

Karyotyping. The hiPSCs were snap-frozen in liquid nitrogen and genomic DNA (gDNA) was extracted using the Blood and Tissue DNA extraction kit (Qiagen). SNP karyotyping analysis of >713,014 SNPs was performed using Genome-Wide HumanOmniExpress-24 BeadChips v1.1 on a HiScan sequencing platform per the manufacturer's directions (Illumina) and analyzed using the KaryoStudio v1.4 software (Illumina).

Cardiomyocyte differentiation. Differentiation towards cardiomyocytes was carried out following a small molecule Wnt-activation/inhibition protocol previously described[37,38]. Briefly, hiPSCs were first treated with CHIR99021 (4-6 μM; Tocris) in RPMI/B27 without insulin (Life Technologies) for 72 hours, and then with IWR (3 μM; Selleck Chemicals) for another 48 hours. The media was then replaced with RPMI/B27 with insulin (Life Technologies) and refreshed every 2 days. Spontaneously beating cells was typically observed 8-10 days post-differentiation. On day 13 post-differentiation, hiPSC-CMs were metabolically selected in RPMI-B27 without D-glucose (Life Technologies) supplemented with 0.2% Sodium DL-lactate (Sigma) for 96 hours. Differentiated hiPSC-CMs were maintained with RPMI/B27 medium. All experiments were conducted by using hiPSC-CMs between 35 and 50 days after culture in maturation media39 (2D baseline contractility assessment, siRNA UPR experiment, XBP-1 splicing reporter) or RPMI/B27 (scRNA-seq, BiX experiments).

CRISPR-Cas9 genome editing. Genome editing was performed in hiPSCs to either correct or introduce the PLN R14del mutation in hiPSCs by CRISPR-Cas9-mediated homology-directed repair (HDR) as described[38]. Briefly, the gRNA with the highest specificity score (gRNA: TTGAGGCATTTCAATGGTTG) was cloned into pSpCas9(BB)-2A-GFP (PX458; a gift from Feng Zhang; Addgene plasmid #48138). The PX458 vector (0.5 µg) and single-stranded oligodeoxynucleotide donor template (ssODN, 4.0 µg) were co-transfected in hiPSCs using 10 µL Lipofectamine Stemfect (Thermo Fisher Scientific). Twenty-four hours after transfection, the cells were dissociated with 1X TrypLE Express (Thermo Fisher Scientific) and GFP+ cells were sorted by FACS. Single-cell colonies were screened by PCR (PLN_Fw: AGGAGAGAAAGAGAGACAGACA; PLN_Rv: TCACTGTCACATATTAACCACCA) and Sanger sequencing to verify the insertion or correction of the PLN R14del mutation. The top eight ranking off-target sites predicted by the COSMID tool40 were also assessed (Tables II-V in the Supplement). The following sequence was used as HDR donor templates:

>PLN R14del ssODN
CTCGACCACTTAAAACTTCAGACTTCCTGTCCTGCTGGTATCATGGAGAAAGTCCAATACCTCACTC-GCTCAGCTATAAGAGCATCAACCATTGAAATGCCTCAACAAGCACGTCAAAAGCTAC

>PLN WT ssODN
CTCGACCACTTAAAACTTCAGACTTCCTGTCCTGCTGGTATCATGGAGAAAGTCCAATACCTCACTC-GCTCAGCTATAAGAAGAGCATCAACCATTGAAATGCCTCAACAAGCACGTCAAAAGC

The primers and ssODNs were synthesized by Integrated DNA Technologies (IDT).

Single-Cell RNA-seq library construction and sequencing. At 45 days after differentiation, cells were dissociated by incubation with 10x TrypLE solution for 10 min at 37 °C. Cells were filtered through a 40 µm cell strainer (BD Falcon), centrifuged at 100g for 3 min, and resuspended in PBS supplemented with 0.1% BSA. Single-cell encapsulation, cDNA generation, and preamplification as well as library preparation were performed using the Chromium Single Cell 3' v2 reagent kit according to the instruction manual. Briefly, about 5,000 cells per sample were encapsulated into microdroplets and the barcoded complementary DNAs (cDNAs) were combined and amplified for library preparation according to the manufacturer's protocol (10x genomics). Libraries were sequenced on the NextSeq 500 sequencing system with a target of 40000 to 50000 reads per cell (Illumina).

Processing and analysis of scRNA-seq data. The raw FASTQ files were processed with the Cellranger software v1.3.0 (10x Genomics) for demultiplexing, mapping to the hg19, and quality control. The absolute unique molecular identifier (UMI) counts were quantified per gene per cell to generate a gene-barcode matrix for each sample. These sparse matrices were

aggregated and pre-processed using SAVER41 to impute missing data prior to downstream analysis. The Seurat package 2.0 implemented in R was used to perform normalization, unbiased clustering, t-distributed stochastic neighbor embedding (t-SNE) visualization, and differential gene expression analysis as described in the tutorials (http://satijalab.org/seurat/)[42]. Briefly, the aggregated cell count matrix was first normalized by dividing the number of UMI for each transcript by the total UMI for the cell, multiplying by 10,000, and log-transformed. Highly variable genes were selected using the FindVariableGenes function in Seurat and used as input for principal component analysis (PCA). Based on the first 20 principal components, cell clusters were identified based on their PCA score. To visualize cells in a high-dimensional space, two-dimensional projections created by t-SNE. To assign identities to these subpopulations, we cross-referenced their marker genes with known cardiac subtype markers from the literature. To detect differentially expressed genes between wild-type and PLN R14del iPSC-CM sub-populations, we performed pairwise comparisons using the non-parametric Wilcoxon rank-sum test through the FindMarkers function. An adjusted P-value (Bonferroni correction) cut-off $< 2\times10^{-6}$ was used to identify differentially expressed genes.

Three-dimensional Engineered Heart Tissues (3D-EHTs). The 3D-EHTs were generated in agarose casting molds using solid silicone racks (EHT Technologies) as described with modifications43. Briefly, about 1x106 iPSC-CMs were suspended in a fibrin hydrogel (100 µL total) composed of 10 µL Matrigel (Corning), 5 mg/mL bovine fibrinogen (2.53 µL of 200 mg/mL fibrinogen reconstituted in 0.9% NaCl) and supplemented with 0.1 mg/mL aprotinin (Sigma Aldrich) and 3 U/mL thrombin (Sigma Aldrich). Once polymerized, the silicone racks with the newly formed fibrin gels were transferred to a new 24-well plate and cultured for 3-4 weeks in culture medium consisting of DMEM:RPMI media (1:1) supplemented with 0.25% dialyzed fetal bovine serum (JR Scientific), 0.5x B27 supplement (Gibco), 5% knock-out serum replacement (Gibco), 1% penicillin/streptomycin (Gibco), and 33 µg/mL aprotinin. The culture medium was refreshed every 3-4 days. Videos of the deflecting posts were recorded at 75 frames/s using the SI8000 Cell Motion Imaging System (Sony), at baseline and 72 hours following BiX treatment. The video recordings were processed by MuscleMotion44 to quantify the contraction amplitudes. Absolute force values were derived from calibrated measurements of post displacement considering an elastic modulus of 1.7 MPa, a post radius of 0.5 mm and a distance between posts (length) of 10 mm.[37]

High-throughput contractility analysis. The hiPSC-CMs were plated on Matrigel-coated surfaces at a density of 20,000 cells per well in a 384-well plate (Greiner Bio-One) in 100 µL of replating media (RPMI-B27, 10% knock out serum replacement). The replating media was gradually transitioned to RPMI/B27 by replacing 50% of the media every 2 days for 6-8 days prior to analysis. For siRNA-mediated knockdown, hiPSC-CMs were transfected with

siRNAs (Silencer Select, Ambion) with 0.2 µL Lipofectamine RNAiMax (Invitrogen) 20 nM final concentration. Prior to analysis, the iPSC-CMs cells were loaded with Tetramethylrhodamine methyl ester dye (TMRM, 400 nM) and fluorescent time-lapse images were acquired automatically using the IC200 KIC instrument (Vala Sciences) at an acquisition frequency of 100 Hz for a duration of 10s using a 20x objective (0.75 NA). The contractility image analysis was performed using custom particle image velocity software as previously described[45].

XBP1-splicing reporter / AAV production. The F-XBP1 and F-XBP1ΔDBD7 were a kind gift from Dr. Miura (University of Tokyo). The two XBP1 splicing reporters were cloned into the pAAV-CMV vector (Takara). HEK293T cells were co-transfected (Lipofectamine 2000, Thermo) with pAAV-F-XBP1 (or pAAV-F-XBP1ΔDBD), pRC2, and pHelper (Takara).). After 3 days the cells were collected and the AAV particles extracted from the cell pellets using the AAVpro extraction solutions (Takara). The AAV2 particles were incubated at 37 °C for 30 minutes with Cryonase Cold-active Nuclease (2 U/µl) and purified with a resin-based approach according to manufacturer's instructions (AAVpro purification kit, Takara). The purity was evaluated by the SDS-PAGE and the amount of viral genome was quantified using a real-time qPCR assay using the ITR sequence of AAV2 as a target according to the manufacturer's protocol (Takara). The hiPSC-CMs were seeded in a 384-well at 20,000 cells per well and infected with $5x10^3$ viral genomes per cell. Fluorescent images were acquired with the IC200 KIC (Vala Sciences, San Diego, CA). For quantification, nuclear expression (F-XBP1) was calculated as a percentage of positive nuclei to total nuclei (Hoechst 33342, Invitrogen), and cytoplasmic expression (F-XBP1ΔDBD) was calculated as integrated fluorescent density Patient RNA sequencing for UPR genes.

Human cardiac tissue collection. This study was approved by the Biobank Research Ethics Committee, University Medical Center Utrecht, Utrecht, the Netherlands (protocol number WARB 12/387). Written informed consent was obtained or in certain cases waived by the ethics committee when obtaining informed consent was not possible due to the death of the individual. Heart samples collected at autopsy or transplantation were obtained from a homogeneous cohort of patients who all carried the same pathogenic PLN R14del mutation (n = 6). Four control hearts obtained from rejected organ donors (n = 3) or from autopsy (n =1) were used as a reference.

Human heart tissue immunohistochemistry. Human heart tissue was obtained from the local tissue biobanks of the Departments of Pathology from the University Medical Center Utrecht and the University Medical Center Groningen, The Netherlands. Three explanted hearts from heart failure patients carrying the heterozygous pathogenic PLN R14del variant and autopsy heart tissue from three sudden death patients with the PLN R14del variant expected to harbor PLN aggregates in cardiomyocytes were included. Immunohistochemistry

was also performed on explanted hearts from patients with arrhythmogenic cardiomyopathy (ARVC) negative for the pathogenic PLN R14del variant, ischemic cardiomyopathy (ICM), and control autopsy hearts (genetic variants are shown in Table I in the Supplement). Tissue sections (3 µm) of formalin-fixed and paraffin-embedded (FFPE) myocardium were stained for PLN and different UPR sensors using immunohistochemistry. Sections were manually stained for PLN (PLN ser-10 Bradilla, A010-10AP, 1:200), BiP (GRP78/BiP, Proteintech, 66574-1-Ig, 1:200), PDI (PDI, Proteintech, 66422-1-Ig, 1:200) using antigen retrieval solution pH9 (PLN, BiP) and pH6 (Hsp70, PDI) and incubation overnight at 4 °C. For each heart three hotspot areas were selected: outer-and inner compact myocardium and trabecular myocardium. In each hotspot 250 cells were counted using 400X magnification. Positive cardiomyocytes were averaged as a mean score per patient. The PLN aggregates were examined by their characteristic features as described previously.[13] Specifically, the size, shape, and localization were used to identify and characterize the aggresomes. BiP and PDI positive cells were scored according to dark red staining that was localized perinuclear or more diffuse in the cytosol. All cases were examined by two independent observers and guided by a certified pathologist.

Protein expression analysis. The hiPSC-CMs were washed with cold PBS and lysed in RIPA buffer (Thermo Fisher) supplemented with 1X Protease and Phosphatase Inhibitor Cocktail (Sigma) for 30 minutes on ice. For BiX experiments, hiPSC-CMs were treated with 0.1 µM BiX or vehicle control (DMSO) for 72 hours prior to cell lysis. Protein quantification was performed using the BCA method according to manufacturer's protocol (Pierce), and an equal amount of protein (10-20 µg) was loaded on a precast 4-20% polyacrylamide gel (Bio-Rad), followed by blotting onto a PVDF membrane using the Trans-blot Turbo system (Bio-Rad). Membranes were blocked in 5% BSA in TBS for 1 hour at room temperature. After blocking, the membranes were incubated with primary antibodies overnight while shaking at 4 °C. After incubation with anti-mouse or anti-rabbit horseradish-coupled secondary antibody, the bands were visualized with FluroChem E (Protein Simple) imager. The antibodies used for the Western Blot analyses are shown in Table VI in the Supplement.

Intracellular Calcium analysis. For ratiometric calcium imaging, dissociated hiPSC-CMs were seeded on Matrigel-coated 35 mm dishes with a 20 mm coverglass bottom (Matek). After 7 days, the cells were treated with BiX (0.1 µM) or DMSO. Seventy-two hours later, the cells were loaded with 5 µM Fura-2AM (Thermo Fisher Scientific) with 0.02% Pluronic F-127 (Thermo Fisher Scientific) in Tyrode's solution for 10 min at room temperature. Following two washes in Tyrode's solution, Ca^{2+} traces were acquired using the MultiCell HTS system (Ionoptix). The cells were electrically paced at 1.0 Hz at 37 °C. Calcium transient analysis was performed using the IonWizard software (Ionoptix).

Patient RNA sequencing for UPR genes. Human cardiac tissue collection was approved by the Biobank Research Ethics Committee, University Medical Center Utrecht, Utrecht, the Netherlands (protocol number WARB 12/387). Written informed consent was obtained or in certain cases waived by the ethics committee when obtaining informed consent was not possible due to the death of the individual. Heart samples collected at autopsy or transplantation were obtained from a homogeneous cohort of patients who all carried the same pathogenic PLN R14del mutation (n = 6). Four control hearts obtained from rejected organ donors (n = 3) or from autopsy (n =1) were used as a reference. RNA was isolated using ISOLATE II RNA Mini Kit (Bioline) according to the manufacturers' instructions with minor adjustments. After the selection of mRNA, libraries were prepared using the NEXTflexTM Rapid RNA-seq Kit (Bio Scientific). Libraries were sequenced on the Nextseq500 platform (Illumina), producing single-end reads of 75bp. Reads were aligned to the human reference genome GRCh37 using STAR v2.4.2a[46]. Picard's AddOrReplaceReadGroups v1.98 (http://broadinstitute.github.io/picard/) was used to add read groups to the BAM files, which were sorted with Sambamba v0.4.5[47] and transcript abundances were quantified with HTSeq-count v0.6.1p1[48] using the union mode. Subsequently, reads per kilobase per million mapped reads (RPKMs) were calculated with edgeR's RPKM function[49].

hiPSC-CM RNAseq. Total RNA was isolated from PLN R14del hiPSC-CMs at 72h post-treatment with BiX (0.1 μM) or DMSO control. Sequencing libraries were generated using the NEBNext Ultra Directional RNA Library Prep Kit for Illumina. Clustering of the index-coded samples was performed on a cBot Cluster Generation System using TruSeq PE Cluster Kit v3-cBot-HS (Illumina). Sequencing was carried out on an Illumina HiSeq platform. For each sample 30 to 40 million 150-base paired-end reads were acquired, and data were analyzed using the ENCODE-DCC RNA-seq pipeline (https://github.com/ENCODE-DCC/rna-seq-pipeline). Briefly, reads were aligned to the human genome (GRCh38) using STAR, version 2.5.1b, and gene and transcript quantifications were performed by RSEM (1.2.31). Differential expression analysis was performed in R version 3.4 using the DESeq2 package[50]. Heat maps of gene expression were generated using the online tool Morpheus.

RESULTS

Modeling DCM Contractility Defect With hiPSC-CMs

To model PLN R14del DCM, we recruited 2 unrelated families carrying the mutation (**Figure I in the Data Supplement**) to generate hiPSCs from carriers. Isogenic control lines in which the genetic background is identical are important for unequivocal assignment of phenotype to the underlying gene variant. Therefore, we corrected the R14del mutation in both patient hiPSC lines through CRISPR/Cas9–mediated genome editing and similarly introduced the R14del mutation into an hiPSC line derived from an individual with no history of heart disease (healthy donor [HD]; **Figure 1A and 1B**). We generated 3 pairs of isogenic models that differ only in the PLN R14del mutation (**Figure 1C, Figure II, and Tables I-IV in the Data Supplement**). Impaired contractility is a pathological hallmark of DCM; therefore, we assessed the contractile function of the hiPSC-CMs. Consistent with previous studies,[5] hiPSC-CMs carrying the PLN R14del mutation (patient and HD R14del introduced) showed decreased contractility in 3-dimensional engineered heart tissues (**EHTs; Figure 1D and 1E**) and 2-dimensional monolayer cultures (**Figure 1F and 1G**). Therefore, the isogenic paired hiPSCs lines recapitulated the contractile deficit, providing a quantifiable model for determining the molecular mechanisms that underlie the development of DCM.

scRNA-seq Analysis Reveals UPR Activation

Single-cell transcriptomic analysis makes it possible to deconvolute the complex transcriptional responses that occur naturally across populations of cells into clusters of similarly responding cells. We used a high-throughput droplet-based scRNA-seq method (10X Genomics) to examine the transcriptional effects caused by introducing the PLN R14del mutation into an HD hiPSC line. Unbiased t-distributed stochastic neighbor embedding clustering parsed 9244 single-cell transcriptomes from PLN wild-type (WT) hiPSC-CMs (5279 cells) and PLN R14del hiPSC-CMs (3965 cells) into 10 distinct subpopulations (**Figure 2A**). The heterogeneity of the cardiomyocyte cultures was similar to previous scRNA-seq studies.[6] Despite this heterogeneity, t-distributed stochastic neighbor embedding analysis revealed close clustering of the PLN mutant line with its isogenic counterpart, indicating that the transcriptomes and cell type composition are preserved across isogenic populations (**Figure 2B**). To assign cellular identity, subpopulations were classified on the basis of known marker genes. Most of the cell clusters appeared to be cardiomyocytes based on their specific patterns of gene expression (clusters 1–4 and 6–7 expressed marker genes TNNT2, MYL2, and MYH7). Two clusters, clusters 5 and 8, were identified as fibroblasts (expressing marker genes COL3A1, COL1A1, and FN1), and 1 cluster with very few cells, cluster 9, was identified as smooth muscle cells (with marker genes ACTA2 and TAGLN; **Figure 2C and 2D**).

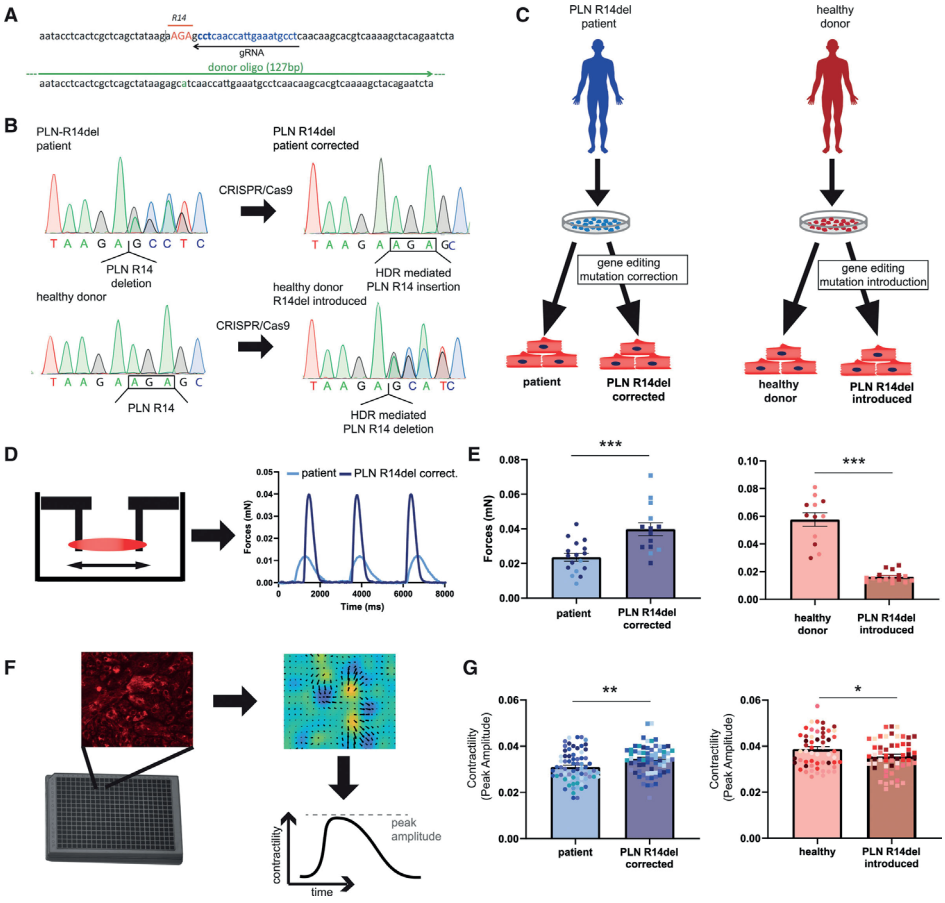

Figure 1. Phospholamban (PLN) loss of arginine at position 14 (R14del) human induced pluripotent stem cell (hiPSC) disease modeling and functional assessment of contractility. A, Schematic overview of the strategy to precisely modify the PLN sequence using CRISPR/Cas9 and single-stranded donor oligonucleotides complementary to the guide RNA (gRNA). B, Sanger sequencing analysis showing the correction and introduction of the R14del variant sequence in hiPSCs generated from dilated cardiomyopathy and healthy individual hiPSCs, respectively. C, Schematic representation of hiPSC lines used in the study. D and E, Assessment of force generation of hiPSC–derived cardiomyocytes (CMs) carrying the PLN R14del mutation and their corresponding isogenic controls in 3-dimensional engineered heart tissues (EHTs; 2 batches, n=5–12 EHTs each). F and G, Two-dimensional monolayer contractility measurements of hiPSC-CMs carrying the PLN R14del mutation and their corresponding isogenic controls (12 batches, n=5–10 wells each). Colors represent experimental batches. Data are presented as mean±SEM. HDR indicates homology-directed repair. *P<0.0005.

Next, we explored the transcriptional changes associated with the R14del mutation. An advantage of single-cell over bulk RNA sequencing is that it affords greater statistical power to resolve differential expression because it focuses within cell-identity clusters rather than across the broader heterogeneous population in which cell type–specific information remains obscure. On the basis of the t-distributed stochastic neighbour embedding clustering and canonical marker expression, we restricted the analysis to the cardiomyocyte subclusters 1 to 4 and 6 to 7. Seventy-seven genes (Wilcoxon ranksum test) were differentially expressed in PLN R14del hiPSC-CMs compared with the isogenic control hiPSC-CMs (**Figure 2E**). Gene enrichment analysis revealed genes associated with pathways related to ER stress and UPR signaling pathway (**Figure 2F**). Further bioinformatics analysis showed that several hallmark genes related to UPR pathway were activated in PLN R14del hiPSC-CMs, including gene members of the protein disulfide isomerase (PDIA3 and PDIA4), heat shock protein 90 (HSP90A1 and HSP90B1), and HSPA5 (also known as BiP [binding immunoglobulin protein]) compared with isogenic PLN WT controls. Comparison of the gene expression profiles of the cell cluster identified as fibroblasts showed no significant differences in the expression of the UPR hallmark genes between the PLN R14del and PLN WT cells (**Figure 2G**). We further corroborated the activation of UPR markers in the hiPSC-CMs at the protein level using Western blot analysis (**Figure 2H**). Finally, we monitored the activity of the UPR pathway in living hiPSC-CMs using an XBP1-splicing reporter construct[7] (**Figure 2I**) and observed a significant increase in UPR activity in patient PLN R14del cells. Because adrenergic drive activates UPR response in cardiomyocytes,[8,9] we also measured the UPR reporter activity on isoproterenol stimulation. Under adrenergic stress conditions (72 hours of treatment with 1 µmol/L), we noticed an increase in UPR signaling in PLN WT cells but an exaggerated (4-fold higher) response in hiPSC-CMs containing the mutation. Taken together, these data suggest that the PLN R14del mutation activates the UPR transcriptional program and sensitizes R14del hiPSC-CMs to adrenergic stress.

Histopathologic Characterization of the UPR in PLN-R14del Patient Myocardium

The accumulation of protein aggregates is often associated with dysfunctional UPR responses, for instance, in neurodegenerative diseases.[10] Protein aggregation has been noted as a histopathologic characteristic of end-stage PLN R14del DCM hearts but not in hearts representative of other forms of DCM.[11–13] Therefore, we examined human myocardial samples of PLN R14del hearts for evidence of UPR involvement. We also analyzed myocardial tissue from desmosomal arrhythmogenic right ventricular cardiomyopathy and ischemic cardiomyopathy hearts (Figure III and Table V in the Data Supplement). Consistent with previous studies,[13] PLN immunolabeling revealed perinuclear aggregations in PLN R14del tissues (7±2%), but these aggregations were absent in arrhythmogenic right ventricular cardiomyopathy, ischemic cardiomyopathy, and control hearts (**Figure 3A–3D and 3M**). BiP is an essential regulator of the UPR that monitors ER stress, and its expression is markedly increased in the presence of unfolded proteins in the ER.[14,15] Accordingly, we observed the highest BiP levels in PLN R14del

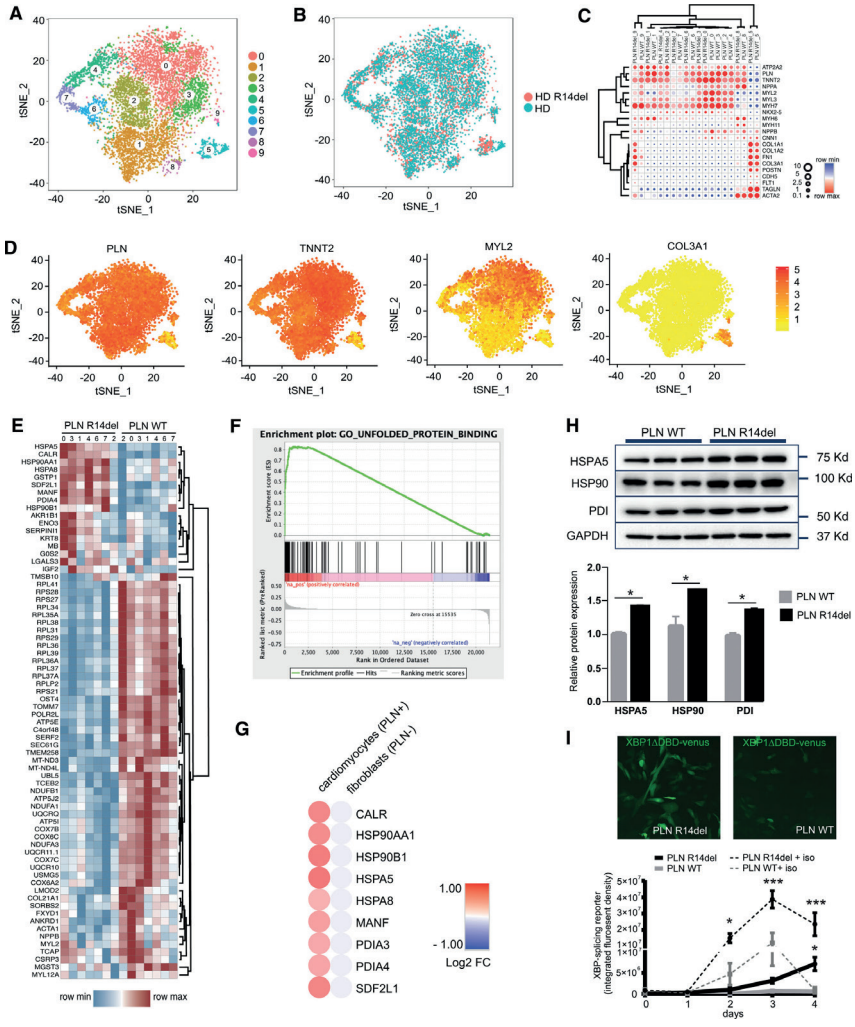

Figure 2. Single-cell RNA sequencing of isogenic human induced pluripotent stem cell–derived cardiomyocytes (hiPSC-CMs) carrying the phospholamban (PLN) loss of arginine at position 14 (R14del) mutation. A and B, Unbiased identification of cell clusters using t-distributed stochastic neighbor embedding (tSNE)–based clustering of single-cell transcriptomes showing a 2-dimensional visualization with distinctly isolated cell subpopulations (n=5279 cells, healthy donor [phospholamban wild-type (PLN WT)]; n=3965 cells, healthy donor PLN R14del introduced [PLN R14del]). C and D, Subpopulations were classified according to canonical marker gene expression. E, Heat map display of 77 differentially expressed genes in the cardiomyocyte subpopulations. F, Gene set enrichment analysis pathway enrichment analysis. G, Comparison of unfolded protein response (UPR) hallmark differential gene expression between cardiomyocyte and noncardiomyocyte subpopulations in a healthy donor (HD) and R14del introduced hiPSC-CMs. H, Western blot expression analysis of UPR proteins from paired isogenic hiPSC-CM lines (n=3 batches). I, Assessment of the UPR activity in living hiPSC-CMs (PLN R14del and PLN WT) transduced with AAV-F-XBP1ΔDBD (3 batches, n=4–6 wells each). Statistical significance represented as differences between PLN WT and PLN R14del in either control or isoproterenol (iso) conditions. Data are presented as mean±SEM. *P<0.0005.

(23±5%), but we also detected comparable BiP expression in desmosomal arrhythmogenic right ventricular cardiomyopathy (16±5%) and ischemic cardiomyopathy (17±2%) relative to control hearts (2±1%; **Figure 3E–3H and 3M**), consistent with UPR activation in failing hearts.[16–18] Protein disulfide isomerase, a protein folding facilitator, is another chaperone that is induced by protein misfolding.[19] A striking protein disulfide isomerase presence was detected in the myocardium of patients with PLN R14del (46±29%) relative to subjects with desmosomal arrhythmogenic right ventricular cardiomyopathy (7±6%), those with ischemic cardiomyopathy (6±4%), and control subjects (3±3%; **Figure 3I–3M**). In addition, RNA sequencing showed that UPR genes are upregulated in the myocardium of R14del patient cardiac tissue relative to that of healthy individuals (**Figure 3N**). Taken together, the histological manifestations of PLN R14del share hallmarks of neurodegenerative disease wherein the accumulation of protein aggregates is associated with abnormal levels of ER stress response.[20,21]

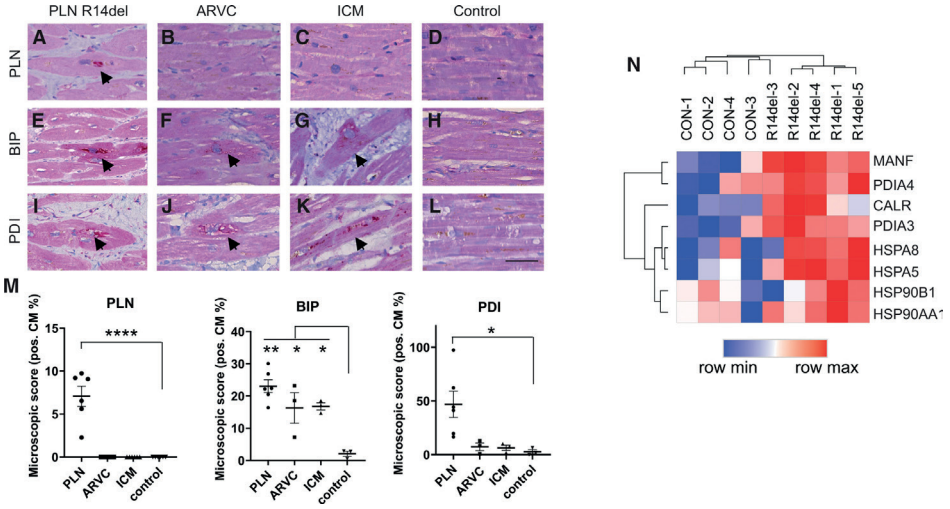

Figure 3. Determination of the unfolded protein response (UPR) status in phospholamban (PLN) loss of arginine at position 14 (R14del) disease and other forms of cardiomyopathies. Histological analysis of human myocardium from patients with PLN R14del, desmosomal arrhythmogenic cardiomyopathy (ARVC), and ischemic cardiomyopathy (ICM) vs control (CON; healthy) hearts. A through D, Abnormal accumulation of PLN in perinuclear aggregates (arrows) in severely affected cardiomyocytes (CMs) in PLN R14del and absent in ARVC, ICM, and control. E through H, Diffuse moderate immunolabeling (arrows) for BiP (binding immunoglobulin protein) in PLN 14del and present to a lesser extent in ARVC and ICM. I through L, High immunolabeling for dotted cytoplasmic protein disulfide isomerase (PDI; arrows) in PLN 14del and low PDI presence in ARVC and ICM (scale bar=25 µm). M, Quantification of immunostaining in PLN R14del (n=6 patients), ARVC (n=3 patients), ICM (n=3 patients), and control (n=3 patients). N, RNA sequence analysis of UPR gene expression from healthy and PLN R14del myocardium from patient samples. Data are presented as mean±SEM. *P<0.00005.

UPR Activity Protects Contractile Function in hiPSC-CMs Harboring PLN-R14del

In principle, UPR could have a pathological or beneficial effect on the PLN R14del cardiomyocytes. To establish the role of the UPR, we carried out a loss-of-function experiment in which we attenuated the main transducers of the UPR (IRE1, ATF6, and PERK; **Figure 4A**). These interconnected signaling branches of the UPR provide the cells with an adaptive response to ER stress to restore proteostasis.[22] Under baseline conditions, targeting each of the 3 branches by siRNA did not significantly affect the contractility in either PLN WT (HD and patient R14del corrected) or PLN R14del (patient and HD R14del introduced) hiPSC-CMs, although a trend toward decreased function (≈10%) was observed with siRNA against IRE1 and PERK in PLN R14del (**Figure 4B and 4C**) hiPSC-CMs. Given that long-term adrenergic stimulation dramatically increased UPR fluxes in hiPSC-CMs harboring PLN R14del (**Figure 2I**), we next evaluated the impact of the loss of function in the presence of isoproterenol. Under adrenergic stress, the contractility of PLN WT hiPSC-CMs remained unchanged after the siRNA-mediated knockdown of IRE1 and ATF6, but we observed significantly decreased contractile function after PERK knockdown (14.3±3.7%; **Figure 4D**). In contrast, we observed a significant contractility deficit in PLN R14del hiPSC-CMs upon knockdown of each of the 3 UPR arms compared with control siRNA treated (siRNA against IRE1, –15.5±4.2%; siRNA against ATF6, –16.7±4.1%; siRNA against PERK, –36.6±5%), indicating that the mutant hiPSC-CMs were sensitized to a loss of UPR signaling in a genotype-specific manner (**Figure 4E**). Taken together, these data suggest that activation of the UPR in PLN R14del hiPSC-CMs preserves cell function and therefore plays a protective role in alleviating ER stress and potentially blunts disease pathogenesis.

Pharmacological Targeting the UPR in PLNR14del Ameliorates Contractility

Next, we evaluated whether pharmacologically stimulating the UPR pathway in PLN R14del hiPSC-CMs beyond basal levels would have a positive effect on cardiomyocyte function. BiP protein inducer X (BiX) is a small molecule proteostasis regulator that increases expression of the BiP protein to consequently induce UPR and protect neurons from ER stress.[23,24] In both PLN R14del (patient and HD R14del introduced) and PLN WT (HD and patient R14del corrected) hiPSC-CMs, treatment with BiX induced a dose-dependent increase in a reporter for XBP1-splicing (indicative of activated UPR). The maximal effect was higher in PLN R14del than in corresponding isogenic control hiPSC-CMs (Emax=33.1±7% versus 56.8±7% XBP-1 splice positive cells in normal versus R14del hiPSC-CMs, respectively; **Figure IVb and IVc in the Data Supplement**). BiX (0.1 µmol/L) significantly enhanced contractility in PLN R14del and PLN WT hiPSC-CMs as detected in 2-dimensional cell sheets (**Figure 4G and 4H**). In the EHTs, this translated to an increase in force from about 20 µN in untreated EHTs to 40 µN in treated EHTs, corresponding to a level statistically indistinguishable from isogenic control EHTs (**Figure 4I and 4J**). Remarkably, the increase in peak contractility was more pronounced in the PLN R14del hiPSC-CMs, and BiX treatment (0.1 µmol/L) led to a nearly complete restoration of

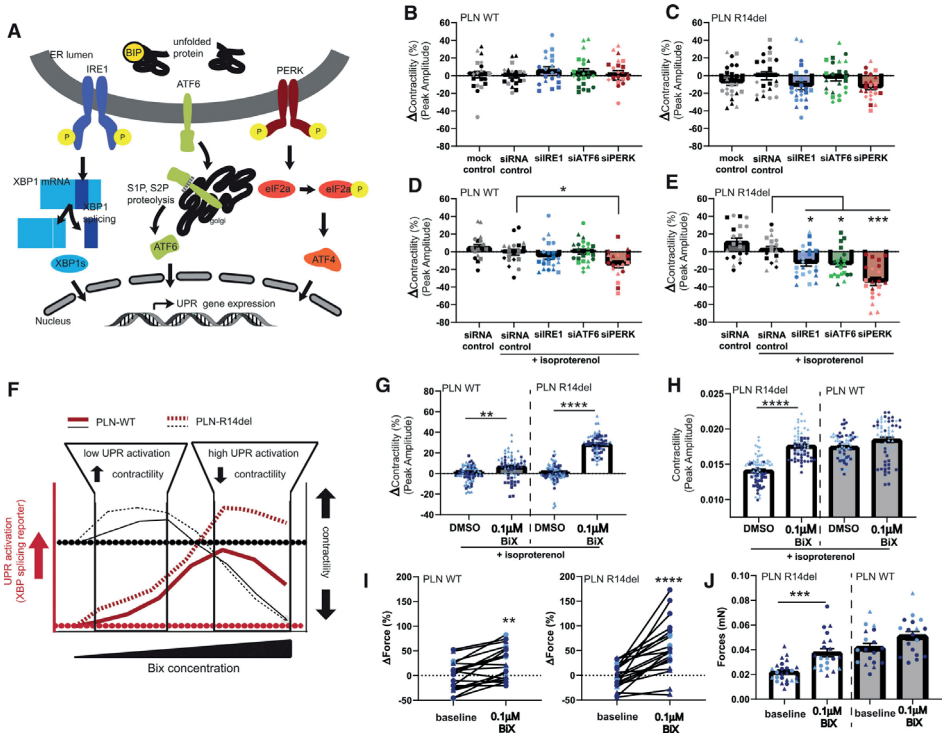

Figure 4. Defining the role of the unfolded protein response (UPR) pathway in human induced pluripotent stem cell–derived cardiomyocytes (hiPSC-CMs) with loss of arginine at position 14 (R14del). A, Schematics of UPR signaling including stress sensors IRE1, ATF6, and PERK at the endoplasmic reticulum (ER) membrane and the 3 corresponding downstream transcriptional effectors. B through E, Functional analysis of UPR pathway perturbation in isogenic hiPSC-CMs. Cells were transfected with the indicated siRNAs, and 2-dimensional (2D) monolayer contractility was measured after 4 days either under baseline conditions (B and C) or with 0.1 μmol/L isoproterenol (D and E). Contractility represented as percent change from control siRNA (6 batches, n = 2–3 wells each). , , , and represent experimental batches; dark symbols represent hiPSC-CMs from healthy donor background; light symbols represent hiPSC-CMs from the patient background. All data are presented as mean±SEM. **P<0.005; ****P<0.00005 vs DMSO vehicle controls (G and H). I and J, Force generation of 3-dimensional engineered heart tissues (EHTs) derived from isogenic hiPSC-CMs at baseline and after treatment with BiX for 72 hours. Force generation is represented as percent change from baseline (I) or as total generated force (J; 4 batches, n=2–8 EHTs each). WT indicates wild-type. **P<0.005; ***P<0.0005; ****P<0.00005 by paired Student t test.

the contractile deficit without increasing the expression levels of myofilament proteins (**Figure V and Table VI in the Data Supplement**). At high concentrations, BiX decreased contractility in both the PLN R14del and isogenic controls (Emax=–25% at 10 μmol/L for both R14del and isogenic controls; **Figure IVa in the Data Supplement**). We considered whether the beneficial effect of BiX is mediated through the modulation of the calcium handling properties of PLN R14del hiPSC-CMs. Compared with a dimethyl sulfoxide control, there was no significant difference in the intracellular calcium handling kinetics in PLN R14del hiPSC-CMs

treated with BiX (**Figure VI in the Data Supplement**). In agreement, the expression levels of PLN and other key calcium handling proteins, including SERCA2a, NCX1 (sodium-calcium exchanger), RYR2 (ryanodine receptor 2), and CASQ2 (calsequestrin 2), were similar between BiX and dimethyl sulfoxide–treated PLN R14del hiPSC-CMs (**Figure VII and Table VI in the Data Supplement**). Collectively, these data suggest that stimulating the UPR pathway in PLN R14del hiPSC-CMs restored contractility to levels of isogenic controls without affecting calcium homeostasis.

DISCUSSION

Human iPSCs provide an opportunity for modeling DCM in vitro to understand the molecular consequences of pathogenic mutation such as PLN R14del. However, the inherited heterogeneity caused by a mixture of cell types in hiPSC-CM differentiation cultures and the genetic background of the donor present confounding factors for defining disease-specific phenotypes. To overcome these challenges, we generated multiple isogenic hiPSC lines carrying the R14del mutation and performed scRNA-seq on these genotype-defined hiPSC lines. This experimental approach can be widely used to define the specific contributions of pathogenic mutation in DCM and cardiomyopathies more broadly. Using this approach, we revealed that the PLN R14del mutation activates the UPR, an integrative intracellular signaling pathway that plays a critical role in the maintenance of proteostasis in the ER.[25] Proteostasis, the balance among protein synthesis, folding, refolding, and degradation, is essential for the long-term preservation of cell and tissue function. With age, the ability of many cells and organs to maintain proteostasis is gradually compromised.[26] Accumulating evidence suggests that UPR is activated in response to a loss of proteostasis in the ER and the corresponding accumulation of protein aggregates, which characterizes age-related diseases and protein folding disorders such as Alzheimer disease, Parkinson disease, and amyotrophic lateral sclerosis.[10] Reminiscent of these diseases, aggregation of PLN protein is a hallmark of PLN R14del DCM,[12] suggesting that the disruption of proteostasis plays a role in disease presentation. It is tempting to speculate that the altered stability and folding kinetics of the PLN R14del mutant directly activate the UPR in mutant hiPSC-CMs and human heart tissues. It will be of interest to explore this hypothesis further in the future. Our isogenic models allowed us to perform high-throughput genetic and pharmacological assays both to understand the underlying pathological mechanisms and to identify therapeutic targets to prevent or treat such diseases. We found that activation of UPR in PLN R14del hiPSC-CMs is protective because molecular inhibition of each of the 3 UPR sensors, IRE1, PERK, and ATF6, exacerbated the contractile dysfunction. Conversely, pharmacological enhancement of UPR by the small molecule agonist BiX ameliorated the contractility defect in PLN R14del hiPSC-CMs. BiX activates the chaperone BiP, thereby increasing the activity of the UPR pathway. These observations are consistent with previous studies showing that activation of UPR suppressed disease onset and progression in cellular and animal models of neurodegenerative

diseases[27–31] and prevented damage in the heart caused by ischemia/reperfusion.[32–34] These findings suggest that enhancing the expression or activity of individual proteostasis network components could be therapeutically beneficial in PLN R14del DCM. Here, we showed that the small molecule BiX improved contractile performance without affecting Ca^{2+} transients in PLN R14del hiPSC-CMs. BiX preferentially activates ER stress response elements upstream of the BiP gene, a molecular chaperone, thereby increasing the activity of the UPR pathway.[22] BiX showed a detrimental effect at high doses in hiPSC-CMs, suggesting a narrow therapeutic window between the effective doses and those at which it causes adverse toxic effects. The underlying mechanism for the biphasic response is unclear. It is possible that BiX is a ubiquitous ER stressor, limiting its application as a therapeutic strategy because it may activate several pathways of the UPR, including the ER stress–induced apoptotic pathways. Although the inotropic mechanisms of BiX are unprecedented, our findings suggest that selective modulation of UPR components could improve cardiac function in PLN R14del DCM and potentially avoid the deleterious effects that can occur with drugs that target calcium signaling or other upstream regulators of contraction. In conclusion, by combining scRNA-seq, human cardiac tissue samples, and disease modeling in vitro using isogenic hiPSC-CMs, our findings implicate the UPR pathway in PLN R14del DCM pathogenesis. Furthermore, stimulating the UPR with the small molecule BiX led to functional rescue of the contractility deficit in PLN R14del hiPSC-CMs in vitro in a genotype-specific manner, suggesting UPR as a potential new therapeutic target. Finally, because disease penetrance in PLN R14del DCM is age related,[35] we theorize that the decline in the proteostasis network capacity associated with aging[36] may enhance the propensity of R14del PLN proteins to form aggregates, increasing disease susceptibility. Our study provides important proof of concept that activation of proteostasis mechanisms has a protective effect on PLN R14del-associated DCM in vitro and could be harnessed therapeutically to delay the onset or slow the progression of disease.

ACKNOWLEDGEMENTS

The authors are thankful to the patients and their families for providing valuable material for research purposes. They thank the Stanford CVI iPSC Biobank for providing the patient hiPSC lines and Dr Masayuki Miura for providing the XBP1-reporter vector. They gratefully acknowledge the help of Christian Snijders Blok and Dr Jan Willem Buikema.

REFERENCES

1. MacLennan DH, Kranias EG. Phospholamban: a crucial regulator of cardiac contractility. Nat Rev Mol Cell Biol. 2003;4:566–577. doi: 10.1038/nrm1151
2. Rosenbaum AN, Agre KE, Pereira NL. Genetics of dilated cardiomyopathy: practical implications for heart failure management. Nat Rev Cardiol.2020;17:286–297. doi: 10.1038/s41569-019-0284-0
3. Haghighi K, Kolokathis F, Gramolini AO, Waggoner JR, Pater L, Lynch RA, Fan GC, Tsiapras D, Parekh RR, Dorn GW 2nd, et al. A mutation in the human phospholamban gene, deleting arginine 14, results in lethal, hereditary cardiomyopathy. Proc Natl Acad Sci USA. 2006;103:1388–1393. doi: 10.1073/pnas.0510519103
4. van der Zwaag PA, van Rijsingen IA, Asimaki A, Jongbloed JD, van Veldhuisen DJ, Wiesfeld AC, Cox MG, van Lochem LT, de Boer RA, Hofstra RM, et al. Phospholamban R14del mutation in patients diagnosed with dilated cardiomyopathy or arrhythmogenic right ventricular cardiomyopathy: evidence supporting the concept of arrhythmogenic cardiomyopathy. Eur J Heart Fail. 2012;14:1199–1207. doi: 10.1093/eurjhf/hfs119
5. Stillitano F, Turnbull IC, Karakikes I, Nonnenmacher M, Backeris P, Hulot JS, Kranias EG, Hajjar RJ, Costa KD. Genomic correction of familial cardiomyopathy in human engineered cardiac tissues. Eur Heart J. 2016;37:3282–3284. doi: 10.1093/eurheartj/ehw307
6. Friedman CE, Nguyen Q, Lukowski SW, Helfer A, Chiu HS, Miklas J, Levy S, Suo S, Han JJ, Osteil P, et al. Single-cell transcriptomic analysis of cardiac differentiation from human PSCs reveals HOPX-dependent cardiomyocyte maturation. Cell Stem Cell. 2018;23:586–598.e8. doi: 10.1016/j.stem.2018.09.009
7. Iwawaki T, Akai R, Kohno K, Miura M. A transgenic mouse model for monitoring endoplasmic reticulum stress. Nat Med. 2004;10:98–102. doi: 10.1038/nm970
8. Ayala P, Montenegro J, Vivar R, Letelier A, Urroz PA, Copaja M, Pivet D, Humeres C, Troncoso R, Vicencio JM, et al. Attenuation of endoplasmic reticulum stress using the chemical chaperone 4-phenylbutyric acid prevents cardiac fibrosis induced by isoproterenol. Exp Mol Pathol. 2012;92:97–104. doi: 10.1016/j.yexmp.2011.10.012
9. Zhuo XZ, Wu Y, Ni YJ, Liu JH, Gong M, Wang XH, Wei F, Wang TZ, Yuan Z, Ma AQ, et al. Isoproterenol instigates cardiomyocyte apoptosis and heart failure via AMPK inactivation-mediated endoplasmic reticulum stress. Apoptosis. 2013;18:800–810. doi: 10.1007/s10495-013-0843-5
10. Hetz C, Saxena S. ER stress and the unfolded protein response in neurodegeneration. Nat Rev Neurol. 2017;13:477–491. doi: 10.1038/nrneurol.2017.99
11. Karakikes I, Stillitano F, Nonnenmacher M, Tzimas C, Sanoudou D, Termglinchan V, Kong CW, Rushing S, Hansen J, Ceholski D, et al. Correction of human phospholamban R14del mutation associated with cardiomyopathy using targeted nucleases and combination therapy. Nat Commun. 2015;6:6955. doi: 10.1038/ncomms7955
12. Te Rijdt WP, van der Klooster ZJ, Hoorntje ET, Jongbloed JDH, van der Zwaag PA, Asselbergs FW, Dooijes D, de Boer RA, van Tintelen JP, van den Berg MP, et al. Phospholamban immunostaining is a highly sensitive and specific method for diagnosing phospholamban p.Arg14del cardiomyopathy. Cardiovasc Pathol. 2017;30:23–26. doi: 10.1016/j.carpath.2017.05.004
13. Te Rijdt WP, van Tintelen JP, Vink A, van der Wal AC, de Boer RA, van den Berg MP, Suurmeijer AJ. Phospholamban p.Arg14del cardiomyopathy is characterized by phospholamban aggregates, aggresomes, and autophagic degradation. Histopathology. 2016;69:542–550. doi: 10.1111/his.12963
14. Bertolotti A, Zhang Y, Hendershot LM, Harding HP, Ron D. Dynamic interaction of BiP and ER stress transducers in the unfolded-protein response. Nat Cell Biol. 2000;2:326–332. doi: 10.1038/35014014
15. Patil C, Walter P. Intracellular signaling from the endoplasmic reticulum to the nucleus: the unfolded protein response in yeast and mammals. Curr Opin Cell Biol. 2001;13:349–355. doi: 10.1016/s0955-0674(00)00219-2
16. Gao G, Xie A, Zhang J, Herman AM, Jeong EM, Gu L, Liu M, Yang KC, Kamp TJ, Dudley SC. Unfolded protein response regulates cardiac sodium current in systolic human heart failure. Circ Arrhythm Electrophysiol. 2013;6:1018–1024. doi: 10.1161/CIRCEP.113.000274
17. Okada K, Minamino T, Tsukamoto Y, Liao Y, Tsukamoto O, Takashima S, Hirata A, Fujita M, Nagamachi Y, Nakatani T, et al. Prolonged endoplasmic reticulum stress in hypertrophic and failing heart after aortic constriction: possible contribution of endoplasmic reticulum stress to cardiac myocyte apoptosis. Circulation. 2004;110:705–712. doi: 10.1161/01.CIR.0000137836.95625.D4

18. Azfer A, Niu J, Rogers LM, Adamski FM, Kolattukudy PE. Activation of endoplasmic reticulum stress response during the development of ischemic heart disease. Am J Physiol Heart Circ Physiol. 2006;291:H1411–H1420. doi: 10.1152/ajpheart.01378.2005

19. Perri ER, Thomas CJ, Parakh S, Spencer DM, Atkin JD. The unfolded protein response and the role of protein disulfide isomerase in neurodegeneration. Front Cell Dev Biol. 2015;3:80. doi: 10.3389/fcell.2015.00080

20. Hoozemans JJ, van Haastert ES, Nijholt DA, Rozemuller AJ, Eikelenboom P, Scheper W. The unfolded protein response is activated in pretangle neurons in Alzheimer's disease hippocampus. Am J Pathol. 2009;174:1241–1251. doi: 10.2353/ajpath.2009.080814

21. Hoozemans JJ, van Haastert ES, Eikelenboom P, de Vos RA, Rozemuller JM, Scheper W. Activation of the unfolded protein response in Parkinson's disease. Biochem Biophys Res Commun. 2007;354:707–711. doi: 10.1016/j.bbrc.2007.01.043

22. Hetz C, Chevet E, Oakes SA. Proteostasis control by the unfolded protein response. Nat Cell Biol. 2015;17:829–838. doi: 10.1038/ncb3184

23. Kudo T, Kanemoto S, Hara H, Morimoto N, Morihara T, Kimura R, Tabira T, Imaizumi K, Takeda M. A molecular chaperone inducer protects neurons from ER stress. Cell Death Differ. 2008;15:364–375. doi: 10.1038/sj.cdd.4402276

24. Oida Y, Izuta H, Oyagi A, Shimazawa M, Kudo T, Imaizumi K, Hara H. Induction of BiP, an ER-resident protein, prevents the neuronal death induced by transient forebrain ischemia in gerbil. Brain Res. 2008;1208:217–224. doi: 10.1016/j.brainres.2008.02.068

25. Walter P, Ron D. The unfolded protein response: from stress pathway to homeostatic regulation. Science. 2011;334:1081–1086. doi: 10.1126/science.1209038

26. Kaushik S, Cuervo AM. Proteostasis and aging. Nat Med. 2015;21:1406–1415. doi: 10.1038/nm.4001

27. Valenzuela V, Jackson KL, Sardi SP, Hetz C. Gene therapy strategies to restore ER proteostasis in disease. Mol Ther. 2018;26:1404–1413. doi: 10.1016/j.ymthe.2018.04.004

28. Hu Y, Park KK, Yang L, Wei X, Yang Q, Cho KS, Thielen P, Lee AH, Cartoni R, Glimcher LH, et al. Differential effects of unfolded protein response pathways on axon injury-induced death of retinal ganglion cells. Neuron.2012;73:445–452. doi: 10.1016/j.neuron.2011.11.026

29. Zuleta A, Vidal RL, Armentano D, Parsons G, Hetz C. AAV-mediated delivery of the transcription factor XBP1s into the striatum reduces mutant Huntingtin aggregation in a mouse model of Huntington's disease. Biochem Biophys Res Commun. 2012;420:558–563. doi: 10.1016/j.bbrc.2012.03.033

30. Gorbatyuk MS, Shabashvili A, Chen W, Meyers C, Sullivan LF, Salganik M, Lin JH, Lewin AS, Muzyczka N, Gorbatyuk OS. Glucose regulated protein 78 diminishes α-synuclein neurotoxicity in a rat model of Parkinson disease. Mol Ther. 2012;20:1327–1337. doi: 10.1038/mt.2012.28

31. Sado M, Yamasaki Y, Iwanaga T, Onaka Y, Ibuki T, Nishihara S, Mizuguchi H, Momota H, Kishibuchi R, Hashimoto T, et al. Protective effect against Parkinson's disease-related insults through the activation of XBP1. Brain Res. 2009;1257:16–24. doi: 10.1016/j.brainres.2008.11.104

32. Jin JK, Blackwood EA, Azizi K, Thuerauf DJ, Fahem AG, Hofmann C, Kaufman RJ, Doroudgar S, Glembotski CC. ATF6 decreases myocardial ischemia/reperfusion damage and links ER stress and oxidative stress signaling pathways in the heart. Circ Res. 2017;120:862–875. doi: 10.1161/CIRCRESAHA.116.310266

33. Martindale JJ, Fernandez R, Thuerauf D, Whittaker R, Gude N, Sussman MA, Glembotski CC. Endoplasmic reticulum stress gene induction and protection from ischemia/reperfusion injury in the hearts of transgenic mice with a tamoxifen-regulated form of ATF6. Circ Res. 2006;98:1186–1193. doi: 10.1161/01.RES.0000220643.65941.8d

34. Blackwood EA, Azizi K, Thuerauf DJ, Paxman RJ, Plate L, Kelly JW, Wiseman RL, Glembotski CC. Pharmacologic ATF6 activation confers global protection in widespread disease models by reprograming cellular proteostasis. Nat Commun. 2019;10:187. doi: 10.1038/s41467-018-08129-2

35. van Rijsingen IA, van der Zwaag PA, Groeneweg JA, Nannenberg EA, Jongbloed JD, Zwinderman AH, Pinto YM, Dit Deprez RH, Post JG, Tan HL, et al. Outcome in phospholamban R14del carriers: results of a large multicentre cohort study. Circ Cardiovasc Genet. 2014;7:455–465. doi:10.1161/CIRCGENETICS.113.000374

36. Hipp MS, Kasturi P, Hartl FU. The proteostasis network and its decline in ageing. Nat Rev Mol Cell Biol. 2019;20:421–435. doi: 10.1038/s41580-019-0101-y

37. Lian X, Hsiao C, Wilson G, Zhu K, Hazeltine LB, Azarin SM, Raval KK, Zhang J, Kamp TJ, Palecek SP. Robust cardiomyocyte differentiation from human pluripotent stem cells via temporal modulation of canonical Wnt signaling. Proc Natl Acad Sci USA. 2012;109:E1848–E1857. doi:10.1073/pnas.1200250109

38. Levitas A, Muhammad E, Zhang Y, Perea Gil I, Serrano R, Diaz N, Arafat M, Gavidia AA, Kapiloff MS, Mercola M, et al. A novel recessive mutation in SPEG causes early onset dilated cardiomyopathy. PLoS Genet.2020;16:e1009000. doi: 10.1371/journal.pgen.1009000

39. Feyen DAM, McKeithan WL, Bruyneel AAN, Spiering S, Hörmann L, Ulmer B, Zhang H, Briganti F, Schweizer M, Hegyi B, et al. Metabolic maturation media improve physiological function of human iPSC-derived cardiomyocytes. Cell Rep. 2020;32:107925. doi: 10.1016/j.celrep.2020.107925

40. Cradick TJ, Qiu P, Lee CM, Fine EJ, Bao G. COSMID: a web-based tool for identifying and validating CRISPR/Cas off-target sites. Mol Ther Nucleic Acids. 2014;3:e214. doi: 10.1038/mtna.2014.64

41. Huang M, Wang J, Torre E, Dueck H, Shaffer S, Bonasio R, Murray JI, Raj A, Li M, Zhang NR. SAVER: gene expression recovery for single-cell RNA sequencing. Nat Methods. 2018;15:539–542. doi: 10.1038/ s41592-018-0033-z

42. Satija R, Farrell JA, Gennert D, Schier AF, Regev A. Spatial reconstruction of single-cell gene expression data. Nat Biotechnol. 2015;33:495–502. doi: 10.1038/nbt.3192

43. Schaaf S, Eder A, Vollert I, Stöhr A, Hansen A, Eschenhagen T. Generation of strip-format fibrin-based engineered heart tissue (EHT). Methods Mol Biol. 2014;1181:121–129. doi: 10.1007/978-1-4939-1047-2_11

44. Sala L, van Meer BJ, Tertoolen LGJ, Bakkers J, Bellin M, Davis RP, Denning C, Dieben MAE, Eschenhagen T, Giacomelli E, et al. MUSCLEMOTION: a versatile open software tool to quantify cardiomyocyte and cardiac muscle contraction in vitro and in vivo. Circ Res. 2018;122:e5–e16. doi:10.1161/CIRCRESAHA.117.312067

45. Sharma A, Burridge PW, McKeithan WL, Serrano R, Shukla P, Sayed N, Churko JM, Kitani T, Wu H, Holmstrom A, et al. High-throughput screening of tyrosine kinase inhibitor cardiotoxicity with human induced pluripotent stem cells. Sci Transl Med. 2017;9:eaaf2584. doi: 10.1126/scitranslmed.aaf2584

46. Dobin A, Davis CA, Schlesinger F, Drenkow J, Zaleski C, Jha S, Batut P, Chaisson M, Gingeras TR. STAR: ultrafast universal RNA-seq aligner. Bioinformatics. 2013;29:15–21. doi:10.1093/bioinformatics/bts635

47. Tarasov A, Vilella AJ, Cuppen E, Nijman IJ, Prins P. Sambamba: fast processing of NGS alignment formats. Bioinformatics. 2015;31:2032–2034. doi: 10.1093/bioinformatics/btv098

48. Anders S, Pyl PT, Huber W. HTSeq: a Python framework to work with high-throughput sequencing data. Bioinformatics. 2015;31:166–169. doi: 10.1093/bioinformatics/btu638

49. Robinson MD, McCarthy DJ, Smyth GK. edgeR: a bioconductor package for differential expression analysis of digital gene expression data. Bioinformatics. 2010;26:139–140. doi: 10.1093/bioinformatics/btp616

50. Love MI, Huber W, Anders S. Moderated estimation of fold change and dispersion for RNA-seq data with DESeq2. Genome Biol. 2014;15:550. doi: 10.1186/s13059-014-0550-8

SUPPLEMENTARY

The **supplementary methods, supplementary table 1-6** and **supplementary figure 1-7** can be downloaded from: https://www.ahajournals.org/action/downloadSupplement?-doi=10.1161%2FCIRCULATIONAHA.120.049844&file=CIRC_CIRCULATIONAHA-2020-049844_supp1.pdf

Or:

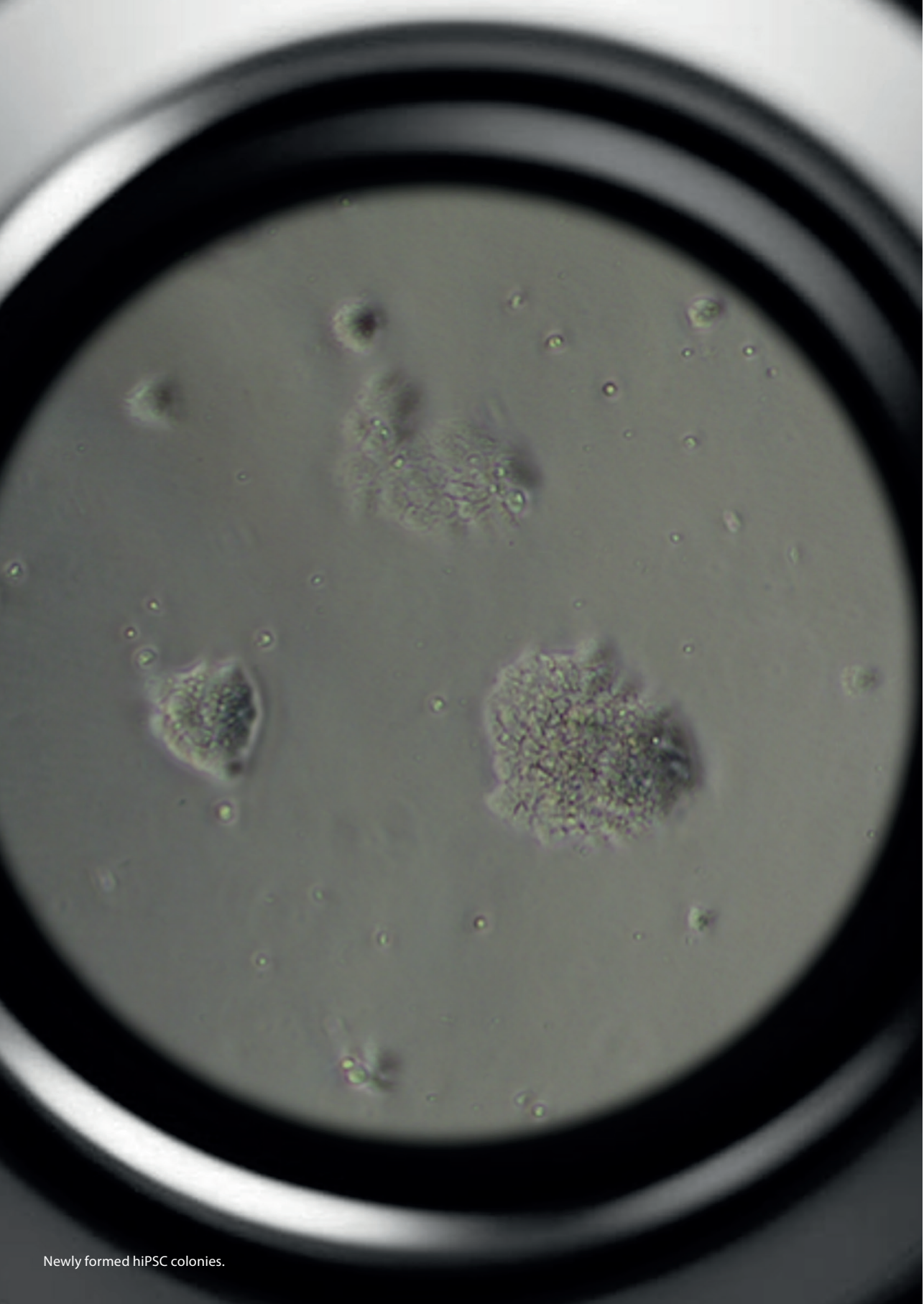

Newly formed hiPSC colonies.

Chapter 10

Generation of Human Induced Pluripotent Stem Cell (hiPSC) Lines Derived from Six Patients Carrying the Pathogenic Phospholamban-R14del (PLN-R14del) Variant and Two Non-Carrier Family Members

Manuscript in preparation

Renée G.C. Maas, Floor van den Dolder, Pieter A Doevendans,
Magdalena Harakalova, Joost P.G. Sluijter

ABSTRACT

The phospholamban (PLN) p.Arg14del mutation was identified in patients diagnosed with dilated cardiomyopathy (DCM) and/or arrhythmogenic cardiomyopathy (ACM), with the molecular disease mechanisms incompletely understood. Human-induced pluripotent stem cells (hiPSCs) clones were generated from three symptomatic and three non-symptomatic individuals carrying the Phospholamban (PLN) p.Arg14.del variant and two healthy probands from families carrying the mutation by reprogramming peripheral blood mononuclear cells (PBMCs) using integration-free Sendai viral vectors. The established hiPSCs clones had normal ES-like morphology, expression of pluripotency markers, karyotyping, and potential for mesoderm-cardiac lineage differentiation. The reported hiPSC lines would be a useful model for in vitro modeling of the PLN-R14del cardiomyopathy.

1. Resource utility

The clinical spectrum of disease phenotype caused by PLN-R14del varies from healthy carriers to early stage ECG and ultrasound strain abnormalities to moderate stage consisting of decreased left ventricular function, and ultimately progression into congestive biventricular failure with/or arrhythmias. To unravel this variability in onset and disease penetrance, hiPSC clones were generated from the peripheral blood mononuclear cells (PBMCs) of symptomatic and non-symptomatic carriers from the PLNR14del mutation or from healthy family probands. The recent development of PLN-R14del mouse and zebrafish models, have helped identifying early-stage molecular mechanisms of PLN-R14del disease. Together with the clinical data and animals. However, animal models could give different outcomes than those found in clinical data and in vitro studies using hiPSC-derived cardiomyocytes. The generated hiPSC lines represent additional tools to compare symptomatic R14del carriers and the non-symptomatic carriers, for elucidating the molecular mechanism of the deletion of arginine 14 in dilated and arrhythmogenic cardiomyopathies.

2. Resource Table 1

Unique stem cell lines identifier	**UMCUi001-A, UMCUi002-A, UMCUi003-A, UMCUi003-B, UMCUi003-C, UMCUi004-A, UMCUi005-A, UMCUi006-A, UMCUi006-B, UMCUi006-C, UMCUi007-A, UMCUi007-B, UMCUi008-A, UMCUi008-B.**
Alternative name(s) of stem cell lines	PLN-R14del-2AC3 (UMCUi001-A) PLN-R14del-3AC7 (UMCUi002-A) PLN-R14del-6BC2 (UMCUi003-A) PLN-R14del-6BC7 (UMCUi003-B) PLN-R14del-6BC13 (UMCUi003-C) PLN-R14del-7AC13 (UMCUi004-A) PLN-R14del-10AC21 (UMCUi005-A) PLN-R14del-10BC12 (UMCUi006-A) PLN-R14del-10BC13 (UMCUi006-B) PLN-R14del-10BC15 (UMCUi006-C) PLN-1CC2 (UMCUi007-A) PLN-1CC6 (UMCUi007-B) PLN-5AC1 (UMCUi008-A) PLN-5AC2 (UMCUi008-B)
Institution	Utrecht Regenerative Medicine Center, Circulatory Health Laboratory, University Utrecht, Department of Cardiology, Experimental Cardiology Laboratory, University Medical Center Utrecht, 3508 GA Utrecht, the Netherlands
Contact information of distributor	Joost Sluijter, j.sluijter@umcutrecht.nl
Type of cell lines	iPSC
Origin	Human
Additional origin info	PLNR14del carriers: UMCUi001-A, Age: 25, Sex: M, UMCUi002-A, Age: 31, Sex: F, UMCUi003-A/UMCUi003-B/UMCUi003-C, Age: 65, Sex: M, UMCUi004-A, Age: 63, Sex: F, UMCUi005-A, Age: 66, Sex: F, UMCUi006-A/UMCUi006-B/UMCUi006-C, Age: 64, Sex: F. Healthy proband donors: UMCUi007-A/UMCUi007-B, Age: 67, Sex: M, UMCUi008-A/UMCUi008-B, Age: 44, Sex: M.
Cell Source	Total PBMCs
Clonality	Clonal
Method of reprogramming	Sendai virus reprogramming (OCT4, SOX2, KLF4, and c-MYC)
Genetic Modification	Yes
Type of Genetic Modification	Hereditary
Evidence of the reprogramming transgene loss	Taqman (Kit)
Associated disease	Dilated and arrhythmogenic cardiomyopathies
Gene/locus	PLN/6q22.31 c.40_42delAGA (p.Arg14del)
Date archived/stock date	11/03/2021
Ethical approval	Medical Ethical Committee (TCBio) of University Medical Center (UMC) Utrecht; approval number: 12–387

3. Materials & Methods

Ethics statement. The generation and characterisation of these hiPSC lines were approved by the Medical Ethical Committee (TCBio) of University Medical Center (UMC) Utrecht; approval number 12–387. The study was performed according to the approved ethics protocol, including the receipt of informed consent.

PBMC collection and reprogramming. 9 ml of whole blood was collected from each donor into Lithium heparin Vacutainer blood collection tubes. PBMCs were isolated using Ficoll density gradient and cultured in StemPro-34 SFM with 100 ng/mL SCF, 100 ng/mL FLT-3, 20 ng/mL TPO and 20 ng/mL IL-6 (Thermofisher Scientific). Reprogramming was performed using the Cytotune 2.0 Sendai Virus Kit (Thermofisher Scientific at the appropriate MOI (i.e., KOS MOI=5, hc-Myc MOI=5, and hKlf4 MOI=3). Colonies exhibiting hiPSC-like morphology were manually selected 2–3 weeks post-transduction and maintained on 0.1 mg/mL growth factor reduced Matrigel (Corning) and Essential 8 (Thermofisher Scientific) with a 7-day passage cycle in the first 1-5 passages, after that the splitting ratio was increased to 1:10-1:15. hiPSCs were cultured by a medium change every day and a 4-day passage cycle. To improve cell survival, split ratio reliability, and to reduce selective pressure, for the first 10 passages a concentration of 10 μM ROCK inhibitor (Calbiochem) was used. Thereafter the concentration of rock was decreased in steps till 20 μM was achieved.

Maintenance of hiPSC. The hiPSCs were non-enzymatically passaged using 0.5 mM EDTA (Invitrogen, 15575-038) every 4 days. In brief, 1 ml 0.5 mM EDTA-PBS was added per 9.6 cm2 surface area. Cells were incubated at room temperature for 3-5 minutes until cells began to separate uniformly throughout the colonies. PBS-EDTA was removed and hiPSC colonies were washed off swiftly using 1 ml E8 medium. WhiPSC clumps were passaged in a splitting ratio of 1:10-1:15 routinely at 80% confluence. Additionally, 20 μM ROCK inhibitor (Calbiochem) was used in the first 24 hrs. To maximize the flexibility in experimental workflow, hiPSCs were cryopreserved and recovered as clumps or single cells using the PSC Cryopreservation Kit (Thermofisher Scientific).

Immunocytochemistry. hiPSC were cultured on a Matrigel-coated 384 wells plate, fixed in paraformaldehyde (4%) for 15 minutes, and permeabilized in blocking/permeabilization buffer (5% BSA/0.3% Triton-X-100 in PBS) for 30 minutes. Primary antibodies were added as shown in Table 2 and incubated in 1:5 diluted blocking/permeabilization buffer DPBS overnight at 4°C. Cells were washed four times with PBS for 5 minutes and incubated with Alexa-conjugated secondary antibodies (life technologies) diluted in 1:5 diluted blocking/permeabilization buffer (Table 2) in the dark at room temperature for 1 hour. Cells were washed four times

with PBS for 5 minutes and nuclei were stained using 1 µg/ml Hoechst (Life Technologies) for 15 minutes. Coverslips were mounted using Fluoromount-G (Southern Biotech) and images were acquired using Leica DMi8 confocal microscope.

RNA isolation and cDNA synthesis. Total RNA was isolated from cells using TriZol (Ambion) according to the manufacturer's instructions. DNase treatment was carried out using RNase-Free DNase Set (Qiagen). Two units of DNase were used to treat 1 µg of RNA for 15 minutes at 42°C and DNase was inactivated for 5 minutes at 65°C. One µg of DNase-treated RNA was converted to cDNA using the iScript™ cDNA Synthesis Kit (Quatetect). After reverse transcription (15 min 42°C) and RT inactivation (3 min 95°C), the cDNA was diluted 20X with MilliQ before qRT-PCR.

qRT-PCR. Relative gene expression was determined by qRT-PCR using the (5'–3') primers listed in Table 2. The following cycling parameters were used for qPCR: Incubation at 95°C for 3 minutes, followed by 40 three-step cycles, each consisting of 95°C for 10 seconds (denaturation), 58°C for 10 s (annealing), and 72°C for 30 s (elongation), followed by melting curve analysis. qPCR was performed using SYBR Green Master Mix (Biorad) in a CFX96 Touch™ Real-Time PCR Detection System (Bio-Rad). All experiments were performed in duplicate and values were normalized to the housekeeping gene RPL32. The ΔΔCt was determined by comparing it to control gene expression and the relative fold increase in expression was calculated by 2^-ΔΔCt.

Table 2. Reagent Details

Classification		Result	Data
Morphology	Brightfield imaging		Fig. 1A
Phenotype	Immunocytochemistry	Positive for pluripotency markers NANOG and OCT4.	Fig. 1D
	RT-qPCR	Expression of pluripotency genes was assessed by qPCR	Fig. 1E
Genotype	Karyotype (ddPCR)	Banding quality	Supplementary Fig. 1
Identity	Microsatellite PCR	Not performed	N/A
	STR analysis	16 loci analyzed, ruled out cross-contamination	Not yet performed
Mutation analysis	TaqMan Genotype Assay	Not performed	N/A
Microbiology and virology	Mycoplasma	MycoAlertTM Mycoplasma Detection Kit: All negative	Data not shown
Differentiation potential	Directed differentiation	All hiPSC lines showed full differentiation capacity towards mesodermal(cardiac) germ layer and CM expansion potential.	Fig. 1B, 1C
List of recommended germ layer markers	Trilineage differentiation qPCR array	Not performed	N/A
Donor screening (OPTIONAL)	HIV 1 + 2 Hepatitis B, Hepatitis C	Not performed	N/A

4. Resource details

PLN is a major regulator of calcium homeostasis in the SR and acts through the inhibition of the sarcoplasmic reticulum Ca^{2+} ATPase (SERCA).[1] During β-adrenergic signalling, PLN is phosphorylated at Ser16 by PKA, or at Thr17 by calcium/calmodulin-dependent protein kinase II (CaMKII) or protein kinase B (Akt), which reverses the inhibitory effect on SERCA.[2] Although the specific cardiac pathology and onset of disease vary, most patients present in the clinics with cardiac dilatation, hypertrophy, decreased ejection fraction, and ventricular arrhythmias. In this regard, the pathogenic c.40_42delAGA (p.Arg14del) mutation is associated with severe heart failure and a poor prognosis from late adolescence.[3] Therefore, it is crucial to generate hiPSCs of patients with the PLN-R14del genetic mutation to elucidate the disease mechanism of this cardiomyopathy. This study establishes novel hiPSC, lines, of which six carry the genetic variant PLN-R14del c.40_42delAGA, where 3 carriers experienced cardiomyopathy-related symptoms.

In this study, whole blood was collected from individuals carrying the PLN-R14del mutation, and healthy family probands. The PLN-R14del carriers can be either non-symptomatic up to now (2A, 3A, and 10A), or display already severe clinical symptoms (6B, 7A, and 10B). The peripheral blood mononuclear cells (PBMCs) were reprogrammed by the CytoTune-iPS 2.1 Sendai Reprogramming Kit using the manufacturer's protocol in feeder-dependent culture conditions. The hiPSC clones displayed a normal human-induced pluripotent stem cell (hiPSC) morphology by light microscopy (**Fig. 1A**), and positive immunostaining for NANOG and OCT4 in all hiPSC colonies (**Fig. 1B**). To further confirm the expression of pluripotency genes was confirmed via RT-qPCR analysis for SOX2, MYC, NANOG, OCT4, and ZFP42 (**Fig. 1C**). Karyotyping of the hiPSC lines was carried out by a ddPCR iCS-Digital™ PSC 24 probes test (Stemgenomics), which will ensure to catch 90% of most frequent genomic defects at high resolution such as the sub-karyotypic 20q.11.21 amplification, which accounts for 20% of all hiPSC abnormalities detected worldwide.[4] All the lines showed no abnormal copy number variants (CNVs) and the normal expression of chromosome X for either male (0-1) or female (1-2) copy number expression (**Supplementary Fig. 1)**. Microbiological contaminations were investigated on a regular basis by the MycoAlertTM Mycoplasma Detection Kit and were all negative (data not shown). A directed cardiac differentiation assay revealed that mesodermal cell types were detectable in all the lines (**Fig. 1D**). Hereafter, the generated hiPSC-CMs showed the capacity for cardiac expansion (**Fig. 1E**) before cryopreservation.[5] All investigations were performed around passages p16–p20. In summary, we describe the generation described the generation hiPSC lines generated of three symptomatic PLN-R14del individuals, three non-symptomatic PLN-R14del individuals, and two non-carrier family members. All eight of the generated hiPSC lines have passed almost all the tests or the test are undergoing (**Table 2**). After all the tests are performed, the hiPSC lines are a useful model to study PLN-R14del cardiomyopathy in vitro.

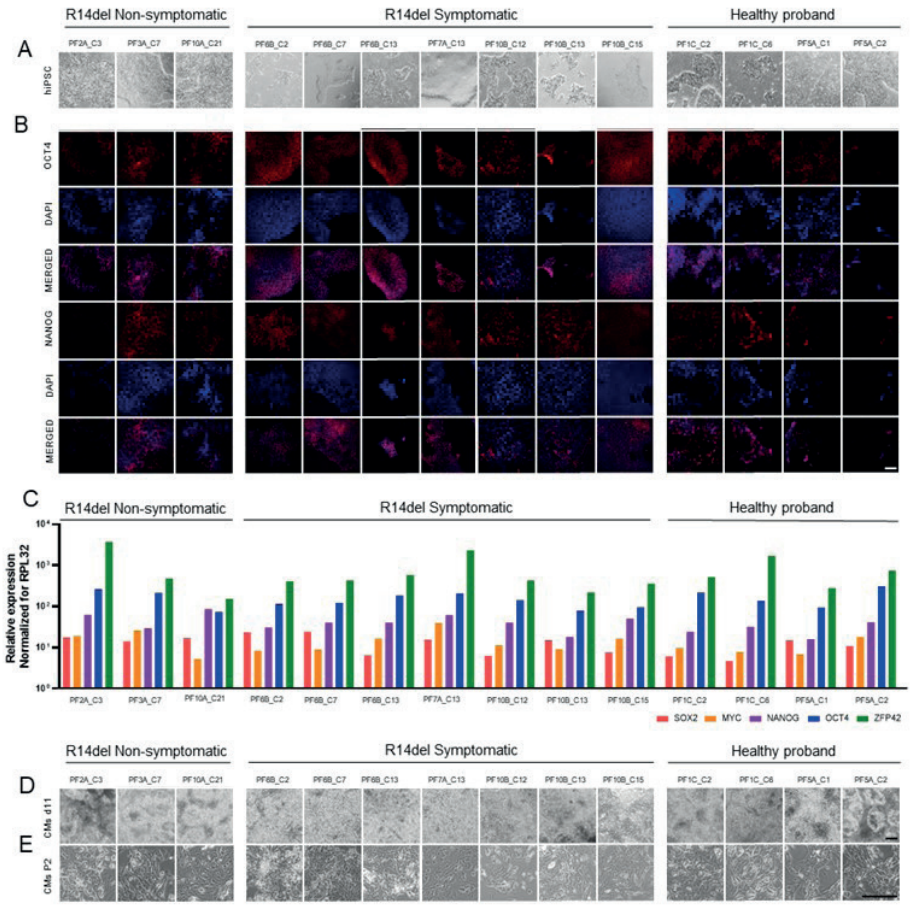

Figure 1. Generation and characterization of hiPSCs. (**A**) Typical round-shape colony morphology with small, tightly packed cells. (**B**) Expression of pluripotency-associated markers (OCT4, NANOG, and DAPI) by immunofluorescence. (**C**) The qRT-PCR analysis confirmed the expression of SOX2, MYC, NANOG, OCT4, and ZFP42. Total RNA from hiPSC-derived fibroblasts was used as negative control and reference. (**D**) Cardiac differentiation potential of hiPSC clones on day 11 (d11) post differentiation. (**E**) hiPSC-CMs show the capacity to expand up to passage 2 (P2). Scale bars represent 200 uM.

Table 3. Characterization and validation.

Antibodies used for immunocytochemistry			
	Antibody	**Dilution**	**Company Cat #**
Pluripotency Markers	Rabbit anti-NANOG	1:100	Cell Signaling, Cat# D73G4
	Mouse anti-OCT3/4	1:200	Santa Cruz, Cat# sc-5279
Secondary antibody	Goat anti-Rabbit IgG, Alexa Fluor 555	1:500	Thermo Fisher, Cat# A-21428
Primers			
	Target	**Forward primer (5′-3′)**	**Reverse primer (5′-3′)**
Pluripotency markers (qRT-PCR)	SOX2	TGGACAGTTACGCGCACAT	CGAGTAGGACATGCTGTAGGT
	MYC	GCGAACCCAAGACCCAGGCCTGCTCC	CAGGGGGTCTGCTCGCACCGTGATG
	NANOG	TGCAAGAACTCTCCAACATCCT	ATTGCTATTCTTCGGCCAGTT
	OCT4	AGGTGTTCAGCCAAACGACC	TGATCGTTTGCCCTTCTGGC
Housekeeping marker	ZFP42	TAGAATGCGTCATAAGGGGTGA	TCTTGCCTGTCATGTACTCAGAA
	RPL32	AGGCATTGACAACAGGGTTC	GACGTTGTGGACCAGGAACT

Declaration of Competing Interest

The authors declare that they have no known competing financial interests or personal relationships that could have appeared to influence the work reported in this paper.

Acknowledgments

This work was commissioned and completely supported by the Foundation PLN. A few additional chemicals were provided by NWO VENI grant (no. 016.176.136 to MH).

REFERENCES

1. Kranias, E. G. & Hajjar, R. J. Modulation of Cardiac Contractility by the Phopholamban/SERCA2a Regulatome. Circ. Res. (2012) doi:10.1161/CIRCRESAHA.111.259754.
2. Grimm, M. & Brown, J. H. β-Adrenergic receptor signaling in the heart: Role of CaMKII. J. Mol. Cell. Cardiol. 48, 322 (2010).
3. van der Zwaag, P. A. et al. Editor's choice: Phospholamban R14del mutation in patients diagnosed with dilated cardiomyopathy or arrhythmogenic right ventricular cardiomyopathy: evidence supporting the concept of arrhythmogenic cardiomyopathy. Eur. J. Heart Fail. 14, 1199 (2012).
4. Halliwell, J. A. et al. Nanopore Sequencing Indicates That Tandem Amplification of Chromosome 20q11.21 in Human Pluripotent Stem Cells Is Driven by Break-Induced Replication. Stem Cells Dev. 30, (2021).
5. Massive expansion and cryopreservation of functional human induced pluripotent stem cell-derived cardiomyocytes. STAR Protocols 2, 100334 (2021).

SUPPLEMENTARY FIGURES

Supplementary Figure 1 - ddPCR results for karyotyping

PF1A_C2

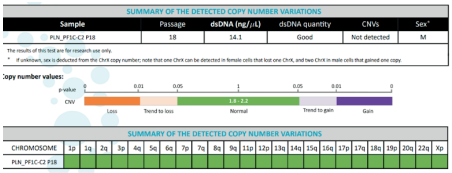

PF1A_C6

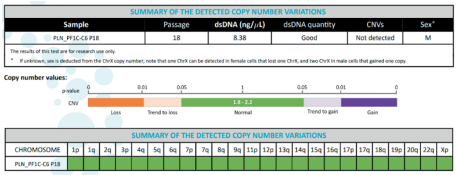

PF2A_C3

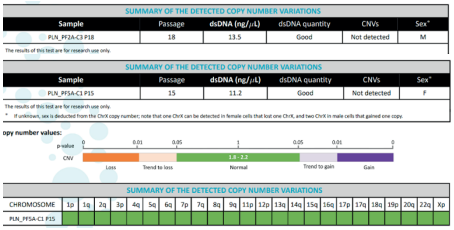

PF3A_C7

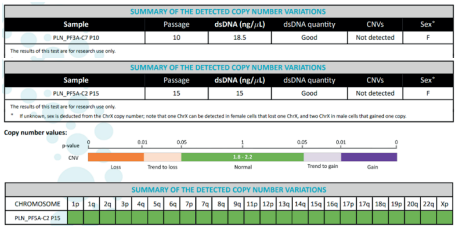

PF6B_C2

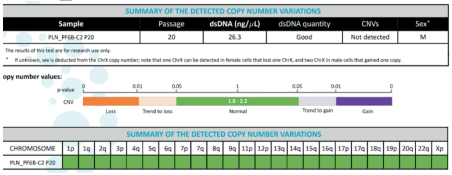

PF6B_C7

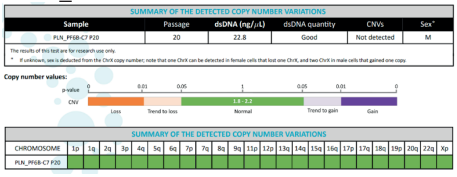

PF6B_C13

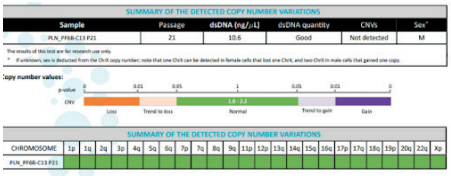

PF7A_C13

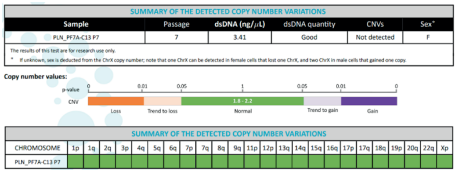

PF10A_C21

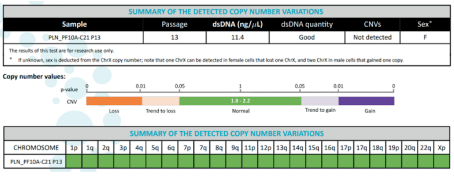

PF10B_C12

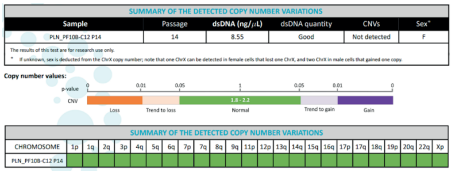

PF10B_C13

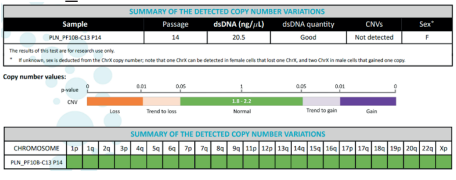

PF10B_C15

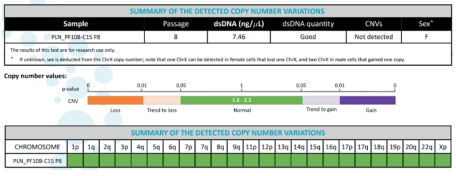

Supplmenetary Figure 2 – Example of hiPSC Datasheet

UMC Utrecht

Data Sheet: hiPSC line generated by the RMCU (PLN foundation)

STICHTING GENETISCHE HARTSPIERZIEKTE PLN

Product Information

hiPSC line	Gender	Genotype	Phenotype	Age at PBMC withdraw (2018)
Sendai RMCU_PF6B_C13	M	PLN R14del mutation	Yes	61

Description

The patient-derived human induced pluripotent stem cells (hiPSC) lines are generated from peripheral blood mononuclear cells (PBMCs). Reprogramming was performed using the Cytotune 2.0 Sendai Virus Kit (Thermofisher Scientific at the appropriate MOI (i.e., KOS MOI=5, hc-Myc MOI=5, hKlf4 MOI=3). The resulting hiPSC were selected using morphological criteria. One cell vial contains enough cells to start culturing in 12-well format (± 0.5-1.0 x 10^6 iPSC). For thawing and culturing instructions please see supplementary protocol 1 and 2.

hiPSC line Quality information

Pluripotency testing:

Expression of pluripotency markers are quantified using PCR and immunofluorescent stainings. The PF6B_C13 hiPSC line displays a healthy iPSC morphology (**Figure 1A**) and is positive for the pluripotency markers Alkaline phosphathase (AP), TRA-160, NANOG, OCT3/4 and SOX2 by immunofluorescent (IF) and immunohistochemistry (IHC) stainings (**Table 1, Figure 1B**, scale bar; 200 µM). The PF6B_C13 hiPSC line is positive for the pluripotency markers NANOG, MYC, SOX2, ZFP42, OCT4 by RT-qPCR (**Table 1, Figure 1C**).

Table 1: Pluripotency expression confirmation

Assay	Genes	Positive	#P
qPCR	NANOG	Yes	21
qPCR	OCT4	Yes	21
qPCR	ZFP42	Yes	21
qPCR	MYC	Yes	21
qPCR	SOX2	Yes	21
qPCR	EIF1AY	Yes, Male	21
IF	Tra-160	Yes	21
IF	AP	Yes	21
IHC	NANOG	Yes	21
IHC	OCT3/4	Yes	21

Figure 1 – hiPSC characterization

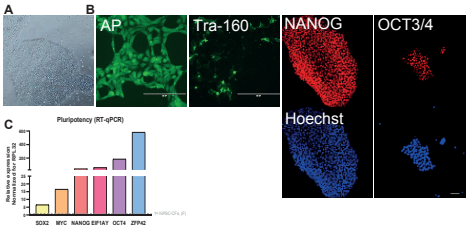

Myocplasma testing: PF6B_C13 hiPSC line is regularly tested for sterility for mycoplasma every 1-2 months.

Karyotyping: ddPCR analysis on the gDNA by the iCS-digital™ PSC test kit (Stem genomics) allows analysis of the most common genomic defects occurring in hiPSC lines. In the PF6B_C13 hiPSC line (Passage 21) no CMVs were detected (**Page 2**).

hiPSC-CM differentiation:
We obtained hiPSC derived cardiomyocytes (hiPSC-CMs) using the original RPMI/B27 monolayer directed differentiation protocol in this hiPSC line.[1,2] 6-8 µM CHIR09921 was used for cardiac differentiation. The most optimal CHIR concentration for the PF6B_C13 hiPSC line is displayed in table 2, -; no beating observed, +/-; some beating observed, +; over 50% beating observed, ++; over 70% beating observed, +++; over 90% beating observed.

CHIR (µM)	Differentiation #1	Differentiation #2	Differentiation #3
6	++	+	++
7	+++	+++	++
8	+++	+++	+++

[1] Lian X. Robust cardiomyocyte differentiation from human pluripotent stem cells via temporal modulation of canonical wnt signaling. Proc. Natl. Acad. Sci. U S A. 2012;109:1848–1857.

[2] Maas, R.G.C et al. Massive expansion and cryopreservation of functional human induced pluripotent stem cell-derived cardiomyocytes. Cell STAR protocols 2021 Feb 9;2(1):100334. doi: 10.1016/j.xpro.2021.100334.

Shipping, storage, and handling

The shipping will take place on dry ice. After shipment either thaw for immediate use or store in liquid nitrogen. Cells stored for more than 1 day at −80°C quickly lose viability. This product is stable for at least 6 months from the date of receiving when stored as directed.

Biosafety Level 2 Users should treat all human and animal cells as potential pathogens. Wear protective clothing and eyewear. Practice appropriate disposal techniques for potentially pathogenic or biohazardous materials.

Supplementary Protocols

Supplementary protocol 1: hiPSC thawing protocol
Supplementary protocol 2: hiPSC culturing protocol
Supplementary protocol 3: hiPSC-CM differentiation protocol

Terms and Conditions

This product is property of the PLN foundation and for research/ pharma use only; not intended for human or animal diagnostic or therapeutic uses.

Contact: Renee Maas (r.g.c.maas-4@umcutrecht.nl) ; PLN foundation (Annet@plnheart.org)

UMC Utrecht

Data Sheet: hiPSC line generated by the RMCU (PLN foundation)

STICHTING GENETISCHE HARTSPIEROZE PLN

Page 2

iCS digital PSC test report (Stem Genomics) – Passage 21

stemgenomics cell integrity

iCS-digital™ PSC test report

CONTACT PERSON		
Name: Renee Maas	Phone: +31618810035	E-mail: r.g.c.maas-4@umcutrecht.nl
INSTITUTION / COMPANY		
Name: UMC Experimental cardiology		
Address: Uppsalalaan 8		

PURCHASE ORDER (DATE)	REMAINING TEST
QUOT220304-1 - QUOT220421-2	0 - 16

TEST DATE	CONTROL VALIDATION
April 26, 2022	Normal DNA control for the 24 probes: Passed

SUMMARY OF THE DETECTED COPY NUMBER VARIATIONS

Sample	Passage	dsDNA (ng/µL)	dsDNA quantity	CNVs	Sex*
PLN_PF6B-C13 P21	21	10.6	Good	Not detected	M

The results of this test are for research use only.
* If unknown, sex is deducted from the ChrX copy number; note that one ChrX can be detected in female cells that lost one ChrX, and two ChrX in male cells that gained one copy.

Copy number values:

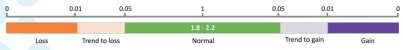

SUMMARY OF THE DETECTED COPY NUMBER VARIATIONS

CHROMOSOME	1p	1q	2q	3p	4q	5q	6q	7p	7q	8q	9q	11p	12p	13q	14q	15q	16q	17p	17q	18q	19p	20q	22q	Xp
PLN_PF6B-C13 P21																								

COPY NUMBER VARIATION

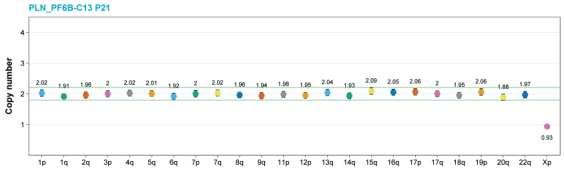

Elena Hauser
Platform Manager

Stem Genomics • IRMB - Hôpital Saint Eloi • 80 avenue Augustin Fliche - 34295 Montpellier Cedex 5 • France • +33 (0)9 85 03 61 60

Contact: Renee Maas (r.g.c.maas-4@umcutrecht.nl) ; PLN foundation (Annet@plnheart.org)

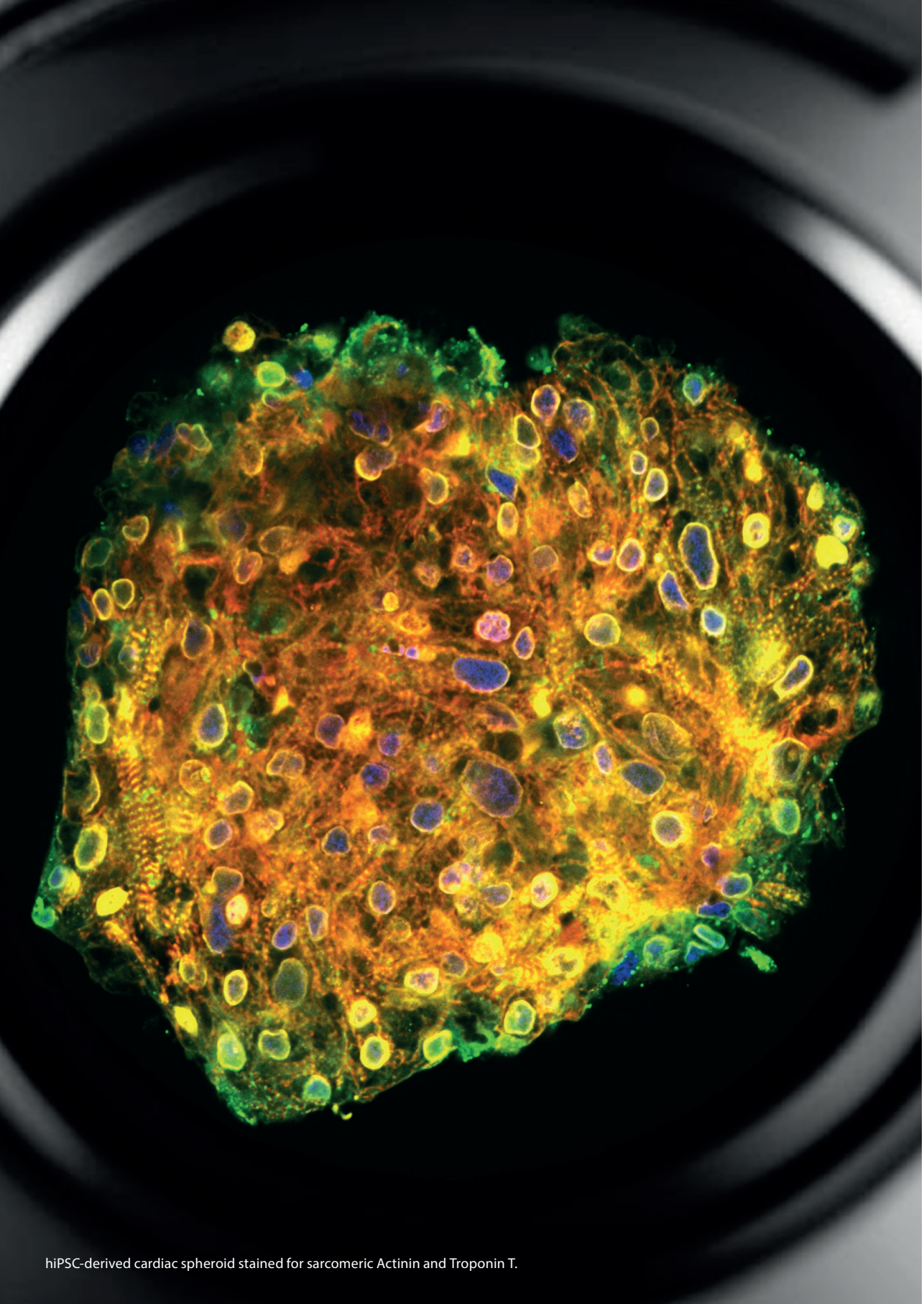

hiPSC-derived cardiac spheroid stained for sarcomeric Actinin and Troponin T.

Chapter 11

Generation, High Throughput Screening, and Biobanking of Human iPSC-Derived Cardiac Spheroids

Published in: Journal of Visualized Experiments (JoVE), 2023

Renée G.C Maas, Tess Beekink*, Nino Chirico*, Christian J.B. Snijders Blok, Inge Dokter, Vasco Sampaio-Pinto, Alain van Mil, Pieter A. Doevendans, Jan W. Buikema, Joost P.G. Sluijter§ and Francesca Stillitano§

*These authors contributed equally

§These authors contributed equally.

SUMMARY

Presented is a set of protocols for the generation and cryopreservation of cardiac spheroids (CSs) from human induced pluripotent stem cell-derived cardiomyocytes (hiPSC-CMs) cultured in a high throughput multidimensional format. This three-dimensional (3D) model functions as a robust platform for disease modeling, high throughput screenings, and the screening of functional CSs after cryopreservation.

ABSTRACT

Human-induced pluripotent stem cell-derived cardiomyocytes (hiPSC-CMs) are of paramount importance for human cardiac disease modeling and therapeutics. We recently published a cost-effective strategy for the massive expansion of hiPSC-CMs in two dimensions (2D). Two major limitations are the cell immaturity and lack of three-dimensional (3D) arrangement and scalability in high-throughput-screening platforms. To overcome these limitations, the expanded cardiomyocytes form an ideal cell source for the generation of 3D cardiac cell culture and tissue engineering techniques. The latter holds great potential in the cardiovascular field, providing the next generation of more physiologically relevant high-throughput screens (HTS). Here, we present a scalable, HTS-compatible workflow for the generation, maintenance, and optical analysis of cardiac spheroids (CSs) in a 96-well-format. These small cardiac spheroids are essential to fill the gap present in current *in vitro* disease models and/or generation for 3D tissue engineering platforms. The resulting CSs possess a highly homogeneous morphology, size, and cellular composition. Furthermore, hiPSC-CMs cultured as CSs, display increased maturation. CSs present several functional features of the human heart such as spontaneous calcium handling and contractile activity. By automating the entire workflow from CSs generation to functional analysis, we enhance intra- and inter-batch reproducibility as demonstrated via high-throughput (HT) imaging and calcium handling analysis. The described protocol allows modeling of cardiac diseases and assessing drug/therapeutic effects at the single-cell level within a complex 3D cell environment in a fully automated HTS workflow. In addition, the study describes a straightforward procedure for whole-spheroids biobanking, thereby, providing researchers the opportunity to create next-generation living biobanks. HTS combined with long-term storage will substantially contribute to translational research in a wide range of areas, including drug discovery and testing, regenerative medicine, and the development of personalized therapies.

INTRODUCTION

The discovery of human-induced pluripotent stem cells (hiPSCs) offered unprecedented opportunities to study human development and disease at the cellular level. Over the past decade, using developmental lessons, various protocols were established to ensure the efficient differentiation of hiPSCs into cardiomyocytes (CMs)[1–4]. hiPSC-derived cardiomyocytes (hiPSC-CMs) can serve as a resource for modeling genetically inheritable cardiovascular diseases (CVDs), testing cardiac safety for new drugs, and cardiac regenerative strategies[5–8]. Despite directed cardiac differentiation of hiPSCs, indefinite cardiomyocyte numbers remain a challenge in the cardiac field since matured hiPSC-CMs generally are non-proliferative, and primary human cells are not available in high quantities. Recently, we described that concomitant Wnt signaling activation with low cell-density culture resulted in a massive proliferative response (up to 250 fold) of hiPSC-CMs[9,10]. This cost-effective strategy for the massive expansion of hiPSC-CMs via serial passaging in culture flask format facilitates standardization and quality control in large batches of functional hiPSC-CMs. Additionally, to keep up with the demand for large batches of hiPSC-CMs from various donors, the biobanking of hiPSC-CMs has been described[10]. However, cardiomyocyte monolayers seeded in these standard culture dishes are not representative of the complex 3D structure present in the heart. Moreover, the immaturity of hiPSC-CMs has remained an obstacle, thus falling short in mimicking the biological and physiological phenotype of the *in vivo* cardiovascular environment. Novel 3D *in vitro* models have been developed where hiPSC-CMs show closer physiological behavior such as self-organization processes[11,12], ECM remodeling[13], enhanced maturation[14–16], and synchronized contraction[17–19]. Hereto, 3D models have been utilized for drug discovery, drug cardiotoxicity testing, disease modeling, regenerative therapies, and even the first clinical trials[20–24]. One of the most used models is the fibrin-based engineered heart tissue (EHT), which exhibits a tissue-like arrangement and cardiac contractility[13,17,25]. Previously, we showed that EHTs generated from expanded hiPSC-CMs displayed comparable contractility to those from unexpanded hiPSC-CMs, demonstrating uncompromised cellular functionality after expansion[9]. Nevertheless, even though the generation of EHTs from hiPSC-CMs has been well established, further developments are anticipated regarding the establishment of an HT assessment platform. Here, the rapid generation of large numbers of self-aggregating CS in 96-wells format allows an improvement in 3D conditions for HTS purposes. Overall, the advantage of a CSs as 3D cell culture is the option of using semi-automatic methods to produce spheroids such as pipetting robots for filling multi-well plates, exchanging medium, drug treatments, and finally analyzing the samples in high-content readers[20]. Here, we describe optimized protocols to generate high-purity and high-quality 3D CSs, which can be efficiently cryopreserved and screened for cardiac function by performing Ca^{2+} transient measurements using an optical calcium acquisition and analysis system. This model provides a simple, yet powerful, tool to perform high throughput screens on hundreds-thousands of spheroids.[17,18]

PROTOCOL

hiPSC-CMs used in this study were generated according to previously described hiPSC culturing and CM differentiation protocols[26,27]. Optionally, the hiPSC-CMs can be expanded and cryopreserved as recently published before starting the CSs protocol[10].

1. Preparation of Media

1. Prepare basal RPMI medium

Equilibrate pen/strep and the basal medium (RPMI 1640) to room temperature (RT). Ensure that the supplement has thawed completely. Mix 500 mL of the basal medium and 5 mL of Pen/strep. Store at 4 °C.

2. Prepare RPMI + B27.

1. Equilibrate the B27 supplement and the basal medium (RPMI 1640) to RT. Ensure that the supplement has thawed completely. Mix 485 mL of the basal medium, 5 mL of Pen/strep, and 10 mL of the 50x supplement. Store at 4 °C for up to 2 weeks, equilibrate to 37 °C before use.

3. Prepare CM re-plating media (RM)

1. Add Rho-associated, coiled-coil containing protein kinase (ROCK) inhibitor (2 µM final concentration) and Knockout Serum Replacement (Knockout SR, 10% final concentration) to RPMI + B27 media. Store at 4 °C for up to 1 week, equilibrate to 37 °C before use.

4. Preparez CM thawing media

1. Add Revitacell (100X) and Knockout SR (20% final concentration) to RPMI + B27 media and equilibrate to 37 °C before use.

5. Prepare maturation media

1. Equilibrate the B27 supplement, Knockout SR, pen/strep, maturation medium[28], and the basal DMEM no-glucose medium to RT. Ensure that the supplement has thawed completely. Mix 435 mL of the basal medium and 10 mL of the 50X B27 supplement, 5 mL of pen/strep, 5 mL Knockout SR, and 45 mL of maturation medium aliquot as previously described[28] and filter using a 0.22 µm vacuum-driven filter. Store at 4 °C for up to 2 weeks, equilibrate to 37 °C before use.

6. Prepare fluor bright medium

1. Equilibrate, pen/strep, and the basal DMEM Fluorobrite medium to RT. Ensure that the supplement has thawed completely. Mix 500 mL of the basal medium and 5 mL of pen/strep. Store at 4 °C, equilibrate to 37 °C before use.

7. Prepare Pluronic solution

1. Mix pluronic powder F-127 (20% final concentration) and PBS. Filter using a 0.22 µm vacuum-driven filter and store at 4 °C. Equilibrate to RT before use.

8. Prepare calcium dye medium

1. Mix the Pluronic F-127 solution (final concentration of 0.04%) and the Cal-520 AM (1:1000) in fluor bright medium: In a 50 mL conical tube, add 10 uL of Cal520, 20 µL of Pluronic solution. Mix until fully dissolved. Keep the solution in the dark.

2. Preparation of Buffers

Prepare Permeabilization and blocking buffer: This buffer contains PBS, 5% BSA, and 0,3% Triton-X-100.

Prepare the Flow cytometry buffer: This buffer contains 50 ml of PBS and 1% BSA and 0.3% Triton-X-100.

Prepare the Flow cytometry washing buffer: This buffer contains 50 ml of PBS and 1% BSA.

Prepare Spheroid washing buffer: This buffer contains 1 mL Triton-X-100, 2 mL of 10% (w/v) SDS, and 2g BSA in 1L PBS. NOTE: OWB can be stored at 4 °C for up to 2 weeks.

Prepare the FUnGI solution: This solution contains 50% (v/v) glycerol, 9.4% (v/v) dH2O, 10.6 mM tris base, 1.1 mM EDTA, 2.5M fructose, and 2.5 M urea. Note: FUnGI can be stored at 4 °C in the dark. FUnGI should not be heated as fructose caramelizes at higher temperatures. Preparation time = 1 day.

Prepare PBT buffer. This buffer contains PBS/Tween-20 (0.1% v/v)): For 1L of PBS add 1mL Tween-20.

3. Preparation of Small Molecules

NOTE: Reconstitute all small molecules in DMSO unless otherwise stated.

1. Reconstitute 10 mM aliquots of 50 µL each of Thiazovivin (ROCK inhibitor) and store at -20 °C.
2. Prepare 2.5 mM aliquots of 10 µL each of Cal-520 AM and store them at -20 °C.

4. Cardiac spheroid generation

1. Three weeks before performing the Ca^{2+} transient measurements or any functional analysis, add 1 mL of sterile TrypLE Select Enzyme to each well. Incubate the plate at 37 °C for 15 min.
2. Using a 5 mL pipette, mechanically dissociate the cells by flushing with 2 mL warm basal RPMI medium so that single cells can be seen when observed under a microscope.
3. Transfer the cells to a sterile 15 mL conical tube. Centrifuge for 3 min at 300*xg*.
4. Aspirate the supernatant and resuspend the cells in CM replating media (RM).
5. Using a 1,000 mL pipette tip, mechanically dissociate the cell pellet until the solution appears homogeneous.
6. Transfer 10,000 cells in 100 µL RM to each ultra-low attachment round bottom 96-wells well. Place the plate of CSs on an orbital shaker at 70 rpm in a 37°C incubator for 24 h.
   NOTE: For more CSs/well; seed 1 million CMs in a 6wells-format ultra-low attachment plate with 2 mL RM.
7. Aspirate 50 µL of medium from each well and add 100 µL RPMI + B27 medium per well for the first 48 h.
   NOTE: Always keep 50 µL of the medium in the 96-well to avoid accidental aspiration and spheroid rupture.
8. Aspirate 100 µL of medium from each well and add 100 µL maturation medium per well. Maintain cells in maturation media, changing media every 2-3 days until ready for functional analysis.

5. Cryopreservation of cardiac spheroids

Cardiac spheroids can be cryopreserved for long-term storage. Cryopreservation can be performed from day 3 after the generation of CSs. CSs can be cryopreserved directly in the wells of a 96 wells plate or as a CSs suspension in cryovials.

1. Pre-chill the plate to 4°C by placing the plate on ice for 10 min.
2. Centrifuge spheroid plate for 3 min at 70*xg*.
3. Remove the supernatant till 50 µL remains and resuspend each well in STEMdiff hiPSC Freezing Medium. Use 200 µL medium per well.
   NOTE: Keep the cell suspension on ice.
   NOTE: In case of a 6 wells plate with spheroids; freeze one well in 500 µL freezing medium cryovial.
4. Freeze the plate at –80°C for a minimum of 4 h in a CoolCell.
5. Transfer the plate to liquid nitrogen or –150°C for long-term storage.

6. Thawing of cardiac spheroids

1. Prepare 20 mL of 37°C-preheated RPMI medium in a 50-mL tube.
2. Collect the cell plate with CSs from the liquid nitrogen and place it in the incubator for 15 min.
   NOTE: Do not thaw more than one plate at a time to ensure a quick thawing process.
3. Remove the supernatant till 50 µL remains and resuspend each well in RPMI medium. Use 200 µL medium per well.
4. Centrifuge for 3 min at 70*xg*.
5. Repeat steps 3 and 4.
6. Remove the supernatant till 50 µL remains and resuspend each well in CM thawing medium. Use 200 µL medium per well.
7. Place the plate of spheroids on an orbital shaker at 70 rpm in a 37°C incubator for 24 h. The incubator conditions should be set to 37°C, 5% CO2, 21% O2, and 90% humidity.
8. Aspirate 50 µL of medium from each well and add 100 µL RPMI + B27 medium per well for the first 48 h.
9. Aspirate 100 µL of medium from each well and add 100 µL maturation medium per well. Maintain cells in maturation media, changing media every 2-3 days until ready for functional analysis.

7. Assessment of Intracellular Ca^{2+} Transients

1. After 1 week of culture, the thawed CSs are optimal for calcium handling optical imaging.
   NOTE: As indicated previously, the spheroids are in culture for the optimal timing of 3 weeks, two weeks before freezing, and one week after thawing. The 'fresh' controls are age-matched.
2. Treat them with 100 µL per well of calcium dye medium and incubate at 37 °C for 60 min.
   NOTE: Cal520AM is light-sensitive. Perform all loading procedures and experiments in the dark.
3. Prepare the calcium acquisition and analysis system.
   1. Power the Leica Thunder microscope system ensuring the environmental control option is on.
   2. Adjust the camera and framing aperture dimensions to minimize background area.

   NOTE: Here, the Leica Thunder DMi8 microscope was used, but other microscope systems might be applicable as well, considering that it allows a frame rate of over 30 frames/second.
4. Begin recording of a video collecting a consistent stream of 2–10 peaks within 10 seconds and scan across the 96wells plate, initially moving to the left, then downwards in a zig-zag fashion to cover the whole plate.
5. Once the Ca^{2+} transients are acquired, analyze the data with the fluorescence traces analysis software according to the manufacturer's instructions.

8. Flow cytometry analyses of dissociated cardiac spheroids

1. Collect the spheroids in a 15 mL tube, and centrifuge for 3 min at 70*xg*.
2. Aspirate the supernatant and add 1 ml PBS.
3. Centrifuge for 3 min at 200*xg* for 5 min.
4. Aspirate the supernatant and dissociate the CSs by adding 1 mL of TrypLE Select Enzyme solution.
5. Incubate the tube at 37 °C for 15 min.
6. Using a 5 mL pipette, mechanically dissociate the cells by flushing with 2 mL RPMI-1640 so that single cells can be seen when observed under a microscope.
7. Centrifuge for 3 min at 200*xg* for 5 min.
8. Aspirate the supernatant and add fix the CMs with 200 µl 4% PFA.
9. Incubate for 10 minutes at room temperature.
10. Centrifuge for 3 min at 200*xg* for 5 min.
11. Aspirate the supernatant and add 1 ml PBS.
    NOTE: Pause Point: The fixed hiPSC-CMs can be stored at 4°C for up to 4 weeks.
12. Transfer the cell suspension to a FACS tube.
13. Centrifuge for 3 min at 200*xg* for 5 min.
14. Aspirate the supernatant and resuspend 1×10^5 cells in 50 µl of permeabilization buffer.
15. Incubate the cells for 30 min at 4 °C.
16. For immunofluorescence flow cytometry analysis:
    16.1 Resuspend in 50 µl of flow cytometry buffer containing the α-actinin antibody (1:300 dilution) and in another FACS tube resuspend 1×10^5 cells in 50 µl of flow cytometry buffer with the respective isotype control (e.g., FITC mouse IgM, κ isotype (1:200 dilution)) and 1×10^5 cells in 50 µl of flow cytometry buffer for negative control.
    16.2 Incubate the cells for 30 min at 4°C.
    16.3 Wash the cells with 2.5 ml of flow cytometry buffer and centrifuge at 200*xg* for 5 min at 4°C; discard the supernatant and repeat the wash two more times.
    16.4 Resuspend in 50 µl of flow cytometry buffer containing the secondary-antibody Goat-anti-mouse (1:300 dilution).
    NOTE: Place the tube in the dark since the secondary-antibody solution is light-sensitive.
17. For viability check with propidium iodide (PI), add 1:1000 PI and incubate for 15 min.
    NOTE: Place the tube in the dark since the PI solution is light-sensitive.
18. Analyze the cells with a flow cytometer, adjusting the gates according to the standard gating strategy as shown in supplementary figure 1.

9. Immunofluorescence staining of whole 3D spheroids

NOTE: during the procedure, all pipet tips and tubes can be coated with 1% BSA-PBS to prevent the spheroids from sticking to plastics.

1. Collect the spheroids (approx. 20-50 spheroids per antibody combination) into a 15 mL coated tube by using a 5 mL pipet.
   NOTE: Be careful not to damage the spheroids.
2. Centrifuge for 3 min at 70*xg* and aspirate the supernatant.
3. Carefully resuspend the organoids in 1 mL of ice-cold PFA using a coated 1 mL tip.
4. Fix at 4 °C for 45 min. Gently resuspend the spheroids halfway through the fixation time using a coated 1 mL tip to ensure even fixation among all spheroids.
5. Add 10 mL of ice-cold PBT to the tube, gently mix by inverting the tube, incubate for 10 min and spin down at 70 x g, both at 4 °C.
   NOTE: From this step onwards coating of tips is generally not needed as most organoid types do not stick to the tip after fixation. However, some organoids may require coated plastics even after fixation.
6. Block the spheroids by resuspending the pellet in ice-cold OWB (at least 200 µL of OWB per well) and transfer the spheroids to a 24-well suspension plate.
   NOTE: Organoids from one large pellet can be split over multiple wells to perform different stainings. Use approx. 20-50 spheroids per antibody combination.
7. Incubate at 4 °C for at least 15 min.
8. Pipette 200 µL of OWB in an empty well to serve as a reference well .
   NOTE: The immunolabeling can also be performed in 48- or 96-well plates to reduce antibody usage. However, the user should be aware that both staining and washing performance could be reduced due to the smaller volume.
9. Allow the spheroids to settle at the bottom of the plate, by leaving the plate at 45° for 5 minutes.
10. Remove OWB leaving the organoids in 200 µL of OWB (use the reference well to estimate 200 µL).
11. Add 200 µL of OWB with primary antibodies 2x concentrated (e.g., Alpha-actinin [1:200] and Troponin T [1:200] for results in Figures 1C and 4D and incubate overnight at 4 °C while mildly rocking/shaking (40 rpm on horizontal shaker).
12. The next day, add 1 mL of OWB.
13. Allow the spheroids to settle at the bottom of the plate by leaving the plate at 45° for 5 minutes.
14. Remove OWB leaving 200 µL in the plate. Add 1 mL of OWB and wash for 2 h with mild rocking/shaking.
15. Repeat steps 13 and 14 for two more times.
16. Allow the organoids to settle at the bottom of the plate by leaving the plate at 45° for 5 minutes.

17. Remove OWB leaving 200 µL in the well.
18. Add 200 µL of OWB with secondary antibodies, conjugated antibodies, and dyes 2x concentrated (e.g., DAPI [1ug/mL], mouse-AF488 [1:500], rabbit-AF568 [1:500], for results in Figure 1C and 4D and incubate overnight at 4 °C while mildly rocking/shaking.
19. The next day, repeat steps 13 and 14 for two more times.
20. Carefully transfer the spheroids to a 1.5 mL tube and spin down at 70x*g* for 3 min.
21. Remove as much as possible the OWB by pipetting without disrupting the spheroids.
22. Add FUnGI (at least 50 µL, RT) using a 200 µL tip with the end cut off and resuspend gently to prevent bubble formation. Incubate at RT for 20 min.
23. In the meantime, create a square container on a glass slide with either nail polish or silicone sealant.
24. Cut off the end of a 200 µL tip and transfer the spheroids in FUnGI to the middle of the square container.
25. Place a square coverslip on top. To minimize trapped air bubbles, place the left side of the coverslip first, then slowly lower the coverslip from left to right until there is no trapped air and then release the coverslip.
26. Gently apply pressure on all edges of the coverslip to firmly attach it to the silicone sealant.
27. Leave the slide overnight on RT. The next day, the slide is ready for imaging.
    NOTE: Optical clearing by FUnGI may cause minor tissue shrinkage. This will not affect the general morphology of monolayered and multilayered spheroids. The protocol can be paused here and samples can be stored at 4 °C (for at least 1 week) or at -20 °C (for at least 6 months).

Representative Results

The protocol shown in **Figure 1A** describes the generation of CSs from previously expanded hiPSC-CMs. The CSs acquire a 3D structure by day 1 post-seeding in ultra-low attachment round-bottom plates and can be cultured for up to 6 weeks (**Figure 1B**). As assessed by immunofluorescence staining, the majority of the cells in 3-week-old CSs expressed sarcomeric proteins such as alpha-actinin and troponin T, and displayed regular sarcomere organization (**Figure 1C**). For quantification of α-actinin-positive cells, flow cytometry analysis was performed. In accordance with the immunofluorescence results, the flow cytometry data demonstrated comparable high levels of α-actinin in both day 0 (76.9±16.6%) and 3 week-old CSs (71.1±22.7%) (**Figure 1D**), indicating a constant and highly pure cellular composition during culturing.

Subsequently, the functional properties of CSs including beating rate and Ca^{2+} handling were assessed at different time points (**Figure 2**). Calcium transient parameters such as rise time, peak time, decay time, and calcium transient duration (CTD90) were evaluated as indicated in **Figure 2A-B**. The percentage of beating CSs is similar in the first 3 weeks post-generation

but significantly dropped in Wk6-CSs (**Figure 2C**). The beating rate was significantly reduced at Wk3 compared to Wk1 and, similar to the percentage of beating CSs, dramatically dropped at Wk 6 (**Figure 2D**). At Wk6, CSs deterioration was observed, which could explain the drop in both beating rate and number of beating CSs. Measurement of calcium transient parameters indicated a significantly higher peak value at Wk2 (**Figure 2E**), while the rise time, decay time, and CTD90 were significantly increased at Wk3 compared to Wk1 (**Figure 2F-H**). Taken together, these results show that hiPSC-CM-derived spheroids are functional optimal round weeks 2 and 3 post-generation.

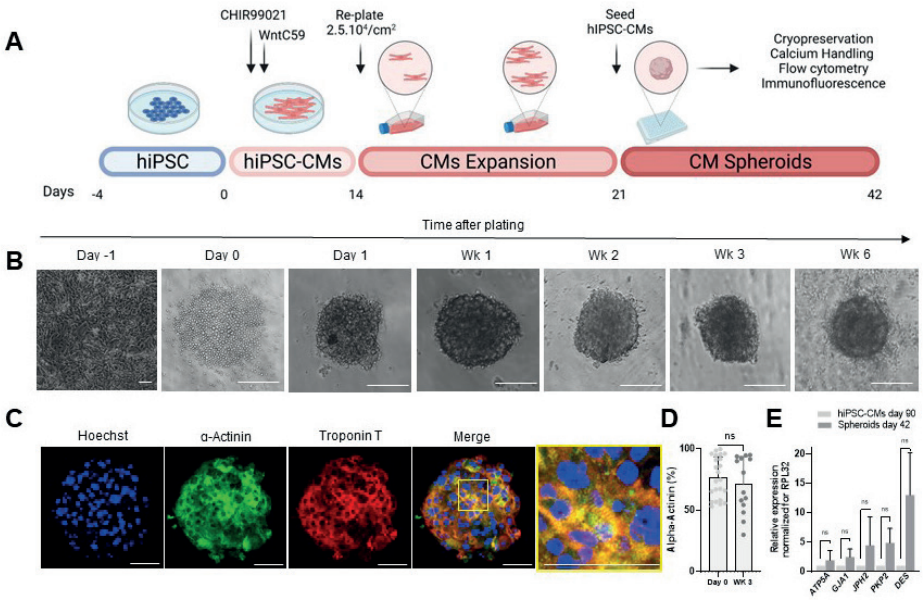

Figure 1: Generation of cardiac spheroids. (**A**) Schematic representation of Wnt-based directed cardiac differentiation, the subsequent expansion of hiPSC-CMs, and the generation of CSs. Created with biorender.com. (**B**) Bright-field images at different time points of CSs culturing. Scale bar, 200 µm. (**C**) Representative immunofluorescence images for cardiac sarcomeric proteins α-actinin and troponin-T in 3-week-old CSs. Immunofluorescence: Hoechst (blue), α-actinin (green), and troponin T (red). The merged picture on the right displays the sarcomere organization. Scale bar, 50 µm. (**D**) Flow cytometry quantification of α-actinin positive cells before (day 0) and 3 weeks after the formation of CSs. (n= 14-23 per condition. Data are represented as mean ± SD).

Figure 3 shows the effect of spheroid size on the beating rate and calcium handling. CSs were generated by seeding 2.5, 5, 10, and 20x10^4 hiPSC-CMs in a well of a 96-well plate, for a total of 24 CSs/wells per condition (**Figure 3A**). As expected, the spheroid size increased as the number of cells used increased, ranging from 178±36 to 351±65 µM (**Figure 3A**, right panel). Ca^{2+} transients were measured in 3-week-old CSs at the four different seeding densities (**Figure 3B**). Measurements of beating CSs indicated that only about 50% of the smaller size-CSs (2.5K- and 5K-CSs) were beating, while the percentage of bigger size-beating CSs (10K-

and 20K-CSs) was significantly higher (about 85%) (**Figure 3C**). 5K-, 10K- and 20K-CSs showed similar beating rate (about 28 bpm) which was significantly higher compared to 2.5K-CSs (**Figure 3D**). The peak values of calcium images were similar in all tested conditions (**Figure 3E**), however, rise time (**Figure 3F**), decay time (**Figure 3G**), and CTD90 (**Figure 3H**) were significantly increased in bigger size-CSs (10K-, and 20K-CSs) compared to the smaller ones (2.5K- and 5K-CSs). Taken together, these results show that hiPSC-CM-derived spheroids are optimal for calcium handling screening when a seeding density between 10K- and 20K hiPSC-CMs/well is used.

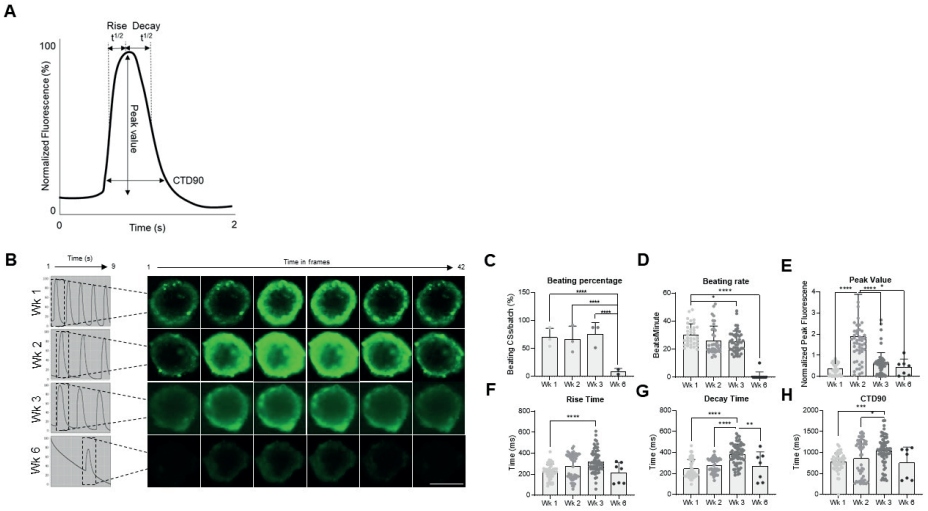

Figure 2: Beating rate and Calcium handling in CSs at different weeks post generation. (**A**) Examples of calcium transient parameters calculated by the Vala sciences analysis algorithm in Cyteseer Software. (**B**) Representative calcium transient traces and time-lapse images of the CSs at different time points (weeks) post-generation. Scale bar, 200 µm. (**C**) Time course quantification of spontaneous beating activity is expressed as the percentage of beating CSs. (**D**) Beating rate of CSs during culturing time. (**E-H**) Quantification of the calcium transients showing peak value, rise time, decay time, and CTD90. Data shown are mean ± SD. Biological replicates = 3 technical replicates = 38,50,66 and 7, respectively. $*p < 0.05$, $****p < 0.001$; one-way ANOVA followed by Tukey's post hoc multiple-comparisons test. Abbreviations; CTD= Calcium transient duration, wk= week, CSs= human cardiac spheroids.

Next, we evaluated the impact of cryopreservation on CS's viability and function. Before analysis, thawed CSs were maintained in culture for 1 week (**Figure 4A**). As shown by both flow cytometry (**Figure 4B**) and Calcein-AM (**Figure 4C**) cell viability tests, cryopreservation did not affect cell viability within the CSs. Additionally, thawed CSs showed similar expression levels of sarcomeric proteins as compared to the fresh age-matched CSs (**Figure 4D**). These data indicate that CSs can be efficiently cryopreserved for subsequent cardiac function analysis and high throughput screening.

Finally, the beating activity and Ca^{2+} handling were measured in both fresh and cryopreserved CSs (**Figure 5**). The percentage of beating CSs was measured at different time points after thawing, respectively at 2, 5 and 7 days. While most of the fresh CSs showed beating activity over time, clearly the cryopreserved CSs needed up to a week of culturing in order to recover their beating activity (**Figure 5B**). There was no significant change in the beating rate of thawed CSs versus fresh, however no spontaneous beating activity was observed in some frozen CSs (**Figure 5C**). Although peak values were significantly reduced in frozen/thawed CSs compared to fresh (**Figure 5D**), no significant changes were observed in rise time, decay time and the CTD90 of frozen/thawed CSs compared to fresh (**Figure 5E-G**). These data indicate that, after thawing, it is important to let the CSs recover in the incubator for at least 1 week before measuring beating activity and Ca^{2+} transient.

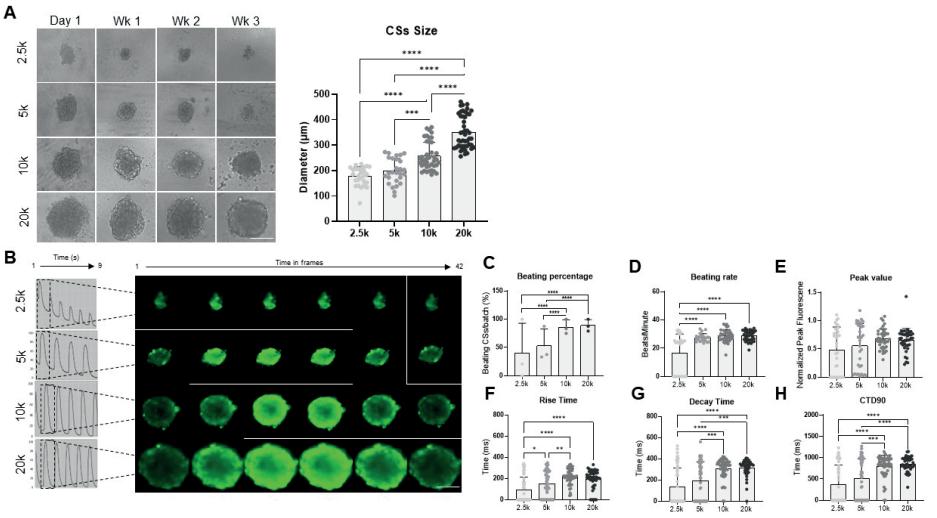

Figure 3: Beating rate and calcium handling in CSs generated using different cell seeding densities. (**A**) Bright-field imaging (left) and size measurements (right) of CSs generated using different numbers iPSC-CM. Scale bar, 200 µm. (**B**) Representative calcium transients traces and time-lapse images of the 2.5K-20K-CSs. (**C-D**) Beating percentage and beating rate of 2.5K-20K-CSs. (**E-H**) Peak value, rise time, decay time, and CTD90 in 2.5K-20K-CSs. Data are mean ± SD. Biological replicates = 3, technical replicates = 28-39. $*p < 0.05$, $****p < 0.001$; one-way ANOVA followed by Tukey's post hoc multiple-comparisons test. Abbreviations: CTD = Calcium transient duration, wk = week, k = x1000 cells, CSs = Cardiac spheroids.

Taken together, these results show that cryopreservation of hiPSC-CM-derived spheroids, using PSC Cryopreservation Kit, preserves cardiomyocyte viability, the sarcomeric structure and their functional characteristics such as the spontaneous beating activity and calcium handling. Thus, hiPSC-CM-derived spheroids represent a suitable model to accurately recapitulate cardiac electrophysiology *in vitro*.

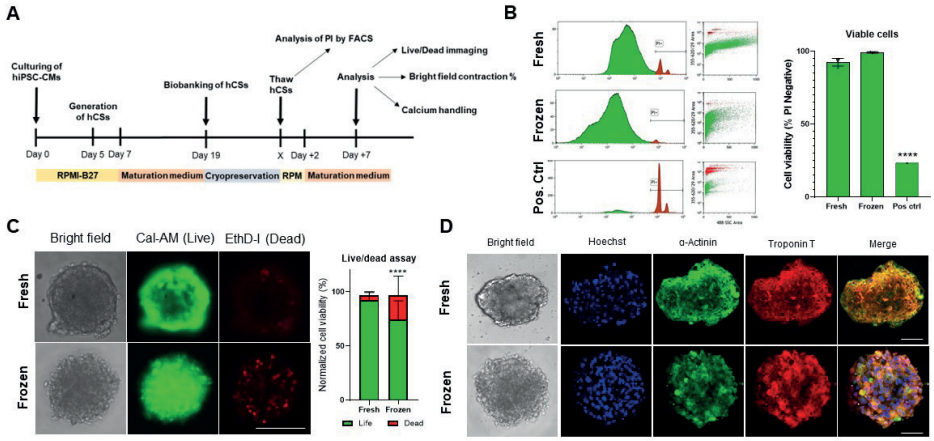

Figure 4. Effect of cryopreservation on cardiac spheroids viability and structure. (**A**) Schematic representation of CSs generation, subsequent biobanking, and thawing. (**B**) Flow cytometry cell viability test in both fresh and cryopreserved CSs. As a positive control, a treatment with 10% Triton-X solution for 5 min was used. (n = 4 per condition). Data are represented as mean ± SD.****p < 0.001; one-way ANOVA followed by Tukey's post hoc multiple-comparisons test. (**C**) Calcein-AM cell viability test in fresh *vs.* thawed CSs after 7 days of culturing (n = 15-17 per condition, ****p < 0.001, by paired t-test, scale bar, 200 µm). (**D**) Representative bright-field (left) and immunofluorescence staining for α-actinin and troponin T expression in fresh and thawed CSs. Immunofluorescence: Hoechst (blue), α-actinin (green), and troponin T (red). The merge pictures on the right display sarcomere striations in the CSs. Scale bar, 50 µm. Abbreviations: X = Thawing day of choice, PI = Propidium iodide, Cal-AM = calcein-AM, EthD-I = Ethidium Homodimer I.

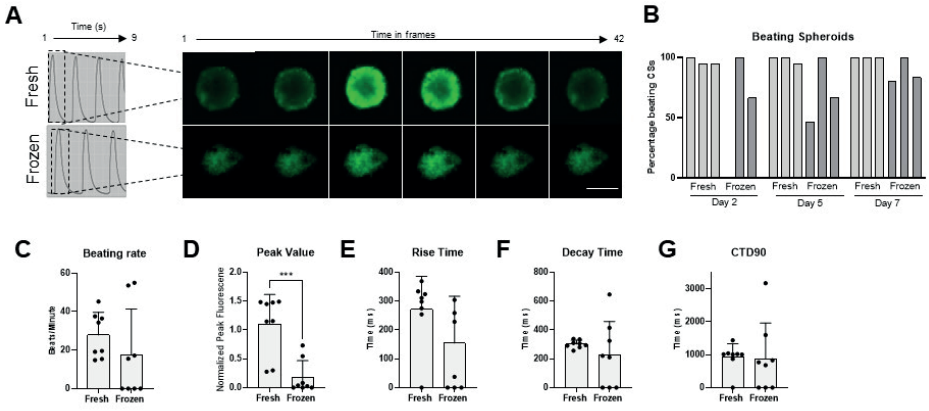

Figure 5: Calcium transients in fresh vs thawed CSs. (**A**) Representative calcium transient traces and time-lapse images of the CSs before cryopreservation and one week after thawing. (**B-C**) Beating percentage and beating rate of fresh and frozen/thawed cardiac spheroids. (**D-G**) Quantification of calcium transient parameters: peak value, rise time, decay time, and CTD90. Data are mean ± SD. *p<0.05, ****p<0.001; one-way ANOVA followed by Tukey's post hoc multiple-comparisons test. Abbreviations; CTD = Calcium transient duration, CSs = cardiac spheroids.

DISCUSSION

Cardiac drug discovery is hampered by the reliance on non-human animal and cellular models with inadequate throughput, and physiological fidelity, to accurately perform readouts. The hiPSC-cardiomyocyte biology coupled with HT instrumentation and physiological probes has the potential to re-introduce human models into the earliest stages of cardiac disease modeling and drug discovery. We developed a 3D cardiac tissue generation method that produces high-quality and functional CSs for an optimal cardiac disease modeling and drug screening platform. Our method relies on several crucial factors and is a variant of existing protocols[9,10,28]. These methods include; 1) generation of 3D tissue constructs, 2) the optimal cell number and timing before the screening, 3) improving sensitivity and high throughput capacity of instruments, and 4) being able to freeze the spheroids before any functional analysis. Unlike the previously described protocols, the proposed protocol describes the generation of up to 1500 spheroids per day and the suitability for HTS. Conventional analysis of a hundred compounds over 6 x ½ log doses for 10 replicates using existing 96-well calcium imaging systems or 24-well multiplexed engineered heart tissues would require approximately 500 million to 3 billion hiPSC-CMs[31]. The proposed application makes cardiac screenings less costly and time effective compared to the conventional systems since the 96 wells plates required only 10% of the seeding density compared to the described method. This small 3D model mimics the biological and physiological phenotype of the *in vivo* cardiovascular environment. As previously demonstrated, calcium transients dramatically increase in 3D cardiac tissue constructs as compared to 2D monolayer cell cultures[32].

Next, we found that the seeding density and proper culturing time are also critical factors for a successful CS screening. The densities of 10K-20K hiPSC-CMs per spheroid and the screening between week 2-3 after generation seemed optimal, whereas too small or too old spheroids show disturbed calcium handling (**Figure 2** and **Figure 3**). Therefore, it is of importance to maintain seeding densities as consistently as possible, since size influences the functional parameters. Also, although this optical method provides good results for live 3D cultures as a whole tissue, obtaining data within larger spheroids at (sub-)cellular level is challenging without relying on time-consuming histology methods. Recently, several approaches have been published that used "optically clearing", which enables the acquisition of whole 3D organoids with the opportunity for single-cell quantification of markers. Here, we adapted a three-day protocol from hCS harvesting to image analysis, which is optimized for 3D imaging using confocal microscopy[29](**Figure 1C** and **Figure 4D**).

Lastly, with the increase in 3D cardiac tissue applications and commercial applications, the demand for long-term storage and patient-specific biobanking from various donors is rising. Cryopreservation is an effective strategy to generate HTS-plates from multiple batches over time. The freezing of hiPSC-CMs has been described previously and is not different compared to other cultured cell types[10,33,34]. Recently, approaches for freezing plates with 2D cells have

been described[35]. Here, we found the PSC Cryopreservation Kit is the most optimal condition as compared to 3 others (data not shown) and used this medium for the efficient freezing of spheroids. After cryopreservation, viability remains high (**Figures 4B** and **Figure 4C**), but CSs' electrophysiological properties are affected and a period of incubation after thawing is required. Indeed, one week after thawing, CSs displayed spontaneous beating activity and calcium handling. However, it has been described that fresh and recovered hiPSC-CMs do not always show identical molecular and physiological properties[36]. This limitation needs to be considered when cryopreserved hiPSC-CMs are used for assessing drug-induced cardiac read-outs. Overall, we propose a step-by-step protocol to efficiently generate CSs which are suitable for downstream applications such as disease modeling and HT drug screening.

Disclosures

The authors have nothing to disclose.

Acknowledgments

We would like to acknowledge VALA sciences for the Cyteseer software package and optimization of the automated 3D calcium analysis. We wish to acknowledge grant support from the PLN foundation (RM). P.A.D. and F.S. are supported by CUREPLaN Leducq. J.P.G.S. is supported by H2020-EVICARE (#725229) of the European Research Council (ERC). J.W.B. is supported by the UMC Utrecht Clinical Fellowship, Netherlands Heart Institute Fellowship, and CVON-Dosis young talent grant; Netherlands Heart Foundation (CVON-Dosis 2014–40). NC is supported by the Gravitation Program "Materials Driven Regeneration" by the Netherlands Organization for Scientific Research (RegmedXB #024.003.013), and the Marie Skłodowska-Curie Actions (Grant agreement RESCUE #801540). V. S.-P. is supported by the Alliance Fund (UMCU, UU, TU/e). A.v.M. is supported by the EU-funded project BRAVE (H2020, ID:874827)

REFERENCES

1. Burridge PW, Matsa E, Shukla P, Lin ZC, Churko JM, Ebert AD, et al. Chemically Defined and Small Molecule-Based Generation of Human Cardiomyocytes. Nat Methods. 2014;11: 855.
2. Kattman SJ, Witty AD, Gagliardi M, Dubois NC, Niapour M, Hotta A, et al. Stage-specific optimization of activin/nodal and BMP signaling promotes cardiac differentiation of mouse and human pluripotent stem cell lines. Cell Stem Cell. 2011;8: 228–240.
3. Lian X, Hsiao C, Wilson G, Zhu K, Hazeltine LB, Azarin SM, et al. Robust cardiomyocyte differentiation from human pluripotent stem cells via temporal modulation of canonical Wnt signaling. Proc Natl Acad Sci U S A. 2012;109. doi:10.1073/pnas.1200250109
4. Paige SL, Osugi T, Afanasiev OK, Pabon L, Reinecke H, Murry CE. Endogenous Wnt/beta-catenin signaling is required for cardiac differentiation in human embryonic stem cells. PLoS One. 2010;5. doi:10.1371/journal.pone.0011134
5. Gintant G, Burridge P, Gepstein L, Harding S, Herron T, Hong C, et al. Use of Human Induced Pluripotent Stem Cell-Derived Cardiomyocytes in Preclinical Cancer Drug Cardiotoxicity Testing: A Scientific Statement From the American Heart Association. Circ Res. 2019;125: e75–e92.
6. Ahmed RE, Anzai T, Chanthra N, Uosaki H. A Brief Review of Current Maturation Methods for Human Induced Pluripotent Stem Cells-Derived Cardiomyocytes. Front Cell Dev Biol. 2020;0. doi:10.3389/fcell.2020.00178
7. Liu C, Feng X, Li G, Gokulnath P, Xiao J. Generating 3D human cardiac constructs from pluripotent stem cells. EBioMedicine. 2022;76: 103813.
8. Musunuru K, Sheikh F, Gupta RM, Houser SR, Maher KO, Milan DJ, et al. Induced Pluripotent Stem Cells for Cardiovascular Disease Modeling and Precision Medicine: A Scientific Statement From the American Heart Association. Circ Genom Precis Med. 2018;11: e000043.
9. Buikema JW, Lee S, Goodyer WR, Maas RG, Chirikian O, Li G, et al. Wnt Activation and Reduced Cell-Cell Contact Synergistically Induce Massive Expansion of Functional Human iPSC-Derived Cardiomyocytes. Cell Stem Cell. 2020;27: 50–63.e5.
10. Maas RGC, Lee S, Harakalova M, Snijders Blok CJB, Goodyer WR, Hjortnaes J, et al. Massive expansion and cryopreservation of functional human induced pluripotent stem cell-derived cardiomyocytes. STAR Protoc. 2021;2: 100334.
11. Tremblay C, Ruel J, Bourget JM, Laterreur V, Vallières K, Tondreau MY, et al. A new construction technique for tissue-engineered heart valves using the self-assembly method. Tissue Eng Part C Methods. 2014;20. doi:10.1089/ten.TEC.2013.0698
12. Lewis-Israeli YR, Wasserman AH, Gabalski MA, Volmert BD, Ming Y, Ball KA, et al. Self-assembling human heart organoids for the modeling of cardiac development and congenital heart disease. Nat Commun. 2021;12: 1–16.
13. Goldfracht I, Efraim Y, Shinnawi R, Kovalev E, Huber I, Gepstein A, et al. Engineered heart tissue models from hiPSC-derived cardiomyocytes and cardiac ECM for disease modeling and drug testing applications. Acta Biomater. 2019;92. doi:10.1016/j.actbio.2019.05.016
14. Fleischer S, Jahnke H-G, Fritsche E, Girard M, Robitzki AA. Comprehensive human stem cell differentiation in a 2D and 3D mode to cardiomyocytes for long-term cultivation and multiparametric monitoring on a multimodal microelectrode array setup. Biosensors and Bioelectronics. 2019. pp. 624–631. doi:10.1016/j.bios.2018.10.061
15. Branco MA, Cotovio JP, Rodrigues CAV, Vaz SH, Fernandes TG, Moreira LM, et al. Transcriptomic analysis of 3D Cardiac Differentiation of Human Induced Pluripotent Stem Cells Reveals Faster Cardiomyocyte Maturation Compared to 2D Culture. Sci Rep. 2019;9: 9229.
16. Ergir E, La Cruz JO-D, Fernandes S, Cassani M, Niro F, Sousa D, et al. Generation and Maturation of Human iPSC-derived Cardiac Organoids in Long Term Culture. doi:10.1101/2022.03.07.483273
17. Lemoine MD, Mannhardt I, Breckwoldt K, Prondzynski M, Flenner F, Ulmer B, et al. Human iPSC-derived cardiomyocytes cultured in 3D engineered heart tissue show physiological upstroke velocity and sodium current density. Sci Rep. 2017;7: 5464.
18. Kofron CM, Kim TY, Munarin F, Soepriatna AH, Kant RJ, Mende U, et al. A predictive in vitro risk assessment platform for pro-arrhythmic toxicity using human 3D cardiac microtissues. Sci Rep. 2021;11: 1–16.

19. Human-iPSC-Derived Cardiac Stromal Cells Enhance Maturation in 3D Cardiac Microtissues and Reveal Non-cardiomyocyte Contributions to Heart Disease. Cell Stem Cell. 2020;26: 862–879.e11.

20. Richards DJ, Li Y, Kerr CM, Yao J, Beeson GC, Coyle RC, et al. Human cardiac organoids for the modelling of myocardial infarction and drug cardiotoxicity. Nature Biomedical Engineering. 2020;4: 446–462.

21. Tenreiro MF, Louro AF, Alves PM, Serra M. Next generation of heart regenerative therapies: progress and promise of cardiac tissue engineering. npj Regenerative Medicine. 2021;6: 1–17.

22. Hansen A, Eder A, Bönstrup M, Flato M, Mewe M, Schaaf S, et al. Development of a drug screening platform based on engineered heart tissue. Circ Res. 2010;107: 35–44.

23. McDermott-Roe C, Lv W, Maximova T, Wada S, Bukowy J, Marquez M, et al. Investigation of a dilated cardiomyopathy–associated variant in BAG3 using genome-edited iPSC-derived cardiomyocytes. JCI Insight. 2019. doi:10.1172/jci.insight.128799

24. Safety and Efficacy of Induced Pluripotent Stem Cell-derived Engineered Human Myocardium as Biological Ventricular Assist Tissue in Terminal Heart Failure - Full Text View - ClinicalTrials.gov. [cited 29 Apr 2022]. Available: https://clinicaltrials.gov/ct2/show/NCT04396899

25. Ronaldson-Bouchard K, Ma SP, Yeager K, Chen T, Song L, Sirabella D, et al. Advanced maturation of human cardiac tissue grown from pluripotent stem cells. Nature. 2018;556: 239.

26. Oh JG, Dave J, Kho C, Stillitano F. Generation of Ventricular-Like HiPSC-Derived Cardiomyocytes and High-Quality Cell Preparations for Calcium Handling Characterization. JoVE (Journal of Visualized Experiments). 2020; e60135.

27. Lian X, Zhang J, Azarin SM, Zhu K, Hazeltine LB, Bao X, et al. Directed cardiomyocyte differentiation from human pluripotent stem cells by modulating Wnt/β-catenin signaling under fully defined conditions. Nat Protoc. 2013;8: 162.

28. Feyen DAM, McKeithan WL, Bruyneel AAN, Spiering S, Hörmann L, Ulmer B, et al. Metabolic Maturation Media Improve Physiological Function of Human iPSC-Derived Cardiomyocytes. Cell Rep. 2020;32: 107925.

29. van Ineveld RL, Ariese HCR, Wehrens EJ, Dekkers JF, Rios AC. Single-Cell Resolution Three-Dimensional Imaging of Intact Organoids. J Vis Exp. 2020 [cited 19 May 2022]. doi:10.3791/60709

30. Ding B, Sun G, Liu S, Peng E, Wan M, Chen L, et al. Three-Dimensional Renal Organoids from Whole Kidney Cells: Generation, Optimization, and Potential Application in Nephrotoxicology In Vitro. Cell Transplant. 2020;29: 963689719897066.

31. Denning C, Borgdorff V, Crutchley J, Firth KSA, George V, Kalra S, et al. Cardiomyocytes from human pluripotent stem cells: From laboratory curiosity to industrial biomedical platform. Biochim Biophys Acta. 2016;1863: 1728.

32. Daily NJ, Yin Y, Kemanli P, Ip B, Wakatsuki T. Improving Cardiac Action Potential Measurements: 2D and 3D Cell Culture. J Bioeng Biomed Sci. 2015;5. doi:10.4172/2155-9538.1000168

33. Preininger MK, Singh M, Xu C. Cryopreservation of Human Pluripotent Stem Cell-derived Cardiomyocytes: Strategies, Challenges, and Future Directions. Adv Exp Med Biol. 2016;951: 123.

34. Kim YY, Ku SY, Liu HC, Cho HJ, Oh SK, Moon SY, et al. Cryopreservation of human embryonic stem cells derived-cardiomyocytes induced by BMP2 in serum-free condition. Reprod Sci. 2011;18. doi:10.1177/1933719110385130

35. Daily MI, Whale TF, Partanen R, Harrison AD, Kilbride P, Lamb S, et al. Cryopreservation of primary cultures of mammalian somatic cells in 96-well plates benefits from control of ice nucleation. Cryobiology. 2020;93: 62–69.

36. Zhang JZ, Belbachir N, Zhang T, Liu Y, Shrestha R, Wu JC. Effects of Cryopreservation on Human Induced Pluripotent Stem Cell-Derived Cardiomyocytes for Assessing Drug Safety Response Profiles. Stem Cell Reports. 2021;16: 168–181.

SUPPLEMENTARY FIGURES

Supplementary figure 1 can be downloaded from: https://www.jove.com/files/ftp_upload/64365/figures%20version%202_6-end.pdf

Or:

SUPPLEMENTARY MATERIALS LIST

The supplementary materials list can be downloaded from: https://www.jove.com/pdf-materials/64365/jove-materials-64365-generation-high-throughput-screening-biobanking-human-induced

Or:

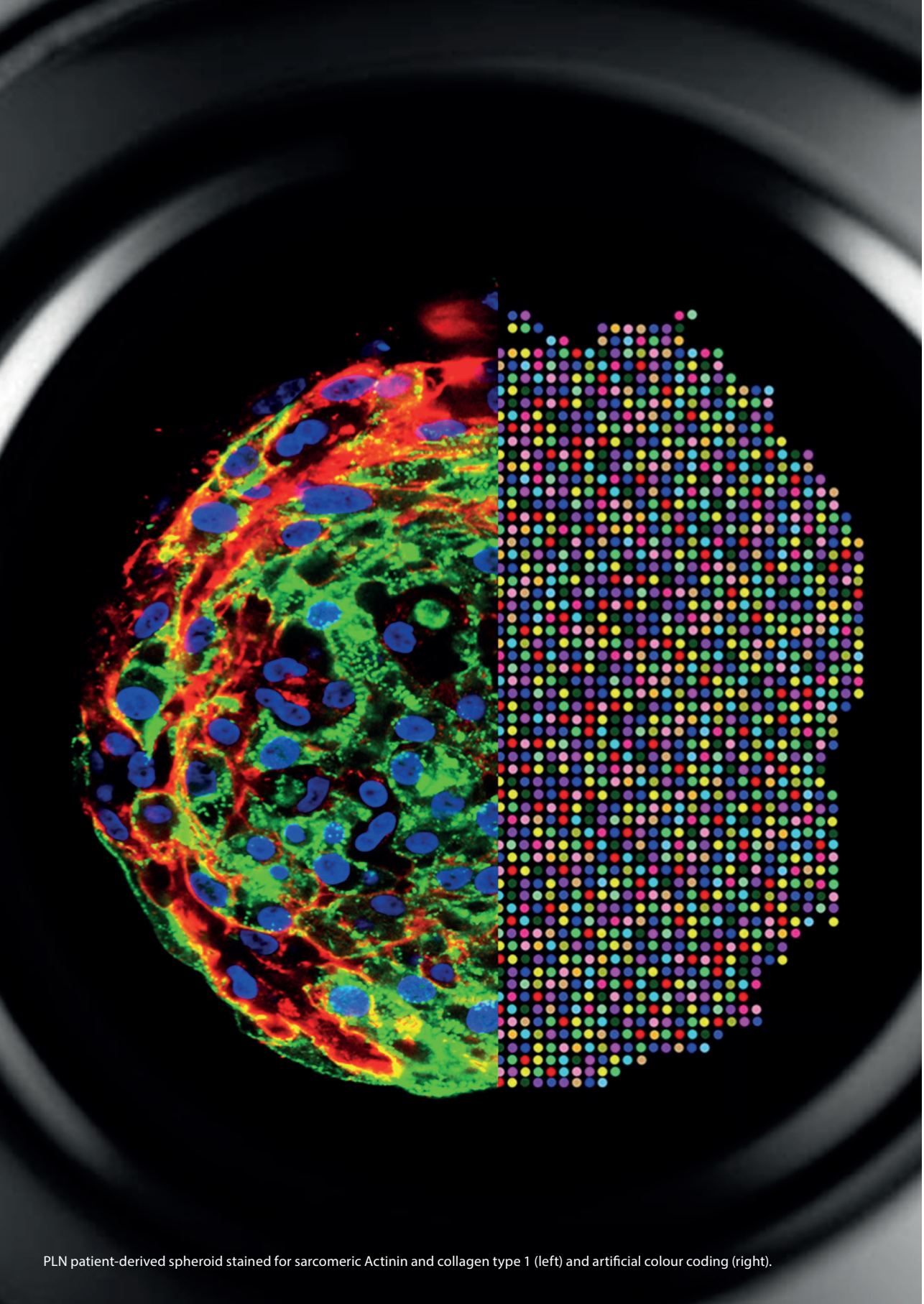

PLN patient-derived spheroid stained for sarcomeric Actinin and collagen type 1 (left) and artificial colour coding (right).

Chapter 12

Modeling and Rescue of PLN-R14del Cardiomyopathy Phenotype in Human Induced Pluripotent Stem Cell-Derived Cardiac Spheroids

Manuscript in preparation

Renée G.C. Maas, Floor W. van den Dolder, Tess Beekink, Remco E. Hoogervorst Magdalena Harakalova, Jan W. Buikema, Roger Hajjar, Francesca Stillitano, Jorg J.A. Calis, Pieter A. Doevendans, Joost P.G. Sluijter.

ABSTRACT

A deleterious mutation of the arginine 14 codon in the phospholamban (PLN) gene (PLN-R14del)) in dilated cardiomyopathy patients is associated with severe ventricular arrhythmias, contractile dysfunction, heart failure, and sudden cardiac death. Using induced pluripotent stem cells (hiPSCs) generated from three symptomatic patients with the PLN-R14del mutation, we established a 3D cardiac spheroid (hCS) *in vitro* model that displayed an increase in spheroid size, nuclei number, and decreased CM number upon culturing, as compared to isogenic and healthy control lines. Single-cell RNA sequencing revealed patient-like pathological phenotypes, among others, mitochondrial dysfunction, increased fibrosis, affected unfolded protein response, and reduced calcium (Ca^{2+}) handling and contraction in PLN-R14del patient-derived cardiac spheroids. For the first time, we further revealed fibroblast activation, decreased expression of cardiac-specific genes, and decreased Ca^{2+} handling in PLN-R14del 3D spheroids, thereby confirming various human PLN-R14del cardiomyopathy features. Adeno-associated virus (AAV)-mediated overexpression of constitutively active inhibitor-1 (I-1c) partially rescued the disease phenotype of the PLN-R14del hCSs, by restoring spheroid size, cardiac gene expression levels, preventing fibroblast activation and improving contractility and Ca^{2+} handling functionality. This study provides evidence for (1) the feasibility of generating 3D hCS for high-throughput screenings to model the PLN-R14del phenotype *in vitro* and (2) efficient gene augmentation in hCSs as a potential therapeutic strategy for genetic cardiomyopathies.

INTRODUCTION

The pathogenic Phospholamban (PLN) p.Arg14del (PLN-R14del) founder mutation accounts for approximately 10% of all cases of dilated cardiomyopathy (DCM) and 15% of all cases of arrhythmogenic cardiomyopathy (ACM) in the Netherlands.[1] PLN is a sarcoplasmic reticulum (SR) protein that reversibly binds to SERCA2a pumps, reducing its affinity for calcium (Ca^{2+}), and thereby decreasing Ca^{2+} re-uptake into the SR. PLN is phosphorylated by protein kinase A (PKA) or Ca^{2+}-calmodulin-dependent protein kinases (CaMKII) during -adrenergic signaling.[2] Phosphorylation abolishes PLN's inhibitory effects, resulting in increased Ca^{2+} flux into the SR, which transports approximately 70% of all Ca^{2+} ions in the human heart.[4] Dysregulation of SERCA and PLN and concomitant Ca^{2+} dysfunction have been correlated with dysfunctional contractility and heart diseases.[3] The clinical spectrum of disease phenotypes caused by PLN-R14del ranges from early-stage ECG and ultrasound strain abnormalities to a moderate disease stage consisting of decreased left ventricular function and, ultimately, progression into congestive biventricular failure.[5–7] Moreover, a more severe biventricular phenotype is characterized by dilation of the heart and/or myocardial fibrofatty tissue replacement, which provides the risk for ventricular arrhythmias.[8] The previously described disturbed Ca^{2+} regulation[9], identification of protein aggregates[10], and increase in fibrosis[11] in PLN-R14del patient hearts have been observed in young homozygous PLN-R14del mice, which also demonstrated inducibility of ventricular arrhythmias (VAs), suggestive of aberrant Ca^{2+} handling.[12]

Recent in vitro studies by us and others have shown reduced contractility in human induced pluripotent stem cells (hiPSC)-derived cardiomyocytes (hiPSC-CM) from individuals carrying the R14del heterozygous mutation, which was mediated by an elevated Unfolded Protein Response (UPR)/Endoplasmic Reticulum (ER) stress response[13,14] and impairment of cardiac metabolism.[14,15] Moreover, frequent episodes of irregular Ca^{2+} waves have been observed in hiPSC-CMs harboring the PLN-R14del mutation.[16] The mechanistic understanding of how the PLN-R14del mutation contributes to disease progression and whether this can be mitigated via disease-specific therapeutic strategies remains unknown. Three-dimensional (3D) cardiac cell culture and tissue engineering techniques reflect better human cardiac physiology compared to regular 2D culturing. Human cardiac spheroids (hCSs) are small and have been proven to recapitulate developmental stages, tissue organization, and function, as seen in whole organs.[17–19] Moreover, the development of an hCS screening platform could be essential not only to better recapitulate pathophysiological phenotypes and study molecular mechanisms but also to allow testing therapeutic strategies in an unbiased, high-throughput manner.

In this study, we established a human cardiac spheroid model of PLN-R14del patient-derived hiPSC and observed the presence of various pathophysiological phenotypes of the PLN-R14del cardiomyopathy, including fibrosis, metabolic dysfunction, UPR/ER stress, and Ca^{2+} handling/contractile dysfunction. We explored the therapeutic potential of a constitutively active inhibitor-1 (I-1c) delivered by AAV2/8 to improve PLN phosphorylation and restore cardiomyocyte function.

METHODS

hiPSC reprogramming and cell lines. Dermal fibroblasts were obtained from a skin biopsy of a 52-year-old PLN-R14del (D4iR14del) patient following informed consent (Stanford Institutional Review Board and Stem Cell Research Oversight Committee). Genome editing was performed in hiPSCs to correct the PLN-R14del mutation in hiPSCs by CRISPR-Cas9-mediated homology-directed repair (HDR), as described to generate the C31iCTR line.[13] One previously established[20] healthy individual hiPSC line was used for this study (SCVI-273 = 273iCTR, Sendai virus reprogrammed, PBMCs, 42-year-old female). Following informed consent (UNRAVEL, UMCU METC 12/387), peripheral blood mononuclear cells (PBMCs) were collected from one healthy proband relative of the D4iCTR (1CiCTR, 62-year old male), and 2 PLN-R14del patients (6BiR14del, 61-year old male, and 10BiR14del, 60-year old female). The blood was collected in heparin-coated tubes and diluted 1:1 with phosphate-buffered saline (PBS). Per 15 mL Ficoll (Thermo Scientific) 20 mL of blood-PBS was added and centrifuged for 30 minutes at 400×g. PBMCs were isolated by transferring the PBMC layer to a new tube, washed, and resuspended in StemPro-34 SFM media (Life Technologies) supplemented with cytokines stem cell factor (SCF, 100 ng/mL), Fms Related Receptor Tyrosine Kinase 3 (FLT-3, 100 ng/mL), and interleukin-6 (IL-6, 20 ng/mL). Cells were maintained for 3 days at 5% CO2, at 37°C, before use. PBMCs were reprogrammed to hiPSCs using the CytoTune-iPS 2.0 Sendai Reprogramming Kit (Thermo Fisher Scientific) according to the manufacturer's instructions with small modifications. Briefly, 2 x105 PBMCs were transduced with the three CytoTune 2.0 reprogramming vectors per well (24-well plate) in 0.5 mL in complete StemPro-34 SFM. Twenty-four hours post-transduction the PBMCs were pelleted by centrifugation, resuspended in fresh complete StemPro-34 SFM, and plated in one Matrigel-coated well of a 24-wells plate. Three days later, the medium was replaced with StemPro-34 SFM without cytokines and cultured for an additional 3 days. Next, cells were exposed to and maintained in the E8 stem cell medium. Approximately two weeks post-transduction, stem cell-like colonies were manually picked and expanded in E8 stem cell media (Life Technologies) on Matrigel (0.1 mg/mL, BD Biosciences)-coated plates under standard culture conditions (5% CO2, 37ºC). Cells were dissociated with 0.5 mM EDTA-PBS (Invitrogen) with E8 medium supplemented with 2.5 µM Y-27632 (SelleckChem). All hiPSC lines were routinely checked for mycoplasma and characterized as shown in **Supplementary Figure 1**.

Differentiation of hiPSC to CMs. Cardiomyocyte (CM) differentiation was carried out following a small molecule Wnt-activation/inhibition protocol, as previously described.[21] Briefly, hiPSCs were first treated with CHIR99021 (8 µM; Tocris) in RPMI+ 2% B27 without insulin (Life Technologies) for 72 hours, and then with Wnt C-59 (2 µM; Selleck Chemicals) for another 48 hours. Media was replaced with RPMI + 2% B27 with insulin (Life Technologies) and refreshed every 2 days. Spontaneously beating cells were typically observed 8-10 days post-differentiation induction. On day 9 of differentiation, hiPSC-CMs were metabolically selected in RPMI-B27 without D-glucose (Life Technologies) supplemented with 2% B27 for 48

hours. Differentiated hiPSC-CMs were maintained with RPMI + 2% B27 medium. All subsequent experiments were conducted by using hiPSC-CMs differentiated for 20 to 30 days.

Differentiation of hiPSC to CFs. Cardiac fibroblast (CF) differentiation was carried out following a small molecule Wnt-activation protocol as previously described.[22] Briefly, hiPSCs were first treated with CHIR99021 (12 µM; Tocris) in RPMI+ 2% B27 without insulin (Life Technologies) for 24 hours, and then in RPMI+ 2% B27 without insulin for another 24 hours. Media was replaced every other day with CFBM medium consisting of DMEM, high glucose (Gibco) supplemented with 500 µg/mL HAS (Sciencell), 0.6 µM Linoleic Acid (Sigma-Aldrich), 0.6 µg/mL Lecithin(Sigma-Aldrich), 50 µg/mL Ascorbic Acid (Sigma-Aldrich), 7.5 mM GlutaMAX (Thermo Scientific), 1.0 µg/mL Hydrocortisone Hemisuccinate (Millipore Sigma), 5 µg/mL recombinant human Insulin (Sigma-Aldrich) and the fresh addition of 75 ng/ml bFGF (Sigma-Aldrich). All subsequent experiments were conducted by using hiPSC-CFs that were differentiated for at least 20 days and passaged 3-6 times.

Cardiac spheroid generation. Human cardiac spheroid (hCS) generation was achieved following a protocol that was previously described.[23] Briefly, hiPSC-CMs were digested by TrypLE Select Enzyme (10X, Thermo Fisher Scientific) for 15 min at 37°C. Next, 10.000 hiPSC-CM were collected and added to a 96- or 384-well ultra-low attachment multiple-well plate (Corning) in RPMI-B27 supplemented with 10% knockout serum replacement (KOSR) and 10 µM Y-27632 (Tocris). The hCSs culture plates were kept on a rotation plate, 70 rpm at 37°C, and 5% CO2. Medium change was performed after 24 hours with a basal medium without KOSR and Y-27632. After 21 days, the hCSs were used for downstream analysis.

Spheroid maturation. Spheroid maturation was achieved by a previously described maturation medium used for hiPSC-CMs.[24] The maturation medium consists of DMEM without glucose (Thermo Fisher Scientific, 11966025) supplemented with 3mM glucose (Sigma Aldrich, G7021), 10mM L-lactate (Sigma Aldrich, 71718), 5µg/ml Vitamin B12 (Sigma Aldrich, V6629), 0.82µM Biotin (Sigma Aldrich, B4639), 5mM Creatine monohydrate (Sigma Aldrich, C3630), 2mM Taurine (Sigma Aldrich, T0625), 2mM L-carnitine (Sigma Aldrich, C0283), 0.5mM Ascorbic acid (Sigma Aldrich, A8960), 1x NEAA (Thermo Fisher Scientific, 11140), 0.5% (w/v) Albumax (Thermo Fisher Scientific, 11020021), 1x B27 and 1% KOSR (Thermo Fisher Scientific, 10828028). After 48 hours, the medium was replaced by the maturation medium for 1, 2, 3, or 6 weeks, which metabolically matured hCSs.

Parse single-cell RNA sequencing. The samples for single-cell RNA sequencing were prepared by dissociating day 75 cardiac spheroids with TrypLE Select Enzyme for 45 minutes

and processed with a fixation kit (Parse Biosciences). Fixed samples were combined, barcoded, and sequenced according to the Parse barcoding protocol. Sequencing data was analyzed with the split-pipe software from Parse to obtain cell/gene expression matrices for each sample.

Single-cell RNA sequencing analysis. Single-cell RNAseq (scRNAseq) data was analyzed using the Seurat package (version 4.0.5) in R (version 4.1.0). The scRNAseq data of all hCSs samples was combined and analyzed, and cells with at least 750 features were selected from three control and three PLN-R14del mutated samples. A reference data set from Grancharova et al.[25] comprising hiPSC-CM cultures that were matured for 12, 24, or 90 days was used for mapping combined with the MapQuery function in Seurat (**Supplementary Figure 4A-B**). ScTransformed expression data was used to obtain variably expressed genes. RNA count data was regularly normalized and scaled with regression of mitochondrial gene expression levels and the number of expressed genes (nFeature). The normalized data was used to generate a PCA plot from the variable genes. PCA values were used to integrate cells of different samples via the harmony method (function: runHarmony[25,2626]). Harmony scores were used for dimensionality reduction of the cells using UMAP, and to cluster cells. Cell type categories were assigned to each cell cluster after examination of expressed marker genes. Differential gene expression was modelled and assessed using the glmQLFit functions in edgeR[27] with added per-cell gene detection rate information as recommended by Soneson et al.[28] Hereby, expression was modelled using a linear model that included cell type and PLN genotype information next to the gene detection rate.

AAV Treatment. I-1c cDNA, under the control of the CMV promoter, was packaged in an AAV2i8.[29] AAV.I-1c was prepared to a final titer of 4.73 × 10^14 viral genomes (VG)/mL. To determine the optimal multiplicity of infection (MOI), transduction with an MOI of 1000, 10.000, 100.000, and 500.000 was used in one-week-old PLN-R14del hCSs, whereafter the spheroids were cultured for two more weeks before harvested. The endogenous I-1C expression was determined by RT-qPCR while the Ca^{2+} handling function was determined by optical Ca^{2+} transient analysis of peak value, decay time, and beating rate parameters of the hCSs (**Supplementary Figure 6**). For the final experiments, hCSs were incubated with a MOI of 10.0000 in 100 µL media for 24 h. After 24 hours, 200 µL of the spheroid medium was added to each well. Every 2-3 days, half of the medium was replaced with maturation medium for 14 days post AAV transduction.

Optical Ca^{2+} transient analysis. Ca^{2+} transient analysis was performed to evaluate Ca^{2+} handling properties in both control and PLN-R14del hiPSC-CMs with and without AAV treatments. Briefly, cells were loaded for 30 min in FluoroBrite DMEM Media (Thermo Fisher),

supplemented with 1.25 µM Cal-520 (Abcam) and 0.02% Pluronic F-127 solution (Sigma Aldrich). Spontaneous Ca^{2+} transients were recorded three weeks after plating. Video streams of Cal-520 (green channel) lasting 10 seconds at 33 fps were automatically scanned by a Leica Thunder microscope. Image analysis was conducted using Cyteseer (Vala Sciences, California, USA), as previously described.[30,31] The physiological parameters; decay time, peak value (normalized area under the peak trace), rise time, and Ca^{2+} Transient Duration (CTD) on 10% (CTD10) and 90% (CTD90) of the peak width and beats per minute were automatically calculated for each time series.

Spheroid immunolabeling and confocal imaging. For immunofluorescent stainings, whole 3D microtissues were used to image at a single-cell resolution, adapted from a recently published protocol.[32] In short, 1 mil. hiPSC-CMs were seeded in 6 wells (ultra-low attachment, corning). After 3 weeks of culturing, half of the medium was carefully aspirated and 1 mL of cold phosphate-buffered saline (PBS) was added. The hCSs were carefully collected by BSA-coated tips (Roche) into BSA-coated tubes. The hCSs were washed with 10 mL ice-cold PBS and spun down for 3 min at 70xg and 4° C. Next, the hCSs were resuspended in 1 mL 4% paraformaldehyde (PFA, Santa Cruz) solution and fixed for 45 min at 4°C. After the fixation, the hCSs were spun down for 3 min at 70xg and 4° C, and washed with 10 mL ice-cold PBS 3 times. HCSs were then blocked for 15 min at 4°C in spheroid washing buffer (SWB), consisting of 0,1% Triton X-100 (Sigma), 0,2% of 10% (w/v) SDS (Sigma), and 0,2% bovine serum albumin (BSA, Sigma) in PBS (stored at 4°C up to 2 weeks). After fixation and blocking, the hCSs were transferred to a 24-well suspension plate where immunolabeling was performed. hCSs were incubated with various primary antibodies (**Supplementary Table 1**). DNA Hoechst staining was used for nuclei labelling (Thermo Fisher Scientific) and was added together with the secondary antibodies (0.5 µg/mL Goat Anti-mouse 488, and 0.5 µg/mL goat anti-rabbit-568, Thermo Fisher Scientific). For the direct Nile Red labelling, 10 µg/ml Nile Red (Sigma) was added to the secondary antibody mix. Specimens were mounted on microscope glasses using FUnGI consisting of 50% (v/v) glycerol (Sigma), 9.4% (v/v) dH2O, 10.6 mM tris base (Roche), 1.1 mM EDTA (Sigma), 2.5 M fructose (Sigma) and 2.5 M urea (Sigma). Fluorescent imaging was done using an SP8 Confocal Microscope (Leica). Optical sectioning along the Z-axis was performed and the images collapsed into a single focal plane using the manufacturer's software.

Flow cytometry analysis. The hCSs were digested by TrypLE Select Enzyme for 30 min at 37°C. The single CMs were fixed with 4% paraformaldehyde (Santa Cruz) for 10 minutes at 37°C. Cells were then permeabilized using 1% ice-cold BSA-PBS and 0.3% Triton-X-100 for 30 minutes on ice. The primary antibody against alpha-actinin (0.25 µg/mL dilution)(mouse, A7811 MilliporeSigma) was incubated for 1 hour while the secondary antibody goat anti-mouse Alexa Fluor-488 (0.25 µg/mL dilution) (Thermo Fisher Scientific) was incubated with

cells for 30 minutes at room temperature. The total recorded events were 1000-25,000. Acquired data were analyzed with FlowJo Version 7.6.2 (Treestar Software, Ashland, OR, USA).

RNA Extraction and qPCR. Day 21 cardiac organoids were subjected to RNA extraction by the chloroform method as previously described.[33] cDNA synthesis was performed using 500 ng RNA per sample in the qScript cDNA Synthesis Kit (Quantabio). The cDNA produced was then diluted 20 times with nuclease-free water and stored at -20°C for subsequent analysis. qPCR was carried out on an Applied Biosystems CFX384 Fast Real-Time PCR system using the SYBR Green method using 5 µL cDNA per duplicate. Data from the qPCR were normalized to RPL32, which was chosen due to its consistency across the sample groups. Integrated DNA Technologies Primers were designed and are displayed in **Supplementary Table 1**.

Engineered Heart Tissue (EHT) generation. Engineered Heart Tissues were generated with small modifications, as previously described.[34] Briefly, hiPSC-CMs were detached and resuspended in RPMI supplemented with 2% B27, 10% KOSR and 10 µM Y-27632. EHTs of 1x106 cardiomyocytes were casted by mixing the reconstitution mix consisting of 79 µl cell suspension, 15.5 µL 2x DMEM (Gibco), and 2,5 µL (0.5 mg) of fibrinogen (Sigma) with 3 µl (100 U/ml) thrombin (Sigma) and pipetting it into the casting molds. Fibrin polymerization (37°C, 7% CO2, 98% RH, 2 h) led to the formation of a muscle strip. The EHTs were transferred to a culture medium (Dulbecco's modified Eagle's medium) containing 10% horse serum, 1% penicillin/streptomycin, 10 µg/ml insulin, and 33 µg/ml aprotinin and maintained at 21% oxygen, 7% CO2 and 37°C in a humidified cell culture incubator for 17 days. Contractility measurements were performed in a culture medium, as described before.[34]

Statistical Analysis. Statistical analysis was carried out on GraphPad Prism 9. Data were subjected to one-way-, two-way- ANOVA (Tukey), and/or unpaired t-tests, as indicated in the different figure legends. Significance was determined as a p-value of < 0.05.

RESULTS

PLN-R14del hCSs show reduced Ca^{2+} amplitude and impaired Ca^{2+} handling

To evaluate the PLN-R14del phenotype, we used patient-specific hiPSC lines (D4iR14del, 6BiR14del, and 10BiR14del) and compared them to control hiPSC lines derived from 1) a healthy proband of the D4iR14del line (1CiCTR), 2) an individual with no history of heart disease (273iCTR), and 3) an isogenic control of the D4iR14del line corrected by CRISPR-Cas9 (C31iCTR) (**Supplementary Figure 1**). As three-dimensional (3D) hCSs more closely recapitulate intercellular biomechanics, we generated 3D spheroids after step-wise differentiation, in which guided mesodermal induction of human induced pluripotent stem cells (hiPSC) was followed by cardiomyocyte (CM) differentiation.[21] After 11 days, the differentiated CMs were re-plated to T75 culture flasks to induce controlled CM expansion, as previously described.[35,36] After differentiation and subsequent expansion of the CMs, 10.000 CMs were placed in one well to induce spheroid formation as previously described[23] (**Figure 1A**).

PLN-R14del is generally associated with susceptibility to Ca^{2+} handling, and multiple electrophysiological abnormalities, resulting in heart failure.[1,16,37] Therefore, we assessed Ca^{2+} handling in hCSs at 1,2, 3, and 6 weeks after their generation in 96-well plates (**Supplementary Figure 2**). The previously reported consistent difference in all Ca^{2+} handling parameters between C31iCTR and D4iR14del PLN-R14del hCSs was present at weeks 2 and 3 (**Supplementary Figure 2C**). We extended these analyses on 2 control lines; 1CiCTR, 2731CTR, and PLN-R14del; 6BiR14del and 10BiR14del, and recorded spontaneous Ca^{2+} sparks and observed reduced Ca^{2+} intensity (**Figure 1B**) and a very 'spiky and narrow' peak width in the PLN-R14del hCSs (**Figure 1C**). Next, we performed automated high-throughput screening of the spontaneous Ca^{2+} transients' parameters (**Figure 1D**). We observed significantly decreased decay and rise times, peak amplitude, and Ca^{2+} transient durations of 10% (CTD10) and 90% (CTD90) (**Figure 1E-I**), which hint towards a decreased Ca^{2+} handling function. Hence, we observed an increase in the beating rate in all hCSs from the PLN-R14del lines (**Figure 1J**).

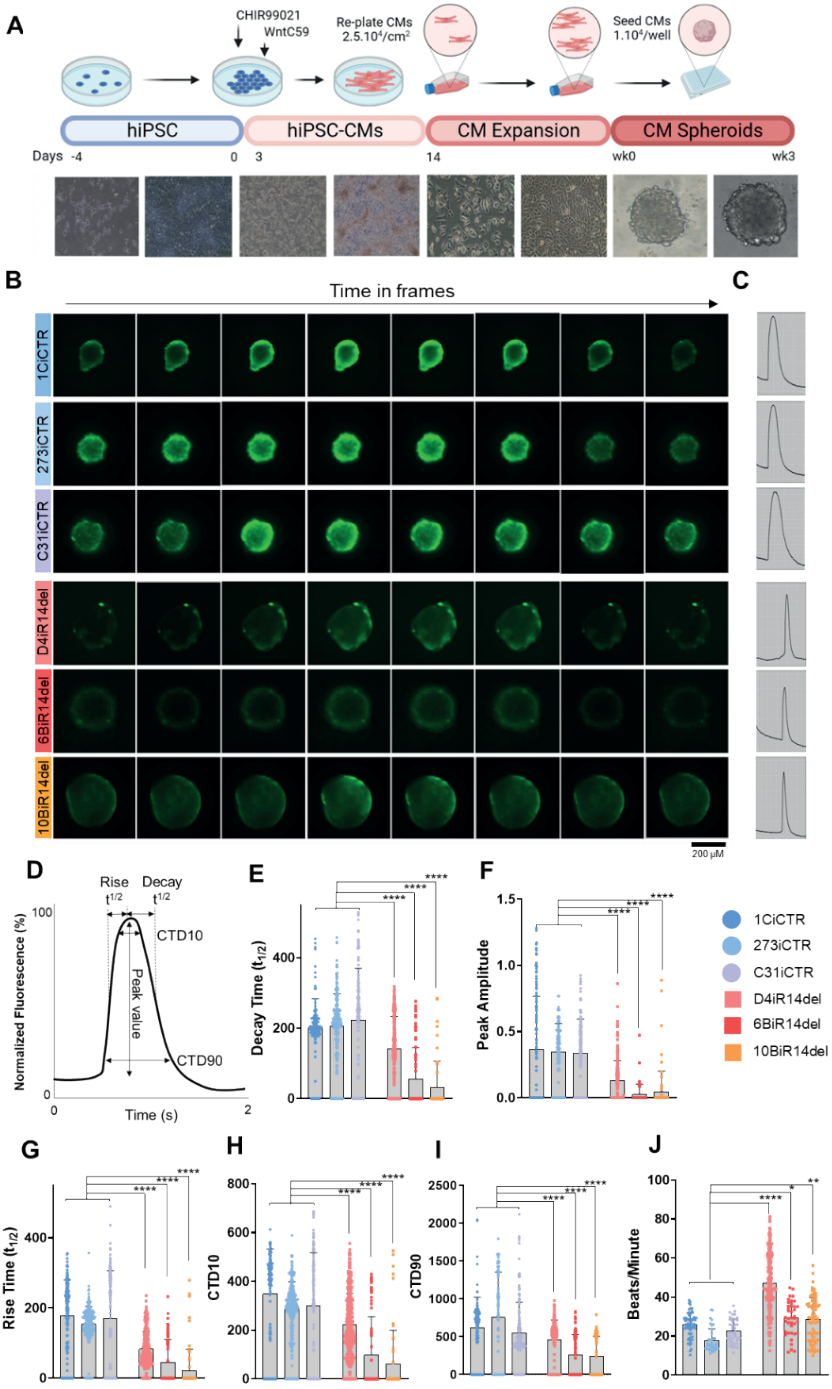
A
CHIR99021
WntC59
Re-plate CMs
2.5.10⁴/cm²
Seed CMs
1.10⁴/well
hiPSC
hiPSC-CMs
CM Expansion
CM Spheroids
Days -4
0
3
14
wk0
wk3
B
Time in frames
C
1CiCTR
273iCTR
C31iCTR
D4iR14del
6BiR14del
10BiR14del
200 µM
D
Rise t1/2
Decay t1/2
CTD10
Peak value
CTD90
Normalized Fluorescence (%)
Time (s)
E
Decay Time (t1/2)
F
Peak Amplitude
1CiCTR
273iCTR
C31iCTR
D4iR14del
6BiR14del
10BiR14del
G
Rise Time (t1/2)
H
CTD10
I
CTD90
J
Beats/Minute

◀Figure 1. Comparison of Ca^{2+} handling properties between hCSs from wild type (CTR lines) and PLN-R14del patients (R14del lines). (**A**) Schematic representation of Wnt-based directed cardiac differentiation, the subsequent expansion of hiPSC-CMs, and the generation pipeline for hCSs. Created with biorender.com (**B**) Time-lapse Ca^{2+} imaging of spontaneous Ca^{2+} release in hCSs. Scale bar: 200 µm (**C**) Representative recordings of time-lapse Ca^{2+} transients. (**D**) Measurement of Ca^{2+} handling parameters from automated recorded data. Comparison of (**E**) Decay time (Tau), (**F**) Ca^{2+} transient amplitude, (**G**) Rise time, (**H**) transient duration 10% (CTD10), (**I**) transient duration 90% (CTD90), and (**J**) beating rate in 1CiCTR (biological replicates=3, n=120), 273iCTR (biological replicates=5, n=217), C31iCTR (biological replicates =3, n=138), D4iR14del (biological replicates=5, n=287), 6BiR14del (biological replicates=3, n=89), and 10BiR14del (biological replicates=3, n=60) hCSs. **** $P < 0.0001$ vs. control lines by One-Way ANOVA. Each dot represents one individual spheroid and 3 biological (=b) per condition were included in this analysis.

Morphological characterization of PLN-R14del hCSs

Notably, when culturing the hCS, we observed an overall increase in the size of the hCSs, both in the controls and PLN-R14del-derived lines. Remarkably, spheroid size in PLN-R14del was massively increased when compared to controls (**Figure 2A**, **Supplementary Figure 3A**), already after 7 days of culturing. PLN-R14del hCSs showed a significantly larger diameter compared to controls at days 7, 14, and 21 (**Figure 2B**), with a final average size of 1092.87 µM (± 597.28) vs 422.94 µM (± 251.97) of 21 days old hCSs (**Figure 2C**). The number of nuclei per spheroid was significantly increased compared to controls, with an average number of 460 (± 306) vs 163 (± 101) of 21-day-old hCSs (**Figure 2D**). To ensure comparable CM numbers for initial spheroid generation, we enriched hiPSC-CMs to >80% purity through metabolic selection before hCS generation for all lines. The purity of the hiPSC-CMs used for the generation of hCSs was not significantly different between cell lines when hCSs spheroids were generated (78.04 ± 10.31 % alpha-actin positive cells) (**Figure 2E**, **Supplementary Figure 3B**). However, after 3 weeks of spheroid culturing, the PLN-R14del hCS showed a significant 50% reduction in alpha-actinin positive cells (43.33 ± 9.10) compared to healthy control spheroids (70.71 ± 3.38) (**Figure 2F**, **Supplementary Figure 3C**). The increased spheroid size, nuclei number, and reduced purity indicate an increase in PLN-R14del spheroid cell number. The observed increase in cell number was confirmed by a significant increase in expression of the proliferation marker ki67 from 0.21 (±0.47) to 37.46 (±76.3) fold (**Figure 2G**).

Effect of hiPSC-CF and hiPSC-CM ratios in PLN-R14del vs isogenic control hCSc size

Next, we controlled and gradually changed the ratio of hiPSC-derived cardiac fibroblasts to hiPSC-CMs (100%-0%, 90%-10%, 70%-30%, and 50%-50%, per hCS respectively) derived from the same donor. Interestingly, we observed again an increase in the PLN-R14del spheroid size after 14-21 days in culture (**Figure 3A**). The size of the isogenic control hCSs was not affected by the addition of different ratios with CFs (**Figure 3B**), whereas a significant increase in spheroid size in the PLN-R14del hCSs was observed (**Figure 3C**). Interestingly, when modulating the ratio into +50% hiPSC-CMs, the PLN-R14del hCSs size significantly increased after 14 and 21 days of spheroid culturing (**Supplementary Figure 4**). This suggests that over time cardiomyocyte-specific cell interaction mediates the increase in size rather than the proliferation of existing hiPSC-derived fibroblasts in the hCSs, which is dramatically enhanced in the PLN-R14del patient lines.

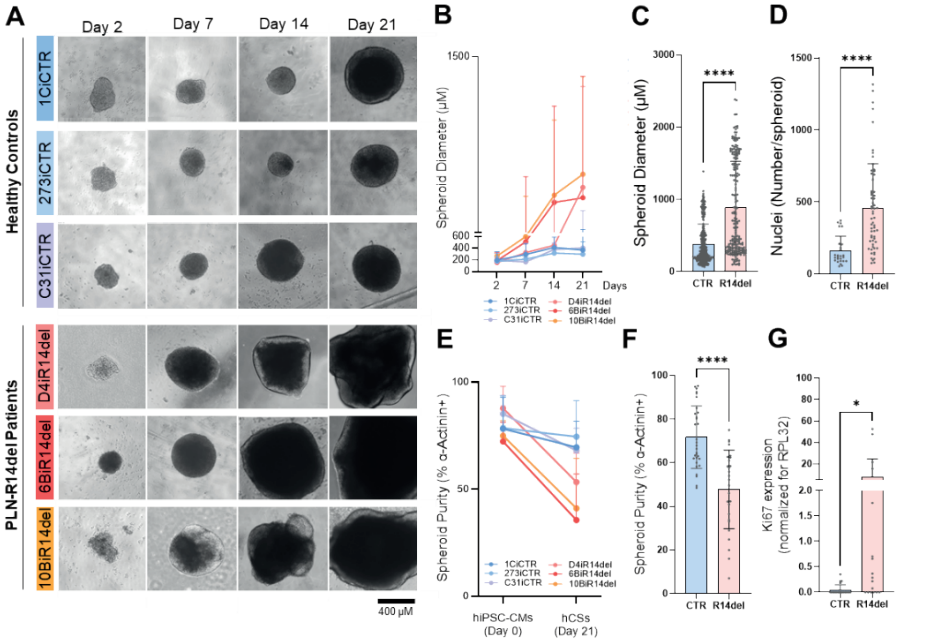

Figure 2. Comparison of morphology and cell numbers between hCSs from wild type (CTR lines) and PLN-R14del patients (R14del lines). (**A**) Cardiac spheroid morphology at days 2, 7, 14, and 21. Scale bar: 400 µm. Each dot represents the average of 27-304 spheroids, while 3-7 biological differentiations per condition were included in this analysis. (**B**) Quantification of spheroid size at day 21. **** P < 0.0001 by unpaired T-test. CTR = size measurement per spheroid of the 3 control lines, R14del = size measurement per spheroid of the 3 PLN-R14del lines. (**C**) Quantification of spheroid nuclei number at day 21. **** P < 0.0001 by unpaired T-test. CTR = nuclei number per spheroid of the 3 control lines, R14del = nuclei number per spheroid of the 3 PLN-R14del lines. Each dot represents one individual spheroid, and 2-3 biological, while 3-8 technical replicates per condition were included in this analysis. (**D**) Flow cytometry analysis of alpha-actinin positive cells before the generation of spheroids and after 21 days post-generation. (**E**) Quantification of alpha-actinin after 21 days post spheroid generation. **** P < 0.001 by Student's unpaired T-test. Each dot represents the average of 5-25 flow cytometry measurements of 25.000 cells. 2-3 biological differentiations per condition were included in this analysis. (**F**) mRNA expression of proliferation marker ki67. Each dot represents one batch of hCSs (n=21 vs. n=18). 3 biological replicates per condition were included in this analysis. * P< 0.05 as calculated by an unpaired t-test. Abbreviations; hiPSC; human induced pluripotent stem cell-derived cardiomyocytes, CMs; Cardiomyocytes, CTR; Control hCSs (1CiCTR, 273iCTR, C31iCTR), R14del; PLN-R14del hCSs (D4iR14del, 6BiR14del, 10BiCTR). All data are represented as mean ± SD.

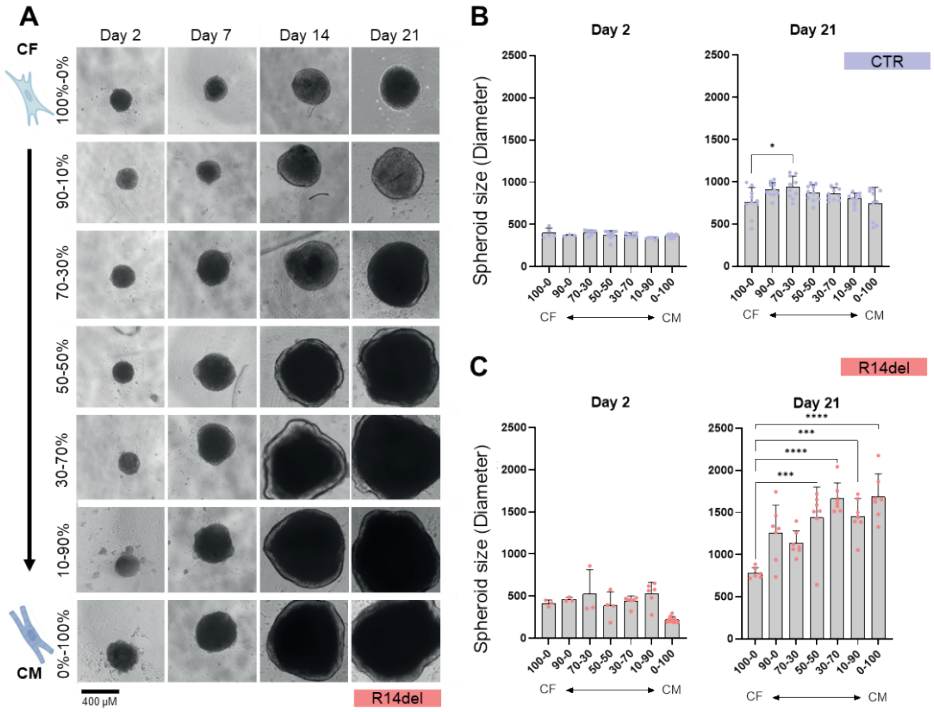

Figure 3. Contribution of Cardiac Fibroblast (CF) numbers to hCSs size. (**A**) Representative cardiac spheroid morphology at D2, D7, D14, and D21 after the controlled generation of hCSs containing hiPSC-derived fibroblasts (hiPSC-CFs) and hiPSC-CMS, both derived from the PLN-R14del (D4iR14del) line in the ratios 100% hiPSC-CFs (top) to 100% hiPSC-CMs (bottom) and 5 different ratios in between. Scale bar: 400 µm. (**B**) Bar graphs of the size quantification from C31iCTR (CTR) spheroids on day 2 and day 21 post-hCS generation. (**C**) Bar graphs of the size quantification from D4iR14del spheroids on day 2 and day 21 post-hCS generation. Biological replicates = 1, technical replicates 5-8 hCSs per group. * P< 0.05 - **** P < 0.0001 vs. hiPSC-CF only group by one-way ANOVA.

Single-cell sequencing reveals cellular diversity and PLN-R14del phenotype pathways

To investigate the cardiac spheroid composition and functional heterogeneity, we performed split-pool ligation-based transcriptome sequencing (SPLiT-seq) of 760 single cells from PLN-R14del spheroids (total 386 cells) and healthy or isogenic corrected spheroids (total 374 cells) (**Figure 4A**, **Supplementary Figure 5**). Based on previous clustered mapping[25] (**Supplementary Figure 5A-B**), we partitioned these cells into three clusters, which were annotated as cardiomyocytes group 1 (CM1), cardiomyocytes group 2 (CM2), and fibroblasts (fibro) (**Figure 4B**, **Supplementary Figure 5C**). We found that the healthy CTR spheroids were mainly composed of CM1 and CM2 grouped cells (**Supplementary Figure 5D**). The CM1 cluster is distinguished from the CM2 group by the abundance of genes; deleted in colorectal cancer (DCC), a large transmembrane receptor of netrin-1, critical for mediating netrin-1's cardioprotective function and sodium leak channel non-selective channel protein (FAM155A)

(DCC/FAM155A^{high} CMs) (**Supplementary Figure 5E**). The CM2 cluster is highlighted by the presence of classical cardiac genes such as sarcomeric protein TNNT2 and the Ca^{2+} handling protein Ryanodine receptor 2 (RYR2) (TNNT2/RYR2^{high} CMs). While the expression levels of cardiac markers troponin T (TNNT2) and myosin heavy chain 7 (MYH7) did not reveal an overall significant difference between conditions (**Supplementary Figure 5F**), PLN-R14del spheroids contained more cells in the CM2 and fibroblast-like single cells, cluster 3, were detected in 7.51% of PLN-R14del cells compared to the control (1.87%) confirming the increased fibroblast number after culturing PLN-R14del cells (**Supplementary Figure 5D**). Cluster 3 is highlighted by fibroblast matrix proteins Fibronectin 1 (FN1) and type I collagen (COL1A1) (**Supplementary Figure 5G-H**). Gene set enrichment analysis of the top 100 pathways revealed differences in specific pathways that were previously described to be affected by the PLN-R14del mutation (**Figure 4D**). Multi-omics integration13 and mitochondrial functional assays12 have shown an impaired mitochondrial function and decreased fatty acid oxidation metabolism in PLN-R14del hiPSC-CMs. Here, we showcase 4 pathways involved in mitochondrial function (**Figure 4D**, yellow bars), such as fatty acid oxidation, biogenesis, oxidative phosphorylation, and triglyceride catabolism, that were all significantly decreased in the PLN-R14del single cells. Moreover, previous single-cell RNA sequencing revealed the induction of the unfolded protein response (UPR) pathway (**Figure 4D**, red bars) in PLN R14del compared with isogenic control hiPSC-CMs.[13] Similarly, we found autophagy, UPR activation, and aggrephagy pathways all significantly increased in the PLN-R14del single cells, confirming our previous findings.[13]

A decreased force in engineered heart tissues has revealed impaired contractility in PLN-R14del CMs[13,14], which was confirmed by our pathway analysis of muscle contraction and dilated and hypertrophic cardiomyopathies (DCM/HMC) related protein expressions in PLN-R14del single cells (**Figure 4D**, blue bars). Furthermore, increased arrhythmic Ca^{2+} cycling[16] and decreased decay time and amplitude[37] revealed a critical role of abnormal Ca^{2+} handling in the pathogenesis of PLN-R14del. We observed a significant decrease in the cardiac conduction, Arrhythmogenic Right Ventricular Cardiomyopathy (ARVC), and myogenesis pathways, whereas the Ion homeostasis was decreased in PLN-R14del single cells although not significantly (**Figure 4D**, purple bars). Most PLN-R14del hearts develop significant cardiac fibrosis, mainly in the posterolateral left ventricle wall. Interestingly, to the best of our knowledge, we show for the first time that pathways involved in fibrosis are affected in *in vitro* cardiac spheroids by our single-cell sequencing approach (**Figure 4D**, orange bars). Specifically, we found significantly different expressed pathways in the extracellular matrix (laminin/ECM) and pathways involved in EIF and PI3K/AKT in PLN-R14del single cells, indicating a profibrotic response in spheroids harboring the PLN-R14del mutation.

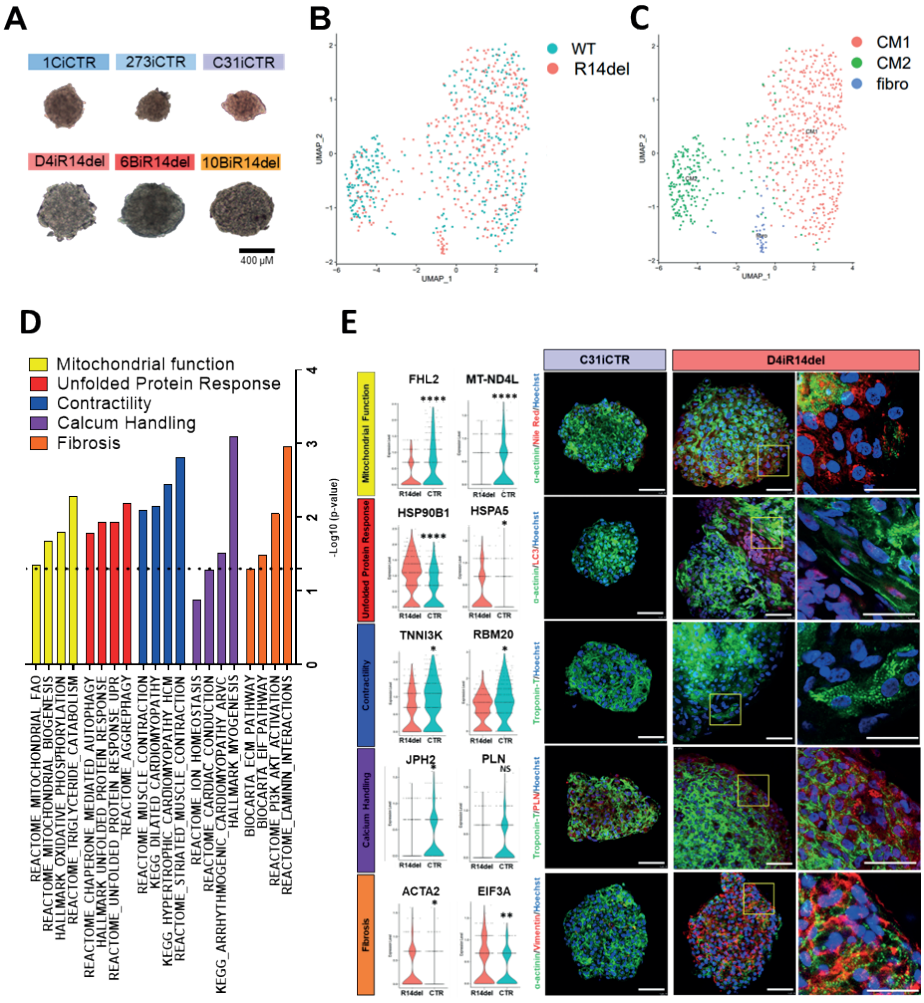

Figure 4. Single-cell transcriptional profiling of cardiac spheroids from PLN-R14del spheroids and healthy controls. (**A**) Bright-field images of the spheroids used for split-pool ligation-based transcriptome sequencing (SPLiT-seq). (**B**) UMAP of single cell profile with each cell color-coded for cells from healthy controls (WT, blue) and PLN-R14del spheroids (R14del, red). (**C**) Unsupervised Uniform Manifold Approximation and Projection (UMAP) clustering of single cells after QC and data filtering using Harmony integration. Expression patterns of hiPSC-derived cardiac spheroids from 374 healthy control and 384 PLN-R14del single cells were clustered using the Jaccard-Louvain method (3 clusters indicated by colors) and visualized using Uniform Manifold Approximation and Projection (UMAP). Cluster IDs were assigned after clustering based on cluster size, with Cluster 1 containing the most cells and Cluster 3 containing the least. (**D**) Gene Ontology (GO) enrichment analyses with the top hundred biological processes, cellular components, and molecular functions of the differentially expressed genes between PLN-R14del and healthy cardiac spheroid cells. GO-pathways are selected for 5 PLN-R14del phenotype classes; mitochondrial function (yellow), Unfolded protein Response (Red), Contractility (blue), Ca^{2+} handling (Purple), and Fibrosis (orange). A vertical black dotted line indicates the cut-off level for significance ($P < 0.05$). P-values were adjusted by Benjamini-Hochberg correction for multiple testing. (**E**) The differential expression levels of 5 PLN-R14del phenotype classes genes in

the SPLIT-seq dataset and corresponding immunofluorescent stainings. * P< 0.05, ** P<0.01, **** P<0.0001 vs. CTR group by Student's unpaired T-test. Scale bars indicate 50 uM and the yellow box indicates the zoomed-in location of the PLN-R14del spheroid (right picture). Abbreviations; CTR; Control hCSs (1CiCTR, 273iCTR, C31iCTR), R14del; PLN-R14del hCSs (D4iR14del, 6BiR14del, 10BiCTR), FHL2; Four And A Half LIM Domains 2, MT-ND4L; Mitochondrially Encoded NADH Ubiquinone Oxidoreductase Core Subunit 4L, HSP90B1; Heat Shock Protein 90 Beta Family Member 1, BIP/HSPA5; Immunoglobulin heavy-chain-binding protein, LC3; Microtubule-associated protein 1A/1B-light chain 3, TNNI3K; Troponin I-interacting kinase 3, RBM20; RNA binding motif protein 20, JPH2; Junctophilin, PLN; Phospholamban, ACTA2; Actin Alpha 2 and EIF3A; Eukaryotic Translation Initiation Factor 3 Subunit A.

Next, we investigated genes involved in the pathological mechanisms of the 5 pathways described in the PLN-R14del disease; mitochondrial function, UPR, contractility, Ca^{2+} handling, and fibrosis. The top 20 of differentially expressed genes revealed the expression of genes involved in all 5 pathways described in the PLN-R14del disease, such as Polyubiquitin-C (UPR) but also Golgi and ER protein modification, which could also be involved in protein toxicity (GOLGA1, ICMT) (**Supplementary Table 2**). The top 20 differentially expressed genesets revealed mainly the reduced contraction genes. PLN-R14del cells also expressed upregulated Netrin-1 genesets, which are involved in embryonic development and are upregulated in cancer-associated fibroblasts.[38] Additionally, Gli protein expression was elevated in PLN-R14del, which is known to be involved in cell fate determination, proliferation, and patterning in many cell types and most organs during embryo development[39] (**Supplementary Table 3**). We additionally selected 2 genes of the SPLiTSseq dataset in each PLN-R14del pathway and performed immunofluorescent imaging to visualize pathological protein patterns within the PLN-R14del spheroids. We observed mitochondrial genes Four And A Half LIM Domains 2 (FHL2) and Mitochondrially Encoded NADH Ubiquinone Oxidoreductase Core Subunit 4L (MT-ND4L) to be significantly decreased and the Nile red staining revealed visually increased lipid droplet size in PLN-R14del spheroid cells as compared to control (**Figure 4E**). The expression levels of the UPR genes; Heat Shock Protein 90 Beta Family Member 1 (HSP90B1) and Immunoglobulin heavy-chain-binding protein (BIP or HSPA5) were also significantly upregulated, and autophagy was confirmed with an increased protein imaging of LC3 (**Figure 4C**). The contractility genes; Troponin I-interacting kinase 3 (TNNI3K) and RNA binding motif protein 20 (RBM20) and the immunofluorescent staining of cardiac sarcomere protein alpha-actinin, which showed a significant reduction in the gene expression and a visually reduced presence of sarcomere positive cells in the PLN-R14del spheroids (**Figure 4E**). Next, the Ca^{2+} handling gene Junctophilin (JPH2) was significantly decreased, indicating the decreased junctions in the PLN-R14del spheroid cells. However, the PLN expression levels were not significantly decreased, although we could observe, for the first time, PLN protein aggregates in the PLN-R14del spheroids (**Figure 4D**). Lastly, we analysed the fibroblast genes; Actin Alpha 2 (ACTA2) and Eukaryotic Translation Initiation Factor 3 Subunit A (EIF3A) and the ECM protein vimentin were increased in PLN-R14del spheroid cells as compared to control (**Figure 4E**). The increased lipid droplets, fibrotic ECM accumulation, elevated autophagy, PLN aggregates, and reduced sarcomere-positive cells prove the spheroid capability to mimic the PLN-R14del pathological mechanisms *in vitro*.

PLN-R14del hCSs express an increased fibroblast activation pattern.

Interestingly, the pathological mechanisms observed in PLN-R14del spheroids were observed in various stages of severity in spheroid size and sarcomeric marker alpha-actinin (-ACT) presence. In some PLN-R14del spheroids, one or multiple non-positive holes were observed, whereas some spheroids did reveal only a few nuclei with sarcomere expression (**Figure 5A**). However, all PLN-R14del spheroids revealed nuclei with no sarcomere proteins present (**Figure 5A**), and a significant reduction of -ACT area/nucleus (**Figure 5B**). Many nuclei in the PLN-R14del spheroids were found positive for the proliferation marker Ki67 and were observed in different locations, either in the middle or on the outer layers (**Figure 5B**), whereas the collagen production was mainly found in the outer layer of the spheroids (**Figure 5E**). Quantification of proliferation showed an increase in Ki67-positive nuclei (**Figure 5D**) and a significant increase in Pro-COL1A1 accumulation (**Figure 5F**). RT-qPCR analyses revealed that PLN-R14del hCSs displayed a significant increase in activated fibroblast genes (aSMA (ACTA2), COL1A1, FN1), proliferation gene ki67, fetal genes (NPPA/MYH7) and a significantly reduced expression of genes that regulate cardiomyocyte function e.g. CASQ2, ATP2A, PLN, PKP2, GJA1, TNNI3 and ACTA1 (**Figure 5G**). A heat map was generated using Euclidean distance showing hierarchical clustering of control and PLN-R14del hCSs, based on log2 fold expression of the genes described in Figure 3G (**Figure 5H**), confirming similar expression patterns between control hCSs and the three PLN-R14del patient hCSs. The reduction of cardiac markers and increase in proliferation and collagen expression is variable in each PLN-R14del spheroid but could be the result of CM depletion and replacing fibrosis also observed in the myocardium of PLN-R14del patients.

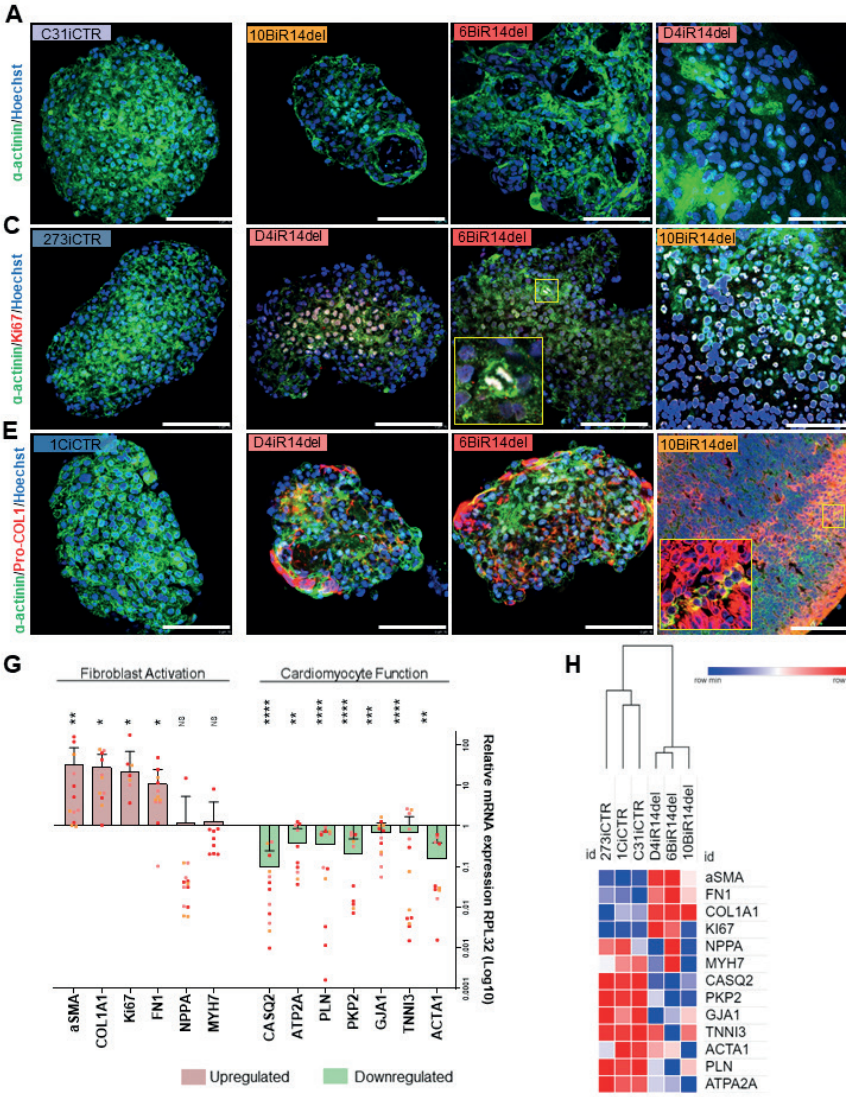

Figure 5. Increased fibroblast activation expression and protein expression in PLN-R14del spheroids. (**A**) Representative immunofluorescent imaging of alpha-actinin (green). (**B**) Representative immunofluorescent imaging of alpha-actinin (green) co-stained with Ki67 (red). (**C**) Representative immunofluorescent imaging of alpha-actinin (green) co-stained with Pro-Collagen 1 (red). Hoechst is used to stain the nuclei (Blue). Scale bar: 500 µm. Immunofluorescent quantification of hCSs α-Actinin expression (**D**), proliferation marker Ki67 (**E**), and Pro-Collagen 1 (**F**) per nuclei. ** P< 0.01 vs. CTR group by Student's unpaired T-test. Each dot represents one individual spheroid and 2-3 biological and 3-10 technical replicates per condition were included in this analysis. (**G**) qPCR analysis of various genes involved in fibroblast activation or cardiomyocyte function in PLN-R14del hCSs vs. controls. Each dot represents the expression of one sample containing 20 hCSs, normalized for average control spheroid expression. (**H**) Heat map and hierarchical clustering of gene expression data. Log 2-fold changes of gene expression are represented and the color scale indicates the level of change (blue, low; red, high). The hierarchical clustering was generated using the Euclidean distance correlation metric based on the square root of the sum of the square differences (https://software.broadinstitute.org/morpheus).

AAV-mediated overexpression of I-1c rescues spheroid morphology and cardiac expression patterns and improves contractility in PLN-R14del spheroids

Next, we asked whether gene augmentation with I-1c might alleviate the disease phenotype by restoring cardiac spheroid function. I-1c decreases protein phosphatase 1 (PP1) activity, thereby upstream regulating the SERCA2a/phospholamban complex, and is also closely linked to the β-adrenoceptor system.[40] Upon activation of I-1c, PP1 is suppressed, thereby increasing SERCA2a activity and phospholamban phosphorylation which leads to improved basal cardiac performance.[41] AAV.I-1c previously demonstrated clinically meaningful benefits in ischaemic heart failure pigs by improving left ventricle ejection fraction (LVEF), contractility, and decreased fibroblast activation[42], whereafter AAV2/8.I-1c is currently in clinical trials[43]. In this gene augmentation approach, the constitutively active I-1c is used to restore Ca^{2+} An increased MOI rate demonstrated an exponential increase in expression of I-1c from 28 up to 34.000-fold in PLN-R14del transduced hiPSC-CMs over non-transduced cells (**Supplementary Figure 6A**). The percentage of functional contracting spheroids was similar in all conditions, suggesting that AAV.I-1c does not affect spheroid viability (**Supplementary Figure 6B**). Interestingly, AAV.I-1v improved Ca^{2+} handling in PLN-R14del hCSs by all used MOIs. An MOI of 10,000 was selected for the rest of the experiments based on physiological levels of I-1v and significant changes in Ca^{2+} handling (**Supplementary Figure 6C**). Seven-day-old healthy control and PLN-R14del spheroids were transduced with AAV.I-1c at an MOI of 10.000 (**Figure 6A**) and subsequently analyzed after 14 days for spheroid size. When PLN-R14del hCSs were generated in 6 wells, we again observed large spheroids with reduced Ca^{2+} flux activity (**Figure 6B**). After a single dose of AAV.I-1c treatment, we observed increased Ca^{2+} intensity and more regular peak widths in treated PLN-R14del hCSs (**Figure 6C**). AAV.I-1c reduced spheroid size in all 3 PLN-R4del patients hCSs (462 ± 55 µm versus 931 ± 200 µm in non-transduced PLNR14del hCS) (**Figure 6D**) while not affecting the size of healthy control spheroids (306 ± 50 µm versus 294 ± 62 µm in non-transduced control hCS) (**Figure 6E**). Moreover, to study the effect of AAV.I-1c on contractility, Engineered Heart Tissues (EHTs) were generated of all hiPSC lines as previously reported.[34] The administration of AAV.I-1c for 7 days improved contraction in both the CTR spheroids and significantly in the PLN-R14del EHTs (**Figure 6F**). Secondly, gene expression after transduction of control and PLN-R14del spheroids with AAV.I-1c was evaluated by RT-PCR analysis. Interestingly, treatment of AAV.I-1c decreased the expression of fibroblast activation genes such as α-Smooth muscle actin (aSMA), Fibronectin 1 (FN1), and Pro-collagen 1 (COL1A1), and the proliferation marker Ki67 in PLN-R14del spheroids (**Supplementary Figure 7A**). The hypertrophy-responsive genes, such as atrial natriuretic peptide (NPPA) and Myosin Heavy chain 7 (MYH7), did not significantly reduce after AAV.I-1c treatment (**Supplementary Figure 7B**), whereas both plakophilin-2 (PKP2) and calsequestrin 2 (CASQ2) showed a non-significant trend towards higher levels (**Supplementary Figure 7C**). The thin myofilament genes Troponin I (TNNI3) and -actinin (ACTA1) did not significantly increase (**Supplementary Figure 7D**), however, both PLN and SERCA2A gene expression was

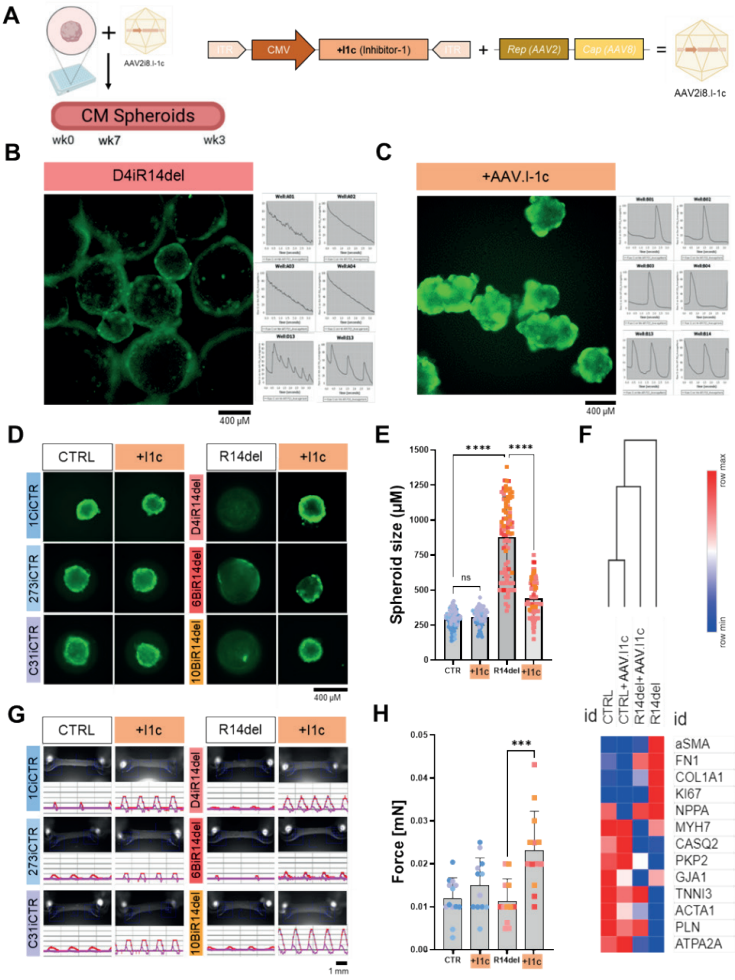

Figure 6. hCS morphology after AAV.I-1c treatment. (**A**) Schematic overview of the expression cassette containing the cytomegalovirus (CMV) promoter, the inhibitor-1 (I-1c), and Inverted terminal repeats (ITR) and the AAV vector design, combining the Rep protein of AAV2 with the Capsid protein AAV8. hCSs transfected with AAV.Ic-1 MOI.10.000 for 14 days before the Ca^{2+} analysis was performed. (**B**) Representative cardiac spheroid morphology and 6 representative 10-second Ca^{2+} transients of non-treated hCSs from the PLN-R14del (D4iR14del) line. Scale bar: 400 µm. (**C**) Representative cardiac spheroid morphology and 6 representative 10-second Ca^{2+} transients of AAV.I-1c treated hCSs from the PLN-R14del (D4iR14del) line. Scale bar: 400 µm. (**D**) Representative size of all hiPSC lines of untreated and AAV.I-1c treated hCSs. Scale bar: 400 µm. (**E**) Bar graphs of the size quantification from untreated vs. AAV.I-1c treated hCSs spheroids. Each dot represents one individual spheroid. (**F**) Bar graph of engineered heart tissue (EHT) force analysis from non-treated vs. AAV.I-1c treated EHTs. Each dot represents one individual EHT. *** $P < 0.001$, **** $P < 0.0001$ untreated vs AAV.I-1c of each group by Student's T-Test or one-way ANOVA. (**G**) Heat map and hierarchical clustering of gene expression data. Log 2-fold changes of gene expression are represented, and the colour scale indicates the level of change (blue, low; red, high). The hierarchical clustering was generated using the Euclidean distance correlation metric based on the square root of the sum of the square differences (https://software.broadinstitute.org/morpheus). (**H**) Representative bright field of an EHT and a 4-second force transient from all hiPSC lines of untreated and AAV.I-1c treated EHTs. Scale bar: 1 mm. (**I**) Bar graph of engineered heart tissue (EHT) force analysis from non-treated vs. AAV.I-1c treated EHTs. Each dot represents one individual EHT. *** $P < 0.001$, **** $P < 0.0001$ untreated vs AAV.I-1c of each group by Student's T-Test or one-way ANOVA.

significantly increased after AAV.I-1c treatment in the PLN-R14del hCSs (**Supplementary Figure 7E**). Interestingly, AAV.I-1c overexpression did not significantly affect gene expression patterns in healthy control hCSs compared to the non-transduced controls (**Supplementary Figure 7A-E**). Based on the log2 fold expression of these genes, a heat map was generated using Euclidean distance to study the hierarchical clustering of control and PLN-R14del hCSs with or without AAV.Ic1 treatment (**Figure 6G**). PLN-R14del hCSs treated with the AAV.I-1c clustered towards the CTRL and CTRL+AAV.I-1c, rather than with the PLN-R14del untreated group, indicating a gene expression profile shift towards the healthy control group after AAV.I-1c treatment.

AAV-mediated overexpression of I-1c restores Ca^{2+} handling in PLN-R14del spheroids

The Ca^{2+} intensity and peak amplitude showed improvements after 14 days by a single dose of the AAV. I-1c (MOI of 10.000) (**Figure 7A-B**), which was further quantified and reflected in improved decay time in both control and PLN-R14del hCSs (**Figure 7D**), increased peak amplitude (**Figure 7E**) while both rise time and CTD10 partially increased but not to healthy control levels (**Figure 7F-G**). In contrast, Interestingly, CTD90 did significantly improve in both transduced controls and PLN-R14del spheroids (**Figure 7H**). Lastly, the beating rate was reduced upon AAV.I-1c transduction and declined from 38±22 beats per minute (BPM) to 30±22 BPM, which is more similar to non-transduced (23±7 BPM) or transduced (22±7 BPM) controls (**Figure 7I**). To exclude beating-rate variability in Ca^{2+}-handling, we normalized for beating rates and observed that PLN-R14del spheroids had similar reduced trends in Ca^{2+} parameters while these were normalized by AAV.I-1c supplementation (**Supplementary Figure 8**). Together, these results indicate that AAV.I-1c was able to restore Ca^{2+} handling in PLN-R14del cardiac spheroids, which makes the AAV.I-1c gene therapy a potential therapeutic option for PLN-R14del patients.

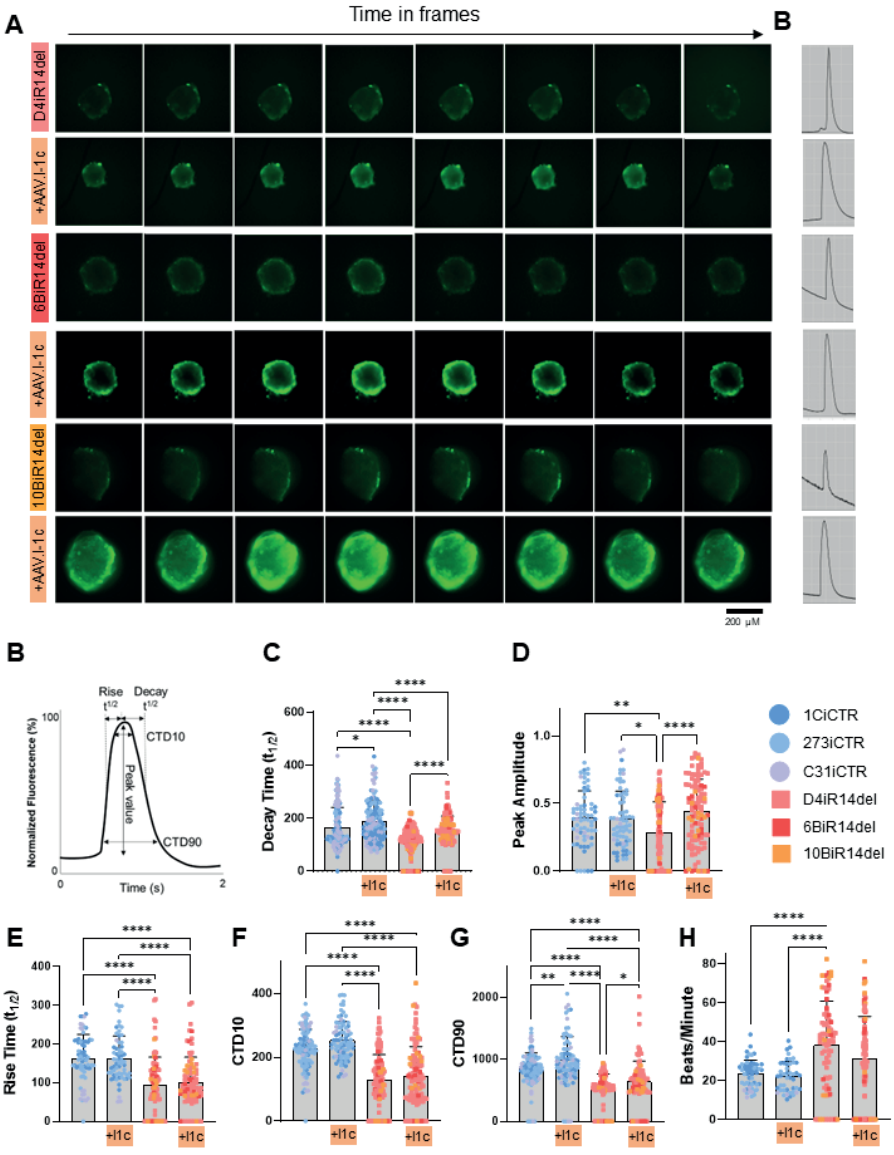

Figure 7. Comparison of Ca^{2+} handling properties between cardiac hCSs from (isogenic) controls and PLN-R14del patients. (**A**) Frames in time of spontaneous Ca^{2+} release in hCSs. Scale bar: 200 µm (**B**) Representative recording of time-lapse Ca^{2+} transients. (**C**) Measurement of Ca^{2+} handling parameters from automated recorded data. Comparison of (**D**) decay time (Tau), (**E**) Ca^{2+} transient amplitude, (**F**) Rise time, (**G**) transient duration 10% (CTD10), (**H**) transient duration 90% (CTD90), and (**I**) beating rate (BPM) among the combined groups of control lines (biological replicates=2-3, n=188), controls + AAV.Ic-1 (biological replicates=2-3, n=151), PLN-R14del lines (biological replicates=2-3, n=243), and the PLN-R14del + AAV.Ic-1 (biological replicates=2-3, n=204) groups. * P< 0.05 - **** P < 0.0001 vs. each group by two-way ANOVA. Each dot represents the raw data of one individual spheroid without batch normalization.

DISCUSSION

Various pathogenic genetic variants cause severe heart failure, including mutations in the coding region of the PLN gene. Specifically, the deletion of the arginine 14 codon in the PLN gene (PLN-R14del) is associated with prevalent ventricular arrhythmias, fibrosis, dilatation of the heart, and sudden cardiac death.[9] The pathogenic signature of how the PLN-R14del contributes to the overall clinical presentation is limited, especially in *in vitro* models. This unknown pathogenic signature translates back into the current lack of disease-specific therapeutic screening strategies. Patient-derived hiPSC-CM models provide a platform for modelling various genetic cardiomyopathies *in vitro* to understand the underlying pathological mechanisms. However, the complexity of the human heart by the cellular composition and conduction characteristics presents a limiting factor to defining the total disease-specific phenotype *in vitro*. To overcome these challenges and explore further PLN-R14del phenotypes, we generated 3D human cardiac spheroids (hCSs) from healthy controls, an isogenic control, and three PLN-R14del patient lines. The hiPSC-CMs for hCSs were successfully generated in a highly reproducible way from 6 individual patients, which can be frozen for later usage without altering their functional properties.[23] hCSs were formed from just 10,000 cells by self-aggregation in 96/384 wells plates and cultured for an optimal time of 21 days.

In contrast to other 3D systems, including engineered heart tissues (EHT)[44], our hCS model allows automated analysis of Ca^{2+} transients in a high-throughput fashion. Here, we showed, for the first time, that the optical 3D construct analysis in 384-well plates revealed decreased Ca^{2+} handling and Ca^{2+} peak amplitude in PLN-R14del hCSs (**Figure 1**). Interestingly, even after 7 days of culturing, a reduced decay time and CTD10 were observed, hinting toward the first functional pathological phenotype of this disease. However, the reduction in all Ca^{2+} handling parameters after 21 days, including rise time, decay time, and the Ca^{2+} transient duration, indicates an overall reduced Ca^{2+} flux in PLN-R14del hCSs, instead of a prolonged decay time as previously described. Indeed, the reduced Ca^{2+} handling parameters were all decreased, despite the increased beating rate in the PLN-R14del spheroids (**Supplemetary Figure 2**). Genetic analysis of the PLN-R14del hCSs revealed a decreased expression of Ca^{2+} channels JPH2, PLN, and CACNA1G and an increase in CPNE5. The gene CPNE5 is a poorly characterized Ca^{2+}-dependent membrane protein[45] and merits further attention. Taken together, an aberrant Ca^{2+} handling and amplitude due to the R14 deletion in PLN was observed in the hCSs. Recently, a decreased decay time was observed in 2D hiPSC-CMs of an unrelated PLN-R14del patient, which was described to be caused by an enhanced SERCA2a activity.[37] Pharmacological SERCA2a activation by PST3093 did not alleviate the accelerated systolic and diastolic Ca^{2+} dynamics by the overserved enhanced SR function. Cardiac DWORF overexpression in homozygous PLN-R14del mice delayed cardiac fibrosis and heart failure. However, these mice displayed an already enhanced Ca^{2+} reuptake, wherefore the DWORF overexpression did not improve Ca^{2+} S/ER reuptake.[46] The authors state that the PLN

aggregation could trigger cardiomyocyte dysfunction, leading to cardiomyocyte cell loss and fibrosis, which finally culminates in severe cardiac dysfunction and death. Given the recently described increased enhanced Ca^{2+} reuptake in both PLN-R14del 2D hiPSC-CMs and mice, the interpretation of Ca^{2+} handling and potential interventions may need to be re-evaluated.

We used the single-cell SPLiT-seq technique, which represents a new approach to determining gene expression variability at the single-cell level. Here, we used comprehensive transcriptome analysis of 386 (PLN-R14del) and 374 (healthy control) single cells from cardiac spheroids to classify them in an unbiased manner, independent of any prior knowledge of cell subtypes (**Figure 4**). To study the late stage of the PLN-R14del cardiomyocytes, we removed very large (fibrotic) spheroids and used smaller spheroids after 3 weeks of culturing from all 6 donors. Our day 75 3D spheroid cells cluster similarly to a previously described expression pattern in 2D day 90 CMs[25], indicating the enhanced maturity of the spheroid cells upon sequencing. We classified the spheroid cells into three groups; CM1 (DCC/FAM155A^{high} CMs), CM2 (TNNT2/RYR2^{high} CMs) and fibro (FN1/COL1A1^{high}) The CM1 group contained cells positive for alpha-actinin but was also distinguished from the CM2 group by the abundance of the genes DCC and FAM155A, which are involved in organogenesis/cardiomyocyte survival[47] and sodium leak channel[48]. Interestingly, even though we removed very large spheroids, the fibro group was more present in the PLN-R14del cells, indicating the increased fibroblast presence in the PLN-R14del spheroids despite the initial smaller size. When comparing GO-term pathway analysis, and the top 20 genes and genesets, we observed significant differences in pathways that were previously described in the PLN-R14del pathophysiology and pathology. The mitochondrial genes FHL2 and TMEM71 were downregulated, which were also previously described to be downregulated in hypertrophic cardiomyocytes.[49,50] In the top 20 genesets, triglyceride metabolism and cholesterol biosynthesis were found to be significantly expressed in PLN-R14del compared to the control. Both triglycerides and cholesterol have been found to accumulate in lipid droplets.[51] Lipid droplets have been observed in the PLN-R14del spheroids (**Figure 4E**), showcasing the detrimental outcome of mitochondrial dysfunction in the PLN-R14del disease. The impairment of the ER/mitochondria compartment and fatty acid oxidation has been previously described[14,15], which was confirmed in PLN-R14del cardiac spheroids. The top differentially expressed gene we found is Ubiquitin C (UBC), a polyubiquitin precursor activated by proteotoxic stress to degrade misfolded proteins. Other highly expressed genes include HSP90B1 and HSPA5, both members of the UPR. The geneset 'aggrephagy' was also significantly increased in the PLN-R14del CMs from the cardiac spheroids and was confirmed by the presence of autophagy protein LC3. The activation of the UPR has also previously been observed as the top significant pathway in day 42-old 2D hiPSC-CMs by single-cell sequencing.[13] Our model revealed both lipid droplets and additonally PLN accumulation, which has not been observed *in vitro* before. Hence, the mechanism connecting impaired lipid droplet biogenesis to UPR activation remains unclear. Recent findings indicate that the UPR can be directly activated by altering the lipid composition of the ER.[52] In contrast,

the highly upregulated UPR pathway in 21-day-old hCSs and aggregates could indicate that the elevated UPR could trigger the accumulation of lipid droplets. For example, activating the UPR branch ATF6 is known to down-regulate PPARα causing a reduction in β-oxidation and an accumulation of lipid droplets in mice.[53] Similar to ATF6, sterol regulatory element-binding proteins (SREBPs) are ER-resident proteins possessing transcription factor activity to activate a large number of genes involved in the synthesis of FA derivatives and cholesterol. The reactome of 'gene expression by SREBP is significantly upregulated in the PLN-R14del CMs geneset analysis. Additionally, autophagy leads to the release of lipids from protein breakdown, of which a portion of autophagy-released lipids is immediately re-esterified to form triacylglycerol. This process is under the control of the master growth regulator, mTOR complex 1 (mTORC1)[54], which is also significantly upregulated in the PLN-R14del CMs geneset. Contractility-associated genes that were affected by the PLN-R14del included sarcomere kinases and regulators TNNI3K, RBM20, and SPHKAP. TNNI3K has been described in atrial tachyarrhythmia and dilated cardiomyopathy[55], the loss of RBM20 causes an abnormal intracellular Ca^{2+} handling, and arrhythmias[56] and SPHKAP is a membrane-anchoring protein in the Z-bodies associated with heart failure[57]. Three of the top twenty genesets involved in cardiac contractility; myogenesis, muscle contraction, and HCM, were significantly downregulated in PLN-R14del CMs. We and others have shown a significant decrease in contractile force in EHTs.[13,14] We have not analyzed contraction in our cardiac spheroids, although this model could improve high-throughput analysis of contractile parameters.

In addition to the reduced Ca^{2+} handling and known PLN-R14del pathological metabolic and UPR expression patterns, we observed a striking 2.4-fold increase in PLN-R14del hCS size after 21 days of 3D culturing (**Figure 2**). This observed size increase was not related to the initial cell number, size, or purity of the CMs. Previously, a 3-fold size increase has been observed in vascularized cardiac spheroid after the addition of doxorubicin, a known inducer of myocardial fibrosis.[58] We did observe increased expression of the proliferation marker ki67, collagen production, and in multiple genes such as α-SMA (ACTA2), and EIF3A, in PLN-R14del CMs of hCSs. EIF3A and ITGB3 are involved in fibrosis through via regulation of the TGF-b1/SMAD3 signaling pathway.[59,60] Cardiac fibroblasts and the differentiation to myofibroblasts underlie the development of pathological cardiac fibrosis, leading to arrhythmias and heart failure. Matured myofibroblasts are characterised by increased α-smooth muscle actin (α-SMA) fiber expression, secretion of collagens, and changes in proliferation.[61,62] Additionally, a controlled addition of hiPSC-CFs and hiPSC-CMs, creating various cell ratios, did not induce the hCSs size increase (**Figure 3**). Interestingly, the addition of >50% hiPSC-CM derived from a PLN-R14del background initiated this massive increase in size, suggesting that this phenotype is linked to the CM PLN-R14del mutation. Importantly, the significant upregulation of all fibroblast genes is accompanied by the decrease of cardiomyocyte-specific genes. This confirms the reduced cells positive for the sarcomeric protein alpha-actinin that we observed by the immunofluorescent imaging. Currently, the underlying molecular mechanisms of cardiomyocytes causing fibroblast activation

remain unknown. The PLN-R14del cardiomyopathy has been described to cause severe fibrosis in post-mortem histology samples of both humans[11] and mice[63]. In PLN-R14del carriers, a distinct fibrotic pattern in the subepicardial layer of the LV posterolateral wall was observed before a decrease in LV systolic function was observed.[64] This suggests that fibrosis is an early feature of PLN-R14del cardiomyopathy. Moreover, recent data show that total collagen turnover correlates weakly to moderately with clinical parameters in PLN-R14del patients.[5] In homozygous R14del/R14del mice, extensive myocardial fibrosis was observed throughout the left and right ventricles, and fibrotic genes were elevated in 8-week-old mice, whereas 3-week-old mice did not show any signs of fibrosis.[63] At the same time, these mice presented PLN aggregation, similar to human patients. Consistently, heterozygous WT/R14del mice did not reveal fibrosis or PLN aggregation until 18 months of age, but both pathological phenotypes co-existed at the same time, suggesting a link between the PLN aggregation and fibrotic response of the heart. Interestingly, we showed for the first time, PLN aggregation in an *in vitro* system (**Figure 4E**). Both findings in humans and mice harboring the PLN-R14del mutation could suggest that in fact, the fibrosis is linked to increased mechanical and molecular stress, consistent with the presence of PLN aggregates and an elevated UPR. However, in other mutations of the PLN gene (R9C, R9L, R9H, Leu-39stop, and R25C) no PLN aggregation was described, instead only abnormal Ca^{2+} cycling before the onset of overt cardiac remodeling, which leads to heart failure in human carriers.[65–67]

Next to the elevated UPR, the underlying molecular mechanisms of cardiomyocytes causing fibroblast activation could be caused by the mechanical remodelling of the cells. In patients, the inferolateral wall is more vulnerable due to regional molecular changes caused by the mutation or the regional susceptibility which could result from exposure to higher mechanical stress.[10] The disruption in mechanical junctions like desmosomes and gap junctions have been described to increase cardiac fibrosis and arrhythmias.[68] RT-qPCR revealed a significant decrease in the desmosomal gene PKP2 and gap-junction Cx43, and the geneset analysis revealed a downregulation of the cell-cell adhesion pathway in the PLN-R14del CMs. This suggests the possibility that loss of these interactions may play a contributory role in the activation of fibroblasts and the onset of the PLN-R14del disease.

Given the multifactorial etiology of 'PLN-myopathies', it is unclear whether reduced Ca^{2+} uptake by SERCA, secondary to the disturbed PKA-mediated phosphorylation of PLN may represent a 'final molecular stress pathway' underlying the disease onset in PLN-R14del patients. Since we found the first Ca^{2+} abnormalities in PLN-R14del hCSs after 7 days, the massive increase in spheroid size could indicate a possible secondary response of replacement fibrosis due to Ca^{2+} handling dysfunction. Still, how PLN mutations affect cardiac contractility and if the Ca^{2+} handling is linked to fibroblast activation has not been extensively studied in human *in vitro* models. In pre-DCM hearts of PLN-R9 mutation mice, contractile performance was normal, yet an increased proliferation of non-myocytes, early fibroblast activation, and an altered metabolic gene expression in CMs were detected.[69] The mechanism by which

the latter is regulated by PLN is not certain, but it could be related to paracrine signaling to nonmyocytes such as fibroblasts, possibly via cardiomyocyte-specific expression of cytokine (as reviewed elsewhere).[70] Moreover, profibrotic factors could modulate the endoplasmic reticulum Ca^{2+} release and Ca^{2+} influx into fibroblasts, which could result in an increased cytosolic Ca^{2+} concentration, thereby initiating fibrosis-promoting proliferation/differentiation of fibroblasts.[71] In a disease state, CFs undergo activation to a myofibroblast phenotype, characterized by increased proliferation, ECM production, and decreased contractility.[72] Interestingly, geneset enrichment analysis revealed the top 1 and 4 elevated genesets to be Netrin-1 signalling. Netrin-1 is a laminin-like protein, which is involved in embryonic development and is upregulated in cancer-associated fibroblasts.[38] Despite the role of Netrin-1 in the heart has not been fully elucidated, this protein is highly expressed in muscle tissue.[73] A study in neonatal rat cardiomyocytes revealed that the downregulation of Netrin-1 was found to significantly alleviate the degrees of myocardial hypertrophy, fibrosis, apoptosis, and heart failure.[74,75] Future studies are required to investigate the role of netrin-1 in the PLN-R14del cardiomyopathy. Transient receptor potential (TRP) channels play an important role in the differentiation of fibroblasts to myofibroblasts, ECM remodelling, and the fibrogenesis cascade and have emerged as the most important ion channels that mediate Ca^{2+} signals in cardiac fibroblasts.[76–78] TRP mechanosensitive Ca^{2+}-permeable channels 3 and 4 (TRPM3/4) were significantly upregulated in PLN-R14del hCSs, hinting towards a potential role of TRP in the onset of fibroblast activation in PLN-R14del CMs.

Further unbiased and spatiotemporal RNA sequencing and proteomics attempts could identify key regulators of cytosolic Ca^{2+} overload-mediated cardiac dysfunction, fibroblast activation, and fibrogenesis. It would be of great interest to further study all of the disease-specific traits of the PLN-R14del disease in an earlier stage versus the disease state. Knowing when and why these pathophysiological traits derail would be the key to unravelling the optimal time window and most suitable therapeutic intervention. Our hCSs model largely mimics the cardiomyopathy characteristics seen in the PLN-R14del disease: mitochondrial dysfunction, UPR activation, PLN aggregation, reduced contractility, and impaired Ca^{2+} handling, which therefore could be used as a high-throughput screening tool to identify novel therapeutic targets. Additionally, our hCSs model showed the important role of activated CFs in PLN-R14del, indicating the importance of fibrosis for the pathogenesis of ACM/DCM and potential therapeutic interventions. Importantly, the identification of clinically relevant fibroblast activation may inform us of disease pathology and hint at other potential therapeutic opportunities.

In the last years, three clinical trials using AAV-mediated gene replacement have been designed targeting heart failure (reviewed elsewhere[79]). We note that to date, only a fairly limited number of reports have employed organoids to study AAV gene therapy (summarized here[80]). In this study, we show, for the first time, the feasibility of using a cardiac spheroids platform to test AAV-delivered gene augmentation as a therapeutic strategy for genetic

cardiomyopathies. Previous studies have demonstrated that the administration of a constitutively active I-1c delivered by this cardiotropic AAV2i8 (BNP116) virus in ischaemic-induced heart failure pigs improved LV cardiac function with an EF of 5.7%.20 Additionally, investigators reported that the delivery of I-1c was safe in three non-ischemic cardiomyopathy patients who exhibited LVEF improvements of 10.5%, 22%, and 6%, respectively, at 12 months of follow-up.[81] We observed that a single dose of AAV.I-1c was sufficient to rescue PLN-R14del spheroids size, Ca^{2+} function, EHT contractility, and cardiac expression patterns (**Figure 6**). It is important to note that contractile function is strongly decreased in PLN-R14del myocytes and EHT constructs.[13,14] Additionally, we observed an overall increase in all Ca^{2+} handling parameters after a single dose of AAV.I-1c treatment (**Figure 7**). However, we observed a prolonged decay time and CTD90 compared to non-transduced spheroids, indicating a decreased SR Ca^{2+} uptake. The increase in decay time might be caused by the overall increased total amount of Ca^{2+} as indicated by the increase in peak value. Additionally, we observed a 3 to 5-fold increase in SERCA2A expression compared to non-transduced control and PLN-R14del hCSs respectively. Increased I-1c levels suppress SR-associated PP1 activity, thereby increasing SERCA2a activity, and PLN phosphorylation at both Ser16 and Thr17 and enhancing contractility both basally and after β-adrenergic stimulation.[82] Indeed, the upregulation of I-1c increases SERCA2A activation and Ca^{2+} transient amplitude, possibly decreasing PP-1 activity and improving phospholamban phosphorylation. Lastly, I-1c gene augmentation has a positive effect on mRNA levels of proteins associated with fibrosis and Ca^{2+} handling function (**Supplementary Figure 7**). For instance, COL1A1 and FN1, which are known to be higher in activated myofobroblasts[83], were significantly reduced after 14 days of AAV.I-1c therapy. AAV.I-1c increased mRNA levels of Ca^{2+} handling proteins, confirming the observed improvement in cardiac function. While the restoration of the hCSs size, gene expression, contractility, and Ca^{2+} handling was evident in our study, further studies are required to define the link between the fibroblast activation, cardiomyocyte function, and the protective role of AAV.I-1c we observed. Our work on AAV2i8-based gene augmentation with the constitutively active I-1c complements animal studies with a human-specific system and evaluates the rescue of PLN-R14del phenotype, which may constitute a therapeutic strategy in failing hearts. We are aware that additional systematic testing of different AAV-mediated strategies such as WT PLN overexpression might lead to a more direct improvement, as previously demonstrated by AAV6-mediated overexpression of PLN, which induced downregulation of endogenous PLN-R14del transcripts and sufficient to improve CM function.[16] Nevertheless, this is the first proof of concept of AAV-mediated gene augmentation in cardiac spheroids.

Based on our results, we hypothesize the potential pathological mechanism underlying the PLN-R14del cardiomyopathy to be the toxic cytosolic Ca^{2+} overload due to the reduced Ca^{2+} handling and protein misfolding by PLN-R14del. Multiple pathological pathways emerge, from UPR activation, metabolic dysfunction, and reduced contractility to the activation of myofibroblasts (**Figure 8**).

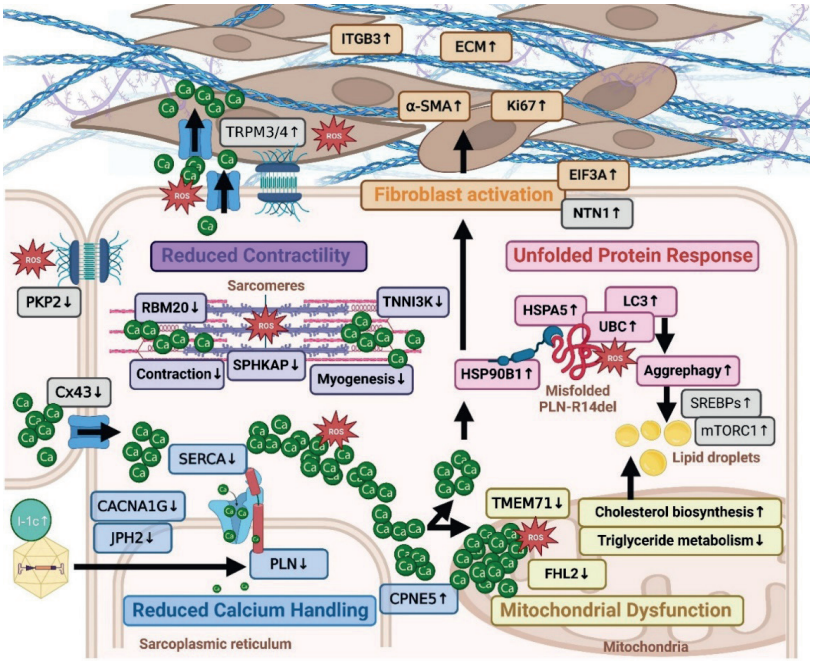

Figure 8. The schematic hypothesis of the PLN-R14del-mediated pathological mechanisms in the PLN-R14del cardiomyopathy. Purple; reduced contractility by potential Ca^{2+} overload and the observed downregulation of RNA-binding motif protein 20 (RBM20), cardiac troponin I-interacting kinase (TNNI3K), SPHK1 Interactor, AKAP Domain Containing (SPHKAP) and genesets muscle contraction and myogenesis. **Red**; Activation of the unfolded protein response pathway by misfolded PLN-R14del proteins and activation of (HSP90B1), (HSPA5), (UBC), (LC3), and the aggrephagy geneset. Upregulation of autophagy relates genes Sterol regulatory element-binding proteins (SREPBs) and Mechanistic target of rapamycin complex 1 (mTORC1) could also influence the lipid accumulation in PLN-R14del CMs. **Yellow**; Mitochondrial dysfunction by potential Ca^{2+} overload and downregulation of the mitochondrial genes Four And A Half LIM Domains 2 (FHL2) and Transmembrane Protein 71 (TMEM71). Geneset downregulation of triglyceride metabolism and upregulation of cholesterol biosynthesis could also increase lipid droplet accumulation due to reduced fatty acid metabolism. **Blue**; Reduced Ca^{2+} handling by PLN-R14del malfunction and reduced expression of Ca^{2+} channel/binding proteins sarcoplasmic/endoplasmic reticulum Ca-ATPase (SERCA), Connexin 43 (Cx43), Ca^{2+} Voltage-Gated Channel Subunit Alpha1 G (CACNA1G), Junctophilin 2 (JPH2) and Copine 5 (CPNE5), potentially leading to a toxic cytosolic Ca^{2+} overload. The AAV.I-1c therapy suppresses SR-associated PP1 activity, thereby increasing SERCA2a activity, and PLN phosphorylation, thereby enhancing Ca^{2+} handling and contractility. **Orange**; fibroblast activation by potential Ca^{2+} overload or increased mechanical stress by the upregulation of transient receptor potential Ca^{2+}-permeable channels 3 and 4 (TRPM3/4) and downregulation of desmosomal gene Plakophilin 2 (PKP2). Laminin-like protein Netrin 1 (NTN1) and transcription factor Eukaryotic Translation Initiation Factor 3 Subunit A (EIF3A) could also play a role in the activation of fibroblasts. After fibroblast activation, fibroblast proliferation is increased as indicated by proliferation marker ki67 and the mature myofibroblasts express excessive extracellular matrix (ECM), ECM receptor Integrin Subunit Beta 3 (ITGB3), and α-smooth muscle actin (-SMA) stress fibers. Abbreviations: Ca^{2+}; Calcium, I-1c; Inhibitor-1, ROS; Reactive Oxygen Species,. The illustration is created with Biorender.com.

In conclusion, the generation of patient-derived spheroids is simple, scalable, and rapid, and works robustly for a range of different pluripotent stem cell lines of both HF patients, isogenic controls, and healthy individuals. Cardiac spheroids represent a new preclinical model that mimics the sophisticated spatiotemporal processes of the PLN-R14del disease. Here, our findings support that this experimental approach can be broadly used to identify additional processes that contribute to pathogenic mutations in genetic cardiomyopathies and demonstrate the feasibility of using AAV-delivered I-1c as a promising therapeutic option that may represent a potential antiarrhythmic concept in cardiomyopathy patients. The evaluation of the efficacy of therapeutic options in a 3D model, such as hCSs, represents an intermediate step toward clinical application for these patients. Still, further studies with a large animal model harboring the PLN-R14del cardiomyopathy are required to test AAV doses and delivery before going to the first-in patient.

STUDY LIMITATIONS

HiPSC-CM presents a readily available human cardiomyocyte model that can be generated on demand in large quantities, making it a promising model for investigating electrophysiological abnormalities in patients with inherited cardiac arrhythmias. However, our data showed that the hCSs decreased in their Ca^{2+} handling and beating rate after 6 weeks of culturing (**Supplementary Figure 2**). This observation is in line with another study describing an apoptotic response in CM-only spheroids cultured for 8 weeks. Interestingly, spheroids generated from all four cardiac-cell types, in the ratio of CMs, Ecs, SMCs, and CFs (4:2:1:1) remained viable throughout the culture period, by presumably following the distribution trends found in human myocardium.[69] Recently, several studies have investigated the role of a controlled combination of hiPSC-CMs, cardiac fibroblasts, and cardiac endothelial cells, which showed enhanced maturation and allowed the disease modeling of ACM and strikingly recapitulated features of the disease, indicating a multicell-type cause of genetic cardiomyopathies.[19,70] This finding suggests the importance of physiological ratios of all cell types of the heart, to study the full cell-cell communication *in vitro* and could be also of value in this model. Another explanation for the reduced Ca^{2+} handling and beating rate after 6 weeks of culturing is an edge effect, which we observed possibly due to the evaporation of the cell culture medium, which plays a critical role in multi-well-based cellular assays because it can deteriorate assay performance compared to 6-wells cultured hCSs (data not shown). Another limitation of the model is that not every aspect of the disease mechanism can be mimicked with the current spheroid model (e.g., using immature hiPSC-CMs, contractile force, and the lack of inflammatory cells). Additionally, the mechanisms underlying the decreased Ca^{2+} handling are beyond the scope of the present study. Nevertheless, altered mRNA expression of the underlying Ca^{2+} regulators SERCA2A and PLN renders intrinsic differences of its expression levels between PLN-R14del and healthy control hCSs likely. Further analysis

of the specific Ca^{2+} regulation and PLN function is required, which is thought to be mainly due to the reduced PKA-dependent phosphorylation on Serine 16.

Although the single-cell sequencing technique used in this study was effective in determining the pathological pathway patterns and gene expression profiles, the challenges that arose were severalfold. First, the dissociation of the spheroids before fixation could be optimized, thereby avoiding sequencing bias of non-CMs due to CM damage and loss during the dissociation. Secondly, the cell type identification was challenging since the cardiac spheroids were generated solely from hiPSC-CM differentiations. Further cell-type analyses of cardiac spheroids would establish a better understanding of cellular complexity. Lastly, by using specific primer labeling with this SPLiT-sequencing technique, allelic expression per cell could be studied. This experiment could provide insights into each cardiomyocyte's allelic imbalance and genetic makeup harboring the PLN-R14del mutation. Additionally, RNA sequencing on multiple spheroid ages could identify the spatiotemporal processes to identify mechanistic insights in the 'first to fail' mechanism of the PLN-R14del cardiomyopathy.

The AAV therapy described in this study is hopeful, but further analysis of the transduction efficiency of this AAV.I-1c *in vitro* and in vivo needs to be performed using immunofluorescent label detection. Additionally, future studies focussing on the effect in comparison to the modulation of PLN activity are required. For example, AAV-mediated Cas9-mediated exon excision in Duchenne muscular dystrophy can correct up to 7% of the genome, which was sufficient to avoid fibrosis of the left ventricle in a large animal model.[84] Another study showed that the MYBPC3 gene replacement strategy circumvents haploinsufficiency of cMyBP-C (restoration of a correct amount of protein) and reduces CM hypertrophy.[85] In this study, collagens (COL1A1 and COL3A1), and fibronectin (FN1) were significantly reduced and Ca^{2+} handling genes were upregulated after the MYBPC3 gene transfer, indicating that PLN gene transfer might efficiently eliminate the PLN disease phenotype. However, in one of the largest AAV clinical trials (CUPID2), the AAV-mediated upregulation of SERCA2A resulted in no safety issues or adverse effects, but the low-dose delivery of SERCA2A by AAV1 did not improve symptoms of heart failure in patients.[86] In contrast, much higher levels of viral transgene DNA (range 8000–42,000 ssDNA copy number/µg DNA) were used in preclinical small and large animal models of HF where SERCA2A was tested. Therefore, the gene delivery, toxicity, and clinical impact need to be identified and addressed and aid the design of future trials in this field.

AUTHOR CONTRIBUTIONS

Manuscript writing; R.G.C.M. Collection of data; R.G.C.M, F.v.D and T.B. Analysis of data: R.G.C.M, T.B. Supervision and manuscript editing; J.P.G.S, P.A.D, J.C, F.S, R.H., and J.W.B. All authors have read and agreed to this thesis version of the manuscript.

ACKNOWLEDGMENTS

We thank Vala Sciences directors Jeffrey H. Price and Patrick M. McDonough for the Cyteseer Software package to analyze the Ca^{2+} transients in the hCSs. We thank Prof. Joseph C. Wu from Stanford University for providing the control line 273iCTR. We thank Prof. Mark Mercola from Stanford University for providing the isogenic control line C31iCTR and the PLN-R14del patient line D4iR14del. We thank Stef Houweling for the Ca^{2+} handling screenings, and Christian Snijders Blok for the flow cytometry analysis. We thank the PLN foundation for providing the proband control line 1CiCTR and the PLN-R14del patient lines; 6BiR14del and 10BiR14del

FUNDING

R.G.C.M is supported by the PLN Foundation and the grant HARVEY (18747 NWO-OTP). P.A.D. is supported by CUREPLaN Leducq. J.P.G.S. is supported by H2020-EVICARE (#725229) of the European Research Council (ERC). P.A.D and J.P.G.S are supported by ZonMW Psider-Heart and HARVEY (18747 NWO-OTP). J.W.B. is supported by a Dekker grant from the Dutch Heart Foundation (03-003-2021-T025), Netherlands Heart Institute Fellowship, and CVON-Dosis young talent grant; Netherlands Heart Foundation (CVON-Dosis 2014–40).

CONFLICTS OF INTEREST

The authors declare that there is no conflict of interest regarding the publication of this paper.

REFERENCES

1. van der Zwaag, P. A. *et al.* Phospholamban R14del mutation in patients diagnosed with dilated cardiomyopathy or arrhythmogenic right ventricular cardiomyopathy: evidence supporting the concept of arrhythmogenic cardiomyopathy. *Eur. J. Heart Fail.* **14**, 1199–1207 (2012).
2. MacLennan, D. H. & Kranias, E. G. Phospholamban: a crucial regulator of cardiac contractility. *Nat. Rev. Mol. Cell Biol.* **4**, 566–577 (2003).
3. Dridi, H. *et al.* Intracellular calcium leak in heart failure and atrial fibrillation: a unifying mechanism and therapeutic target. *Nat. Rev. Cardiol.* **17**, 732–747 (2020).
4. Bers, D. M. & Bridge, J. H. Relaxation of rabbit ventricular muscle by Na-Ca exchange and sarcoplasmic reticulum calcium pump. Ryanodine and voltage sensitivity. *Circ. Res.* **65**, 334–342 (1989).
5. van der Voorn, S. M. *et al.* Exploring the Correlation Between Fibrosis Biomarkers and Clinical Disease Severity in PLN p.Arg14del Patients. *Front Cardiovasc Med* **8**, 802998 (2021).
6. Regnier, M. & Childers, M. *Familial Cardiomyopathies: Methods and Protocols*. (Springer Nature, 2023).
7. Verstraelen, T. E. *et al.* Prediction of ventricular arrhythmia in phospholamban p.Arg14del mutation carriers-reaching the frontiers of individual risk prediction. *Eur. Heart J.* **42**, (2021).
8. Maione, A. S. *et al.* Fibrosis in Arrhythmogenic Cardiomyopathy: The Phantom Thread in the Fibro-Adipose Tissue. *Front. Physiol.* **11**, 279 (2020).
9. Haghighi, K. *et al.* A mutation in the human phospholamban gene, deleting arginine 14, results in lethal, hereditary cardiomyopathy. *Proc. Natl. Acad. Sci. U. S. A.* **103**, (2006).
10. Te Rijdt, W. P. *et al.* Phospholamban p.Arg14del cardiomyopathy is characterized by phospholamban aggregates, aggresomes, and autophagic degradation. *Histopathology* **69**, 542–550 (2016).
11. Sepehrkhouy, S. *et al.* Distinct fibrosis pattern in desmosomal and phospholamban mutation carriers in hereditary cardiomyopathies. *Heart Rhythm* **14**, (2017).
12. Eijgenraam, T. R. *et al.* Protein Aggregation Is an Early Manifestation of Phospholamban p.(Arg14del)-Related Cardiomyopathy: Development of PLN-R14del-Related Cardiomyopathy. *Circ. Heart Fail.* **14**, e008532 (2021).
13. Feyen, D. A. M. *et al.* Unfolded Protein Response as a Compensatory Mechanism and Potential Therapeutic Target in PLN R14del Cardiomyopathy. *Circulation* **144**, 382–392 (2021).
14. Cuello, F. *et al.* Impairment of the ER/mitochondria compartment in human cardiomyocytes with PLN p.Arg14del mutation. *EMBO Mol. Med.* **13**, e13074 (2021).
15. Harakalova, M. *et al.* Transcriptional regulation profiling reveals PPARA-mediated fatty acid oxidation as a novel therapeutic target in phospholamban R14del cardiomyopathy. (2022) doi:10.21203/rs.3.rs-1902254/v1.
16. Karakikes, I. *et al.* Correction of human phospholamban R14del mutation associated with cardiomyopathy using targeted nucleases and combination therapy. *Nat. Commun.* **6**, 6955 (2015).
17. Yan, Y. *et al.* Cell population balance of cardiovascular spheroids derived from human induced pluripotent stem cells. *Sci. Rep.* **9**, (2019).
18. Scalise, M. *et al.* From Spheroids to Organoids: The Next Generation of Model Systems of Human Cardiac Regeneration in a Dish. *Int. J. Mol. Sci.* **22**, (2021).
19. Giacomelli, E. *et al.* Human-iPSC-Derived Cardiac Stromal Cells Enhance Maturation in 3D Cardiac Microtissues and Reveal Non-cardiomyocyte Contributions to Heart Disease. *Cell Stem Cell* **26**, (2020).
20. Lee, C. *et al.* Generation of three iPSC lines from dilated cardiomyopathy patients carrying a pathogenic LMNA variant. *Stem Cell Res.* **59**, 102638 (2022).
21. Lian, X. *et al.* Robust cardiomyocyte differentiation from human pluripotent stem cells via temporal modulation of canonical Wnt signaling. *Proc. Natl. Acad. Sci. U. S. A.* **109**, (2012).
22. Zhang, J. *et al.* Functional cardiac fibroblasts derived from human pluripotent stem cells via second heart field progenitors. *Nat. Commun.* **10**, 2238 (2019).
23. Maas, R. G. C. *et al.* Generation, High-Throughput Screening, and Biobanking of Human-Induced Pluripotent Stem Cell-Derived Cardiac Spheroids. *J. Vis. Exp.* (2023) doi:10.3791/64365.
24. Feyen, D. A. M. *et al.* Metabolic Maturation Media Improve Physiological Function of Human iPSC-Derived Cardiomyocytes. *Cell Rep.* **32**, 107925 (2020).

25. Grancharova, T. *et al.* A comprehensive analysis of gene expression changes in a high replicate and open-source dataset of differentiating hiPSC-derived cardiomyocytes. *Sci. Rep.* **11**, (2021).

26. Korsunsky, I. *et al.* Fast, sensitive and accurate integration of single-cell data with Harmony. *Nat. Methods* **16**, 1289–1296 (2019).

27. Robinson, M. D., McCarthy, D. J. & Smyth, G. K. edgeR: a Bioconductor package for differential expression analysis of digital gene expression data. *Bioinformatics* **26**, 139–140 (2010).

28. Soneson, C. & Robinson, M. D. Bias, robustness and scalability in single-cell differential expression analysis. *Nat. Methods* **15**, 255–261 (2018).

29. Alexandra Ward, M. A. Novel Gene Therapy for Heart Failure Shows Initial Promise of Efficacy, Safety at 12 Months. *CGTlive™* https://www.cgtlive.com/view/novel-gene-therapy-heart-failure-shows-initial-promise-efficacy-safety-12-months (2022).

30. Katz, A. M., Tada, M. & Kirchberger, M. A. Control of calcium transport in the myocardium by the cyclic AMP-Protein kinase system. *Adv. Cyclic Nucleotide Res.* **5**, 453–472 (1975).

31. McKeithan, W. L. *et al.* Reengineering an Antiarrhythmic Drug Using Patient hiPSC Cardiomyocytes to Improve Therapeutic Potential and Reduce Toxicity. *Cell Stem Cell* **27**, 813–821.e6 (2020).

32. van Ineveld, R. L., Ariese, H. C. R., Wehrens, E. J., Dekkers, J. F. & Rios, A. C. Single-Cell Resolution Three-Dimensional Imaging of Intact Organoids. *J. Vis. Exp.* (2020) doi:10.3791/60709.

33. Chomczynski, P. & Sacchi, N. Single-step method of RNA isolation by acid guanidinium thiocyanate-phenol-chloroform extraction. *Anal. Biochem.* **162**, 156–159 (1987).

34. Hansen, A. *et al.* Development of a Drug Screening Platform Based on Engineered Heart Tissue. *Circ. Res.* (2010) doi:10.1161/CIRCRESAHA.109.211458.

35. Buikema, J. W. *et al.* Wnt Activation and Reduced Cell-Cell Contact Synergistically Induce Massive Expansion of Functional Human iPSC-derived Cardiomyocytes. *Cell Stem Cell* **27**, 50 (2020).

36. Maas, R. G. C. *et al.* Massive expansion and cryopreservation of functional human induced pluripotent stem cell-derived cardiomyocytes. *STAR protocols* **2**, (2021).

37. Badone, B. *et al.* Characterization of the PLN p.Arg14del Mutation in Human Induced Pluripotent Stem Cell-Derived Cardiomyocytes. *Int. J. Mol. Sci.* **22**, (2021).

38. Sung, P. J. *et al.* Cancer-Associated Fibroblasts Produce Netrin-1 to Control Cancer Cell Plasticity. *Cancer Res.* **79**, (2019).

39. Niewiadomski, P. *et al.* Gli Proteins: Regulation in Development and Cancer. *Cells* **8**, (2019).

40. Nicolaou, P., Hajjar, R. J. & Kranias, E. G. Role of protein phosphatase-1 inhibitor-1 in cardiac physiology and pathophysiology. *J. Mol. Cell. Cardiol.* **47**, 365–371 (2009).

41. Nicolaou, P. *et al.* Inducible expression of active protein phosphatase-1 inhibitor-1 enhances basal cardiac function and protects against ischemia/reperfusion injury. *Circ. Res.* **104**, 1012–1020 (2009).

42. Ishikawa, K. *et al.* Cardiac I-1c overexpression with reengineered AAV improves cardiac function in swine ischemic heart failure. *Mol. Ther.* **22**, (2014).

43. Ishikawa, K., Weber, T. & Hajjar, R. J. Human Cardiac Gene Therapy. *Circ. Res.* **123**, (2018).

44. Mannhardt, I. *et al.* Human Engineered Heart Tissue: Analysis of Contractile Force. *Stem cell reports* **7**, (2016).

45. Tomsig, J. L. & Creutz, C. E. Copines: a ubiquitous family of Ca(2+)-dependent phospholipid-binding proteins. *Cell. Mol. Life Sci.* **59**, 1467–1477 (2002).

46. Stege, N. M. *et al.* DWORF Extends Life Span in a PLN-R14del Cardiomyopathy Mouse Model by Reducing Abnormal Sarcoplasmic Reticulum Clusters. *Circ. Res.* (2023) doi:10.1161/CIRCRESAHA.123.323304.

47. Ziegon, L. & Schlegel, M. Netrin-1: A Modulator of Macrophage Driven Acute and Chronic Inflammation. *Int. J. Mol. Sci.* **23**, (2021).

48. Kschonsak, M. *et al.* Structure of the human sodium leak channel NALCN. *Nature* **587**, (2020).

49. Friedrich, F. W. *et al.* FHL2 expression and variants in hypertrophic cardiomyopathy. *Basic Res. Cardiol.* **109**, 451 (2014).

50. Laggner, M. *et al.* EGR1 Is Implicated in Right Ventricular Cardiac Remodeling Associated with Pulmonary Hypertension. *Biology* **11**, (2022).

51. Olofsson, S. O. *et al.* Triglyceride containing lipid droplets and lipid droplet-associated proteins. *Curr. Opin. Lipidol.* **19**, (2008).

52. Volmer, R., van der Ploeg, K. & Ron, D. Membrane lipid saturation activates endoplasmic reticulum unfolded protein response transducers through their transmembrane domains. *Proc. Natl. Acad. Sci. U. S. A.* **110**, 4628–4633 (2013).

53. Jao, T.-M. *et al.* ATF6α downregulation of PPARα promotes lipotoxicity-induced tubulointerstitial fibrosis. *Kidney Int.* **95**, 577–589 (2019).

54. Zoncu, R. *et al.* mTORC1 senses lysosomal amino acids through an inside-out mechanism that requires the vacuolar H(+)-ATPase. *Science* **334**, 678–683 (2011).

55. Theis, J. L. *et al.* TNNI3K mutation in familial syndrome of conduction system disease, atrial tachyarrhythmia and dilated cardiomyopathy. *Hum. Mol. Genet.* **23**, 5793–5804 (2014).

56. Lennermann, D., Backs, J. & van den Hoogenhof, M. M. G. New Insights in RBM20 Cardiomyopathy. *Curr. Heart Fail. Rep.* **17**, 234–246 (2020).

57. Aye, T.-T. *et al.* Reorganized PKA-AKAP associations in the failing human heart. *J. Mol. Cell. Cardiol.* **52**, 511–518 (2012).

58. Figtree, G. A., Bubb, K. J., Tang, O., Kizana, E. & Gentile, C. Vascularized Cardiac Spheroids as Novel 3D in vitro Models to Study Cardiac Fibrosis. *Cells Tissues Organs* **204**, 191–198 (2017).

59. Li, B. *et al.* Knockdown of eIF3a ameliorates cardiac fibrosis by inhibiting the TGF-β1/Smad3 signaling pathway. *Cell. Mol. Biol.* **62**, 97–101 (2016).

60. Sarrazy, V. *et al.* Integrins αvβ5 and αvβ3 promote latent TGF-β1 activation by human cardiac fibroblast contraction. *Cardiovasc. Res.* **102**, 407–417 (2014).

61. Hinz, B., Dugina, V., Ballestrem, C., Wehrle-Haller, B. & Chaponnier, C. Alpha-smooth muscle actin is crucial for focal adhesion maturation in myofibroblasts. *Mol. Biol. Cell* **14**, 2508–2519 (2003).

62. Hall, C. *et al.* Chronic activation of human cardiac fibroblasts in vitro attenuates the reversibility of the myofibroblast phenotype. *Sci. Rep.* **13**, 12137 (2023).

63. Eijgenraam, T. R. *et al.* The phospholamban p.(Arg14del) pathogenic variant leads to cardiomyopathy with heart failure and is unreponsive to standard heart failure therapy. *Sci. Rep.* **10**, (2020).

64. Te Rijdt, W. P. *et al.* Distinct molecular signature of phospholamban p.Arg14del arrhythmogenic cardiomyopathy. *Cardiovasc. Pathol.* **40**, (2019).

65. Schmitt, J. P. *et al.* Dilated cardiomyopathy and heart failure caused by a mutation in phospholamban. *Science* **299**, (2003).

66. Medeiros, A. *et al.* Mutations in the human phospholamban gene in patients with heart failure. *Am. Heart J.* **162**, (2011).

67. Landstrom, A. P., Adekola, B. A., Bos, J. M., Ommen, S. R. & Ackerman, M. J. PLN-encoded phospholamban mutation in a large cohort of hypertrophic cardiomyopathy cases: summary of the literature and implications for genetic testing. *Am. Heart J.* **161**, (2011).

68. Pellman, J., Zhang, J. & Sheikh, F. Myocyte-fibroblast communication in cardiac fibrosis and arrhythmias: Mechanisms and model systems. *J. Mol. Cell. Cardiol.* **94**, 22–31 (2016).

69. Burke, M. A. *et al.* Molecular profiling of dilated cardiomyopathy that progresses to heart failure. *JCI insight* **1**, (2016).

70. Hall, C., Gehmlich, K., Denning, C. & Pavlovic, D. Complex Relationship Between Cardiac Fibroblasts and Cardiomyocytes in Health and Disease. *J. Am. Heart Assoc.* **10**, (2021).

71. Nattel, S. & Harada, M. Atrial remodeling and atrial fibrillation: recent advances and translational perspectives. *J. Am. Coll. Cardiol.* **63**, (2014).

72. MacLean, J. & Pasumarthi, K. B. Signaling mechanisms regulating fibroblast activation, phenoconversion and fibrosis in the heart. *Indian J. Biochem. Biophys.* **51**, (2014).

73. Tissue expression of NTN1 - Summary - The Human Protein Atlas. https://www.proteinatlas.org/ENSG00000065320-NTN1/tissue.

74. Wu, G. *et al.* Suppression of Netrin-1 attenuates angiotension II-induced cardiac remodeling through the PKC/MAPK signaling pathway. *Biomed. Pharmacother.* **130**, 110495 (2020).

75. Wang, N., Cao, Y. & Zhu, Y. Netrin-1 prevents the development of cardiac hypertrophy and heart failure. *Mol. Med. Rep.* **13**, 2175–2181 (2016).

76. Du, J. *et al.* TRPM7-mediated Ca2+ signals confer fibrogenesis in human atrial fibrillation. *Circ. Res.* **106**, 992–1003 (2010).

77. Adapala, R. K. *et al.* TRPV4 channels mediate cardiac fibroblast differentiation by integrating mechanical and soluble signals. *J. Mol. Cell. Cardiol.* **54**, 45–52 (2013).

78. Ji, C. & McCulloch, C. A. TRPV4 integrates matrix mechanosensing with Ca2+ signaling to regulate extracellular matrix remodeling. *FEBS J.* **288**, 5867–5887 (2021).

79. Korpela, H. *et al.* Gene therapy for ischaemic heart disease and heart failure. *J. Intern. Med.* **290**, 567–582 (2021).

80. Ramamurthy, R. M., Atala, A., Porada, C. D. & Almeida-Porada, G. Organoids and microphysiological systems: Promising models for accelerating AAV gene therapy studies. *Front. Immunol.* **13**, 1011143 (2022).

81. Surià Albà, R. American Society of Gene and Cell Therapy (ASGCT) - 25th Annual Meeting. Washington, D.C./ Virtual - May 16-19, 2022. *Drugs Future* (2022) doi:10.1358/dof.2022.47.8.3455366.

82. Kranias, E. G. & Hajjar, R. J. Modulation of cardiac contractility by the phospholamban/SERCA2a regulatome. *Circ. Res.* **110**, 1646–1660 (2012).

83. Herum, K. M. *et al.* Cardiac fibroblast sub-types reflect pathological cardiac remodeling. *Matrix Biol Plus* **15**, 100113 (2022).

84. Moretti, A. *et al.* Somatic gene editing ameliorates skeletal and cardiac muscle failure in pig and human models of Duchenne muscular dystrophy. *Nat. Med.* **26**, 207–214 (2020).

85. Prondzynski, M. *et al.* Evaluation of MYBPC3 trans-Splicing and Gene Replacement as Therapeutic Options in Human iPSC-Derived Cardiomyocytes. *Mol. Ther. Nucleic Acids* **7**, 475–486 (2017).

86. Lyon, A. R. *et al.* Investigation of the safety and feasibility of AAV1/SERCA2a gene transfer in patients with chronic heart failure supported with a left ventricular assist device - the SERCA-LVAD TRIAL. *Gene Ther.* **27**, (2020).

SUPPLEMENTARY FILES

Supplementary Table 1: Antibodies and qPCR Primer sequences used in this study.

Genes		***Sequence (5'-3')***	***Annealing Temperature (°C)***
CASQ2	Forward	CAAACTGGAAGTCCAAGCCTT	55,7 - 63
	Reverse	GGCTCATCCATAAATGGCTCAT	
ATP2A2	Forward	ACCCACATTCGAGTTGGAAG	57.1-65
	Reverse	CAGTGGGTTGTCATGAGTGG	
PLN	Forward	ACCTCACTCGCTCAGCTATAA	52.8-63.2
	Reverse	CATCACGATGATACAGATCAGCA	
MYH7	Forward	TCTTTCCCTGCTGCTCTC	52.8-63.2
	Reverse	GACTGCCATCTCCGAATC	
ACTN1	Forward	GACGAGAAGCTGGCTTGTATAG	60
	Reverse	CATAATACCTGAGCCTTGTCCC	
FN1	Forward	AGCAGACCCAGCTTAGAGTT	60
	Reverse	GCAGAAGTGTTTGGGTGACT	
TNNI3	Forward	CCAACTACCGCGCTTATGC	60
	Reverse	CTCGCTCCAGCTCTTGCTTT	
NPPA	Forward	CAACGCAGACCTGATGGATTT	60
	Reverse	AGCCCCCGCTTCTTCATTC	
Col1a1	Forward	CTGCTGGACGTCCTGGTGAA	60
	Reverse	ACGCTGTCCAGCAATACCTTGAG	
GJA1	Forward	TGGTAAGGTGAAAATGCGAGG	57.1-65
	Reverse	GCACTCAAGCTGAATCCATAGAT	
CASQ2	Forward	CAAACTGGAAGTCCAAGCCTT	55,7 - 63
	Reverse	GGCTCATCCATAAATGGCTCAT	
PKP2	Forward	GGTAGGAGAGGTTATGAAGAATGC	60
	Reverse	AAGCGATGAGAAGATGTGACG	
RPL32	Forward	AGGCATTGACAACAGGGTTC	60
	Reverse	GACGTTGTGGACCAGGAACT	
aSMA	Forward	ACTGAGCGTGGCTATTCCTCCGTT	58
	Reverse	GCAGTGGCCATCTCATTTTCA	
Ki67	Forward	GAAAGAGTGGCAACCTGCCTTC	60
	Reverse	GCACCAAGTTTTACTACATCTGCC	

Supplementary Table 2: Differentially expressed genes in CMs from PLN-R14del and CTL spheroids.

Gene	Abbreviation	Function	P Value	FDR	Phenotype Class
Polyubiquitin-C	UBC	Increases ubiquitin necessary to remove unfolded proteins	1.02E-21	1.06E-17	Unfolded Protein Response
Golgin subfamily A member 1	GOLGA1	Participates in glycosylation and transport of proteins/lipids	4.94E-20	2.55E-16	N/A
RNA, U4 Small Nuclear 2	RNU4-2	Affiliated with the snRNA class	1.87E-17	6.46E-14	N/A
Transmembrane Protein 71	TMEM71	Mitochondrial membrane protein involved in immune and inflammatory response, cell proliferation and cell migration	4.09E-14	1.06E-10	Mitochondrial function
Long Intergenic Non-Protein Coding RNA 1099	LINC01099	Affiliated with the lncRNA class	7.64E-14	1.58E-10	N/A
AC092957.1	AC092957.1	N/A	2.99E-13	5.16E-10	N/A
AFG3 Like Matrix AAA Peptidase Subunit 1, Pseudogene	AFG3L1P	Mitochondrial protein processing	2.14E-12	3.16E-09	Mitochondrial function
Heat Shock Protein 90 Beta Family Member 1	HSP90B1	Chaperone functions in folding stabilization	6.96E-12	8.99E-09	Unfolded Protein Response
Sphingosine Kinase Type 1-Interacting Protein	SPHKAP	Protein kinase A binding activity in Z disc	7.74E-11	8.88E-08	Contractility
Copine 5	CPNE5	Calcium-dependent membrane-binding protein	6.93E-10	7.17E-07	Calcium Handling
Integrin Subunit Beta 3	ITGB3	Cell adhesion as well as cell-surface mediated signalling	7.72E-10	7.25E-07	Fibrosis
Transmembrane Protein 132D	TMEM132D	Methylation during stress	8.87E-10	7.64E-07	Unfolded Protein Response
Isoprenylcysteine Carboxyl Methyltransferase	ICMT	Modifies isoprenylated C-terminal cysteine residues of proteins in ER	9.97E-10	7.93E-07	N/A
Thioredoxin Interacting Protein	TXNIP	Major regulator of cellular redox signaling which protects cells from oxidative stress	1.18E-09	8.68E-07	Unfolded Protein Response
Mitochondrially Encoded Cytochrome C Oxidase III	MT-CO3	Enable electron transfer activity and oxidoreduction-driven active transmembrane transporter activity in mitochondria	1.77E-09	1.22E-06	Mitochondrial function
SWI/SNF Related, Matrix Associated, Actin Dependent Regulator Of Chromatin, Subfamily D, Member 3	SMARCD3	Member of the SWI/SNF family of proteins, display helicase and ATPase activities and regulates transcription of certain genes by altering the chromatin structure around those genes.	2.29E-09	1.48E-06	N/A
Arginine And Glutamate Rich 1	ARGLU1	Enables cadherin binding activity	4.79E-09	2.91E-06	N/A

Gene	Abbreviation	Function	P Value	FDR	Phenotype Class
Homeobox A3	HOXA3	Encodes for a DNA-binding transcription factor, regulating gene expression, morphogenesis, and differentiation	5.6E-09	3.21E-06	N/A
Plexin A4	PLXNA4	Regulates cell migration, mediator of amyloid-β/tau pathology.	7.15E-09	3.89E-06	Unfolded Protein Response
Calcium Voltage-Gated Channel Subunit Alpha1 G	CACNA1G	Encodes a T-type, low-voltage activated calcium channel	9.09E-09	4.7E-06	Calcium Handling

Supplementary Table 3: Differential expressed gene modules in CMs from PLN-R14del and CTL spheroids.

Module name	Up /down	Description of module	P-value	FDR	Phenotype Class
REACTOME_NETRIN_1_SIGNALING	Up	Netrin-1 signaling	0.0002	0.17976	N/A
REACTOME_GLI_PROTEINS_BIND_PROMOTERS_OF_HH_RESPONSIVE_GENES_TO_PROMOTE_TRANSCRIPTION	Up	GLI proteins bind promoters of Hh responsive genes to promote transcription	0.0002	0.17976	N/A
HALLMARK_MYOGENESIS	Down	Development of skeletal muscle (myogenesis)	0.0008	0.34865	Contractility
REACTOME_NETRIN_MEDIATED_REPULSION_SIGNALS	Up	Netrin mediated repulsion signals	0.0010	0.34865	N/A
REACTOME_LAMININ_INTERACTIONS	Down	Laminin interactions	0.0011	0.34865	Fibrosis
KEGG_ANTIGEN_PROCESSING_AND_PRESENTATION	Up	Antigen processing and presentation	0.0012	0.34865	N/A
REACTOME_STRIATED_MUSCLE_CONTRACTION	Down	Striated Muscle Contraction	0.0015	0.38054	Contractility
REACTOME_SCAVENGING_BY_CLASS_F_RECEPTORS	Up	Scavenging by Class F Receptors	0.0020	0.38876	N/A
REACTOME_IMMUNOREGULATORY_INTERACTIONS_BETWEEN_A_LYMPHOID_AND_A_NON_LYMPHOID_CELL	Up	Immunoregulatory interactions between Lymphoid - non-Lymphoid	0.0020	0.38876	N/A
REACTOME_IRAK1_RECRUITS_IKK_COMPLEX	Up	DIRAK1 recruits IKK complex	0.0026	0.45041	N/A
REACTOME_LIGAND_RECEPTOR_INTERACTIONS	Up	Ligand-receptor interactions	0.0034	0.50318	N/A
KEGG_HYPERTROPHIC_CARDIOMYOPATHY_HCM	Down	Hypertrophic cardiomyopathy (HCM)	0.0036	0.50318	Contractility
REACTOME_DSCAM_INTERACTIONS	Up	DSCAM interactions	0.0042	0.50318	N/A
REACTOME_RRNA_PROCESSING	Up	rRNA processing	0.0042	0.50318	N/A
REACTOME_REGULATION_OF_COMMISSURAL_AXON_PATHFINDING_BY_SLIT_AND_ROBO	Up	Regulation of commissural axon pathfinding by SLIT and ROBO	0.0044	0.50318	N/A
REACTOME_TRIGLYCERIDE_CATABOLISM	Down	Triglyceride catabolism	0.0051	0.50318	Mitochondrial function
REACTOME_NONSENSE_MEDIATED_DECAY_NMD	Up	Nonsense-Mediated Decay (NMD)	0.0060	0.50318	N/A
REACTOME_RAB_GEFS_EXCHANGE_GTP_FOR_GDP_ON_RABS	Down	RAB GEFs exchange GTP for GDP on RABs	0.0060	0.50318	N/A
REACTOME_CHOLESTEROL_BIOSYNTHESIS	Up	Cholesterol biosynthesis	0.0063	0.50318	Mitochondrial function
REACTOME_AGGREPHAGY	Up	Aggrephagy	0.0064	0.50318	Unfolded Protein Response

SUPPLEMENTARY FIGURES

Supplementary Figure 1

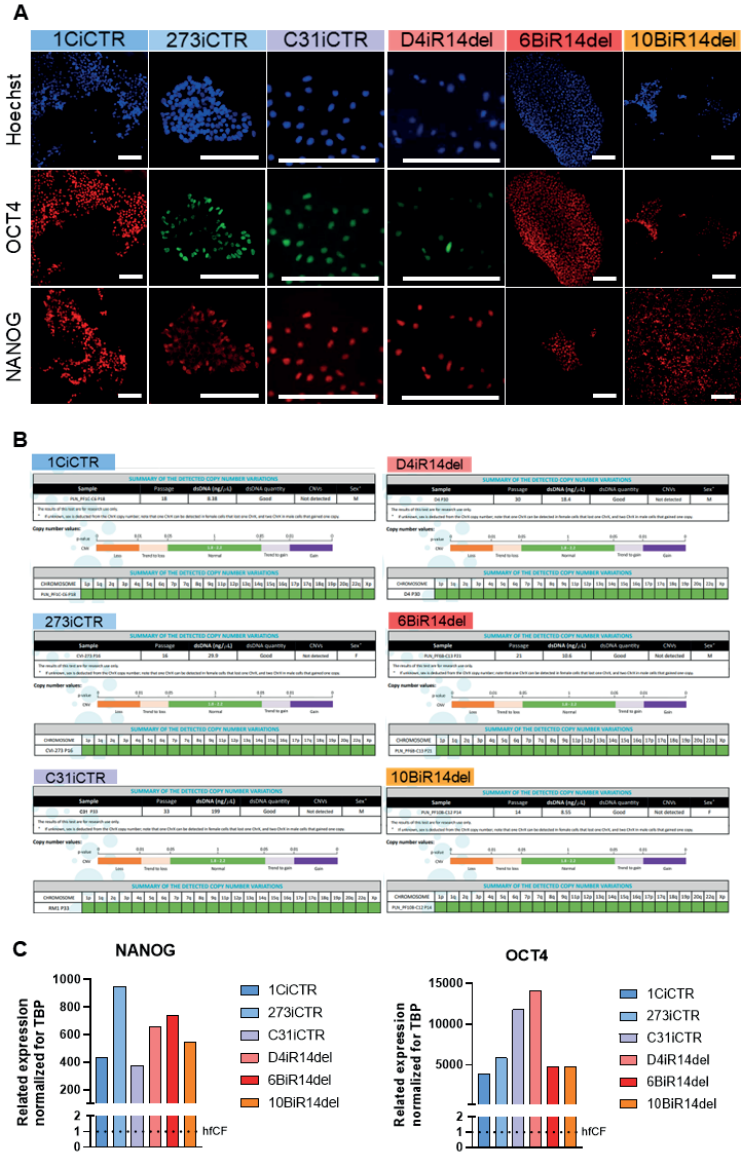

Supplementary Figure 1. Generation and characterization of hiPSCs. (**A**) Bright-field imaging revealed demarcated colony morphology of the newly generated lines 1CiCTR, 6BiR14del, and 10BiR14del. (**B**) Trilineage differentiation potential was shown with positive immunostainings of endodermal (SOX17), mesodermal (Brachyury T), and ectodermal (OTX2) markers in the newly generated lines 1CiCTR, 6BiR14del, and 10BiR14del. Scalebar = 400µm.(**C**) The qRT-PCR expression levels of NANOG and OCT4. Total RNA from human fetal cardiac fibroblasts (hfCF) was used as negative control and reference. (**D**) Expression of pluripotency-associated markers (OCT4, NANOG, and Hoechst) by immunofluorescence. (E) ddPCR summary of the detected copy number variations in the iPSC genome for karyotyping.

Supplementary Figure 2

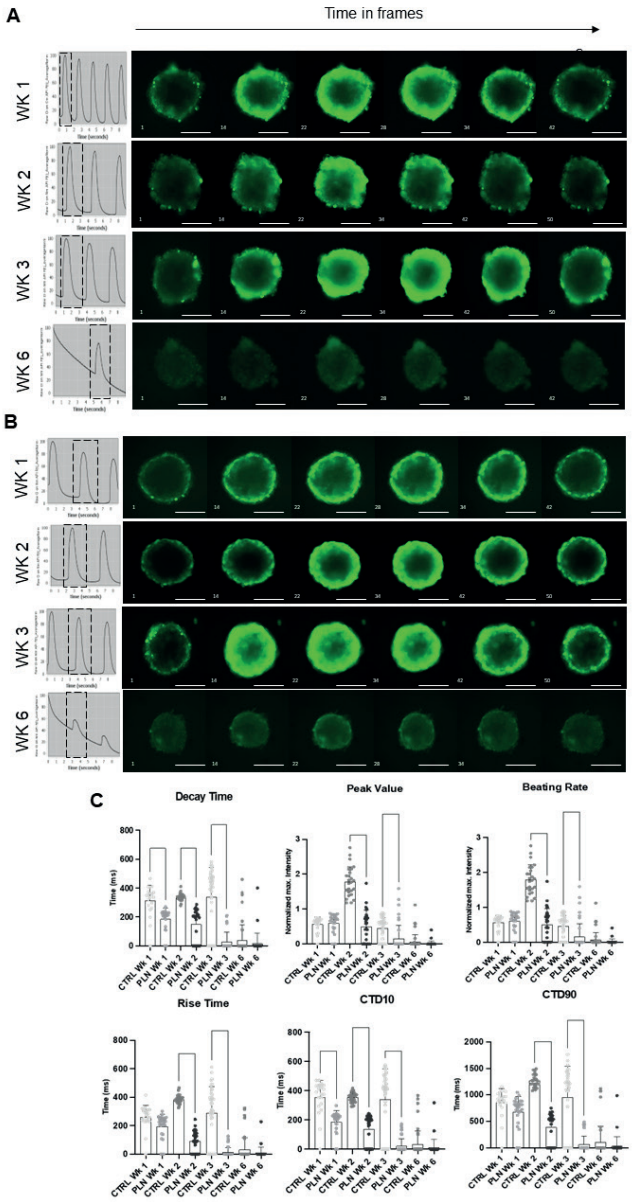

Supplementary Figure 2. Optimization of high throughput optical recordings of the Cal520 dye during the culturing of hCSs. (**A**) Representative Ca^{2+} transients and images of the optical recording over time in control hCSs (273iCTR line). (**B**) Representative Ca^{2+} transients and images of the optical recording over time in PLN-R14del hiPSC-derived CM spheroids (D4iR14del line). (**C**) Ca^{2+} transient parameters, including decay time, beating rate, duration at 10% decline from maximum amplitude (CTD10), and duration at 90% decline from maximum amplitude (CTD90). Each dot represents one individual spheroid and 3 biological (3 different differentiations of one hiPSC line) per condition were included in this analysis.

Supplementary Figure 3

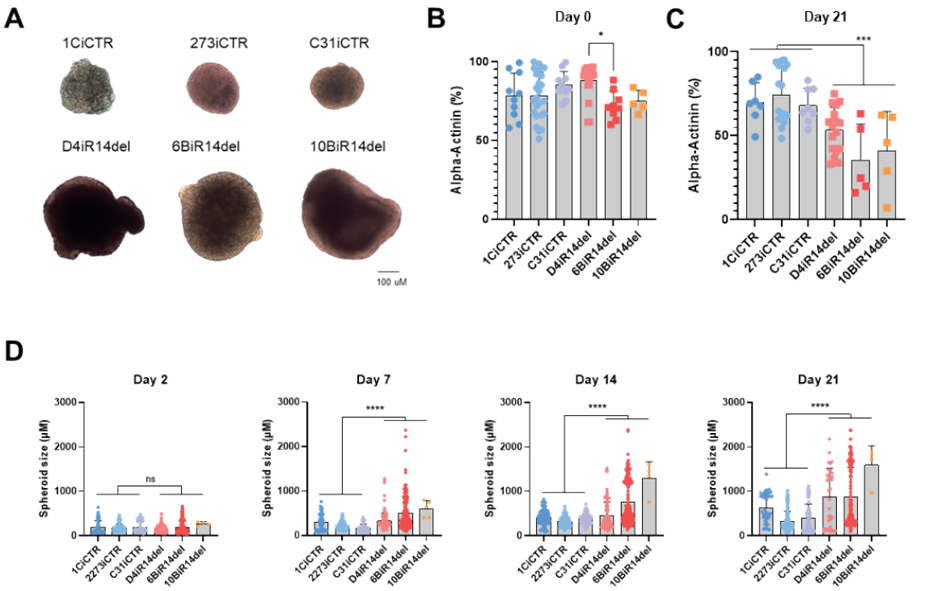

Supplementary Figure 3. Morphology, Purity, and Size of hCSs from healthy or isogenic controls (CTR; 1CiCTR, 273iCTR, C31iCTR) lines and PLN-R14del patients (R14del; D4iR14del, 6BiR14del, 10BiCTR) lines. (**A**) Bright-field images demonstrating the size of the hCSs after 21 days. Scale bar: 100 µm. (**B**) Flow cytometry quantification of alpha-actinin purity of each spheroid cell line before the generation of hCSs (Day 0). (**C**) Flow cytometry quantification of alpha-actinin purity of each spheroid cell line after 3 weeks of spheroid culturing (Day 21). (**D**) Quantification of spheroid size in the individual cell lines during culturing (Day 2, 7, 14, and 21). * P< 0.05 - **** P < 0.0001 vs. CTR group or each cell line by Student's unpaired T-test or 2-way ANOVA. Each dot represents one individual spheroid and 2-3 biological replicates per condition were included in this analysis.

Supplementary Figure 4

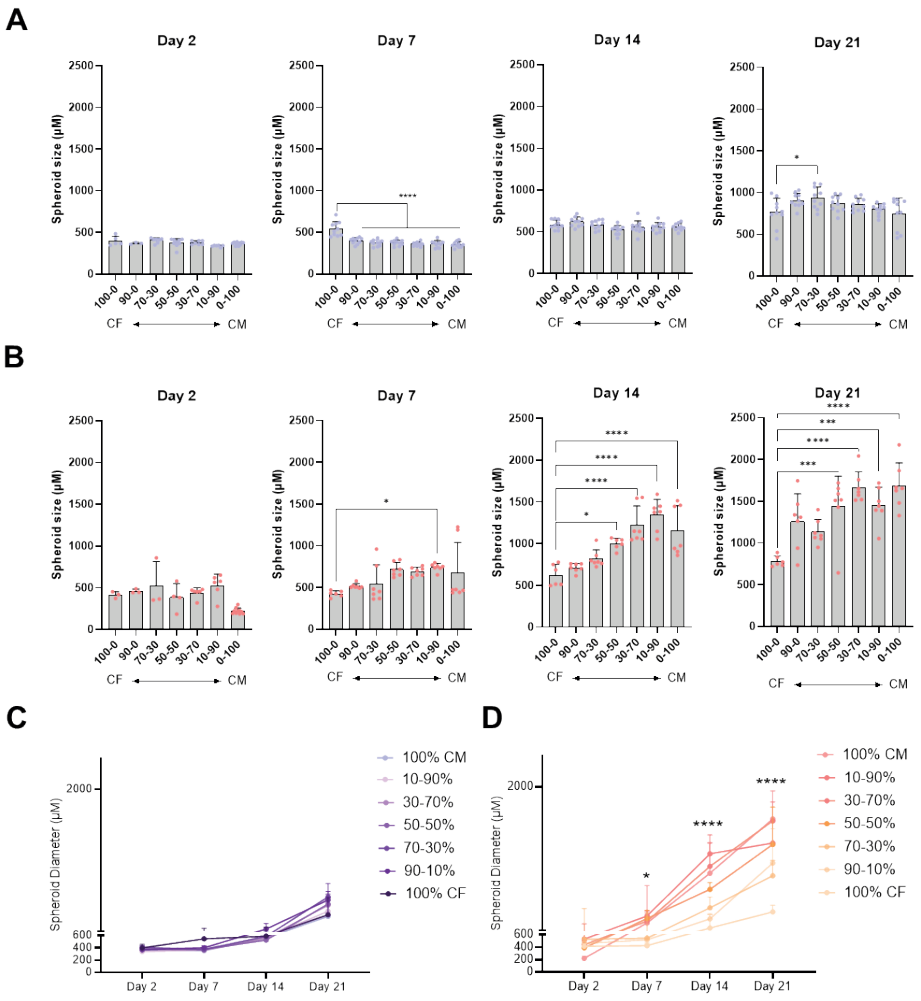

Supplementary Figure 4. Size measurements of hCSs with various ratios of hiPSC-CMs + hiPSC-CFs from wild type (CTR lines) and PLN-R14del patients (R14del lines). (**A**) Quantification of spheroid size in the isogenic control line (C31iCTRL) with 100% hiPSC-CFs (left), the various ratios (middle), and 100% hiPSC-CMs (right) during culturing (Day 2, 7, 14, and 21). (**B**) Quantification of spheroid size in the PLNR14del line (D4iR14del). * P< 0.05 - **** P < 0.0001 vs. hiPSC-CF hCSs group analyzed by 1-way ANOVA. Each dot represents one individual spheroid and 2 biological replicates per condition were included in this analysis. (**C**) Overtime quantification of the isogenic control (C31iCTR) line spheroid size. (**D**) Overtime quantification of the D4iR14del line spheroid size as displayed in A.

Supplementary Figure 5

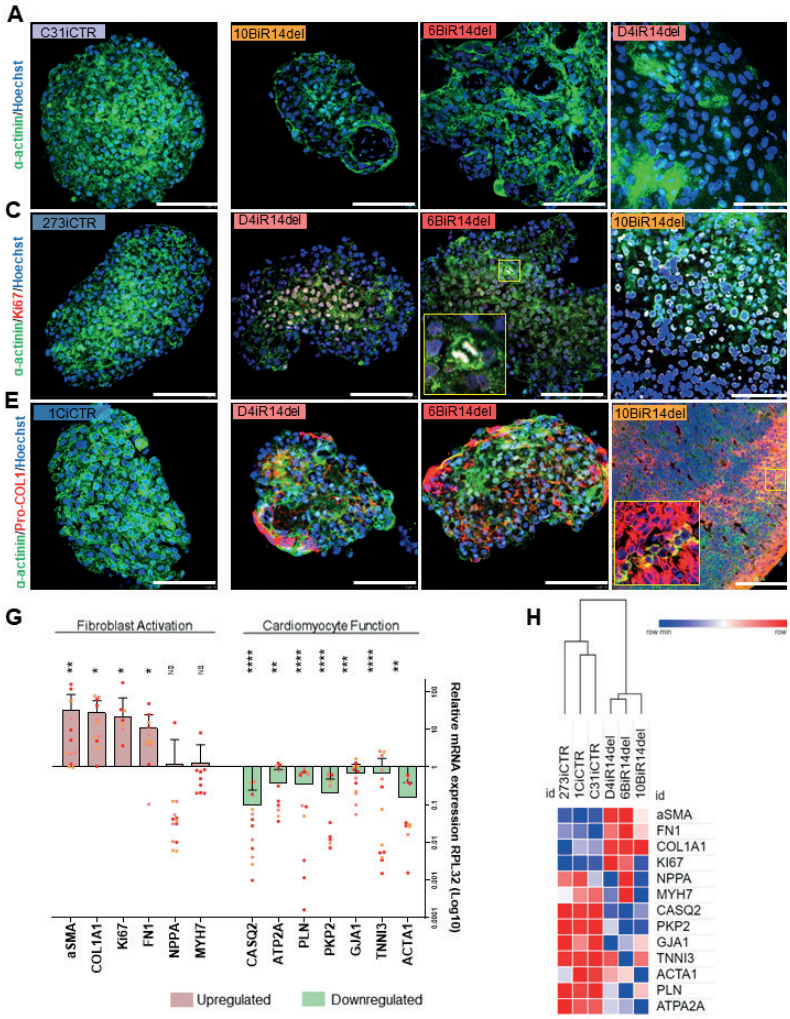

Supplementary Figure 5. SPLiT Sequencing mapping, sources of biological variability in hiPSC donors and cell type-specific gene patterns. (**A**). UMAP plot of single-cell profile with each cell color-coded for D12, D24, and D90 cardiomyocytes (Grancharova et al.,). Different cell clusters are colored and labeled as indicated. (**B**) clustered mapping of all labels based on mapping in A (Grancharova et al.,) (**C**) UMAP of the individual cells derived from cardiac spheroid per iPSC donor. (**D**) Fraction of cells for the three cell types; CMs group 1 (CM1), CMs group 2 (CM2), and fibroblasts (fibro) in healthy controls and PLN-R14del spheroid groups. (**E**) Top 10 genes of each cell cluster. Wilcoxon rank-sum test identifies differentially expressed genes in each cluster and the top 10 genes are displayed in a heatmap. (**F**) Expression levels of cardiac genes TNNT2 and MYH7 per individual cells derived from cardiac spheroid per iPSC donor. (**G**) UMAP from Fig. 3 colored by transcript abundance of DCC and FAM155A, highlighting cardiomyocyte cluster 1, TNNT2, and RYR2, highlighting cardiomyocyte cluster 2 and FN1 and COL1A1, highlighting the fibroblast cluster. (H) Transcript abundance distributions are shown for CM1, CM2, and fibroblast clusters. Max value = maximum value of log1p normalized counts; dot = median.

Supplementary Figure 6

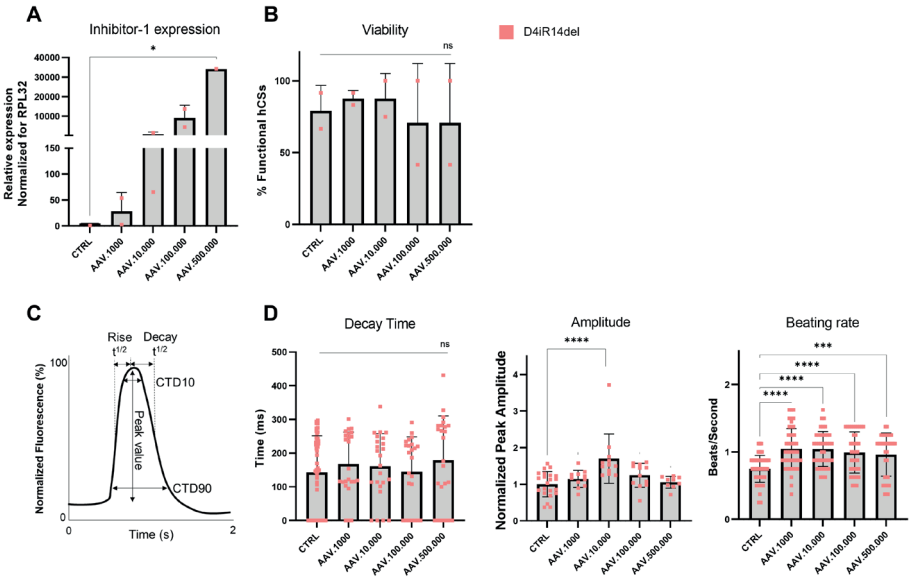

Supplementary Figure 6. Optimization of AAV.I-1c dosage in the D4iR14del line. (**A**) qPCR analysis of Inhibitor 1 (I-1c) expression after different MOI concentrations of AAV.I-1c treatment. * $P < 0.05$ vs. untreated control (CTRL) by one-way ANOVA. Each dot represents a sample of 20 spheroids and 1-2 biological replicates per condition were included in this analysis. (**B**) Functional beating viability of hCSs after different MOI concentrations of AAV.I-1c treatment. Each dot represents the percentage of beating hCSs per experiment. N=2 per condition. (**C**) Measurement of Ca^{2+} handling parameters from automated recorded data (**D**) Comparison of decay time (Tau), Ca^{2+} transient amplitude, and beating rate after different MOI concentrations of AAV.I-1c treatment. * $P< 0.05$ - **** $P < 0.0001$ vs. each group by one-way ANOVA. Each dot represents one individual spheroid, n=48-24 spheroids, and 2 biological replicates per condition were included in this analysis.

Supplementary Figure 7

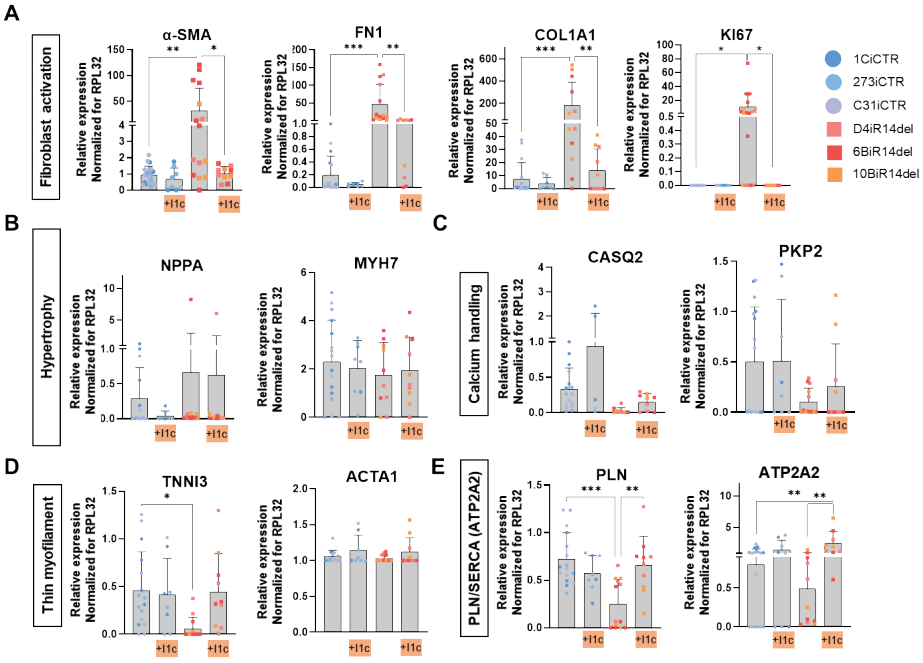

Supplementary Figure 7. hCS gene expression after AAV.I-1c treatment. (**A**) qPCR analysis of various genes involved in fibroblast activation (A), hypertrophy (**B**), Ca^{2+} handling (**C**), Thin myofilaments (**D**), and PLN and SERCA (**E**) expression in controls, PLN-R14del hCSs, and the treatment with AAV.I-1c. **** $P < 0.0001$ vs. each group by 2-way ANOVA. Each dot represents one individual spheroid and 2-3 biological replicates per condition were included in this analysis.

Supplementary Figure 8

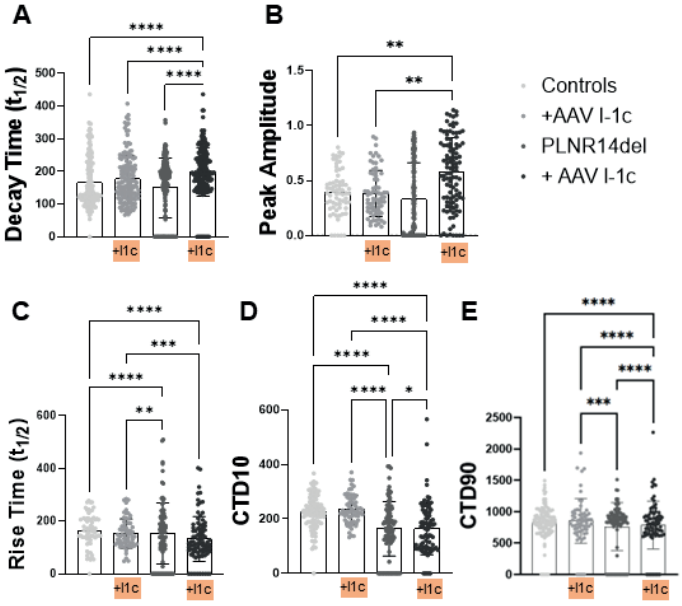

Supplementary Figure 8. Ca^{2+} transient analysis normalized for beating rate. Ca^{2+} handling parameters include (**A**) decay time, (**B**) peak amplitude, (**C**) Rise time, (**D**) duration at 10% decline from maximum amplitude (CTD10), and (**E**) duration at 90% decline from maximum amplitude (CTD90). Each dot represents one individual spheroid and 3 biological (3 different differentiations of one hiPSC line) per condition were included in this analysis. The combined groups of control lines (biological replicates=2-3, n=188), controls + AAV.Ic-1 (biological replicates=2-3, n=151), PLN-R14del lines (biological replicates=2-3, n=243), and the PLN-R14dels + AAV.I-1c (biological replicates=2-3, n=204) were normalized for beating rate. * P< 0.05 - **** P < 0.0001 vs. each group by two-way ANOVA. Each dot represents the raw data of one individual spheroid without batch normalization. Abbreviations: Controls; healthy or isogenic control hCSs (1CiCTR, 273iCTR, C31iCTR), PLNR14del; PLN-R14del hCSs (D4iR14del, 6BiR14del, 10BiCTR).

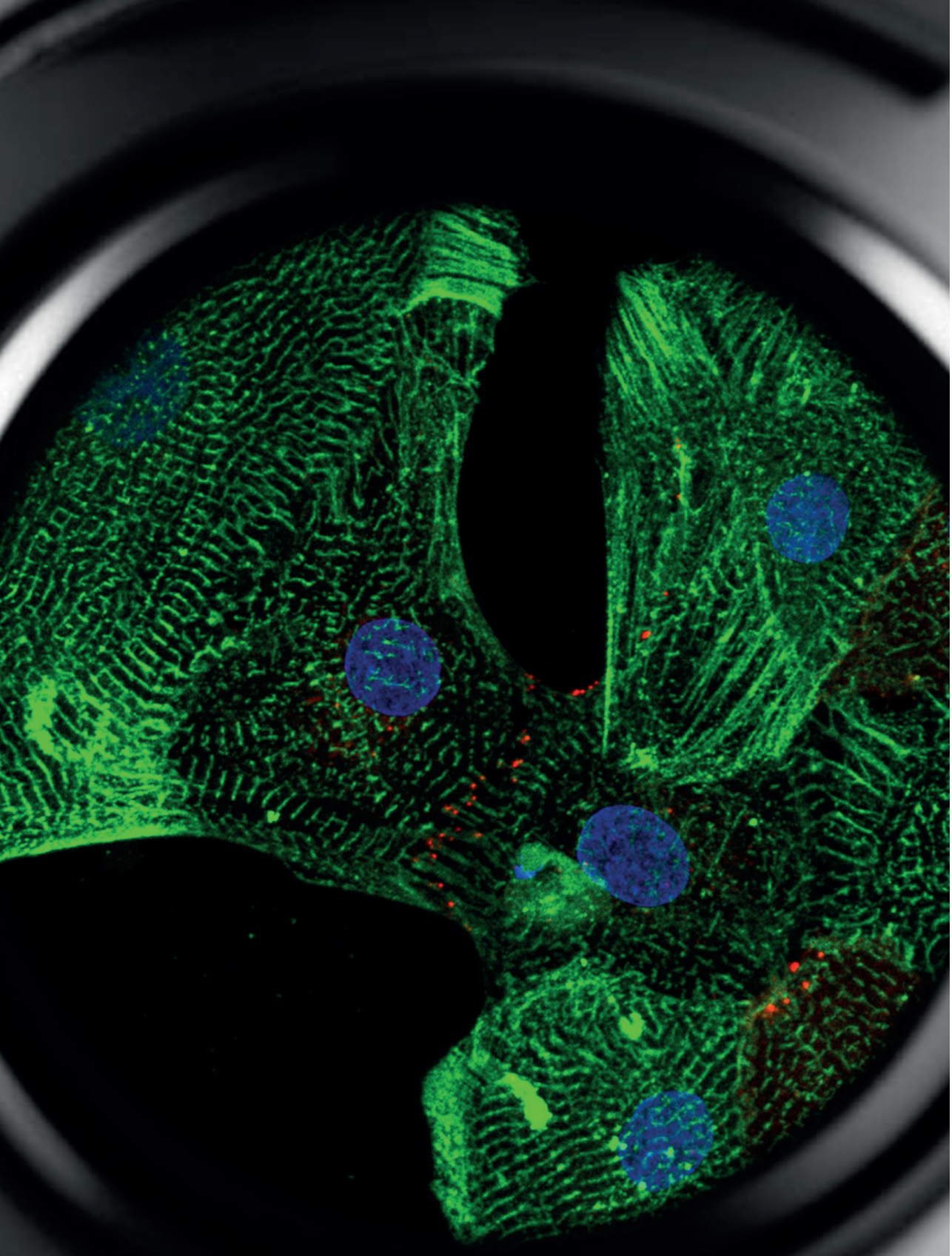

Metabolically matured hiPSC-CMs stained for sarcomeric Actinin and Gap-junction protein Connexin 43.

Chapter 13

General Discussion - hiPSC-CMs Disease Modelling and Future Perspectives

Renée G.C. Maas

Cardiomyopathies are disorders of the myocardium caused by a wide variety of factors, leading to cardiac dysfunction, aggravated by arrhythmias, heart failure, and sudden cardiac death. The prevalence is estimated based on genetic screenings, as high as 1:500 for hypertrophic cardiomyopathy (HCM), 1:250 for dilated cardiomyopathy (DCM), and 1:1000 for arrhythmogenic cardiomyopathy (ACM).[1,2] These numbers, however, are probably underestimated as the majority of individuals have incomplete and/or late-onset disease expression. Numerous mutations in various pathways crucial for cardiac function have been linked to these cardiomyopathies. However, the underlying genetic mutation has only been identified in approximately 35% of DCM, and 50% of the HCM and ACM cases.[1] Genetic mutations unfortunately have low predictability when it comes to the onset of disease and progression. Therefore, cell models used in the early phases of drug discovery and the significant difference in treatment responses among patients hold promise as predictors for the phenotype onset in the patients. Moreover, the understanding of the pathophysiological and molecular mechanisms that underlie the onset of pathological features of genetic cardiomyopathies is crucial to developing novel targets for therapeutics.

In vitro disease modeling can help to model the onset of the first variable phenotypic presentations and, therefore, forms a scalable platform for human disease modeling, drug discovery, and the clinical validation of novel therapeutic developments. In this thesis, we used the crucial pathways in cardiogenesis for a recent discovery in the massive expansion and biobanking of hiPSC-CMs. Next, we used this technology and combined metabolically matured hiPSC-CMs to produce both 2D and 3D *in vitro* models. Importantly, *in vitro* models are suitable for modeling healthy and pathological cardiac tissues, and we provide several lines of evidence to confirm this hypothesis. Finally, we combine findings from the previous chapters with insights from other studies and discuss the current developments in cardiac *in vitro* models, pathophysiology, and the underlying pathways of PLN-R14del cardiomyopathy. In addition, new tools are being developed to facilitate our progress. We finally suggest a roadmap for employing these non-animal platforms in assessing early-onset disease phenotyping and novel therapeutic screening.

PART ONE: CLUES FROM HEART DEVELOPMENT TOWARDS OPTIMIZED HIPSC-CMS MODELS

From cardiogenesis to in vitro proliferation of human cardiomyocytes

Cell cycle activity in human adult CMs decreases within the first months after birth and is very sparse in the human adult myocardium. As described in **Chapter 2**, many pathways have been investigated over the past decades for their capacity to regulate heart growth versus the molecular targets that promote *in vitro* cardiomyocyte proliferation. Pushing the level of understanding of the mechanisms controlling human cardiomyocyte proliferation

provides a framework for advanced basic and translational cell biology applications. From here, methods for defined culture, efficient differentiation, and the upscaling of hiPSC-CMs for the generation of large batches of cardiomyocytes are elucidated. As presented in **Chapter 3**, we identified the earliest and most potent mitogen to stimulate the canonical Wnt signal via the LEF/TCF pathway to delay hiPSC-CM maturation. Notably, we found that persistent CM proliferation required both LEF/TCF activity and AKT phosphorylation, which was independent of yes-associated protein (YAP) signaling. Importantly, in this study, we also investigated the contractility of previously expanded hiPSC-CMs in 3D microtissues and showed the uncompromised cellular functionality after expansion compared to non-expanded hiPSC-CMs. The massive expansion of hiPSC-derived cardiomyocytes via Wnt/β-catenin signaling modulation holds great potential for the generation of large batches of cardiomyocytes (**Chapter 3**). Biobanking of expanding hiPSC-CMs, as performed in **Chapter 4**, now allows scientists and clinicians to generate an ''off-the-shelf'' human cardiomyocyte source. Through these recent developments to generate and biobank billions of cardiomyocytes, hiPSC-CMs will be useful for drug screening, disease modeling, and regenerative approaches in cardiovascular medicine. In addition, we were one of the first to report on sarcomere distribution during cardiac mitosis, followed by cytokinesis, multinucleation, or self-duplication in massively expanding human cardiomyocytes (**Chapter 5**). Interestingly, we found that both mono- and binuclear hiPSC-CMs give rise to mononuclear daughter cells or binuclear progeny, which give novel insights into the potential proliferative strategy in adult CMs. However, the specific role of mononuclear and diploid cardiomyocytes during cardiac repair following myocardial infarction remains unclear[3], although small case studies have shown evidence of postnatal human heart recovery post-injury in a newborn and 6 years old child suffering from myocardial dilation or infarction.[4,5] More research is required to discover and combine new mechanisms to manipulate the cardiomyocyte cell cycle and cell-cell contact in adults to induce cardiomyocyte mitosis. Future research could focus on combining the overexpression of cell cycle promoters (cyclins and CDKs), cell cycle progression pathways (neuregulin/ERBB2/ERBB4), cell cycle arrest pathways (hippo-YAP), and miRNA modulation.[6] However, these processes should be tightly controlled to avoid tumorigenesis, endoreplication, or endomitosis. The verification of the massive expansion of human CMs *in vivo* is still pending, which is of significant interest to cardiovascular investigators to restore the adult myocardium.

Cardiomyocyte maturation, are we close enough?

Although scalability has improved for the majority of hiPSC-derived cell types, the immaturity of the differentiated cells, specifically hiPSC-CMs, limits their clinical potential.[7] Many biochemical and biophysical strategies have been invented to induce a mature phenotype of hiPSC-CMs. For example, during prolonged culture time, hiPSC-CMs displayed more mature phenotypes in morphology (increased cell size), structure (sarcomeric organization),

proteasome activity (PKA/HSP90 signaling), metabolic homeostasis (fatty acid oxidation), physiology (calcium handling, increased contractility, and β-adrenergic response).[8–10] Next, we and others showed that alterations in energy sources are a simple, yet effective method to metabolically switch hiPSC-CMs from glucose to fatty acid oxidation by providing oxidative substrates adapted to the metabolic needs of hiPSC-CMs.[11–13] According to a recent article in Nature, a fatty acid called γ-linolenic acid (GLA) found in the milk of nursing mice has been found to trigger a transformation in the metabolic pathways by binding retinoid X receptors (RXRs), enabling the cells to rapidly mature after birth.[14] This unexpected finding reveals a role for GLA in promoting the early murine heart maturation, which could be applied to improve hiPSC-CM maturation. In **Chapter 6,** we demonstrate that prolonged cultured and metabolically stimulated cardiomyocytes increase hypoxia susceptibility, which is more reminiscent of adult CMs. The metabolic maturation of hiPSC-CMs represents an improved *in vitro* model to study human ischemic heart disease and genetic cardiomyopathies.[11,15]

In this thesis, we combined biochemical strategies such as prolonged culturing of a monolayer with metabolic and hormonal supplements to induce maturation *in vitro*. Here, sarcomeric organization, CM length, and sarcomere spacing were improved, resulting in a morphology similar to human adult CMs (**Figure 1A**). Although many of the measurable maturation parameters such as; surface area, bi-nuclearity, gene expression, M-banding, and sarcomere spacing are improved in these hiPSC-CMs to mimic the human adult CM level, the upstroke velocity, resting membrane potential, and T-tubuli are almost reaching the parameter levels (**Figure 1B**). Nevertheless, if the maturation status of hiPSC-CMs could even further improve or accelerate in the described parameters, a significant increase in disease modeling can be expected. For example, increased gene expression levels of ventricular ion channels and calcium-handling genes are considered to be hallmarks of maturation.[16] Still, complex mRNA-based mechanisms driven by alternative splicing and RNA-binding proteins may need to be manipulated to improve CM maturation further.[17] Abolishing depolarization-associated genes *HCN4, CACNA1H,* and *SLC8A1*, along with overexpressing the ion channel *KCNJ2* changes extensively as hiPSC-CM grafts mature *in vivo*, thereby reducing arrhythmic events after cell graft transplantation.[18] However, the one major challenge remaining is to localize the fully functional gap junction protein Connexin 43 (Cx43) in the intercalated discs. In metabolically matured hiPSC-CMs, a rather low Cx43 expression and localization are found (**Figure 1C**), causing a significant reduction of intercellular coupling and leading to slow electrical signal propagation.[19]

The formation of functional gap junctions is essential for modulating cardiac electric activities and the absence of Cx43 leads to the incidence of ventricular tachyarrhythmias.[20] Interestingly, even during the development and maturation of human cardiomyocytes, spatiotemporal localization of Cx43 takes 7 years to move from the lateral membranes to the intercalated disks.[21] In summary, after 70 years of many cell culture improvements, we now have create

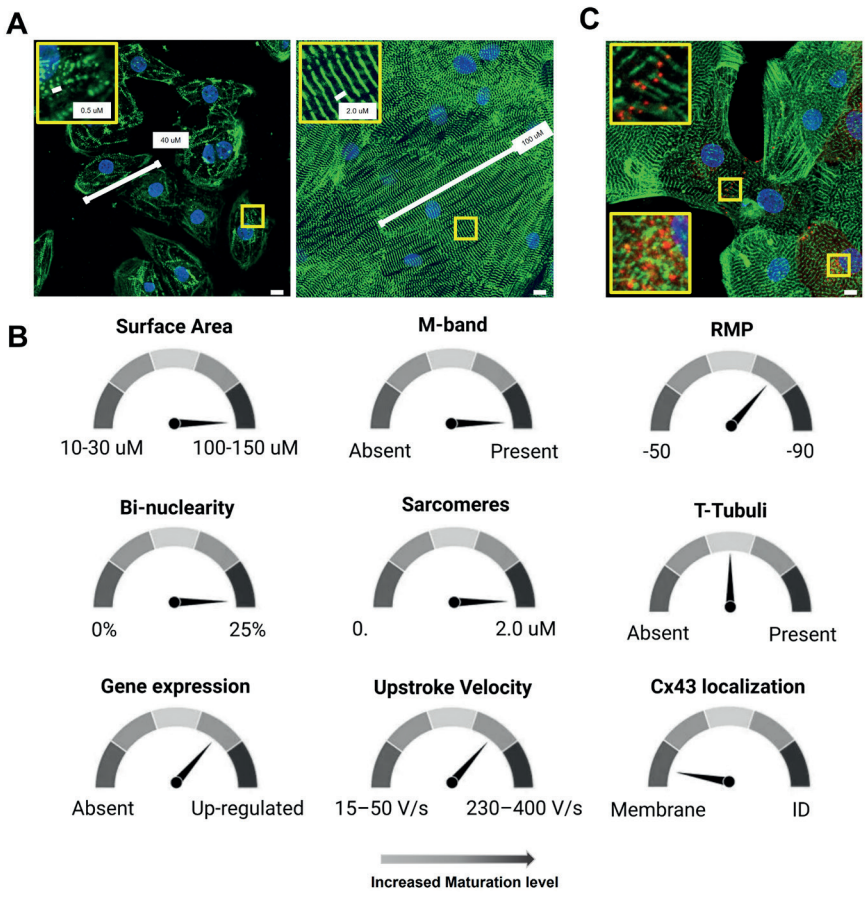

Figure 1. Induced maturity in hiPSC-CMs. (**A**) Sarcomeric organization, cell length, and sarcomere spacing on immunofluorescent labeled 2D cultured hiPSC-CMs by alpha-actinin. Scale bar: 8 uM. (**B**) The major measurable parameters of biological processes in cardiomyocyte maturation. The arrow indicates the level of the specific maturation parameters in hiPSC-CMs, the left indicates low, and the right means high maturation levels compared to adult myocytes. Abbreviations; RMP; resting membrane potential, ID; intercalated disc. (**C**) Connexin43 (Cx43) organization and localization on immunofluorescent labeled 2D cultured hiPSC-CMs by alpha-actinin (green) and Cx43 (red). Scale bar: 8 uM. Created with BioRender.com.

'enough-matured' hiPSC-derived CMs that can be used for disease modeling, testing of drug-induced toxicity, and drug refinement/discovery. Although convenient, 2D cell culture techniques have unfortunately proven to be ineffective in mimicking the contractile deficit in titin patient-derived hiPSC-CMs. Instead, the titin mutant hiPSC-CMs in the engineered heart tissue (EHT) model showed the obvious insufficient contractile force of the patient-derived hiPSC-CMs.[22] RNA sequencing revealed 22 transcription factors (TFs) whose expression was progressively increased in the 3D culture systems as compared to 2D differentiations.[23] By overexpressing three of the 22 identified TFs (KLF15, ESRRA, and HOPX), Kumar *et al.* could

significantly improve calcium handling, metabolic function, and hypertrophy in day 17 2D hiPSC-CMs. Another study used single-cell RNA sequencing to compare hiPSC-CM monolayers versus 3D sheets, tissue strips, and organoid chambers, revealing increasing levels of maturity by increasing tissue complexity. Interestingly, myofibril structure was shown to be the first to mature, followed by electrophysiological function and oxidative metabolism.[24] In summary, the limited maturation and predictivity in the current hiPSC-CM models pose the question if these methods can yield mature enough cells, in a realistic, large-scale, and financially appropriate culture time frame. Combining the current strategies such as long-term culturing, 3D tissue engineering, and metabolic supplementation with future improvements such as TFs/Cx43/KCNJ2 enhancement could take us to the final steps in getting as close as possible to our 'holy grail'; an hiPSC derived adult-like CM.

PART TWO: MODELING THE PHOSPHOLAMBAN R14DEL MUTATION USING PATIENT-SPECIFIC HIPSC-CMS

In **Part 1**, we discussed the substantial technological innovations observed from cardiac development regarding the differentiation, proliferation, and maturation of hiPSC-CMs. Especially with the advanced hiPSC technology, the possibility arises to create essentially limitless numbers of hiPSC-derived CMs, harboring a diversity of patient genetics. Genetic cardiac hiPSC-CM models have been constructed using hiPSCs derived from patients suffering from ACM, DCM, HCM, non-compaction cardiomyopathy (NC), and lysosomal storage disorders which were thoroughly reviewed elsewhere.[25–27] In this thesis, we study the deletion of arginine 14 (R14) in the phospholamban protein (PLN-R14del), causing the panoply of DCM and ACM manifestations in heart failure patients. By systematically reviewing the current evidence of all studies describing PLN-R14del mutation, we summarized the potential molecular mechanisms contributing to the disease pathophysiology (**Chapter 7**). We emphasized how the discovery of PLN-R14del fuelled insights into the basic biology of calcium handling, protein toxicity, metabolism, and fibrosis, and we reinforced the idea that PLN is a crucial dynamic regulator of SERCA2a (ATP2A2) that contributes to the speed and force of calcium-driven muscle contraction.

Metabolic maturation and multi-omics analysis of hiPSC-CMs reveal the pathological features of the R14del cardiomyopathy in vitro.

RNA sequencing (RNA-seq) is a genomic approach for the detection and quantitative analysis of messenger RNA molecules to study cellular gene expression. In **Chapter 5**, we used whole genome RNA-seq to study the gene expression patterns in expanding hiPSC-CMs, versus hiPSC-CMs that were metabolically matured for +77 days. As expected, genes associated with embryonic signaling pathways and mitosis were upregulated in proliferating hiPSC-CMs, whereas the expression of sarcomere genes was upregulated in matured CMs and human

heart tissue. This RNA-seq data showed that in hiPSC-CMs, the cell cycle gene expression is inversely correlated to sarcomere gene expression and maturity of CMs. In **Chapter 8**, we used the metabolic maturation of patient-derived hiPSC-CMs, to provoke the molecular scenery of the cardiomyocytes from a PLN-R14del patient. To clarify the cell regulation on all levels, we combined the transcriptional regulation analysis in human primary tissue and validated this expression in a unique long-term (160 days) matured hiPSC-CM model. First, the multi-omics integration hinted us to disturbed mitochondrial function and (lipid) metabolism in PLN-R14del hearts based on the changed histone acetylation levels of annotated gene promoters, predicted transcription factor binding motifs (TFBMs), and altered gene expression. Next, we demonstrated, that PLN-R14del hiPSC-CMs displayed a lower fatty acid oxidation (FAO) profile than the controls at both mRNA and functional levels, the suppression pattern remained consistent even though PLN-R14del hiPCS-CMs were given excessive amounts of FAs or glucose, indicating the profoundly impaired lipid metabolism. Additionally, to the best of our knowledge, we showed for the first time, the potential of bezafibrate in re-activating mitochondrial FAO and improving Ca^{2+} transients, which provides a novel strategic path for developing precision medicine for PLN-R14del patients, such as targeting FAO upstream regulators (i.e. PPARA). In a recent study, multi-omics analysis (plasma/cardiac tissue metabolomics, genome-wide RNA-seq, and proteomic studies) revealed profound metabolic abnormalities in human failing hearts in 87 explanted human hearts from 39 patients with end-stage HF compared with 48 non-failing donors.[28] Substantial reductions in fatty acids and acylcarnitines were observed in these failing hearts, despite plasma elevations, suggesting the same defective import of FA into cardiomyocytes as we described in **Chapter 8** and **Chapter 12**. As a result, the glucose levels were elevated in the end-stage HF hearts, similar to our glucose dependency of the PLN-R14del hiPSC-CMs. This study proved that starting with ChiP-sequencing and RNA-seq from failing hearts identify gene pattern alterations, which could be confirmed by the RNA-seq of hiPSC-CMs of heart failure patients in the early stage of the disease.

Next, we showed that single-cell transcriptomic analysis of metabolically matured patient-derived hiPSC-CMs revealed the induction of the unfolded protein response (UPR) pathway in PLN-R14del hiPSC-CMs as compared to isogenic control hiPSC-CMs (**Chapter 9**). Additionally, this disturbance of UPR expression was also detected in bulk RNA-sequencing of human hearts from PLN-R14del patients. Next, we used both 2D and 3D *in vitro* models to evaluate the impact of modulating disease-relevant pathways in PLN-R14del hiPSC-CMs. hiPSC-CM contractility analysis in both the 2D and 3D models recapitulated the contractile deficit associated with the disease *in vitro*, which could be restored by activating the UPR with a small molecule activator. Both studies (**Chapter 8** and **Chapter 9**) provided insight into the transcriptional regulation of both human tissues and hiPSC-CMs of PLN-R14del patients to understand the molecular consequences of the pathogenic mutation and subsequent development of therapeutic interventions.

Additionally, the present focus on applying second- and third-generation sequencing technologies may lead to optimization in the full analysis of the underlying epigenetic and genetic regulation in each cardiomyocyte. For example, second-generation sequencing by Split-Pool Ligation-based Transcriptome sequencing (SPLIT-seq) has been used to define the *in vivo* cell composition from 27 healthy donors and 18 dilated cardiomyopathy patient hearts.[29] Notably, cardiomyocytes displayed the common disease-associated cell states, whereas fibroblasts and myeloid cells undergo dramatic diversification. Fibroblasts in the DCM hearts displayed a robust activation signature that included *αSMA* and *COL1A1* expression. Interestingly, we observed a similar upregulation of the fibroblast activation signature (*COL1A1, αSMA, and FN1*) in DCM patient-derived spheroids harboring the PLN-R14del mutation (**Chapter 12**). Together, this study provided a comprehensive analysis of the cellular and transcriptomic landscape of DCM hearts and uncovered cell type-specific transcriptional programs and disease-associated cell states, which is a valuable resource for the investigation of human heart failure.[29] However, future unbiased and spatiotemporal RNA sequencing and proteomics attempts could identify key regulators of the pathological features of the R14del cardiomyopathy.[30] Importantly, the identification of clinically relevant pathological features may inform us of disease pathology and hint at other potential therapeutic opportunities. Finally, knowing when and why these pathophysiological traits derail would be the key to unravelling the optimal time window to apply the most suitable therapeutic intervention.

Another option is third-generation sequencing (long-range sequencing), by direct RNA sequencing by Oxford Nanopore Technologies, which makes the direct sequencing of full-length RNA transcripts and post-transcriptional RNA modifications analysis possible. However, both SPLIT-seq and Nanopore sequencing suffer from high costs, and limited sequencing depth, something the single-cell community has not had huge success with, including ourselves. However, with the optimization of large hiPSC-CM batches, and improved knowledge of the fixation and library preparations, it would be a matter of time before these second- and third-generation techniques can be applied to study 3D *in vitro* hiPSC-CM models for the initial complete disease genome evaluation. Although transcriptomics is currently the most readily-used single-cell-omics level analysis, post-translational protein modifications can affect protein interactions and also play a major role in disease pathogenesis. Quantitative proteomic analysis of hiPSC-CM reveals lineage-specific protein profiles in hiPSC-derived Marfan syndrome smooth muscle cells[31] and titin-mutated hiPSC-CMs[32]. Still, combined analysis of modified proteomics (for example phosphorylated proteomics) with proteomics is rare. Here, the development of micro- and modified-proteomics will allow wide protein dynamic ranges and high levels of identifications in low numbers of cells.[33] The advancement of RNA-seq and proteome technology opens a new chapter in the study of the pathological mechanisms, as displayed recently in hiPSC-CMs from hypoplastic left heart disease patients.[34] At this point, we can only reinforce the importance of multi-omics analysis of hiPSC-based 3D structures for the initial *in vitro* screening of pathological mechanisms. Clearly, by integrating

multi-omics approaches, researchers could establish purely the computational blueprints for development, differentiation, and drug response in hiPSC-CMs.

From *in vivo* to *in vitro* - from organ to organoid.

As discussed, hiPSC-CMs could bypass the limitation represented by the impossibility of mechanistic studies on the pathogenesis and progression of cardiomyopathies in tissues from living patients. Moreover, patient-specific hiPSC-CMs create the possibility of analyzing the molecular mechanism of cardiomyopathies in an early stage, before the cardiac remodeling or end-stage pathological levels are reached. Both 2D and 3D hiPSC-CMs have their advantages and disadvantages as discussed below. Still, the best model is one that is fit for purpose; as simple as possible, yet, as complex as necessary.

The 2D patient-derived hiPSC-CMs models we used in this thesis showed multiple significant characteristics of the studied disease, including the metabolic disturbance (**Chapter 8**) and upregulation of UPR (**Chapter 9**). On the contrary, 2D cell culture techniques have proven to be ineffective for the prediction of cancer drug efficacy[35] or mimicking the contractile deficit in titin patient-derived hiPSC-CMs. Instead, the titin mutant hiPSC-CMs in a 3D EHT model showed the obvious insufficient contractile force of the patient-derived hiPSC-CMs.[22] Both examples have been attributed to the fact that cells grown in a 2D culture lack maturity, complex structure, and multicellular organization instead of a 3D model. A recent study by Biendarra-Tiegs *et al*. showed that atrial fibrillation can be modeled in day 60 old-hiPSC-CMs cultured on a micropatterned linear chip, which enhances the conduction velocity compared to the 2D planar culturing as this chip matched the conduction velocity measured *in vivo* human hearts and *ex vivo* human atrial tissue slices.[36] This example nicely illustrates that, although the model is not a perfect copy of the human adult myocardium, specific traits can be used for disease modeling and ultimately for novel therapeutic screening. However, finding the right molecular phenotype to model the disease can be quite complex, especially when patients with the same mutation manifest the disease phenotype with a diverse severity. As described in **Chapter 7**, the variability in penetrance of the PLN-R14del cardiomyopathy, including the diversity in disease onset, varies from young symptomatic patients and elderly asymptomatic mutation carriers. Primary tissues from multiple human donors are problematic as there is not enough *ex vivo* primary tissue from a single donor to accommodate testing multiple concentrations of drugs and a single donor approach can not predict the outcome for the complete patient population. 2D i*n vitro* hiPSC-CMs can overcome the single donor limitation as we can generate multiple hiPSC lines from genetic cardiopathy donors (**Chapter 10**).

Despite the discovered metabolic disturbance (**Chapter 8**) and upregulation of UPR (**Chapter 9**) by using 2D hiPSC-CMs, we developed micro 3D tissues, called spheroids (**Chapter 11**) to study the morphology, PLN-R14del pathology and the cell-cell interactions (**Chapter**

12). These cardiac spheroids were metabolically matured for several weeks. Here, we found that the spheroids cultured for 2 and 3 weeks were efficient in predicting the disturbed calcium handling in PLN-R14del hiPSC-CMs. Remarkably, however, 6-week-old spheroids showed a non-viable morphology and decreased calcium function. These findings suggest that the spheroids created with cells consisting of +80% hiPSC-CM, could represent a non-physiological condition, rather than mimicking the cell types in the human myocardium. Recently, several studies have investigated the role of a controlled combination of hiPSC-CMs, cardiac fibroblasts, and cardiac endothelial cells, which showed enhanced maturation and allowed high reproducibility across lines and differentiated cell batches of over a thousand microtissues. Interestingly, these three-cellular microtissues generated from an ACM patient, strikingly recapitulated features of the disease, indicating a multicell-type cause of genetic cardiomyopathies.[37] Moreover, in another study, apoptotic cells became apparent in CM-only spheroids cultured for 8 weeks. Interestingly, spheroids generated from all four cardiac-cell types, in the ratio of CMs, ECs, SMCs, and CFs (4:2:1:1) remained viable throughout the culture period, by presumably following the distribution trends found in human myocardium.[38] Where cardiac spheroids are simple 3D structures typically consisting of a cluster of cells, organoids are complex structures that aim to replicate the architecture and function of specific organs or tissues.[39] Human heart organoids have been created since the mid-2010s, but only recently have significantly faithful models been achieved.[40,41] The delay, when compared to other organoid types, is due to the specific obstacles posed by cardiac tissue. For example, nutrient distribution in organoids is a challenge, often resulting in a necrotic core and thereby limiting the maximum organoid size. Vascularization[42] or long-term culture[43] can promote the development and maturation of organoids, making them larger and more functional. The generation of human heart organoids by the self-assembly of hiPSCs could offer another possibility to mimic and culture human myocardium *in vitro*. Cardiac organoids generated by a three-step Wnt signaling modulation strategy mimic the age-matched human fetal cardiac tissues at the transcriptomic, structural, and cellular level[44], cardiac proliferation[45], and were able to model ischemic injury[46]. Subsequently, the improvement of cardiac spheroids and organoids by the combination of multiple cell types could improve physiological functions. However, this application on a very large scale, would remain challenging and very costly culture-wise. Moreover, mimicking the localization and interaction of the endocardial, myocardial, and epicardial layers in *in vitro* models would allow studying, for example, ventricular arrhythmias and stress-induced hypertrophy.[47,48] Finally, the fusion of two subregional organoids, as shown with brain organoids[49], could be a promising technique. For example, constructing specific-chambered hCOs with both ventricle-like and atrial-like structures or combining hCOs with vascular organoids[50] may open the field of "next-generation" organoid technology in the near future. At this point, cardiac microtissues mimicking the 3D environment, yet remaining scalable and controllable[51] offer a great opportunity for 3D disease modeling in a high-throughput screening (HTS) platform.

hiPSC-CMs for drug screenings, cardiotoxicity, and disease modeling

After the initial identification of the molecular mechanism by multi-omics and the subsequent experiments for the gene/protein expression and localization, the complex discoveries need to be studied in the automated screening of many individuals, and in well-controlled hiPSC-CM models. These hiPSC lines could not only serve as a proxy for a clinical trial but also have no limitation in the number of different "people" that could be used for screenings. In statistical sample size estimation studies, a sample size of four different cell lines could show the drug toxicity/sensitivity probability of the observations in 34%[52], whereas 22 individual lines, roughly the number of individuals in the phase I clinical trial, would achieve a 90% probability of predicting events that occur in 10% of the population. With 250 lines, the assay could predict events in 1% of the population with a 90% probability.[53] Moreover, a new successful drug can take more than 10 years to form and be approved, with costs of approximately 2 billion for the whole process. This disappointing reality of promising preclinical findings failing in 89% of the studies from animal models into effective therapies has raised serious concerns within the scientific community.[54] The recent FDA Modernization Act 2.0 has opted a way for alternative methods such as hiPSC to bolster the preclinical data pipeline, aiming to reduce the dependence on animal models.[55] The combination of bioengineered 3D techniques with hiPSC currently represents our best hope for improving our preclinical-to-clinical trial pipeline for new therapeutics. The costs of these hiPSC-derived microtissues are very low, resulting in the cost for a screening of 22 lines with 5 drug concentrations and 5 replicates per condition to be under 200 euros (±0.22 per spheroid[37]). This enables big pharma to reduce drug development costs by enabling drug screenings that have a high probability of failing in clinical trials while continuing the development of drugs that are safe for human administration. These phase II-like CTiDs could follow the same principles as the ones of a clinical trial, with similar donor cohort design, scale, and confidence in the prediction. In **Chapter 10**, we demonstrated that 8 hiPSC lines could be efficiently generated from 6 individuals carrying the PLN-R14del mutation and 2 healthy family members. Moreover, the massive expansion and biobanking described in **Chapter 4**, and the generation of 3D microtissues in a 96-well (**Chapter 11**) and 384-well format (**Chapter 12**) offer great potential for high-throughput (HT) disease modeling and subsequent screening of therapeutic interventions.[56] After the efficient development of hiPSC-CM models from any cardiomyopathy and any patient, now more than ever, hiPSC-CMs can be used as "clinical trials in a dish" (CTiD). Unfortunately, not many studies have used 4 or more individuals' hiPSC-CMs for the prediction of drug response, cardiac toxicity, or disease modeling (**Table 1**).

In practice, the validation of hiPSC-CM-based cardiotoxicity as studies described a good correlation between *in vitro* cardiotoxicity and the clinical incidence of cardiotoxicity. Contrary to expectations, however, a recent study investigating the overlap between the drug response to dofetilide and moxifloxacin in 16 hiPSC lines of both subjects and the corresponding subject-derived hiPSC-CMs, failed to find a significant correlation.[62] Therefore, to study

cardiotoxicity maybe even more than 16 hiPSC lines need to be considered. The variability appears to be less relevant for hiPSC-CM disease modeling and drug screening but still, studies with more than one line should be considered. Overall, the recapitulation of the prediction in hiPSC-CM models could be impeded by the baseline differences in the hiPSC cultures (e.g., hiPSC line ancestry, HLA haplotype, differentiation efficiency, hiPSC-CM maturity level, and epigenetics). Here, the individual genetic variation in ion channels, sarcomeric protein expression, and drug response in healthy control hiPSC-CM supports the request for isogenic controls or multiple hiPSC clones and the standardization and automatization of many patient-derived hiPSC-CMs in our scientific community.

High-throughput drug screening of hiPSC-CMs models

As discussed, studies using more than 4 hiPSC lines for cardiac research *in vitro* are rare, yet elaborating the molecular mechanism of complex CM features requires many more hiPSC lines in future *in vitro* hiPSC-CM models. A predictive, quantitative, and reproducible high-throughput screening (HTS) pipeline is required to design, mimic the clinical issues, and guide the development of phenotypic-specific therapeutics. For phenotypic HTS fixed-endpoint assays such as the identification and localization of proteins of interest can be used to evaluate the static properties of cardiac cells. In this thesis, we observed significant increases in lipid droplets due to metabolic disruption (**Chapter 8**), followed by the activation of XBP-1, indicative of activated UPR (**Chapter 9**), and the increased fibroblast activation (**Chapter 12**) in hiPSC-CMs of patients with PLN-R14del mutation.These findings provided valuable information about the cardiac pathophysiology and the molecular mechanism, such as the ability to ameliorate the phenotype in hiPSC-CM models.

As previously described in this thesis, 2D models have proven to be less effective for the prediction of drug efficacy and disease modeling. Here our published framework from **Chapter 4** (expanded hiPSC-CMs) and **Chapter 11** (cardiac spheroids) in a 384 wells HTS format could provide an improved hiPSC-CM model, for the initial screening of morphological, cell death, gene, protein, and functional assessments. To screen complex physiological phenomena such as CM function, a more complex analysis with optical Ca^{2+} or voltage sensors, action potential, or force can be performed. Previously, the multi-/micro-electrode array (MEA) system has provided a non-invasive user-friendly platform consisting of dot-like electrodes measuring fluctuations in the extracellular field potential of a complete monolayer for detailed electrophysiological analysis. Although both MEA and macro-tissue platforms have the advantage of plug-and-play commercial read-out platforms, both have some throughput-limiting disadvantages of expensive and high-cell number plate formats, analogous levels of process-induced and batch-to-batch variations, as the CM-specific event could be obscured by averaging the complete field of view of a culture well.

Table 1. Overview of all studies using four or more hiPSC-lines for cardiac drug response, toxicity, and disease modeling *in vitro*.

Study type	hiPSC lines (number)	hiPSC-CMs maturation status	Analysis	Assesment	Outcome	ref.
Drug response	Healthy subjects (10)	~50 days (EHTs)	Contractile parameters, RNA Nanostring analysis	Screening of 7 inotropic indicator compounds.	Baseline phenotypes of healthy control cell lines differ considerably, drug responses were qualitatively similar.	[57]
Drug response	RyR2 (6)	~30-50 days	Calcium transients by machine learning	Anti-arrhythmic effect of dantrolene after adrenaline administration	Classification accuracy of 65.6% and sensitivities (true positive rates) of 79.7% for responders	[58]
Drug response	Healthy subjects (6)		Qualitative differences in action potentials	8 different classes of pharmacological reagents	Female iPSC-CMs more sensitive to dofetilide/cisapride. Male hiPSC-CMs less sensitive to two hERGs. Some donor hiPSC-CMs showed different responses to drugs and external stimulation.	[59]
Cardiotoxicity	Healthy subjects (10)	~40 days	MEA array (FPD), RNA Microarray	Risk of moxifloxacin-induced long QT in patients vs. hiPSC-CMs	Significant correlation of FDP response to the inter-individual differences observed *in vivo*	[60]
Cardiotoxicity	Healthy subjects (14)	~50 days	MEA array (FPD), patch-clamp analysis, RNAseq	Risk prediction in hiPSC-CMs from patients with low (7) or high (7) sensitivities to Sotalol-induced long QT	Strong correlation of FDP response to the inter-individual differences observed *in vivo*	[61]
Cardiotoxicity	Healthy subjects (16)	~30 days	APD recordings (CellOPTIQ)	Risk of dofetilide or moxifloxacin-induced long QT in patients vs. hiPSC-CMs.	No significant correlation between the *in vitro* hiPSC-CM and the clinical response of the same subject	[62]

Study type	hiPSC lines (number)	hiPSC-CMs maturation status	Analysis	Assesment	Outcome	ref.
Cardio-toxicity	Healthy subjects (11)	~40 days	Kinetic high-content contractility analysis	'Cardiac safety index' screen of 21 chemother-apeutic kinase inhibitors	Good correlation between the *in vitro* cardiotoxicity and the clinical incidence of cardiotoxicity	[63]
Cardio-toxicity	Healthy subjects (27)	~40 days	Ca^{2+} flux assay, cytotoxicity, TempO-Seq, mitochondrial high content cell imaging	Feasibility of hiPSC-CMs as population-based *in vitro* model for inter-individual variability	hiPSC-CMs can be used to characterize inter-individual responses in untreated and chemical-treated hiPSC-CMs	[64]
Cardio-toxicity	homozygous HLA donors (13)	48 days	1536-well plate dead cell screening, MEA array, TUNEL	Screening of 2,375 clinically approved compounds for cardiotoxicity	hiPSC-CMs screening confirms known cardiotoxic compounds, and identifies several unknown cardiotoxic compounds.	[65]
Disease modelling	RYR2 (6) TPM1 (2) MYBPC3 (2), KCNQ1(2), HERG (4) LMNA (2) and Healthy subjects (2)	~30-50 days	Calcium transients by machine learning	Analysis of 12 variables in calcium peaks for the separation of disease vs control	Efficient classification accuracy of 87% between the disease group and controls.	[66]
Disease modelling	DMD (4)	~20 days	LC–MS, patch clamp, EM, confocal microscopy	Study if DMD hiPSC-CM are associated with metabolic deficits	DMD hiPSC-CMs recapitulated some disease phenotypes, metoprolol improved myofilament organization	[67]
Disease modelling	TNNT2 (4)	20-50 days	Sarcomere distribution, MEA, patch clamp, calcium, contractility analysis	Analyze functional properties, describe the potential underlying etiology, and test metoprolol	Impairment in myofilament regulation, Ca^{2+} handling, and force production of individual CMs, explain DCM clinical phenotype	[68]

Study type	hiPSC lines (number)	hiPSC-CMs maturation status	Analysis	Assesment	Outcome	ref.
Disease modelling	MYH7 (5) Proband (5)	20-60 days	Optical Ca^{2+} imaging, MEA, patch clamp, confocal microscopy, single-cell qPCR	Elucidate mechanisms underlying HCM and test pharmacological restoration	MYH7 hiPSC-CMs recapitulate HCM phenotype. Screening of 13 drugs revealed Ca2+/Na2+ blocking drugs most efficient to restore beating frequency. Verapamil prevented hypertrophy.	[69]
Disease modelling	Healthy subjects (6)	30 days	Overall distribution of action potential	Variability of arrhythmias per cell line, per differentiation protocol and batch	Even the same cell line and differentiation protocol reveals variability, indicating importance in modeling arrhythmias in hiPSC-CMs.	[70]

Kinetic image cytometry (KIC) can analyze any individual cells within a full field of view, thereby increasing the identification of heterogeneous proarrhythmic events in each CM, such as early afterdepolarizations. Here, a study by McKeithan *et al.* proved that hiPSC-CMs from patients with LQTS type 3, facilitated the rapid medicinal chemical refinement of analogs of the drug mexiletine to improve the therapeutic potential and reduce the undesired proarrhythmic activity of this drug.[71] Thus, the optical modalities with Ca^{2+} sensors for recording intracellular Ca^{2+} concentration used in this study hold a great opportunity for high-throughput (HT) physiological recording. The 3D HT model we described in **Chapter 12** has proven to be sufficient for the translation of *in vivo* clinical data to *in vitro* to elucidate the full molecular mechanism of the PLN-R14del mutation. Additionally, to the best of our knowledge, we showed for the first time, the kinetic analysis of cardiac pathophysiology by the functional assessment of Ca^{2+} in an HT 3D spheroid model. Our data compare similarly to alternative cardiac spheroids studies, which used imaging and cellular viability endpoints.[72–74] We observed, similarly to the study from McKeithan, that our 3D cardiac spheroids recapitulated decreased Ca^{2+} handling, as predicted to be disturbed in the PLN-R14del mutation (**Chapter 7**).

As we initiated in **Chapter 12**, the implementation of more complex 3D *in vitro* models in HT platforms would be the most suitable for screening disease manifestations with cell-autonomous mechanisms, such as cardiomyopathies with morphological, electrophysiological,

metabolic, and contractile pathogenesis. Here, an integrated screening approach that combines the HT analysis with first a physiological function screening, whereafter the same cells are subsequently followed by a secondary screening for the protein/gene expression that is affected by the disease would be optimal. However, to fulfill this promise, it must be understood that HTS platforms require more than the simple linear extension of a single cell line approach by adding additional cell lines. Thus, future HTS research should focus on a standardized approach for all the different aspects before the screening, as almost every study now uses only a few hiPSC lines, variable differentiation protocols (**Chapter 2, Figure 3**), and different maturation stages of hiPSC-CMs (**Table 1**). Moreover, without the proper maturation of hiPSC-CMs, there is a potential risk of uncovering biology relevant to a fetal rather than an adult disease manifestation.

Taken together, the HTS of hiPSC-CM models is more complicated than the present *in vitro* testing approaches, and optimization is, in many ways a study itself, demanding its unique protocols, robotics, standardization, and automated data analysis. Given the above, it can be assumed that hiPSC-CM models could eventually be included in regulatory documents as the first CTiD screen before drug evaluation in patients. Next, the combination of the clinical findings with the CTiD data with machine learning algorithms could help the clinical choices of care by cardiologists. Moreover, eventually, the HTS platform holds the promise of reducing the need for *in vivo* studies, although the secondary effects in pharmacodynamic, tissue interaction, and metabolite activity remain challenging to study in *in vitro*.

Studying PLN-R14del hiPSC-CMs reveals multiple pathological mechanisms

The PLN-R14del mutation causes ventricular arrhythmias, decreased contractility, protein aggregation/toxicity, mitochondrial dysfunction, fibrosis, and inflammation. However, identifying the primary effect leading to this phenotype is crucial to determining 'at-risk' patients, which is important for disease prediction and prevention.

We were, to our knowledge, the first to report the altered Ca^{2+} transient parameters in PLN-R14del spheroids, corresponding to the decreased cardiac function (**Chapter 12**). The SERCA2a/PLN complex plays a pivotal role in mediating intracellular calcium homeostasis and aberrant calcium handling by the decreased SERCA2a activity is a consistent finding in heart failure. As described in **Chapter 7**, data converging to argue for PLN p.Arg14del may cause the 'super-inhibition' of SERCA2a, due to increased PLN-R14del/SERCA2a binding.[75] The decreased activity of SERCA2a by PLN-R14del is expected to cause prolonged calcium reuptake by SERCA2a, therefore increasing the decay time. However, calcium analysis data from others (**Figure 2A**)[76] and our calcium data (**Figure 2B, Chapter 12**) displayed a very similar pattern of decreased decay time in hiPSC-CMs. These observations raised the question of ''which alternative mechanisms could connect PLN-R14del defects in Ca^{2+} handling with low-force development?''

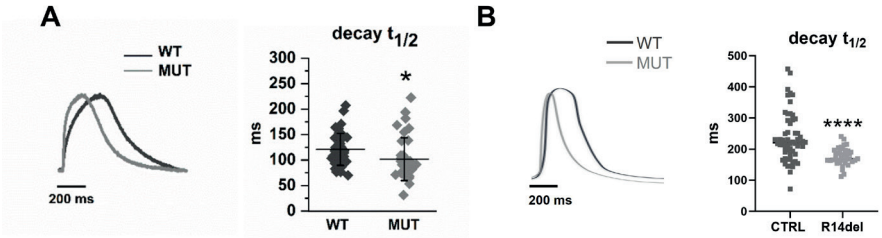

Figure 2. Intracellular calcium cycling in PLN-R14del hiPSC-CMs compared to control. (**A**) Calcium transient and corresponding decay time modified from the study by Badone et al.[76] (**B**) Calcium transient and corresponding decay time modified from **Chapter 12**.

SERCA2a function is modulated by the binding of PLN. Over the last decade, more PLN-binding partners have been described, including HAX-1 and GM, the anchoring subunit of protein phosphatase 1 (PP1), as well as AKAP the anchoring subunit of protein kinase A (PKA), allowing the fine-tuning of the PLN binding/phosphorylation status and thus, SERCA activity.[77] PP1 dephosphorylates PLN, causing PLN to inhibit SERCA2a's Ca^{2+} pumping. Upon β-adrenergic stimulation, PKA activity increases, whereby PKA phosphorylates PLN, relieving SERCA2a inhibition and enhancing SR Ca^{2+} transport as well as cardiac relaxation.[78] The β-AR mediated phosphorylation of PLN has been shown to occur mainly through the effects of PKA at serine 16, illustrating the importance of this mechanism for beta-adrenergic-induced cardiac relaxation.[79] Importantly, multiple studies described that the deletion of arginine 14 in the PLN-R14del disease, disrupts its R-R-X-S motif.[80,81] This protein motif is required for the phosphorylation by PKA, on only two amino acids higher, serine 16. The missense of arginine 14 could be associated with conformational changes in PLNs coil domain, which is believed to provide flexibility associated with PLN phosphorylation and impaired SERCA2a regulation.[77,82] If the PKA-Ser16 phosphorylation is hampered, the release of PLN from SERCA2a could be delayed. Together, we can hypothesize that the reduced PLN phosphorylation by PKA-Ser16, could result in impaired SERCA2a activation, thereby reducing the SR Ca^{2+} transport (**Figure 3**). Previously, it was described that even if the PLNR14del can be phosphorylated by PKA, it will not reverse the inhibition of SERCA activity, leading to the super-inhibition of SERCA2a.[83] Although SERCA2a super-inhibition by very strong PLN binding in the basal state has been described to be a suitable explanation for the clinical phenotype in PLN-R14del patients, after our observations, this hypothesis makes it difficult to agree with completely. The observed decreased decay time and contractile incompetence in mice and multiple human cardiomyocyte studies provide evidence of the delayed release of PLN-R14del from SERCA2a due to disturbed phosphorylation.[76,84,85] Thus, our observation of decreased calcium parameters (such as amplitude and decay time) and decreased PLN and SERCA2a expression in PLN-R14del spheroids confirmed the decreased SERCA2a activity upon PKA phosphorylation in PLN-R14del CMs (**Chapter 12**). In failing hearts, increased PP1 activity, coupled with

decreased cAMP-pathway signaling, contributes to a decreased cardiac function. The effect of the R14del on the dephosphorylation of PLN by PP1, remains still, unknown. Interestingly, we demonstrated that the AAV-mediated activation of inhibitor-1 (I-1c), an endogenous inhibitor of PP1, restored the PLN-R14del calcium handling abnormalities (**Chapter 12**).

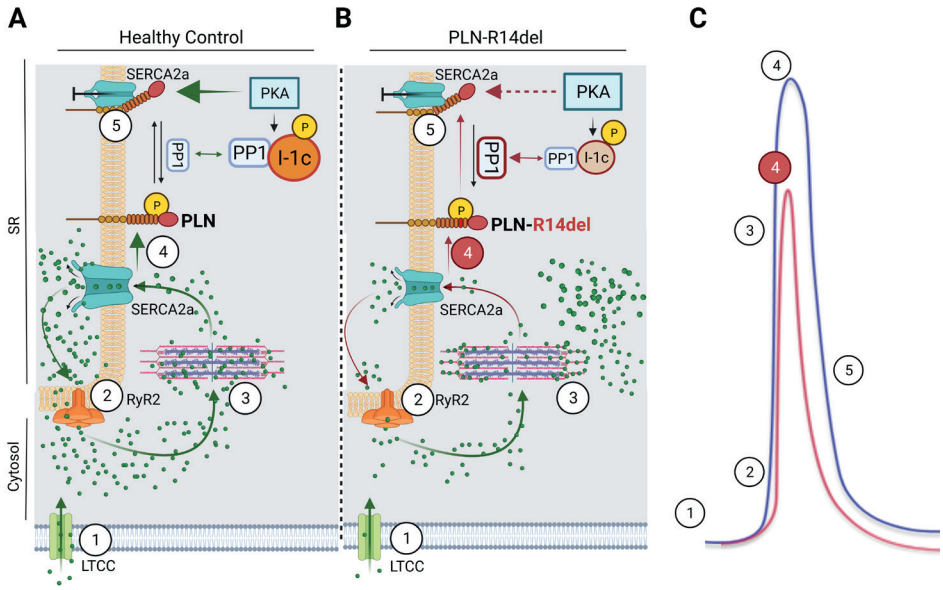

Figure 3. Overview of the calcium handling in healthy cardiomyocytes vs the suggested disturbed calcium handling in PLN-R14del cardiomyocytes. (**A**) Calcium regulation in healthy controls. **A1**) The Ca^{2+} transient begins when membrane depolarization opens L-type Ca^{2+} channels (LTCC). **A2**) The Ca^{2+} influx leads to a sharp rise in Ca^{2+} within the dyadic space, triggering the opening of ryanodine receptors (RyRs) and the release of Ca^{2+} from the sarcoplasmic reticulum (SR). **A3**) Ca^{2+} then binds to the myofilaments, triggering myocyte contraction. **A4**) The Ca^{2+} transient is terminated as RyRs close and Ca^{2+} is removed from the cytosol by the Sarco/endoplasmic reticulum Ca^{2+} ATPase 2a (SERCA2a). **A5**) Relaxation is mediated mainly by PKA phosphorylation of PLN and thereby the dissociation from SERCA2a, increasing the rate of calcium reuptake into the SR. (**B**) Suggested disturbed calcium handling in PLN-R14del cardiomyocytes. **B4**) Impaired phosphorylation of PLN by PKA results in increased cytosolic calcium leading to reduced contractility, UPR activation, mitochondrial dysfunction, and fibroblast activation. (**C**) Ca^{2+} transient time course in cardiac spheroids of isogenic control (blue) and derived from a PLN-R14del patient hiPSC-CMs (red). Numbers around the peak height correspond to the calcium handling regulation order described in **3A** and **3B**. Created with BioRender.com.

If SERCA2a does not function as well in removing Ca^{2+} from the sarcoplasm, this could lead to two consequences: 1) there is an increase in resting sarcoplasmic Ca^{2+} that contributes to reduced relaxation and diastolic dysfunction; and 2) there is less Ca^{2+} released from the sarcoplasmic reticulum during contraction, which means that the force of contraction is reduced. The decreased contractile function has been described in patients[86], mice[87], and hiPSC-CMs[84] harboring the PLN-R14del mutation. In **Chapter 9**, we also observed a 50% force reduction in EHTs from PLN-R14del hiPSC-CMs. The rapid change in free Ca^{2+} levels in the

cytoplasm is essential for the proper initiation of muscle contraction and relaxation. Therefore, the chronic accumulation of Ca^{2+} in the cytosol due to the reduced SERCA2a activation can affect the contractile function in PLN-R14del. Additionally, upon high cytosolic Ca^{2+} levels, the protein folding capacity of the endoplasmic reticulum (ER) is reduced, which leads to the accumulation and aggregation of unfolded proteins, resulting in ER stress. As a result, this ER stress leads to the activation of three ER-resident transmembrane proteins of the unfolded protein response (UPR). The UPR can greatly impact the folding capacity and can eventually induce ER stress-mediated apoptosis. In the myocardium of PLN-R14del patients, we observed the aggregation of PLN proteins, similarly, we observed the increased presence of UPR regulators in both PLN-R14del hearts and the metabolically matured hiPSC-CMs (**Chapter 9**). So, the observed ER stress by the Ca^{2+} imbalance could be described as another pathological result of the PLN-R14del.

Moreover, mitochondria regulate Ca^{2+} dynamic oscillation due to their high Ca^{2+}-buffering capacity.[88] Mitochondrial Ca^{2+} overload in the PLN-R14del CMs could therefore, increase mitochondrial Ca^{2+} uptake, which in turn leads to altered metabolism and increased production of ROS.[89] In **Chapter 8**, we studied the decline of fatty acid oxidation (FAO) metabolism transcription in both PLN-R14del hearts and hiPSC-CMs. Here, we found, for the first time, that PLN-R14del hiPSC-CMs displayed a lower FAO profile than the controls at both mRNA and functional levels. Additionally, we observed many PLN-R14del hiPSC-CMs filled with large lipid droplets, indicating the profoundly impaired lipid utilization metabolism. Recently, De Bortoli *et al*. revealed similar a lower overall density of sodium current and a higher intracellular lipid accumulation in ACM patient-derived hiPSC-CMs compared to asymptomatic hiPSC-CMs.[90] Therefore, it is tempting to speculate that the Ca^{2+} overload in PLN-R14del CMs could induce mitochondrial dysfunction, which could lead to a reduction in the FAO metabolism. However, the precise pathophysiological effect of the overload on mitochondrial Ca^{2+} transport machinery needs further exploration.

Lastly, cardiac fibrosis has been found in histological examination of heart tissues from PLN-R14del patients with end-stage disease.[91,92] Interestingly, a specific predominance of fibrosis in the inferolateral wall of the left ventricle in PLN-R14del carriers was observed, together with a preserved LV systolic function.[93] This finding could suggest that cardiac fibrosis is an early feature of PLN-R14del cardiomyopathy before LV function decreases. In fact, recent data show that total collagen turnover correlates weakly to moderately with clinical parameters in PLN-R14del patients.[94] In **Chapter 12**, we described for the first time, the upregulation of multiple markers known for myofibroblast activation in an *in vitro* PLN-R14del model by single-cell sequencing. Interestingly, we found that the cardiac spheroids massively increased in size over time, together with the loss of calcium-handling activity. Moreover, in **Chapter 12**, we combined hiPSC-derived cardiac fibroblasts and CMs in various ratios and observed the increase of PLN-R14del spheroid size when combining 50% or more hiPSC-CMs in the spheroids. This preliminary experiment suggests that the increase in size is caused by the PLN-

R14del CMs, rather than the initial amount of cardiac fibroblasts in the spheroids. Recently, cardiac spheroids treated with ISO/hypoxia/TGFβ1 to induce cardiac injury revealed the downregulation of several calcium handling, ion channels, fatty acid metabolism-related genes, and the upregulation of ECM and fibroblast activation genes.[95] Nonetheless, the exact pathophysiological mechanism and trigger behind the fibroblast activation in PLN-R14del cardiomyopathy remains to be investigated.

The chicken or the egg? What is the first trigger of the PLN-R14del phenotype?

In patients, the first described subclinical PLN-R14del disease alteration before the onset of heart failure symptoms is the post-systolic shortening in the left ventricular apex, which is detected by echocardiographic deformation imaging.[96] Accordingly, it was hypothesized by these authors that the dysregulation of intracellular calcium handling in PLN-R14del mutation carriers could lead to altered myocardial mechanical behavior observed in these pre-symptomatic mutation carriers.[97]

In this thesis, we used hiPSC-CMs and described the impaired SERCA2a activation, reduced contractile force, the activation of ER stress, fibroblast activation, and the reduced FAO metabolism in the PLN-R14del disease. However, one big question remains; *What is the first trigger of the PLN-R14del phenotype?* Meaning; *Which came first, the chicken or the egg?* Understanding the underlying pathophysiology of the PLN-R14del disease would improve insights into a patient's disease course and would create the opportunity for conceiving treatment strategies. After so many intense years of studying the PLN-R14del phenotype *in vitro*, the onset of the observed PLN-R14del hiPSC-CMs phenotypes described in this thesis differs. First, on day 30 (spheroids week 1), impaired calcium handling is observed (**Chapter 12**). Next, on day 42 post differentiation, we described the reduced contractility and UPR activation (**Chapter 9**). The fibroblast activation seems to occur after 2 weeks of spheroids culturing, also around differentiation day 42 (**Chapter 12**). Later, between days 60 and 180, lipid droplet accumulation in hiPSC-CMs is observed (**Chapter 8**). However, both contractility and the metabolic phenotype have been described in earlier 2D and 3D models (day ~30).[84] Together, in this thesis we successfully recapitulate the diverse phenotype, highlighting the utility of hiPSC-CMs in modeling more complex cardiac diseases.

Overall, a reduced SERCA2a activity has been described to increase cytosolic Ca^{2+} levels, resulting in mitochondrial and ER stress, ventricular arrhythmias, reduced contractility, and eventually heart failure.[98,99] After combining all our data described in this thesis, we would like to propose the following onset of the PLN-R14del phenotype hypothesis (**Figure 4**).

1) First, The mutation of arginine 14 causes a conformation change, resulting in the reduced PLN phosphorylation by PKA-Ser16 and thereby delayed release of PLN from SERCA2a, 2) The impaired SERCA2a activation, reduces the SR Ca^{2+} transport, leading to Ca^{2+} overload.

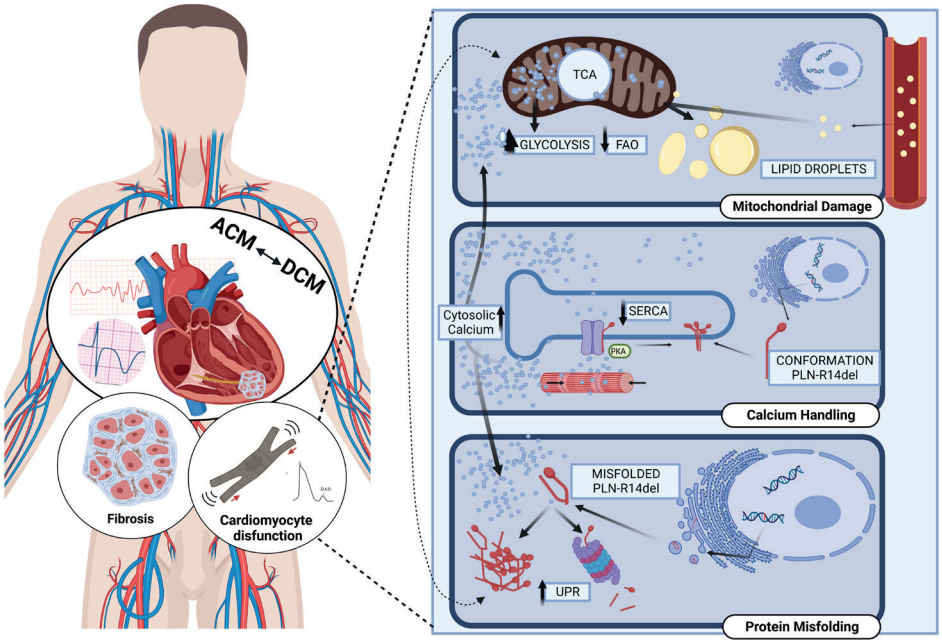

Figure 4. Overview of the potential pathological mechanisms leading to PLN-R14del induced heart failure. Right panels display the initial molecular mechanisms and the effect of the PLN-R14del on the PLN conformation leading to a reduced SERCA activity, increased cytosolic calcium, increased mitochondrial damage and glycolysis, and misfolded PLN-R14del leading to increased UPR and protein aggregation. Left panels describe the secondary effect of the mutation, with cardiomyocyte dysfunction and fibrosis, leading to an ACM and/or DCM phenotype in the PLN-R14del patient. Abbreviations: TCA; The tricarboxylic acid cycle, FAO; Fatty acid oxidation pathway, PKA; protein kinase A. ACM; Arrhythmogenic cardiomyopathy, DCM; Dilated cardiomyopathy. Created with BioRender.com.

3) The Ca^{2+} overload may increase the Ca^{2+} in different structures (e.g. SR, cytoplasm, and mitochondria) to an excessive level, which induces electrical and mechanical abnormalities such as arrhythmias and a decrease in the force of contraction. 4) Additionally, toxic levels of Ca^{2+} in the ER can severely impact folding capacity. The toxic increase of mitochondrial Ca^{2+} leads to altered metabolism and increased production of ROS, triggering cell death. Intracellular Ca^{2+} activates the calcineurin/NFAT, ERK1/2, ROS/RhoA, and sFRP2 pathways to promote profibrotic gene expression.[100] For the last 3 pathologic observations, however, it remains unknown which pathway fails first, triggering the others to fail as well, or if all events happen at the same time. For example, high UPR activation in the CM could cause mitochondrial UPR activation and trigger mitochondrial damage, or the increased mitochondrial Ca^{2+} concentration triggers mitochondrial damage, thereby activating the UPR. Additionally, the activation of profibrotic pathways could also be caused by cardiomyocyte apoptosis, rather than elevated intracellular Ca^{2+} levels. Finally, since the PLN-R14del

disease leads to multiple pathological phenotypes, gaining a better understanding of the Ca^{2+} signaling function, and how the delayed SERCA2a activation influences contractility, mitochondrial damage, UPR activation, and fibrosis, is an important challenge. As proposed in **Chapter 12**, multi-omics approaches such as RNA sequencing and proteomics with spheroids from different culture ages could identify the spatiotemporal processes to identify mechanistic insights in the 'first to fail' mechanism of the PLN-R14del cardiomyopathy. These outcomes will provide new insights into finding a therapeutic target that could delay or even better, prevent the disruption of phosphorylation-mediated calcium cycling abnormality in the PLN-R14del-associated cardiomyopathy.

Towards the future - Therapeutic interventions for genetic cardiomyopathies

Detailed signaling pathways that promote cardiac pathology have been unraveled, and we continue to discover important molecular targets that have important roles in the pathologic pathway regulation of cardiomyopathies. Many therapeutic interventions have been tested in both animal models and hiPSC-CMs to cure PLN-R14del cardiomyopathy. For example, two promising drugs targeting myosin (the sarcomeric motor protein); activator Omecamtiv Merabil (FDA approved) and inhibitor Mavacamptem (Clinincal Trial III) have been tested in humanized PLN-R14del mice. Myosin activation by Omecamtiv Merabil could improve contractile dysfunction in RV myocytes, while the myosin inhibitor Mavacamptem had no effects.[101] Since Omecamtiv Merabil did not improve Ca^{2+} handling parameters and the continuous activation of resting myosin ATPase, could limit its clinical benefits in the current treatment options for the PLN-R14del cardiomyopathy. Another therapeutic intervention, the antifibrotic agent Epelerone, did not improve the contractile dysfunction or reduce disease progression in both PLN-R14del mice nor in a clinical trial with 42 presymptomatic PLN-R14del carriers.[87,102] Taken together, unfortunately, targeting the contractile dysfunction or fibrosis did not improve the PLN-R14del phenotype.

As previously described in this thesis, we explored the potential therapeutic strategies for activating the FAO metabolism (**Chapter 8**), modulating the UPR pathway (**Chapter 9**), and SERCA activity (**Chapter 12**) for curing the PLN-R14del cardiomyopathy. In **Chapter 8**, we showed for the first time, the potential of bezafibrate in re-activating mitochondrial FAO and improving Ca^{2+} transients, suggesting future therapeutic strategies for PLN-R14del patients by targeting FAO regulators (i.e. PPARA). In **Chapter 9**, we used a compound called BiX (binding immunoglobulin protein) inducer X), to modulate the UPR activation in PLN-R14del hiPSC-CMs. BiX showed a dose-dependent amelioration of the contractility deficit in both 2-dimensional cultures and 3-dimensional models without affecting the calcium homeostasis. However, the detrimental effect at high doses limits the application of BiX as a therapeutic strategy because it may activate the ER stress pathway, inducing apoptosis. In a recent study by Ouwerkerk *et al*., genomic, transcriptomic, proteomic, and clinical data from 1738 patients with heart failure identified pathways related to the progression of heart failure and early mortality.[103] ERBB

receptors and their downstream effects on the PI3K and MAPK pathways were identified as the strongest pathways for cardioprotective effects. Interestingly, Neuregulin, an ERBB receptor ligand, is currently in the early phase of clinical development in patients with HFrEF.[104] Both metabolic and cell stress interventions are important for the modulation of downstream pathways that are affected by the PLN-R14del mutation.

As PLNs main function is the regulation of calcium by the modulation of SERCA, multiple therapeutic strategies have been tested to modulate calcium handling. The CaMKII inhibitor KN93 reversed the proarrhythmic phenotype in myocytes of PLN-R14del mice, consequently suggesting its anti-arrhythmic application and especially potentially preventing SCD.[105] On the contrary, Metoprolol (β-blocker) significantly decreased the heart rate and showed no increase in the survival rate of PLN-R14del mice.[87] Given the molecular effects of β-blocker are not based on a modulation of CaMKII, it seems the community is open and motivated for new pharmacologic drugs for CaMKII inhibition. Ca^{2+}-binding proteins GCaMP6f and parvalbumin mainly reduced the UPR expression and led to dynamic alterations within the ER-mitochondrial compartment.[84] Interestingly, GCaPM6f was associated with significantly improved force development in PLN-R14del EHTs, but not parvalbumin. Recently, in homozygous PLN-R14del mice, reduced calcium handling, PLN aggregation, and fibrosis were all observed within 5 weeks of age. The overexpression of Dwarf open reading frame (DWORF) counteracts the PLN regulatory calcium handling function in the sarco/endoplasmic reticulum (S/ER) and reveals delayed PLN aggregates and prolonged the life span in PLN-R14del Cardiomyopathy Mice.[85] Both therapeutic strategies targeting Ca^{2+}-binding and regulation revealed mainly the cardioprotective effect in ER/UPR alternations, rather than a direct effect on improved calcium regulation or contractility. If the PLN-R14del results in enhanced calcium reuptake, rather than the previously described super-inhibition, increasing calcium S/ER reuptake could be ineffective in PLN-R14del cardiomyopathy and need to be further evaluated before more therapeutic testing.

Therapeutic therapies targeting intracellular gene expression hold great promise for the modification of deranged intracellular signaling that is often difficult to target in cardiomyopathies with traditional drug therapies. For genetic cardiomyopathies, we have the opportunity to target or restore the genetic abnormality affected by the genetic mutation, rather than improving only the affected downstream pathways. Therapeutic genes can be delivered either by using genetic material or by non-viral or viral carriers containing the DNA or RNA of interest. Viral vector transgene delivery vehicles such as lentiviruses, adenoviruses, and adeno-associated viruses (AAV), are more efficient than naked or non-viral vector delivery in crossing the cardiomyocyte membrane. AAVs contain single-stranded DNA, producing long-term expression, with a low immune response. All of the viral vectors provide safe gene delivery but their gene-transduction efficacy in the human heart remains suboptimal. To overcome this limitation, AAVs have the possibility to design tissue tropism from 13 serotypes and the ability to transduce both dividing and non-dividing cells, making this viral

approach the most interesting for the human heart. One phase IIb trial (CUPID2) explored the upregulation of SERCA2a, for the treatment of heart failure. Here, no safety issues or adverse effects were observed, but unfortunately, the delivery of SERCA2a by AAV1 did not improve symptoms of heart failure in patients [106], possibly due to the low intravenous AAV dosage. Other therapeutic strategies targeting SERCA activity, such as istraoxime and PST3093, have been tested to alleviate the PLN-R14del phenotype. Although Istraoxime in zebrafish ameliorates the *in vivo* Ca^{2+} dysregulation and improves cardiac relaxation[107], PST3093 was not effective in PLN-R14del hiPSC-CMs[76] and mice[108] but affected Ca^{2+} dynamics parameters in the isogenic hiPSC-CMs. These therapeutic outcomes argue against SERCA2a super-inhibition as a mechanism of PLN-R14del.

In an *in vitro* study, hiPSC-CMs harboring the PLN-R14del disease were treated with a combinatorial gene therapy approach by the overexpression of a miRNA-resistant PLN in an AAV6 vector to achieve the PLN gene correction. Interestingly, AAV6-mediated overexpression of PLN reduced the frequency of arrhythmogenic episodes when compared with non-infected cells.[109] However, the hypertrophy markers, ANF, and BNP were significantly increased after AAV6 infection, suggesting a general stress response of AAV vectors in CM homeostasis. Therefore, the transgene expression of different serotypes could be used to improve the targeting of the organ of interest and thereby reduce the off-target effect and immune response. Interestingly, instead of AAV1 or AAV6, AAV9 has now become the method of choice for introducing genetic material into the heart, due to its ability to effectively transduce adult rodent hearts[110] and hiPSC-CMs[111]. Recently, capsid re-engineering of adeno-associated vectors to a hybrid AAV2/8 and AAV2/9 virus has been reported to have up to 5-100 fold higher efficiency for transgene delivery as compared to AAV2 serotypes and are proven safe in rodent cardiomyocytes.[112–114] Overall, the advanced AAV technology using suitable serotypes and hybrids, enables the generation of safe, effective viral delivery for any gene of interest. However, cardiac-specific delivery of therapeutic materials *in vivo* remains challenging, due to the invasive high systemic doses that potentially could lead to cardiomyocyte toxicity and systemic inflammation. For example, recently a young man with Duchenne Muscular Dystrophy died just days after receiving AAV9 due to an innate immune reaction that caused multi-organ failure including his heart, attributed to the high dose of the gene therapy.[115]Here, extracellular vesicles hold immense potential for the delivery of therapeutic agents, as this carrier is stable, biocompatible, and therefore non-mutagenic, less immunogenic, and non-cytotoxic.[116] Moreover, lessons from the improved transfection efficiency in expanding hiPSC-CM (**Chapter 5**) could help to identify factors that regulate cardiac uptake of therapeutic materials in adult CMs. Likely, the molecular insights of this promising pro-proliferative factor CHIR99021 (CHIR) contribute to not only optimizing the generation of hiPSC-CM but also potential transfection, and transduction, which is essential to overcoming the current delivery inefficiency. Unfortunately, we showed that the *in vivo* administration of CHIR during late gestation resulted in a 1.8-fold increase in mitotic CMs, while we observed a progressive decline in the proliferative capacity of postnatal mouse cardiomyocytes (**Chapter**

3). This finding indicates that GSK-3β inhibition alone is not sufficient to stimulate cardiac proliferation in the postnatal and adult phases.

Previously, the administration of a constitutively active inhibitor-1 (I-1c) delivered by the cardiotropic AAV2/8 (BNP116) virus in ischaemic heart failure pigs improved cardiac function (LV EF +5.7%).[117] I-1 decreases protein phosphatase 1 (PP1) activity, thereby upstream regulating the SERCA2a/phospholamban complex, and is also closely linked to the β-adrenoceptor system. Upon activation of I-1c, PP-1 is suppressed, thereby increasing SERCA2a activity and phospholamban phosphorylation and enhancing basal cardiac function.[118] In heart failure patients, PP-1 levels are increased, resulting in a decreased PLN phosphorylation.[119] Decreased PLN phosphorylation promotes binding to SERCA2a, leading to decreased SERCA2a activity.[120] The reduced SERCA2a activity is associated with a defect in cardiomyocyte Ca^{2+} cycling and impaired cardiac contractility.[121] As described in this discussion (**Chapter 13**), the PLN-R14del mutation causes a reduced sensitivity of Ser16 phosphorylation by PKA, causing the loss of SERCA2a activation. Thus, we hypothesized that PLN-R14del will be amenable to treatment by AAV-mediated overexpression of I-1c, by alleviating the detrimental effects of SERCA2a regulation through specific modulation of the PLN-coupled PP1 activity. In **Chapter 12**, we aimed to test this hypothesis, by first modeling the cellular phenotype of the PLN-R14del disease in 3D spheroids grown in 384-wells for 3 weeks. After 2-3 weeks, PLN-R14del spheroids recapitulated the cellular phenotype associated with the clinical features of the disease, including abnormal structure, decreased calcium handling activity, increased fibrosis, and decreased cardiac gene expression. Next, we treated the spheroids with a single addition of the AAV-based I-1c gene therapy for 1 week and used kinetic high-throughput screening analysis of intracellular calcium handling activity. AAV-mediated I-1c gene augmentation therapy restored normal calcium handling function, increased cardiac gene expression, and reduced the fibroblast activation in patient-derived and genome-edited PLN-R14del hiPSC lines. To the best of our knowledge, we showed in **Chapter 12** the first proof of concept that the I-1c AAV2/8-based gene therapy has the potential to be used for the treatment of genetic cardiomyopathy modeled in hiPSC-CMs. Although the partial restoration of the calcium function and structure may be enough to preserve cardiac function in patients with PLN-R14del cardiomyopathy, the therapeutic targeting of the PLN-gene itself could hold even better promise for the genetic modification of the PLN-R14del disease. As previously described, the AAV6-mediated overexpression of PLN reduced the frequency of arrhythmogenic episodes in a PLN-R14del patient.[109] The combination of AAV2/8, AAV9, or AAV2/9 with the overexpression of PLN could offer the perfect strategy for efficient delivery and optimal restoration of the PLN-R14del phenotype.

In the far future, gene editing approaches such as CRISPR-CAS or prime editing will allow the editing of the specific gene causing the pathologic mutation[122], although the limitations of the off-target effects, delivery, and immunogenic toxicity need to be overcome. Therefore,

until safe gene-editing therapies are developed, preimplantation genetic diagnosis (IVF) for the disease-causing variant could be considered, although this decision causes a significant emotional burden.[123]

Can we use hiPSC-CMs to find a cure for genetic cardiomyopathies?

hiPSCs represent individual donor genetics and with the recent hiPSC reprogramming technology, creating many patient-derived hiPSC lines is now feasible. Subsequently, we speculate on the potential broader future implications of hiPSC-CM models and this chapter will conclude with an attempt to answer the central question of this thesis: ''*Can we use hiPSC-CMs to find a cure for genetic cardiomyopathies?''* Here, the motivation towards realizing the hiPSC-CMs full potential of precision medicine is two-fold: first, to study and elucidate the molecular mechanisms caused by a pathological variant; and second, to screen for new therapeutic strategies for these cardiac pathologies.

The prediction of the individual phenotype of hiPSC-CM could make it possible to focus on preventive actions and avoid the disease burden from those without any signs of disease at the heart failure level. Interestingly, in this thesis, we observed that individual cardiomyocytes can develop different degrees of lipid droplet accumulation (**Chapter 8**) or UPR activation and PLN aggregates (**Chapter 9**). A potential hypothesis for this phenotypic mosaic pattern in some of the PLN-R14del cardiomyocytes could be the allelic imbalance. In heterozygous patients with mutations that alter protein function and biomechanical properties of a cell, the imbalanced allelic expression may cause functional heterogeneity from cell to cell, which could exacerbate disease phenotype. Previously the allelic imbalance has been demonstrated in both DCM[124] and HCM hearts[125] which could be linked to the genetic or epigenetic risk for disease and the biological traits of an individual cell.[126,127] An improved understanding of the influence of both environmental and genetic modifiers should ultimately be studied in the future to understand the causal genetic variation in each cardiomyocyte and patient. These findings will contribute to the longevity of CMs despite the imbalance transcription of the PLN-R14del mutation and could predict and prevent the onset of the disease in each individual.

In this thesis, we showed that multi-omics analysis of metabolically matured hiPSC-CMs could be considered the first fingerprinting for the pathological features of the disease (**Chapter 8**, **Chapter 9**). In the human body, cells do not function in mono-lineage isolation. Thus, the understanding of disease may require multi-cellular, integrated platforms, which exhibit distinct advantages over mono-lineage analyses. Microtissues such as organoids or spheroids could be used, allowing the study of hundreds of 3D conditions with relatively low amounts of cells and costs. Cardiac spheroids offer great potential for the biobanking and personalized screening of all therapeutic strategies for personalized disease modeling in cardiomyopathy patients (**Chapter 11**, **Chapter 12**). Automated kinetic analysis of individual cells and 3D constructs offers the opportunity for high-throughput screenings of many individuals' hiPSC-CMs. As previously

described, the hiPSC-CM offers a robust and reproducible platform "clinical trials in a dish" (CTiD) with a future reality of commercialization by revolutionizing our thinking about the applications of HTS in the field of drug discovery across the pharmaceutical industry. The implementation of hiPSC-CMs allows the testing of therapeutic targets and hit compounds during the early stages of drug discovery and chemical optimization. Still, any of these deviations could potentially raise differences between lines' subsequent responses and could be an artifact of variation during the screening, rather than a reflection of the underlying biological pathology[128]. Therefore, we advise increasing and testing the inter- and intra-batches coefficient, thereby allowing the identification of ''physiological'' and ''pathological'' differences. Still, we would recommend the improvement of hiPSC-CM standardization and quality control, as well as clear guidelines for designing and executing any *in vitro* studies testing therapeutic strategies, including CTiD studies. Then, in the future, it may be possible to study the chronic side effects of prolonged treatment and rare drug effects may be rapidly identified *in vitro*.

One impressive example of *in vitro* 3D models for personalized medicine is the discovery of rectal organoids in Dutch cystic fibrosis (CF) patients. Within only 4 years, the first person received treatment for CF based on drug efficacy in CF organoid swelling assays.[129] Now, over 700 organoid models derived from rectal biopsies of CF patients, representing over 100 clinically relevant mutations, are biobanked.[130] The future could hold the potential to biobank every CF patient (1500 in the Netherlands) to improve research and to evaluate *in vitro* the effectiveness of novel compounds. Instead of subscribing to a drug based on the largest statistical population, these CF organoids could be cheap avatars for a patient's personalized disease modeling, characterizing the disease even before these young patients develop symptoms. However, only five classes of CF gene mutations exist to disturb protein production, processing, gating, conduction, and function. Therefore, the *in vitro* modeling and screening of cardiomyopathies might be far more challenging, considering that over 50 individual genes (and counting) are affected, causing completely variable pathophysiological phenotypes such as DCM, HCM, and ACM.[131–134] Still, the impressive CF *in vitro* disease modeling set the example for the future of personalized medicine in individuals with a risk of developing heart failure. The generation of such a system will not only help patients but will also allow prevention of the onset of the disease and predict the drug efficacy and toxicity for each individual.[135] This allows cardiologists to move from the current 6 types of standard heart failure medication to the best match for treating or even preventing the disease as early as possible.

In summary, the work described in this thesis has contributed to a realistic view of the possibilities and current limitations of hiPSC-CMs for the disease modeling of genetic cardiomyopathies. While keeping eventual clinical implications in mind, hiPSC-CM research was taken from the basic to the translational level (**Figure 5**). The journey from many hiPSC lines to the HTS of thousands of spheroids that predict the disease and potential therapeutic targets is paving the way for the future of predicting, preventing, and personalized medicine of all cardiomyopathies.

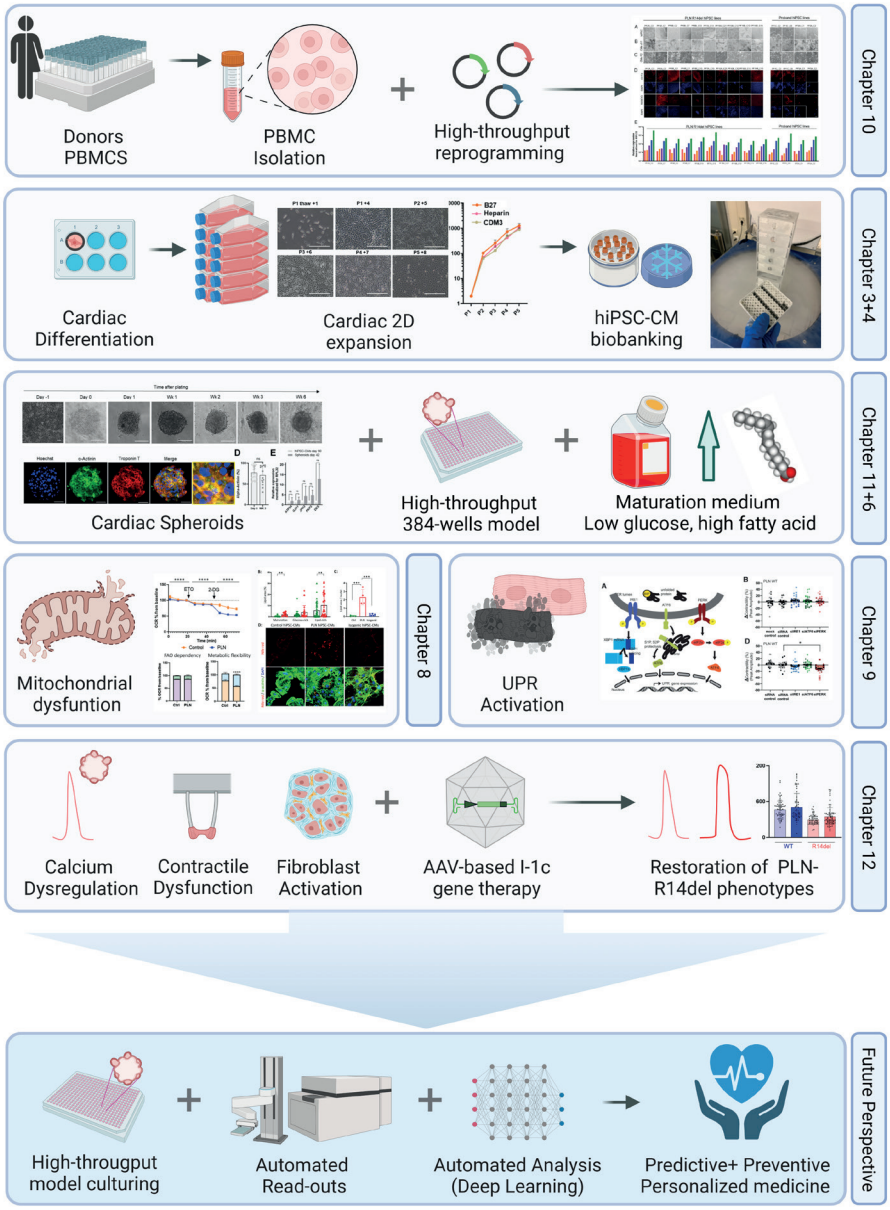

Figure 5: Roadmap for employing high-throughput platforms in assessing disease phenotyping and novel therapeutic screening for predictive, preventive, and personalized medicine. Created with BioRender.com.

REFERENCES

1. McKenna, W. J. & Judge, D. P. Epidemiology of the inherited cardiomyopathies. Nat. Rev. Cardiol. 18, 22–36 (2020).
2. He, J. et al. Arrhythmogenic Left Ventricular Cardiomyopathy: A Clinical and CMR Study. Sci. Rep. 10, 1–12 (2020).
3. Becker, C. & Hesse, M. Role of Mononuclear Cardiomyocytes in Cardiac Turnover and Regeneration. Curr. Cardiol. Rep. 22, (2020).
4. Macmahon, H. E. Hyperplasia and Regeneration of the Myocardium in Infants and in Children. Am. J. Pathol. 13, 845–854.5 (1937).
5. Haubner, B. J. et al. Functional Recovery of a Human Neonatal Heart After Severe Myocardial Infarction. Circ. Res. 118, 216–221 (2016).
6. Johnson, J., Mohsin, S. & Houser, S. R. Cardiomyocyte Proliferation as a Source of New Myocyte Development in the Adult Heart. Int. J. Mol. Sci. 22, (2021).
7. Multi-lineage Human iPSC-Derived Platforms for Disease Modeling and Drug Discovery. Cell Stem Cell 26, 309–329 (2020).
8. Kamakura, T. et al. Ultrastructural maturation of human-induced pluripotent stem cell-derived cardiomyocytes in a long-term culture. Circ. J. 77, (2013).
9. Lundy, S. D., Zhu, W. Z., Regnier, M. & Laflamme, M. A. Structural and functional maturation of cardiomyocytes derived from human pluripotent stem cells. Stem Cells Dev. 22, (2013).
10. Ebert, A. et al. Proteasome-Dependent Regulation of Distinct Metabolic States During Long-Term Culture of Human iPSC-Derived Cardiomyocytes. Circ. Res. 125, 90–103 (2019).
11. Feyen, D. A. M. et al. Metabolic Maturation Media Improve Physiological Function of Human iPSC-Derived Cardiomyocytes. Cell Rep. 32, 107925 (2020).
12. Chirico, N. et al. Small molecule-mediated rapid maturation of human induced pluripotent stem cell-derived cardiomyocytes. Stem Cell Res. Ther. 13, 531 (2022).
13. Hu, D. et al. Metabolic Maturation of Human Pluripotent Stem Cell-Derived Cardiomyocytes by Inhibition of HIF1α and LDHA. Circ. Res. (2018) doi:10.1161/CIRCRESAHA.118.313249.
14. Paredes, A. et al. γ-Linolenic acid in maternal milk drives cardiac metabolic maturation. Nature 618, 365–373 (2023).
15. Peters, M. C. et al. Metabolic Maturation Increases Susceptibility to Hypoxia-induced Damage in Human iPSC-derived Cardiomyocytes. Stem Cells Transl. Med. 11, (2022).
16. Maurya, S. et al. Outlining cardiac ion channel protein interactors and their signature in the human electrocardiogram. Nature Cardiovascular Research 2, 673–692 (2023).
17. Ottaviani, D., Ter Huurne, M., Elliott, D. A., Bellin, M. & Mummery, C. L. Maturing differentiated human pluripotent stem cells in vitro: methods and challenges. Development 150, (2023).
18. Marchiano, S. et al. Gene editing to prevent ventricular arrhythmias associated with cardiomyocyte cell therapy. Cell Stem Cell 30, 396–414.e9 (2023).
19. Kucera, J. P., Prudat, Y., Marcu, I. C., Azzarito, M. & Ullrich, N. D. Slow conduction in mixed cultured strands of primary ventricular cells and stem cell-derived cardiomyocytes. Frontiers in cell and developmental biology 3, (2015).
20. Poelzing, S. & Rosenbaum, D. S. Altered connexin43 expression produces arrhythmia substrate in heart failure. Am. J. Physiol. Heart Circ. Physiol. 287, (2004).
21. Vreeker, A. et al. Assembly of the cardiac intercalated disk during pre- and postnatal development of the human heart. PLoS One 9, (2014).
22. Hinson, J. T. et al. Titin Mutations in iPS cells Define Sarcomere Insufficiency as a Cause of Dilated Cardiomyopathy. Science 349, 982 (2015).
23. Kumar, A., He, S. & Mali, P. Systematic discovery of transcription factors that improve hPSC-derived cardiomyocyte maturation via temporal analysis of bioengineered cardiac tissues. APL bioengineering 7, (2023).

24. Cheng, S. et al. Single-cell RNA sequencing reveals maturation trajectory in human pluripotent stem cell-derived cardiomyocytes in engineered tissues. iScience 26, (2023).

25. van Mil, A. et al. Modelling inherited cardiac disease using human induced pluripotent stem cell-derived cardiomyocytes: progress, pitfalls, and potential. Cardiovasc. Res. 114, 1828–1842 (2018).

26. Sacchetto, C., Vitiello, L., de Windt, L. J., Rampazzo, A. & Calore, M. Modeling Cardiovascular Diseases with hiPSC-Derived Cardiomyocytes in 2D and 3D Cultures. Int. J. Mol. Sci. 21, (2020).

27. Khedro, T., Duran, J. M. & Adler, E. D. Modeling Nonischemic Genetic Cardiomyopathies Using Induced Pluripotent Stem Cells. Curr. Cardiol. Rep. 24, 631–644 (2022).

28. Flam, E. et al. Integrated landscape of cardiac metabolism in end-stage human nonischemic dilated cardiomyopathy. Nat Cardiovasc Res (2022) doi:10.1038/s44161-022-00117-6.

29. Koenig, A. L. et al. Single-cell transcriptomics reveals cell-type-specific diversification in human heart failure. Nat Cardiovasc Res 1, 263–280 (2022).

30. Mori, T. et al. eSPRESSO: topological clustering of single-cell transcriptomics data to reveal informative genes for spatio-temporal architectures of cells. BMC Bioinformatics 24, (2023).

31. Iosef, C. et al. Quantitative proteomics reveal lineage-specific protein profiles in iPSC-derived Marfan syndrome smooth muscle cells. Sci. Rep. 10, 1–15 (2020).

32. Schick, R. et al. Functional abnormalities in induced Pluripotent Stem Cell-derived cardiomyocytes generated from titin-mutated patients with dilated cardiomyopathy. PLoS One 13, (2018).

33. Alexovič, M., Sabo, J. & Longuespée, R. Microproteomic sample preparation. Proteomics 21, (2021).

34. Ma, L. et al. Single-Cell RNA Sequencing and Quantitative Proteomics Analysis Elucidate Marker Genes and Molecular Mechanisms in Hypoplastic Left Heart Patients With Heart Failure. Frontiers in cell and developmental biology 9, (2021).

35. Shoemaker, R. H. The NCI60 human tumour cell line anticancer drug screen. Nat. Rev. Cancer 6, 813–823 (2006).

36. Biendarra-Tiegs, S. M. et al. An iPS-derived in vitro model of human atrial conduction. Physiol Rep 10, e15407 (2022).

37. Giacomelli, E. et al. Human-iPSC-Derived Cardiac Stromal Cells Enhance Maturation in 3D Cardiac Microtissues and Reveal Non-cardiomyocyte Contributions to Heart Disease. Cell Stem Cell vol. 26 862–879.e11 Preprint at https://doi.org/10.1016/j.stem.2020.05.004 (2020).

38. Kahn-Krell, A. et al. A three-dimensional culture system for generating cardiac spheroids composed of cardiomyocytes, endothelial cells, smooth-muscle cells, and cardiac fibroblasts derived from human induced-pluripotent stem cells. Front. Bioeng. Biotechnol. 0, (2022).

39. Kostina, A., Volmert, B. & Aguirre, A. Human heart organoids: current applications and future perspectives. Eur. Heart J. (2023) doi:10.1093/eurheartj/ehad841.

40. Ma, Z. et al. Self-organizing human cardiac microchambers mediated by geometric confinement. Nat. Commun. 6, 1–10 (2015).

41. Kim, H., Kamm, R. D., Vunjak-Novakovic, G. & Wu, J. C. Progress in multicellular human cardiac organoids for clinical applications. Cell Stem Cell 29, 503–514 (2022).

42. Voges, H. K. et al. Vascular cells improve functionality of human cardiac organoids. Cell Rep. 42, (2023).

43. Ergir, E. et al. Generation and maturation of human iPSC-derived 3D organotypic cardiac microtissues in long-term culture. Sci. Rep. 12, 1–21 (2022).

44. Lewis-Israeli, Y. R. et al. Self-assembling human heart organoids for the modeling of cardiac development and congenital heart disease. Nat. Commun. 12, 1–16 (2021).

45. Hesselbarth, R. et al. CHIR99021 Promotes hiPSC-Derived Cardiomyocyte Proliferation in Engineered 3D Microtissues. Advanced Healthcare Materials vol. 10 2100926 Preprint at https://doi.org/10.1002/adhm.202100926 (2021).

46. Voges, H. K. et al. Development of a human cardiac organoid injury model reveals innate regenerative potential. Development 144, 1118–1127 (2017).

47. Antzelevitch, C. The Role of Spatial Dispersion of Repolarization in Inherited and Acquired Sudden Cardiac Death Syndromes. Am. J. Physiol. Heart Circ. Physiol. 293, H2024 (2007).

48. Meier, A. B. et al. Epicardioid single-cell genomics uncovers principles of human epicardium biology in heart development and disease. Nat. Biotechnol. 41, 1787–1800 (2023).

49. Xiang, Y. et al. Fusion of Regionally Specified hPSC-Derived Organoids Models Human Brain Development and Interneuron Migration. Cell Stem Cell 21, (2017).

50. Meijer, E. M. et al. 3D Human iPSC Blood Vessel Organoids as a Source of Flow-Adaptive Vascular Cells for Creating a Human-Relevant 3D-Scaffold Based Macrovessel Model. Advanced biology 7, (2023).

51. Moriwaki, T. et al. Scalable production of homogeneous cardiac organoids derived from human pluripotent stem cells. Cell reports methods 3, (2023).

52. Noordzij, M. et al. Sample size calculations: basic principles and common pitfalls. Nephrol. Dial. Transplant 25, 1388–1393 (2010).

53. Challenges in designing and executing clinical trials in a dish studies. J. Pharmacol. Toxicol. Methods 94, 73–82 (2018).

54. Van Norman, G. A. Phase II Trials in Drug Development and Adaptive Trial Design. JACC. Basic to translational science 4, (2019).

55. Zushin, P.-J. H., Mukherjee, S. & Wu, J. C. FDA Modernization Act 2.0: transitioning beyond animal models with human cells, organoids, and AI/ML-based approaches. J. Clin. Invest. 133, (2023).

56. Denning, C. et al. Cardiomyocytes from human pluripotent stem cells: From laboratory curiosity to industrial biomedical platform. Biochim. Biophys. Acta 1863, 1728–1748 (2016).

57. Comparison of 10 Control hPSC Lines for Drug Screening in an Engineered Heart Tissue Format. Stem Cell Reports 15, 983–998 (2020).

58. Juhola, M., Penttinen, K., Joutsijoki, H. & Aalto-Setälä, K. Analysis of Drug Effects on iPSC Cardiomyocytes with Machine Learning. Ann. Biomed. Eng. 49, 129 (2021).

59. HiPSC-CMs from different sex and ethnic origin donors exhibit qualitatively different responses to several classes of pharmacological challenges. J. Pharmacol. Toxicol. Methods 99, 106598 (2019).

60. Shinozawa, T. et al. Recapitulation of Clinical Individual Susceptibility to Drug-Induced QT Prolongation in Healthy Subjects Using iPSC-Derived Cardiomyocytes. Stem Cell Reports 8, 226 (2017).

61. Stillitano, F. et al. Modeling susceptibility to drug-induced long QT with a panel of subject-specific induced pluripotent stem cells. Elife 6, (2017).

62. Blinova, K. et al. Clinical Trial in a Dish: Personalized Stem Cell–Derived Cardiomyocyte Assay Compared With Clinical Trial Results for Two QT-Prolonging Drugs. Clin. Transl. Sci. 12, 687 (2019).

63. Sharma, A. et al. High-throughput screening of tyrosine kinase inhibitor cardiotoxicity with human induced pluripotent stem cells. Sci. Transl. Med. 9, (2017).

64. Grimm, F. A. et al. A human population-based organotypic in vitro model for cardiotoxicity screening. ALTEX 35, 441 (2018).

65. Population-based high-throughput toxicity screen of human iPSC-derived cardiomyocytes and neurons. Cell Rep. 39, 110643 (2022).

66. Juhola, M., Joutsijoki, H., Penttinen, K., Shah, D. & Aalto-Setälä, K. On computational classification of genetic cardiac diseases applying iPSC cardiomyocytes. Comput. Methods Programs Biomed. 210, (2021).

67. Willi, L. et al. Bioenergetic and Metabolic Impairments in Induced Pluripotent Stem Cell-Derived Cardiomyocytes Generated from Duchenne Muscular Dystrophy Patients. Int. J. Mol. Sci. 23, (2022).

68. Sun, N. et al. Patient-Specific Induced Pluripotent Stem Cell as a Model for Familial Dilated Cardiomyopathy. Sci. Transl. Med. 4, 130ra47 (2012).

69. Lan, F. et al. Abnormal calcium handling properties underlie familial hypertrophic cardiomyopathy pathology in patient-specific induced pluripotent stem cells. Cell Stem Cell 12, (2013).

70. Carvalho, A. B. et al. Action potential variability in human pluripotent stem cell-derived cardiomyocytes obtained from healthy donors. Front. Physiol. 13, (2022).

71. McKeithan, W. L. et al. An Automated Platform for Assessment of Congenital and Drug-Induced Arrhythmia with hiPSC-Derived Cardiomyocytes. Front. Physiol. 8, 766 (2017).

72. Polonchuk, L. et al. Cardiac spheroids as promising in vitro models to study the human heart microenvironment. Sci. Rep. 7, (2017).

73. Takeda, M. et al. Development of In Vitro Drug-Induced Cardiotoxicity Assay by Using Three-Dimensional Cardiac Tissues Derived from Human Induced Pluripotent Stem Cells. Tissue Eng. Part C Methods 24, (2018).

74. Archer, C. R. et al. Characterization and Validation of a Human 3D Cardiac Microtissue for the Assessment of Changes in Cardiac Pathology. Sci. Rep. 8, 1–15 (2018).

75. Haghighi, K. et al. A mutation in the human phospholamban gene, deleting arginine 14, results in lethal, hereditary cardiomyopathy. Proc. Natl. Acad. Sci. U. S. A. 103, 1388–1393 (2006).

76. Badone, B. et al. Characterization of the PLN p.Arg14del Mutation in Human Induced Pluripotent Stem Cell-Derived Cardiomyocytes. Int. J. Mol. Sci. 22, (2021).

77. Vafiadaki, E., Haghighi, K., Arvanitis, D. A., Kranias, E. G. & Sanoudou, D. Aberrant PLN-R14del Protein Interactions Intensify SERCA2a Inhibition, Driving Impaired Ca Handling and Arrhythmogenesis. Int. J. Mol. Sci. 23, (2022).

78. Liu, Y., Chen, J., Fontes, S. K., Bautista, E. N. & Cheng, Z. Physiological and pathological roles of protein kinase A in the heart. Cardiovasc. Res. 118, 386 (2022).

79. Kuschel, M. et al. Ser16 prevails over Thr17 phospholamban phosphorylation in the beta-adrenergic regulation of cardiac relaxation. Am. J. Physiol. 276, (1999).

80. Vostrikov, V. V., Soller, K. J., Ha, K. N., Gopinath, T. & Veglia, G. Effects of naturally occurring arginine 14 deletion on phospholamban conformational dynamics and membrane interactions. Biochim. Biophys. Acta 1848, 315–322 (2015).

81. Qin, J. et al. Structures of PKA–phospholamban complexes reveal a mechanism of familial dilated cardiomyopathy. (2022) doi:10.7554/eLife.75346.

82. Kim, J. et al. Dysfunctional conformational dynamics of protein kinase A induced by a lethal mutant of phospholamban hinder phosphorylation. Proc. Natl. Acad. Sci. U. S. A. 112, (2015).

83. Vostrikov, V. V., Soller, K. J., Ha, K. N., Gopinath, T. & Veglia, G. Effects of naturally occurring arginine 14 deletion on phospholamban conformational dynamics and membrane interactions. Biochim. Biophys. Acta 1848, (2015).

84. Cuello, F. et al. Impairment of the ER/mitochondria compartment in human cardiomyocytes with PLN p.Arg14del mutation. EMBO Mol. Med. 13, (2021).

85. Stege, N. M. et al. DWORF Extends Life Span in a PLN-R14del Cardiomyopathy Mouse Model by Reducing Abnormal Sarcoplasmic Reticulum Clusters. Circ. Res. 133, (2023).

86. van der Zwaag, P. A. et al. Phospholamban R14del mutation in patients diagnosed with dilated cardiomyopathy or arrhythmogenic right ventricular cardiomyopathy: evidence supporting the concept of arrhythmogenic cardiomyopathy. Eur. J. Heart Fail. 14, 1199–1207 (2012).

87. Eijgenraam, T. R. et al. The phospholamban p.(Arg14del) pathogenic variant leads to cardiomyopathy with heart failure and is unreponsive to standard heart failure therapy. Sci. Rep. 10, (2020).

88. Xu, H.-X., Cui, S.-M., Zhang, Y.-M. & Ren, J. Mitochondrial Ca2+ regulation in the etiology of heart failure: physiological and pathophysiological implications. Acta Pharmacol. Sin. 41, 1301 (2020).

89. Abdullah, C. S. et al. Cardiac Dysfunction in the Sigma 1 Receptor Knockout Mouse Associated With Impaired Mitochondrial Dynamics and Bioenergetics. J. Am. Heart Assoc. 7, (2018).

90. De Bortoli, M. et al. Modeling incomplete penetrance in arrhythmogenic cardiomyopathy by human induced pluripotent stem cell derived cardiomyocytes. Comput. Struct. Biotechnol. J. 21, (2023).

91. Ritterhoff, J. & Tian, R. Metabolism in cardiomyopathy: every substrate matters. Cardiovasc. Res. 113, (2017).

92. Sepehrkhouy, S. et al. Distinct fibrosis pattern in desmosomal and phospholamban mutation carriers in hereditary cardiomyopathies. Heart Rhythm 14, 1024–1032 (2017).

93. Te Rijdt, W. P. et al. Myocardial fibrosis as an early feature in phospholamban p.Arg14del mutation carriers: phenotypic insights from cardiovascular magnetic resonance imaging. Eur. Heart J. Cardiovasc. Imaging 20, 92–100 (2019).

94. van der Voorn, S. M. et al. Exploring the Correlation Between Fibrosis Biomarkers and Clinical Disease Severity in PLN p.Arg14del Patients. Front Cardiovasc Med 8, 802998 (2021).

95. Fernandes, I., Funakoshi, S., Hamidzada, H., Epelman, S. & Keller, G. Modeling cardiac fibroblast heterogeneity from human pluripotent stem cell-derived epicardial cells. Nat. Commun. 14, 1–19 (2023).

96. Early Mechanical Alterations in Phospholamban Mutation Carriers: Identifying Subclinical Disease Before Onset of Symptoms. JACC Cardiovasc. Imaging 14, 885–896 (2021).

97. Taha, K. et al. Optimal echocardiographic assessment of myocardial dysfunction for arrhythmic risk stratification in phospholamban mutation carriers. Eur. Heart J. Cardiovasc. Imaging 23, 1492–1501 (2022).

98. MacLennan, D. H. & Kranias, E. G. Phospholamban: a crucial regulator of cardiac contractility. Nat. Rev. Mol. Cell Biol. 4, (2003).

99. Lipskaia, L., Chemaly, E. R., Hadri, L., Lompre, A.-M. & Hajjar, R. J. Sarcoplasmic reticulum Ca2+ ATPase as a therapeutic target for heart failure. Expert Opin. Biol. Ther. 10, 29 (2010).

100. Feng, J. et al. Ca2+ Signaling in Cardiac Fibroblasts and Fibrosis-Associated Heart Diseases. Journal of Cardiovascular Development and Disease 6, (2019).

101. Kumar, M. et al. Myofilament Alterations Associated with Human R14del-Phospholamban Cardiomyopathy. Int. J. Mol. Sci. 24, (2023).

102. de Brouwer, R. et al. A randomized controlled trial of eplerenone in asymptomatic phospholamban p.Arg14del carriers. Eur. Heart J. 44, 4284–4287 (2023).

103. Ouwerkerk, W. et al. Multiomics Analysis Provides Novel Pathways Related to Progression of Heart Failure. J. Am. Coll. Cardiol. 82, 1921–1931 (2023).

104. A Phase II, Randomized, Double-Blind, Multicenter, Based on Standard Therapy, Placebo-Controlled Study of the Efficacy and Safety of Recombinant Human Neuregulin-1 in Patients With Chronic Heart Failure. J. Am. Coll. Cardiol. 55, 1907–1914 (2010).

105. Haghighi, K. et al. Impaired Right Ventricular Calcium Cycling Is an Early Risk Factor in R14del-Phospholamban Arrhythmias. Journal of Personalized Medicine 11, (2021).

106. Greenberg, B. et al. Calcium upregulation by percutaneous administration of gene therapy in patients with cardiac disease (CUPID 2): a randomised, multinational, double-blind, placebo-controlled, phase 2b trial. Lancet 387, 1178–1186 (2016).

107. Kamel, S. M. et al. Istaroxime treatment ameliorates calcium dysregulation in a zebrafish model of phospholamban R14del cardiomyopathy. Nat. Commun. 12, 1–15 (2021).

108. Maniezzi, C. et al. Early consequences of the phospholamban mutation PLN-R14del+/- in a transgenic mouse model. bioRxiv 2023.04.05.535536 (2023) doi:10.1101/2023.04.05.535536.

109. Karakikes, I. et al. Correction of human phospholamban R14del mutation associated with cardiomyopathy using targeted nucleases and combination therapy. Nat. Commun. 6, 1–10 (2015).

110. Bish, L. T. et al. Adeno-Associated Virus (AAV) Serotype 9 Provides Global Cardiac Gene Transfer Superior to AAV1, AAV6, AAV7, and AAV8 in the Mouse and Rat. Hum. Gene Ther. 19, 1359 (2008).

111. Ambrosi, C. M., Sadananda, G., Han, J. L. & Entcheva, E. Adeno-Associated Virus Mediated Gene Delivery: Implications for Scalable in vitro and in vivo Cardiac Optogenetic Models. Front. Physiol. 10, (2019).

112. Wang, Z. et al. Adeno-associated virus serotype 8 efficiently delivers genes to muscle and heart. Nat. Biotechnol. 23, (2005).

113. Ferla, R. et al. Non-clinical Safety and Efficacy of an AAV2/8 Vector Administered Intravenously for Treatment of Mucopolysaccharidosis Type VI. Molecular Therapy. Methods & Clinical Development 6, 143 (2017).

114. Liu, Z. et al. Comparative analysis of adeno-associated virus serotypes for gene transfer in organotypic heart slices. J. Transl. Med. 18, 1–12 (2020).

115. Lek, A. et al. Death after High-Dose rAAV9 Gene Therapy in a Patient with Duchenne's Muscular Dystrophy. N. Engl. J. Med. 389, (2023).

116. Mentkowski, K. I. & Lang, J. K. Exosomes Engineered to Express a Cardiomyocyte Binding Peptide Demonstrate Improved Cardiac Retention in Vivo. Sci. Rep. 9, 10041 (2019).

117. Ishikawa, K. et al. Cardiac I-1c Overexpression With Reengineered AAV Improves Cardiac Function in Swine Ischemic Heart Failure. Mol. Ther. 22, 2038 (2014).

118. Nicolaou, P. et al. Inducible expression of active protein phosphatase-1 inhibitor-1 enhances basal cardiac function and protects against ischemia/reperfusion injury. Circ. Res. 104, (2009).

119. Nicolaou, P., Hajjar, R. J. & Kranias, E. G. Role of protein phosphatase-1 inhibitor-1 in cardiac physiology and pathophysiology. J. Mol. Cell. Cardiol. 47, (2009).

120. Funk, F. et al. Phospholamban pentamerization increases sensitivity and dynamic range of cardiac relaxation. Cardiovasc. Res. 119, (2023).

121. Zhihao, L. et al. SERCA2a: a key protein in the Ca2+ cycle of the heart failure. Heart Fail. Rev. 25, (2020).

122. Nishiyama, T., Bassel-Duby, R. & Olson, E. N. Toward CRISPR Therapies for Cardiomyopathies. Circulation 144, 1525–1527 (2021).

123. Yeates, L. et al. Decision-making and experiences of preimplantation genetic diagnosis in inherited heart diseases: a qualitative study. Eur. J. Hum. Genet. 30, 187–193 (2021).

124. Heinig, M. et al. Natural genetic variation of the cardiac transcriptome in non-diseased donors and patients with dilated cardiomyopathy. Genome Biol. 18, (2017).

125. Burkart, V. et al. Transcriptional bursts and heterogeneity among cardiomyocytes in hypertrophic cardiomyopathy. Front. Cardiovasc. Med. 0, (2022).

126. Yan, H., Yuan, W., Velculescu, V. E., Vogelstein, B. & Kinzler, K. W. Allelic variation in human gene expression. Science 297, 1143 (2002).

127. He, L., Loika, Y. & Kulminski, A. M. Allele-specific analysis reveals exon- and cell-type-specific regulatory effects of Alzheimer's disease-associated genetic variants. Transl. Psychiatry 12, (2022).

128. Matsa, E. et al. Transcriptome profiling of patient-specific human iPSC-cardiomyocytes predicts individual drug safety and efficacy responses in vitro. Cell Stem Cell 19, 311 (2016).

129. Dekkers, J. F. et al. A functional CFTR assay using primary cystic fibrosis intestinal organoids. Nat. Med. 19, 939–945 (2013).

130. HUB Organoid model development. HUB Organoids https://www.huborganoids.nl/biobank/ (2022).

131. Cahill, T. J., Ashrafian, H. & Watkins, H. Genetic Cardiomyopathies Causing Heart Failure. Circ. Res. (2013) doi:10.1161/CIRCRESAHA.113.300282.

132. Jacoby, D. & McKenna, W. J. Genetics of inherited cardiomyopathy. Eur. Heart J. 33, 296 (2012).

133. Richard, P., Villard, E., Charron, P. & Isnard, R. The Genetic Bases of Cardiomyopathies. Journal of the American College of Cardiology vol. 48 A79–A89 Preprint at https://doi.org/10.1016/j.jacc.2006.09.014 (2006).

134. Albakri, A. Inherited cardiomyopathies: A review and pooled analysis of pathophysiology, diagnosis and clinical management. Internal Medicine and Care vol. 3 Preprint at https://doi.org/10.15761/imc.1000135 (2019).

135. Bertero, E., Heusch, G., Münzel, T. & Maack, C. A pathophysiological compass to personalize antianginal drug treatment. *Nat. Rev. Cardiol.* **18**, (2021).

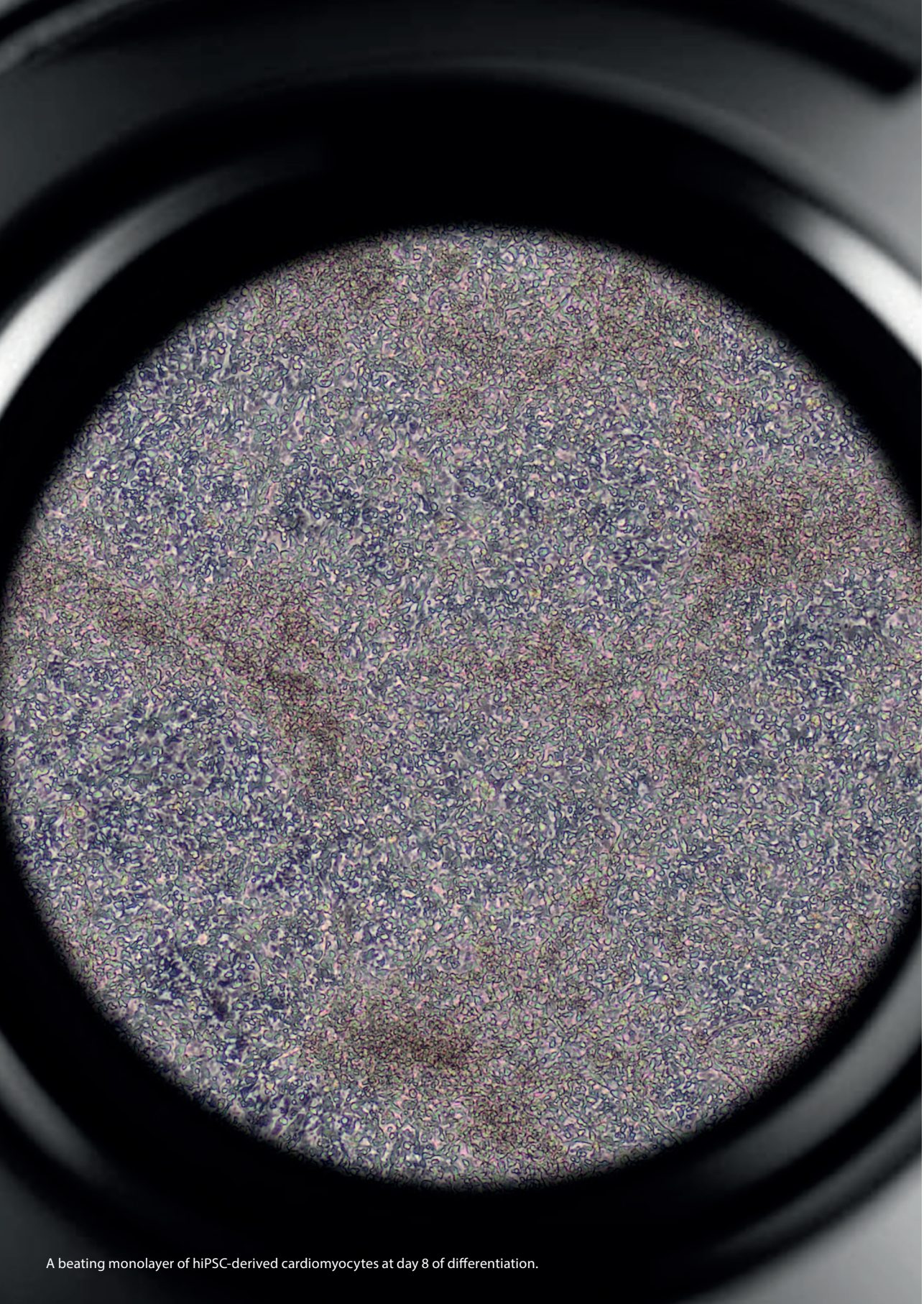

A beating monolayer of hiPSC-derived cardiomyocytes at day 8 of differentiation.

Chapter 14

General Summary

Renée G.C. Maas

GENERAL SUMMARY

The general aim of this thesis was to investigate the potentials of stem cell-derived cardiomyocytes to answer the question ''Can we use stem cell-derived cardiomyocytes to find a cure for genetic cardiomyopathies?''. This aim was achieved using two main parts. In part I, we examined the developmental cues leading to efficient differentiation, expansion, and maturation to study cardiomyocyte division, gene manipulation, and ischemic disease modeling of stem cell-derived cardiomyocytes (hiPSC-CMs) *in vitro*. In part II, disease modeling and therapeutic strategies for the genetic cardiomyopathy PLN-R14del are described.

In **Chapter 1**, we gave a general introduction to the clinical significance of a genetic variation in cardiomyopathies. We highlighted the knowledge derived from cardiogenesis and reproducible methods for the efficient generation of hiPSC-CMs to study the molecular mechanisms of genetic cardiomyopathy processes and contemporary challenges encountered in drug research.

PART I: FROM HEART DEVELOPMENT TOWARDS OPTIMAL CARDIAC IN VITRO MODELS

In **Chapter 2**, we summarize the signals that control human heart size and describe pivotal roles for Wnt and Hippo signaling during embryonic and fetal heart growth. Next, we compared the pathways regulating heart growth *in vivo* with the molecular targets that promote *in vitro* cardiomyocyte proliferation. Lastly, we provide a complete overview of Wnt-signalling-based cardiomyocyte differentiation and cardiomyocyte expansion strategies. With this, we highlight the interaction of signaling pathways in heart development and discuss how this knowledge has been translated into current technologies for cardiomyocyte production.

In **Chapter 3**, we achieved massive expansion of functional hiPSC-CMs in vitro through concomitant GSK-3β inhibition and removal of cell-cell contact. Mechanistically, we demonstrate that GSK-3β inhibition suppresses CM maturation via LEF/TCF activity while stimulating the cell cycle activation by AKT T308 phosphorylation, independent from upregulation of YAP activity. As a proof-of-concept, we demonstrated uncompromised cellular morphology and functionality in engineered heart tissues generated with previously expanded hiPSC-CMs. Lastly, we assessed the late gestational and postnatal CM proliferation *in vivo* and found that CHIR treatment is effective during late gestation but is not sufficient for cardiac regeneration in the postnatal and adult phases of the heart. We conclude that expanded cardiomyocytes have uncompromised cellular functionality making them suitable for multiple translational/regenerative applications.

In **Chapter 4**, we offer a detailed protocol that allows massive expansion (up to a 250-fold increase of CM number within 3-5 weeks) from multiple hiPSC lines. After low cell-density

replating of hiPSC-CMs in culture flasks, the addition of CHIR to the cardiac culture medium efficiently induces hiPSC-CM proliferation up to 37% and subsequent passaging. Moreover, we estimated a price reduction of ~70% when compared to producing the same number of day 20 hiPSC-CMs following the standard Wnt-based differentiation protocol. Lastly, we describe the cryopreservation of expanded cardiomyocytes at passages 1-2 to allow the biobanking of large batches of hiPSC-CMs. We conclude that the removal of cell-cell contact in combination with GSK-3β inhibition is a cost-effective strategy for the massive expansion (> 250-fold) that will greatly facilitate in vitro disease modeling, large-scale drug screening, and in vivo tissue engineering applications.

In **Chapter 5**, we provided insights into sarcomere disassembly during cardiac mitosis and created a tool for gene manipulation studies in hiPSC-CMs. We utilized time-lapse recordings to study the sequence of sarcomere distribution during mitosis, followed by cytokinesis, multinucleation, or self-duplication in massively expanding hiPSC-CMs. We observed that cytokinesis occurred in 13–40%, self-duplication in 1.5–2.5%, and multinucleation in 0.6–1.7% of events. Multinucleation as a result of binuclear cells going through the M phase formed a rare event (0.1–0.2%). We observed that during mitosis of hiPSC-CMs, sarcomere breakdown is predominantly activated during the metaphase, anaphase, and telophase and cells transiently stop contracting during cytokinesis. After cytokinesis and the following G0 or G1/S/G2 phases, the sarcomeres are restored, and spontaneous beating is reinitiated. Secondly, we found that CHIR administration in hiPSC-CMs increased the transfection efficiency to over 30%, which is in the range of conventional non-cardiomyocyte (HEK293) cells. We conclude that sarcomere disassembly is required during cardiomyocyte mitosis and that the increase in sarcomere disassembly allows efficient non-viral vector incorporation.

In **Chapter 6**, we studied the hypoxic effect in hiPSC-CMs cultured in a maturation medium. The immaturity of hiPSC-CMs remains a roadblock for disease modeling. This study shows that only after metabolic maturation in low glucose, high oxidative substrate media, hiPSC-CMs become susceptible to hypoxia-induced cellular damage. Secondly, we validated the cardioprotective effects of necroptosis inhibitor (nec-1) and confirmed that nec-1 prevented the hypoxia-induced decrease in mitochondrial respiration and cell death in the hiPSC-CMs cultured in a maturation medium. We conclude that metabolic maturation renders the susceptibility of hiPSC-CMs to hypoxia further toward a clinically representative phenotype, thereby creating a valid and predictive human *in vitro* model of ischemic heart disease.

PART II: MODELING THE PHOSPHOLAMBAN R14DEL MUTATION USING PATIENT-SPECIFIC HIPSC-CMS

In **Chapter 7**, we systematically reviewed the effect of the deletion of arginine 14 (p.Arg14del) in the phospholamban protein (PLN-R14del) and summarized all the current studies that

have been reported about PLN-R14del cardiomyopathy. We described the impact that the discovery of PLN-R14del had on fuelling insights into the molecular mechanisms and the potential therapeutic approaches that have been tested in both *in-vitro* and *in-vivo* models.

In **Chapter 8**, we identified the disturbance in the mitochondrial function and (lipid) metabolism in histone acetylation activities and the transcriptome regulation in PLN-R14del hearts and PLN-R14del hiPSC-CMs. Functional assessment of the mitochondria revealed reduced metabolic flexibility and increased glucose utilization, and morphological assessment revealed large lipid droplet accumulation and decreased cell viability in PLN-R14del hiPSC-CMs. We assessed the therapeutic potential of a PPARA agonist (bezafibrate) and showed improved calcium handling parameters and increased mitochondrial trifunctional protein expression in PLN-R14del hiPSC-CMs. We concluded that restoration of the impaired FAO, lipid accumulation, and Ca^{2+} handling shed light on future therapeutic strategies for PLN-R14del patients.

In **Chapter 9**, we identified the activation of the Unfolded Protein Response (UPR) in hiPSC-CMs and hearts of PLN-R14del patients by (single-cell) RNA sequencing. The UPR is a cellular stress response and is activated in response to an accumulation of unfolded or misfolded proteins. In hiPSC-CMs, the PLN-R14del mutation activates the UPR transcriptional program and sensitizes R14del hiPSC-CMs to adrenergic stress. We conformed to the previously described aggregation of PLN proteins in the myocardium of PLN-R14del patients and observed an increased presence of UPR regulators. Secondly, we found that activation of UPR in PLN-R14del hiPSC-CMs is protective because molecular inhibition of each of the 3 UPR sensors, IRE1, PERK, and ATF6, exacerbated the contractile dysfunction. Lastly, we assessed the therapeutic potential of activating the UPR with a small molecule activator, BiP (binding immunoglobulin protein) inducer X, and showed a dose-dependent amelioration of the contractility deficit in PLN-R14del hiPSC-CMs. We concluded that the UPR exerts a protective effect and increasing the UPR activity could be therapeutically beneficial in PLN R14del cardiomyopathy.

In **Chapter 10**, we generated 8 hiPSC lines, from 6 individuals carrying the PLN-R14del mutation, and 2 healthy proband family members. We showed efficient reprogramming by the characterization of pluripotency and healthy karyotyping of all hiPSC lines. These hiPSC lines increase the hiPSC sample size in order to improve the probability of identifying specific disease modeling phenotypes and predicting cardiac toxicity and therapeutic drug responses.

In Chapter 11, we developed a high-throughput screening (HTS)-compatible workflow with easy scalability for the generation, maintenance, and optical analysis of human cardiac spheroids (hCSs). We observed a highly homogeneous morphology, size, maturation, functional calcium handling, and contractile activity in CSs. We automated the entire workflow from CSs generation to functional analysis, to enhance intra- and inter-batch reproducibility as demonstrated via HTS- imaging and -calcium handling analysis. In addition, we described

a straightforward procedure for whole-spheroids biobanking, providing the opportunity to create next-generation living biobanks. We conclude that this step-by-step protocol produces high-quality and functional CSs for an optimal cardiac disease modeling and drug screening platform.

In **Chapter 11**, we developed a high-throughput screening (HTS)-compatible workflow with easy scalability for the generation, maintenance, and optical analysis of human cardiac spheroids (hCSs). We observed a highly homogeneous morphology, size, maturation, functional calcium handling, and contractile activity in CSs. We automated the entire workflow from CSs generation to functional analysis, to enhance intra- and inter-batch reproducibility as demonstrated via HTS- imaging and -calcium handling analysis. In addition, we described a straightforward procedure for whole-spheroids biobanking, providing the opportunity to create next-generation living biobanks. We conclude that this step-by-step protocol produces high-quality and functional CSs for an optimal cardiac disease modeling and drug screening platform.

In **Chapter 12**, we investigated the molecular mechanism of PLN-R14del in 3D human cardiac spheroids (hCSs) from healthy controls, an isogenic control, and three PLN-R14del patient lines. We observed a striking pathological increase of 2.4-fold in PLN-R14del hCSs size. We confirmed the decreased contractility and calcium handling, mitochondrial function, lipid droplet accumulation, and ER/UPR stress, thereby confirming various human PLN-R14del cardiomyopathy features. Interestingly, single-cell sequencing analysis revealed additional pathological pathways involved in fibroblast activation and ECM secretion such as netrin-1 and transient receptor potential channels to be significantly different in the PLN-R14del spheroid cells, indicating the importance of fibrosis for the pathogenesis of ACM/DCM and potential therapeutic interventions. In this final thesis study, we revealed fibroblast activation, PLN aggregates, and a decreased Ca^{2+} handling in PLN-R14del spheroids, which have not been described in previous hiPSC-CMs studies. Lastly, we assessed the therapeutic potential of AAV-based I-1c gene therapy and showed improved calcium handling, contractility, and decreased fibroblast activation expression in PLN-R14del hCSs. We concluded that hCSs represent the pathological phenotypes of the PLN-R14del disease and that I-1c AAV2/8-based gene therapy can potentially be used for the treatment of genetic cardiomyopathy modeled in hiPSC-CMs.

PART III: GENERAL DISCUSSION AND SUMMARY

In **Chapter 13**, we put the aforementioned findings into methodological, mechanistic, and clinical perspectives. We use the insights from cardiogenesis to improve cardiomyocyte proliferation and maturation for therapeutic strategies to repair the damaged heart. Secondly, we discuss multiple examples of hiPSC-CM models for the understanding of the pathophysiological and molecular mechanisms of genetic cardiomyopathies. We address

currently unanswered questions about which triggers underlie the onset of pathological features in PLN-R14del cardiomyopathy. Lastly, we discuss the usage of hiPSC-CMs to assess therapeutic options to cure genetic cardiomyopathies. We conclude that further improvement of the standardization, quality metrics, and algorithms, as well as clear guidelines for designing and executing any *in vitro* studies testing clinical therapeutic strategies, are required for the optimization of the choice of therapeutic intervention. Considering the output from more than five years of translational hiPSC-CM research summarized in this thesis, we conclude to have—hopefully—not only added data that will improve these 'mini-hearts' to predict, prevent and cure the burden of cardiomyopathies in people we try to help so hard - the patients.

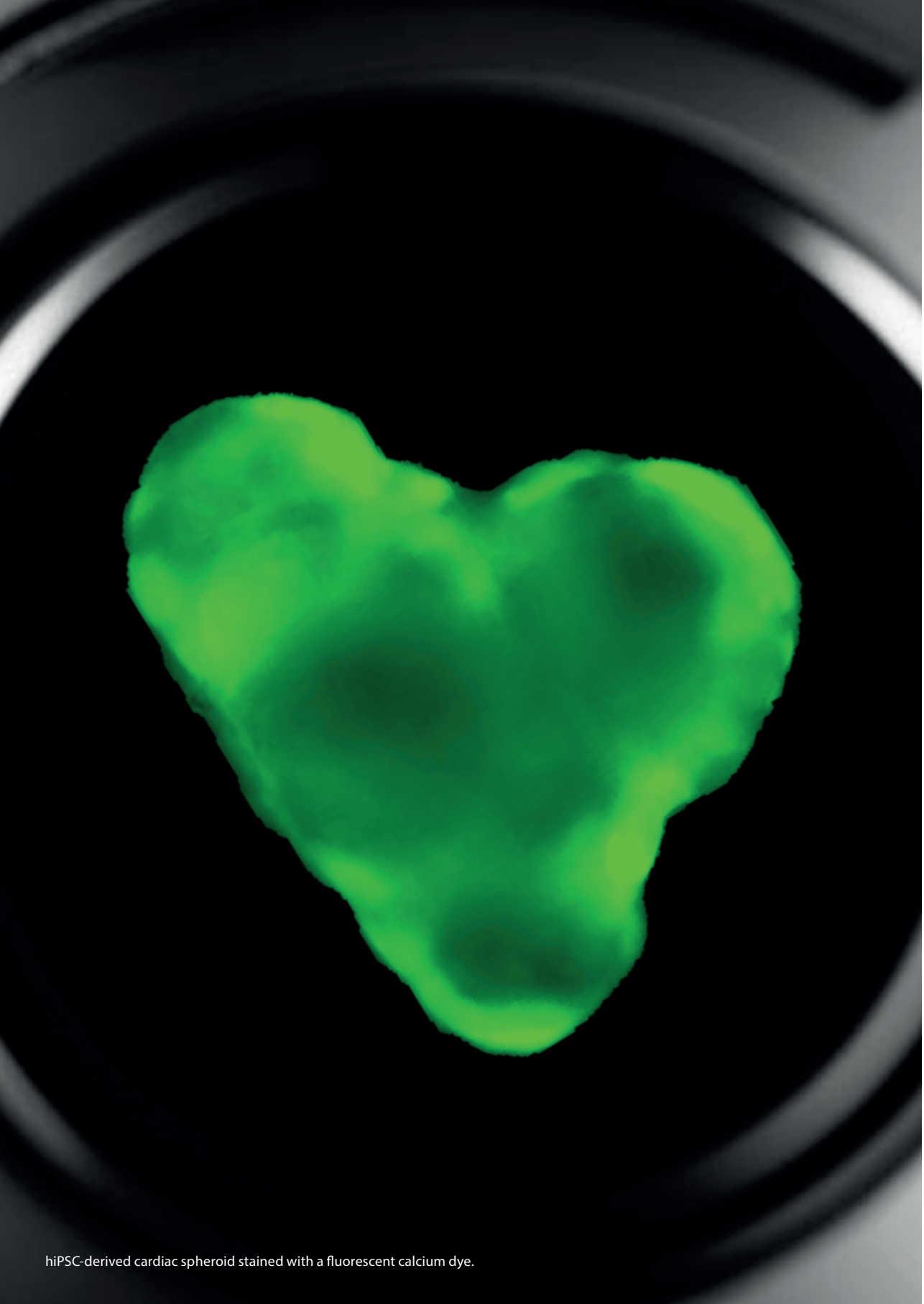

hiPSC-derived cardiac spheroid stained with a fluorescent calcium dye.

Appendices

Renée G.C. Maas

NEDERLANDSE SAMENVATTING

In dit proefschrift worde de mogelijkheden van humane geïnduceerde stamcellen en de daarvan gemaakte hartspiercellen (vanaf nu hiPSC-CMs genoemd) beschreven om antwoord te geven op de vraag ''Kunnen we hiPSC-CMs gebruiken voor het vinden van een geneesmiddel voor genetische cardiomyopathieën?''. Dit proefschrift bestaat uit twee delen. In deel 1 wordt de hartontwikkeling beschreven en is deze kennis gebruikt voor de efficiënte differentiatie, celdeling en maturatie van deze hiPSC-CMs. Daarnaast beschrijven we technieken voor het verhogen van hartspiercel deling, genetische manipulatie en de modellering van ischemische cardiomyopathie. In deel 2 wordt het gebruik van hiPSC-CMs voor ziektenabootsing en therapeutische strategieën van de genetische cardiomyopathie PLN-R14del beschreven.

In **hoofdstuk 1** geven we een algemene inleiding over de klinische en genetische variatie in cardiomyopathieën. Ook worden de methoden voor het efficiënt genereren van hiPSC-CMs besproken om het onderzoek naar de moleculaire mechanismen van genetische cardiomyopathieën en de hedendaagse uitdagingen in geneesmiddelenonderzoek te verbeteren.

DEEL 1: VAN HARTONTWIKKELING NAAR OPTIMALE HARTSPIERMODELLEN

In **hoofdstuk 2** geven we een algemeen overzicht van hartontwikkeling signalen en beschrijven we de specifieke rol van Wnt- en Hippo-signalering tijdens embryonale en foetale hartgroei. We gebruiken kennis over de hartgroei regulatie in het hart om de celdeling in hiPSC-CMs te bevorderen. Ten slotte geven we een compleet overzicht van de Wnt-signalering die belangrijk is voor zowel de hartspiercel differentiatie als hartspier deling. In dit hoofdstuk belichten we de interactie tussen de hartontwikkeling signalen en bespreken we hoe deze kennis vertaald kan worden naar technologieën voor de massa productie van hiPSC-CMs voor regeneratieve toepassingen.

In **hoofdstuk 3** beschrijven we een uitvinding voor de celdeling stimulatie van hiPSC-CMs die bereikt werd door de remming van GSK-3β signalering en het voorkomen van cel-cel contact tijdens de hartspiercel kweek. We laten zien dat door het gebruik van een GSK-3α/β inihitor, genaamd CHIR, de hiPSC-CM maturatie wordt onderdrukt en daardoor de hiPSC-CMs langer en meer kunnen vermeerderen. Ook vonden we dat deze celcyclus wordt gestimuleerd door AKT/T308 fosforylering, die onafhankelijk is van de YAP regulatie. Daarbij toonden we aan dat de cel morfologie en functie onveranderd is na deze massale expansie van hiPSC-CMs. Tot slot bekeken we de hartspiercel deling in embryonale en foetale muizen harten. CHIR was effectief voor de celdeling tijdens de embryonale fase, maar was niet voldoende voor hartregeneratie in de foetale en volwassen fases van het hart. In dit hoofdstuk concluderen

we dat geëxpandeerde hartspiercellen hetzelfde functioneren als niet geëxpandeerde hartspiercellen, waardoor deze geschikt zijn voor meerdere transnationale en regeneratieve toepassingen.

In **hoofdstuk 4** beschrijven we een gedetailleerd protocol dat grootschalige hartspiercel productie mogelijk maakt (tot een 250-voudige toename van het aantal hartspiercellen binnen 3-5 weken) van meerdere stamcel lijnen. Na het toevoegen van de GSK-3α/β inihitor CHIR, observeerden we een celdeling in 37% van de hartspiercellen. Bovendien kunnen we de prijs van de hartspiercel productie hiermee met ~70% verlagen vergeleken met het standaard differentiatieprotocol op basis van Wnt signalering. Tot slot beschrijven we een methode voor het invriezen van geëxpandeerde hartspiercellen tijdens de eerste 1 á 2 passages om de biobanking van vele hartspiercellen mogelijk te maken. In dit hoofdstuk concluderen we dat het verwijderen van cel-cel contact in combinatie met CHIR, een kostenverlagende strategie die verschillende processen zoals het nabootsen van ziekten, grootschalige screenings van medicijnen en regeneratieve toepassingen aanzienlijk zal vergemakkelijken.

In **hoofdstuk 5** gaven we inzicht in de afbraak en opbouw van sarcomeren (de spierbundels van hartspiercellen) tijdens de hartspiercel deling en beschrijven we een techniek voor gemakkelijke genetische manipulatie in hiPSC-CMs. We bestudeerden time-lapse foto's van de sarcomeer afbraak en opbouw tijdens de celdeling en analyseerden de hoeveelheid celkernen en/of celdeling in expanderende hiPSC-CMs. We zagen dat cytokinese optrad in 13-40%, mitose in 1,5-2,5% en multinucleatie in 0,6-1,7% van de gevallen. Multinucleatie als gevolg van binucleaire cellen in de M-fase was een zeldzame gebeurtenis (0,1-0,2%). We zagen dat tijdens de celdeling de afbraak van sarcomeren voornamelijk geactiveerd wordt tijdens de metafase, anafase en telofase en dat deze hartspiercellen tijdelijk stoppen met hun contractie. Tijdens de G0- of G1/S/G2-fasen, worden de sarcomeren vervolgens weer hersteld en wordt de spontane contractie hervat. Ten tweede ontdekten we dat tijdens de toediening van de GSK-3α/β inihitor CHIR, de transfectie-efficiëntie hiPSC-CMs verhoogd werd tot meer dan 30%, wat overeenkomt met andere celtypes. In dit hoofdstuk concluderen we dat de afbraak van sarcomeren nodig is voor de celdeling van hartspiercellen en dat meer sarcomeer afbraak in hartspiercellen de incorporatie voor genetische manipulatie in de hartspier verbeterd.

In **hoofdstuk 6** bestudeerden we het effect van hypoxie (zuurstof vermindering) op hiPSC-CMs gekweekt in een maturatie medium. Wanneer hartspiercellen niet genoeg gematureerd zijn, representeren deze niet het volwassen humane hart en zorgt dit voor een belemmering van studies naar hartziekes. Het geteste maturatie medium bevat een laag suiker gehalte en meer vetten, waardoor dit meer overeenkomt met de omgeving in het volwassen hart. In deze studie tonen we aan dat hiPSC-CMs zijn pas gevoelig voor hypoxie en cellulaire schade nadat deze gekweekt zijn in het maturatie medium. Ten tweede valideerden we het beschermende effect van de necroptose-inhibitor (nec-1) in hiPSC-CMs gekweekt in maturatie medium en hypoxie. We bevestigden dat nec-1 de cellulaire schade na de hypoxie kon voorkomen, wat

vergelijkbaar is aan eerder beschreven klinische resultaten. In dit hoofdstuk concluderen we dat maturatie medium de gevoeligheid van hiPSC-CMs in hypoxie verhoogd, en dat deze methode, een gevalideerd en voorspellend humaan celmodel is voor het bestuderen van ischemische hartziektes.

DEEL II: HET MODELLEREN VAN DE PHOSPHOLAMBAN R14DEL MUTATIE MET PATIËNTEN HIPSC-CMS

In **hoofdstuk 7** geven we een systematisch overzicht van alle studies die zijn gerapporteerd over de deletie van arginine 14 (p.Arg14del) in het phospholamban eiwit (PLN-R14del) en beschrijven we wat het gevolg is van deze mutatie voor patiënten. We beschreven de impact die de ontdekking van PLN-R14del had op het creëren van inzichten in de moleculaire mechanismen en de potentiële therapeutische strategieën die zijn getest in zowel patienten, diermodellen als hiPSC-CMs.

In **hoofdstuk 8** gebruikten we histonacetylering en transcriptoomregulatie sequencing technieken waarbij een verstoring van de mitochondriale functie en het (vet)-metabolisme in zowel PLN-R14del harten als hiPSC-CMs werd geobserveerd. De analyse van mitochondriën functie onthulde een verminderde metabole flexibiliteit en verhoogd glucose gebruik. Morphologische kleuringen onthulden ophoping van grote vet druppels en verminderde metabole eiwitten in PLN-R14del hiPSC-CMs. Hierna bestudeerden we het therapeutische effect van PPARA-agonist (bezafibrate) en toonden een verbeterde calcium regulatie en verhoogde mitochondriale eiwitexpressie aan in PLN-R14del hiPSC-CMs. Na deze studie concluderen we dat de verbetering van mitochondriale functie een optie is als therapeutische strategie voor PLN-R14del patiënten.

In **hoofdstuk 9** gebruikten we (single-cell) RNA-sequencing en identificeerden we de activering van de Unfolded Protein Response (UPR) in zowel hiPSC-CM's als in de harten van PLN-R14del patiënten. De UPR is een cellulair stress mechanisme dat geactiveerd wordt na een ophoping van ongevouwen of verkeerd gevouwen eiwitten. We observeerden verhoogde UPR-specifieke RNA en eiwitten, die nog meer geactiveerd raakten tijdens adrenerge stress. Al eerder werd er PLN-eiwit samenklontering geconstateerd in PLN-R14del harten. Wij observeerden gelijke uitkomsten, maar constateerden ook de verhoogde aanwezigheid van UPR-regulatoren in hartcellen van PLN-R14del harten. Ten tweede vonden UPR activatie een bescherming mechanisme is, omdat moleculaire remming van elk van de 3 UPR-sensoren, IRE1, PERK en ATF6, de contractie verergerde. Tot slot bestudeerden we het therapeutische effect van BiX (binding immunoglobuline protein inducer X), een klein molecuul, die de UPR regulatoren activeert. We toonden aan dat er een contractie verbetering optrad na een lage dosis BiX, maar een te hoge concentratie BiX juist de contractie verstoorde. In dit hoofdstuk concludeerden we dat de UPR een beschermend effect heeft en dat het verhogen van de UPR activiteit een therapeutische optie is voor de genezing van de PLN R14del cardiomyopathie.

In **hoofdstuk 10** creëerden we 8 stamcel lijnen, waarvan 6 personen drager zijn van de PLN-R14del mutatie, en 2 gezonde familieleden. We toonden aan dat witte bloedcellen van deze personen efficiënt en met een lage dosering virale vectoren gereprogrammeerd konden worden tot stabiele stam cel lijnen. In alle lijnen werd een normaal chromosoompatroon geconstateerd, en alle stamcellen bezaten de benodigde pluripotente eigenschappen. Met deze 8 stamcel lijnen vergroten de stamcel biobank, om de onderzoeken voor het nabootsen van de PLN-R14del ziekte en therapeutische screenings te vergroten.

In **hoofdstuk 11** ontwikkelden we een protocol voor het maken, onderhouden en optisch analyseren van 3-dimentionale cardiale sferoïden (hCS) van hiPSC-CMs. Deze hCS zijn van micro-formaat en kunnen daardoor gekweekt worden in grote getalen voor 'high-throughput' screenings. We observeerden een homogene morfologie, grootte en maturatie, en daarnaast bezaten de hCS functionele calcium regulatie en contractie. We automatiseerden het protocol voor de hCS generatie tot screening, waardoor de batch-tot-batch reproduceerbaarheid van de calcium analyse werd verbeterd. Ten tweede hebben we een eenvoudige procedure beschreven voor het invriezen van intacte sferoïden, wat de mogelijkheid biedt voor een kant en klare biobank van vele patiënten voor het screenen van medicatie. We concluderen dat met behulp van dit protocol, functionele hCS van hoge kwaliteit geproduceerd kunnen worden die optimaal zijn voor het nabootsen van de PLN-R14del ziekte en therapeutische screening platformen.

In **hoofdstuk 12** gebruikten we het humane cardiale sferoïden (hCS) model uit hoofdstuk 11 om het moleculaire mechanisme van de PLN-R14del mutatie te onderzoeken. Hierbij vergeleken we hCS van gezonde individuen, een isogene controle (waarvan de mutatie is gecorrigeerd) en drie PLN-R14del patiënten. Opvallend was dat de PLN-R14del hCS een pathologische toename van de diameter tot wel 2.4-fold lieten zien. We observeerden een verminderde contractiliteit en calcium regulatie, mitochondriale dysfunctie, ophoping van vet druppels en ER/UPR-stress activering zoals al eerder beschreven in de PLN-R14del mutatie. Daarnaast observeerden wij met behulp van individuele cel sequencing, ook pathologische mechanismes die nog niet eerder beschreven waren in eerdere kweekmodellen. Zo toonden wij aan dat de PLN-R14del sferoïden een verhoogde fibroblast activering en extracellulaire matrix afscheiding gensets tot expressie brachten (zoals netrin-1) en receptor potentiaal kanaal genen. Deze bevindingen bevestigen het belang van fibrose voor de pathogenese van aritmogene/gedilateerde cardiomyopathieën en voor mogelijke therapeutische interventies. In deze laatste proefschrift studie, onthullen we PLN aggregaten, fibrose, en bleek de calcium regulatie verstoord, wat nog niet eerder is beschreven in vorige hiPSC-CMs studies. Tot slot bestudeerden we het therapeutische effect van een adeno associated virus (AAV)-gebaseerde inhibitor-1 (I-1c) gentherapie en toonden we een verbeterde calcium regulatie, contractie en een verminderde genexpressie van fibroblast activering aan. In dit hoofdstuk concludeerden we dat hCSs de pathologische fenotypes van de PLN-R14del ziekte bezitten en dat I-1c gentherapie gebruikt kan worden als een therapeutische optie voor de genezing van de PLN R14del cardiomyopathie.

DEEL III: ALGEMENE DISCUSSIE EN SAMENVATTING

In **hoofdstuk 13** plaatsen we de bovengenoemde bevindingen in methodologisch, mechanistisch en klinisch perspectief. We gebruiken de kennis van hartontwikkeling voor de stimulatie van celdeling en verbetering van maturatie in hiPSC-CMs om beschadigde harten te herstellen. Ten tweede bespreken we voorbeelden van hartspiercel modellen die gebruikt worden om pathofysiologische en moleculaire mechanismen van genetische cardiomyopathieën te kunnen bestuderen. Daarnaast behandelen we de momenteel onbeantwoorde vragen over welke triggers ten grondslag liggen aan het ontstaan van pathologische kenmerken in PLN-R14del cardiomyopathie. Tot slot bespreken we of hiPSC-CMs geschikt zijn voor het selecteren van de beste therapeutische optie om genetische cardiomyopathieën te genezen. We concluderen dat er meer standaardisatie, kwaliteitscontroles en algoritmen nodig zijn, evenals duidelijke richtlijnen voor het ontwerpen en uitvoeren van therapeutische screenings, voordat er een definitieve beslissing genomen over de beste therapie. Dit proefschrift vat vijf jaar translationeel hiPSC-CM onderzoek samen, waarna we kunnen concluderen dat dit proefschrift bijdraagt aan de ontwikkeling van 'mini-harten' die een verbetering geven om cardiomyopathieën te voorspellen, voorkomen en te genezen bij mensen die we zo hard proberen te helpen - de patiënten.

LIST OF PUBLICATIONS

Published (chronological order)

Somers T*, Siddiqi S*, **Maas RGC**, Meuwissen TJ, Russel FGM, Morshuis WJ, Schirris TJJ. Statins affect human iPSC-derived cardiomyocytes by interfering with mitochondrial function and intracellular acidification. *Basic Research in Cardiology*.

Van de Wakker S.I, Bauzá-Martinez J, Carla Ríos Arceo C.R, Manjikian H, Snijders Blok C.J.B, Roefs M.T, Willms E, **Maas RGC**, Pronker M.F, de Jong O.G, Wu W, Görgens A, El Andaloussi S, Sluijter J.P.G.*, Vader P*. "Size matters: Functional differences of small extracellular vesicle subpopulations in cardiac repair responses" *Journal of Extracellular Vesicles*.

Fang J, **Maas RGC***, Yang Q*, Buono M, Meijlink B, Bruinenberg D.M, Benavente E.D, Mokry M, van Mil A, Qian L, Schiffelers R, Lei Z*, Sluijter J.P.G*. Vitamin C enhances the direct reprogramming of fibroblasts into cardiomyocytes by suppressing reactive oxygen species production. *Stem Cell Research & Therapy*.

Maas RGC, van den Dolder F.W.[#], Yuan Q[#], van der Velden J, Wu SM, Sluijter JPG[$], Buikema JW[$]. Harnessing developmental cues for cardiomyocyte production. *Development*. 2023 Aug 1;150(15):dev201483. doi: 10.1242/dev.201483.

Maas RGC, Beekink T*, Chirico N*, Snijders Blok CJB, Dokter I, Sampaio-Pinto V, van Mil A, Doevendans PA, Buikema JW, Sluijter PG*,Francesca Stillitano F*. Generation, High Throughput Screening, and Biobanking of Human Induced Pluripotent Stem Cell-Derived Cardiac Spheroids. *Journal of Visualized Experiments (JoVE)*. 2023 Mar 10,(193);e64365, doi:10.3791/64365.

Chirico N*, Kessler EL*, **Maas RGC**, Fang J, Qin J, Dokter I, Daniels M, Šarić T, Neef K, Buikema JW, Lei Z, Doevendans PA, Sluijter JPG, van Mil A. Small Molecule-Mediated Rapid Maturation of Human induced Pluripotent Stem Cell Derived Cardiomyocytes. *Stem Cell Research & Therapy*. 2022, 531 doi:10.1186/s13287-022-03209-z.

Meijer EM*, Koch SE*, **Maas RGC**[#], van Dijk CG[#], Chrifi I, Szymczyk W, Besseling PJ, Pomp L, Koomen VJCH, Buikema JW, Bouten CVC, Verhaar MC, Smits AIPM[$], Cheng C[$]. 3D Human iPSC Blood Vessel Organoids as a Source of Flow-Adaptive Vascular Cells for Creating a Human-Relevant 3D-Scaffold Based Macrovessel Model. *Advanced Biology*. 2022 Oct 27:e2200137. doi:10.1002/adbi.202200137.

Maas RGC*, Pei J*, Gaar-Humphreys KR, Gho JMIH, Nagyova E, Snijders Blok CJB, van Adrichem I, van Es R, Sepehrkhouy S, Feyen DAM, van den Dungen NAM, Lansu N, Calis J, van de Kaaij N, de Jonge N, van Laake LW, te Riele ASJM, Huibers MM, de Weger RA, Verhaar MC, van Tintelen JP, Vaz FM, Burgering B, van Mil A, Buikema JW, Vink A, Karakikes I, Mercola M, Doevendans PA, Sluijter JPG, van Steenbeek FG, Cheng C, Mokry M[$], Asselbergs FW[$], Harakalova M[$]. Transcriptional Regulation Profiling Reveals PPARA-mediated Fatty Acid Oxidation as a Novel Therapeutic Target in Phospholamban R14del Cardiomyopathy. *Research Square*. 2022. DOI: 10.21203/rs.3.rs-1902254/v1.

Peters MMC, **Maas RGC**, Adrichem I, Doevendans PAM, Mercola M, Šarić T, Chamuleau SAJ, Sluijter JPG, Hnatiuk AP[$], Neef K[$]. Metabolic Maturation Increases Susceptibility to Hypoxia-induced Damage in Human iPSC-derived Cardiomyocytes. *Stem Cells Translational Medicine*. 2022 Oct 10;11(10):1040–1051, doi:10.1093/stcltm/szac061

Maas RGC*, Yuan Q*, Brouwer ECJ, Pei J, Snijders Blok CJB, Popovic MA, Paauw NJ, Bovenschen N, Hjortnaes J, Harakalova M, Doevendans PA, Sluijter JPG, van der Velden J, Buikema JW. Sarcomere Disassembly and Transfection Efficiency in Proliferating Human iPSC-Derived Cardiomyocytes. *Journal of Cardiovascular Development and Disease*. 2022; Jan 21 9(2):43. Doi:org/10.3390/jcdd9020043

Feyen DAM*, Perea-Gil I*, **Maas RGC**, Harakalova M, Gavidia AA, Wu T, Vink A, Pei J, Suurmeijer AJ, te Rijdt W, Vu M, Amatya PL, Prado M, Zhang Y, Sallam K, Asselbergs FW, Mercola M, Karakikes I. Unfolded Protein Response as a Compensatory Mechanism and Potential Therapeutic Target in PLN R14del Cardiomyopathy. *Circulation*. 2021 Aug 3;144(5):382-392. doi: 10.1161/CIRCULATIONAHA.120.049844.

Maas RGC*, Lee S*, Harakalova M, Snijders Blok CJB, Goodyer WR, Hjortnaes J, Doevendans PA, van Laake LW, van der Velden J, Asselbergs FW, Wu J, Sluijter J, Wu SM[$], Buikema JW[$]. Massive Expansion and Cryopreservation of Functional Human Induced Pluripotent Stem Cell-Derived Cardiomyocytes. *Cell STAR protocols*. 2021 Feb 9;2(1):100334. doi: 10.1016/j.xpro.2021.100334.

Buikema JW*, Lee S*, **Maas RGC**[#], Goodyer WR[#], Chirikian O[#], Li G, Miao Y, Paige SL, Lee D, Wu H, Paik DT, Rhee S, Tian L, Galdos FX, Puluca N, Beyersdorf B, Hu J, Beck A, Venkamatran S, Swami S, Wijnker P, Schuldt M, Dorsch LM, van Mil A, Red-Horse K, Wu JY, Geisen C, Hesse M, Serpooshan V, Jovinge S, Fleischmann BK, Doevendans PA, van der Velden J, Garcia KC, Wu JC, Sluijter JPG, Wu SM. Wnt Activation and Reduced Cell-Cell Contact Synergistically Induce Massive Expansion of Functional Human iPSC-Derived Cardiomyocytes. *Cell Stem Cell*. 2020 Jul 2;27(1):50-63.e5. doi: 10.1016/j.stem.2020.06.001

Feyen DAM, McKeithan WL, Bruyneel AAN, Spiering S, Hormann L, Ulmer B, Zhang H, Briganti F, Schweizer M, Hegyi B, Liao Z, Pölönen RP, Ginsberg KS, Lam CK, Serrano R, Wahlquist C, Kreymerman A, Vu M, Amatya PL, Behrens CS, Ranjbarvaziri S, **Maas RGC**, Greenhaw M, Bernstein D, Wu JC, Bers DM, Eschenhagen T, Metallo CM, Mercola M. *Metabolic Maturation Media Improve Physiological Function of Human iPSC-derived Cardiomyocytes*. *Cell Reports*. 2020 Jul 21;32(3):107925. doi:10.1016/j.celrep.2020.107925.

Garnier S, Harakalova M, Weiss S, Mokry M, Regitz-Zagrosek V, Hengstenberg C, Cappola TP, Isnard R, Arbustini E, Cook SA, van Setten J, Callis J, Hakonarson H, Morley MP, Stark K, Prasad SK, Li J, O'Regan DP, Grasso M, Müller-Nurasyid M, Meitinger T, Empana JP, Strauch K, Waldenberg M, Marguiles KB, Bick AG, Seidman CE, Meder B, Boutouyrie P, Lacolley P, Jouven X, Erdman J, Blankenberg S, Wichter T, Ruppert V, Tavazzi L, Dubourg O, Aumont MC, Roizes G, Dorent R, DeGroote P, Fauchier L, Trochu JN, Gibelin P, Aupetit JF, Germain M, Völker U, Daiane H, Raji I, Bacq-Daian D, Proust C, Lenhert K, **Maas RGC**, Olaso R, Saripella G, Felix SB, Ginn SM, Dubosqu-Bidot L, van Mil A, Fontaine V, Blanché-Koch H, Keating B, Pavia PG, Curjol A, Boland A, Komajda M, Cambien F, Deleuze JF, Dörr M, Asselbergs FW, Villard E[$], Trégouët DA[$], Charron P[$]. Genome-wide Association Analysis in Dilated Cardiomyopathy Reveals Two New Key Players in Systolic Heart Failure on Chromosome 3p25.1 and 22q11.23. *European Heart Journal*. 2021 May 21;42(20):2000-2011. doi: 10.1093/eurheartj/ehab030.

Under review

Maas RGC, Kerckhaert L, Broersma J, Doevendans PA, Sluijter JPG, Stillitano F. Phospholamban p.Arg14del Cardiomyopathy: a systematic review of the pathophysiological mechanisms. *Circulation Research*. - *Under review* 2023 Dec.

Kelters I.R, Verbueken D, Beekink T, Van Laake L.W, Sluijter J.P.G, Buikema J.W*, **Maas RGC***. Generation of Human Induced Pluripotent Stem Cell (hiPSC) Lines Derived from Three Patients Carrying the Pathogenic CRYAB (A527G) Mutation and One Non-Carrier Family Member. *Stem Cell Research - Under review* 2023 Sept.

Margarida V, Bebelman M, **Maas RGC**, Verweij F, Seinen C, de Jager S, Vader P, Pegtel DM, JPG Sluijter. Hypoxia and TNF-alpha modulate extracellular vesicle release from human induced pluripotent stem cell-derived cardiomyocytes. *Journal of Extracellular Vesicles* - under review 2024 February.

Abstracts

Van Mil A, Castilho M, Chirico N, Ainsworth MJ, Dokter I, **Maas RGC**, Buikema JW, Malda J, Sluijter JPG. Next generation bioengineerd human myocardium. *Tissue Engineering*. 2022 Apr. Part A. 28, p. S430-S43.

Chirico N, Ainsworth M, Buikema JW, Dokter I, **Maas RGC**, Malda J, Castilho M, van Mil A, Sluijter JPG. Bioengineered transmural cardiac constructions with hexagonal microarchitectural resolution. *Tissue Engineering*. 2022 Apr. Part A. 28, p. S381-S381

Yuan Q, **Maas RGC**, Brouwer E, Sluijter JPG, Van der Velden J, Buikema JW. Sarcomere disassembly and transfection efficiency in proliferating human iPSC-derived cardiomyocytes. *European Heart Journal*. 2023, 44 (Suppl 2).

Research output and activities on societal impact

Talent under 35. 2024 - Het Financiel Dagblad

Experimental Translational Medicine: PLN case. 2021. *Bachelor Research hub, UMC Utrecht*

YouTube video: '' Massive expansion and biobanking of stem cell derived-cardiomyocyte''. 2021. *Circulatory health, UMC Utrecht*

Interview; Belang van de Hartenbank. 2020. Stichting PLN.

ACKNOWLEDGEMENTS

The last part of this thesis is dedicated to expressing my appreciation for all those who have contributed to the conduct of my academic endeavors, my professional growth, and personal wellbeing for the past years. During this time, I faced many challenges but in which I also have made fantastic memories and many revoked un my mind while writing. Having said this, it brings me much joy to specifically thank who made my journey possible during these last years.

De promotie- en beoordelingscommissie

Zonder twijfel is mijn belangrijkste mentor in de afgelopen jaren, **prof.dr. Joost Sluijter** geweest die niet alleen mijn eerste promotor was, maar die mij in 2015 de kans gaf om met stages en als analist mij aan te sluiten bij de experimentele cardiologie. Jouw brede kennis, positiviteit en je persoonlijke betrokkenheid zijn een grote bron van inspiratie. Daarnaast heb ik natuurlijk ook genoten van alle uitstapjes, BBQ pool-partys in Vlijmen, escape-rooms en etentjes. Ondanks dat we de compleet 'tegenovergestelde kleur' zijn, heb ik onze discussies en je kritische vragen altijd enorm gewaardeerd. Deze hebben mij geholpen om te floreren in de wetenschappelijke wereld en mij op alle vlakken verder te ontwikkelen. Bedankt voor je gestelde vertrouwen in mij en de ondersteuning die je me de afgelopen jaren hebt gegeven en nog steeds geeft. Ik hoop dat ik, en vele andere onderzoekers, nog lang jouw kwaliteiten daar in mogen ervaren bij toekomstige wetenschappelijke ondernemingen.

Als tweede wil ik mijn waardering en dank uitspreken naar **dr. Jan Willem Buikema**, de enigste stamcel-kwekende cardioloog die ik ken. Ik herinner me nog goed dat ik jou als student voor de eerste keer ontmoette tijdens de 1ste DCVA translational research meeting waarna we dit vervolgens met een koffie op de Stanford campus bankje voortzetten. Als copromotor heb jij mij fanatisch begeleid, zowel inhoudelijk als persoonlijk. Je gaf op de juiste momenten wat bijsturing of liet de touwtjes los. Toch kon ik altijd op je rekenen voor tips voor het rekenen van praktische zaken, commentaar op manuscripten, of als klankbord. Dankzij jou heeft dit proefschrift een zeer sterke fundamentele (en exponentiele) basis gekregen. Jouw enthousiasme voor hartontwikkeling is uiteindelijk een drijfveer geweest voor veel projecten uit dit proefschrift. Ik koester ook de etentjes, honden-dates (want ja onze bruine trouwe viervoeters zijn de beste vriendjes) en de academische discussies onder het genot van een goed frans wijntje. Bedankt voor je vertrouwen in mij ondanks mijn enorme eigenwijsheid en eigenzinnigheid. Na de prachtige laudatio die je mij gaf tijdens mijn master diploma, sluiten we opnieuw een hoofdstuk samen af. Ik hoop dat we in de toekomst dan ook nog vele nieuwe bladzijden, dan wel hoofstukken, aan onze samenwerking kunnen toevoegen.

Naast Joost en Jan Willem nam zitting in de promotiecommissie **dr. Magdalena Harakalova** en **prof.dr. Pieter Doevendans**, de man in het PLN-web die met zijn deskundigheid en diplomatieke capaciteiten in korte e-mails een voorbeeld is voor vele onderzoekers waaronder

mijzelf. Onze gesprekken stonden dan ook meestal in het teken van PLN en vooral de beste behandelmethode. Ik bewonder je inzet in de strijd tegen deze ziekte; niet alleen op wetenschappelijk gebied, maar ook door 568 km op één dag te fietsen om geld op te halen voor PLN onderzoek. Ook herinner ik mij nog goed de fantastische kerstborrels, met het beroemde 'Chinese likeurtje', en de interessante reizen die het CurePLaN consortium mogelijk heeft gemaakt. Ik stond bij jou bekend als 'het meisje met de gouden celkweek-handen' waarvan ik hoop dat ik je daarin niet heb teleurgesteld. Nu mijn nieuwe carrière op het punt van beginnen staat mag jij bijna je toga aan de wilgen hanen. Het was een eer om jou als promotor te hebben en ik hoop dat we over een paar jaar een mooie fles kunnen chambreren en proosten op een behandeling voor PLN-R14del.

Daarnaast is **prof.dr. Folkert Asselbergs** de eerste fase van mijn PhD betrokken geweest als promotor, en waarbij ik wil opmerken dat het verontrustend blijft dat hij het instituut helaas heeft verlaten. Jouw kritische blik en je overzicht hebben mij altijd geïnspireerd om met enthousiasme onderzoek te doen. Ook de beoordelingscommissie van mijn manuscript wil ik bedanken, bestaande uit **prof.dr Niels Boverschen**, **prof.dr Robert Passier**, **prof.dr Eva van Rooij**, **prof.dr Jeffrey Beekman** onder leiding van **prof.dr. Peter van Tintelen**, dank voor uw interesse in mijn proefschrift en uw bereidheid om zitting te nemen in deze beoordelingscommissie.

Team Experimental Cardiology

This team wouldn't exist without the unrelenting enthusiasm and belief of all members (and former members) of the 'Sluijter' group. Without a doubt, I am greatly indebted to **Alain**, who gave me the chance to join the lab for an internship as an unexperienced HBO student, almost 10 years ago. Your stamina, respect for our collaborators, and witticisms have been a joy so far and will hopefully continue to be for many years to come. **Zhiyong**, the CRISPR-wizard of G2. Thank you for all your help with genius constructs that made our research more efficient and just a bit 'fancier'. The Nobel price nomination seems every year closer! **Klaus**, thank you for all your input during the PLN discussions, the AAV-coordination and Cologne city-tips, I still need to go back to do them all. Also I have to thank **Saskia**, **Pieter** and **prof. Hester**, your scientific experience was an inspiration to us and often resulted in you nudging us in the right direction during meetings. The PLN research team would not be the same without **Francesca**, who I truly admire for your experimental expertise and the input you gave in so little time while in our lab. I hope we will continue our fruitful PLN collaborations in the future. Finally, Quid pro Quo, the very illustrious academic company of the RMCU and G2 locations, cannot remain unmentioned. **Margarida**, **Juntao**, **Nino**, **Simon**, **Yao**, **Jort**, **Clara** and **Vasco**, thank you for our collaborations. Your expertise and skills in your scientific fields are truly admirable! **Aina**, **Aria**, **Aoife**, **Barbara**, **Elisa**, **Qianbing**, **Jian**, **Xin**, **Songpu**, **Marian, Ernest, Diantha, Eloi, Anil, Geng, Xin, Lantian, Qianbing, Tian,**

Tim, **Yang**, **Jasmijn**, **Evelien**, **Jiabin**, **Talitha**, **Anna,** even though we did not work together every day, I am happy that I got to know you guys well and I really enjoyed our conversations. Thanks for the fun during borrels and other (lab) events! **Karen**, with whom I had memorable – and sometimes not very much memorable (given the amount of cocktails and disco-dance-floors involved) – super gezellige times together. I admire the workload you take on your shoulders although I will kidnap you for coffee before your thesis gets bigger than mine. **Ilse**, jouw klinische blik én medemenselijkheid zijn ijzersterk. Je talent om iedereen bij elkaar te krijgen hebben ertoe geleid dat ik (maar ik denk nog veel meer mensen) een super gezellige tijd in het lab beleven. De klinische discussies die ik met jou de afgelopen jaren heb kunnen voeren tijdens de koffie time-outs heb ik buitengewoon gewaardeerd en hoop ik nog vele jaren te kunnen voortzetten totdat je te druk bent voor mij als cardioloog. Before and during my PhD, I was also lucky enough to surround myself with amazing technicians forming the 'backbone' of our organization. Van één kreeg ik bijna 10 jaar geleden de eerste iPSC lijn, waarna ze gelukkig een functie als 'iPSC meester' bij ons voortzette. **Inge**, jouw nuchtere blik, pragmatische benadering en Q-music foute-uur voorliefde geeft ons allemaal een fantastische tijd in het iPSC lab. De ander kwam ik tegen bij een FACS machine, die vervolgens gelukkig ook bij ons aansloot. **Christian**, je onuitputtelijke will-to-help resulteerden erin dat je nooit 'nee' zei tegen nog éééén flowcytometrie analysetje die dan ook eigenlijk morgen al klaar moest zijn. Dank voor al je kennis, hulp en flexibiliteit! Nog een andere bouwsteen voor deze 'backbone' kwam ik tegen in een NMR-lab, en wisten we gelukkig bij ons binnen te halen als 'lab-papa' van G2. **Mark**, ook jou hulp en komische opmerkingen waardeer ik enorm! **Daniek**, wat een onuitputtelijke drive heb jij, en ik hoop je in de toekomst nog af en toe te mogen storen als ik weer eens iets zoek. **Ingrid**, uiteraard kan ik jou niet vergeten! Hoe hou je toch alle ballen in de lucht, en dat altijd met een glimlach en een politiek correcte (creatieve) oplossing. Je onuitputtende inzet en e-mails (vaak tot laat in de avond) van bijvoorbeeld tientallen MTAs en niet te vergeten snelle-belletjes hebben mij enorm geholpen met de onderzoeks-werkzaamheden. Last, but not-least, I would like to take a moment to remember al the precious but previous members of the experimental cardiology group such as **Juntao**, **Elise**, **Marieke**, **Mudit**, **Nazma**, **Casper**, **Iris**, **Eveliene**, **Emma**, **Patricia**, **Corina**, **Peter-Paul**, **Tom** en **Janine**, it was a pleasure working together on the same goal; curing heart failure.

Regenerative Medicine Center Utrecht

Gedurende mijn tijd als onderzoeker in het RMCU ben ik gezegend met ontmoetingen met vele inspirerende mensen. Allen die hieraan bijgedragen hebben zijn wij zeer erkentelijk, in het bijzonder de 'buren' van nefrologie, **Petra dB**, **Christian**, **Paul**, **Petra dG**, **Bas, Krista**, **Melanie**, ik heb genoten van jullie gezelligheid en dank voor alle hulp gedurende de RMCU jaren! Door zich te ontwikkelen van een zeer gewaardeerde collega naar het managen van haar eigen onderzoeksgroep heeft **Marijn** mijn respect meer dan verdient. Ik hoop nog vele jaren naast je te morgen werken en ik benieuwd naar je nieuwe papers! **Mattie**, **Ihsane** en

Joost F, hartelijk dank voor jullie technische en organisatorische hulp de afgelopen jaren. Het RMCU zou het RMCU niet zijn als er geen mensen zijn die zich dagelijks inzetten voor de service, schoonmaak, faciliteiten en bestellingen. In bijzonder de mannen van de technische dienst **Elroy**, **Bart**, en **Richard**. Dan **Rob** die niet alleen de vissen verzorgd maar ook iedereen van bier tijdens de RMCU borrels. Mijn PhD programma in het RMCU zou niet compleet zijn zonder **Paul** en **Koen**, hartelijk dank voor al jullie hulp en organisatie de afgelopen jaren, ik heb enorm veel geleerd in het RM programma! Ook heb ik genoten van de RM feestjes, die ik met de rest van het PhD comité, **Karen**, **Katrin**, **Robine**, **Simon**, **Lorenzo**, **Leonardo** en **Joachin**, mocht organiseren.

UMC Utrecht

Ook de samenwerkingen met alle andere Utrechtse onderzoekers waardeer ik ten zeerste, en ik vermoed dat ik velen nog terug zal zien. Ik heb veel geleerd van de frisse inzichten, kritische vragen, en wetenschapsfilosofische gesprekken die ik met velen heb gevoerd. Hieronder wil ik een aantal personen in het bijzonder danken. Bij de afdeling cardiologie heb ik mijn plekje mogen vinden binnen de groep onder leiding van **prof.dr. Pim van der Hast** en heb ik in het verleden en heden goede discussies mogen voeren met **Sander**, **Jessica**, **Arjan**, **Feddo**, **Alicia**, **Ayoub**, **Floriaan**, **Klaske**, **Laurens**, **Marion**, **Michael**, **Noortje** en **Mimoet**. Allen erg veel dank daarvoor! In het bijzonder, maar zonder mensen tekort te doen, onze wel gerespecteerde en gewaardeerde patholoog **prof.dr. Arjan Vink**, *in memoriam*, en rechterhand **Petra** die een fantastische bijdrage hebben geleverd voor alle histologie studies in dit proefschrift. Binnen de kliniek wil ik ieder bedanken die bloed heeft afgenomen, alle OK-medewerkers en iedereen die hartweefsel verzameld/bewaard heeft, zonder dit waren deze studies niet mogelijk. **Prof.dr. Linda van Laake** met genoegen heb ik gezien hoe jij je de brug slaat tussen de kliniek en hoogwaardig (ritmisch) translationeel onderzoek; ik hoop dat veel collega's in de toekomst die kwaliteit van je mogen overnemen. Het STRAIN-team, **Karim**, **Arko**, **Rene**, **Maarten Jan**, jullie methodologische en medisch(-technologische) hulp heb ik enorm gewaardeerd. **Toon**, je langetermijnvisie en efficiëntie hebben in belangrijke mate bijgedragen aan onze gemeenschappelijke projecten en dank voor het openstellen van jullie 'elektrofysiologische' deuren. **Teun**, jouw vooruitstrevendheid, pragmatische aanpak en cellulaire elektrofysiologische rolodex worden zeer gewaardeerd. **Willem**, dank voor jouw onverminderde aandacht voor het optimaliseren van calcium analyses en je zeer prettige omgang. Ik kijk met genoegen uit naar onze gemeenschappelijke wetenschappelijke ondernemingen in de nog te ontginnen data**. Boudewijn**, **Maaike** en **Miranda**, jullie kennis met de seahorse analyses is absoluut benijdenswaardig. **Annette** en **Mark**, jullie inzichten en werklust in de (likely) pathogenic variants zijn buitengewoon en bleek van grote waarde binnen onze groep. **Prof.dr. Peter van Tintelen**, **Esmee**, jullie genetische analytische en consistente benadering van de PLN-mutatie is fantastisch en de consortiummeetings zijn met jullie altijd plezierig. Peter, dank voor jouw support in het starten van mijn BKO traject.

Dat brengt mij bij de academische visie, opleidingsgedachtes en zeer sterke educatieve vaardigheden van **Sandra**, **Toine**, **Emma** en **Michael** in de **Research Hub** Utrecht onder leiding van **prof.dr. Niels Boverschen**. Dank voor jullie onverminderde kans om PLN onderzoek te doen en jonge studenten de kunst van onderzoek te berde brachten. Helaas lieten de proefschrift pagina's het niet toe om ook dit avontuur als hoofdstuk te includeren.

The educational journey

I still remember my first internship with **Sekka** under supervision of **prof.dr. Gerald de Haan** in the ERIBA institute, where the fundamental basis for my future academic carrier was born. Ook was ik niet gepromoveerd geweest als **Joost Koedam** niet zo genereus was geweest om mij toe te laten tot de master *cancer, stem cells & developmental biology*. Hartelijk dank voor deze mogelijkheid! Ook dank voor het lachen, studiemaatjes; **Kaylee**, **Bram** en **Daniel**! I also have enjoyed the supervision of many talented students. Thank you all for your efforts, you have done a lot of work and generated beautiful data regarding; **Niek**; het iPSC/CM differentiatie overzicht, **Moui**; the extensive review on the role of the UPR in Cardiac Disease, **Najrana**; review on cardiac 'organoids', **Puck**; het eerste 3D PLN-R14del model, **Adriana**; 'single-cell' spheroid imaging, **Judy**; de start van het PLN-review, **Kaylin**; the first calcium analyses, **Saskia**; de rol van de UPR in genetische cardiomyopathieën, **Stef**; zo veel calcium video analyses!, **Tess**; 2 prachtige co-auteurschappen en een huidige analisten functie waarbij je mijn CM differentiatie efficiency record hebt gebroken! **Jelle**; drugscreenings van de PLN-spheroids, en de nieuwste talenten; **Brian** en **Cosme**; voor jullie 3D contractility analyses. Good luck to all with your future carriers, I hope to cross academic paths in the future!

(Inter)national collaborations

Beste co-auteurs, dear coauthors: I would like to thank you all for our successful (national and international) collaborations, without you this thesis would not have existed. Special tanks go to **prof.dr Mark Mercola**, for giving me the opportunity to work on the UPR and PLN-R14del which have led to very impressive results described in chapter 9. Your scientific track record is dazzling to any investigator, but it is nothing compared to your kindness and accessibility, approaching any researcher with equal regard. **Ioannes**, thank you for being critical, you strongly influenced the way how I perform research and my perception of science, bot practically and philosophically. **Dries Feyen**, thank you for the chance you gave me to join the lab. During these years you not only helped me to develop scientifically but also personally. Stanford superstars; **Wesley**, **Arne**, **Maricela** and **Michelle**, I miss our weekend-westernblots, Arne's annoying Britney Spears-moments and our California food-trips. **Prof.dr. Joseph Wu** thank you for the past and future collaborations regarding the hiPSC lines. **prof. dr. Sean Wu** and **Soah**, is was a great honour to collaborate with you on the CM expansion papers. Cardiologie collega's van het UMC Groningen, **Wouter**, **Albert** en **Herman** hartelijk dank voor het beschikbaar stellen van PLN-hartweefsel en de zeer inspirerende discussies om

PLN-R14del te genezen. **Jorg**, jouw nuchtere blink en enorme sequencing expertise hebben de SPLiTseq data in hoofdstuk 12 tot prachtige inzichten gebracht! I would like to thank **Jiayi** for our collaboration by combining your amazing sequencing expertise with the PLN-R14del hiPSC-CMs, which resulted in the metabolic mechanism manuscript in part II of this thesis. I am happy to see that your hard work paid off and that you found your place! Tea soon? **Prof.dr. Caroline Cheng** en **prof.dr. Marianne Verhaar**, ik dank jullie voor de productieve en vooral prettige 'vasculaire-organoid' samenwerking. Ik wil ook graag **prof. Jeroen Bakkers** en zijn team; **Lotte**, **Sarah** en **Mara** bedanken voor de plezierige samenwerking. **Jesper**, dank voor je input en goede discussies de afgelopen jaren! Het EHT model is mij van zeer grote waarde gebleken en ik wil dan ook **prof.dr Jolanda van der Velden** bedanken voor de mogelijkheid deze techniek onder de knie te krijgen. Tijdens al deze jaren van samenwerking met het Amsterdam UMC heb ik binnen jouw groep een voortreffelijk en divers spectrum wetenschap mogen ervaren. **Larissa**, **Maaike** en **Remco,** hartelijk dank voor al jullie inzet en fantastische metingen! **Diederik**, het ontbrak het van jouw kant nooit aan kritische vragen of hulp, dank! **Qiangliang**, thank you for the wonderful projects we shared, resulting in multiple chapters of this thesis. It was a pleasure working with you and I wish you the best of luck with the completion of your PhD! **Birgit**, leuk om de favor terug te kunnen geven na jouw dankwoord. Ik heb onze 'rode' omgang ook enorm gewaardeerd en super leuk om met iemand te sparren die zo op 1 lijn lag met mijn gedachtes. Ik schiet ook nog steeds in de lach bij het woord ''stellage'', je weet wel waarom. Ik heb de aanvraag voor een landelijke hiPSC-CM meeting ook als enorm fijn ervaren. Ik hoop dat we de samenwerking of het aanvragen van meetings (en feesten) kunnen voortzetten. Tenslotte wil ik **Salay** en **Tim** bedanken voor jullie prettige samenwerking omtrent de statine projecten. **Tim**, ik wens je nog veel succes met de afronding van je PhD en ik gun je een schitterende opleidingsplek!

Stichting PLN

Ik ben meer dan schatplichtig aan de ongelofelijke inzet van de PLN stichting en in het bijzonder natuurlijk **Pieter Glijnis** om PLN-R14del de wereld uit te helpen. Ik bewonder je tomeloze inzet voor deze ziekte, met helaas een persoonlijk belang en ik deel dan ook je frustratie als het even niet snel genoeg gaat. Wat je de afgelopen 10 jaar hebt opgezet en hebt bereikt met deze stichting is bewonderenswaardig. Ik koester de momenten waarbij ik publiekelijk heb mogen vertellen over deze vreselijke ziekte voor de mensen die we zo hard proberen te helpen - de patiënten. **Wouter**, **Evert**, **Jan**, **Yolande**, **Eric**, **Nikki**, **Marise**, **Luuk**, **Annet**, **Annette**, **Corne**, **Margreet** en **Marianne**, jullie zijn van groot belang in de stichting, in het leven van vele patiënten en vervullen je taak met verve. We zijn er bijna! **Marise**, de officemanager; een functieomschrijving die kennelijk de lading 'ruggengraat' moet dekken. Belast met werkelijk het meest uiteenlopende takenpakket lukt het jou om zowel de pipetten als de mensen van het kantoor bij elkaar te houden. Ik kijk dan ook met bewondering terug op de tijd dat we samen sparden over het inrichten van een complete 'bloedbus', dat is jullie

dan ook meer dan gelukt en tegenwoordig gelukkig met versterking van '**M&M**'. Hartelijk dank voor je nominatie als FD talent **Nikki**, wat heb jij een onuitputtelijke positiviteit en drive om alle belangrijke en moeilijke onderwerpen de wereld in te slingeren! **Luuk**, ik waardeer onze discussies en samenwerking voor het grootste PLN onderzoek overzicht tot nu toe. Ik hoop nog veel met je te mogen samenwerken als kersverse PhD-student!

Amici

Door het bekende adagium: wie goed doet, goed ontmoet is gedurende mijn studententijd een van mijn bijzonderste vriendschappen ontvouwen. **Inge**, ik had mijn HBO niet kunnen halen zonder jou, jouw studiementaliteit en de door jou verplichte ophokplicht van mij tijdens tentamens sleepten mij door de jaren heen. Ik koester alle momenten, en moet nog vaak terugdenken aan de 'first-paper' party die je voor mij organiseerde. Ik ben je zeer, zeer dankbaar voor je rol als vriendin, getuige en ik hoop dat je mij in mijn wetenschappelijke geloftes ook scherp zult houden. De vriendschappen ontstaan tijdens mijn jumbo-shifts met **Mara**, en daarna op de manage met **Shalana** en **Nina** zijn in de jaren daarna met goud waard gebleken; ze echoën al vele jaren door. Jullie loyaliteit naar mij ondanks mijn onhebbelijkheden is mij zeer dierbaar, op de voet gevolgd door jullie dansmoves. Ook **Anneke, Sandy, Elaine**, **Martijn** en **Janine**, konden niet aan mijn promotie bejammer ontgelden en gesprekken tijdens heerlijke diners in de afgelopen jaren heb ik buitengewoon gewaardeerd. **Jose,** je bent mij zeer dierbaar, al was het maar vanwege jouw prachtige PIDDDs behandelingen die iedereen 'recht' en gezond houdt. Indrukwekkender dan de behandelingen zijn je medemenselijkheid, je ongelofelijke eigengereidheid en onverminderde positiviteit. **Bianca**, die mij altijd weer terug in de realiteit weet te brengen, of uit de modder-greppel trekt. Ik heb de afgelopen jaren niet alleen de kunst van obedience geleerd met mijn trouwe viervoeters, maar ook de waarde van vertrouwen, precisie en rust, waardoor jouw trainingen voor mij veel meer hebben opgeleverd dan alleen een tweemaals Nederlands Kampioenschaps titel met Iro. Ondanks dat zij dit niet kunnen lezen wil ik ook **Iro** en **Charley** bedanken voor hun schaamteloze vraag om aandacht die mij weer een frisse neus liet halen als ik uren aaneen schreef.

Het dankwoord behoort vaak tot het meest gelezen deel van de thesis. Van het dankwoord zelf worden dan weer vaak de laatste zinnen het meest gelezen. Vandaar om te beginnen op deze plek grote dank naar mijn twee **paranimfen**. **Elana**, het is verbazingwekkend om te zien hoe veel onze levenswegen overeenkomen. Jouw ijver, eerlijkheid, onverschrokkenheid en nuchterheid zijn een voorbeeld voor iedere jonge onderzoeker. Je stond daarnaast ook altijd klaar voor mij, als ik er even doorheen zat of als we gewoon allebei een Genmab-koffie pauze nodig hadden. **Floor**, waar begin ik. Je organisatorische kwaliteiten, overzicht en zorgvuldigheid zijn absoluut onontbeerlijk en verdienen groot respect. Ik geniet van jouw wijde interesses, belezenheid, je vriendelijkheid en flexibiliteit en je loyaliteit naar familie en vrienden. Dank voor onze vele wetenschappelijke overpeinzingen, persoonlijke gesprekken en gezellige weekendjes uitwaaien aan zee.

La Familia

Als een kind zijn aangeboren gevoel van verwondering levend wil houden, heeft hij een volwassen gezelschap nodig die het kan delen en samen met hem de vreugde, opwinding en het mysterie van de wereld waarin we leven, kan herontdekken. **Opa den Hertog**, hier is het proefschrift dan eindelijk. Volgens mij heeft niemand zich meer op dit moment verheugd. Ik koester de herinneringen waarbij u met mijn op insecten-zoeken-avontuur ging of met **Oma den Hertog**, mijn 'eigen' land ontdekken en waardeer onze huidige fijne koffie gesprekken ten zeerste. Ook koester ik de momenten met **Opa** en **Oma Maas**, waarbij ik altijd mijzelf heb mogen zijn en mijn creativiteit ten volste mocht benutten. Ik hoop van mijn artistieke hondenhotel collage nog eens werkelijkheid te kunnen maken. Mijn broertjes **Jeldi** en **Patrick**, voor het voornamelijk belachelijk maken van mijn kloppende celconstructen die mij weer met beide benen op de grond hielden. Kleine **Jayla**, Ti auguro anche di possedere il dono della curiosità e di nutrire sempre un profondo desiderio di conoscere la verità. **Anna** en **Andries**, voor al jullie steun de afgelopen jaren, betere schoonouders zou mij niet durven wensen. **Pap**, **Mam**, ondanks gek om jullie in één zin te benoemen, dank jullie wel voor het te zegenen met mijn meest nuttige talent, de gave van nieuwsgierigheid en een verlangen naar waarheid. **Gerard**, jouw visie, loyaliteit en onzelfzuchtigheid zijn je grootste troef, die ik gelukkig met eigen ogen elke dag mag ervaren. Desondanks jij niet voor een academische carrière bent weggelegd, heb je telkens het geduld voor mij, mijn stamcel-weekenden en nachtelijke laptopmomenten weten op te brengen. Ik kijk uit naar de komende jaren, met hopelijk iets meer tijd omhanden om samen van het leven te genieten.

ABOUT THE AUTHOR

Renée G.C. Maas was born on February 9th, 1994, and raised in Amersfoort. At 17, she moved to Groningen to study: *Biological and Medical Laboratory Research at the Hanze Hogeschool*. For her second internship, she moved back to her home town Amersfoort and generated the first human induced pluripotent stem cell-derived cardiomyocytes (hiPSC-CMs) within the University Medical Center Utrecht. After her graduation in 2015, she continued working as a technician for 6 months whereafter she started her master's *Cancer, Stem cells, and Developmental biology* at the Utrecht University in 2016. During her master's, she received numerous travel grants (4) including the prestigious 'Nederlandse Hartstichting' travel scholarship to study the Phospholamban mutation in the lab of Prof. Mercola at Stanford cardiovascular institute, California for 9 months.

In 2018 Renée started her Ph.D. research on hiPSC-CMs disease modeling in the UMC experimental cardiology lab and joined the Utrecht University Regenerative Medicine program. Prior and during her Ph.D., Renée successfully arranged numerous grants from the PLN foundation to cover her own salary for 2.5 years of her Ph.D. Renée has (co-)authored over 19 manuscripts including the journals *cell stem cell* and *circulation*. During her Ph.D, she was a daily supervisor of 13 bachelor and master students, participated as a university teacher in the Experimental Translational Medicine course, and was involved in a bachelor Regenerative Medicine lab training course. Renée was also a member of the Regenerative Medicine Ph.D. committee and the DCVA NLHI Translational Cardiovascular Research Meeting event committee. She has attended many meetings, presented during patient information days, participated in a national consortium HARVEY (NWO), and an international research consortia CurePLaN (Leducq). Additionally, she participated in many initiatives such as interviews, videos, and presentations to inform patients about the research effort we are performing to cure their disease. She recently was invited to be a reviewer for the journal; *Reviews in Cardiovascular Medicine*. Since 2023, Renée is now a scientific officer within the PLN foundation where she contributed to set up a laboratory and mobile bus for the collection of patient blood samples to perform more PLN patient related research. She was also selected to display her immunofluorescent microscopic images at an art exhibition (I Art my Science in 2021 and 2022). Last year, she was selected to be one of the 15 candidates in the Dutch Cardiovascular Alliance program to 'steer my career'. This year, Renée is selected as one of the Talents 2024 by the 'Financiel Dagblad' - 50 Talents under 35 years of age. She successfully received over half a million euros to perform her personal research. With the last two travel scholarships grants from the 'Vrienden van de Cardiologie' and NWO-ZonMw-RUBICON she will spend 24 months in the Biodiscovery Institute within the Denning lab at the University of Nottingham, UK. Here, she will study; "Pathological traits and genetic modifiers in monogenic

cardiomyopathies to cure heart failure". Renée will investigate common patterns of heart muscle function and gene expression in hiPSC-CMs from different genetic cardiomyopathy patients. She will also test potential therapies to improve or even prevent heart muscle degradation in patients with heart failure. Her ultimate dream is to start her own lab after completing her postdoc and carry out further research into disease modelling and therapeutic screenings to treat cardiomyopathies.

UU PHD PORTFOLIO

PhD training	Year	Workload (ECTs)
EMBO publishing	2018	0.3
PhD retreat	2018	1
PhD retreat	2019	1
This Thing Called Science	2020	2
PhD retreat	2021	1
Academic teaching (EMT course, Research Hub)	2022	3
Scientific Method courses		
FACS masterclass (LTI)	2019	0.3
Fundamentals of Biofabrication	2020	3
Specific Courses		
Regenerative Medicine Technologies	2018	1.5
Cardiovascular Regenerative Medicine course	2018	1
Intro to stem cells	2019	2.6
Materials driven regeneration	2019	1.8
Intro to Regenerative Medicine	2019	1.5
Cardiovascular training course (Hartstichting)	2021	1
Seminars, workshops and master classes		
CVON Masterclass on Cardiomyopathies	2019	0.6
Masterclass by Professor Heribert Schunkert	2020	0.15
Steer your Career Training Program (DCVA)	2023	1
Conferences & Presentations		
3rd Translational Cardiovascular Research meeting, poster	2019	0.6
Dutch Society for Stem Cells Research (DSSCR), presentation	2020	0.3
4th Translational Cardiovascular Research Meeting, Presentation	2020	0.3
International Society for Stem Cell Research (ISSCR), abstract	2020	0.9
5th Translational Cardiovascular Research Meeting, poster	2021	0.6
European Society of Cardiology (ESC), presentation	2021	0.3
6th Translational Cardiovascular Research Meeting, poster	2021	0.6
International Society for Stem Cell Research (ISSCR), poster	2021	0.9
I Art my Science, Virtual Art Exhibition	2022	0.1
7th Translational Cardiovascular Research Meeting, poster	2022	0.6
RM network and poster event, poster	2022	0.5
I Art my Science, Art exhibition	2023	0.1
PLN Gala	2023	0.1

(inter)national meetings		
Leducq consortium CurePlaN, Philadelphia, USA	2019	n/a
Leducq consortium CurePlaN, Athens, Greece	2023	n/a
Young@Heart Spring Meeting, Driehoek, Utrecht	2023	0.3
DCVA and RegMed XB valorization event, Karel V, Utrecht	2023	0.1
Leducq consortium CurePlaN, Philadelphia, USA	2023	n/a
Other		
Research meeting Dept. Exp Cardiology	2015-2024	n/a
Research meeting Dept. Cardiology	2015-2024	n/a
Research meeting Circulatory Health	2020-2024	n/a
Regenerative Medicine floormeetings	2018-2024	1
National Journal club hiPSC-CM, virtual	2020-2024	n/a
Teaching		
Supervising Bachelor writing internships (6 students)	2019-2020	n/a
Supervising MLO/Bachelor student research internships (4 students)	2019-2022	n/a
Supervising master student research internships (3 students)	2020-2023	n/a
	Total:	**30.05 ECTs**

Parameters of Esteem	
Travel grants	
Nederlandse Hartstichting travel scholarship	2017
Jo Kolk travel scholarship	2017
Quintus travel scholarship	2017
KF Hein travel scholarship	2017
DCVA/Vrienden van de cardiologie travel fellowship	2023
Personal grants	
Personal Cure PLN grand PhD fund 1 year (PLN foundation)	2018
Bachelor research hub – ETM (PLN foundation)	2019
Personal Cure PLN grand PhD fund half year (PLN foundation)	2020
Personal Cure PLN grand PhD fund half year (PLN foundation)	2021
Bachelor research hub - ETM course (PLN foundation)	2021
Rapid high-throughput production of cellular systems to model PLN R14del disease, 1 year (PLN foundation)	2021
Functional screening of AAV-I1c in hiPSC-CMs (AskBio)	2023
Private funding for screening facility RMCU (PLN gala)	2023
Rubicon "Pathological traits and genetic modifiers in monogenic cardiomyopathies to cure heart failure" (NWO)	2023-2025
Other activities	
Peer-reviewed for Reviews in Cardiovascular Medicine	2022
Member of the PhD committee, Regenerative medicine program	2021-2022
Member of the DCVA translational meeting committee	2023-2024